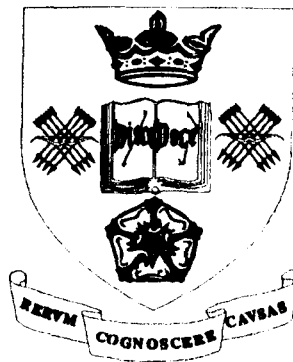


OPTIMISATION OF THE SHOT PEENING PROCESS IN TERMS OF FATIGUE RESISTANCE

José Solis Romero

Thesis submitted to the University of Sheffield in partial fulfilment
of the requirements for the degree of

Doctor of Philosophy
in
Mechanical Engineering



Faculty of Engineering
Department of Mechanical Engineering
THE UNIVERSITY OF SHEFFIELD

Sheffield, U.K., April 2002

Summary

This research studies the modifications on the surface and subsurface of the aluminium alloys 2024-T351 and 7150-T651 caused by a stream of minute, relatively hard particles or shots that are used in the shot peening process. Residual stresses (RS), strain hardening (Hv) and surface roughness (Kt) were identified as the main changes or effects induced in the surface layers of the material, which are intrinsically related to the fatigue resistance of the peened material. The magnitude of these effects depends on the choice of the peening parameters, such as shot (type/size), intensity, incidence angle and coverage, which define a peening condition. From these, shot and incidence angle are controlled directly while the others are measured. A thorough characterisation of the shots used (cast steel S110, S230, S330 and conditioned steel SCCW20) revealed significant variations in size and roundness of the shots, which affect the elastic stress concentration factor and coverage. For shot peening to be consistent, effective and reproducible, a method to obtain the peening intensity at saturation point is presented. Similarly, a theoretical and experimental investigation into the development of coverage is described.

Application of the design of experiments concepts established the major peening factors influencing each of the peening effects (RS, Hv, Kt) and allowed the estimation of the optimum combinations of such factors with their corresponding levels, in order to attain the maximum RS, Hv and minimum Kt. An assessment of the peening effects yielded the optimum and worst conditions for fatigue resistance. These were, optimum: shot S110, 200% coverage and 45° incidence angle; worst: CCW20, 100% and 45° for AA 2024-T351. Optimum: S230, 100%, 89° and worst: S110, 200%, 30° for AA 7150-T651.

The fatigue testing results from the predicted optimum and worst peening conditions for the AA 2024-T351 were found to give only marginal improvement in fatigue resistance. However, the optimum condition was shown, overall, to render slightly better fatigue results, whilst the worst condition, although it did not improve life, neither decreased it. In contrast, the optimum condition in AA 7150-T651 was shown to give lower fatigue results even than the unpeened condition, whilst the worst peening condition yielded the best fatigue results. Peened specimens exhibited subsurface initiation, whilst typical surface initiation was evident in the unpeened specimens, which relates to the influence of peening on fatigue behaviour.

Peening effects were incorporated into the Navarro-de los Rios micromechanical-model. Fatigue life predictions showed relatively good agreement with the experimental results for peened specimens and even better for unpeened results.

The usefulness of the peening process in terms of fatigue resistance depends on the competition between its beneficial and detrimental effects, thus the role of the peened effects was analysed in these terms. Surface roughness, deemed to be the detrimental factor, was discussed by means of the N-R micromechanical model and the Kitagawa-Takahashi diagram. It was shown that the effect of the stress concentration induced by shot peening roughness is considerably detrimental for AAs.

The use of the finest shot did provide the best fatigue performance in both AAs. Surface integrity degradation or the depth of the plastic deformation layer is the precursor of fatigue damage. Peen indents are primary damage features.

Preface

This thesis is based upon the findings of research conducted in the Department of Mechanical Engineering at the University of Sheffield.

The content of this thesis is original except where specific references are made to other work. No part of this thesis has been submitted to any other University.

**J. Solis Romero
Sheffield, April 2002**

Acknowledgements

The study carried out in the present thesis was possible thanks to The Consejo Nacional de Ciencia y Tecnología (CONACyT), the Secretaria de Educación Pública through the Dirección General de Institutos Tecnológicos (SEP-DGIT) and the Instituto Tecnológico de Tlalnepantla, México. I gratefully acknowledge the financial support and period of leave, which made the pursuit of this degree achievable. I would also like to thank British AirBus, U.K., especially Andrew Levers, for their funding and technical aid.

The undertaking of this research programme would have been impossible without the assistance of many people. In first place, I am extremely grateful to Dr Eduardo de los Rios, my supervisor, for his kindness, expert guidance and constant support through the period of this research, his approval helped me persevere when 'the going got tough'. I would also thank him for carefully having read this manuscript providing me with valuable comments and discussions.

I would like to thank Dr C.A. Rodopoulos for his help and useful guidance during my first steps in fracture mechanics, specifically, the fatigue damage maps. I would also like to thank Sean Curtis for his technical assistance during the fatigue testing. Thanks also go to Mr John Goodliffe for being kind and willing to help me set up the fatigue machine at SIRIUS. I am very grateful to Mr J. Talamantes for his invaluable computing help but especially for his friendship, which helped make these years a profitable and enjoyable time during my research at the University of Sheffield. I also thank to Mr J. Chitty, Mr J. Verduzco, Mr A. Bedolla, Mr J. Gonzalez, Mr S. Almaguer, and Mr Gabriel Acosta from the Department of Engineering Materials for their technical assistance and friendship.

In the course of my research, I regularly required support and assistance of all technical and administrative Staff of the Department of Mechanical Engineering. I am grateful to all and each of people working there. In particular, I am very grateful to Mrs Jean Edwards from the purchase office, for her kindness and comprehension to me and to all international students.

I would like to acknowledge the sacrifices made by my family while I was a postgraduate student. Although I have fully enjoyed my research experience at the University of Sheffield, I regret spending so much time away from my family. I have no words to express my infinite thankfulness to my beloved wife Betty, my grown up Jose and my little Jacqueline. I hope they can forgive me for all the inconveniences and disappointments that I have caused. This work is dedicated to them.

I would like to thank my Dad, Mum, Father and Mother in law for their continued love, support and encouragement. I also regret having separated them from their grandchildren for long time. I would like to thank my brothers Juan, Jaime, Genaro and sister Judith for keeping me informed regarding relatives and friends. I would equally like to thank Martin, Daniel, Isabel, Luisa, Laura, Ricardo, and Alejandro for their frequent trips to U.K. to bring us food supplies and gifts but especially their love. In particular, I would like to thank Ruben who has taken exceptionally good care of my house over the past few years.

My life in Sheffield has been a fruitful and unique experience, thanks to the Weger-Berenguer family and Mr Paul, Mattie and Berlie Doherty whom I trust I have fully expressed my appreciation.

**A mi esposa Betty,
mis hijos José y Jacqueline.**

TABLE OF CONTENTS

SUMMARY	ii
PREFACE	iii
ACKNOWLEDGEMENTS	iv
NOMENCLATURE	xi
CHAPTER 1. INTRODUCTION	1
1.1 MOTIVATION	1
1.2 OUTLINE OF THE THESIS	4
1.3 PUBLICATIONS	5
CHAPTER 2. LITERATURE SURVEY	7
2.1 FATIGUE OF METALLIC MATERIALS	8
2.1.1 Development of fatigue cracks	9
2.1.2 Regimes of crack propagation	10
2.1.2.1 Microscopic stages of fatigue crack growth	10
2.1.2.2 Macroscopic modes of fracture	12
2.1.3 Characterisation of fatigue crack propagation	13
2.1.3.2 Elastic-plastic fracture mechanics (EPFM)	15
2.1.4 Characterisation of the crack growth rate (long cracks)	17
2.1.4.1 Crack closure on propagation	19
2.1.5 Short fatigue cracks	20
2.1.5.1 The effect of fatigue crack closure on SCs	24
2.1.6 The behaviour of SCs : microstructural analysis	25
2.1.6.1 The three zone micromechanical model (TZMMM)	26
2.1.6.2 Description of crack arrest in terms of the TZMMM	29
2.1.6.3 Crack propagation rate in terms of the TZMMM	32
2.1.7 Fatigue resistance of metallic materials	33
2.2 AN ENGINEERING SURFACE TREATMENT: SHOT PEENING (SP)	35
2.2.1 Brief history of SP	35
2.2.2 The mechanism of the SP method	37
2.2.3 Shot peening nomenclature and control parameters	42
2.2.3.1 Shot Peening Media	42
2.2.3.2 Incidence angle	44
2.2.3.3 Saturation condition	45
2.2.3.4 Intensity	47
2.2.3.5 Coverage	48
2.2.3.6 Velocity	50
2.2.4 Shot peening effects and fatigue	50
2.2.4.1 Residual stresses (RS)	53
2.2.4.2 Microstructure	56
2.2.4.3 Topography (surface roughness)	57
2.2.5 SP control parameters correlations with life behaviour	58
2.3 SUMMARY	61
2.4 COMMERCIAL 2024-T351 AND 7150-T651 ALUMINIUM ALLOYS (AAS)	63
2.4.1.1 Characteristics of AAs classes	63

2.4.1.2	Fundamentals of the heat treatable AAs	65
2.4.1.3	Constituent phases or microstructures	66
2.4.1.4	Metallurgical factors on fracture toughness and fatigue performance..	67
	67
CHAPTER 3.	ANALYTICAL FRAMEWORK	70
3.1	FATIGUE CRACK PROPAGATION IN SHOT-PEENED COMPONENTS.....	71
3.2	MODELLING THE MATERIAL STATE FOLLOWING SHOT PEENING	75
3.2.1	Residual stresses.....	75
3.2.2	Work hardening.....	77
3.2.3	Kt gradient concept from surface roughness	79
3.3	SUMMARY	82
CHAPTER 4.	MATERIALS AND EXPERIMENTAL METHODS	83
4.1	PEENING MATERIALS AND PROCEDURES.....	85
4.1.1	Shot peening equipment: Introductory background	85
4.1.2	The experimental peening facility	88
4.1.3	The experimental peen media	90
4.1.3.1	Geometric features (the size, shape factor and aspect ratio).....	91
4.1.3.2	Hardness features.....	94
4.1.3.3	Density characterisation	95
4.1.4	Evaluation of the peening process parameters.....	95
4.1.4.1	Determination of the intensity	95
4.1.4.2	Peening process parameters.....	97
4.1.5	Coverage	101
4.1.6	Velocity and strain rate estimations	104
4.2	INVESTIGATED MATERIALS.....	106
4.2.1	Tested materials.....	106
4.2.2	Specimen design.....	106
4.2.3	Specimen preparation and manufacture.....	108
4.3	EXPERIMENT DESIGN	110
4.3.1	Design of experiments (DoE): Introductory background	110
4.3.1.1	Three types of analysis statistics: signal-to-noise ratio (S/N).....	115
4.3.1.2	The predictive model	116
4.3.2	Experiment design.....	117
4.4	EXPERIMENTAL TECHNIQUES FOR DETERMINING THE PEENING	
	EFFECTS	119
4.4.1	Surface roughness.....	119
4.4.1.1	Roughness parameters.....	119
4.4.1.2	Equipment	120
4.4.1.3	Experimental technique.....	120
4.4.2	Residual stresses.....	121
4.4.2.1	Selection of the suitable method.....	121
4.4.2.2	The hole drilling concept.....	123
4.4.2.3	Equipment and materials.....	124
4.4.2.4	Experimental procedure	127
4.4.2.5	Analysis methods of nonuniform Stress Fields	128
4.4.3	Work hardening (hardness measurements).....	129
4.5	FATIGUE TESTING.....	131
4.5.1	Test practice	131
4.5.2	Fatigue crack propagation: Surface replication.....	132
4.5.3	Fatigue and fracture surface characterisation.....	133

4.5.4	Summary	133
CHAPTER 5.	EXPERIMENTAL RESULTS	135
5.1	SHOT PEENING EFFECTS	136
5.1.1	Stress concentration.....	137
5.1.2	Residual stresses.....	144
5.1.3	Work hardening.....	153
5.2	THE DESIGN OF EXPERIMENT ANALYSIS.....	159
5.2.1	Significant factors for each peening effect in AA-2024-T351	159
5.2.2	Optimum and worst peening conditions for AA-2024-T351.....	164
5.2.3	Significant factors for each peened effect in AA 7150-T651	166
5.2.4	Optimum and worst peening conditions for the AA 7150-T651	168
5.3	FATIGUE TESTING.....	170
5.3.1	Fatigue results	170
5.3.1.1	AA 2024-T351.....	170
5.3.1.2	AA 7150-T651.....	172
5.3.2	Crack growth.....	173
5.3.2.1	AA 2024-T351.....	173
5.3.2.2	AA 7150-T651.....	176
5.3.3	Crack growth rate.....	178
5.3.4	Fracture surface observations.....	180
5.3.4.1	AA 2024-T351.....	180
5.3.4.2	AA 7150-T651.....	184
5.3.5	Application of the Navarro-de los Rios Model to fatigue results	187
5.3.6	Summary	190
CHAPTER 6.	DISCUSSION	192
6.1	BENEFICIAL EFFECTS	193
6.1.1	Residual stresses.....	194
6.1.2	Strain hardening	198
6.2	DETRIMENTAL EFFECTS	199
6.2.1	Stress concentration analysis	202
6.2.1.1	Surface roughness effects under crack arrest conditions	202
6.3	ASSUMPTIONS AND LIMITATIONS.....	208
6.4	SUMMARY	211
CHAPTER 7.	CONCLUSIONS	212
7.1	CONTROL PROCESS PARAMETERS	213
7.2	PEENING EFFECTS.....	214
7.3	FATIGUE PERFORMANCE.....	215
CHAPTER 8.	SUGGESTIONS FOR FUTURE WORK	217
CHAPTER 9.	RECOMMENDATIONS	219
9.1	GENERAL RECOMMENDATIONS	219
9.2	PRACTICAL SHOT PEENING GUIDELINES FOR AA 2024-T351 AND AA 7150-T651.	221
APPENDICES	223
APPENDIX I.	GEOMETRIC FEATURES OF THE PEEN MEDIA	223
APPENDIX II.	PEENING MACHINE PERFORMANCE.....	225
APPENDIX III.	COVERAGE DETERMINATIONS	232
APPENDIX IV.	SPECIMENS MANUFACTURING DETAILS	255
APPENDIX V.	ROUGHNESS PARAMETERS.....	257
APPENDIX VI-A.	RESIDUAL STRESS THEORY	259
APPENDIX VI-B.	RESIDUAL STRESS RESULTS	262

APPENDIX VII. WORK HARDENING RESULTS 267
APPENDIX VIII. DESIGN OF EXPERIMENTS 272
APPENDIX IX. FATIGUE RESULTS 276
APPENDIX X. DISCUSSION..... 291
Appendix References 294
REFERENCES 295

NOMENCLATURE

a	crack length
a_0	initial crack length
a_f	final crack length (failure)
A_2	coefficient of the Paris relationship
ASTM	American Society for Testing of Materials
a	notch depth
β	notch half width
b	magnitude of the Burger's vector, slip contribution of a single dislocation
c	position of the crack tip at $\frac{1}{2} iD + r_0$
CTOD	crack tip opening displacement
$C(t + \delta t)$	coverage after an increment of time
D	grain size
d	indentation size
ρ	density of the shot
da/dN	FCG rate with respect to load cycle count
DoE	design of experiments method
E	elastic modulus
E_c	kinetic energy ($mv^2/2$)
EPFM	elasto-plastic fracture mechanics
$\dot{\epsilon}$	strain rate
ϵ	elastic deformation
f_{ij}	a dimensionless function of θ
FCG	fatigue crack growth
G	shear modulus
Hv	microhardness Vickers
h	depth of the dent
i	number of half grains affected by the fatigue process $i= 1, 3, 5, \dots$
J	elastic-plastic stress field near the crack tip
$K=Y\sigma\sqrt{2\pi a}$	stress intensity factor (SIF)
$K_{I, II, III}$	SIF for each different modes of fracture
K_C	critical value of K corresponding to fracture
K_{IC}	fracture toughness
ΔK	cyclic range of K during constant amplitude loading, defined as $K_{max} - K_{min}$
ΔK_{eff}	effective (closure free) portion of ΔK
ΔK_{th}	threshold value of ΔK
K_t	elastic stress concentration
m_1/m_2	effect of grain orientation, evaluated as $m_1/m_2=1+0.5\ln(i)$
MEF	microstructural fracture mechanics
m_2	slope of FCG curve in the Paris regime
m	shot mass, defined as $\frac{4}{3} \rho \pi R_s^3$
LEFM	linear elastic fracture mechanics
N_f	number of cycles to failure
n	condition for propagation at each grain boundary, defined as $2a/iD$
n_c^i	critical value of n , i.e. when the crack is able to overcome the barrier
σ_{ij}	the singular solution of the near-tip stress fields
θ	the polar angle measured from the crack
P	pressure exerted by the shot at the moment of collision
r_0	grain boundary width
r	distance behind the crack tip
R_a	average roughness
R_s	shot radius
RS	Residual stress
R	applied load ratio, defined as $\sigma_{min}/\sigma_{max} = K_{min}/K_{max}$
R_{tm}	mean roughness depth
S_m	mean indentation peak-to-peak distance
σ_1	closure stress acting on the crack flanks
σ_2	resistance of the material to plastic deformations (flow stress)
σ_3	a measurement of the reaction stress developed at barrier due to the PSB blocking

σ_y	yield stress
σ_{ly}	local yield strength
σ	applied stress
σ_{FL}	fatigue limit
σ_{UTS}	ultimate tensile stress
σ_{arrest}^p	magnitude of stress for arrest a crack (no closure stress effect)
$\sigma_{\text{closure}}^{\text{arrest}}$	magnitude of stress for arrest a crack considering the closure stress effect
σ_{FL}^{sp}	fatigue limit of the peened material
τ_c	critical resolved shear stress
ζ	relates the position throughout, in such a way that the crack tip is at $\zeta = n_1$ and the nearest grain boundary at $\zeta = n_2 = x/c$
ν	Poisson's ratio
v	velocity of the shot
x	location of the grain boundaries, defined as $\frac{1}{2} iD$
Z_i	fatigue notch factor

ROBERTSON EQUATION

Y	Variable for vertical (y) axis
x	Depth below surface
$A+B$	Peak value of Robertson equation curve
B	Final (minimum) value of Robertson equation curve
X_d	Depth at which the peak of the Robertson equation curve occurs
W	Width measure of the Robertson equation curve

CHAPTER 1

INTRODUCTION

1.1 MOTIVATION

It is universally established that the two main types of material failure are: deformation and fracture. Because machines, vehicles and structures are seldom free of alternating stress, material failure by fracture, and particularly fatigue, is envisaged to be the major cause of failure of mechanical components within two economically important sectors: motor vehicles and aircraft.

The fatigue strength of a metallic material is dominated by the resistance to crack growth offered by grain or phase boundaries, and in general, all types of barriers to plastic slip present within the material. Simply expressed, this represents the difficulty of an initial stage I shear crack becoming a stage II tensile opening mode crack [1]. Hence, provided crack initiation and early propagation stages are somehow delayed or even halted, the fatigue resistance of the component will be increased. To condition the surface to resist crack propagation, the shot peening process; defined as a bombardment of the surface with hard shot, is routinely employed as it introduces many and varied forms of textural barriers or surface distortion on the surface and subsurface layers. For this reason the microstructural dependant shear stage I propagation is affected and fatigue life increased.

The mechanisms of the fatigue crack growth retardation brought about by shot peening, are [2]:

- A compressive residual stress field induced in the plastic layer due to the clamping action of the elastic material surrounding this zone. The plastic layer results from the elasto-plastic relaxation of the near surface layers as the shot rebounds. The influence of this stress is that of increasing the resistance to the opening of the crack, or closure stress, which reduces the driving force of the crack.
- Strain hardening with the extremely distorted microstructure at the surface and subsurface layers. This makes the generation of crack tip plasticity much more difficult. Additionally, the shape and size of the grains is generally reduced in the through thickness direction. This also contributes to lower crack rate propagation because of the increased number of microstructural barriers.

While peening treatments ameliorate the effect of surface defects, they also have significant disadvantages. One of the main disadvantages is that, due to the level of plastic deformation introduced, there is an associated increase in surface roughness. In terms of fatigue damage, surface roughness represents a potential source for nucleation and early propagation of cracks.

The magnitude and the depth to which the peening effects extend beneath the surface of the component are influenced by a complex interaction of a variety of parameters, characterised both by the shot peening process and material conditions. Peening conditions must be properly selected and controlled in order to obtain beneficial strengthening and to avoid introduction of severe damage (surface crack initiation owing to an excessive penetration of the shot in the material). The most important process control factors are:

- a) The peened component: geometry, material mechanical properties, monotonic and cyclic elastic-plastic behaviour.
- b) The energy of the shot stream (intensity): properties of the shot, velocity, angle of incidence, offset distance, flow rate, etc.
- c) The percentage of indentation of the part surface (coverage): number of passes or duration of the treatment.

As many variables are involved in the peening process, the incorrect choice of any of these variables may degrade rather than enhance the fatigue performance of the workpiece. For this reason, a thorough understanding of the effects of shot peening will lead to an optimisation of the process in terms of fatigue resistance.

Despite having an increasing interest in shot peening as a mechanism of avoiding the early failure of components due to fatigue, very little work has been devoted to assess fatigue damage of peened components from the microstructural point of view. This entails the characterisation of the material properties (fatigue) with consideration of the compressive residual stresses, work hardening and surface roughness. These material changes should be incorporated respectively as a closure stress, a flow stress ahead of the crack tip in the plastic zone and a stress concentration, into the fatigue crack propagation laws. This latter suggestion means that the optimisation of the peening process is a potentially valuable area of study within the fatigue resistance of materials field, particularly in the aircraft industry. Specifically, assessing the influence of the main process control parameters on the peened properties of the material is a necessary research topic, and therefore it represents the major objective of this study. Control parameters include material properties, shot media, equipment settings, velocity, intensity, incidence angle, saturation and coverage. Peened material modifications comprise residual stresses, roughness, hardness and microstructure.

Generally, peening treatments are applied to high-strength materials such as high-strength steel, stainless steel and titanium alloys, where such treatments have been found to be extremely effective in improving fatigue performance [3]. The benefits of peening high-strength aluminium alloys in terms of fatigue resistance are less clear-cut than in the other materials [4]. Furthermore, it has been reported that peening aluminium alloys with steel shot (as used for high-strength steels and titanium alloys) can be fairly detrimental to fatigue life, while peening with lighter media such as glass or ceramic beads can yield some improvement to the fatigue performance, although not as noticeably as for steels or titanium alloys [5]. These aspects represent another rationale for investigating the inherent relationship between the peening conditions and the competing factors (beneficial-detrimental), which determine the fatigue performance of aluminium alloys when using steel shot.

In this thesis, the optimisation of the peening process is undertaken by using four different type/sizes of steel shot media on two aluminium alloys, Al 2024-T351 and Al 7150-T651. These materials are extensively used in the aerospace industry for structural components and frames of commercial and military aircraft units, e.g. in the fuselage, wing skins and other minor parts [6].

1.2 OUTLINE OF THE THESIS

This work aims to establish the optimum peening conditions leading to increased fatigue performance of two high strength aluminium alloys and to examine the effectiveness of this surface treatment by analysing the effect of beneficial and detrimental factors. A description of the process and the main issues associated with fatigue and shot peening fundamentals, and their interaction for increasing the fatigue resistance of metallic materials are discussed in Chapter 2. This Chapter begins with a brief introduction to fatigue of metallic materials, with special attention to short crack behaviour, followed by a detailed description of the mechanics of shot peening, and a comprehensive literature review of the peening control parameters together with a discussion of residual stress, work hardening and surface roughness peening effects and their impact on the fatigue resistance.

In Chapter 3 a characterisation of fatigue damage in peened surfaces in terms of short crack behaviour is addressed. A detailed description on how peening effects for specific and optimised peening conditions are incorporated into a microstructural fracture mechanics methodology (N-R micromechanical model) is provided.

Chapter 4 describes the experimental work, including materials utilised, equipment and machines, the experimental techniques and approaches employed for the optimisation and characterisation. Analysis and discussion, where appropriate, are also dealt with in this chapter.

Experimental results and general analysis are presented in Chapter 5 for both the peening effects and their impact on fatigue performance. Observations of crack initiation sites and other main features by using the scanning electron microscope are given.

In Chapter 6, a detailed discussion of experimental results, theoretical predictions and general observations from the previous chapter is presented. In this chapter, the beneficial and detrimental factors in relation to fatigue damage are discussed, paying particular attention to the role of peening effects on the propagating and arrest of fatigue cracks.

General conclusions are listed in Chapter 7. Future research topics are considered in Chapter 8 and some recommendations for shot peening-related studies on aluminium alloys are presented in Chapter 9.

1.3 PUBLICATIONS

Publications originating from this research programme are:

1. Solis-Romero, J., de los Rios, E.R., Fam, Y.H. and Levers, A., (1999), "Optimisation of the shot peening in terms of the fatigue resistance." In: Shot Peening: Present and Future. The 7th Conference on Shot Peening (ICSP-7). Warsaw, Poland. Ed. Aleksander Nakonieczny. Institute of Precision Mechanics <IMP>: pp. 117-126 (ISBN 83-904574-5-8).
2. Solis-Romero, J., de los Rios, E.R., Levers, A. and Karuppanan, S., (2001), "Toward the optimisation of the shot peening process in terms of fatigue resistance of the 2024-T351 and 7150-T651 aluminium alloys". In: Surface treatment V: Computer methods and experimental measurements for surface treatment effects. Spain. Ed. C.A. Brebbia. Wessex Institute of Technology (WIT) press. Southampton, U.K.: pp. 343-355

3. J. Solis-Romero, E.R. de los Rios, C.A. Rodopoulos, J. R. Yates and S.P. Godfrey (2001) "The effect of shot peening on the fatigue life of unidirectional titanium-based metal matrix composites". In: Composites: from fundamentals to advance structures. Proceedings, 2nd Hellenic conference on composite materials, University of Patras, Greece. Ed. V. Kostopoulos, applied mechanics laboratory. pp. 152-160 (ISBN 960-530-053-2).
4. S.A. Curtis, J.Solis-Romero, E.R. de los Rios, C.A. Rodopoulos and A. Levers. (2001) "Predicting the interfaces between fatigue crack growth regimes in 7150-T651 aluminium alloy using the fatigue damage map. Materials Science & Engineering. To be published.
5. E.R. de los Rios, S. Karuppanan, J.S. Romero, C.A. Rodopoulos and A. Levers (2002). "A theoretical and experimental investigation into the development of coverage in shot peening". In: 8th Conference on shot peening, Garmisch-Partenkirchen, Germany. Chairman L. Wagner. To be published.

CHAPTER 2

LITERATURE SURVEY

The fatigue behaviour of metallic materials is known to be strongly dependent on the surface and near surface conditions. Engineering surface treatments, including shot peening, induce important changes on the surface and subsurface of a metallic component. An understanding of the mechanism behind the change in fatigue strength resulting from applying shot peening will provide the basis for ascertaining the influence of the relevant peening process conditions on the fatigue strength. This constitutes the backbone of the thesis.

In this chapter, a literature survey is carried out on the fatigue resistance of metallic materials and the process of shot peening, identifying the fundamental mechanisms and links relevant to this study. Fundamentals of metal fatigue under conditions of constant amplitude loading are presented first and this is followed by a discussion of the mechanisms expected to improve the fatigue limit and the fatigue life of peened surfaces. Particular attention is given to the latest developments in the study of short crack behaviour and crack growth. Finally, a detailed review of the mechanics of shot peening, including the control of its main process parameters, is undertaken.

2.1 FATIGUE OF METALLIC MATERIALS

It has been known for more than 150 years that the strength and life of structures can be diminished or even progressively damaged if subjected to fluctuating or cyclic loadings. Fatigue cracks are the cause of the delayed failure. The final failure is caused by metal defects initiating fatigue cracks, which will grow to a critical size causing sudden separation of the material [7]. It follows that, unlike the bulk static strength of metallic materials, fatigue is a localised event, i.e. localised stress concentrations, which are sites of fatigue microcrack formation.

The aim of achieving better quality of life has given impetus to the emergence of new technologies and consequently to developments in the understanding of fatigue and fracture. These challenges have attracted a considerable number of scientists and engineers. To highlight the salient topics related to the fatigue of metallic materials, an historical overview of the major contributions is given in table 2.1. It shows that the major milestones in fatigue analysis up to the present day, have been: (a) the work of Wöhler with his first systematic fatigue investigation, which formed the basis of the representative method (the S-N approach) for characterising fatigue behaviour, (b) the work of, firstly Griffith and the mathematical tools for quantitative treatments of fracture in brittle solids, and secondly of Irwin with the introduction of the stress intensity factor K , which are the premises for the advent of the so-called Linear Elastic Fracture Mechanics (LEFM) approach. Finally, (c) the work of Paris for the characterization of the fatigue crack growth in terms of the K , and of Kitagawa-Takahashi, for combining together the S-N curves and crack propagation. This latter work on the boundary between fatigue failure and infinite lives showed that there could eventually be a unified approach to fatigue analysis.

Metal fatigue has received considerable attention in order to understand the processes responsible for such behaviour and the processes that would improve the integrity of metal parts. Among others, it is generally the micro-structural and mechanical condition of the surface layers of the component, which will determine its fatigue resistance [1]. For example, the initiation of a fatigue crack in polycrystalline metals is due to a variety of surface stress concentration features. Hence the initiation of fatigue cracks in

components is generally on the free surface of the component. This latter is almost a universal statement.

AUTHOR(S), INSTITUTIONS	YEAR	STATEMENTS/PROPOSALS
W.A.S. Albert, [8] [9]	1829	It is believed to be the first study on metal fatigue. Repeated load on mine hoist chains were performed.
Poncelet, [9]	1839	Designs mill wheels with cast iron axles. First uses the term 'fatigue' in a book on mechanics.
IMechE, <i>ibid.</i>	1849	Debate on the "Crystallization" theory.
Wöhler, [10]	1850	Conducts first systematic fatigue investigations on axles. Develops the rotating-bending fatigue test, S-N curves and the concept of fatigue limit. Identifies the importance of cyclic and mean stresses.
Bauschinger, [8]	1886	Notion that the elastic limit of metals in reversed loading could be different from that observed in monotonic deformation. Strain-stress hysteresis.
Ewing & Humphrey, [8] [9]	1903	Based on the old crystallization theory, they showed that fatigue damage is due to the formation of slip bands (now commonly referred to as "extrusions and intrusions").
Baird, <i>ibid.</i>	1910	Significant contribution to the stress-strain response during cyclic hardening and softening.
Griffith, [11]	1920	Investigates cracks in glass. The birth of fracture mechanics.
Manson and Coffin, <i>loc. cit.</i>	1955	Plastic strains are responsible for cyclic damage.
G.R. Irwin, [12]	1957	The stress field near a crack tip could be expressed in terms of the stress intensity factor, K.
Paris and Erdogan, [13, 14]	1960	First systematic method for handling crack propagation using fracture mechanics.
Forsyth, [15]	1961	Identified stage I and stage II crack propagation.
Tomkins, [9]	1968	High strain crack propagation law- physical basis for Coffin-Manson.
Kitagawa and Takahashi [16]	1976	Rationalised the fatigue limit and the fatigue threshold.

Table 2.1 Brief historical overview of the fatigue of metallic materials.

2.1.1 Development of fatigue cracks

Research into the creation of fatigue cracks has confirmed that the damage process is related to the forward and backward motion of dislocations along the slip planes of metallic crystals, i.e. the reversed plastic flow. A consequence of these repeated dislocation movements are the creation of small-localised deformations called extrusions and intrusions at sites where the persistent slip bands emerge at the material surface [8]. In this respect, a large number of models have been formulated to explain

nucleation of microcracks [17], thereby making a distinction between intrusions and microcracks. Furthermore, as a consequence of microscopic material defects, such as second-phase particles, inclusions or precipitates, surface notches and machining marks; microstructural features such as grain boundaries, triple points and twin boundaries [9, 18] and also environmental effects like pitting corrosion [19] a local concentration of stress which may exceed the yield strength of the material is developed. Consequently, cyclic plastic deformation due to the higher stresses of these stress concentration sites and also due to the lower degree of constraint of the near surface volumes from a cyclically loaded material is developed. It is well known that fatigue damage occurs only when cyclic plastic strains are generated [20]. Therefore, given the intrinsic heterogeneity of polycrystalline metals, the above conditions, separately or in a variety of combinations, can lead to the nucleation of microcracks. The preferred mechanism of initiation will therefore depend on the microstructure and manufacturing process of the material, the type of loading and shape of the component.

Once nucleated, a microcrack may be arrested by a microstructural barrier or may propagate until reaching a critical size, causing the final failure [21].

2.1.2 Regimes of crack propagation

2.1.2.1 Microscopic stages of fatigue crack growth

Cyclic crack growth is found to be generally divided into three stages. Stage I fatigue crack growth occurs by a shear mechanism in the direction of the primary slip system over a few grains. The crack propagates on planes oriented at approximately 45° to the stress axis¹, i.e., the crack follows the best-orientated grain path, e.g., a high angle grain boundary where, due to the high local stress concentration it will form a new slip band in the next grain giving raise to crack extension [1]. The effect of this crack growth mode is the characteristic zig-zag crack path as defined by Forsyth [15]. At this stage, the crack length may reach a length of a few grains. However, the zone of near-tip plasticity is smaller than the grain dimensions [8].

¹ According to the Schmid's law ($\tau_c = \sigma \cos \theta \cos \phi$, where for θ and ϕ equal to 45°, τ_c is a maximum), plastic deformation occurs when, the applied tensile stress σ , resolved as τ_c on a particular slip plane, exceeds a determined shear stress τ_y . $\tau_y = \sigma_y/2$ if the material observes the Tresca's principles, where σ_y is the corresponding yield stress.

Favourable conditions and higher stress intensity range values (see § 2.1.3 for the stress intensity concept) allow the crack to grow longer, as the plastic zone size increases, and also to be able to overcome the resistance offered by successive barriers. After a certain growth, there is a transition from stage I to stage II crack propagation, where the crack overcomes microstructural barriers with ease and simultaneous shear planes develops, as established by Forsyth *ibid.* At stage II, also known as the Paris regime, crack propagation is driven by the stress normal to the crack face and the mode will change to mode I. It is proposed that at the transition from stage I to stage II, the plastic zone will be of the order of the grain size [22]. Fatigue stages are shown in Fig. 2.1.1.

When the crack tip stress intensity reaches values close to those required for unstable crack propagation, stage III begins [23]. The transition from stage

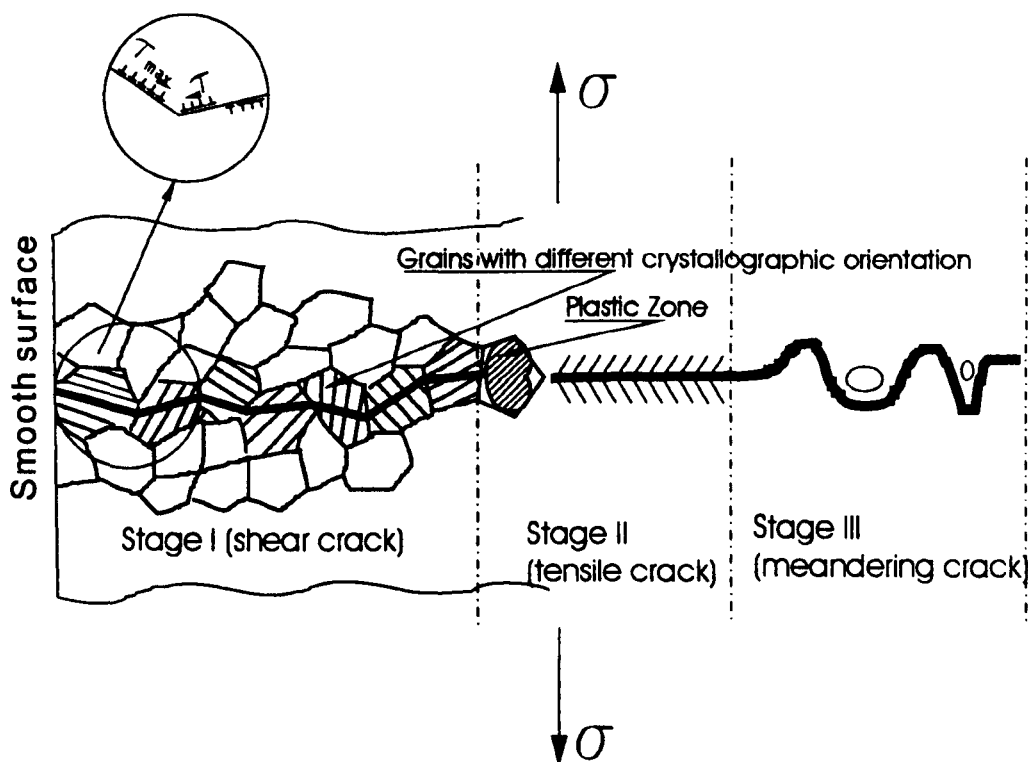


Figure 2.1.1 Schematic representation of the fatigue crack growth stages. As indicated (on the left) is a general dislocation model of crack nucleation from the free surface, at the largest and best-orientated grain, as described by Mutoh [24].

II to stage III crack growth has not been widely studied but it has been observed regularly by E. Hay and M.W. Brown [25]. At this stage, a tearing mechanism is

dominant, and the crack branches from the main crack path (crack meandering) [26] as illustrated in Fig. 2.1.2. In high cycle fatigue, Stage III represents an insignificant proportion of life, i.e., failure follows very rapidly.

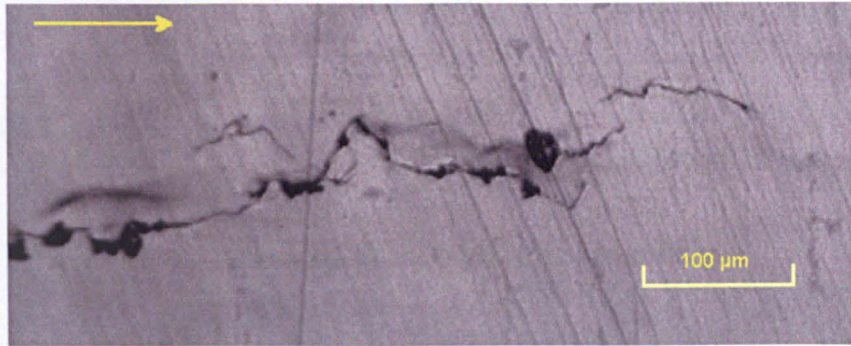


Figure 2.1.2 Crack meandering from the main crack path in stage III of a shot peened specimen (Al 2024-T351) fatigued under four-point bending constant amplitude loading. The general direction of crack extension is indicated by the arrow.

2.1.2.2 Macroscopic modes of fracture

As the fatigue crack propagates through the different stages, different fracture modes are observed. These crack surface displacements are related to the three basic modes of fracture [8, 23], which are schematically shown in Fig. 2.1.3. Mode I, is known as *tensile opening mode* in which the crack faces separate in a direction normal to the plane of the crack. Mode II, is known as *in-plane sliding* or *shear mode* in which the crack faces are mutually sheared in a direction normal to the crack front. Mode III is the *tearing or anti-plane shear mode* in which the crack faces are sheared parallel to the crack front.

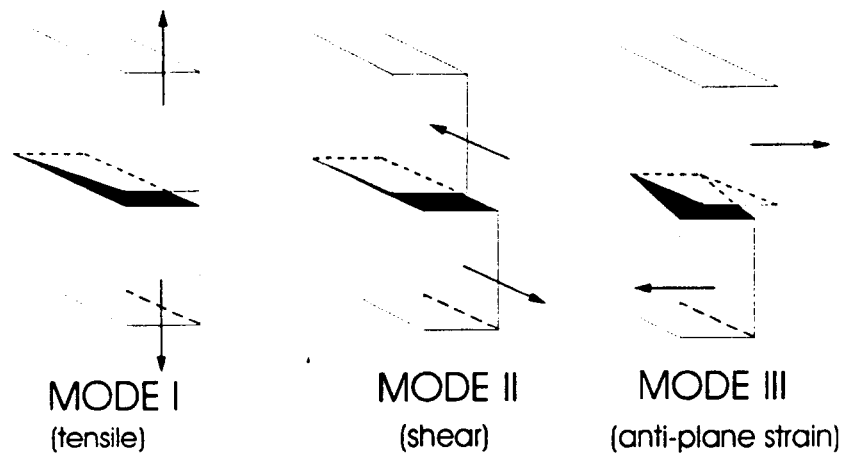


Figure 2.1.3 Basic modes of crack fracture in fatigue.

2.1.3 Characterisation of fatigue crack propagation

Fatigue crack propagation has been successfully characterised by means of the theory of fracture mechanics (FM). The basic formulation on which FM is founded emanates from the studies of A.A. Griffith [11] in 1921, who obtained a relationship between fracture stress and crack length provided the material's work of fracture were known. However, Irwin put forward the concept of plastic flow at the crack tip before the onset of crack extension in 1957 [12]. He introduced the parameter stress intensity factor K which quantifies the near-tip stress fields induced by a crack. This factor K characterises the severity of the crack system as affected by the crack size itself, stress magnitude and geometry or shape.

Each type of crack (long, short and physically small cracks discussed later from § 2.1.5 onwards) requires its own particular scheme of analysis to adequately describe the propagation behaviour [1]. Approaches in terms of linear elastic fracture mechanics (LEFM), elasto plastic fracture mechanics (EPFM) and microstructural fracture mechanics (MFM) are predominantly used for such purposes.

2.1.3.1 Linear elastic fracture mechanics (LEFM)

The theory of fracture mechanics provides the invaluable concept of the stress intensity factor (SIF), denoted by K . As aforementioned, SIF is a measure of the intensity of the

near-tip stress fields. However, when such intensity is under linear elastic conditions the approach used is the so called LEFM. This approach can readily be used to analyse and/or to predict fracture, provided the plastic zone surrounding the crack tip is sufficiently small (small scale yielding) in a way that the K-elastic stress field or K-dominance is not significantly altered. In this respect, and according to Irwin, the singular solutions of the near-tip stress fields, σ_{ij} , are correlated with K as follows:

$$\sigma_{ij} = \frac{1}{\sqrt{2\pi r}} \left\{ K_I f_{ij}^I(\theta) + K_{II} f_{ij}^{II}(\theta) + K_{III} f_{ij}^{III}(\theta) + \dots \right\}, \quad (2.1)$$

where r is the distance from the crack tip, θ the polar angle measured from the crack plane, f_{ij} a dimensionless function of θ at different modes of fracture. K_I, II, III are the SIFs for each loading mode, which is generally expressed for mode I as:

$$K = Y\sigma\sqrt{\pi a},$$

where Y is a non-dimensional function of the loading and crack geometry, σ is the uniform applied stress remote from the crack and a is the real crack length.

It is important to indicate at this point that in LEFM, the initiation of crack propagation under monotonic, quasi-static loading conditions is characterised by the critical value of the SIF, K_C . When the critical value is obtained for mode I stress intensity factor, it is known as fracture toughness and is universally denoted as K_{IC} . In the shearing and tearing modes, fracture toughness is referred to as K_{IIC} and K_{IIIC} , respectively.

It is well recognised, that in Irwin's analysis the plasticity ahead of the crack tip is assumed negligible. However, when the extent of plasticity is not very small compared to the crack length, the application of LEFM can lead to imprecise predictions. In this respect, views concerning the extent to which the elastic based theory is applicable have long been documented, among these are:

- i. The maximum plastic zone at the crack tip taken to be one fiftieth of the crack length provides a small-scale yielding [27].
- ii. The applied stress should be up to two thirds of the cyclic yield stress [23].

In circumstances where the plastic zone size is comparable to the crack length, i.e., small scale yielding conditions are not met; the application of elastic-plastic fracture mechanics is the appropriate approach to employ.

2.1.3.2 Elastic-plastic fracture mechanics (EPFM)

When plastic deformation in the fracture process becomes more pronounced, EPFM concepts have to be used to characterise the crack tip zone of stress and strain. Accordingly, the ability to predict crack initiation under these principles is mainly based on the path-independent line integral, J and the Crack Tip Opening Displacement (CTOD). The integral form was proposed by Rice [29] and the CTOD was introduced by A.A. Wells [30]; together they constitute the basis of EPFM. Whilst the J integral is mathematically more rigorous, the CTOD possesses a clear physical meaning and consequently it has been extensively adopted in engineering practice [31].

The J integral can be used to characterise the singular elastic-plastic stress field near the crack tip, analogous to the factor K in LFM. Based on the deformation theory of plasticity, Hutchinson [32] and Rice & Rosengren [33] proposed the expressions for obtaining such singular elastic-plastic stress field at the crack tip as:

$$\sigma_{ij} = \sigma_y \left(\frac{J}{\alpha \sigma_y \varepsilon_y I_n r} \right)^{\frac{1}{n+1}} \tilde{\sigma}_{ij}(\theta, n), \quad (2.2)$$

where the function $\tilde{\sigma}_{ij}(\theta, n)$ varies with the polar angle θ , the strain hardening exponent n and the state of stress either plane stress or plane strain. The factor I_n is related to the strain hardening exponent n .

In addition, J as a measure of the intensity of crack tip fields under quasi-static loads has been formulated on the basis of a critical value, i.e., the critical amount of potential energy needed to overcome the resistance of material to cracking, namely, $J=J_c$ [8]. The measured critical value of plane strain fracture toughness is denoted as J_{IC} , provided the conditions of J -dominance are met in a plane strain specimen. In this respect, a relationship used to obtain an equivalent K_{IC} value from J_{IC} measurements under linear elastic and plain strain conditions is [8, 31],

$$J_{IC} = \frac{K_{IC}^2}{E} (1-\nu^2) \quad (2.3)$$

The major drawback of the J integral criterion is realised when the fracture is strongly affected by the microstructure of materials, e.g. microstructure-sensitive short fatigue crack propagation, due to the fact that EPFM is still based on continuum solid mechanics.

CTOD on the other hand, is an alternative procedure for characterising elastic-plastic fracture. Crack opening displacement also denoted as δ_t is defined as the opening (distance between two points on the upper and lower crack faces) where 45° lines emanating from the deformed crack tip intercept the crack faces [8]. For cyclic loading the SIF is denoted as, ΔK_I , and the cyclic CTOD as $\Delta\delta_t$, namely:

$$\delta_t \propto \frac{K_I^2}{\sigma_y E} \quad \text{for small-scale yielding (quasi-elastic)} \quad (2.4)$$

For the case of elastic-plastic fracture, Shih [34] deduced the following relationship:

$$\delta_t = d_n \frac{J}{\sigma_y} \quad \text{for large-scale yielding} \quad (2.5)$$

where d_n ranges from 0.3 to 0.8 (material constant) and σ_y is the yield stress.

Despite of its easier physical interpretation, the problem of identifying the critical event in the CTOD test still remains something of a controversy. R.A. Smith [28] claims that the inherent disadvantage of CTOD is in the difficulty of measuring experimentally the

displacements of a crack tip in a region of high uncertainty. As a result, its use in design can be very conservative.

2.1.4 Characterisation of the crack growth rate (long cracks)

Basically, for LEFM to be valid and long cracks be addressed, the crack size must not be less than some microstructural feature size (e.g. grain size) and the plastic zone at the crack tip should be notably much smaller than the crack size. For that reason, propagation in this regime depends fundamentally on the geometry of the crack and the applied stress level but is, however, largely independent of microstructure.

Long crack growth rate has been successfully characterised in terms of SIF, K by P.C. Paris & Erdogan [13, 14]. For a cyclic variation of the imposed stress field under LEFM (quasi-elastic) conditions, the empirical relationship between crack growth increment da/dN and K is given by the power law:

$$\frac{da}{dN} = C \Delta K^m \quad (2.6)$$

Where C and m are experimental constants depending on material microstructure, frequency, environment, temperature and stress ratio $R = \frac{\sigma_{\min}}{\sigma_{\max}} = \frac{K_{\min}}{K_{\max}}$; and ΔK is the stress intensity factor range, defined as $\Delta K = K_{\max} - K_{\min}$.

Crack growth rate data for most engineering alloys is graphically presented in the form of a log-log plot as shown schematically in fig. 2.1.4. Regime A relates to the propagation of cracks at ΔK values just above the threshold level (ΔK_0), below which long cracks propagate at an undetectable rate. For practical purposes, ΔK_0 is frequently considered as a limiting growth rate of 10^{-10} m/cycle. Regime B, is known as the Paris regime, i.e., where LEFM conditions become dominant. In contrast to regime A, regime B stable propagation is seldom influenced by microstructure and is often referred to as stage II growth. At high ΔK values, i.e. regime C, crack growth rates become radically higher than in stable propagation and the $K_{\max} \rightarrow K_c$, i.e., the fatigue fracture tends to

catastrophic failure. In this regime, instability ensues and also static modes of fracture give rise to cleavage, intergranular separation and fibrous failure [35]. A marked sensitivity of propagation rate to microstructure is a consequence of these static modes.

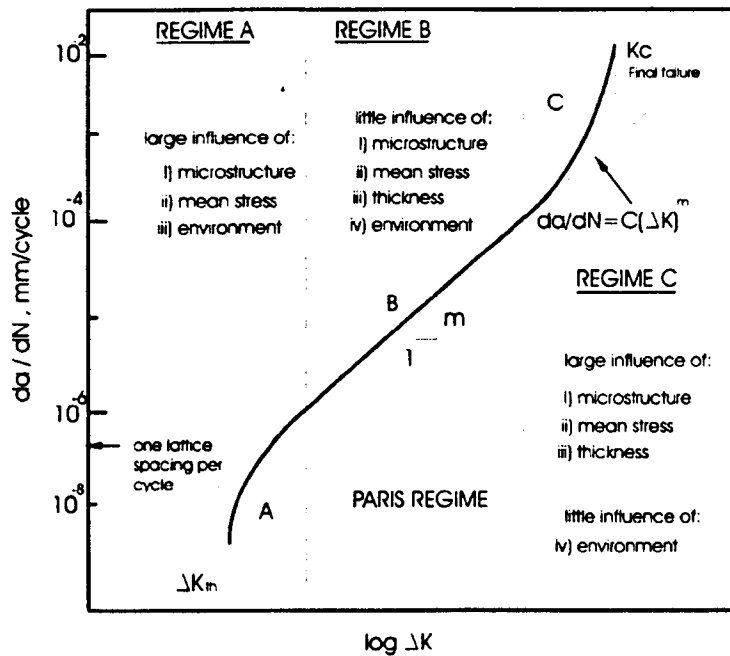


Figure 2.1.4 Schematic illustration of the sigmoidal variation of fatigue long crack propagation (after [8]).

From the above considerations, Eq. (2.6) can lead to inaccurate results when used in the regimes A and C due to (i) microstructural features involved and (ii) premature contact of the fracture surfaces (crack closure) which can lead to a non-uniform reduction of ΔK [36].

For that reason, other approaches have been developed in order to characterise fatigue growth rate in terms of CTOD. Among these, the following two relationships are most relevant [37]:

$$\frac{da}{dN} \propto C_1 \Delta J^{m_1}, \quad (2.7)$$

$$\frac{da}{dN} \propto \Delta \delta_1 (CTOD \text{ or } \phi) \quad (2.8)$$

2.1.4.1 Crack closure on propagation

The crack closure effect first discussed by Elber [36] has increasingly concerned researchers of fatigue crack growth behaviour, particularly in the near-threshold stress intensity levels of long cracks [38, 39]. This is because the fractured surfaces in the wake of an advancing crack tip close when the far-field load is still tensile before the attainment of the minimum load. Premature contact of the fracture flanks occurs and as a result, the crack tip does not experience the full range of ΔK , i.e., the real driving force or effective stress intensity range, ΔK_{eff} ($\Delta K_{\text{eff}} = K_{\text{max}} - K_{\text{op}}$) is lower than the nominal ΔK and therefore a lower da/dN is expected. Here, K_{op} is the stress intensity when the crack is fully opened ($\geq K_{\text{min}}$).

The most accepted mechanism for such an effect is that of the constraint effect on the residual plastically stretched material which is left on the wake of the crack front by the elastic material which surrounds it, when the crack tip continues advancing through the plastic zone. However, several other mechanisms are envisaged as possible, e.g., due to the presence of corrosion debris within the crack (oxide induced closure) [40] and due to the contact between rough fracture surfaces (roughness induced closure) [41].

The application of LEFM to long fatigue cracks characterisation has been studied extensively over the past 30 years. Crack growth at high stresses, which essentially involves EPFM, has also been better understood recently. These concepts have proved to be an invaluable tool for engineering design but despite this, it is subject to limitations, as for example, its inability to describe crack growth in components containing another important group of fatigue cracks, namely, short cracks. This latter group of cracks is of a particular importance when surface treatments (e.g. shot peening processes) are employed. Hence, short crack behaviour will be discussed in the following sections.

2.1.5 Short fatigue cracks

It is well documented that short cracks (SCs) behave markedly different to long cracks. Their growth could occupy a significant portion of the total fatigue life of several structures/components. The short crack (SC) problem was originally proposed by Pearson [42] with his experimental work performed on aluminium alloys. In this pioneer work it was realised that cracks of the order of the grain size tend to propagate at rates far higher than LEFM predictions suggest. In contrast, experimental evidence on 7075-T6 aluminium alloys [43] indicates that SCs propagate at rates slower than that of long cracks subjected to the same nominal ΔK . Moreover, some SCs grow at stress intensities well below ΔK_0 . The crack growth rate decelerates or even arrests in some other SCs. Others cracks are known to reverse such trends and accelerate as much as two orders of magnitude higher than those of corresponding large cracks. The general ‘anomalous’ behaviour of SCs is depicted in Fig. 2.1.5.

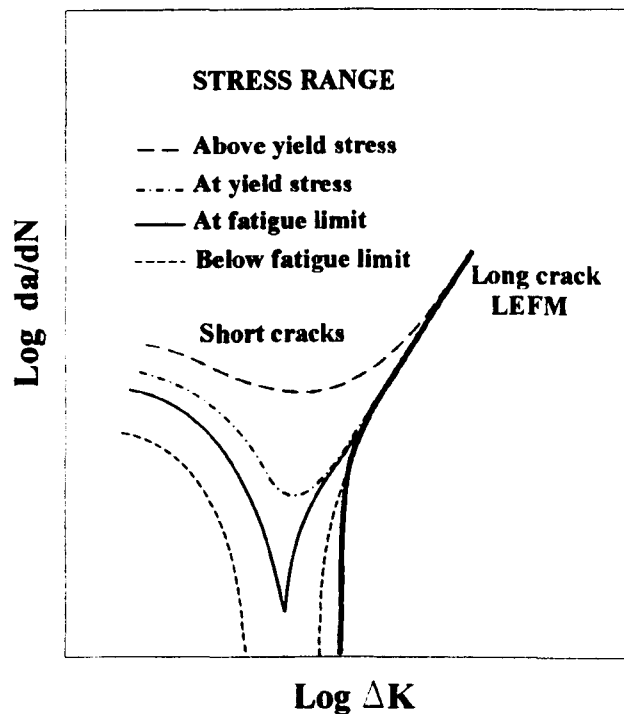


Figure 2.1.5 Schematic representation of the short crack behaviour at different stress levels for a 7075 aluminium alloy [43, 44].

Acceleration, deceleration and crack arrest is commonly attributed as the ‘anomalous’ behaviour of SCs [45]. Lankford [43] suggested that such behaviour is caused by the

difficulty of cracks to nucleate microplasticity in certain crystallographic orientations and/or smaller grains.

A comprehensive review on short fatigue crack behaviour has been published by Miller [46, 47]. Other researchers indicated that SCs may be divided into two primary zones of interest [48]:

- i. The microstructurally short crack zone/regime (MSC) in which the crack is small in relation to the surrounding microstructural features (e.g. cracks which are comparable to the grain size). Crack growth is strongly influenced by microstructure. The micromechanical description of its propagation is expressed by means of the MFM. Fig. 2.1.6.a.
- ii. The physically small cracks (PSC), which are significantly larger than the microstructural dimension and the scale of local plasticity, but are physically small with length typically smaller than a millimeter or two. Here, the microstructure is not the main parameter affecting their propagation but rather, PSC are strongly dependent on the stress level. PSC are conveniently described in terms of EPFM. Fig. 2.1.6.b.

Suresh and Ritchie [38] in turn, suggested a comprehensive classification of SCs which include: microstructurally, mechanically, physically and chemically small cracks.

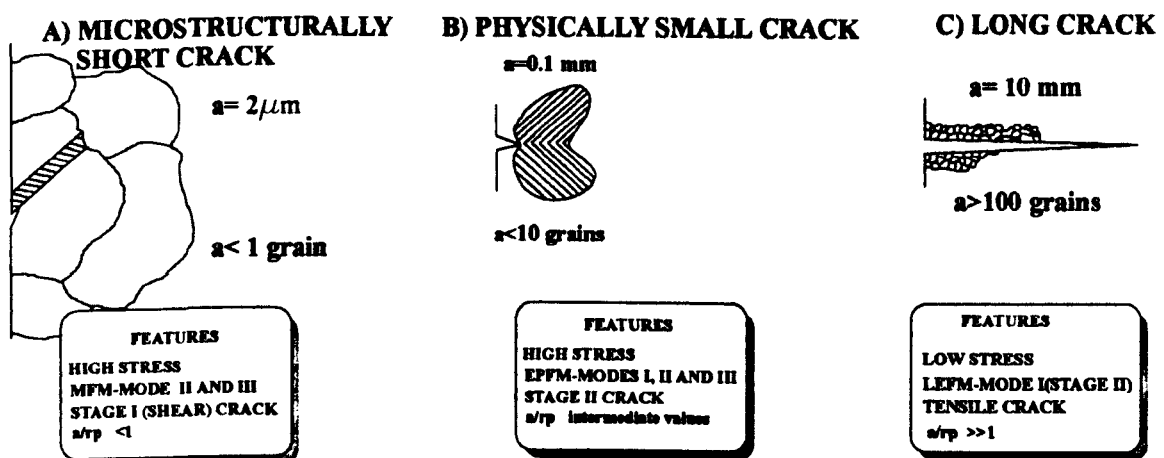


Figure 2.1.6 Classification of SCs: a) MSC, b) PSC and for comparison c) long crack. A briefly description of their main features according to Miller [1] is given (where, a is the crack length and r_p is the plastic zone).

A significant contribution to the understanding of SCs was put forward by Kitagawa and Takahashi [16] who develops the well known Kitagawa-Takahashi diagram (K-T), shown in Fig. 2.1.7. This diagram shows, for a number of metals, that there is a dividing line, considered to be the bounding condition between propagation leading to failure and non-propagating cracks or crack arrest.

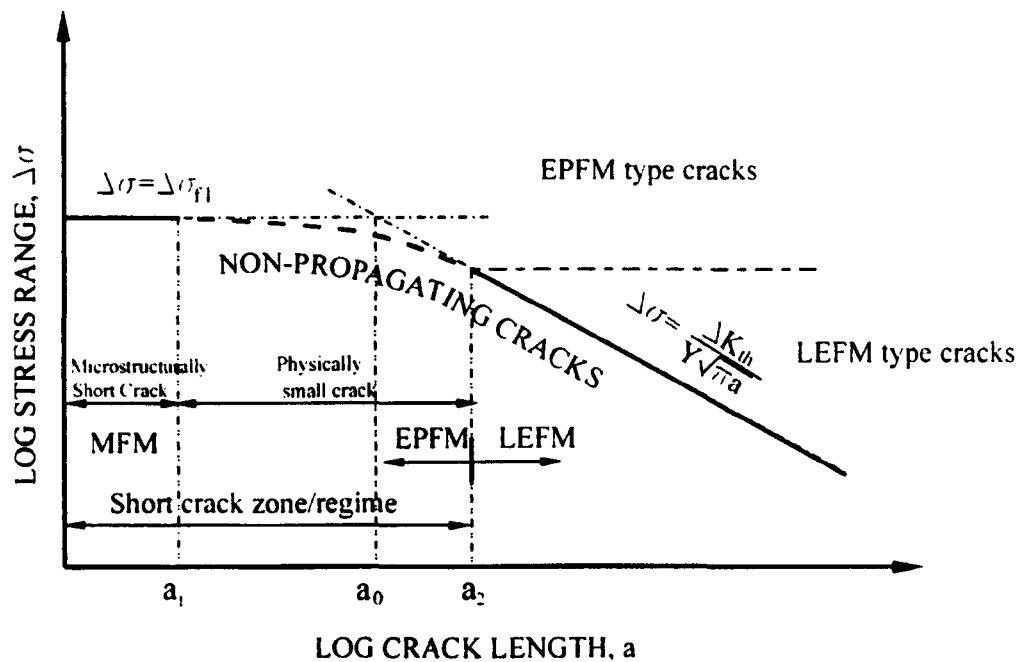


Figure 2.1.7 Schematic Kitagawa-Takahashi diagram [16, 45, 46]. The crack lengths a_1 and a_2 define the deviation of the constant stress and constant stress intensity behaviour respectively. Crack lengths between a_1 and a_2 can be expected to propagate faster and to have lower ΔK_{th} , than cracks larger than a_2 . This latter crack length represents the point below which the use of LEFM and Paris law predictions are non-conservative. On the other hand, the point a_1 represents the crack length below which there is no crack length effect on fatigue strength [49].

The K-T may be approximated by two straight asymptotic lines. The line given by ΔK_{th} represents the low-stress threshold condition below which a crack should not propagate according to LEFM given by [50]:

$$\Delta \sigma = \frac{\Delta K_{th}}{Y\sqrt{\pi a}} \quad (2.9)$$

It follows that,

$$\log \Delta \sigma = \log \left(\frac{\Delta K_{th}}{Y \sqrt{\pi}} \right) - \frac{1}{2} \log(a) \quad (2.10)$$

Where Y is the geometric factor of both the geometry of loading and the geometry of the cracked specimen and a is the crack length.

The horizontal line is the fatigue limit itself, i.e., the limiting conditions for the propagation of a crack in a plane specimen. The intersection of the fatigue endurance and the LFM threshold lines take place at a critical crack length of ≈ 10 grains (PSC) [45, 46]. This assumption supports the fact that a crack must be very much larger than microstructural features for a LFM concept to be valid. More accurately, the intersection occurs when the crack length is:

$$a_2 = \frac{1}{\pi} \left(\frac{\Delta K_{th}}{Y \Delta \sigma_0} \right)^2 \quad (2.11)$$

for short cracks, $\Delta \sigma_0 = \Delta \sigma_{f1}$.

This critical crack length ' a_2 ' (transition crack size) has been employed as an empirical parameter to account for the differences in propagation rates between long and short cracks even when they are under the same driving forces from a LFM standpoint [8]. In this sense, K-T may well illustrate the fracture behaviour under different combinations of stress range levels and crack lengths.

The relevant K-T has been further extended by Brown [23]. The interfaces of several crack propagation mechanisms occurring at different stress levels have been eloquently identified in a fatigue damage map as depicted in Fig. 2.1.8. From the so-called Brown map, it is established that cracks may initiate and propagate at stress levels below of the fatigue limit and LFM threshold. These cracks eventually decelerate until they arrest just below the fatigue limit as a consequence of the existing microstructural barriers (additional discussion regarding microstructural barriers is presented in §2.1.6). Consequently the Brown map is useful for applying more accurately the FM analysis since the dominant mode of growth is correctly established.

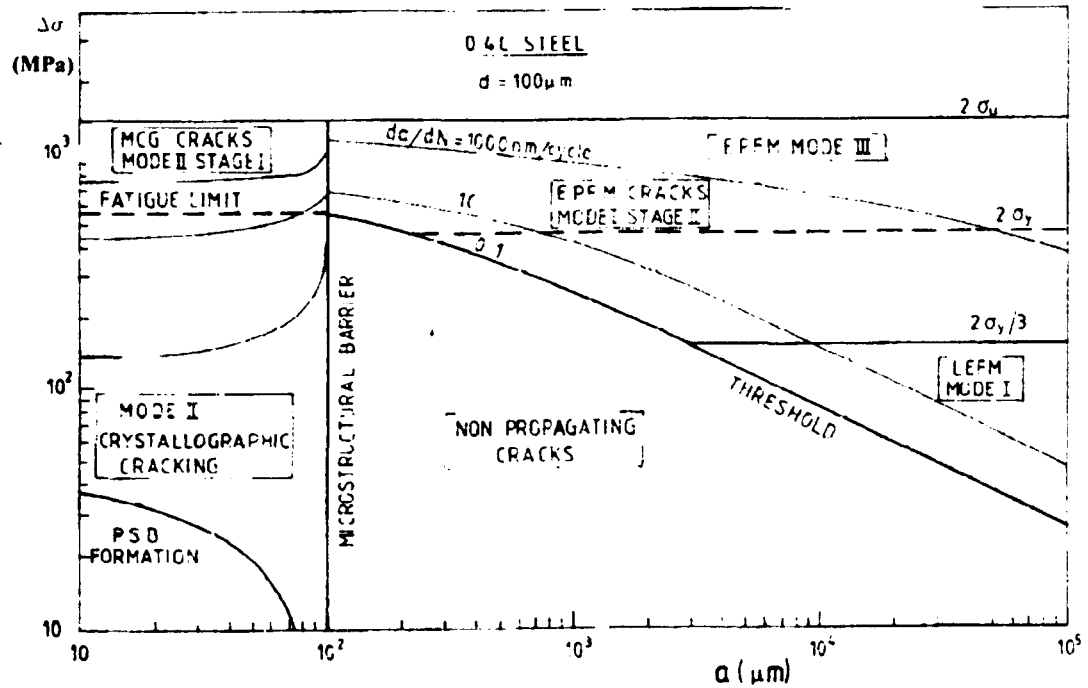


Figure 2.1.8 The Brown map showing the boundary conditions between short, long and non propagating cracks. The fatigue fracture-mode map encompasses six zones, namely; (i) LEFM mode I, (ii) EPFM mode I, (iii) EPFM mode III, (iv) mode II stage I, (v) mode II crystallographic cracks, and (vi) non-propagating modes I/II [23].

2.1.5.1 The effect of fatigue crack closure on SCs

As quoted previously in § 2.1.4.1, the closure phenomena in long cracks has a marked influence on the fatigue crack propagation rate. Nevertheless, both experimental research and numerical simulations have revealed lower closure stress levels for SCs than for long cracks at the same nominal SIF [51] [52] [53]. The above is due to the well known fact that SCs have a limited wake [54]. In the case of peened surfaces, crack closure plays an important role as it is extremely influenced by the residual compressive stresses provoked by the peening action as will be discussed in later sections.

2.1.6 The behaviour of SCs : microstructural analysis

The large number of papers dealing with the quantification of short crack propagation rate behaviour reported in the literature, indicate the importance of this type of fatigue crack in metallic materials. In this sense, modelling of SC propagation rate certainly has contributed to a better understanding of MSC and PSC and subsequently to better fatigue-based designs. Furthermore, attributed to developments on SCs microstructural analysis, it is now possible to incorporate materials effects in an explicit form within the crack system of, e.g., a surface treated by shot peening. This will be reviewed in § 2.2.

The behaviour of SCs has been formulated as an answer to the belief that LEFM principles are violated due to the relatively large cyclic plasticity at the crack tip, which modifies substantially the strength of the stress field ahead of the crack. For example, a strain intensity factor that took into account cracks propagating in cyclic plastic strain fields was proposed by Boettner *et al.* [55], which is believed to be the first attempt to model SC propagation. A model dealing with the blocking action of grain boundaries was analysed by Chang [56], in which critical strain energy must be exceeded at the tip of a crack in order for the crack to propagate. As a result, it is argued that an incubation period arises when cracks encounter grain boundaries. A modified LEFM equation with disorientation between grains analysis was put forward by Chan *et al* [57]. Tanaka [58], on the other hand, considered the effect of grain boundaries on the development of slip bands and formulated the relationship of SC propagation behaviour as a function of crack tip displacement and closure. In the same work, SCs are related to the LEFM threshold stress intensity for long cracks. Hobson, Brown and de los Rios [59, 60], proposed empirical models to quantify both short and long crack propagation rates, which incorporated the effect of the microstructure in Aluminium 7075-T6 and steel. These empirical relationships were later extended by Angelova and Akid [61] in an attempt to describe more precisely short fatigue crack behaviour not only in air but in an aggressive environment.

All the above formulations, either analytically or empirically, have been reasonably successful and have served as the premise for more detailed developments which account for the elastic-plastic interface coincident with a grain boundary at any position,

the successive blocking of the plastic zone by slip barriers and the subsequent initiation of slip in the next grain. A more realistic and comprehensive development is detailed in the extensive work of Navarro-de los Rios [62] who have successfully related short crack propagation rate to the strength of microstructural barriers in a general model to predict the crack growth rate during stages I and II, and for both short and long cracks (applications of this formulation are given elsewhere [63-65]). This model predicts the decreasing crack propagation rate, and alternating fluctuations or intermittent pattern of crack growth within the microstructurally sensitive zone.

2.1.6.1 The three zone micromechanical model (TZMMM)

Based on the analysis of distribution of dislocations by Bilby, Cottrell and Swinden (BCS) [66], Navarro and de los Rios originally proposed a theoretical model for short crack propagation by considering infinitesimal dislocations distributed within two zones, one for the crack itself and the another for the plastic zone [67]. Both bounded and unbounded solutions for the dislocation distribution system were written in a single expression, which was later further extended to incorporate a third zone to represent the situation where the blockage of the plastic zone by grain boundaries takes place [68]. The general solution given the dislocation distribution is as follows:

$$\begin{aligned}
 f(\zeta) = & \frac{1}{\pi^2 A} \left\{ (\sigma_2^i - \sigma_1^i) \left[\cosh^{-1} \left(\left| \frac{1 - n_1^i \zeta^i}{n_1^i - \zeta^i} \right| \right) - \cosh^{-1} \left(\left| \frac{1 + n_1^i \zeta^i}{n_1^i + \zeta^i} \right| \right) \right] \right. \\
 & + \left. (\sigma_3^i - \sigma_2^i) \left[\cosh^{-1} \left(\left| \frac{1 - n_2^i \zeta^i}{n_2^i - \zeta^i} \right| \right) - \cosh^{-1} \left(\left| \frac{1 + n_2^i \zeta^i}{n_2^i + \zeta^i} \right| \right) \right] \right\} \\
 & + \frac{2}{\pi^2 A} \frac{\zeta^i}{(1 - \zeta^{i2})^{\frac{1}{2}}} \left[(\sigma_2^i - \sigma_1^i) \sin^{-1} n_1^i + (\sigma_3^i - \sigma_2^i) \sin^{-1} n_2^i + (\sigma - \sigma_3^i) \frac{\pi}{2} \right]
 \end{aligned} \tag{2.12}$$

where σ is the applied stress; σ_1^i , σ_2^i and σ_3^i are the friction stresses; $A = Gb/2\pi$ for screw dislocations, or $A = Gb/2\pi(1-\nu)$ for edge dislocations, G is the shear modulus, b the Burgers vector, and ν the Poisson ratio. Grain boundaries are situated at $x = \frac{1}{2} iD$ and crack tips at $a_i = n_c$ with $c = \frac{1}{2} iD + r_0$. Here D is the grain diameter and r_0 may be

considered as the width of the grain boundary itself. The variable $\zeta = x/c$ relates the position throughout, in such a way that the crack tip is at $\zeta = n_1^i$ and the nearest grain boundary at $\zeta = n_2^i$. Finally, the value of $i = 1, 3, 5, \dots$ describes the number of half grains affected by the fatigue process.

The friction stress σ_3 represents the stress at the grain boundary and is calculated by making the bracketed term multiplying the singularity in Eq. (2.12) equal to zero, resulting the following relationship [69]:

$$\sigma_3^i = \frac{1}{\cos^{-1} n_2^i} \left[\left(\sigma_2^i - \sigma_1^i \right) \sin^{-1} n_1^i + \sigma_2^i \sin^{-1} n_2^i + \frac{\pi}{2} \sigma \right] \quad (2.13)$$

As the crack propagates σ_3 increases in value and will reach a level equal to the strength of the boundary when the crack reaches a critical length denoted by $n_1^i = n_c^i$. The grain boundary will be overcome and crack tip plasticity is able to extend to the next grain boundary where it is again blocked. However, if σ_3 does not attain the level of the grain boundary strength before the crack tip reaches the barrier, the crack arrests.

The crack system (the term considers the crack, the crack tip plasticity and the barrier zone) can be represented by three zones as shown in Fig. 2.1.9. The first zone represents the crack itself, the second the crack plasticity and the third the barrier. In terms of stresses, the crack is envisaged as stress free unless some closure stress, σ_1^i , is acting on the crack flanks, the plastic zone is subjected to the stress σ_2^i which represents the resistance of the material to plastic deformations (cyclic or monotonic yield stress), and the grain boundary is subjected to a stress, σ_3^i . This stress represents a measurement of the reaction stress developed at barrier due to the PSB blocking.

In general, the crack growth mode predicted by the model is represented by the oscillations of the crack propagation rate, which repeats itself grain after grain until the alternating fluctuations or intermittent pattern ceases, giving rise to a monotonic increase similar to that predicted by LEFM [70]. The above emphasizes the belief that the transition from a short crack behaviour to a long crack behaviour is defined when both cracks experience identical propagation rates under the same nominal ΔK [8].

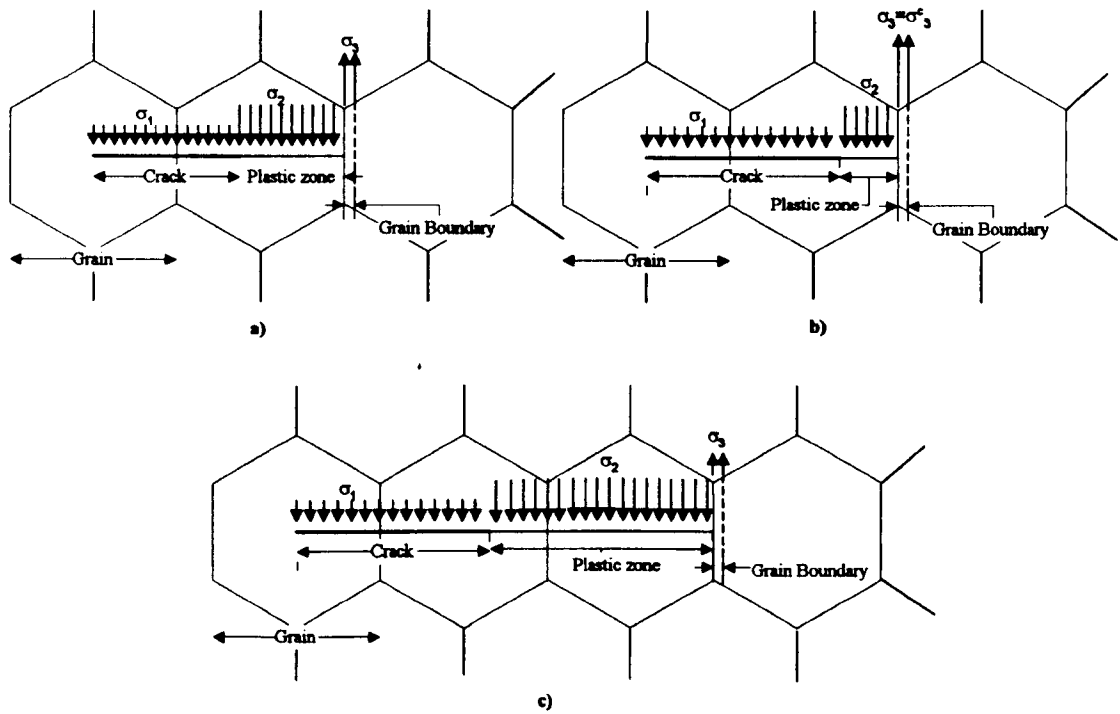


Figure 2.1.10 Schematic representation showing the effect of slip-band locked by the grain boundary on stress concentration in three stages: a) blockage of the plastic zone by the grain boundary which increases σ_3 ; b) further crack propagation until $\sigma_3 = \sigma_3^c$ results into new slip-band development and c) relaxation of σ_3 and yielding on a new grain. The parameters σ_1 and σ_2 represent crack closure stress and cyclic yield stress respectively.

2.1.6.2 Description of crack arrest in terms of the TZMMM

When the crack attains a critical length the stress σ_3 reaches the necessary level to overcome the barrier and the crack is able to propagate through such a constraint (as shown in Fig. 2.1.11). If σ_3 does not achieve the required value before the crack tip reaches the barrier, the crack arrests, which is expressed as $\sigma_3 \leq \sigma_3^c$. The condition for arrest can be obtained from Eq. (2.13) by bearing in mind that when the crack tip reaches the barrier, before plasticity spreads onto the next grain $n_1 = n_2 = 1$ [72]. Thus, the magnitude of stress for crack arrest is:

$$\frac{2}{\pi} \sigma_3^i \cos^{-1} n_2^i + \sigma_1 = \sigma_{\text{arrest}} \quad (2.14)$$

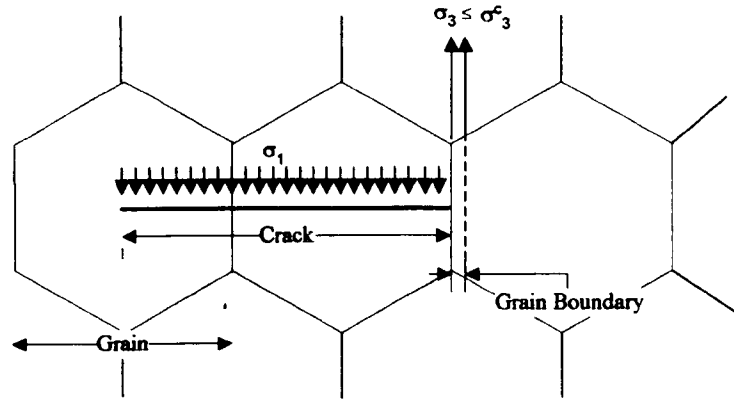


Figure 2.1.11 Schematic representation of crack arrest

As indicated earlier, if σ_3 does not attain the level of σ_3^c before the crack tip reaches the grain boundary the crack arrests. It has been shown [72] that crack arrest is achieved when:

$$\frac{m_i}{m_1} \frac{\sigma_{FL} - \sigma_1}{\sqrt{i}} + \sigma_1 = \sigma_{arrest} \quad (2.15)$$

where $i = \frac{2a}{D}$, σ_1 is the crack closure stress which is set to $\sigma_1 = 0$ for stress free cracks (i.e., untreated surfaces), a is the crack length, D is the grain diameter and σ_{FL} is the fatigue limit. The term $\frac{m_i}{m_1}$ is the effect of grain orientation, which was evaluated and incorporated by de los Rios and Navarro [73] on SC propagation using the following empirical relationship:

$$\frac{m_i}{m_1} = 1 + 0.5 \ln(i) \quad (2.16)$$

The grain orientation factor m_1 is related to the first grain and m_i is the average factor corresponding to other successive grains. In the first grain, the orientation factor should have a value of approximately unity, since crack formation takes place in grains where the critical resolved shear stress is maximum. It should be noted that the grain orientation factor increases monotonically as does i , with the largest increase between

the first and the second grain and the rate of increase slowing down until m_i reaches a value that represents the truly polycrystalline behaviour (Taylor's factor $m_i = 3.07$ for FCC metals [74]).

By combining Eq. (2.15) with Eq.(2.16), the Kitagawa-Takahashi diagram (described previously in § 2.1.5) can be theoretically drawn as shown in Fig. 2.1.12. The effect of having a closure stress σ_1 is that of increasing the stress required for arresting the crack. This is the case when a metallic surface has been treated by, for instance, shot peening, which introduces compressive residual stresses and can be readily assessed in terms of increasing the limit stress for crack propagation.

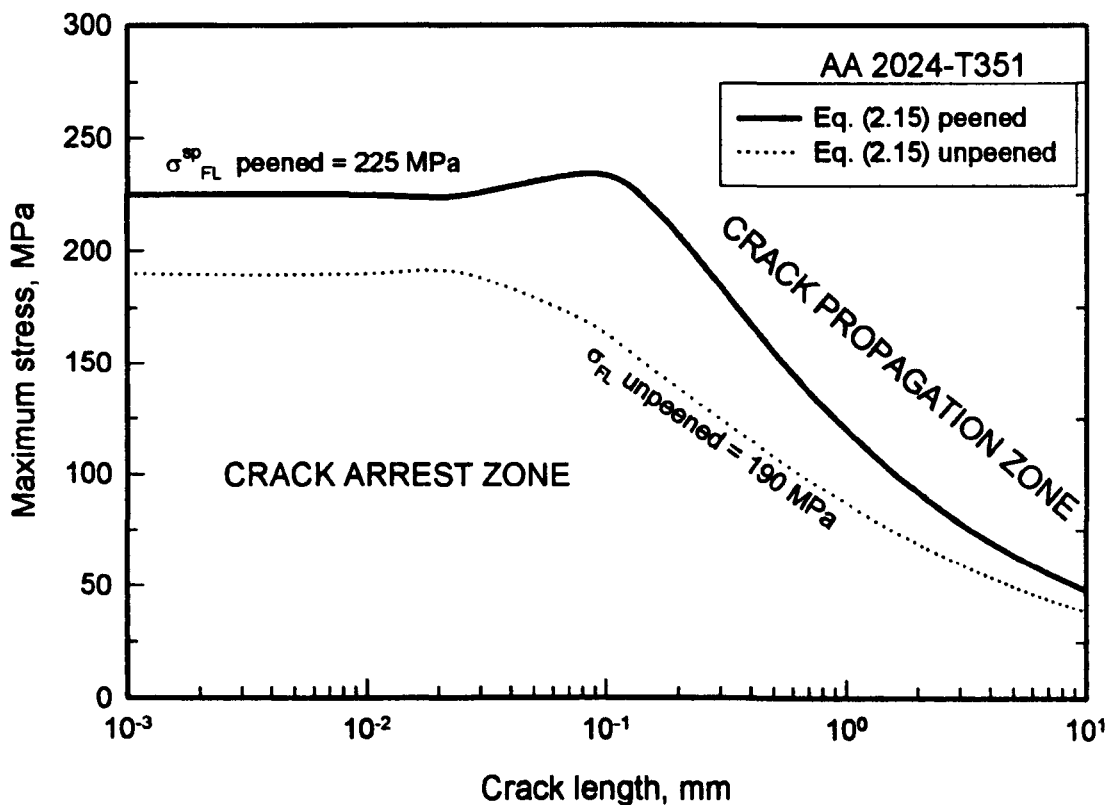


Figure 2.1.12 Fatigue damage curves which conforms to the K-T diagram. Eq. (2.15) was used considering $\sigma_1 = 0$ (no closure stress dashed line) and $\sigma_1 \neq 0$ (introduced compressive residual stresses solid line) for a surface engineering treated material. σ_{FL} is 190 and 225 MPa for untreated and treated material respectively and a grain diameter of $52.8\mu\text{m}$. The surface engineering treatment was the shot peening.

2.1.6.3 Crack propagation rate in terms of the TZMMM

Crack propagation rate is assumed to be proportional to the displacement between the crack surfaces at the crack tip, ϕ , i.e., crack propagation rate as a function of the CTOD, also denoted as ϕ , as annotated in Eq. (2.8) [70], which through a Paris type relationship is given by:

$$\frac{da}{dN} = C \phi^m \quad (2.17)$$

where coefficient C and exponent m are obtained by correlating ϕ with long crack propagation data generated using fracture mechanics specimens.

The equilibrium equation (2.12) incorporates all the forces, internal and external, e.g. applied stress minus resistances and the forces due to the dislocations. A general solution was given in [69]. The application of this solution to the three-zone crack system renders expressions for crack tip open displacement (CTOD) and the constraint stress σ_3 . CTOD is equal to the number of dislocations entering the plastic zone, multiplied by the Burgers vector [75]. It has been mathematically expressed as:

$$\phi_i = \frac{bc}{\pi^2 A} \left\{ -(\sigma_2 - \sigma_1) \left[-\left(2n_1^i \right) \ln \left(\frac{1}{n_1^i} \right) \right] - \right. \\ \left. -(\sigma_3 - \sigma_2) \left[\left(n_1^i - n_2^i \right) \cosh^{-1} \left(\left| \frac{1 - n_2^i n_1^i}{n_2^i - n_1^i} \right| \right) - \left(n_1^i + n_2^i \right) \cosh^{-1} \left(\left| \frac{1 + n_2^i n_1^i}{n_2^i + n_1^i} \right| \right) \right] \right\} \quad (2.18)$$

where b is the Burgers vector, $A = Gb/2\pi$ for screw dislocations and $A = Gb/2\pi(1-\nu)$ for edge dislocations; G is the shear modulus and ν is the Poisson ratio.

Life predictions are obtained by integrating Eq. (2.17) in each grain and then adding together to compute total life. The integration is made between the limits of initial crack length in each grain interval (a_s^i) and final length in each grain interval (a_f^i), as follows:

$$N = \int_{a_i^i}^{a_f^i} \frac{d a_i}{C(\phi_i)^m} \quad (2.19)$$

This total life is given by

$$\sum_{i=1}^{i_f} N_i \quad (2.20)$$

Summarising, the important features of the model described above, are:

- i. The model involves plastic displacements throughout the crack system in such a way that the tip plasticity effects are incorporated.
- ii. With the introduction of the third zone which represents the blockage source or the grain boundary itself, the stress remains finite anywhere in the crack system. The grain orientation factor m_i , which considers the increasing number of grains being traversed by the crack front, has been taken into account (m_i increases from 1 to 3.07). Work hardening has also been incorporated [76], which produces more realistic predictions.
- iii. Even though the model was originally developed for the prediction of short crack propagation, propagation of longer cracks has also been predicted [72].
- iv. As the model is based on EPFM concepts it takes into account cases of large scale yielding.
- v. The friction stresses in the crack wake are not modelled as a continuum closure pressure but as being a resistance to crack opening.
- vi. The model describes the fatigue damage from crack initiation to catastrophic failure.

2.1.7 Fatigue resistance of metallic materials

Following the discussion of important concepts regarding fatigue, crack propagation regimes and quantification of crack growth, some major aspects of long cracks and in more detail short crack features, it is necessary to discuss the meaning of fatigue resistance of metallic materials and its connection with both short cracks and shot peening.

As discussed in the previous section, the effect of the microstructural barriers decreases as crack length increases and the stress concentration at the tip of the crack gets closer and ultimately exceeds that value required to overcome the barriers. If the crack is obstructed in its path by many closely packed barriers, as would occur in microstructures containing small grains, then the crack growth path would be deflected. It is envisaged therefore that fatigue resistance is high. Herein, fatigue resistance may be quantified as the resistance to crack propagation offered by the material. Miller [1] has defined fatigue resistance for multigrain materials as the difficulty of a stage I crack becoming a stage II crack, as illustrated in Fig. 2.1.13.

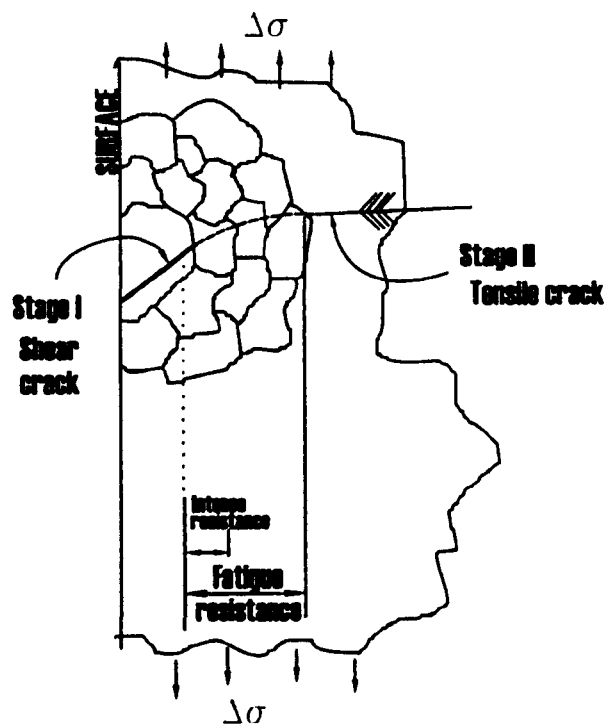


Figure 2.1.13 Schematic illustration of the fatigue resistance threshold for multigrain materials expressed in terms of difficulty of initial stage I crack becoming stage II crack (after Miller [1]).

To condition the surface to resist crack propagation in structural components made of aluminium alloys, the shot peening process is routinely employed for improving fatigue performance. Because this process modifies only the surface and properties of the peened surface, characterisation of fatigue damage needs to be described in terms of short crack behaviour, [77]. The shot peening process and its interaction with fatigue will be considered in detail within the following sections.

2.2 AN ENGINEERING SURFACE TREATMENT: SHOT PEENING (SP)

As commented previously, fatigue resistance for multigrain materials represents the degree of difficulty for a stage I crack becoming a stage II crack. It is also clear from the preceding section that fatigue resistance would increase by introducing compressive residual stresses in the surface layer to compensate for tensile loading stresses. This is also complemented by introducing many and variable forms of textural barriers to hinder the development of stage II crack. The application of suitable surface engineering treatments, alone or combined with other hardening processes, delays the propagation of such cracks. Three different ways have been identified by which fatigue resistance can substantially be affected: Firstly, by machining, secondly by rolling and thirdly by shot peening [78].

The SP process has for some time been described as an effective mechanical surface treatment in tackling fatigue failure. This method is a cold working process that involves bombarding a metal component with a stream of small and relatively hard shot to induce desirable residual compressive stresses and strains within the surface layers of the component.

2.2.1 Brief history of SP

The process is widely identified as a mechanical prestressing method. Rolling, coining, stress peening and hammering are among others prestressing processes. Of those, hammering is the oldest cold working process. Cary [79] found in the literature that mechanical prestressing probably predates 2700 B.C. Hammered gold helmets were found during the Crusades (1100-1400 A.D.), etc. However, the reasons for the improvements in durability were probably not understood.

Shot peening was well accepted as a technological process in the early 1920's, following an accidental observation that components which were routinely sand-blasted for cleaning purposes showed an increase in fatigue life. Kloos, *et al.* [78] compiled

some relevant contributions showing the historical development of SP for the period from 1920 to 1960 as listed in table 2.2.1:

AUTHOR(S),INSTITUTIONS	YEAR	STATEMENTS/PROPOSALS
American automotive industries	1926/28	Steel shot blasting
E.G. Herbert	1927	Work hardening due to abrasion("cloudburst process")
O. Foppl	1929	Cold-hammering improves bending fatigue behaviour of structural steel
German Patent Nr. 573630	1929	Steel shot blasting of springs
E.E. Weibel	1935	Increased fatigue resistance due to shot blasting
J.H. Frye,G.L.Kehi	1938	Influence of cleaning procedures on fatigue behaviour
R.Z. v Manteuffel	1939	Improved fatigue strength of sand blasted steel springs
F.P.Zimmerli	1940	Shot blasting and its effect on fatigue fracture life
H. Wiegand	1940	Increased security of surface treated aircraft motor components against fracture
J,O. Almen	1943	Improved fatigue strength of shot peened engine parts; method for measuring peening effects
EW. Milburn	1945	X-ray diffraction applied to shot peened surfaces
H.O. Fuchs,R.L. Mattson	1946	Residual stress measurement at shot peened springs
A.J. Gould,U.R. Evans	1948	Improved corrosion fatigue behaviour of shot peened parts
J.C Straub,O. May	1949	Stress peening yields superior enhancements of fatigue strength
R.L. Mattson, J G Roberts	1959	Analysis of residual stress states induced by strain peening

Table 2.2.1 Historical development of surface strengthening by hammering and shot blasting or shot peening (after Kloos [78]).

An important contribution to the history of the SP process has been the work of Herbert, which is believed to be the earliest work on SP. The name of SP is directly attributable to Herbert. Equally important was the work of O. Foppl, who was the first scientist to

expound the beneficial influence on the fatigue resistance of metals. Zimmerli [80] presented the results of a systematic study and the influence of a process parameter on the fatigue behaviour of blasted springs. The influence of the process parameters on the effects of the SP in terms of fatigue resistance is particularly relevant to the scope of this work.

In addition to these advances, the contributions of Almen to the development of SP procedures were of particular importance. For example, he was responsible for the formation of the SAE committee on shot peening, and did outstanding work in the residual stress field [81]. Nevertheless, his major contribution was the development of the Almen test strip and gauge [82]. It became a worldwide standard method for specifying the required peening intensity that a component should receive, and an important tool in process control.

The process was initially used in the automotive industry, but is now extensively used in the aerospace industry not only to condition the metal surface of aircraft components, but also for producing curvature in panels [83]. This process requires no dedicated tooling to achieve a given component shape, and can achieve large residual strains. Due to induced compressive stresses on the surfaces, the fatigue life of components is enhanced, which is the opposite effect of most other forming processes [84].

2.2.2 The mechanism of the SP method

A general picture of what constitutes the mechanism by which the peening process can alter the microstructure and properties of the peened layer, would be comprised of the following stages [85, 86]:

- i. Essentially, spherical particles also known as shot, which are made of cast high carbon steel, iron, stainless steel, glass or ceramic beads [82, 87], are purposely projected to strike the surface of a metallic component. The particles are accelerated by means of either compressed air (used in this investigation) or centrifugal forces [88, 89]. Impinging velocities which typically involve approximately $10\text{-}50\text{ m}\cdot\text{s}^{-1}$ for aluminium components [90] are sufficient to

originate an indentation, where the dominant regime is fully plastic. This stage is schematically depicted in Fig. 2.2.1.

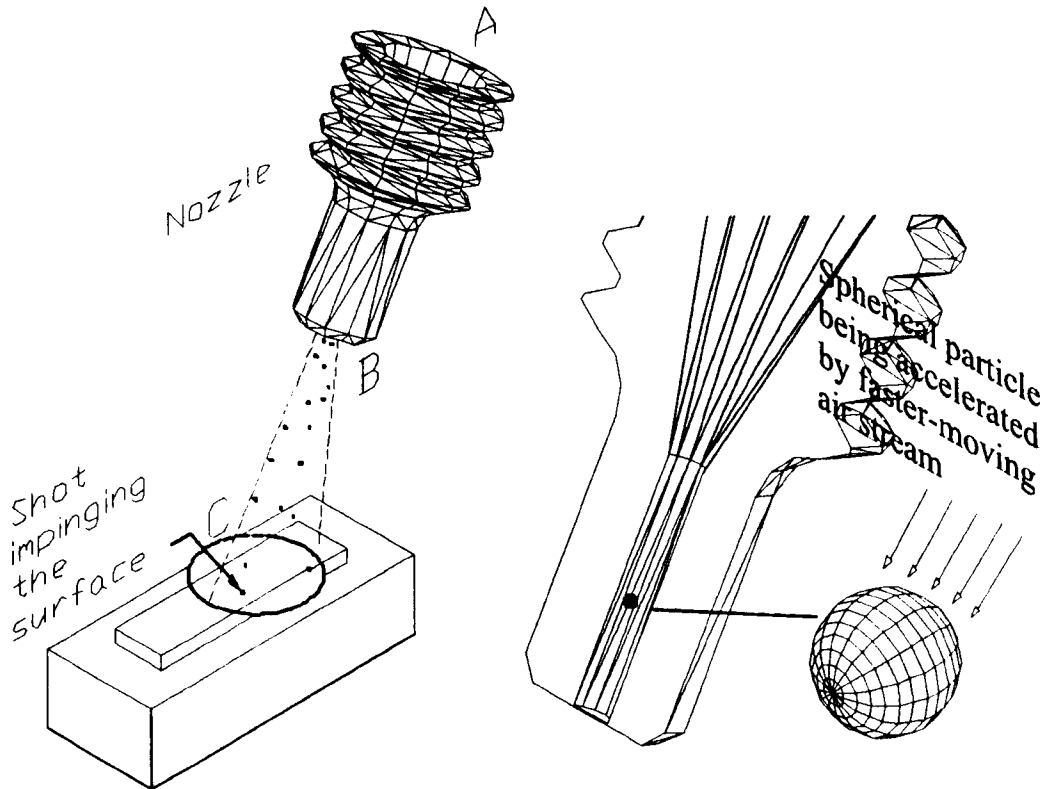


Figure 2.2.1 Schematic representation of the SP process. The particles are propelled by means of compressed air and further accelerated (right side figure) when passing through a nozzle (from point A to B on the left side figure). In point B, the particles highly loaded with kinetic energy are projected to the surface (point C). The shot blast pattern is usually on the shape of a narrow cone with a region highly obliterated at the surface.

- ii. The severity of the impact is directly related to the kinetic energy¹ of the stream. The contact pressures between the shot and target vary with exposure time as the kinetic energy is transferred to the surface during the impact phase and returned to the shot in the rebound phase. Differently expressed: The distinction between the stream kinetic energy W_i and the returning kinetic energy W_r is the sum of the energy stored in the material and in the shot plastic deformations and the energy dissipated in heating, vibration, etc., which can be defined as follows:

¹ $E_i = \frac{1}{2} m v^2$ where $m = \frac{4}{3} \rho \pi R_s^3$ represents the mass of the shot and v is the velocity of the shot at the material surface.

$$\Delta W_{\alpha} = W_p + W_d \quad (2.21)$$

where W_d is the energy dissipated during the impact, which has not been exactly determined [91]. The efficiency of the impact is defined as K , which expresses the ratio of the energy dissipated during the contact to the energy transmitted to the target material. Estimates are from 0.8 to 0.9 for the mechanical impacts [92]. Therefore, the energy transmitted by plastic deformation to the target material is as follows:

$$W_p = \Delta W_{\alpha} K = \frac{1}{2} m V_i^2 \psi(e_r, \alpha) K \quad (2.22)$$

Where $\psi(e_r, \alpha) = [1 - \sin^2 \alpha (e_r^2 + \cot^2 \alpha)]$, V_i = Velocity at the

impingement angle and e_r = Coefficient of restitution given by: $e_r = \frac{V_r \sin \alpha'}{V_i \sin \alpha}$,

here V_r = Velocity after impingement at an angle α' . Values of 1 are characteristic for an elastic contact and 0 for plastic contact.

- iii. Although the process is under dynamic conditions, published work indicates equivalence to those for quasi-static behaviour [91, 93, 94]. In this respect, it has recently been assessed numerically by using finite elements [95] that for shot velocities up to 200 m/s at the moment of the impact; the process can be modelled using a quasi-static approach, ignoring time-dependent effects. Conversely, substantial errors can arise from the application of quasi-static analysis to the simulation of a 300 m/s impact. The discrepancies found are directly attributed to a) time-depending effects (strain-rate sensitivity, elastic-weave, interactions, etc.) and b) non-continuum effects (microcracking and shear-band formations).
- iv. When the dimple is formed on the component surface, a local plastic deformation occurs in the surface layers of the component as shown in Fig. 2.2.2. In order to create the dent, the surface fibres of the material must be yielded in tension. There is a momentary rise in the temperature of the surface, due to transformation of energy, which only affects the plastic flow of the surface fibres. When the material is deformed so rapidly (strain rates in the range of $4 \cdot 10^4 \text{ s}^{-1}$), the generated heat cannot diffuse, and then slip localization known as adiabatic shear

bands may take place [96]. On rebound of the shot, below the surface, the fibres try to restore the surface to its original shape but the continuity of the material in both regions, the elastic and plastic, does not allow this to occur. Consequently, a balanced system of residual stresses is trapped in the component. The plastically deformed zone recovers only some part of the elastic portion of its total strain. The resulting trapped stresses are compressive in a thin sub-surface layer with tensile residual stresses distributed throughout the lower regions (see Fig. 2.2.3).

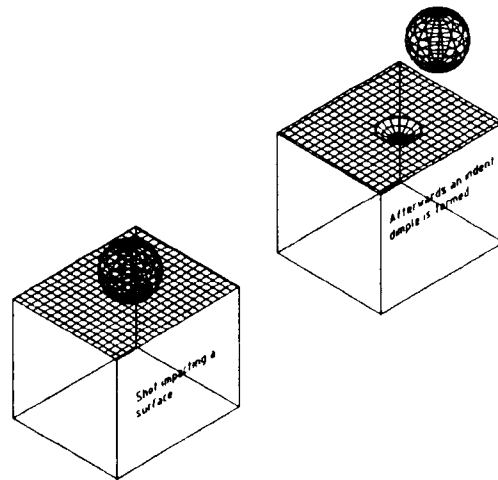


Figure 2.2.2 Schematic illustration of a shot immediately before and after impinging the surface. As a result, a finite plastic deformation in the stressed material beneath the particle occurs in order to dissipate that kinetic energy from the particle leading to formation of a characteristic dimple. This shot is taken from one referred to Fig. 2.2.1.

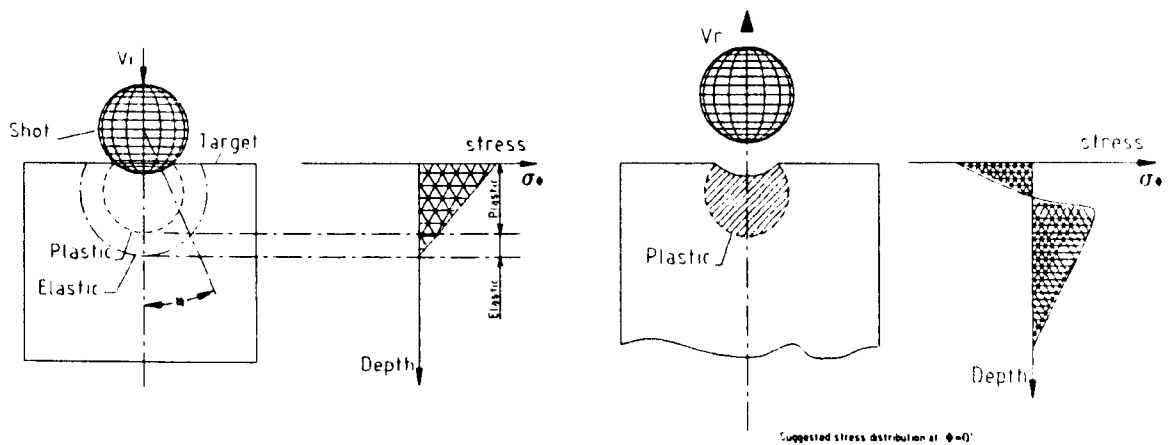


Figure 2.2.3 The heart of the mechanics: (a) a shot impacts a component, which absorbs most of the kinetic energy of the shot and therefore there is a local plastic yielding deformation in the surface layers of the component, i.e. an indentation is formed at each point of impact and (b) on the rebound of the shot a balanced system of compressive residual stresses is trapped in the component.

Initial impacts alternately increase the dislocation density, or create very fast moving dislocations, which result in high impact stresses.

- v. As peening proceeds over the peening schedule, and all the surface becomes indented, these regions of plastic deformation merge to form a permanent global deformed and uniform [97] zone in the surface layers of the material, as showed in Fig.2.2.4. The mechanism occurring at this stage could be explained by the work carried out by Frost and Ashby [98], namely; as the target material becomes saturated, the already higher dislocation density results in lower mean dislocation velocities and accordingly lower impact stresses, i.e., as peening proceeds, the targeted material work hardness and the subsequent impacts become more elastic in nature.

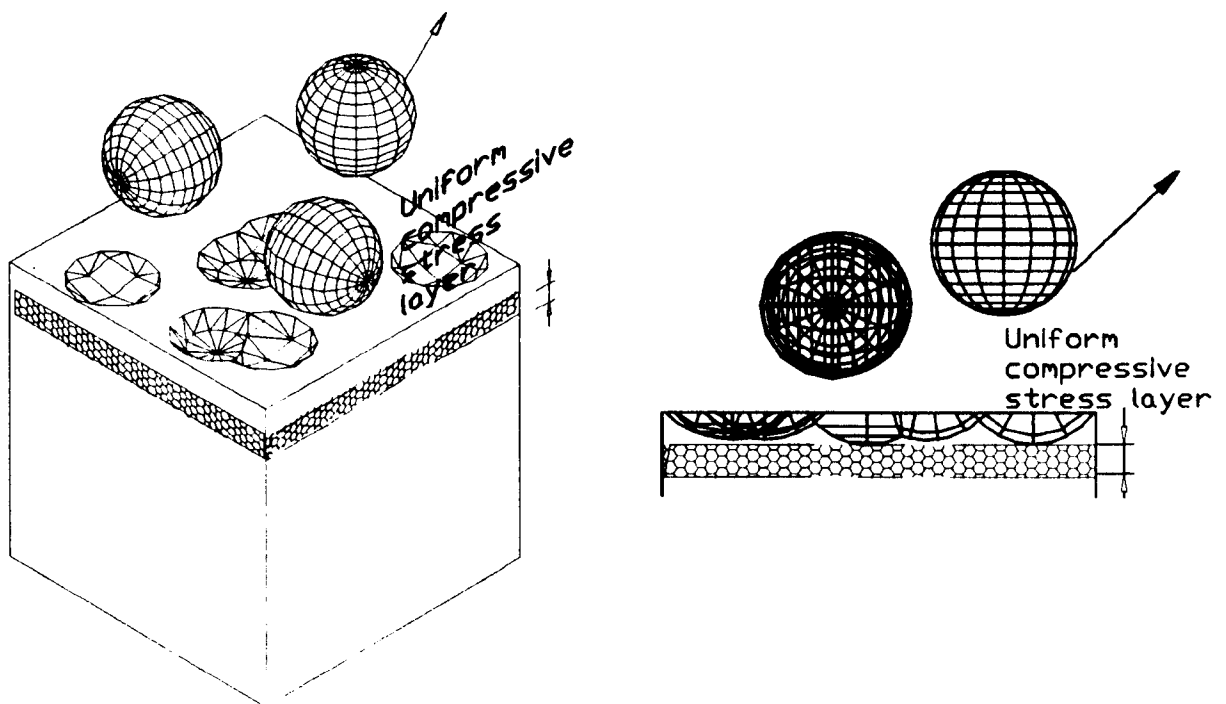


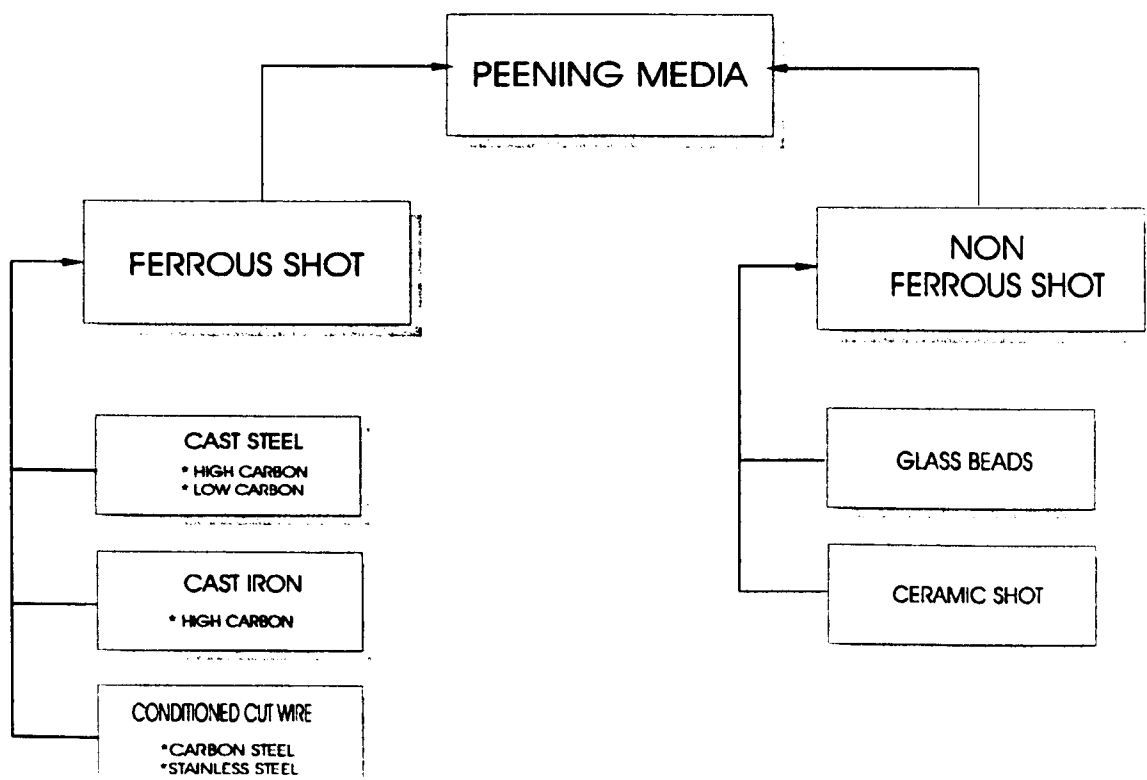
Figure 2.2.4 Schematic diagram of: low coverage (six dimples) produced after impacting of the shots on the left, and a sectioned view of the dents representing the formation of a plastically deformed layer in depth, resulting in an approximately uniform compressive residual stress layer underneath the surface when 100% coverage has been reached. An increase of dislocation density or creation of very fast moving dislocation also takes place.

2.2.3 Shot peening nomenclature and control parameters

There is a considerable body of work which provides evidence that there are primarily six process parameters employed to describe a shot peening condition [82, 85, 87, 99, 100], namely: 1) Shot, 2) Incidence angle, 3) Intensity, 4) Saturation, 5) Velocity and 6) Coverage, as shown in the flow diagram of the process in Fig. 2.2.5. Control parameters are adjusted to obtain desired values of intensity, saturation and coverage. The magnitude of the residual compressive stress and the depth to which it extends beneath the surface of the component must be controlled. It becomes immediately apparent that for shot peening to be consistently effective and reproducible; the shot, intensity and coverage must be closely under control [101].

2.2.3.1 Shot Peening Media

SP media should be spherical in accordance to standardised specifications [82, 102]. There is an extensive range of production media, including:



Cast steel shot has been widely used both in industry and in research for a considerable time [103], although, it is well known that it has a wide size distribution [104, 105] and can also fracture, resulting in debris often being found embedded in the surface layer [87] and can produce lower fatigue life often below that for an unpeened material [106, 107]. Conditioned cut wire is made from steel wire which is cut into pieces of approximately the same length as the wire diameter. The cut wire is conditioned to eliminate sharp edges and form spherical shaped shot [108]. Flavenot [109] found that despite having a greater deviation from perfect spheres than comparable cast steel shot, a more uniform size distribution and better wear properties are normally attributable to this type of media. However, in use, cut wire shot seldom fractures but wears to a small size. There still exist, though controversial statements regarding the effect of peening in terms of fatigue when using cut wire and cast steel shot on aluminium alloys, as reported by Edwards [110]. Glass and ceramic beads have been used for providing better surface finish and, therefore for improving fatigue performance, but due to premature fracture, they are for economic reasons not so often used. In support of this, it has been reported [111] that the mean size of broken ceramic shot is 1.5 times larger than glass beads for the same nominal diameter.

Despite these latter observations, it is difficult to obtain a clear picture regarding the use of ceramic or glass beads since it is claimed [112] that ceramic beads are both economically and technically feasible for implementation into a SP process. Indeed all types of shot wear and fracture to some extent. It becomes immediately apparent that size and shape control of shot media is significantly important in terms of the fatigue resistance. In this respect, Gillespie [106, 113] has contributed in the development of image analysis techniques to provide control on shot shape and size, leading to a more efficient and accurate manner of controlling the media and it may be used together with the classical methodologies recommended in [82, 114].

Direct-pressure and gravity induction machines (described in chapter IV) will handle all types of media. The selection of which media to use will depend on the type of metal part to be peened, the intensity required, and type of shot peening equipment (see appendix I for general guidelines).

PEENING SYSTEM

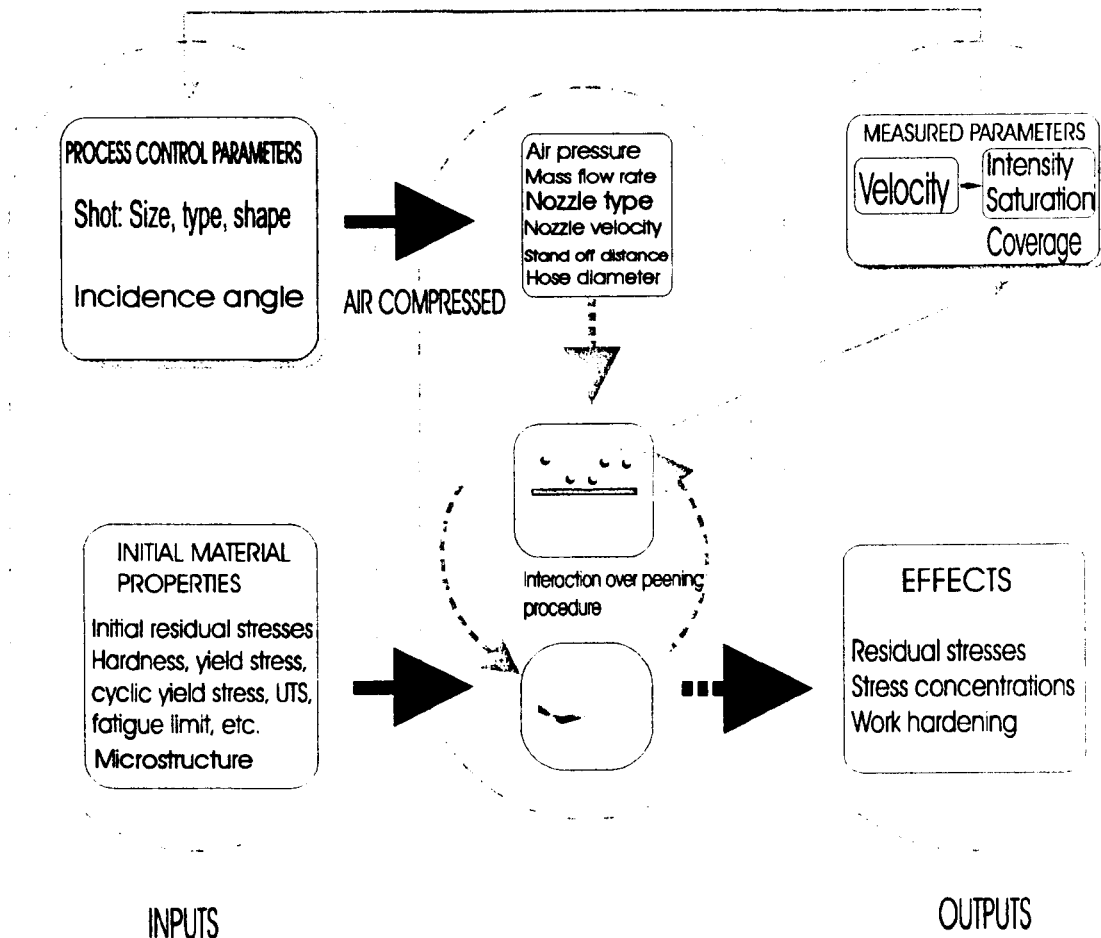


Figure 2.2.5 Control process parameters involved in the SP of a component. These parameters are independent of the machine used. Shot media and angle of incidence are controlled directly, while conversely; saturation, intensity and coverage need to be measured.

2.2.3.2 Incidence angle

The angle formed between the direction of projected particle and the material surface constitutes the incidence angle parameter. Base on experimental work, Iida [115] observed that for the same velocity, the yield zone is symmetric and increases with increase of impact angle. Differently expressed, the indentation produced by normal impact (typically 90°), is larger than that of a shot projected within an inclined angle. This is schematically illustrated in the Fig. 2.2.6. In the case of normal impact, and considering that the shot penetrates elastically into a semi-infinite body without spinning and no sliding, the size of the dent is given by [91]:

$$a = \frac{D}{2} \left(\frac{5}{2} \pi \rho \frac{V_i^2 e_r^2}{E_H} \right)^{\frac{1}{5}} \quad (2.23)$$

Where the parameters ρ , V_i , and e_r , hold for the same meaning as in § 2.2.2. E^* is the equivalent modulus given by $\frac{1}{E_H} = \frac{1-\nu_1^2}{E_1} + \frac{1-\nu_2^2}{E_2}$ where E_1 , ν_1 , E_2 , and ν_2 are the Young's moduli and Poisson's ratios of the shot and of the material respectively. D is the shot diameter.

For the case of inclined impact under the same assumptions, the size of the dent is given by:

$$a = \frac{D}{2} \left(\frac{5}{2} \pi \rho e_r^2 \frac{V_i^2 \sin^2 \alpha}{E_H} \right)^{\frac{1}{5}} \quad (2.24)$$

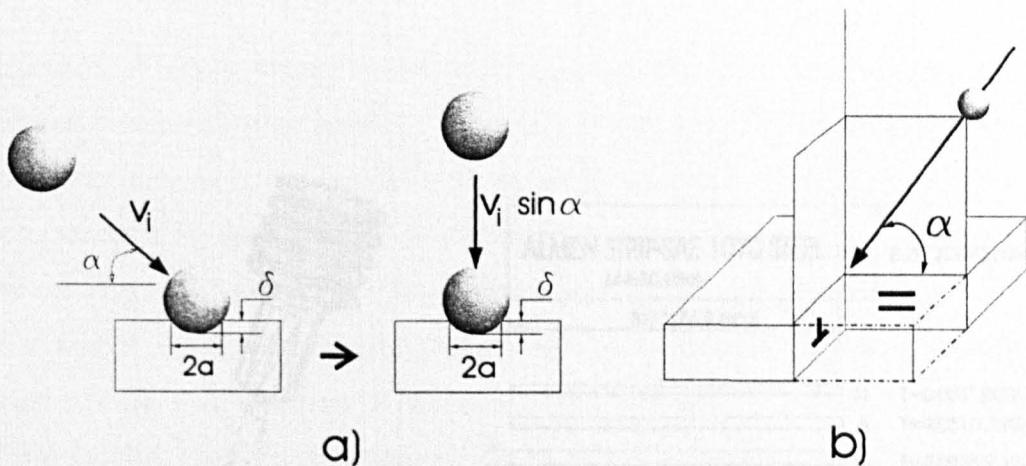


Figure 2.2.6 Schematic representation of: a) Effect of the incidence angle on size of indentation and b) The uniformity of the subsurface yielded layer which is not directional but decreases as the incidence angle increases.

2.2.3.3 Saturation condition

Saturation is used to describe the accumulation of dents on the Almen strip surface (see Fig. 2.2.7) and when achieved implies that plastic strain or work hardening is fairly uniform. In terms of compressive residual stresses in the surface of the Almen strip,

saturation corresponds to the point where further peening induces only a small increase in stress level [116]. Additional peening is useful for ensuring that the residual stress distribution is more uniform, i.e., full coverage. The saturation condition is attained when doubling the exposure time does not lead to an increase more than 10% in Almen strip arc height [82]. Due to the fact that it is fairly common for the saturation condition to be selected based on complete coverage of dimples (often by visual inspection of a peened Almen strip surface), additional peening is then required to complete the saturation curve. If an arc height of T represents the saturation condition, typically three additional measurements of exposure time, corresponding to 0.5T, 2T and 4T points should be obtained [82]. If arc height at 2T condition is less than 10% different from the arc height at the T condition, then the T point is defined as a valid saturation condition [85]. This is depicted in Fig. 2.2.8. Nevertheless, more or less exposure time may be required to attain 100% coverage on the material, i.e., saturation does not imply 100% coverage. This is due to the fact that saturation is characterised by Almen strip, and would only apply to coverage of Almen strip material.

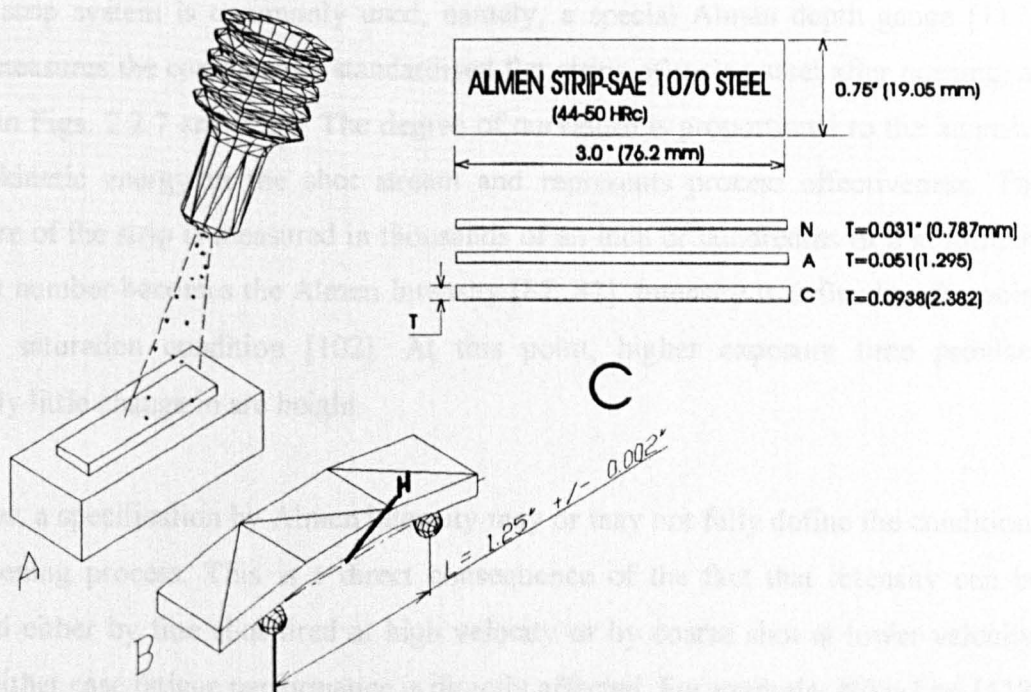


Figure 2.2.7 An Almen strip is exposed to the shot stream (A), provoking strip to deflect a magnitude H (B). The arc height deflection for obtaining saturation condition and intensity values is carried out employing standardised Almen strips (C).

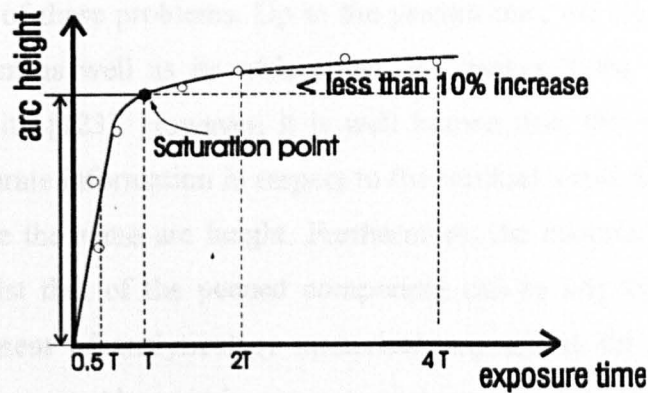


Figure 2.2.8 Schematic representation of the saturation curve showing the saturation point which is needed to define intensity.

2.2.3.5 Coverage

2.2.3.4 Intensity

Coverage is defined as the proportion of the specimen surface that is struck by a given peening type particle [99]. In order to quantify the intensity level, the Almen strip system is commonly used, namely, a special Almen depth gauge [117], which measures the curvature of standardised flat strips of spring steel after peening, as shown in Figs. 2.2.7 and 2.2.8. The degree of curvature is proportional to the intensity of the kinetic energy in the shot stream and represents process effectiveness. The curvature of the strip is measured in thousands of an inch or hundredths of a millimetre and that number becomes the Almen Intensity [82, 87]. Intensity is defined as the point for the saturation condition [102]. At this point, higher exposure time provides relatively little change in arc height.

However, a specification by Almen intensity may or may not fully define the conditions of a peening process. This is a direct consequence of the fact that intensity can be obtained either by fine shot fired at high velocity or by coarse shot at lower velocity, and in either case fatigue performance is directly affected. For example, Niku-Lari [118] obtained different depths of plastic deformation layer with specimens having identical deflection values. As a result, different residual stress distributions can be obtained from the same Almen deflection measurement, as evidenced by Person [119]. On the other hand, Almen strip variability may contribute to uncertainty in the intensity

measurements [120, 121]. All these factors have encouraged researchers such as Kirk [122] to develop new approaches for interactively controlling the SP intensity and so alleviating some of these problems. Up to the present time the clarity and definition of the Almen system as well as its widespread use, makes it the preferred system for measuring intensity [123]. However, it is well known that, this type of measurement cannot yield accurate information in respect to the residual stress field as different stress profiles may give the same arc height. Furthermore, the material used for the strip is pre-defined, whilst that of the peened component can be any different one. For this reason, development of analytical or numerical procedures for relating the residual compressive stresses to Almen strip measurements are increasingly reported because of higher available computer power [124].

2.2.3.5 Coverage

Coverage is defined as the proportion of the exposed surface which has been impacted in a given peening time, usually expressed as a percentage. Coverage also represents a measure of the uniformity of the residual stresses in the subsurface layer. Accordingly, less than complete coverage is ineffective since the unpeened portion of the surface would contribute to an uneven distribution of the residual stresses and consequently, significant reductions in fatigue performance [119]. “100%” coverage is often used to represent approximately complete coverage, i.e., when the entire surface of a reference area has been indented. In theory, “100%” coverage cannot be achieved; since the approach to “100%” coverage is exponential (the probability of a very small area being covered by a new impression becomes smaller with exposure time). The well known Avrami relationship [125, 126] supports such a statement:

$$C(t) = 100 \left\{ 1 - e^{-\pi r^2 R t} \right\} \quad (2.25)$$

where $C(t)$ is the coverage at any particular time, r is the average radius of the indentations, R is the uniform rate of indentation creation and t is the time during which the dimples were being created.

Recently, a theoretical model has been developed by Holdgate which can be used to predict the evolution of the coverage in a general peening system. The proposed model,

which is based on the original relationship used by the Wheelabrator Corporation [85], is given as:

$$C(t + \delta t) = 1 - \left[1 - C(t) \right] \prod_{j=1}^{n_s} \left[1 - \frac{a_j}{S} \right]^{\delta N_j} \quad (2.26)$$

Where $C(t + \delta t)$ is the coverage after an increment of time, δt ; $C(t)$ is the coverage at a known time t ; n_s is the number of peen sources; a_j is the total area of indentation caused by the peens from the j_{th} peen source at time δt ; S is the total area to be peened and δN_j is the number of peens from the j_{th} peen source expected to impact the reference area in an interval of time δt . A graphic representation of these two approaches together with some experimental data is shown in Fig. 2.2.9

From the above, complete coverage is therefore assumed to occur when the observed coverage reaches 98% as established in the related standards [102]. It is common practice that higher than complete coverage, multiples of “100%” are attained. Hence, for instance, 400% coverage is achieved by peening each specimen 4 times longer than that necessary for 100% coverage. Coverage can be assessed qualitatively by visual inspection of the peened surface employing a magnifying glass or by optical microscopy as occur in image analysis or following the dyescan tracer method. Finally, coverage is material-dependent. Softer materials will cover faster than hard materials.

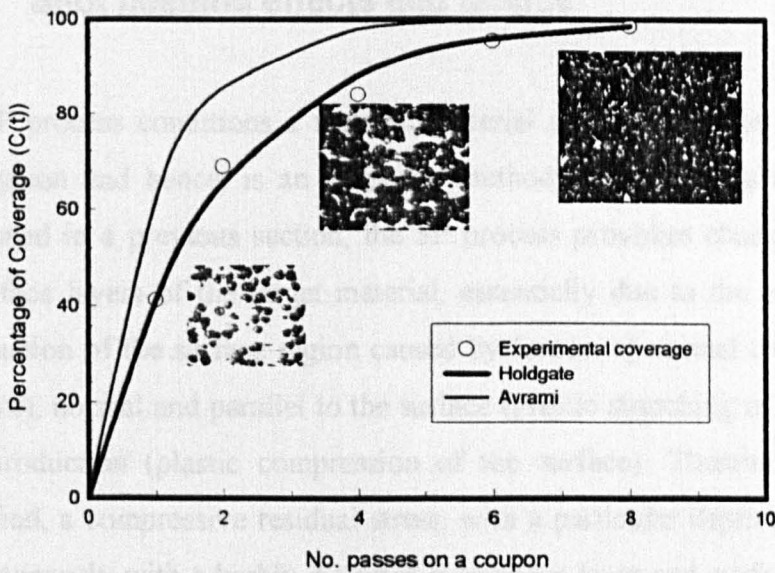


Figure 2.2.9 Experimental and theoretical coverage comparison (Al 2024-T351) with peening conditions: S230 shot, 30° incidence angle and 0.49 mmA (19.3A) intensity.

2.2.3.6 Velocity

Of the several significant peening parameters, velocity is the most important. This is because it characterises the event of impact [127]. Based on the fact that intensity is the kinetic energy transferred to the target material, it appears that the component of the velocity normal to the material surface controls the shot peening intensity. This latter assertion was experimentally confirmed by among others Meguid *et al.* [128], who found that higher velocity shots, whilst keeping other parameters constant, cause a deeper penetration over an Almen strip surface and result in larger arc height values. His findings concerning the effect of the incidence angle show a marked similitude with those of Iida, previously mentioned in § 2.2.3.2.

Velocity measurements have been a major obstacle to the accuracy of the SP process, due to the inherent difficulty presented. Although new devices and algorithms have successfully been incorporated in computer-controlled equipment [129, 130], which reduce considerably the problem of repeatability for that kind of SP machine, such devices are not yet in widespread use and, therefore, a velocity parameter has not been consolidated for process control.

2.2.4 Shot peening effects and fatigue

The SP process conditions a metallic material surface to resist (among others) crack propagation and hence, is an attractive method for improving fatigue resistance. As mentioned in a previous section, the SP process provokes changes in the surface and subsurface layers of the target material, essentially due to the inhomogeneous plastic deformation of the surface region caused by forces: a) normal to the surface (Hertzian pressure), normal and parallel to the surface (plastic stretching of the surface layer) and heat production (plastic compression of the surface). Thereby, as Vöhringer [131] identified, a compressive residual stress, with a particular depth distribution, is created simultaneously with a highly distorted subsurface layer and surface topography effects; all of them largely interrelated to the SP parameters and material conditions. A recent literature survey [132] gives evidence to a general consensus on identifying the major changes in the surface layer of the peened material, namely, residual stresses, hardness,

microstructure and topography as they seem to be the key factor for fatigue improvements. The survey also revealed that the compressive residual stress was considered to be the most effective peening effect for fatigue resistance. Figure 2.2.10 a-c illustrates such effects.

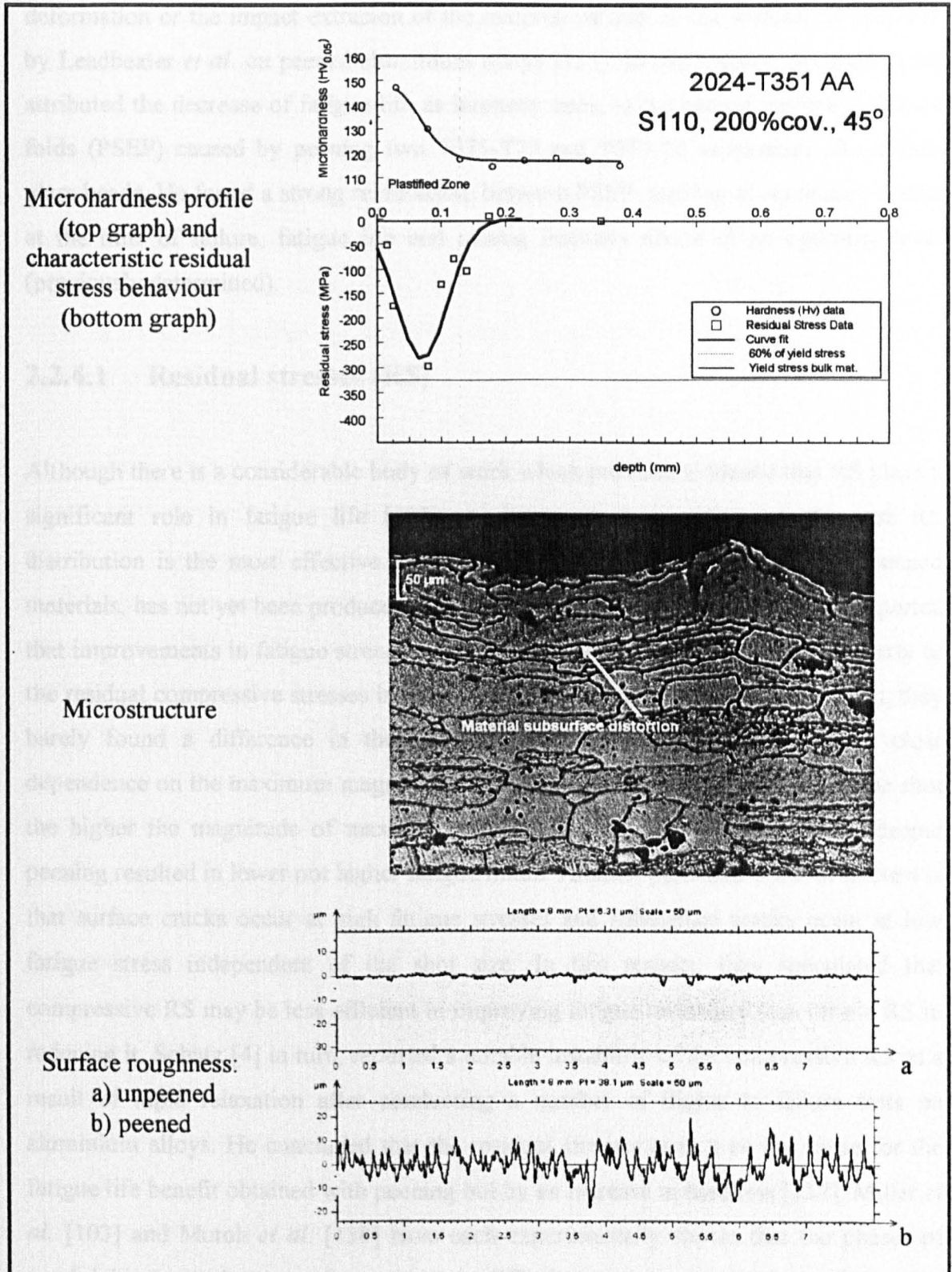


Figure 2.2.10 Different effects induced by particular SP conditions on 2024-T351 aluminium alloy.

Plastic deformation also occurs during the SP process, although the degree of saturation may depend on peening conditions and coverage. Accordingly, SP generates features such as persistent slip bands which are favourable crack nucleation sites and also a certain degree of folding produced on the surface as a function of the local plastic deformation or the impact extrusion of the material parallel to the surface, as observed by Leadbeater *et al.* on peened aluminium alloys [133]. In this respect, Simpson [134] attributed the decrease of fatigue life as intensity rises, to the peened surface extrusion folds (PSEF) caused by peening two 7075-T73 and 7075-T6 aluminium alloys with glass beads. He found a strong relationship between PSEF, number of secondary cracks at the time of failure, fatigue life and raising intensity above of an optimum level (previously determined).

2.2.4.1 Residual stresses (RS)

Although there is a considerable body of work which provides evidence that RS plays a significant role in fatigue life [135], a clear picture regarding whether the RS distribution is the most effective factor affecting the fatigue performance of peened materials, has not yet been produced. For example, Staker and Wohlfahrt [136] reported that improvements in fatigue strengths of carbon steel can only be attributed directly to the residual compressive stresses induced by SP. By using two different shot sizes, they barely found a difference in the surface residual stresses but there was a clear dependence on the maximum magnitudes of the RS distribution, i.e., the larger the shot the higher the magnitude of maximum RS and the deeper it is. In contrast, deeper peening resulted in lower not higher fatigue limits. Another particular point of interest is that surface cracks occur at high fatigue stresses and subsurface cracks occur at low fatigue stress independent of the shot size. In this respect, they speculated that compressive RS may be less efficient in improving fatigue resistance than tensile RS in reducing it. Schutz [4] in turn, reported a notable instability of the compressive RS as a result of rapid relaxation after conducting a number of flights to failure tests on aluminium alloys. He concluded that the residual stresses cannot be the cause for the fatigue life benefit obtained with peening but by an increase in hardness [137]. Miller *et al.* [103] and Mutoh *et al.* [138] have each experimentally shown that the phases of crack initiation and propagation completely differ between peened and those obtained in unpeened samples (carbon steels and aluminium alloys respectively). Whereas crack

initiation tends to accelerate in the early stages of fatigue, crack growth rate during subsequent periods is significantly slower. On the one hand, Miller observed the occurrence of quasi-cleavage fractures involving limited plastic deformation. Since this is a feature of the hardened surface layer, he attributed the crack growth deceleration to the great number of microstructural barriers in the highly deformed grains, the high dislocation density and the compressive residual stresses induced in such a hardened layer. On the other hand, Mutoh attributed the acceleration of crack initiation to the stress concentration in the roughened surface; particularly at fold-like defects caused by SP. After having observed early black fretting debris flowing from the mouth of the crack during testing caused by early closure and rubbing of the fracture facets, he credited the reduction in crack propagation rate, to the action of the RS acting as closure of the crack faces. Analogous conclusions were put forward by Song [139], namely, the resultant growth retardation is assumed to be due to the crack closure.

In contrast, Sharp and Clayton [140] argued that from measurements undertaken on 7050-T7451 aluminium alloy the peak of RS appears stable over fatigue testing. There was a minor amount of stress relaxation due to cyclic loading affecting the average surface value. Similarly, Farrahi [141] attributes the fatigue life improvement directly to the maximum RS and also to the depth of the plastically deformed layer. He found a correlation between the fatigue life and the area of the RS distribution. Contrary to Sharp's observations, the RS decreased during the fatigue stressing. This reduction was found to be a function of the applied stress and the depth of the plastically deformed layer. The RS, however, always remained compressive.

There is a strong consensus of opinion regarding the beneficial effect of the SP treatment on crack growth life. RS have proved to be a crucial factor in the fatigue performance of metallic materials. In this context, a significant amount of work has been done to model, predict or measure the evolution of RS due to particular SP conditions. This body of work is of prime importance in order to develop an understanding of the mechanisms of the creation of RS and to analyse the influence of the relevant parameters in order to obtain the required fatigue life. It is worth mentioning at this point the pioneer contribution of Al-Hassani [142] who analysed the mechanics of the SP from the static and dynamic point of view. Meguid [143, 144] employed 2D finite elements in the analysis of the RS caused by SP. Hills and

Waterhouse *et al.* [93] carried out an analysis of the stress field and correlated the RS distribution with the Almen number. Later, Cao *et al.* [145] was able to correlate more accurately the Almen arc height with RS, and proved the existence of a characteristic double curvature (longitudinal and transverse direction) of the Almen strips after peening. After a comprehensive analysis, Fatallah *et al.* [91] developed a method for predicting RS distributions, while Ogawa and Asano [146] developed a simple procedure based on the stress-strain relationship of the target material and the SP conditions. Recently, Guagliano *et al.* [147] successfully related the SP parameters to the induced RS by running 3D finite element modelling and discussed the optimisation of the process but only in terms of the RS effect.

Boyce, Chen, Hutchinson and Ritchie [95] very recently assessed the residual stresses caused by a spherical projectile upon a flat surface. By using finite elements to characterise the impact event, they found two prominent residual tensile regions as illustrated in Fig. 2.2.11.

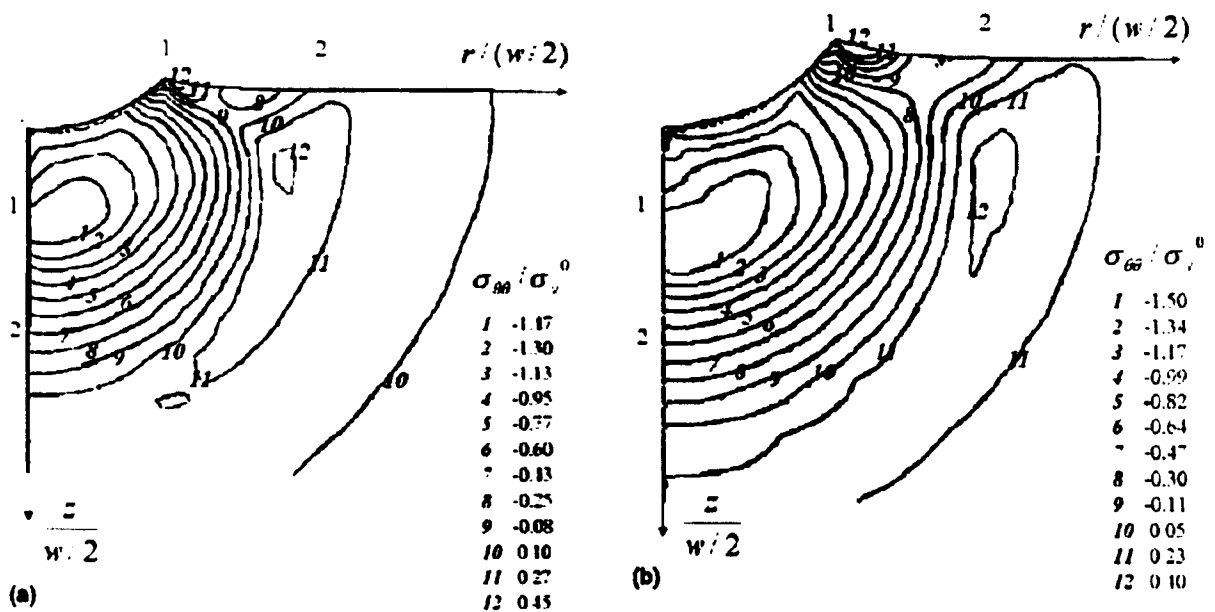


Figure 2.2.11 Residual stresses contours $\sigma_{\theta\theta}$ predicted from finite elements analysis for a) 200 and b) 300 m/s impact velocities. The residual stresses presented were normalised by the yield stress at zero strain rate, σ_y^0 (after [95]).

One of these regions is at the crater rim, and the other located away from the rim and below the surface. These regions of tensile residual stress were shown to increase the local mean stress during subsequent fatigue loading, thereby accelerating the initiation and propagation of fatigue cracks. Significant compressive stresses were found in a large zone beneath the dimple, roughly one dent radius below the dent floor. However, these residual stresses at the indentation rim may be offset by multiple overlapping shots or complete coverage. Nevertheless, incomplete peening coverage of the surface will leave uncompressed rims and consequently important reductions in fatigue life.

2.2.4.2 Work hardening and Microstructure

Fatigue of peened specimens is, in fact, equivalent to stress cycling about a superimposed mean strain. The material on the surface layer undergoes stress fatigue after the cyclic strain during SP. One may appreciate that the tendency of changes of the microstructure in the peening affected surface layer is analogous to the microstructure changes which occur in the fatigue process, even though, the applied cyclic strain is in this case of the compressive type. Evidently this view possesses some degree of controversy. The cyclic hardening in aluminium alloys can act as microstructure strengthening and the cyclic softening in some steels as microstructure weakening. To support these assertions, Lillamand *et al.* [148] very recently has proposed a methodology which describes the SP process by a new cyclic approach: 'In terms of cyclic confined plasticity, the SP conditions do not differ considerably from the low cyclic fatigue of a notched sample where the Chaboche model is often used in such multiaxial loading cases'. However, in the Lillimand's analysis there were major limitations: i) the impacts were normal to the treated surface, ii) the geometrical evolution of the treated surface and the dynamic effects of the impact were neglected, iii) the XX and YY directions were mechanically equivalent with non-zero residual stresses, iv) the interference between two simultaneous impacts was neglected, and v) the successive shot-impacts at the same position were considered.

It is clear, therefore, that for peened samples the fatigue behaviour depends strongly on the RS induced by SP and hence the microstructural effect. Accordingly, the microstructural changes evidenced through the SP, may be seen as:

- i. Development of slip bands due to plastic deformation

- ii. Grain and sub-grain size changes caused by the plastic deformation and the corresponding increased dislocation density.
- iii. Phase transformations originated by the cyclic plastic deformation of the impacting process.

Wang *et al.* [149, 150] have systematically undertaken experimental work finding much evidence of the above assertions. Through X-ray diffraction the dependence of the integrated breadth of the diffraction line on the depth distance from the surface were measured successively on aluminium alloys. He observed that the plastic deformation in the surface layers was homogeneous and hence, the crystal slip was homogeneous. Because of this, fragmentation of sub-grains and an increase of dislocation density may be created giving rise to strengthening of the microstructure in the surface layers. They have reported decreases in sub-grain sizes in René 95 due to SP from 0.179 to 0.015 μm and also observed transformation of γ' (45%) to γ (25%) phase in the surface layer of the same alloy caused by the cyclic plastic deformation of the SP process.

In contrast to the view taken by Wang *et al.*, Timothy and Hutchings [151] observed that plastic deformation beneath the dents was not homogeneous at high velocities (on the order of 50-340 m/s). Adiabatic shear bands were formed for impact conditions corresponding to indentation diameter/shot diameter ratios of around 0.57 to 0.65, which occur for some critical value of strain.

2.2.4.3 Topography (surface roughness)

An increased number of investigations have concluded that the effect of surface roughness may be very pronounced since the fatigue behaviour can change from crack propagation controlled (rough surface condition) to crack nucleation controlled (smooth surface condition) if additional polishing is used after SP. Wagner and Luetjering [152] have shown that easy crack nucleation at rough surface of titanium alloys resulted in a notable loss in fatigue strength. Marked similarities upon the roughness effect on fatigue behaviour (three-point bending) of 2024-T351 and 7075-T7351 aluminium alloys have been reported by Bonnafé and Bathias [153]. Simpson and Probst [154] have also studied the relationship between SP conditions and surface topography of 7075-T6 aluminium alloy and 4340 steel alloy with regards to their effects on axial fatigue

testing. They unequivocally attribute the specimen surface condition in relation to smoothness and lack of surface discontinuities as a contributing factor to attainment of an optimum peening intensity and maximum fatigue life.

There remains little doubt regarding the presence of roughness and its detrimental effect on materials subjected to SP. Unsurprisingly, due to the difficulty in calculating the stress concentration coefficient from many dimples, this effect had been quantitatively ignored from life predictions cf. [2, 136, 155]. The most detailed analysis of the stress concentrations caused by SP is that conducted by Li *et al.* [156]. By using the finite element method, the stress concentration factor (K_t) due to specific surface roughness parameters, R_t (peak dimple depth) and S_m (dimple spacing) over some sample distance is calculated based on simplified modes of indentation. The influence of stress concentration and RS was respectively incorporated as a stress intensifier and mean stress into the Goodman equation to predict fatigue life.

2.2.5 SP control parameters correlations with life behaviour

The notion of a systematic study regarding the influence of process parameters in blasted parts was firstly suggested by Zimmerli [80] as mentioned in § 2.1. He varied not only the time of shot blast but also the ball sizes (0.39-1.19 mm diameter), and stated the effects of the blasting process on the fatigue resistance of springs.

There have been an increasing number of investigations into the effect of the process parameters over the last three decades. Meguid [143] accounted for the effects of the different control parameters on the peened component properties, and studied the mechanics of the SP itself. He managed to predict the residual stresses in target components from the results obtained from single indentations and chosen control parameters, assuming complete coverage. He observed that the larger the shot the deeper the depth of the plastically deformed surface and that smaller shot yielded a shallower but more uniform depth of the plastically deformed zone. This latter finding is highly significant to fatigue performance since the benefit of having a uniform plasticised zone after SP is well known. Finally, he noted that the larger the shot the longer it takes to reach saturation, giving also an increase in arc height for the same

exposure time. However, though, there is an optimum magnitude of intensity which produces maximum fatigue life [154]. Regarding the angle of impact, maximum depth of the compressive residual stress is achieved when using 90° or normal to the target surface, comparable to the results of Iida [115].

The effect of shot peening variables was also reported by Person [119]. For the same intensity level, fatigue life increased with decreasing shot size in aluminium 2025-T6. It would seem to be a contradictory result as it differs from all those in which for equal intensity, larger shot sizes produce higher compressive stresses in aluminium alloys. Higher compressive stresses would be expected to increase fatigue life. However, it is now known [138] that shot impacts produce stress concentrations in the rough peened surface and hence an acceleration of crack initiation (fold-like defects) which reduces markedly fatigue life. The implication of such results supports the fact that a uniform compressive stress layer attained from the use of fine shot enhances fatigue behaviour [104].

On the other hand, Neema and Pandey [157] examined the changes in roughness and hardness by peening a turned surface (0.5%C steel) under controlled conditions. They found that controlled peening can be employed as a post machining operation for improving surface characteristics of the machined components. A design of experiments technique was successfully applied in their investigation for a range of SP control parameters in order to get their best levels and therefore the best target results. Horwath [158] in turn, determined the effects of the shot size, shot velocity and shot flow rate on the magnitude and distribution of residual stress, and on fatigue life of a SAE 1074 steel by using design of experiments concepts. A fractional factorial technique was utilised. Application of the statistics/design of experiments as a medium to quantify benefit/cost ratio has with time become more common in manufacturing processes like shot peening, as pointed out by Vahratian and Garibay [159]. They give comprehensive arguments regarding the employment of relationships between the levels of critical SP process parameters and the fatigue performance of the automotive components, by utilising among others statistical design of experiments methodology. Nevarez and Nelson [160] applied robust design principles to the fatigue life evaluation of a 4340 steel. An extensive set of controllable and uncontrollable parameters for relevant material properties, peening parameters and crack-like micro-discontinuities was identified.

Robust design methodology permitted them to speculate on the mean component life improvements and also the possibility of reducing the variability of that life subjected to the variability in process, material and geometric parameters. Whereas their results are consistent with those reported in the literature, they only use calculated residual stresses as the evaluated effects at high and low levels. This resulted into a limited appreciation of the effects produced by SP on the fatigue resistance.

Freddi *et al.* [161] employed design of experiments to investigate the influence of the main parameters both on the distribution and values of the compressive residual stresses and on fatigue resistance. A classic methodology and a full factorial design of experiments were utilised. Residual stress effects on fatigue life were statistically analysed in order to estimate the optimum values of the process parameters. In this respect, Baragetti [162] put forward a general method that permitted the choice of the shot peening parameters and their relative best levels by using a low alloy steel. It was done by means of design of experiments employing the Taguchi method. This procedure enabled the optimisation of a number of controllable and uncontrollable variables [163]. The experiment was based on the analysis of four factors and two levels: shot diameter (1 and 2 mm), impact speed (80 and 120 m/s), shot material (steel and ceramic) and percentage of coverage (1 and two impacts). Seven different effects (maximum residual stress, depth of the maximum residual stress, surface residual stress, depth of the compressed layer, compressed area, diameter of the trace left by the shot after the impact on the specimen and trace depth or surface roughness) were considered and a fractional factorial array was utilised. These effects were obtained from numerical simulations employing finite elements. As a result, he reported that for the levels considered, all the factors influencing the treatment effects were taken into account. Shot velocity and material had no influence on the effects that enabled the characterisation of the residual stress field, while, to have a better surface finishing, he suggested shot peen with ceramic 1mm diameter shot by using low speeds of impact. In his analysis, he makes clear that if the aim is to optimise the effects that permit the characterisation of the residual stress field (once the magnitude of the surface damage induced by too high peening intensities on the fatigue resistance has been quantified), the shot diameter at level 2mm and the percentage of coverage at 2 impacts were the most important factors.

In Gerald Nachman's perspective [164], modern shot peening technology should be accomplished with the use of engineering models, which would yield optimum shot peening parameters, which include media, residual stress (intensity) and cold work (coverage) specifications. He argued that the goal of any shot peening process must be optimum component life, no matter what the application. In this respect, Fuchs [165] successfully analysed the dependency between the optimum intensity and the distribution of the stresses and self-stresses below the surface, after fatigue testing, in order to estimate the optimum intensity.

2.3 SUMMARY

The formation of fatigue cracks in components is generally on the free surface of the component. The fatigue process consists of the following phases: a) work hardening or softening, b) crack initiation, c) crack propagation and d) instability or final failure. There are many favourable sites for crack initiation, among others: a) slip bands, b) grain boundaries c) inclusions, and d) surface stress concentrators. Crack formation will therefore depend on the microstructure and manufacturing process of the material, the type of loading and shape of the component. There are three major stages of crack growth, i.e., stage I, II and III. In each stage a different separation mechanism or mode operates. Each type of crack (long, short or physically small) requires its particular type of analysis to adequately describe the propagation behaviour. The approaches in terms of linear elastic fracture mechanics (LEFM), elasto plastic fracture mechanics (EPFM) and microstructural fracture mechanics (MFM) are predominantly used for such purposes. Basically, the relative extent of the plastic zone ahead of the crack tip defines the difference between long and short cracks. Increasing attention has been granted to the analysis of short cracks due to their tendency to grow faster than long ones under the same nominal driving force. For that reason, many models have appeared in order to characterise crack propagation. Amongst them, the three zone micro-mechanical model developed by Navarro-de los Rios has been shown to provide realistic results with the possibility of this being extended to incorporate the effect of shot peening. In this respect, shot peening modifies the surface and properties of the peened surface, and

therefore characterisation of fatigue damage need to be described in terms of short crack behaviour.

A shot peening condition can be defined by such variables as: a) Shot, b) Incidence angle, c) Intensity, d) Saturation, e) Velocity and f) Coverage. From these, velocity is likely to be the most important control parameter, but it is, the most difficult to measure. The majority of the existing techniques for measuring velocity of the shot make use of the optical methods (photo detectors), which record the intersection of a beam (white light or laser) into an optical receiving system, e.g. see [90].

SP produces changes to the target material, including modifications to microstructure, and topography and the creation of a compressive residual stress. Some of these changes are beneficial but some can be significantly detrimental. These opposite effects are often difficult to understand and poorly related to the peening conditions. Thus, the balancing between beneficial and detrimental effects makes it difficult to be certain regarding the peening behaviour and its impact on fatigue performance. In general, one can speculate that peening conditions for optimum fatigue strength should result from a surface hardening as high as possible, compressive residual stresses as large as possible with a penetration as deep as possible and with a surface roughness as low as possible. Compromises have to be made, however, (due to the complex interaction) to attain these final conditions.

2.4 THE COMMERCIAL HIGH STRENGTH 2024-T351 AND 7150-T651 ALUMINIUM ALLOYS (AA)

Aluminium alloys (AAs) are widely recognised as the best choice for many engineering applications, mainly because of their high strength to weight ratios and availability in a variety of forms. Commercial AAs provide specific combinations of strength, toughness, corrosion resistance, weldability and fabricability. In the aerospace industry, for either civil or military aircraft, AAs, particularly of the heat-treatable 2xxx (Al-Cu-Mg) and 7xxx (Al-Zn-Mg-Cu) series, have long been used for structural applications in a wide range of operating temperatures and loading rates. The reason for this is that almost all AAs are insensitive to strain rates between 10^{-5} to 1 mm/mm/sec (~ 105 MPa/sec) at room and low temperatures [166]. In this context, nearly, 75% of the structural weight of the Boeing 757-200 aeroplane is comprised of plates, sheets, extrusions and forgings of 2024, 2224, 2324, 7075, and 7150 AAs [167]; common parts include, body frames, fuselage (frames, skins, and substructures), wings (stiffeners, ribs, stringers, and skins), and horizontal stabilisers. Despite facing strong competition from emerging composite technologies, AAs continue to be widely used as the workhorses at the aircraft industry, mainly for economic reasons.

2.4.1.1 Characteristics of AAs classes

AAs are classified in several ways, ASM [166] distinguish them according to their strengthening mechanisms, namely: a) primarily by strain hardening (-H) and b) by solution heat treatment and precipitation ageing (-T). Aluminium Association Standards and data handbook [168] classifies the AAs grouping of wrought AAs by their strengthening method, major alloy element, and relative strength. Another classification system is that of the International Standards Organisation (ISO), which utilises the alloy element abbreviations and the maximum indicated percent of element present. Fig. 2.4.1 shows the main classification of the AAs based on the constituent elements, alloy compositions, and strengthening mechanisms. Commercial aluminium products offer medium-to-high strengths. Of these, 2xxx and 7xxx alloys are commonly utilised in

applications involving highly stressed parts [166]. Basic temper designations are H: strain hardened (wrought products only), H is always followed by two or more digits. T: Heat treated to produce stable tempers, and is always followed by one or more digits [169].

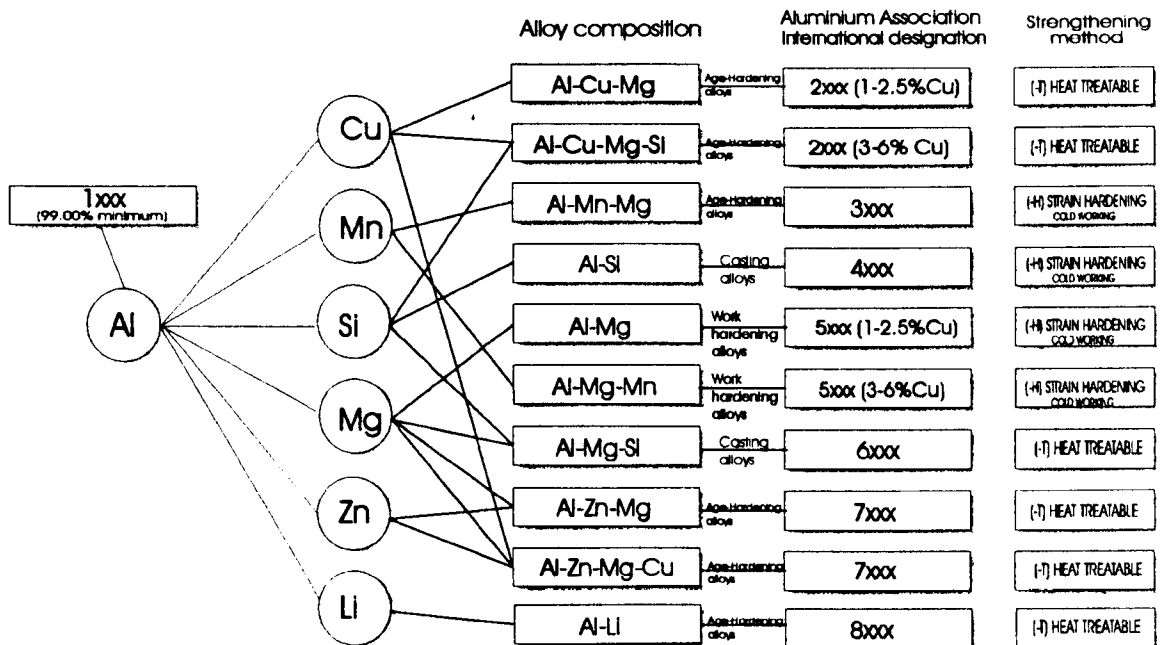


Figure 2.4.1. Principal aluminium alloy elements along with the international designation. The most prominent systems are 2xxx (2024-T351) and 7xxx (7150-T651) series whose major elements are Al-Cu-Mg and Al-Zn-Mg-Cu respectively.

Bearing in mind the above designation system, the specification for the AAs utilised in this work is as follows:

- i. The alloy 2024-T351 is a high strength AA solution heat treated, cold worked (stress relieved by means of a controlled stretching after the solution heat treatment from 1½-to 3% for a product in the form of plate as it is the case for the material used in this research), and naturally aged (room-temperature ageing) to a stable condition.
- ii. The alloy 7150-T651 is a high strength AA solution heat treated, cold worked (stress relieved by means of a controlled stretching after the solution heat treatment from 1½-to 3%), and artificially aged to a stable condition, which

produces mechanical properties to the level of maximum strength and provides some special characteristics as exfoliation corrosion resistance.

2.4.1.2 Fundamentals of the heat treatable AAs.

Broadly speaking, there are two fundamental methods of increasing the strength of aluminium alloys [170]:

- i. Dispersion of second-phase constituents in solid solution and cold working (non-heat treatable alloys).
- ii. Dissolution of the alloy constituents into solid solution and precipitation of coherent submicroscopic particles (heat-treatable or precipitation-hardening alloys).

The most prominent systems are Al-Cu-Mg and Al-Zn-Mg wrought alloys, viz. ternary systems in terms of the solutes involved in developing strength by precipitation. The mechanism of strengthening by age-hardening entails the creation of the coherent clusters of solute atoms, i.e., atoms of solute collected into a cluster but still holding the crystal structure of the solvent phase. As a result, the cluster stabilises dislocations. When dislocations are trapped by coherent solute clusters, the alloy is significantly strengthened and hardened. On the other hand, if precipitates are either: a) semicoherent, i.e., sharing a dislocation-containing interface with the matrix, b) incoherent, when sharing a distorted interface, similar to a large-angle grain boundary, with the matrix, a dislocation can circumvent the particles under the action of an applied shear stress. This effect provides higher strength by obstructing and retarding the movement of the dislocations. It is important to point out that the characteristic by which a precipitate phase is coherent or noncoherent is determined by the closeness of match or the degree of discrepancy between the atomic spacing on the lattice of the matrix and on that of the precipitate.

The solution heat treatment is done at high temperature to maximise solubility, followed by rapid cooling or quenching to obtain a supersaturated solid solution of both solute elements and vacancies (to allow diffusion). The precipitation process involves the solute clusters developed from the saturated solid solution, which contributes to the

formation of transitional (nonequilibrium) precipitates. However, the final structure basically consists of equilibrium precipitates, which contribute to age hardening.

The complete decomposition procedure of the supersaturated solid solution is an extremely complex process which usually includes the formation of the Guinier-Preston (GP) zones, intermediate precipitates and the final equilibrium phase. The GP zones [171] are ordered, solute rich clusters of atoms which have a thin plate shape of uniquely one or two atom planes in thickness. They retain the structure of the matrix, are coherent, and generally finely dispersed.

The high strength is produced by the finely dispersed precipitates formed during the ageing heat treatments, which may include either natural or artificial aging.

2.4.1.3 Constituent phases or microstructures

a) 2024-T3 Alloy

Aluminium-copper alloys are usually complex due to the many additives used for strength, corrosion resistance, or grain structure. A multiphase ingot structure includes the following constituents [168]: $(\text{Mn, Fe})_3\text{SiAl}_{12}$, Mg_2Si , CuAl_2 , and Al_2CuMg , and occasionally $(\text{Fe, Mn})\text{Al}_3$ or $(\text{Mn, Fe})\text{Al}_6$. Successive heating dissolves much of the copper and magnesium though leaving some Al_2CuMg and probably CuAl_2 out of solution. Most of the iron-containing phases experience transformation to $\text{Al}_7\text{Cu}_2\text{Fe}$, possibly accompanied by other minor phases. Simultaneously, manganese is precipitated from solid solution as $\text{Cu}_2\text{Mn}_3\text{Al}_{20}$ dispersoid. Slow cooling causes Al_2CuMg to precipitate in a Widmanstätten pattern. Ming Gao *et al.* [172] identified in detail three constituent phases in the 2024-T3 alloy: Al_2CuMg , Al_2Cu , and an Al-Fe-Mn-Si-Cu rhombohedral phase. They pointed out that other phases were found in the iron-containing particles but were not studied.

b) 7150-T6 alloy

In cast ingot form, this alloy forms one or more variants of $(\text{Fe, Cr})_3\text{SiAl}_{12}$, Mg_2Si , and a pseudobinary eutectic made up of aluminium and MgZn_2 . Subsequent phases contain

Mg(Zn, Cu, Al)₂. Subsequent heating causes the iron-rich phases to transform to Al₇Cu₂Fe. The relatively insoluble Mg₂Si tends to spheroidise somewhat; Mg(Zn, Cu, Al)₂ rapidly dissolves, and at the same time Al₂CuMg precipitates. Cr is precipitated from supersaturated solution as Cr₂Mg₃Al₁₈ dispersoid, heavily concentrated in the primary dendrite regions. Min Gao *et al.*, in turn, identified only two constituent phases: Al₂₃CuFe₄ and amorphous SiO₂.

A major microstructural feature of the 7xxx series alloys is the precipitate free zone (PFZ), i.e., zone adjacent to grain boundaries depleted of precipitates, which is located along both grain and subgrain boundaries [173]. The exact mechanism of this formation is not clear, although its existence has been described as: 1) they may originate adjacent to a grain boundary where the equilibrium phase has nucleated heterogeneously and solute depletion has happened due to the rapid diffusion along the boundary to stimulate the growth of the grain boundary particle, and 2) due to the action of grain boundaries of attracting and thus removing vacancies from the surrounding areas which limits the homogeneous nucleation of strengthening phases [174]. The size of either type of PFZ may be limited by lowering the ageing temperature, since this increases the solute supersaturation, hence providing greater stimulating force for homogeneous nucleation and reducing the diffusion rate which retards the formation of the equilibrium phase. For this reason, commercial ageing treatments usually encompass two stages, the first being at low temperature to produce a structure containing a dense dispersion of fine precipitates with contracted PFZ's and the second at higher temperature to accelerate the growth and transformation of the precipitates [175].

2.4.1.4 Metallurgical factors on fracture toughness and fatigue performance

Hahn and Rosenfield [176] define toughness of AAs as the resistance to crack extension by the ductile or fibrous mode, which includes the growth and linking-up of voids nucleated by the cracking or decohesion of second phase particles. Hence, fracture toughness depends on a) the extent of the heavily strained region ahead of the crack tip, which is a function of yield strength and modulus, b) the size of the ligaments which are related to the volume fraction of cracked particles and c) the work of rupturing the ligaments. The well known second phase particles of interest are [175, 176]:

- i. Large Fe-, Cu-, and Si- rich inclusions of $\sim 0.1-10 \mu\text{m}$ in diameter formed during casting, or coarse particles of normally soluble phases formed during casting or subsequent processing, which crack easily as the matrix deforms plastically. This type of second phase particle is often described as a constituent particle.
- ii. Smaller intermediate particles, typically $\sim 0.1 \mu\text{m}$, Cr-, Mn-, and Zr- rich particles, formed during homogenisation, control recrystallisation and grain growth, and according to Hahn and Rosenfield are more resistant to cracking, and do not appear to be deleterious to toughness. Furthermore, they speculate that the intermediate particles rupture during the void linking-up stage after deformation becomes localised. This type of second phase particle is often described as dispersoid.
- iii. Small precipitates formed during aging from $\sim 0.01-$ to $0.5 \mu\text{m}$ which strengthen the matrix. The loss of toughness is connected with the presence of fine precipitate particles, the loss of strain capacity and the development of local plastic instabilities-superbands and large slip offsets. Strain localisation mechanisms are not well defined yet in AAs. Small precipitates are also known as strengthening precipitates and GP zones are included in these.
- iv. Grain sizes, which are intrinsically related to the precipitation of fine particles at the grain boundaries. Evidence shows that the preferential growth of precipitate particles at the grain boundaries is responsible for intergranular fracture paths and loss of toughness [175, 176]. Evidently, reductions in grain size make an improvement to fracture and fatigue.

It is recognised that, although all the three types of the second phase particles may influence the fatigue performance of AAs, their effect is highly dependent on the type of fatigue test or stress regime chosen for evaluation. Consequently, one should be aware that the fracture toughness response to the constituent particles will proceed to a different extent to that of fatigue behaviour. For instance, there is evidence that reduced iron and silicon contents do not always result in improved fatigue resistance proportionate to the enhancements in fracture toughness [177]. Again, some controversial views are found in related published work. For instance, Hempel [178] and Grosskreutz [179] have each reported that fatigue lifetimes could be enhanced by lowering the Fe and Si content or by careful processing to reduce inclusion content in

Al-Mg-Si, Al-Zn-Mg-Cu, and 2024 AAs. On the other hand, James and Morris suggested that for an overaged commercial Al-Mg-Mn alloy, initiation at coarse intermetallics is dominant in low cyclic fatigue whilst grain boundary initiation is dominant in high cycle fatigue [180].

In terms of fatigue crack propagation (FCP) rates, no consistent differences have been observed for low and high purity 7xxx alloys variants at low to intermediate ΔK levels [181]. Nevertheless, at high ΔK , FCP rates are significantly reduced in low iron and low silicon alloys. This was attributed to the higher fracture toughness of high purity metals. In a given alloy system, slight changes in composition that promote hardening precipitates have hindered the S-N fatigue behaviour of AAs. However, considerable discrepancies have been observed when comparing of alloys of different systems as depicted in Fig. 2.4.2. Thus, 2024-T3 is known to outperform 7075-T6 at stresses within the medium cycle fatigue range ($\sim 10^5$ cycles). The 2024-T3 alloy shows relevant advantages over 7075-T6 and other 7xxx alloys in FCP. Furthermore, this superiority extends over the entire da/dN vs ΔK range (Fig. 2.4.3).

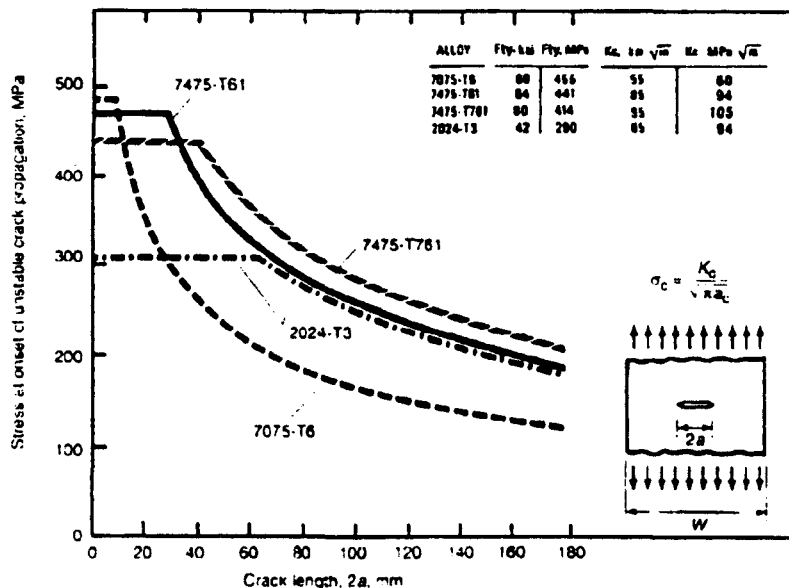


Figure 2.4.2 Initiation of unstable crack propagation vs. crack length of different alloy systems (after [166]).

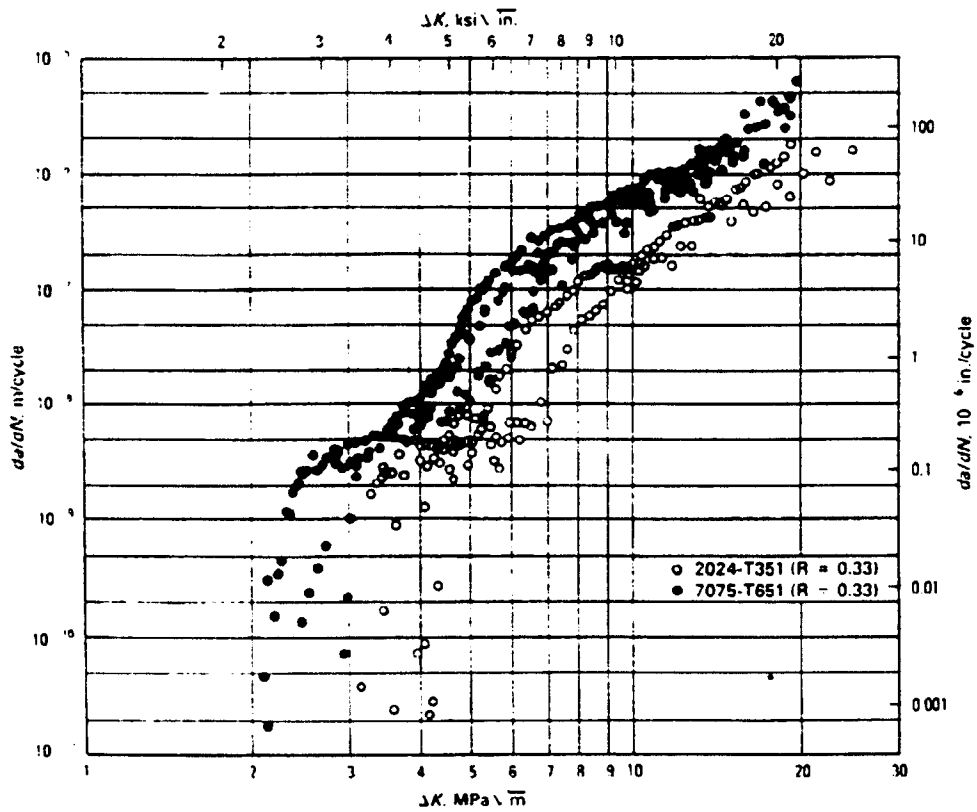


Figure 2.4.3 Fatigue crack propagation rate of 2024-T351 vs. 7075-T651 over entire $da/dN - \Delta K$ range (after [168]).

CHAPTER 3

ANALYTICAL FRAMEWORK

As shot peening alters the microstructure and properties of the peened layer, characterisation of fatigue damage in peened surfaces needs to be done in terms of short crack behaviour. The microstructural fracture mechanics methodology described in the previous chapter makes it now possible to incorporate the mechanical driving force of crack propagation, represented by the applied stress and crack length, and the material crack resistance. There is a clear possibility of including the compressive residual stress and the work hardening effects due to peening into the CTOD assessment, so as to obtain realistic estimations of fatigue life.

This chapter focuses on the definition of the residual stress profile, work hardening behaviour, and stress concentration gradient for specific and optimised peening conditions and on how should they be incorporated in to the N-R representation in order to provide a model for the determination of fatigue damage and life time estimations. These predictions will then be compared to the experimental results.

3.1 FATIGUE CRACK PROPAGATION IN SHOT-PEENED COMPONENTS

If a crack is blocked in its path, by many closely packed barriers of various kinds to delay the development of a stage II crack, then fatigue resistance will intrinsically increase, as discussed in §2.1.7. These assertions underpin the need for modifying the material on a way that would hinder the formation and propagation of these fine cracks. Shot peening (SP) introduces microstructural changes in the material directly affecting the development of stage I cracks and to some extent the stage II cracks.

The changes to the material within the peened depth are primarily, the development of a compressive residual stress, work hardening, and a distortion of the grain structure; also discussed in §2.2.4. However, these effects have to be incorporated into fatigue crack propagation laws in order to develop a methodology for predicting the fatigue behaviour of shot peened components. The approach to follow in this research programme is based on Microstructural Fracture Mechanics principles. A suitable adaptation of the Navarro-Rios model (§2.1.6.1) is utilised for crack analysis and life prediction. This method incorporates variables such as microstructure, initial flaw size, residual stresses, surface topography, work hardened layer, etc. within the system equations. The input variables are: (i) traditional fatigue data for the base material (e.g. long crack da/dN vs ΔK), (ii) initial flaw size (e.g. dimple size, surface damage due to overpeening), (iii) profile of residual stress, (iv) hardness of the work hardened layer, and (v) surface topography.

The residual stress is included as a closure stress at the crack (resistance to the opening of the crack), while the material distortion in the shot peened layer is included as a work hardening term within the resistance to plastic deformation at the crack tip. The closure stress is obtained by calculating the mean value of the function describing the residual stress distribution between $x=0$ and $x=a$ (a represents the crack depth) over the portion of the crack contained within the shot peened layer. Similarly, the resistance to plastic deformation within the plastic zone is obtained by calculating the mean value of the function describing the work hardened flow stress ahead of the crack tip in the plastic

zone. The results are expressed in the form of either cycles to failure for a given applied stress or the S-N curve of the shot-peened material and a fatigue map showing the crack arrest line and the crack instability line. This information can be used by the designer and maintenance engineer to perform safe life calculations or damage tolerance predictions.

There is also a need to control the peening effects and the depth to which they extend beneath the surface of the component, in order to obtain beneficial strengthening and to avoid introduction of severe damage. In this context, Design of Experiments (DoE) concepts are employed in an attempt to achieve the optimum peening conditions.

The basic effects covered in the fracture mechanics approach used for this analysis are described by equations 3.1-3.13. In this respect, the crack growth rate may be thought of as proportional to the crack-tip plastic displacement (CTOD). Thus the classic Paris relationship given in Eq. 2.17 can be rewritten as:

$$\frac{da}{dN} = A_2 \text{CTOD}^{m_2} \quad (3.1)$$

In previous work carried out by De los Rios, *et al.* [182] it was reported that the dominant cracks were mainly corner cracks in both unpeened and peened 2024-T351 AA during a four-point bending fatigue testing (20 Hz and R=0.1). Semi-elliptical (surface) cracks were also observed but only in unpeened specimens. In contrast, corner and semi-elliptical cracks were observed both in peened and unpeened 7150-T651 AA for similar fatigue testing conditions [183]. Hence, the general form of the stress intensity factor (SIF) was obtained from Newman's approach [184] which deals with three-dimensional and constraint factors of quarter-elliptical corner cracks and semi-elliptical surface cracks. The general formulation is given in Eq. (3.2), where c is the depth of the crack, Q is the shape factor for an elliptical crack, F_c is a boundary-correction factor for a corner crack in a plate, and Φ is the parametric angle of the ellipse.

$$\Delta K = \Delta \sigma \sqrt{\frac{\pi c}{Q}} F_c \left(\frac{c}{a}, \frac{c}{t}, \Phi \right) \quad (3.2)$$

ΔK is calculated from Eq. (3.2) for a given crack length a and substituted in $\frac{da}{dN} = A_1 \Delta K^{m_1}$. The corresponding da/dN is then read from the long crack propagation data for these type of AAs [166, 185, 186]. This procedure should be repeated for several crack lengths within the straight-line section of the da/dN vs. ΔK plot. Using the same crack lengths, CTOD is calculated employing Eqs. (2.18) and (2.13). It is assumed that these calculated CTODs produce the same da/dN as their equivalent ΔK s. Then fitting the CTODs to the da/dN s it is possible to obtain the optimum fit coefficient and exponent values A_2 and m_2 . The following results were reported, and will be used for life calculations throughout the present work:

CONDITION/MATERIAL	COEFFICIENT A_2	EXPONENT m_2
¹ Peened-Unpeened/2024-T351	5000	1.8
² Peened-Unpeened/7150-T651	300	1.5

1 After [77]

2 De los Rios and M. Trool, internal report, University of Sheffield.

For propagating cracks, the da/dN curve is numerically integrated within limits for crack length from the initiation size a_0 to the failure size a_f . It follows that crack propagation life, or number of cycles to failure, is:

$$N = \int_{a_0}^{a_f} \frac{da_i}{A_2 CTOD^{m_2}} = \frac{1}{A_2} \sum_{i=1}^{i_f} \int_{a_i^e}^{a_i^f} \frac{da_i}{CTOD^{m_2}} \quad (3.3)$$

Where i_f corresponds to the instability stage, i.e., when the crack propagation rate accelerates dramatically, followed immediately by total failure, $i=1,3,5 \dots i_f$.

In terms of the Navarro-de los Rios model (N-R), the condition for propagation at each grain boundary is determined by the value of n as seen in §2.1.6.1. Therefore, when n reaches a critical value, n_c , the crack is able to overcome the barrier (slip is transmitted and spread at once to the next grain boundary) and propagates into the next grain. The critical value n_c [69] given by the Eq. (3.5) incorporates the orientation factor m_i . This progression of grain orientation described in Eq. (2.16), was later modified by De los

Rios, *et al.* [187] in order to attain a more realistic estimation of such progression, for fcc materials. It is given as:

$$\frac{m_i}{m_1} = 1 + 2.07 \left\{ \frac{2}{\pi} \tan^{-1} [0.522(i-1)] \right\}^{1.86} \quad (3.4)$$

$$n_c^i = c \cos \left[\frac{\pi}{2} \left[\frac{\sigma - \left(\frac{m_i}{m_1} \times \frac{\sigma_{FL} - \sigma_1}{\sqrt{i}} + \sigma_1 \right)}{\sigma_2 - \sigma_1} \right] \right] \quad (3.5)$$

Where:-

n_c^i is the critical value of $n = 2a/iD$; $n_c^i = 2a_c / iD$

σ the applied stress

m_i the grain orientation factor for grain i

m_1 the grain orientation factor for the first grain (=1)

σ_{FL} fatigue limit

σ_1 the closure stress induced by the compressive residual stress after SP

σ_2 flow stress or work hardening after SP

i the number of half grains traversed by the crack.

Considering $c_i = a/n_i = iD/2$ (where, a is the crack length for a corner crack or half-crack length for a surface crack) and taking into account that n_i varies from n_s^i to n_c^i in each

grain, where $n_s^{i+2} = \frac{a_c}{(i+2)\frac{D}{2}}$ and $n_c^i = \frac{a_c}{i\frac{D}{2}}$, then $n_s^{i+2} = n_c^i \frac{i}{(i+2)}$. Thus, it follows

from Eq. (3.3) that [77]:

$$N = \frac{1}{A_2} \sum_{i=1}^{i_r} \int_{n_c^i}^{n_s^{i+2}} \frac{c_i^{1-m_2} d n_i^i}{C T O D^{m_2}} \quad (3.6)$$

3.2 MODELLING THE MATERIAL STATE FOLLOWING SHOT PEENING

The introduction of the compressive residual stress and work hardening effects due to peening into the CTOD will follow the method described in [188]. In addition to this, a method to introduce the effect of surface roughness as a stress concentration factor will be developed in this work.

3.2.1 Residual stresses

The closure stress, σ_1^i , is obtained by calculating the mean value of the function describing the residual stress distribution between $x=0$ and $x=a$ (where a is the crack depth). In this context, the in-depth residual stress measurements are carried out by means of the incremental hole drilling (IHD) technique and/or the X-ray diffraction (XRD) $\sin^2 \psi$ method, which together or separately are widely accepted. Based on prior work by Robertson [189], residual stress profiles can be explicitly represented by the following Gaussian function:

$$f(x) = \sigma_R = A e^{\left[\frac{-2(x-X_d)^2}{W^2} \right]} + B \quad (3.7)$$

Where

σ_R = compressive residual stress

$A+B$ = maximum residual stress

x = depth below the surface

X_d = depth to maximum residual stress

W = a measure of the width of the stress curve

B = preset residual stress (prestressed specimens only)

However, the residual stress function may also be represented in a slightly different and simpler way:

$$f(x) = \sigma_R = A n^{\left[\frac{-2(x-X_d)^2}{W^2} \right]} + B \quad (3.8)$$

where n ranges between 1 and 10. Again, the parameter B is used for prestressed components.

Figure 3.2.1 illustrates an example of some compressive residual stress data plotted together with the resulting curve fit generated using Eq. (3.7) with $B=0$. The experimental data were obtained employing the IHD technique.

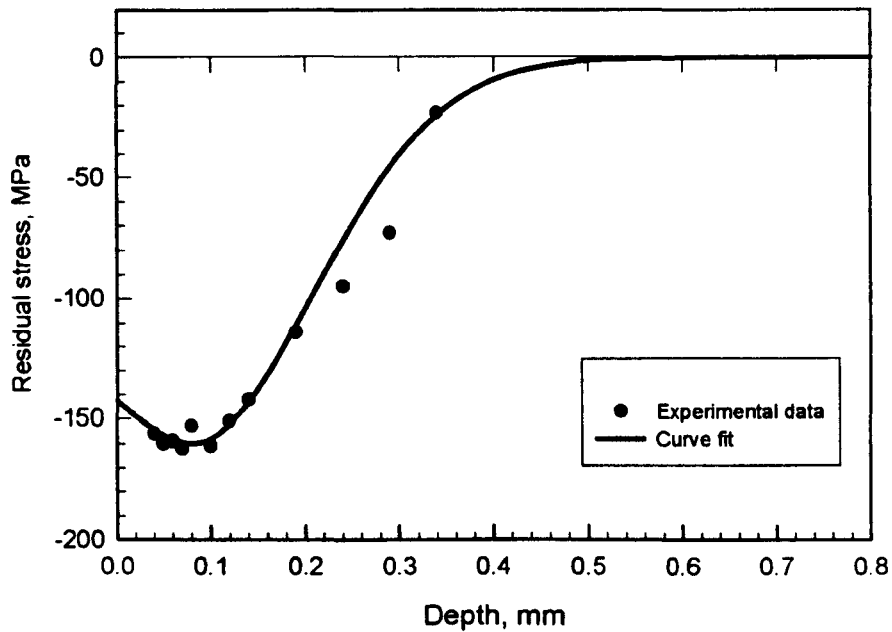


Figure 3.2.1 Residual stress data of the 7150-T651 AA. The corresponding curve fit generated from Eq. (3.7). Peening condition: S110 shot, 0.1524 mmA (6A) intensity, 30° incidence angle, and 400% coverage.

The function describing the residual stresses can now be incorporated, as the closure stress, σ_1^i , into the CTOD estimations, as follows:

$$\sigma_1^i = \frac{\int_0^{a_i} f(x) dx}{a_i} \tag{3.9}$$

where $f(x)$ is described by Eq. (3.7).

The plotting of the closure stress is shown in Fig. 3.2.2.

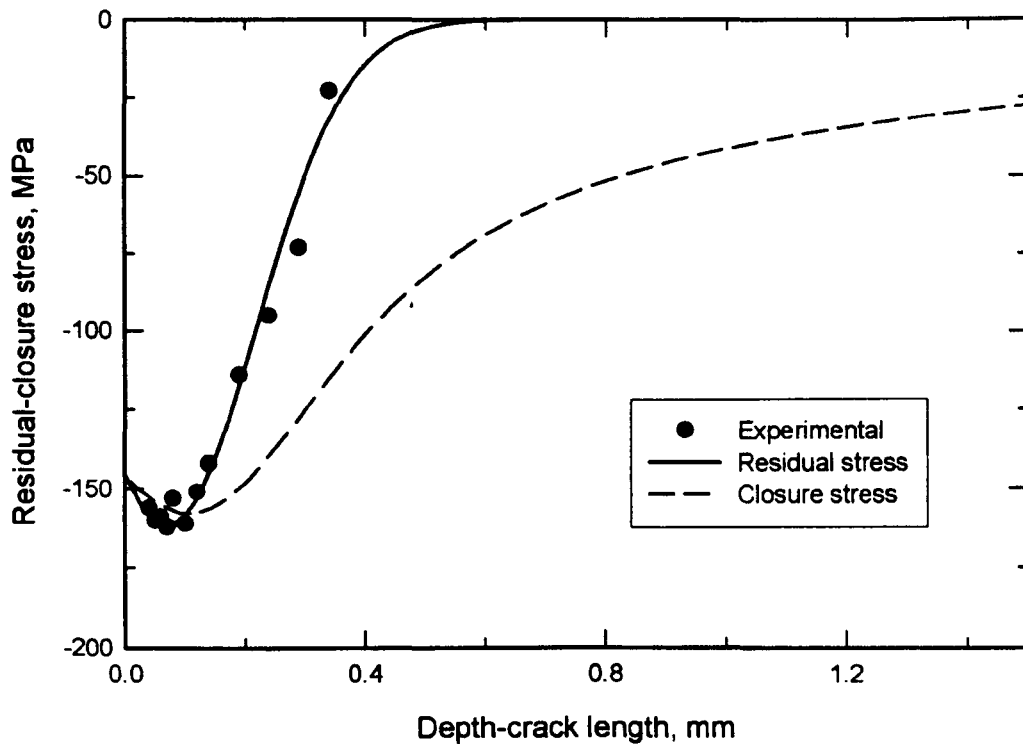


Figure 3.2.2 Evolution of the residual and the corresponding closure stress over the portion of the crack contained within the peened layer. Material and peening conditions as in Fig. 3.2.1.

3.2.2 Work hardening

The resistance to plastic deformation, termed (σ_2) in Eq. 2.18, is increased by the distortion in the shot-peened layer and the corresponding work hardening. The procedure for calculating the stress at the plastic zone is analogous to that of the residual stress, i.e. calculating the mean value of the function describing the work-hardened flow stress ahead of the crack tip between $x=a$ and $x= iD/2$. The mechanical property measured across the section of the peened material is the microhardness. The relationship between hardness and flow stress for 2024-T351 AA was reported by De los Rios *et al.* in [77]. They determined the dependence between these two parameters by deforming the material to different strains and measured the microhardness before and after deformation. The results were reported in the form of a linear function:

$$\sigma_2 = 3.85 H_v - 136.9 \quad (3.10)$$

The expression found for the 7150-T651 was given as:

$$\sigma_2 = 3.125 H_v + 15.548 \quad (3.11)$$

The microhardness distribution may also be determined explicitly by using the Gaussian fitting Eq. (3.7) as depicted in Fig. 3.2.3.

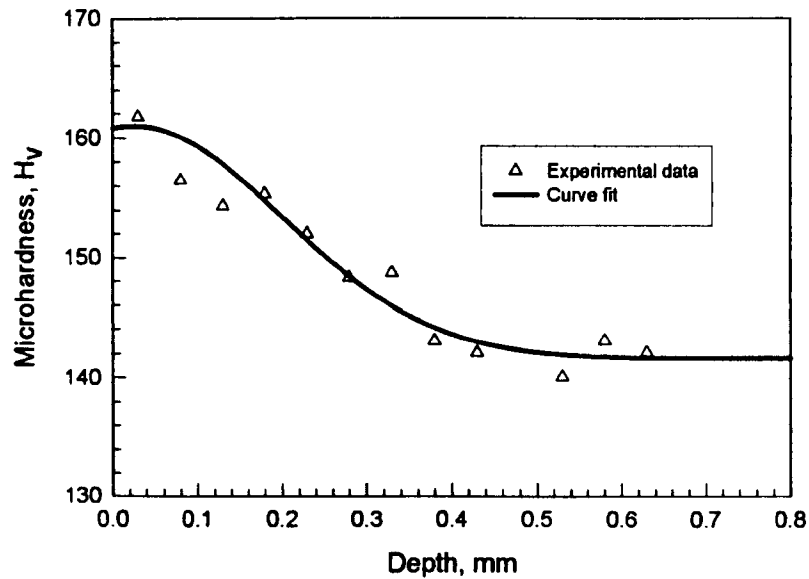


Figure 3.2.3 Work hardening in-depth distribution and the corresponding curve fit generated from Eq. (3.7). Experimental data were determined from a peening condition: S110 shot, 0.1524 mmA (6A) intensity, 30° incidence angle, and 400% coverage

Evolution of the flow stress σ_2^i is therefore calculated by introducing the Gaussian function into Eqs. (3.10 or 3.11) for 2024-T351 and 7150-T651 respectively. The work-hardened flow stress ahead of the crack tip is calculated as the mean value of the resultant function between $x=a$ and $x= iD/2$, analogously to the form described in Eq. 3.9. The distribution of the flow stress in-depth is shown in Fig. 3.2.4

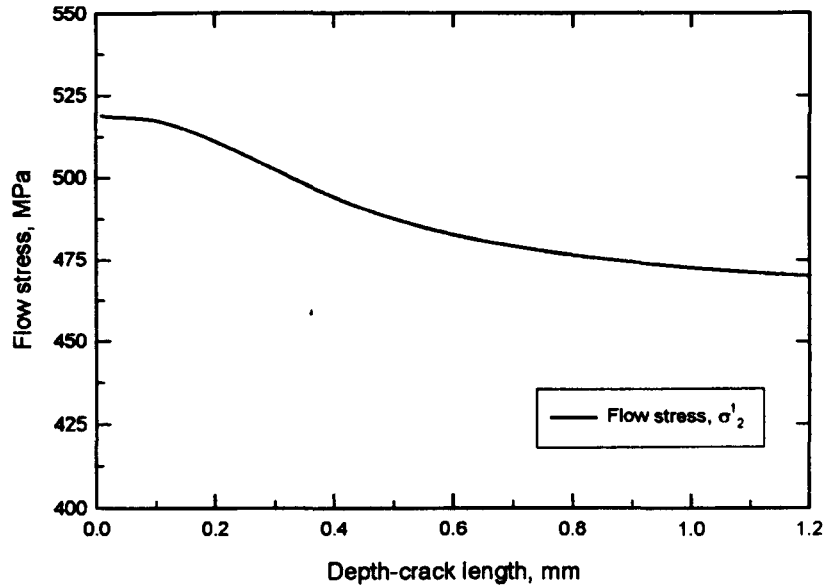


Figure 3.2.4. Evolution of flow stress σ_2^i with in-depth crack length for the same material and peening conditions as in Fig. 3.2.1.

3.2.3 Kt gradient concept from surface roughness

The surface stress will be intrinsically affected by surface topography. The increase in such stress due to stress concentration caused by the dimples on a peened surface should be taken into account in the calculation within the model. A method for estimating a geometric stress concentration factor (Kt) due to multiple indentations was developed by Li, *et al.* [156] where extensive 3D stress analysis using finite elements was carried out and two general relationships for Kt were proposed, as follows:

$$K_t = 1 + 2.1 \left(\frac{R_{tm}}{S_m} \right) \quad \left(\text{for } \frac{R_{tm}}{S} \leq 0.30 \right)^* \quad (3.12)$$

$$K_t = 1 + 4.0 \left(\frac{R_{tm}}{S_m} \right)^{1.3} \quad \left(\text{for } \frac{R_{tm}}{S} < 0.15 \right)$$

* The annotated restrictions are in connection to the approximately linear relationship between the calculated Kt and the ratio H/D (equivalent to R_{tm}/S_m). It is still possible to obtain reasonable results up to $R_{tm}/S_m \leq 0.4$. However, a loss of linearity above this ratio is expected and thus, results can be uncertain.

where R_{tm} represents the mean of all $R_{t,s}$ within an assessment length, and R_t is the maximum peak to valley height of the profile, in one sampling length. S_m is the mean spacing of adjacent local peaks of the profile, measured over the assessment length.

The maximum K_t calculated is used, since it is assumed that a surface crack will tend to initiate at a location that possess the highest local stress concentration.

The stress concentration due to surface roughness in a shot peened specimen is a function of the average width and depth of an impacted dent (aspect ratio), as shown in figure 3.2.5.

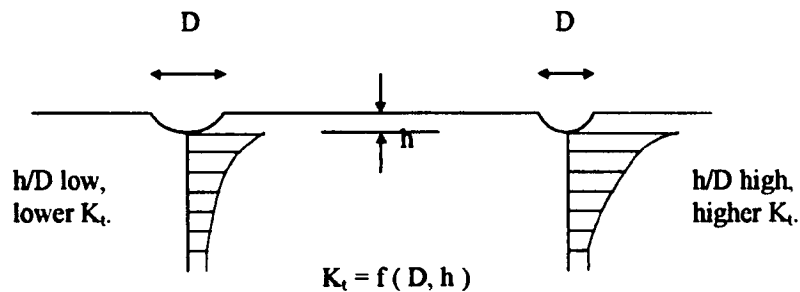


Figure 3.2.5 Geometric stress concentrations due to surface dents with different aspect ratios. K_t varies with the size and depth of the dimple, and is a function distance from the dimple centre.

A quadratic function proposed by De los Rios *et al.* [190] is used to evaluate K_t as a function of the distance from the dent:

$$g(x) = (K_t - 1) \left(\frac{R_{tm}}{x} \right)^2 + 1, \quad \text{for } x \geq R_{tm} \quad (3.13)$$

where K_t is the maximum stress concentration at the root of the dimple.

Figure 3.2.6 shows a typical stress concentration gradient for a peened 2024-T351AA with $R_{tm} = 30.19 \mu\text{m}$ and $K_t = 1.3620$.

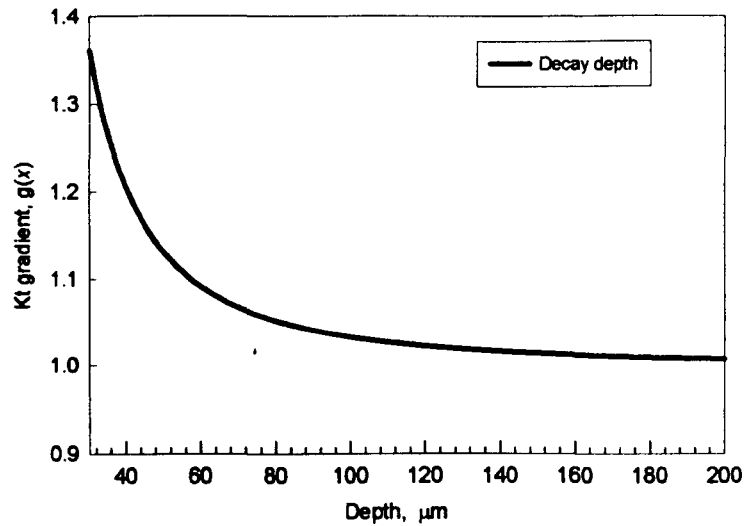


Figure 3.2.6 Variation of K_t with depth. The initial value calculated corresponds to the root of the dent.

The important material parameters affected by shot peening, which are associated with changes in fatigue resistance are:

- Residual stress
- Topography (surface roughness)
- Microstructural work hardening (multiplication of dislocation density)

However, the magnitude of all these effects and the depth to which they extend beneath the surface of the component must be controlled in order to obtain beneficial strengthening and avoid the introduction of unwanted damage. The optimisation of the shot peening in terms of fatigue resistance is done by obtaining the most suitable combination of the peening variables (shot type/size, intensity, coverage, incidence angle) in terms of the changes affected to the material, i.e. maximum residual stress and work hardening, and minimum surface roughness. The analysis of the interaction of these factors will make it possible to: a) find the most significant parameters of the process, and b) examine the interaction amongst the parameters. Chapter 4 discusses the Design of Experiments approach which will identify the relative importance and interaction of the chosen shot peening conditions.

3.3 SUMMARY

In this chapter the necessary elements to characterise the material state due to shot peening in terms of the Navarro-Rios fatigue model were examined. This is necessary because fatigue damage in shot peened components needs to be characterised using short fatigue crack concepts. Thus, to perform predictions of the CTOD and in turn, life determinations, it is essential to incorporate the shot peening effects. The compressive residual stress is included as a closure stress, σ_1 , at the crack flanks whilst work-hardening or material distortion in the peened layer is introduced within the micromechanical model as an extra resistance to plastic deformation, termed σ_2 . Regarding surface roughness, it is proposed that the geometric stress concentration K_t is a suitable factor to measure the effect of the surface topography which affects directly the local stress. In chapter 6, the effect of micro-notches is related to the geometric K_t and the effect of multiple micro-notches is derived.

Closure stress and flow stress are not a linear function of depth; hence, the solution of the equilibrium equation (Eq. 2.13) with the variables $\sigma_1(x)$, $\sigma_2(x)$, and $g(x)$ are obtained using a numerical method.

CHAPTER 4

MATERIALS AND EXPERIMENTAL METHODS

It is evident that a thorough understanding of the induced changes on the surface and subsurface of a metallic component caused by a peening process will lead to an optimisation of the process in terms of fatigue resistance. Since the object of this study is to obtain the best-peened properties of a component, through a characterization of the work hardening, surface stress concentration (roughness) and residual stress, directly from the interaction of the control process parameters and initial component properties; the strategy adopted to achieve this goal was as follows:

1) Peening process

- i. Characterise the experimental peening media employed in order to attain the shape, size and material properties distributions, with the purpose of detecting possible variations from the nominal specifications.
- ii. Produce peening intensity curves under controlled conditions by using the shot (type/size) recommended by the relevant specifications for aluminium alloys. This will, initially, allow exploration of the peening machine operational capacity. It

also will enable to define the corresponding process parameters (mainly pressure, flow rate and stand-off distances) to be used throughout this research.

- iii. Assess the development of peening coverage on the target material by incorporating all the defined peening parameters (Intensity, incidence angle, shot type).

2) Design Experiment approach

Collect as much information as possible regarding the significant peening factors and their interaction within their selected levels by using the design of experiments concept, enabling the best and worst peening conditions in terms of residual stresses, topography and work hardening, to be obtained.

3) Fatigue testing

- i. Validate the determined optimum peening conditions in terms of fatigue resistance by testing peened specimens under constant amplitude axial loading.
- ii. Undertake an analysis of the sensitivity of the fatigue results varying one shot peening factor at a time, and keeping the remainder constant. This will enable the definition of optimum peening conditions for fatigue endurance.
- iii. Obtain experimentally the conditions for crack arrest using pre-cracked peened and unpeened specimens with different initial crack length. The results from these tests will be used to validate theoretical predictions of a fatigue damage map.

In this chapter, the peening equipment used throughout the research is described. Owing to its importance, a characterisation of the peening media was also undertaken. In particular, attention was paid to a methodology for calculating intensity at saturation point. A dedicated section to the procedure for measuring the coverage is reported. Theoretical velocity estimations are also presented. Specimen design and manufacturing preparation are detailed. A brief description of design of experiments theory is included, followed by the selected experiment array. Experimental techniques and procedures for characterising the peening effects are discussed. Finally, the methodology used in the fatigue testing is documented.

4.1 PEENING MATERIALS AND PROCEDURES

4.1.1 Shot peening equipment: Introductory background

In order to gain a clear understanding of the basic technology in the manufacturing of peening equipment, this section offers insight into the classification of peening machines and some of their relevant features, including major advantages.

The equipment used to shotpeen a component may be classified into two major categories: pneumatic and centrifugal systems [85, 87]:

In pneumatic shot peening, a high velocity air stream is used to propel the shot through a (normally circular sectional area) nozzle on to the component surface. These machines may be subdivided into three kinds, depending on the method of introducing the shot into the air stream: *suction-induction*, *gravity-induction* and *direct pressure*. In *suction fed* equipment, shown schematically in Fig. 4.1.1 a, the compressed air passes through a nozzle inducing a negative pressure differential in the shot supply hose. This draws shot from the storage vessel into the air flow, where it is then accelerated to the nozzle exit. *Gravity fed* is similar to suction fed, with a similar nozzle arrangement, but with the nozzle mounted beneath the feed valve of the shot storage vessel so that shot is drawn straight into the air flow without a shot supply hose (Fig. 4.1.1 b). In *direct pressure*, shown schematically on Fig. 4.1.1 c, the shot is stored in a pressure vessel which is maintained at the same pressure as the air, which propels the shot. The shot is fed by gravity into a mixing chamber in the pressure vessel, where it is propelled by air pressure, transported along the boost hose and discharged through a nozzle. This system is the most universally used [89].

For flexibility, the direct pressure method has a number of advantages over the other methods. Among these are: every type of shot may be used with equal ease, pressures are easily adjusted, nozzle stand-off distance and angle of impact may also be varied, ease of handling of small parts. The weakness in the system is the uncontrolled pressure

variation found in the majority of this sort of machines. This system is suitable for laboratory work for economical reasons.

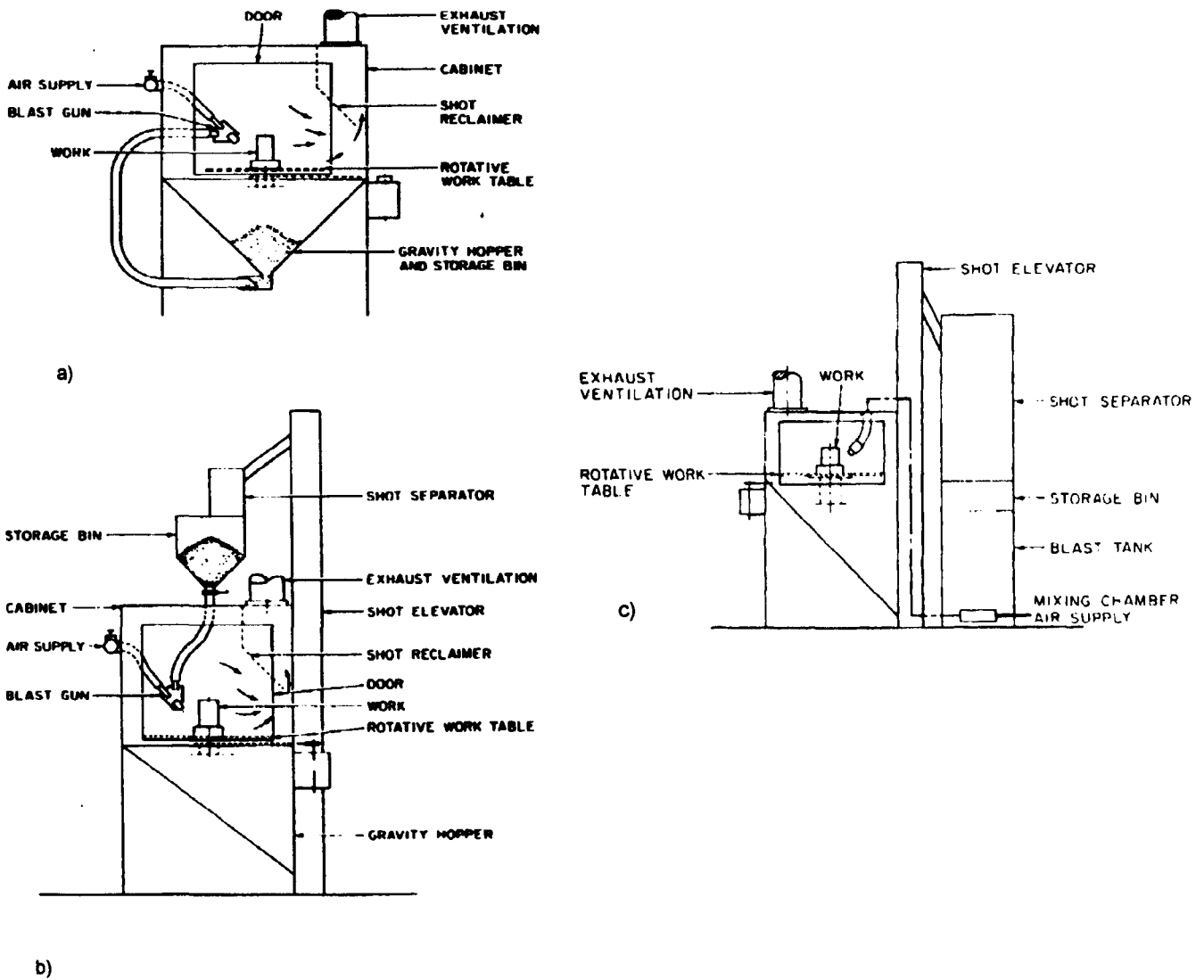


Figure 4.1.1 Schematic diagrams of a) suction fed, b) gravity fed and c) pressure fed air blast shot peening equipment (after [81, 87]).

In the centrifugal system or airless method, a combination of radial and tangential forces to impart the necessary peening velocity to the shot is employed. The impeller may be either a bladed or a tubular wheel. The shot is fed by gravity or low pressure air to the hub of the rotating wheel. By means of a control unit, the shot is directed onto the blades, from whence the shot is thrown into a fan-shaped stream (see Fig. 4.1.2). The airless method of shot propulsion has some advantages over pneumatic. Among these are [85, 88]:

The velocity of the shot in the blast is easily controlled by simply maintaining a constant speed of rotation of the wheel. This is in contrast to an air nozzle in which the velocity of the shot is subject to change due to variation in air pressure, variation in nozzle size (this increases with wear), or changes in shot flow rate. In using an airless wheel, independence from such variation permits uniform control of peening intensity. Due to the high rate of shot flow which can be obtained with a wheel, high production rates can be economically maintained. A standard wheel which will throw 300 pounds (136 kg) per minute at a power input of 15 H.P. (11 kilowatts) while five 3/8" (9.53mm) nozzles are required to throw the same quantity at 80 psi (5.6 kg/cm²) pressure and at power input of 190 H.P. (139.7 kilowatts). The airless wheel is a self-contained unit and does not require the auxiliary equipment needed in the pneumatic one, such as an air compressor of sufficient capacity, pressure regulator, water traps, etc. This kind of equipment is highly recommended for production peening.

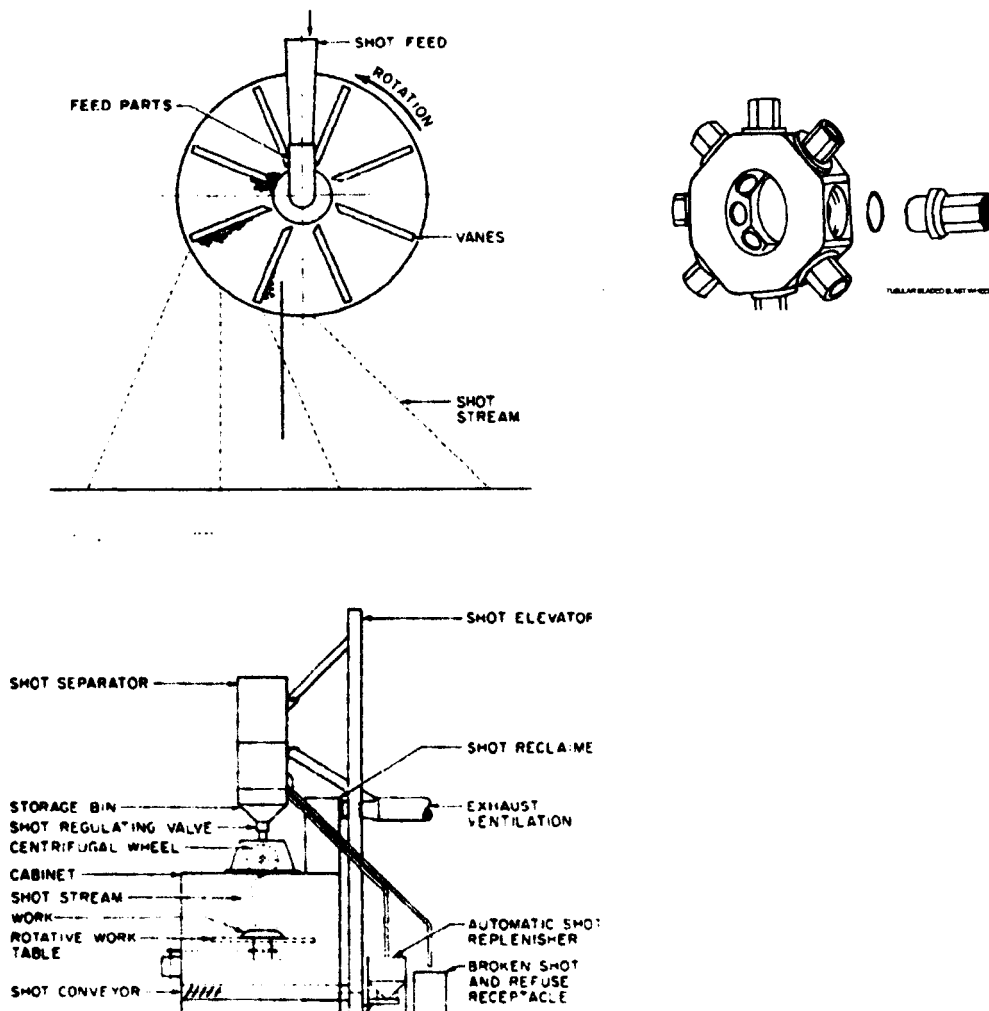


Figure 4.1.2 Schematic designs of centrifugal wheels (top figures) used in a typical centrifugal wheel peening equipment (bottom figure). Ref. [81, 87, 89]

4.1.2 The experimental peening facility

The experimental peening equipment used in this work was that of a direct-pressure type described in § 4.1.1. This equipment, commissioned in July 1998 is a Precifeed system produced by Tealgate. It consists of a standard blast cabinet, an electronically controlled feed valve system, i.e. Magna Valve model No. 368, and a media transfer valve; a pressure vessel, an oscillating nozzle mechanism, a turntable, and a fascia panel containing the main controls. Fig. 4.1.3 details the main components.

The shot is stored in a pressurised container, fed by gravity into a mixing chamber in the pressure vessel, and propelled by air pressure to pass through both a hose and the nozzle to finally strike the work piece, before being fed into the mixing chamber again in a continuous cycle. Fig. 4.1.4 shows schematically the general arrangement of the media flow.

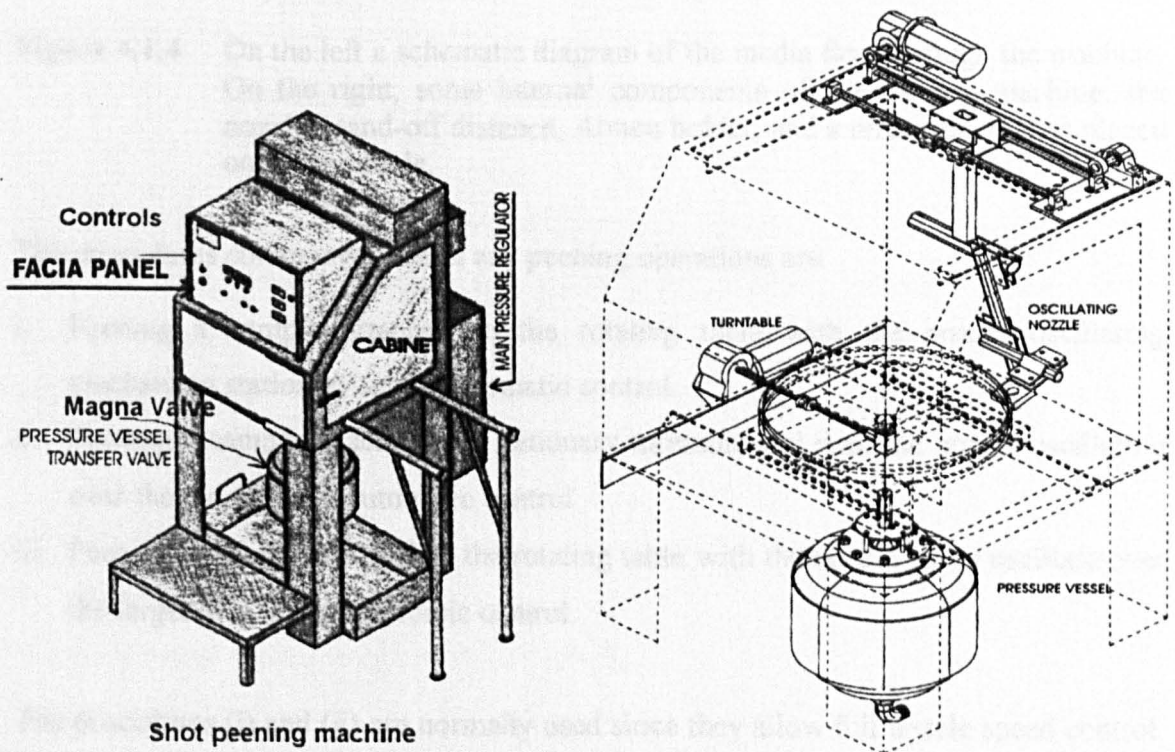


Figure 4.1.3 Schematic illustration of the shot peening machine: External view (on the left) and an isometric representation of the machine showing further internal components (on the right). Ref. [191].

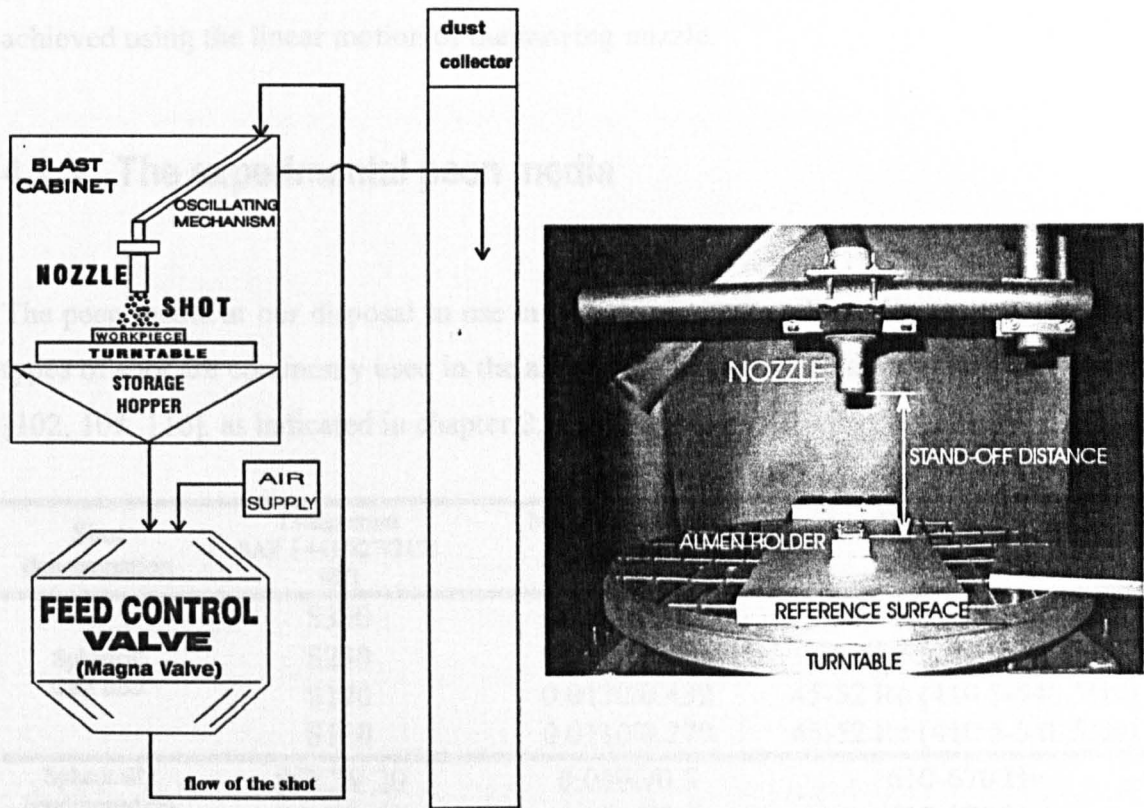


Figure 4.1.4 On the left a schematic diagram of the media flow through the machine. On the right, some internal components of the peening machine: the nozzle, stand-off distance, Almen holder, and a reference surface placed on the turntable.

The procedures commonly used in any peening operations are:

- i. Peening a sample attached to the rotating table with the nozzle oscillating mechanism stationary under automatic control.
- ii. Peening a sample attached to a stationary turntable and with the nozzle oscillating over the target under automatic control.
- iii. Peening a sample attached to the rotating table with the nozzle set to oscillate over the target area under automatic control.

The procedures (i) and (ii) are normally used since they allow full nozzle speed control. The relative speed of the nozzle and the workpiece is not constant in the procedure (iii); hence, the use of this combination is extremely rare. The procedure (ii) was selected in this research due to: it providing the fullest nozzle speed control, wider possibilities for positioning the target material and adequate covering area across the specimens to be

peened. As a result, full covering across the whole length of the peening target was achieved using the linear motion of the moving nozzle.

4.1.3 The experimental peen media

The peen media at our disposal to use in the experiment are listed in table 4.1.2. These types of shot are commonly used in the aircraft industry to peen aluminium components [102, 108, 116], as indicated in chapter 2.

Shot denomination	Designation SAE J 441/827/2175 [87]	Nominal diameter Inches/mm	Specification Hardness
Spherical Cast steel	S330	0.0330/0.838	56-58 Rc (615-668 Hv)
	S230	0.0230/0.584	56-58 Rc (615-668Hv)
	S170	0.0170/0.432	45-52 Rc (410.5-548.5Hv)
	S110	0.0110/0.279	45-52 Rc (410.5-548.5Hv)
Spherically conditioned cut wire steel	SCCW 20	0.0196/0.5	610-670 Hv
	SCCW 23	0.0236/0.6	610-670 Hv

Table 4.1.2 Specifications of the peen media at our disposal for peening aluminium alloys.

Considering that a critical parameter of the peening process is the shot itself, the shot media was sampled and graded at the beginning of the tests to ensure that shot quality met both MIL-S- and SAE requirements, and to observe whether there was any significant variation. The shot characteristics evaluated were those previously identified by Gillespie [106] and also specified by the relevant standards, namely:

- i. Size (diameter).
- ii. Shape factor (roundness).
- iii. Aspect ratio (major length by minor length).
- iv. Hardness (Hv).
- v. Density.

4.1.3.1 Geometric features (the size, shape factor and aspect ratio)

There are three techniques, which either separated or combined, allow these geometric features to be determined [102, 108, 113, 114, 116]:

- i) Visual inspection.
- ii) Sieve analysis.
- iii) Image analysis.

It has been reported that the image analysis¹ (IA) technique allows the measurement of several features of as many individual shot particles as required, with highly descriptive and accurate results, which can be then statistically processed. Conversely, sieve analysis and visual inspection are neither as descriptive nor as accurate as IA. Taking into account the above considerations, the IA technique was adopted for characterising the size, shape factor and aspect ratio of the peen media used in this study. Samples of as received shots were selected randomly by repeat sub-division of a tray of shots until approximately 100 remained as a non-biased sample, in accordance with British Aerospace (Airbus) specifications. A PC-based image analyser software (SigmaScan Pro ver. 5.0 Copyright © SPSS Inc.) and an optical microscope Olympus CH-2 LECO were employed for measuring purposes. The geometric features that were measured on a two-dimensional plane are defined as follows:

- 1) Size in terms of the shot diameter: calculated as the Feret's diameter, which is the diameter of a fictitious circle that has the same area as the shot being measured,

$$\text{given by } \sqrt{\frac{4 \times \text{Area}}{\pi}}$$

- 2) Shape factor: a measure of a shot's circularity, which is given by $\frac{4 \times \pi \times \text{Area}}{\text{Perimeter}^2}$. A

perfect circle has a shape factor of 1. Unacceptably shaped shots have a roundness of less than 0.81.

¹ Image Analysis can be defined as the use of computer to manipulate pictures or images for the purpose of extracting information regarding the features within the images. Image analysis system typically consists of a video camera, magnifying device (optical microscope), computer and specialized software (after [113]).

3) Aspect ratio: a proportion between the major lengths over the minor lengths.
 Acceptable values range between 1 and 1.2 .

Figs. 4.1.5 a-c, show the distributions of size, shape factor and aspect ratio of the S110 shot, respectively.

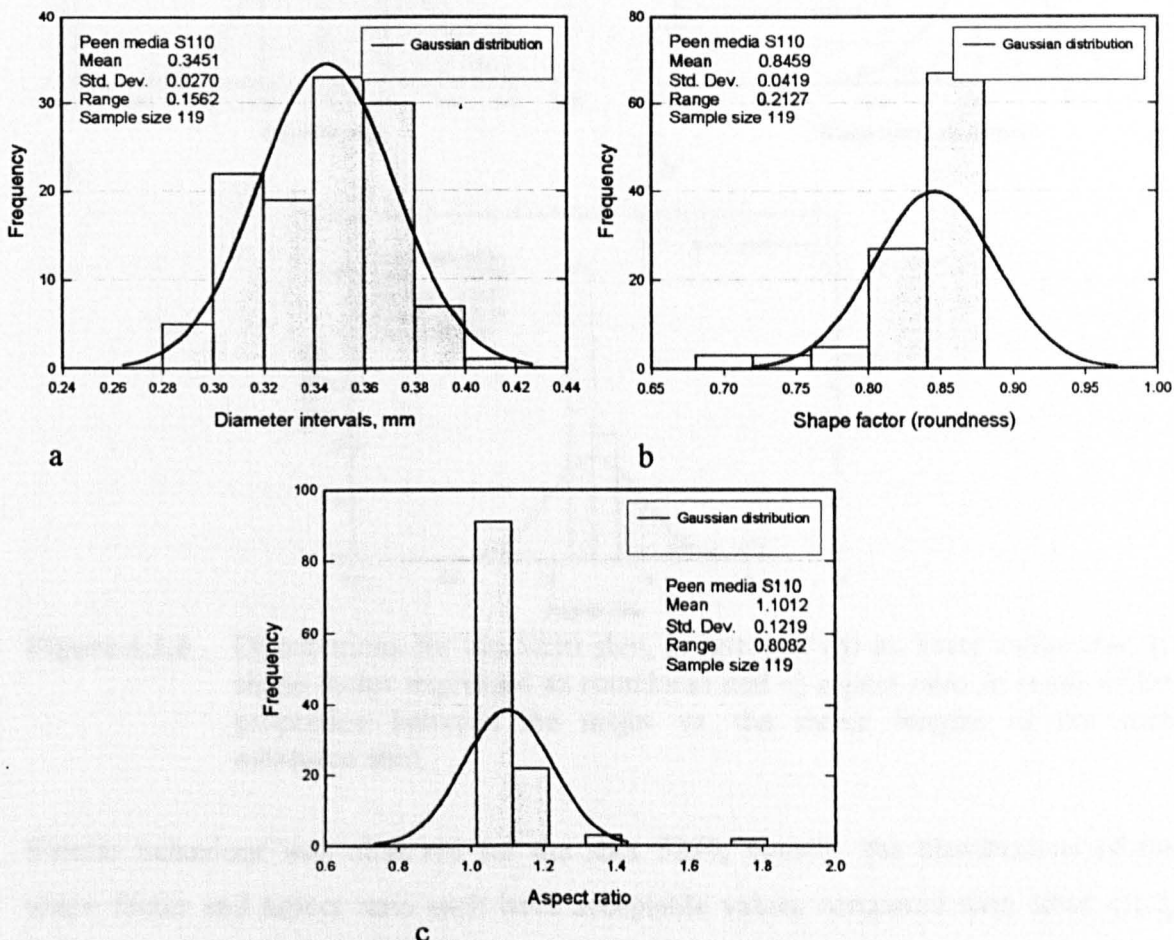


Figure 4.1.5 Distributions for the S110 shot in terms of (a) its Feret's diameter, (b) shape factor expressed as roundness and (c) aspect ratio in terms of the proportion between the major vs. the minor lengths of the each measured shot.

From Figs. 4.1.5, it can be seen that whilst the shape factor and aspect ratio distributions give acceptable values, i.e., the shot was mostly round; the distribution of the shot size presents a significant variability in relation to the nominal diameter, i.e., the shot size ranges between 0.30 to 0.38 mm.

In Figs. 4.1.6 a-c the statistical behaviour of the shot S230 is illustrated.

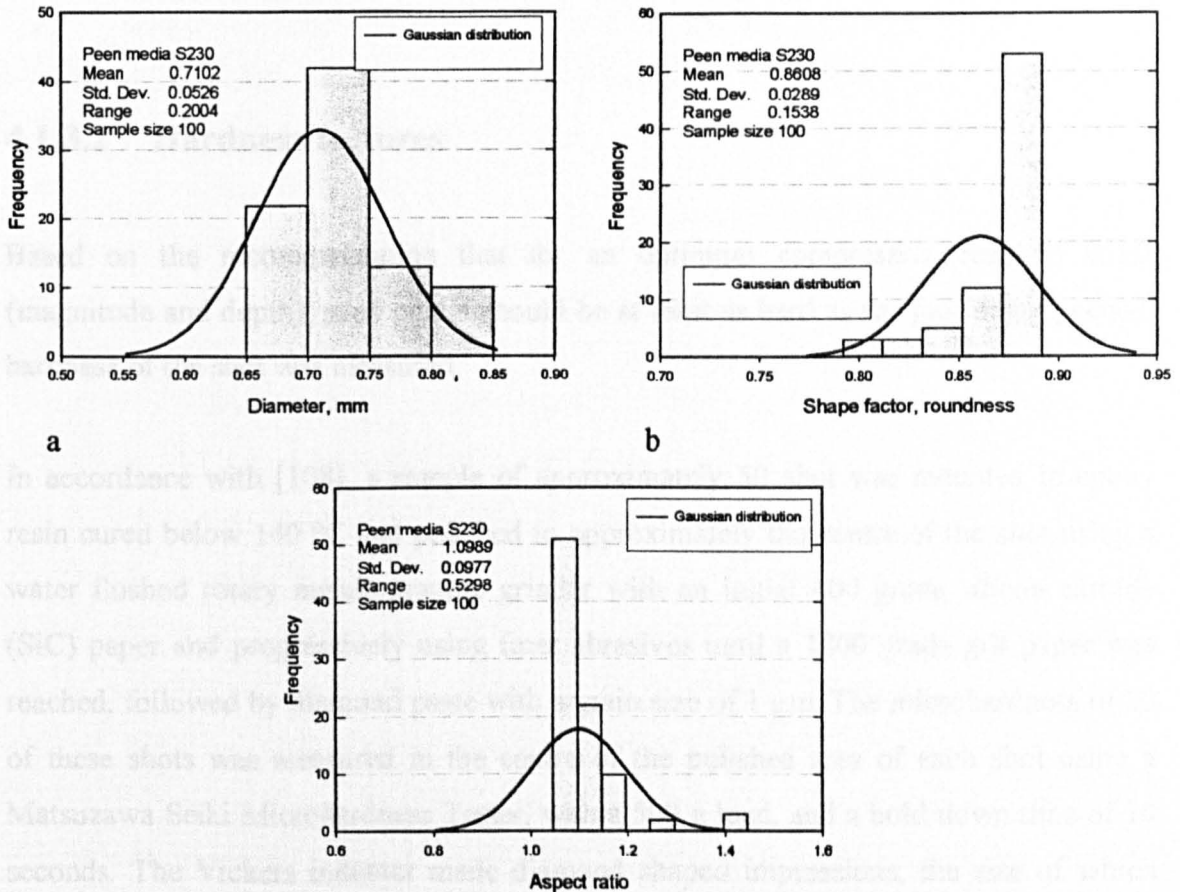


Figure 4.1.6 Distributions for the S230 shot, in terms of (a) its Feret's diameter, b) shape factor expressed as roundness and c) aspect ratio in terms of the proportion between the major vs. the minor lengths of the each measured shot.

Similar behaviour was observed for the shot S230, namely, the distributions of the shape factor and aspect ratio each have acceptable values compared with table 4.1.2, whereas the distribution of the diameter indicates the mean values to be well above the nominal diameter.

Regarding the shot sizes, it was found that there is no clear definition of the tolerances. Significant differences between specifications are reported. For example, whilst the dimensions of the S110 and S230 shots are consistent with MIL-S-13165C [82] specification, these same magnitudes exceed the tolerances observed by SAE-HS84 [87].

The distributions of the geometric characteristics for the remaining media are reported in appendix I.

4.1.3.2 Hardness features

Based on the recommendation that for an optimum compressive residual stress (magnitude and depth), peen media should be at least as hard as the part being peened; hardness of the shot was measured,

In accordance with [108], a sample of approximately 50 shot was mounted in epoxy resin cured below 140 °C and polished to approximately the centre of the shot using a water flushed rotary metallographic grinder with an initial 400 grade silicon carbide (SiC) paper and progressively using finer abrasives until a 1200 grade grit paper was reached, followed by diamond paste with a grain size of 1 µm. The microhardness of 20 of these shots was measured in the centre of the polished area of each shot using a Matsuzawa Seiki Microhardness Tester, with a 500 g load, and a hold-down time of 10 seconds. The Vickers indenter made diamond shaped impressions, the size of which were measured to an accuracy of 0.1µm. The average of twenty microhardness measurements per shot is shown in Fig. 4.1.7.

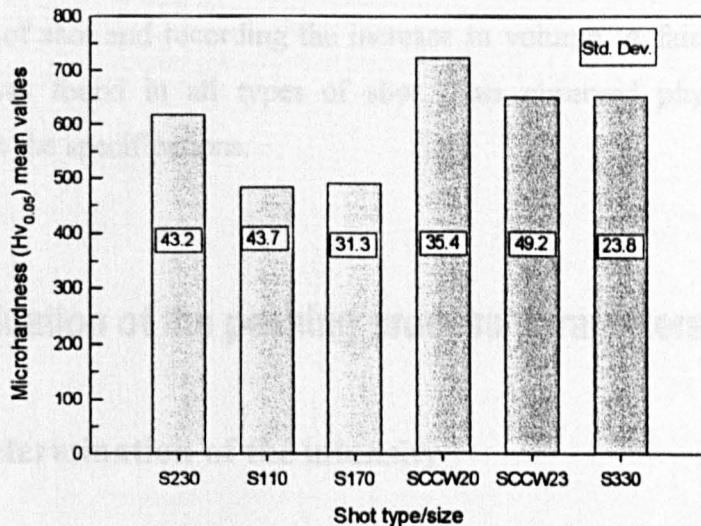


Figure 4.1.7 Microhardness Vickers of the as received peen media.

The evaluated microhardness was found to be consistent with the specifications. Minor deviations were observed in the whole batch examined. Shot types S110 and S170 were softer than S330, S230 and the CCW20 types.

4.1.3.3 Density characterisation

Density measurement can be a quick and valuable indication of the presence of large amounts of voids, porosity or other internal defects in shot particles. Particles with significant internal defects will have low density and tend to shatter and breakdown much faster than solid sound particles, thus reducing average particle size and increasing the amount of unacceptable sharp edge broken pieces. Another important reason to consider density is related to the kinetic energy of a shot (discussed in § 2.2.2), namely, the mass of a particle is the product of its density and volume. As particle density increases, particle mass also increases. Therefore, the media with the higher density will have the highest kinetic energy at equivalent velocities. Media with the highest and most consistent density should produce the highest and most consistent peening intensities with the lowest potential for surface damage.

Density was determined following the SAE specifications. Basically, the procedure adopted consisted of pouring 50 ml of ethanol into a 100 ml graduated glass container, adding 100 g of shot and recording the increase in volume. A fairly uniform value of 7.63 g/cm^3 was found in all types of shot. This observed physical property was consistent with the specifications.

4.1.4 Evaluation of the peening process parameters

4.1.4.1 Determination of the intensity

The effectiveness of the peening process was monitored by recording the arc height deflections of standardised Almen strips at particular exposure times. A standard digital-based Almen gauge [192] with digital accuracy to $0.0002''$ (0.0051 mm) was employed. Saturation curves can readily be built following the method already discussed in § 2.2.3.3. However, a lack as to how to accurately determine the intensity

was identified. Work was undertaken to develop a method to fit a curve for the intensity and time [104, 193].

An equation of the form given in Eq. (4.1) has been adopted for plotting the intensity curve and saturation point, having boundary conditions such that: i) at time =0, Arc height = 0 (imposed directly by the equation), ii) as time approaches infinity arc height approaches a saturation value and iii) each data point has equal weighting.

$$H = \frac{A}{(t+b)^P} - \frac{A}{b^P} \quad (4.1)$$

where, H is the arc height value to determine, t the peening time; A , b and p are fitting parameters.

A full regression analysis to provide the minimum sum of differences from the input data points is used. The normal industrial criteria applied for input data suggests that: a) successive arc height increments reduce, b) time intervals should be doubling (if not then constant increments) and c) successive tangents reduce and show a smooth trend. Details of the main structure of the computer program are given in appendix II. An output of the calculated intensities is depicted in Fig. 4.1.8.

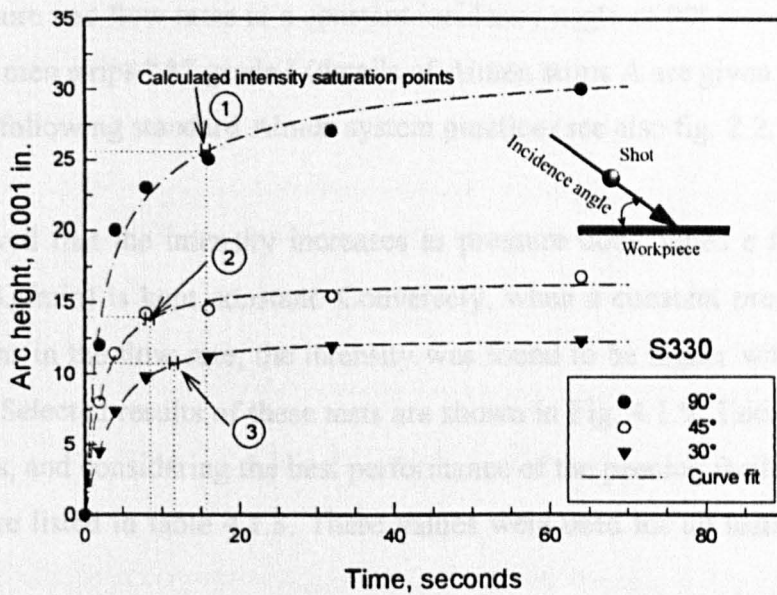


Fig. 4.1.8 Saturation curves of the shot type S330 at different incidence angles. Arrows indicate the calculated intensities saturation points of each fitted curve, obtained from application of Eq. (4.1). The corresponding intensity saturation point values are: 1) $H=25.54A$ (0.65mmA), $t=15.70$ sec., 2) $13.8A$ (0.35mmA), 8.5 sec. and 3) $10.7A$ (0.27mmA), 11.6 sec.

4.1.4.2 Peening process parameters

From the existing peening parameters discussed in § 2.2.3, air pressure, mass flow rate and nozzle velocity were varied to find a common saturated Almen arc height for a selected coarse (S330) and fine (S110) shot, i.e. the extreme shot sizes in the range. However, it was found that the attainment of the same saturated Almen arc height was impossible for such shot sizes and also for the other available peen media. Therefore, these three process parameters were kept constant throughout all peening operations.

The settings were selected according to the recommended levels of pressure and flow rates given by the manufacturer of the experimental facility. A table of the approximate values of intensity as a function of pressure and flow rates for this particular peening machine is reported in appendix II (Fig. II-1). In particular, attention was paid to the acceptable Almen intensities, which according to specifications, intensities between 6-16A (0.15-0.40 mmA) should be acceptable for aluminium alloys.

To determine the appropriate values of these peening parameters, the effect of air pressure and media flow rates on the intensity response was explored. Preliminary tests varying pressure and flow rates at a constant incidence angle of 90° were undertaken. A number of Almen strips “A” grade I (details of Almen strips A are given in appendix II) were peened following standard Almen system practice (see also fig. 2.2.7 c).

It was observed that the intensity increases as pressure does, when a flow rate of 18 lb/min (8.2 Kg/min) is kept constant. Conversely, when a constant pressure was used with variations in the flow rate, the intensity was found to be higher with lower values of flow rate. Selected results of these tests are shown in Fig. 4.1.9. Taking into account these findings, and considering the best performance of the peening facility, the selected parameters are listed in table 4.1.3. These values were used for all tests carried out in this study.

The velocity of the nozzle was tuned to a value such that a single pass of the nozzle along an Almen strip was completed in one second. Stand-off distances between 150-

178 mm (6-7 in.) were found to provide the right intensities. Similar stand-off distances have been used in the peening of aluminium alloys, e.g., ref. [194].

A compilation of the calibrated settings of the nozzle speed and flow rates with different shot types is given in the appendix II (tables II-2-3).

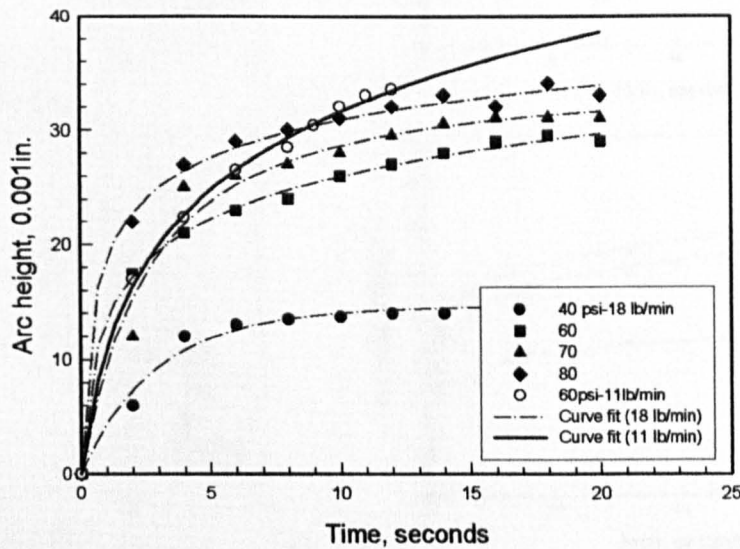


Fig. 4.1.9 Intensity response to varying air pressure and flow rate. “A” Almen strips grade I a standard Almen system for measuring the arc height were used for this preliminary trial. Curve fits were made by using Eq. (4.1). There was an appreciable increase in intensity when the shot flow rate was reduced (from 18 to 11 lb/min-8.2 kg/min) at constant pressure (60 psi-4.21 kg/cm²).

SETTINGS	LEVEL
PRESSURE	50 psi (345 kPa)
NOZZLE* STAND-OFF DISTANCE	6 in. (152.4 mm)
SHOT FLOW RATE	10 lb/min (4.54 kg/min)
* Venturi nozzle size ¼ in. (6.35 mm)	

Table 4.1.3 Experimental peening process parameters

The effect of changing only peening pressure from the settings given in table 4.1.3 is illustrated in Fig. 4.1.10 a-f. Here, the incidence angle was also kept at 90° to the Almen strip surfaces. The corresponding effect of incidence angle on the intensity by using the same peening parameters as in table 4.1.3 is shown in Fig. 4.1.11 a-d.

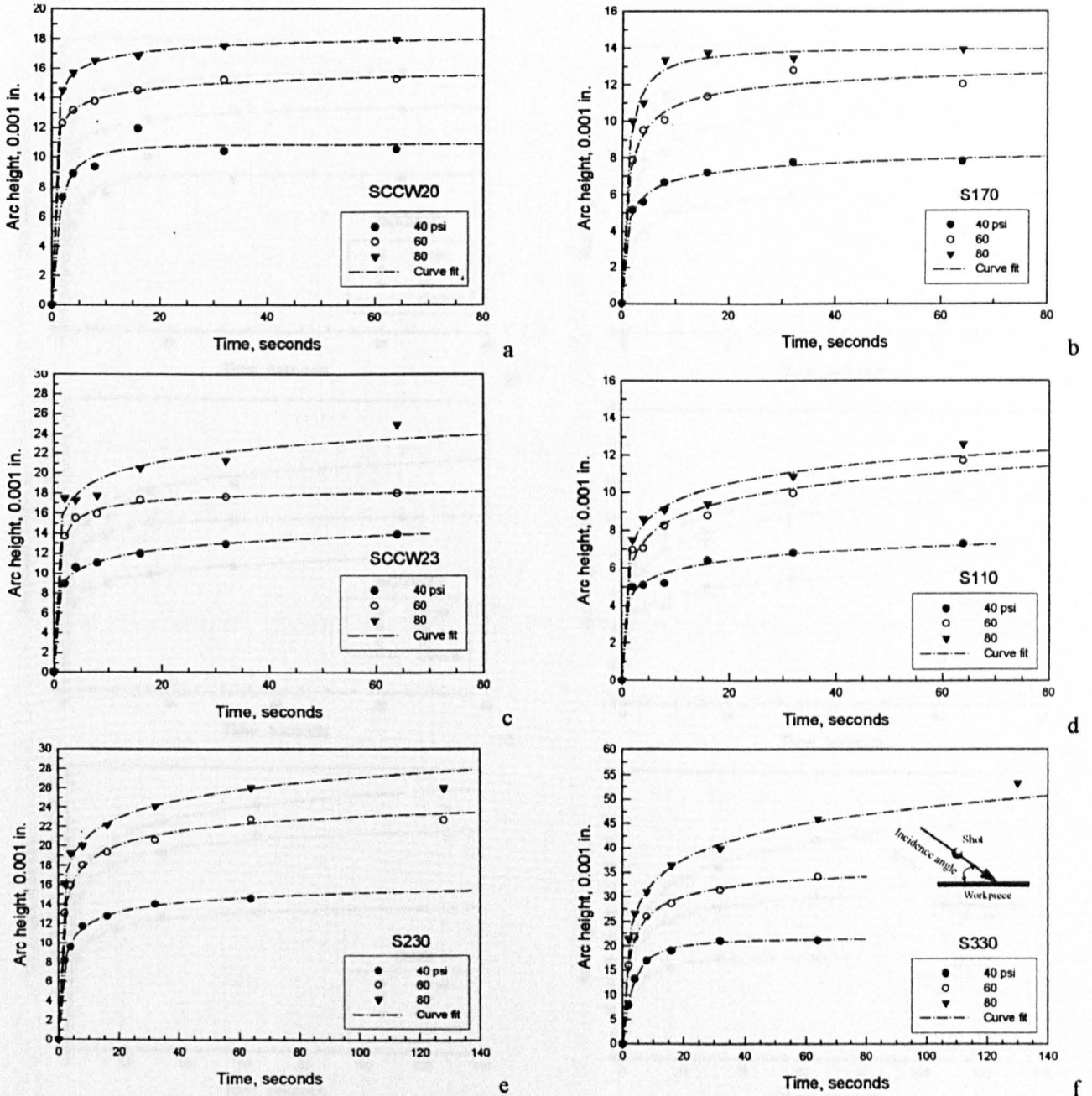


Figure 4.1.10 Saturation curves for different shot size and three different levels of pressure (graphs a-f). Flow rate, stand-off distance, and incidence angle were held at 10 lb/min (4.54 Kg/min), 6 in. (152.4 mm) and 90°, respectively. In Graph (f) the incidence angle of the shot in respect to the impacted surface is also schematically indicated.

4.1.5 Coverage

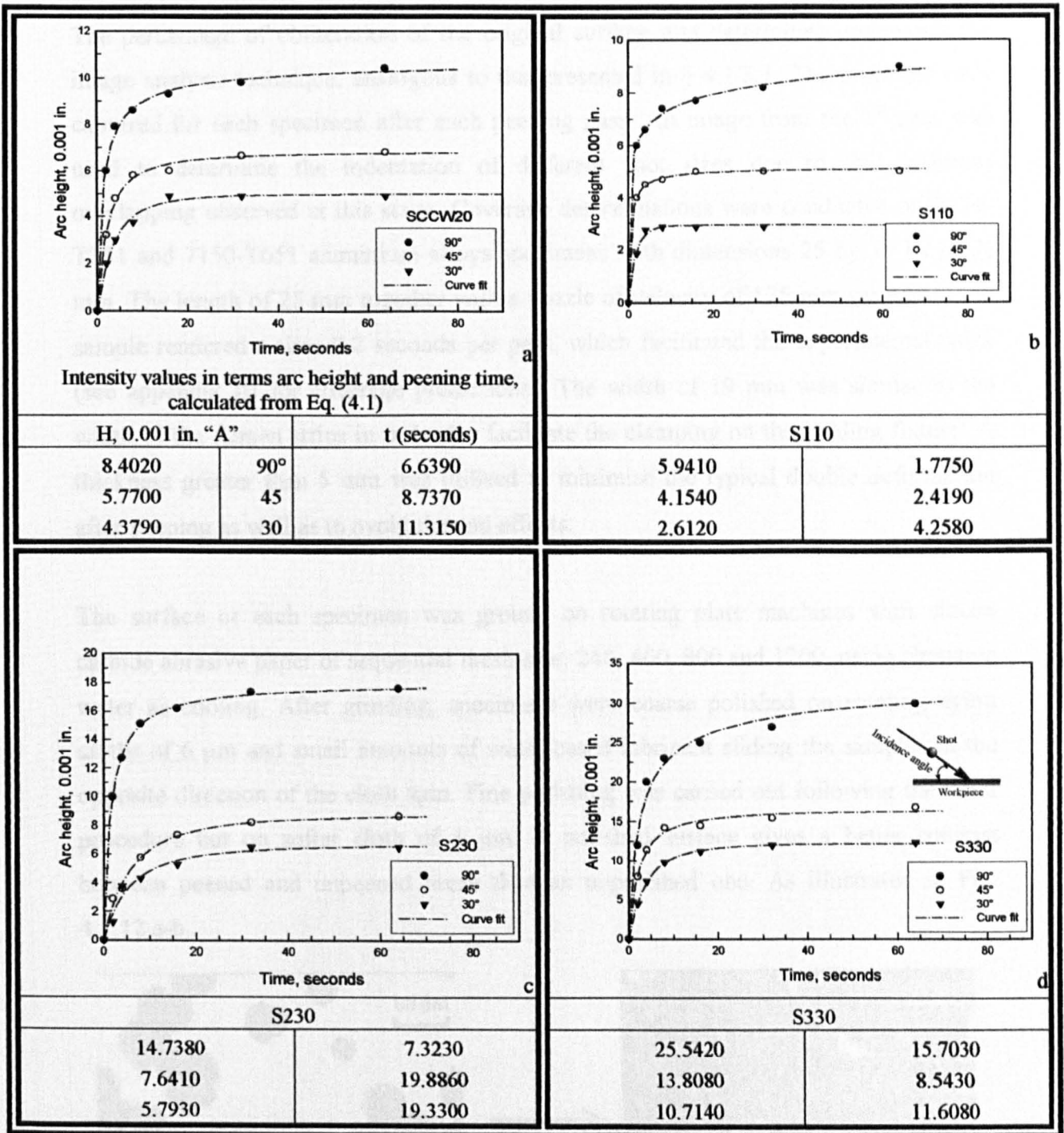


Figure 4.1.11 Saturation curves for different shot size and three different levels of incidence angle (graphs a-d). Flow rate, stand-off distance, and pressure were held at 4.54 kg/min (10 lb/min), 152.4 mm (6 in.) and 345kPa (50 psi), respectively. N.B. four shot types are shown because there were significant variations in intensity with shot type.

4.1.5 Coverage

The percentage of obliteration of the original surface was determined employing the image analysis technique, analogous to that presented in § 4.1.3.1. Three images were captured for each specimen after each peening pass. An image from the 1st pass was used to determine the indentation of different shot sizes due to the minimum overlapping observed at this stage. Coverage determinations were conducted on 2024-T351 and 7150-T651 aluminium alloys specimens with dimensions 25 by 19 by (5-7) mm. The length of 25 mm together with a nozzle of velocity of 125 mm/sec across the sample rendered a time 0.2 seconds per pass, which facilitated the experimental work (see appendix III for coverage predictions). The width of 19 mm was similar to the width of the Almen strips in order for facilitate the clamping on the holding fixture. A thickness greater than 5 mm was utilised to minimise the typical double deformation after peening as well as to avoid the end effects.

The surface of each specimen was ground on rotating plate machines with silicon carbide abrasive paper of sequential mesh size: 240, 400, 800 and 1200, using abundant water as cooling. After grinding, specimens were coarse polished on rotating nylon cloths of 6 μm and small amounts of water-based lubricant sliding the samples in the opposite direction of the cloth spin. Fine polishing was carried out following the latter procedure but on softer cloth of 1 μm . A polished surface gives a better contrast between peened and unpeened areas than an unpolished one. As illustrated in Fig. 4.1.12 a-b.

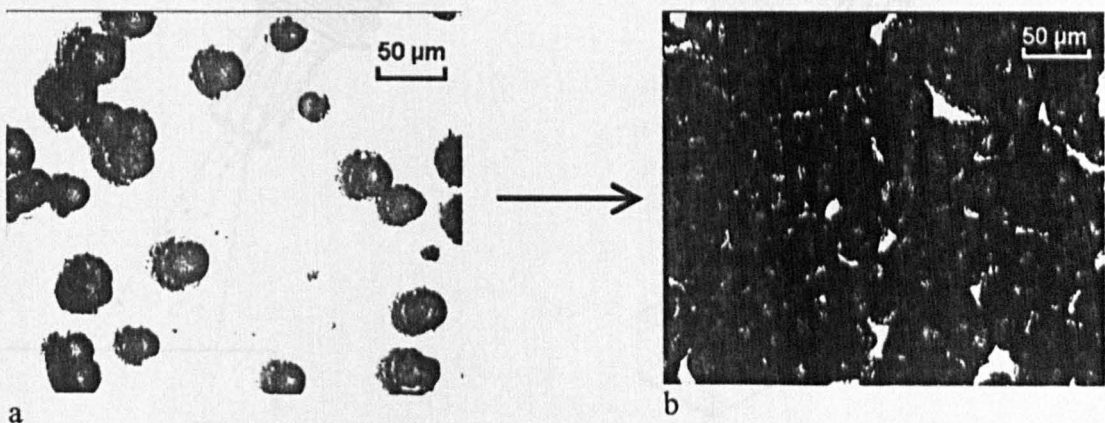


Figure 4.1.12 Images used for measuring coverage captured from peened specimens. The dark regions are the impacted areas which accounts for the coverage.: (a) 22.5% and (b) 98% coverage.

The SigmaScan © was again used for the coverage determinations. A threshold value of image contrast for the unpeened area was predetermined before the analysis. The selected regions were the unpeened areas. Subtracting the unpeened area from the total area in each image yielded the peened area. The ratio of peened area to the total area represented the calculated coverage percentage.

The shot spread or shot stream divergence of each shot type/size and at different incidence angles was also measured. To enable sufficient room for the shot media to freely impact the specimen during the nozzle movement, a large aluminium sheet was utilised. The peening parameters given in table 4.1.3 were kept constant. The shot stream divergence is shown in Fig. 4.1.13 a-b. The detailed geometry of shot stream divergence is depicted in Fig. 4.1.14. It is observed that the width of the spread increases with the distance from the nozzle but reduces with the incidence angle according to the equation:

$$D = \frac{d_n + 2H \tan \alpha}{\sin \theta} \quad (4.2)$$

where, d_n is the nozzle diameter ($\frac{1}{4}$ in = 6.35 mm), H is the stand-off distance, α is the divergence angle and θ is the incidence angle.

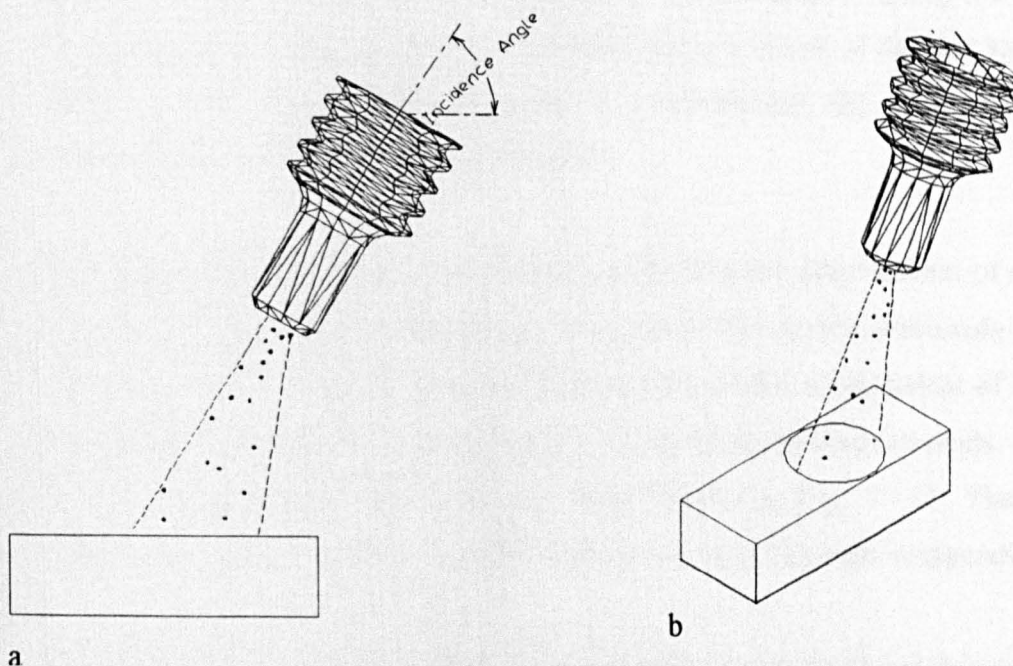


Figure 4.1.13 Schematic representation of the shot stream divergence: (a) the stream diverges at an angle determined by the type and incidence angle of the nozzle, (b) the spreading of the shot upon a surface.

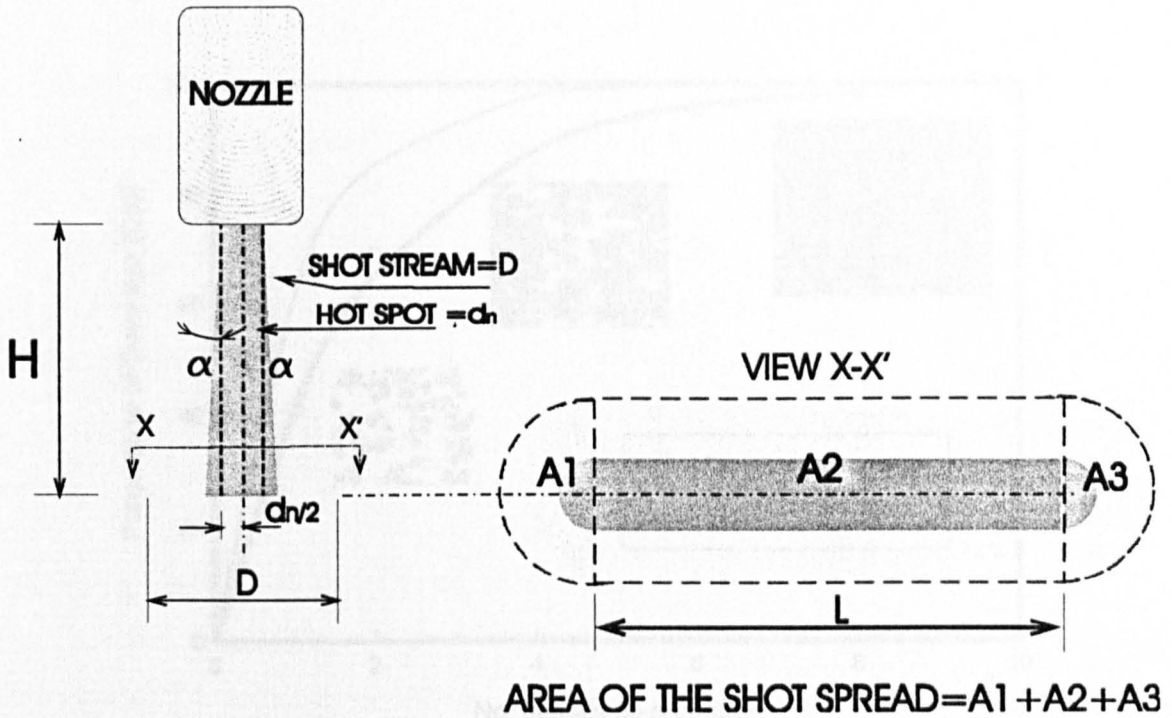


Figure 4.1.14 The basic geometry of the shot stream which diverges at an angle α . It is also shown the shot spread areas denoted as A_1 , A_2 , and A_3 , which themselves represent the three fundamental nozzle movements, namely, the beginning, advancing and stopping, respectively.

In addition, the shot spread was determined theoretically by using the Eq. (4.2) and compared with that measured experimentally using the area of the shot spread indicated in Fig. 4.1.14. A general procedure for determining the shot spread and their measurements are included in appendix III.

Two theoretical models were assessed for predicting the development of coverage from a selected combination of the peening parameters. The models previously discussed in § 2.2.3.5 (Eqs. 2.24 and 2.25) enable the prediction of the development of coverage with reasonable accuracy when compared to the experimental measurements. A comparison between experimental and theoretical data is given in Fig. 4.1.15. The methodology followed for obtaining the coverage predictions is also reported in appendix III.

Bearing in mind the results achieved between the experimental and theoretical coverage, the Holdgate model [195] was adopted for obtaining the evolution of the coverage in this research.

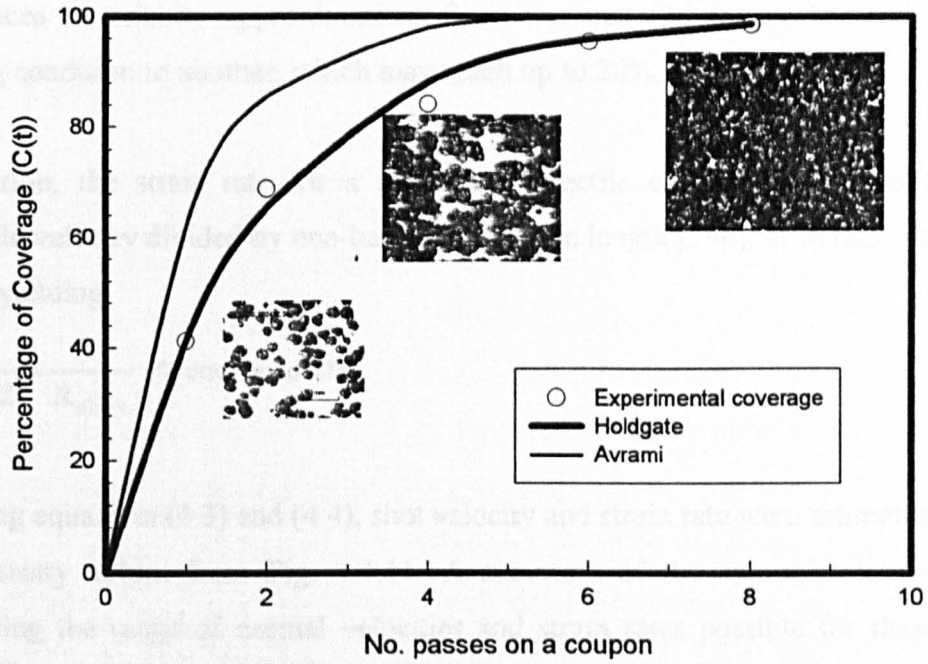


Figure 4.1.15 Experimental and theoretical coverage comparison of a 2024-T351 AA sample with peening conditions: S230, 30° incidence angle and intensity of 19.3A (0.49 mmA).

4.1.6 Velocity and strain rate estimations

Experimental velocity data was not available due to equipment limitations; however, in an attempt to estimate velocity v of a particular shot at the surface of the workpiece for a specific intensity, Iida's relationship [115] was used to determine approximates of impact velocities for peening conditions of interest:

$$v = \left(\frac{1}{1.28} \right)^2 \left(\frac{d}{D} \right)^2 \left(\frac{\sigma_y}{\rho} \right)^{\frac{1}{2}} \quad (4.3)$$

(Further mathematical details regarding Eq. (4.3) are included in appendix III)

where, d represents the dimple diameter, D the shot diameter, σ_y the yield strength of the target material and ρ the shot force density, defined as density/gravitational acceleration.

Errors in the material properties may be as much as ± 10 . The variability in the diameter of the shot may achieve errors up to $\pm 20\%$ (e.g. S110 shot). It is therefore likely to find differences in velocity approximations from one material to another and from one peening condition to another, which may reach up to 20%.

In addition, the strain rate for a spherical projectile can also be estimated as the projectile velocity divided by one-half the projectile length [198], or in this case the shot radius, yielding:

$$\dot{\epsilon} = \frac{v}{L/2} \approx \frac{v}{R_{\text{shot}}} \quad (\% \text{ error up to } 20\%) \quad (4.4)$$

Applying equations (4.3) and (4.4), shot velocity and strain rate were estimated by using the intensity values from Fig. 4.1.11. A summary of the approximate calculations illustrating the range of normal velocities and strain rates possible for these peening conditions is shown in Table 4.1.4. Only the dimple diameters measured at 90° incidence angle were used for velocity determinations of the aluminium alloys, which are reported in appendix III, table III-2. Details of the calculating procedure are incorporated in the same appendix III.

SHOT TYPE INTENSITY (0.001 in, A)	Shot Size, D (mm)	Angle	2024-T351 AA		7150-T651 AA		% variation	
			Velocity	Strain rate	Velocity	Strain rate	Velocity	Strain rate
			v, m/s	$\dot{\epsilon}$ (10^5 s^{-1})	v	$\dot{\epsilon}$		
SCCW20 $I \approx d = 8.402$	0.55	90°	75.6	2.7	84.8	3.1	10.9	12.9
		45°	106.9	3.9	119.9	4.4	10.9	11.4
		30°	87.3	3.1	97.9	3.6	10.9	13.9
S110 5.941	0.34	90	99.4	5.9	113.9	6.7	12.7	11.9
		45	140.6	8.3	161.1	9.5	12.7	12.6
		30	114.8	6.7	131.5	7.7	12.7	12.9
S230 14.738	0.72	90	86.9	2.4	91.6	2.5	5.2	4.0
		45	122.9	3.4	129.6	3.6	5.2	5.6
		30	100.4	2.8	105.8	2.9	5.2	3.5
S330 25.542	0.84	90	97.8	2.3	108.9	2.6	10.2	11.5
		45	138.3	3.3	154.1	3.7	10.2	10.8
		30	112.9	2.7	125.8	3.0	10.2	9.0

Table 4.1.4 Total velocity and strain rates estimates during shot impingement of materials: 2024-T351 and 7150-T651 AA.

4.2 INVESTIGATED MATERIALS

4.2.1 Tested materials

This investigation focuses on attaining the optimum peening conditions in terms of fatigue resistance for two aluminium alloys (AA's) commonly used in aircraft structures, 2024-T351 and 7150-T651. These materials were supplied by Airbus UK. The chemical composition and mechanical properties of each alloy are depicted in table 4.2.5. As these alloys were received in the form of rolled plate they had a preferred grain orientation. The average grain sizes were as follows: 220 μm in the longitudinal direction, 80 μm in the transverse direction and 52 μm in the short transverse direction for the 2024 alloy, and 28.5 μm in the longitudinal direction, 14.3 μm in the transverse direction and 58 μm in the short transverse direction for the 7150 alloy.

Al Alloy	σ_y (MPa)	σ_u (MPa)	E (Gpa)	σ_{FL} (MPa)	Hv (120-130)	Chemical composition (wt %)								
						Si	Fe	Cu	Mn	Mg	Cr	Zn	Ti	Al
2024-T351 ^a	325	470	70	180	120-130	0.5	0.5	3.8-4.9	0.3-0.9	1.2-1.8	0.1	0.25	0.15	Base
7150-T651 ^b	450	575	72.5	300	140-145	0.12	0.15	1.9-2.5	0.1	2-2.7	0.04	5.9-6.9	0.06	

a. Ref. [186]

b. Ref. [199]

Table 4.2.5 Materials: Mechanical properties and chemical composition.

4.2.2 Specimen design

Two different specimen profiles were used to evaluate respectively the surface modifications due to peening and the fatigue resistance: (i) a rectangular plate or coupon for determining the residual stress profile, the surface roughness and the work hardening, and (ii) an hourglass-shaped specimen for a uniaxial constant amplitude fatigue testing. Geometric details are shown in Fig. 4.2.16.

The dimensions of the coupons were based on the size of an Almen strip "A" so as to use the same holder as for the determination of peened intensity. However, a greater thickness was employed to minimise the typical double deformation after peening and also to avoid end effects. The thickness was the same as for fatigue specimens in an

attempt to introduce surface modifications of the same magnitude as in the fatigue specimens.

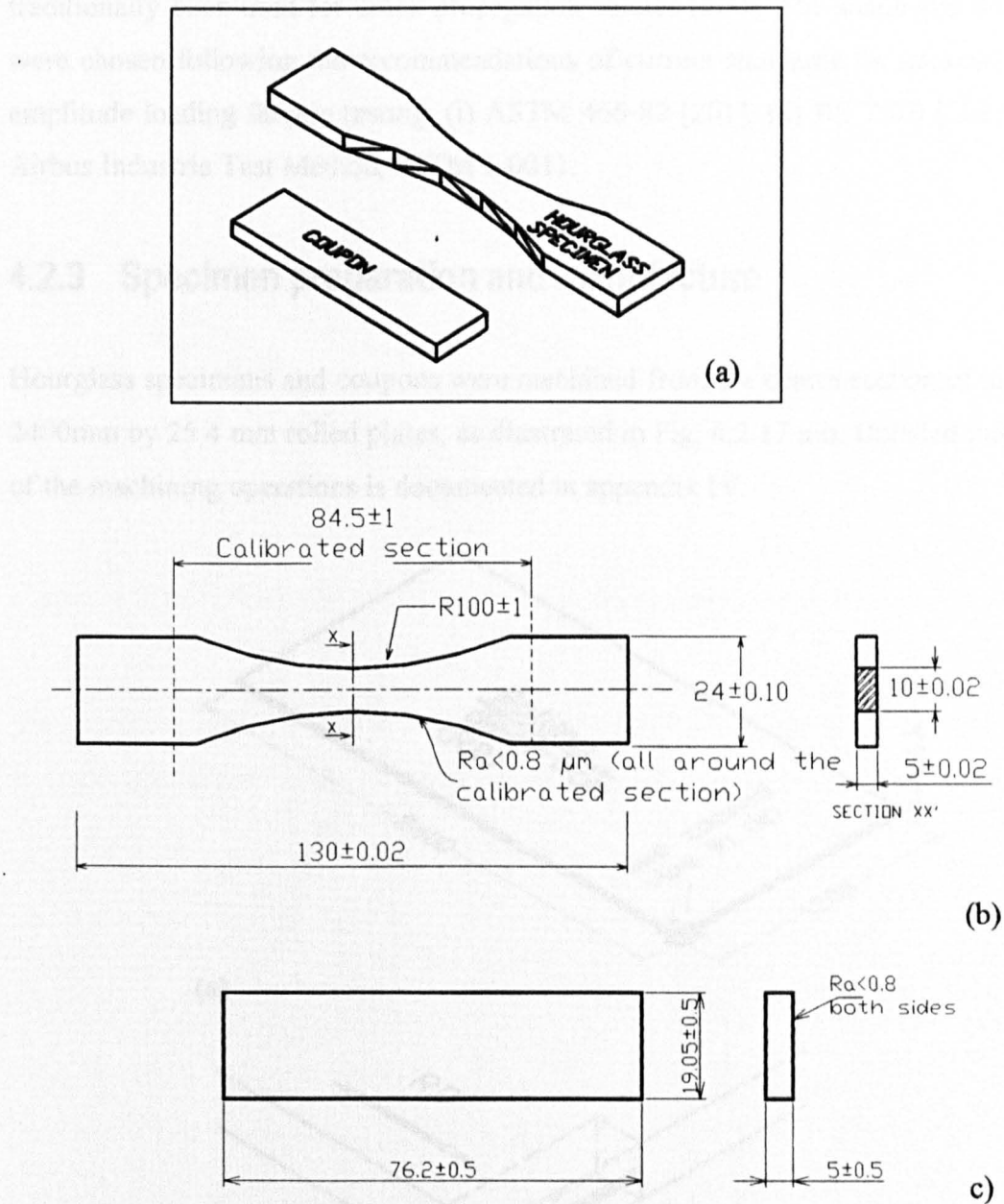


Figure 4.2.16 Specimen profiles (a). Dimensions for the hourglass specimen (b) and coupon (c) are given in mm. The drawings are not to scale.

The hourglass-shaped specimens were employed for determining the S-N curves and crack propagation data using axial fatigue testing. This type of specimen has traditionally been used for crack propagation studies [200]. The shape and dimensions were chosen following the recommendations of current standards for uniaxial constant amplitude loading fatigue testing: (i) ASTM 466-82 [201], (ii) BS 7270 [202] and (iii) Airbus Industrie Test Method, AITM 1-0011.

4.2.3 Specimen preparation and manufacture

Hourglass specimens and coupons were machined from the centre section of the 1200 x 2400mm by 25.4 mm rolled plates, as illustrated in Fig. 4.2.17 a-b. Detailed information of the machining operations is documented in appendix IV.

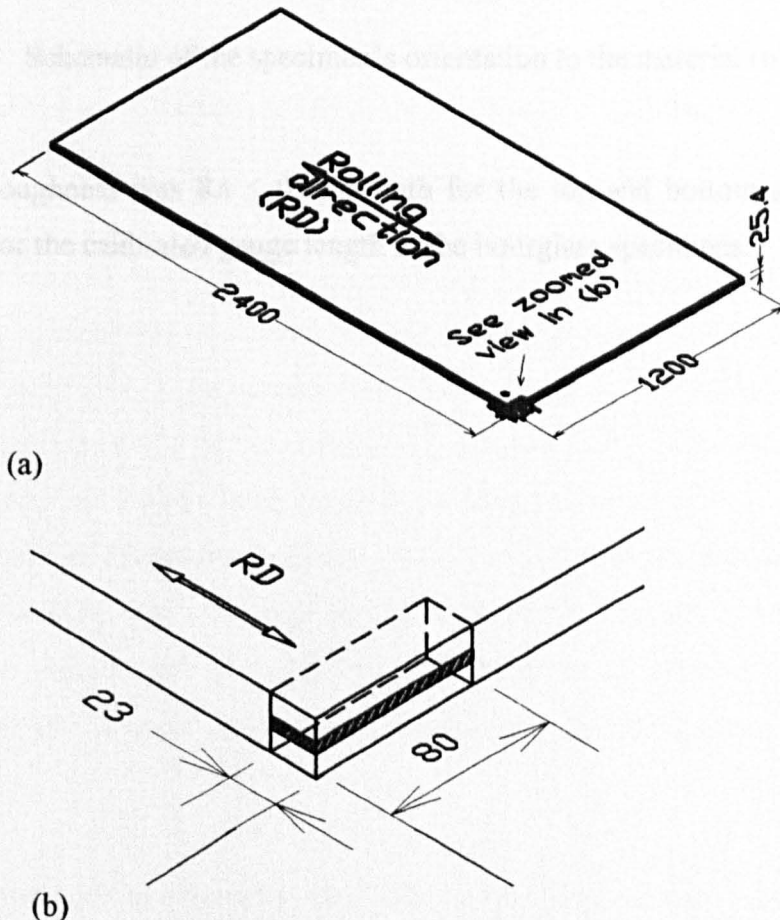


Figure 4.2.17 Rolled plates of both 7150-T651 and 2024-T351 AA (a). Preliminary dimensions of the blanks for machining the coupons are shown in (b). The specimens were machined to their final dimensions from the centre section of the plate, as indicated by the hatched area. All dimensions are in mm and not to scale.

The longitudinal axis of the specimens was orientated perpendicular to the material rolling direction as indicated in Fig. 4.2.18.

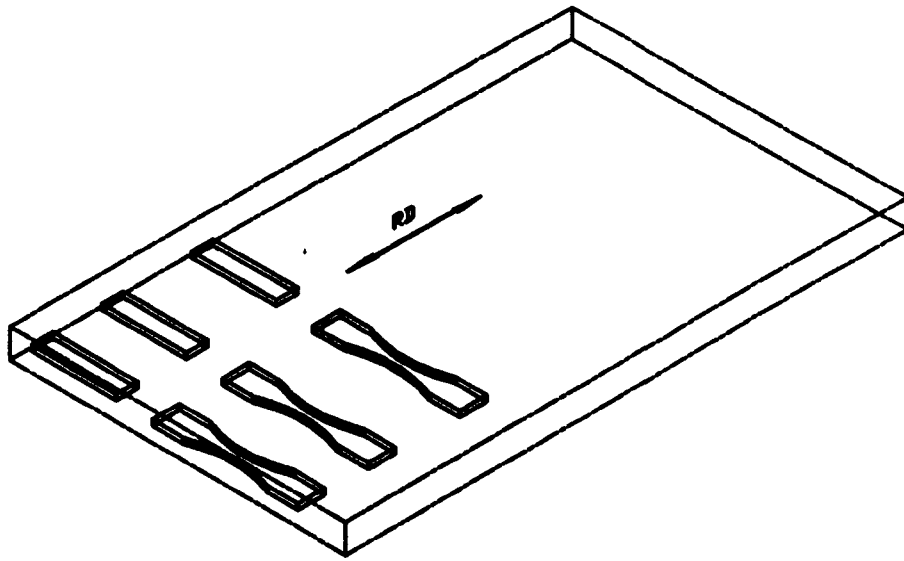


Figure 4.2.18 Schematic of the specimen's orientation to the material rolling direction.

The surface roughness was $R_a \leq 0.8\mu\text{m}$ both for the top and bottom surfaces in the coupons and for the calibrated gauge length in the hourglass specimens.

4.3 EXPERIMENT DESIGN

4.3.1 Design of experiments (DoE): Introductory background

A general methodology suitable for the optimisation of the different shot peening conditions that would enable a rational choice of the peening parameters has been proposed [162]. The shot peening variables and their preferred levels can now effectively be determined on a more scientific basis by means of an analysis of the effects induced on a particular component and the analysis of the interaction among these factors, rather than trusting in empirical considerations and experience. Thus, in order to gain a better understanding of the principles of such a methodology, this section describes the design of experiments and some of their relevant features including major advantages and disadvantages.

Design of experiments is an efficient experimental approach to studying the interaction effects between two or more factors in an experimental program also known as factorial design [203, 204]. The basic concepts were developed by Sir Ronald A. Fisher in England during the 1920's in the agricultural industry [205]. Fisher, together with a mathematician named Frank Yates, developed much of what it is known as the classical Statistical Design of Experiments (DoE). However, in 1949 the classic methodology was brought into the world of engineering, with some substantial modifications, in response to the urgent need to accomplish monumental tasks with very little time and money by Genichi Taguchi, who formally published his contributions in the 1980's [206].

Although design of experiments can take many forms, this strategy aims to quantitatively identify both the main effects of the factors and any interaction between them. This method also allows for conclusions to be drawn that are valid over a range of experimental conditions. The basic steps involved in any design of experiments analysis consist of the following:

To assume a set of variables controlling the output function.

In the design of experiments, selecting the suitable variables or factors is essential to determine the impact of the independent variables x_i on the dependent variable y . This can be expressed by a general function of the type:

$$y = f(x_1, x_2, \dots, x_k + \varepsilon) \quad (4.5)$$

ε is an uncontrolled variable which represents the impact on y of all factors other than x_i .

To select the number of levels of each variable to test.

Each factor is assumed to have a number of levels (≥ 1). If a factor is set up to a minimum and a maximum value, then such variable is assumed to be set to two levels. Considering that c is the number of variables and b is the number of levels, the number of necessary tests in a full factorial experiment is b^c (see § 4.3.1.1 for a complete array standard designation).

To conduct the experiments with a certain number of replications.

The greatest number of items of information will lead to a better process optimisation. Replication or equivalent information on the experimental error will introduce the necessary degree of freedom to estimate ε , that assumes the role of noise in connection with each experiment.

To introduce a predictive model.

This represents a relationship between variables and the system response. Evidently, since Eq. (4.5) is not theoretically derivable, an empirical mathematical model must be established.

To perform the analysis of variance (ANOVA).

An analysis of variance allows evaluation of the impact of every effect on the system response and of the interaction effects among the factors. It distinguishes which variables have statistical significance. If the prediction model is statistically adequate, it

can be used for values of variables not directly tested, and utilised for the optimisation of the process.

The Classic and Taguchi methodologies have already been applied to address the choice of the parameters affecting the surface treatments, such as surface rolling and shot peening [160, 161, 207]. In the last few years however, Taguchi's contribution seems to be the preferred one because it enables the optimisation of complex processes without the necessity of employing rigorous statistical rules and additionally it analyses in a more efficient way, the interaction among the factors of a process [162, 208, 209].

The effect of parameters set at various levels can be studied by following one of the better known experimental design approaches:

One factor at a time.

Full factorial.

Fractional factorial (orthogonal array experiments).

Whereas all three may be used for studying the effects of the variables on the response of the system, not all are equally efficient. One factor at a time has been the traditional method used in academia and industry. However, it has been the most inefficient of all methods as it cannot evaluate any interaction among factors, it is not balanced and very frequently conclusions about factors are never reached and therefore, the optimisation process goes into a loop that does not always converge [210]. Full factorial, will require investigation of all possible combinations, and conclusions are usually apparent well before the experimental data are all collected. This approach is time-consuming and therefore, expensive. The fractional factorial (also called orthogonal array) is a method of setting up experiments that only requires a fraction of the full factorial combinations. It allows information to be obtained on all main effects and interactions, while keeping the size of the experiment manageable and also conducting it in a single, systematic effort [163, 210].

A comparison of sample sizes required for full and fractional factorial experiments of various sizes is depicted in table 4.3.6. It is evident that the more the factors are evaluated the more the advantages of fractional factorial designs.

		Full factorial	Taguchi fractional factorial	
No. of factors (c)	No. of levels (b)	Total runs b^c	Array name	Total runs
3	2	$2^3=8$	L_4	4
7	2	$2^7=128$	L_8	8
11	2	$2^{11}=2048$	L_{12}	12
15	2	$2^{15}=32768$	L_{16}	16
4	3	$3^4=81$	L_9	9
5	4	$4^5=1024$	L_{16}	16
1 7	2 3	$2^1 3^7=4378$	L_{18}	18

Table 4.3.6 Comparison of sample sizes of full and fractional factorial approaches (after [210])

Even though the choice of a particular approach will depend on the number of factors and levels, the use of fractional factorial method represents itself as the most reasonable choice in terms of reducing the number of experiments without loss of quality in the obtained results. Hence, the ensuing sections will be devoted to the orthogonal arrays features as this was the primary strategy used in the designed experiment for the present study.

Fractional factorial orthogonal arrays

Orthogonal arrays are useful tools in which an experiment can readily be constructed by assigning factors to columns of the orthogonal array then matching the different integers of columns with the different factor levels. The latter means that there are many orthogonal arrays which are commonly used for constructing experiment plans. An orthogonal array is a table of integers with a balancing property: every pair of columns contains the same number of each integer and of inverse pairs of integers [209, 211].

The convention for naming the fractional factorial orthogonal arrays is [163, 210]:

$L_a(b^c)$

where

a = the number of experimental runs

b = the number of levels for each factor

c = the number of columns in each array

Although the orthogonal arrays are attributed to Taguchi's methods; these plans were not invented by him [209]. Authors like Plackett-Burman, Rao [212] and many others contributed to the construction of such arrays.

Some examples of the most common orthogonal arrays are shown in table 4.3.7 a-c. The $L_4(2^3)$ can handle three factors at two levels. It is the smallest of the two-level orthogonal arrays. The $L_9(3^4)$ can handle four factors at three levels. The L_{16} is able to handle up to five factors at four levels.

$L_4(2^3)$			
Run	Factor		
	1	2	3
1	1	1	1
2	1	2	2
3	2	1	2
4	2	2	1

(a)

$L_9(3^4)$				
Run	Factor			
	1	2	3	4
1	1	1	1	1
2	1	2	2	2
3	1	3	3	3
4	2	1	2	3
5	2	2	3	1
6	2	3	1	2
7	3	1	3	2
8	3	2	1	3
9	3	3	2	1

(b)

$L_{16}(4^5)$					
Run	Factor				
	1	2	3	4	5
1	1	1	1	1	1
2	1	2	2	2	2
3	1	3	3	3	3
4	1	4	4	4	4
5	2	1	2	3	4
6	2	2	1	4	3
7	2	3	4	1	2
8	2	4	3	2	1
9	3	1	3	4	2
10	3	2	4	3	1
11	3	3	1	2	4
12	3	4	2	1	3
13	4	1	4	2	3
14	4	2	3	1	4
15	4	3	2	4	1
16	4	4	1	3	2

(c)

Table 4.3.7 Standard orthogonal arrays: (a) Three factors at two levels, (b) four factors at three levels and (c) five factors and four levels. After [163, 210, 211].

4.3.1.1 Three types of analysis statistics: signal-to-noise ratio (S/N)

The signal-to-noise metric (S/N) is designed to optimise the robustness of a product or process. The S/N is employed to minimise the performance sensitivity to noise factors. The S/N combines both the variance of predictable performance and the variance of unpredictable performance into a single measure [213]. The fundamental properties of the S/N metric are:

- i. The S/N ratio reflects the variability in the response of a system caused by noise factors.
- ii. The S/N ratio is independent of the adjustment of the mean.
- iii. The S/N ratio measures relative quality¹, because it is to be used for comparative purposes.

The general definition of the S/N can be expressed as:

$$S/N = -10 \log(\text{MSD}) \quad (4.6)$$

where the MSD is the *mean square deviation* expressed in a way that is independent of the adjustment. The MSD average value is referred to as the off-target. The -10 log places the S/N ratio into *decibel units* (dB) and arranges their level in a way that as the value of the MSD decreases, the S/N ratio increases.

The specific S/N that is used in a parameter design experiment depends on whether improved performance is indicated by a small number, a large number, or something closer to a particular target value.

1. In the case when the smaller is better, then

$$S/N = -10 \log \left(\frac{1}{n} \sum_{i=1}^n Y_i^2 \right) \quad (4.7)$$

¹ Quality is based upon the concept of on-target engineering. All deviations of the target imply some loss of quality.

The distinguishing characteristics are: (a) Response values are continuous and nonnegative, (b) the desired value of the response is zero and (c) the goal is simply to minimise the mean and variance simultaneously.

2. In the case when larger is better, then

$$S/N = -10 \log \left(\frac{1}{n} \sum_{i=1}^n \left(\frac{1}{Y_i} \right) \right) \quad (4.8)$$

The distinguishing characteristics are: (a) the response values are continuous nonnegative numbers ranging from 0 to infinity, (b) the desired response is infinity or the largest number possible, and (c) the larger-the better-problems are the reciprocal of the smaller-the-better problems.

When a specific target value is best, then

$$\begin{aligned} S/N &= -10 \log \left(\frac{\bar{y}^2}{S^2} \right) \text{ Type I} \\ S/N &= -10 \log (S^2) \text{ Type II} \end{aligned} \quad (4.9)$$

where Y_i represents the i th replicate numerical measure of process performance and n represents the number of replicates. S is the variance given by

$$S^2 = \frac{1}{n-1} \sum_{i=1}^n (y_i - \bar{y})^2 \text{ and } \bar{y} \text{ is the mean.}$$

4.3.1.2 The predictive model

The general form of the predictive equation is as follows:

$$y_{\text{predicted}} = \bar{y}_{\text{exp}} + (\bar{y}_A - \bar{y}_{\text{exp}}) + (\bar{y}_B - \bar{y}_{\text{exp}}) + (\bar{y}_C - \bar{y}_{\text{exp}}) + \dots \quad (4.10)$$

where \bar{y}_{exp} is the overall average response, i.e. S/N ratio, for the entire fractional factorial array and \bar{y}_A , \bar{y}_B , \bar{y}_C are the response averages for the factors A, B, and C, respectively. The factor effects corresponding to the factor levels being modelled (typically the optimum levels) are used in the predictive equation.

The major advantages offered by the application of DoE are:

- Analysis of the interaction among factors provided these interact during the process.
- Elimination of the effects of the cause without eliminating the causes.
- Velocity of the test execution and rapid data collection and decision making.
- The noise is considered in the experiments (robust design).
- Enables the execution of the screening experiments, which are useful when the aim is to find the most significant parameters of the process and to examine the interaction among the parameters (there is an interaction when a variation in the level of a factor causes a change in the level of another one).

The major disadvantages observed by the Taguchi's contribution are:

- The application of S/N ratio has been seriously questioned by Box, *et al.* [214] as inefficient and unnecessarily complicated.
- The application of orthogonal arrays comes along with interactions and also generates confounding relations among the columns in the arrays. This is frequently difficult to understand [215].
- Two and three levels factors are the preferred arrays published in the literature. The construction of a suitable array results in a complex-time consuming task.

4.3.2 Experiment design

A total of three factors were evaluated at four levels each as shown in table 4.3.7. These chosen factors are of fundamental importance to the aircraft industry and particularly to Airbus UK, who provided the material and some equipment required for this project. A complete full factorial design that would allow for estimation of all main effects and factor interactions would require 4^3 or 64 experiments. Assuming that higher order interactions between factors were negligible, one-fourth fractional factorial design evolving a total of 16 experiments was selected.

FACTOR	LEVEL			
	1	2	3	4
A Steel shot (type)	S230	CCW20	S110	S330
B Coverage (%)	50	100	200	400
C Empty	—	—	—	—
D Incidence angle (degrees)	30	89	45	89
E Empty	—	—	—	—

Table 4.3.7 Summary of shot peen factors evaluated by design of experiment. These factors are of fundamental importance for the aircraft industry.

A fractional factorial $L_{16}(4^5)$ array was used to enable the optimisation of five parameters with each of these set at a maximum of four levels [216]. This approach permitted the estimation of all the main and first order factor interactions. The empty columns, third and fifth factors, were used to verify that all important parameters influencing shot peening effects were considered. The full fractional factorial array together with the selected factors and levels is depicted in table 4.3.8.

Orthogonal array						ASSIGNED FACTORS AND LEVELS				
Run	A	B	C	D	E	SHOT	COVERAGE	EMPTY	ANGLE	EMPTY
1	1	1	1	1	1	S230	50	1	30	1
2	1	2	2	2	2	S230	100	2	89	2
3	1	3	3	3	3	S230	200	3	45	3
4	1	4	4	4	4	S230	400	4	89	4
5	2	1	2	3	4	CCW20	50	2	45	4
6	2	2	1	4	3	CCW20	100	1	89	3
7	2	3	4	1	2	CCW20	200	4	30	2
8	2	4	3	2	1	CCW20	400	3	89	1
9	3	1	3	4	2	S110	50	3	89	2
10	3	2	4	3	1	S110	100	4	45	1
11	3	3	1	2	4	S110	200	1	89	4
12	3	4	2	1	3	S110	400	2	30	3
13	4	1	4	2	3	S330	50	4	89	3
14	4	2	3	1	4	S330	100	3	30	4
15	4	3	2	4	1	S330	200	2	89	1
16	4	4	1	3	2	S330	400	1	45	2

Table 4.3.8 Fractional factorial array $L_{16}(4^5)$ with factors and levels assigned to columns. The orthogonal array was chosen from ref. [216].

The evaluated effects are those obtained from: the measured-calculated residual stresses/depth, the direct measurement of the microhardness/depth and the calculated stress concentration factors (from the direct roughness measurements). The performance statistics utilised, i.e. the parameter MSD, were selected according to the ensuing two modalities:

- i. Larger-the-better statistic for the maximum compressive residual stresses/depth and also for the work hardening (microhardness).
- ii. Smaller-the-better statistic for the stress concentration (roughness).

4.4 EXPERIMENTAL TECHNIQUES FOR DETERMINING THE PEENING EFFECTS

Coupons with dimensions shown in Fig. 4.2.16-c were shot peened according to conditions listed in Table 4.3.8, to determine: (i) surface roughness, (ii) residual stresses profile in depth and (iii) work hardening profile in depth. This sequence was adopted not only to avoid any possible distortion or damage to the original dimpled-surface but to make use of inefficient area to carry out such measurements in many different directions.

4.4.1 Surface roughness

4.4.1.1 Roughness parameters

Three roughness parameters are of interest when quantifying surface roughness of a peened component: (1) average roughness, R_a , (2) roughness depth, R_t , and (3) peak-to-peak distance, S . R_a is utilised comparatively to give a general indication of roughness, however, R_t and S are used to calculate stress concentration factors (K_t) due the roughened surface caused by shot peening as previously described in § 3.2.3. Definition of R_a , R_t and S parameters can be found in Appendix V.

4.4.1.2 Equipment

To carry out the quantification of the surface topography on the peened coupons, the roughness parameters R_a and R_t were determined using, initially, a stylus-tip (electrical contact) instrument (Mitutoyo Surftest 301). More accurate equipment, namely, a Taylor-Hobson Surtronic 3+ machine, in conjunction with computer software¹ was used to obtain 2D profiles of the surface topography of the coupons. This machine allowed for direct readings of R_a and R_t values. Determination of the S parameter was carried out using proprietary software, measuring 30 of the adjacent peak-to-peak distances and averaging the set of measured lengths.

4.4.1.3 Experimental technique

There still is insufficient information regarding the quantification of the topography of shot peened surfaces [217]. Clausen and Stangenbert [218], however, have found that there is no clear dependence between the measured roughness values, the measuring direction and the measuring point in a uniformly peened surface having coverage of $\geq 97\%$. Therefore, they proposed to follow the practice of taking at least ten measurements made at any point and in any direction that is desired, so that the average value can be used to represent the roughness of the surface. The surface roughness can then be expected to have a standard deviation of about 10%. Hence, this practice was adopted for conducting roughness measurements.

An evaluation length of 4mm was chosen, each one containing five sample lengths of 0.8mm. Ten measurements were required in any direction to ensure sufficient accuracy. To reduce the number of measurements required, one measurement of 25mm length (equivalent to six 4mm evaluation lengths), and 4 additional measurements of 4mm length were undertaken. This gave the equivalent of ten profiles of 4mm in length, from which the values for S, R_a and R_t were found, and averaged to give S_m , R_{am} and R_{tm} . The directions in which the profiles were taken are shown in Fig. 4.4.19

¹ *Talyprofile Mountains Technology*, from Digital Surf, France.

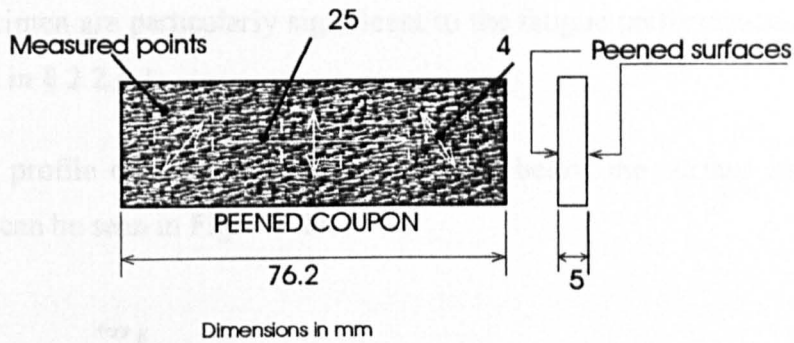


Figure 4.4.19 Location of the measuring points and arrangement of the measuring directions on the peened coupons for each type of aluminium under investigation.

Evaluation lengths were split into sample lengths as indicated in Figure 4.4.20. For a chosen evaluation length, the traverse length of the probe needed to be made slightly longer to allow for run-up and over-travel; this allowance was set to 0.8mm.

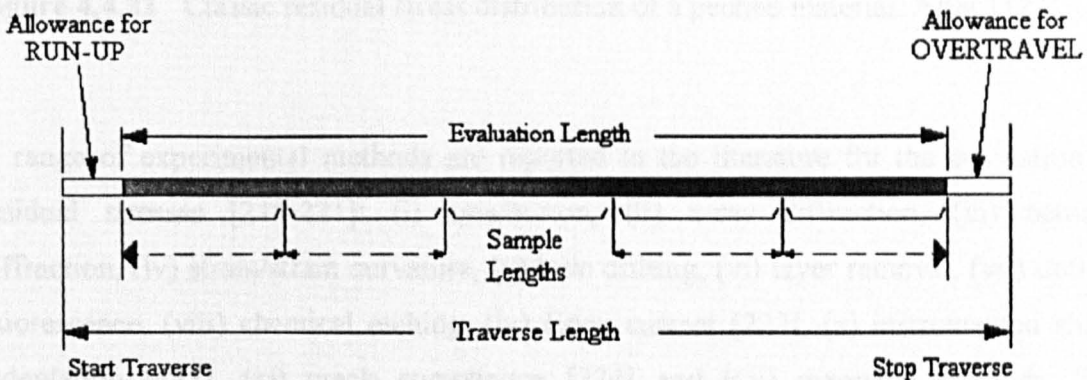


Figure 4.4.20 Schematic representation of the evaluation length when surface roughness is measured.

4.4.2 Residual stresses

4.4.2.1 Selection of the suitable method

It is acknowledged now that shot peening can only be reliably controlled and optimised by measuring, among others, the subsurface residual stress distributions. This is because the stress distributions depend on the properties of the material being peened, prior to processing, and the specific peening parameters used. Residual stresses (RS) for a

peened specimen are particularly significant to the fatigue performance of a component as reviewed in § 2.2.4.1.

The classic profile of residual stress distribution below the surface of a shot peened component can be seen in Fig. 4.4.21.

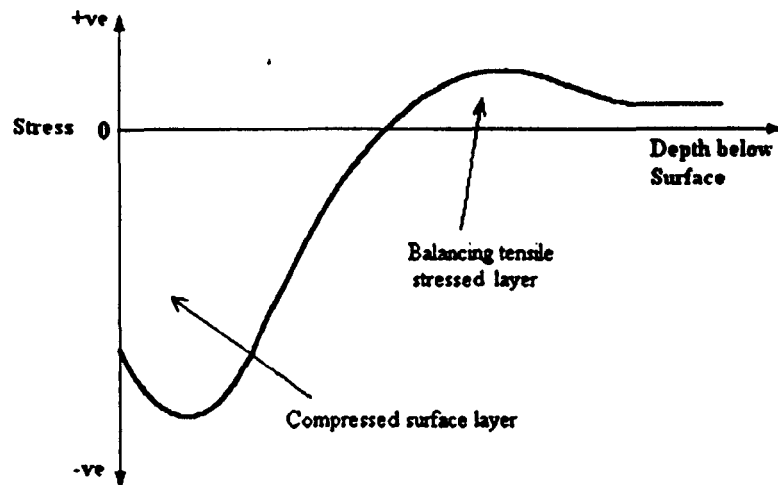


Figure 4.4.21 Classic residual stress distribution of a peened material. After [127].

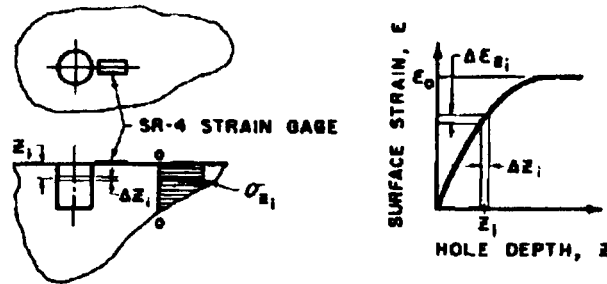
A range of experimental methods are reported in the literature for the estimation of residual stresses [219-221]: (i) synchrotron, (ii) x-ray diffraction, (iii) neutron diffraction, (iv) strain/strain curvature, (v) hole drilling, (vi) layer removal, (vii) optical fluorescence, (viii) chemical etching, (ix) Eddy current [222], (x) instrumented sharp indentation [223], (xi) crack compliance [224] and (xii) magnetic methods. The convenience of measuring residual stresses non-destructively might be preferred. However, from the above techniques, exclusively synchrotron, neutron diffraction (ND) and Eddy current (EC) are non-destructive techniques. In the case of Eddy current, it has not yet achieved wide acceptance as a standardised method of residual stress analysis [225] whilst the use of both synchrotron and ND is literally prohibitive given the expensive equipment required. It is clear, therefore, that the extensive use of each of these techniques for most practical situations present their own inconveniences and/or restrictions because of problems associated with measurement accuracies, spatial resolution; ease and time of measurement, depth profiling; applicability to a broad range of materials and geometries, destructiveness, sensitivity, and the cost, both of equipment and materials employed in their use.

There is little doubt, however, that incremental hole drilling (IHD) and x-ray diffraction (XRD) methods are the most widely accepted standardised methods for measuring residual stresses of peened components, due to their easy and relatively accurate results [226-228]. Between these two techniques, XRD is thought to be more accurate and the best developed means of quantifying RS, although it is also subjected to errors in both measurement and interpretation. The IHD is in turn the most widely used technique in industry [228] with results comparable to XRD. To this regard, a relatively good agreement between the results of both methodologies has been reported [229]. Indeed, it has recently been shown that IHD can successfully be used for measuring residual stresses of a peened component [230].

This discussion and some practical features (listed in appendix VI) led IHD to be selected as the method for measuring the RS of the peened specimens in this research.

4.4.2.2 The hole drilling concept

The hole-drilling strain gauge method for measuring residual stresses, first described by J. Mathar [231], involves drilling a small hole into a specimen containing residual stresses. The relieved surface strains adjacent to the hole can be measured by a special residual stress strain gauge rosette, allowing a back-calculation of residual stress to be made. Theory of elasticity is used to correlate the strain relaxation and the residual stresses existing prior to hole drilling taking into consideration the hole and strain gauge geometry by calibration coefficients. The principles and theory of some relevant features of this method are included in appendix VI. Due to the stresses varying with depth below the peened surface; the residual stresses are not uniformly distributed as indicated in Fig. 4.4.21. In Fig. 4.4.22 a schematic representation of a uniform and a non-uniform stress field is depicted. The measurement of non-uniform residual stresses requires incremental drilling and strain gauge reading [232]. This approach enables incremental changes in measured strains, brought about by drilling specific increments in the hole depth, to be analysed.



(a) UNIFORM STRESS FIELD.



(b) NON-UNIFORM STRESS FIELD.

Figure 4.4.22 Surface strain and hole depth relationships for uniform and non-uniform stress field. In the case of uniform stress field, the incremental change in surface strain, $\Delta \epsilon_{zi}$, for an incremental increase in hole depth, Δz_i is proportional to the magnitude of the stress, σ_{zi} , i.e. for a material that follows the Hooke's law $\epsilon = \frac{\sigma}{E}$. However, in the case of a non-uniform

stress field, the incremental surface strain is not a direct measure of the average residual stress in a given increment of the hole depth and, therefore, a proportionality factor K must be introduced, i.e.,

$$\Delta \epsilon_{zi} = K \frac{\sigma_{zi}}{E}. \text{ After [232].}$$

4.4.2.3 Equipment and materials

For the IHD technique, high-speed drilling equipment, namely, a milling guide RS-200 with air turbine, Measurements Group Inc., was used to create a cylindrical blind hole (a typical hole drilling set-up is shown in Fig. 4.4.23). The equipment is capable of rigidly guiding the progress of the cutter in a straight line during the drilling operation [225]. This action reduces considerably any side pressure on the hole or friction at the non-cutting edge, which is imperative for minimising, in turn, the induced machining effects. Furthermore, due to the use of an ultra-high-speed drill (up to 400,000 rpm when using an air-turbine at 40 psi pressure), this equipment enables continuous drilling of a flat-bottomed hole in precise increments, which is recommended because only minor drilling-induced plastic deformations occur as reported by Flaman in [233].

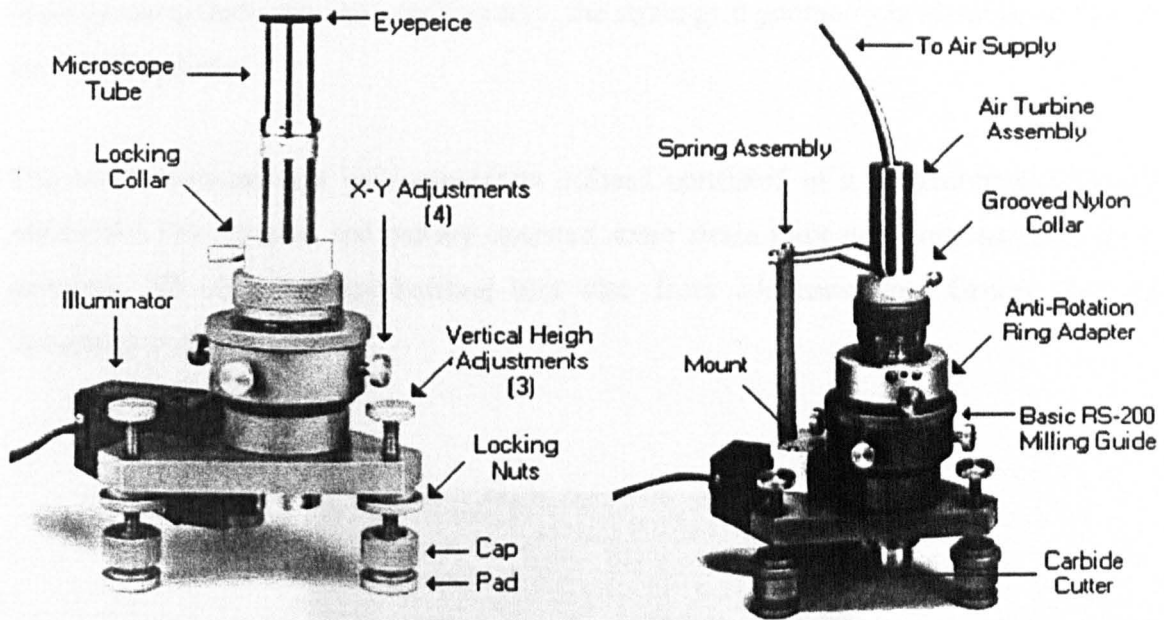


Figure 4.4.23 Hole drilling set up: alignment microscope (left picture) and the milling guide along with the air-turbine assembly (right picture). After [234].

To measure the released strains, high precision strain gauges were used which consisted of three gauge elements specially designed for measuring residual stresses. These rosettes incorporate centering marks for aligning the boring tool precisely at the centre of the gauge circle, since this is critical to the accuracy of the method [225]. Commercial strain gauges more frequently used are pictured in Fig. 4.4.24. The surface strain release of the peened specimens was measured by using the rosette type CEA-06-062UL-120.

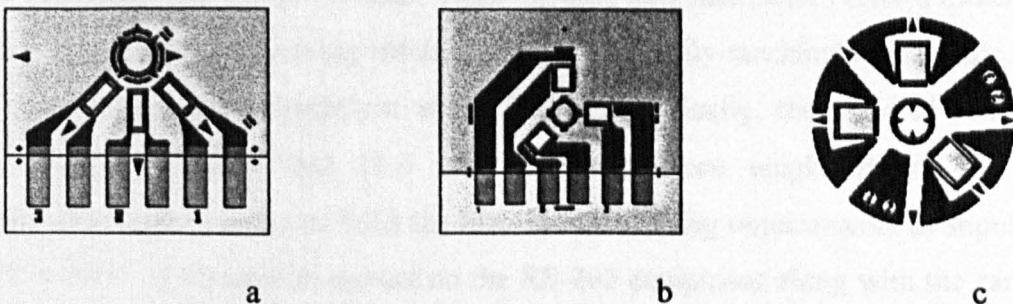


Figure 4.4.24 Schematic representation of the special-purpose strain gauges: (a) CEA-XX-062UM-120, (b) CEA-06-062UL-120 and (c) EA-XX-062RE-120 manufactured by Measurements Group Inc. for measuring residual stresses when the IHD is employed. After [234].

This particular design incorporates integral copper soldering tabs (on one side of the gauge to facilitate lead-wire routing from the gauge site), conformability (it is compatible with all methods of introducing the hole) and its installation time and

expense are greatly reduced. Additionally, the strain grid geometry is identical to that of the 062RE pattern.

The strain-measurement instrumentation utilised consisted of a Measurements Group Model P-3500 portable and battery-operated static strain indicator, supplemented by a precision SB-10-switch-and-balance unit also from Measurements Group, Inc. as illustrated in Fig. 4.4.26.

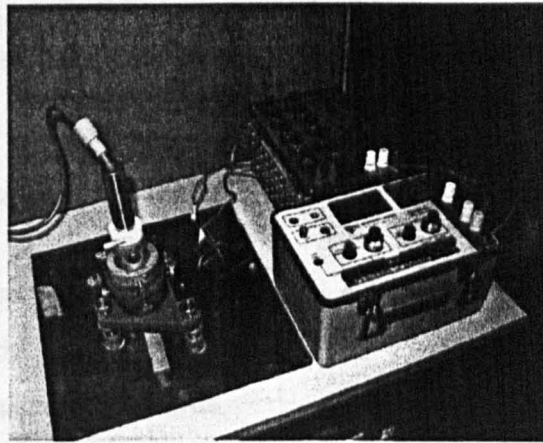


Figure 4.4.26 The strain indicator and balance-unit (yellow boxes) used to record the micro strains.

Finally, a specially dressed end mill cutter from Measurements Group, Inc. was employed which generates the desired flat-bottomed and square-cornered hole shape when a high-speed air turbine is used. These carbide tungsten cutters offer a direct and simple approach when measuring residual stresses on readily machinable materials such as mild steel and some aluminium alloys [225]. Specifically, the inverted-cone and carbide tipped ATC-200-062 (1.6 mm diameter) were employed to drill the corresponding hole in order to fulfil the incremental drilling requirements as stipulated in ASTM E837. A zoomed in picture on the RS-200 equipment along with the carbide tungsten cutter is depicted in Fig. 4.4.27.

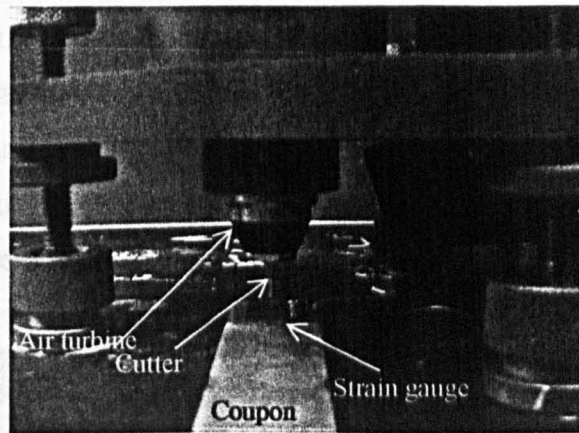


Figure 4.4.27 A view of the RS-200 equipment showing the air turbine assembly (a), the carbide tungsten cutter (b), and a strain gauge already glued to a coupon. The coupon, in turn, is cemented to a steel flat plate.

4.4.2.4 Experimental procedure

The measurement procedure was according to ASTM designation E-837-95 [235] and also in accordance with the recommendations of Vishay Measurements Group [225], which is briefly summarised as follows:

- i. A special three-element strain gauge rosette is glued to a coupon in the required position, according to the manufacturer's guidelines (typical strain gauge installation with M-Bond 200. – Micro-Measurements Instruction Bulletin B-127 from Measurements group, Inc.). The coupon is then cemented to a steel plate in roughly the correct position for drilling.
- ii. Gauge wires are soldered to the relevant contacts and connected to the switch and balance unit, which is in turn, connected to the strain indicator. Figure 4.4.28 shows a coupon with strain gauge and wires attached.
- iii. The drilling tool is aligned with the centre of the gauge using the alignment microscope tube. Once the air-turbine drill is correctly positioned, an initial drilling (approximately 10-20 μm , which is still less than the thickness of the strain gauge) is carried out to cut through the strain gauge.
- iv. The strain gauge readings are set to zero, and drilling is commenced, controlled by the micrometer depth control. In order to access more precisely stress gradients, depth increments of 0.01 mm were used near the surface downwards to 0.1 mm. Beyond this point they were gradually increased to 0.05-0.1 mm at greater depth. The strain readings for each gauge were recorded at each depth

increment, and drilling was continued to a depth 0.4 of the mean diameter of the strain gauge circle ($D=5.13$ mm for the selected type of gauge) where strain values became constant or began to decrease.

- v. The diameter of the hole is recorded as it is fundamental data for calculating the corresponding stresses.

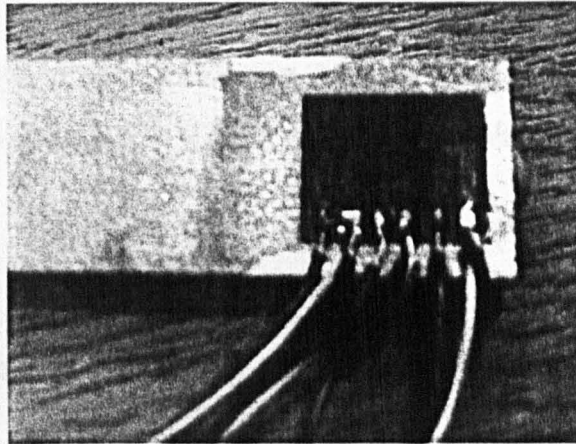


Figure 4.4.29 Photograph of a rosette glued to a coupon with the gauge wires soldered to the contact tabs. There are three strain gauges which hold two numbered contact tabs each. A red wire is soldered to the left numbered tab and the black and white (dummy) wires are connected to the right numbered tab.

4.4.2.5 Analysis methods of nonuniform Stress Fields

It has previously been mentioned that the measurement of in-depth nonuniform residual stresses requires incremental drilling. Once the strains relaxation data are determined, the analytical and empirical equations (referred to in appendix VI) should be employed for determining nonuniform residual stress fields. However, there is not a unique mode for evaluating the residual stresses in-depth and several approaches have been proposed, among the most widely acknowledged are, the Incremental Strain Method [229, 232] and the Average Strain Method [236]. However, following to the advent of the finite element calculation of calibration data, two other improved manners of calculating nonuniform residual stresses from incremental relaxed strain data have been put forward, namely, the Power of Series Method [237] and the Integral Method [229, 238].

A comparison carried out by Schajer [239] showed that the Integral Method gave the best stepped approximation to the actual stress variation with depth, while the Incremental strain and Average stress methods rendered much less satisfactory results.

Schajer concluded that the Incremental and Average methods do not work well with irregular stress fields because they are calibrated using uniform stress field data.

Bearing in mind the above considerations, the residual stresses were determined by utilising the ASTM E837 Incremental Strain Method and compared to the Integral Method. The former was done by using a special off-line Windows®-based computer program (ReStress™) from Measurements Group, Inc. The latter was executed with the help of a special software off-line Windows®-based computer program (H-DRILL© ver. 2.10) from Gary S. Schajer (2505 West Sixth Avenue, Vancouver BC, Canada).

4.4.3 Work hardening (hardness measurements)

Besides introducing residual stresses, shot peening work hardens the peen-affected layer of material, which increases the material resistance to plastic deformation. This was quantified by measuring the microhardness distribution in-depth. A rectangular section of the coupon was cut off as shown in Fig. 4.4.30, using a diamond wheel and sufficient oil-lubricant to avoid introducing further stresses. The cut-off sections were mounted in epoxy resin¹ followed by progressively polishing down to a 1 micron finish (P400, P800 and P1200 silicon carbide abrasive paper, using plenty of water; 6 µm, and 1 µm non ferrous nylon cloth wheels, using small amounts of water based lubricant). Examples of polished epoxy-mounted samples are shown in Fig. 4.4.30.

The samples were tested using a microhardness machine with a Vickers indenter as described in § 2.1.3.2, set to 50 grams force and a hold-down time of 10 seconds. The Vickers indenter made diamond shaped impressions, the size of which were measured to an accuracy of 0.1 µm. Vickers hardness tests were made at depths of 30, 60, 90, 120, 150, 180 and 250 µm from the peened surface, with three indentations made at each depth, the diagonals of which were measured in both directions; so effectively the indentation size at each depth was an average of six measurements. For specimens

¹ Epoxy resin was preferred to bakelite to avoid any possible temperature effects. Epoxy resin is a cold process of encapsulating in which temperatures do not rise more than 150 °C.

peened with shot type S330, the hardness was measured to greater depths (500 μm) to get a complete profile.

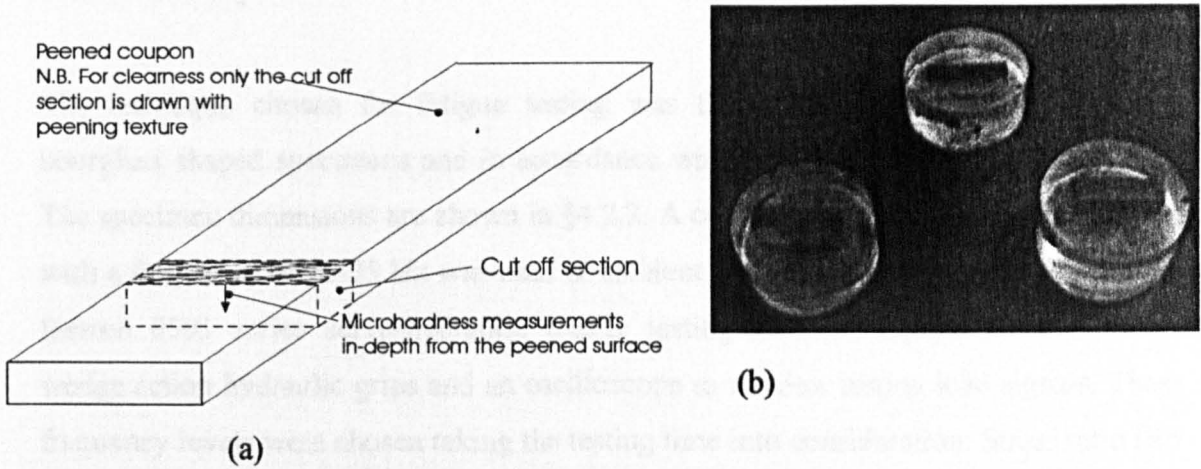


Figure 4.4.30 (a) Schematic representation of the peened cut off section used for measuring the in-depth microhardness distribution. (b) A picture of the mounted sections in epoxy resin is also depicted.

Considering that shot peening causes surface unevenness, the values of hardness will vary depending on the position of the indentation, especially for surfaces peened with low coverage. This is because work hardening will be higher directly underneath the centre of a shot impression than to the side of one. To ensure continuity, all hardness values were taken directly underneath the impressions of the shot peening media that were clearly visible.

4.5 FATIGUE TESTING

4.5.1 Test practice

The technique chosen for fatigue testing was that of tension-tension using plane hourglass shaped specimens and in accordance with British Standards BS-7270 [202]. The specimen dimensions are shown in §4.2.2. A constant amplitude sinusoidal loading with a frequency of 20-25 Hz was used at ambient temperature in a digitally controlled Instron 8501 series servo-hydraulic tensile testing machine equipped with Instron wedge action hydraulic grips and an oscilloscope to monitor testing load signals. These frequency levels were chosen taking the testing time into consideration. Stress ratio ($R = \sigma_{\min}/\sigma_{\max}$, where σ_{\max} is the maximum applied stress and σ_{\min} is the minimum applied stress) was selected at 0.1, fundamentally to preserve a total tensile cyclic stress and to prevent any possible buckling effect. Hence, testing was undertaken under load control up to failure¹ with maximum applied stress ranging between 60 and 120% of the yield stress for each of the materials.

As a result of observed differences in the gauge section dimensions from specimen to specimen, the loading requirement for each test was calculated for each test piece individually. A minimum of 8 specimens with 33% minimum of replication² were tested, following the recommendations of ASTM E 739-91 [240]. The fatigue testing programme adopted was as follows:

- i. A number of unpeened specimens were initially tested to failure in order to plot an S-N curve for both materials under testing.
- ii. The S-N curve and the calculated maximum stresses for breaking a specimen were used to select the stress levels for the peened specimens.
- iii. Optimum and worst peening conditions were tested for both materials. Note that optimum peening condition represents maximum values for the compressive residual stresses/depth and work hardening (microhardness), and minimum values

¹ Failure is broadly speaking defined as the instant when the specimen breaks.

² %replication = $100 [1 - (\text{total number of different stress or strain levels used in testing} / \text{total number of specimens tested})]$. 33% of replication ensured at least three replicated stress levels (two specimens used at each replicated level).

for the stress concentration (roughness). Conversely, worst peening conditions denotes the opposite.

- iv. A sensitivity analysis of selected peening variables was conducted by testing specimens peened to conditions where individual peening variables were investigated.

4.5.2 Fatigue crack propagation: Surface replication

A number of techniques for monitoring cracks and the corresponding methodology for measuring them either directly or indirectly has been successfully developed as reported in [241]. It is clear that each technique may present its particular advantage and disadvantage and therefore, the choice of a specific crack monitoring method will depend among others things on the quality of the information required, the cost of the instrumentation, and the extent and variability of the operation and interpretation of the results. Although more accurate methods of crack monitoring like acoustic microscopy or high amplification travelling microscope with video recorder are suitable for examining the crack growth behaviour of hourglass specimens, restrictions in availability of equipment limited their use for this study.

Experimental crack propagation measurements were made by employing the acetate replication technique. This methodology has been extensively used in short crack growth studies [60, 65, 241]. In this technique, the test is interrupted periodically at the required fraction of life, dousing the specimen surface with acetone, and placing a 30 μm thick cellulose acetate sheet onto the gauge area. Surface tension draws the acetate sheet into cracks and other surface features. Once the replica dried, it was carefully removed (tweezers are the preferred tool to perform this operation) and placed on a microscope glass slide, so that it might observed under optical microscope.

Two replicas were taken each time on opposite sides of the specimen to cover all around the gauge section which would allowed a complete observation of the crack features. All replicas were taken at the mean stress level. It is a usual practice to view the series of replicas in reverse order, as reported elsewhere [241, 242]. Taking into consideration

the S-N data previously produced, the stress levels for replica test were chosen from 300 MPa downwards.

An optical microscope with an integrated video grabber to record the images was employed. Crack propagation measurements were traced manually on a calibrated image by using dedicated image measurement software (SigmaScan Pro ©, ver. 5.0). Calibration of the measuring software was performed using a 49.2 x 49.2 µm grid. The calibration is based on the amount of pixels contained within the specified distance.

4.5.3 Fatigue and fracture surface characterisation

Fatigue surfaces of the specimens cycled to failure were examined by optical microscopy using either a Reichart Polyvar or an Olympus Vanox microscope, and by Scanning Electron Microscopy (SEM) Philips-500. A direct optical microscopy was used to study any secondary cracks and morphologies of the peened surface. SEM examination was in turn, undertaken to identify fracture initiation sites and modes of fracture, particularly regarding the variation of fracture surface features as a function of the depth underneath the surface in order to relate it to the variation of the peening effects (residual stress and microhardness distribution).

4.5.4 Summary

A thorough characterisation of the five different types of shot peening media and a comprehensive assessment of the peening machine capabilities were performed. Among the relevant features characterised were: geometry, hardness and density of the shots. Saturation point, intensity and coverage ranges were determined once optimal working settings and procedures of the peening machine assessment were established.

Two different shape specimens were employed. A rectangular coupon was used to obtain data in relation to the material modifications after peening whilst an hourglass shaped specimen was used to examine the effects of the peening process in terms of fatigue resistance.

A design of experiments (DoE) theory was applied in order to design the corresponding experimental programme. Shot size/type, coverage and incidence angle at four levels were selected as the significant factors. An array of the Taguchi type was found to be appropriate and sixteen peening runs were performed for each of the materials being studied.

A detailed discussion of the procedures adopted for acquiring the peening effects is presented. Surface roughness, residual stress and microhardness in depth distributions are thought to be the main parameters in terms of the fatigue resistance. The generated data were processed employing DoE concepts. A range of optimum and worst peening conditions were determined and experimentally validated. The fatigue testing adopted practice, materials and equipment utilised were also described in this chapter.

CHAPTER 5

EXPERIMENTAL RESULTS

The main goal of the experimental effort was to determine quantitatively the modifications on the surface and subsurface of the AAs 2024-T351 and 7150-T651 caused by shot peening carried out under selected conditions, which may lead to an optimisation of the process in terms of the fatigue resistance. To obtain optimum peening conditions, the significant peening factors and their interaction for the selected levels were determined by using a design of experiments approach. This exercise rendered the best and worst peening conditions in terms of residual stresses, topography and work hardening. Fatigue testing was then undertaken employing such predetermined peening conditions. The peening effects on residual stress, surface roughness and work hardening are shown in this chapter. Significant analysis and estimates of peening conditions from the application of the design of experiment approach are included. Results of the fatigue testing in the form of Wöhler S-N curves, including crack propagation data for each replicated test are presented.

5.1 SHOT PEENING EFFECTS

Based on the design of experiments concepts, a fractional factorial array with 16 combinations of shot types (sizes), coverage, impingement angles and their corresponding intensities evaluated at four levels was used, as described in § 4.3.2. The compiled assignment of the factors and levels is shown in Table 5.1.1. In this respect, the first experimental run was carried out according to the following peening conditions: (i) shot S230, (ii) 50% coverage and (iii) 30° incidence angle of the nozzle and the peening effects: (i) residual stresses, (ii) stress concentration and (iii) work hardening, were obtained. Further runs using SCCW20, S110, S330 followed. The results of each evaluated effect, and the subsequent significance analysis of the peening factors through the design of experiments approach are described next.

Run	Shot	Intensity (mm)	Coverage (%)	Angle (°)
1	S230	0.12A	50	30
2	(0.584 mm)	0.37A	100	89
3		0.21A	200	45
4		0.44A	400	89
5 *	SCCW20	0.14/0.14A	75/71	45
6	(0.5 mm)	0.21A	100	89
7		0.12A	200	30
8		0.25A	400	89
9 *	S110	0.14/0.14A	96/93	89
10	(0.279 mm)	0.11A	100	45
11		0.17A	200	89
12		0.07A	400	30
13	S330	0.57A	50	89
14	(0.838 mm)	0.27A	100	30
15		0.72A	200	89
16		0.4A	400	45

* Al 2024 / Al 7150 conditions.

Table 5.1.1 Factors and levels assigned to columns. The original array (table 4.3.8) was adjusted because it was not possible to attain the required 50% level of coverage for the shot types SCCW20 and S110 for both Al 2024-T351 and 7150-T651 respectively.

5.1.1 Stress concentration

The stress concentration factor, denoted as K_t , is the quantitative characterisation of the peening induced roughness. This factor is a function of the surface roughness parameters, R_{t_m} and S_m (see appendix V for a full description). The calculated averages of the measured parameters R_t and R_a are listed in table 5.1.2. Confidence intervals were quantified by using the Students't-distribution for critical points, i.e. confidence interval $= \mu \pm t \frac{\sigma}{\sqrt{n}}$ where, μ = mean of sample, σ = standard deviation, n = sample size, t = read value from the Students't-distribution table of 90% confidence. The sample size was that of $n = 10$, with the number of degrees of freedom $df = 9$. A value of $t = 1.833$ was read from the corresponding table.

Run	Peening Condition (Shot/Cover/Angle)	Al 2024		Al 7150	
		R_a (μm)	R_{t_m} (μm)	R_a (μm)	R_{t_m} (μm)
1.	S230/50%/30°	3.17 ± 0.41	30.19 ± 2.43	3.08 ± 0.29	33.58 ± 3.1
2.	S230/100%/89°	8.0 ± 0.62	56.53 ± 2.86	7.02 ± 0.22	50.25 ± 3.18
3.	S230/200%/45°	7.83 ± 0.44	59.98 ± 4.68	7.19 ± 0.49	57.14 ± 3.42
4.	S230/400%/89°	8.33 ± 0.23	59.43 ± 2.70	7.63 ± 0.41	61.77 ± 4.17
5(Al 2024).	SCCW20/75%/45°	3.78 ± 0.35	36.23 ± 1.63	-	-
5(Al 7150).	SCCW20/71%/45°	-	-	3.68 ± 0.42	32.95 ± 3.23
6.	SCCW20/100%/89°	5.94 ± 0.22	46.97 ± 3.26	5.477 ± 0.2	43.05 ± 2.84
7.	SCCW20/200%/30°	4.67 ± 0.31	36.27 ± 2.42	4.525 ± 0.35	35.94 ± 2.91
8.	SCCW20/400%/89°	6.72 ± 0.3	50.1 ± 2.91	6.094 ± 0.14	46.37 ± 2.8
9(Al 2024).	S110/96%/89°	4.09 ± 0.15	29.1 ± 1.85	-	-
9(Al 7150).	S110/93%/89°	-	-	3.74 ± 0.14	27.6 ± 2.06
10	S110/100%/45°	3.59 ± 0.12	29.42 ± 1.65	3.73 ± 0.19	27.65 ± 1.04
11	S110/200%/89°	4.25 ± 0.17	33.14 ± 2.29	4.02 ± 0.17	29.19 ± 1.03
12	S110/400%/30°	3.44 ± 0.15	27.43 ± 1.73	3.69 ± 0.15	28.42 ± 1.38
13	S330/50%/89°	5.94 ± 0.57	50.65 ± 4.07	5.81 ± 0.33	46.96 ± 4.23
14	S330/100%/30°	5.67 ± 0.31	46.95 ± 7.0	5.62 ± 0.33	44.36 ± 4.79
15	S330/200%/89°	8.81 ± 0.32	71.95 ± 8.07	8.18 ± 0.44	64.58 ± 6.49
16	S330/400%/45°	9.27 ± 0.39	64.84 ± 4.11	8.72 ± 0.55	68.05 ± 8.65

Table 5.1.2 Averaged values of R_a and R_t roughness parameters for both AA2024-T351 and 7150-T651 measured directly on the peened coupons. R_a is only included as a comparison parameter.

A total of 30 readings of the S values (the adjacent peak-to-peak distances) was obtained for each peening condition from the respective roughness profile plots. The calculated average values are compiled in Table 5.1.3. Examples of the roughness graphical output profiles from where the S measurements were made are illustrated in Figs. 5.1.1 to 5.1.3. These profile plots also highlight the variation in surface topography between peened surfaces using the finest shot (S110) and coarse shot (S330), and the unpeened surface for the same AA.

Run	Peening Condition (Shot/Cover/Angle)	Al 2024		Al 7150	
		Sm (μm)	95% Confidence	Sm (μm)	95% Confidence
1	S230/50%/30°	175.12	±15.12	182.44	±21.97
2	S230/100%/89°	214.63	±20.56	233.82	±22.01
3	S230/200%/45°	191.22	±20.62	241.63	±22.94
4	S230/400%/89°	202.76	±22.23	236.1	±22.04
5 (Al 2024)	SCCW20/75%/45°	136.75	±11.49	-	-
5 (Al 7150)	SCCW20/71%/45°	-	-	158.21	±13.72
6	SCCW20/100%/89°	136.26	±13.77	158.21	±12.98
7	SCCW20/200%/30°	120.33	±11.03	125.69	±12.22
8	SCCW20/400%/89°	125.04	±14.94	130.89	±15.0
9 (Al 2024)	S110/96%/89°	110.89	±7.82	-	-
9 (Al 7150)	S110/93%/89°	-	-	129.76	±11.34
10	S110/100%/45°	107.15	±8.26	132.36	±8.95
11	S110/200%/89°	122.28	±8.73	124.55	±9.17
12	S110/400%/30°	107.81	±8.48	106.83	±9.16
13	S330/50%/89°	234.15	±34.76	231.71	±24.27
14	S330/100%/30°	228.62	±25.19	194.63	±23.75
15	S330/200%/89°	265.04	±30.26	286.67	±27.6
16	S330/400%/45°	251.06	±26.9	219.51	±30.08

Table 5.1.3 Adjacent peak-to-peak averaged distances, denoted as S_m . The 95% confidence intervals are also shown.

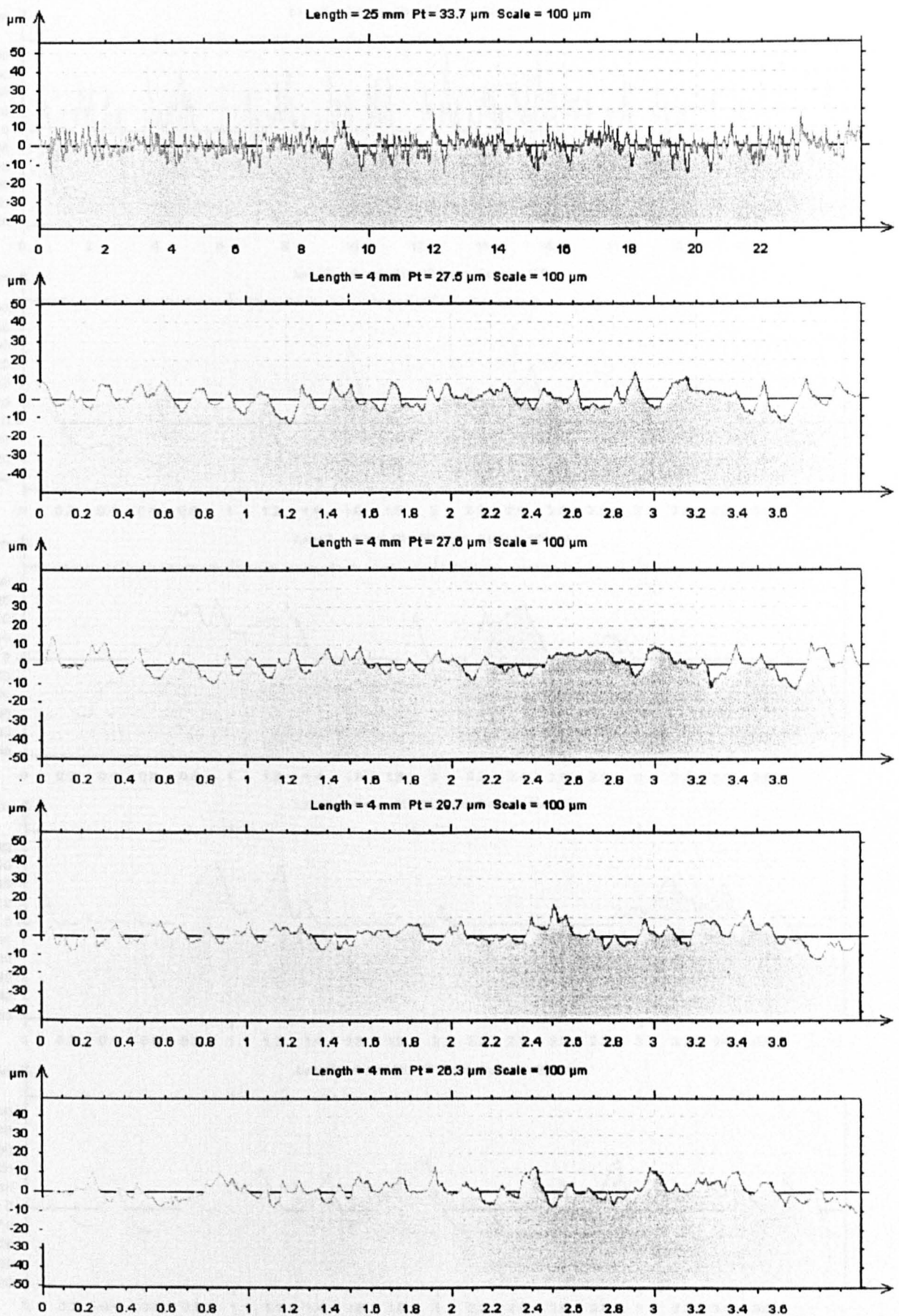


Figure 5.1.1 Roughness profile graphs from an AA-2024-T351 coupon with peening conditions: S110 (finest shot), 100% coverage and 45° incidence angle. A large profile of 25 mm and 4 profiles of 4 mm each are shown.

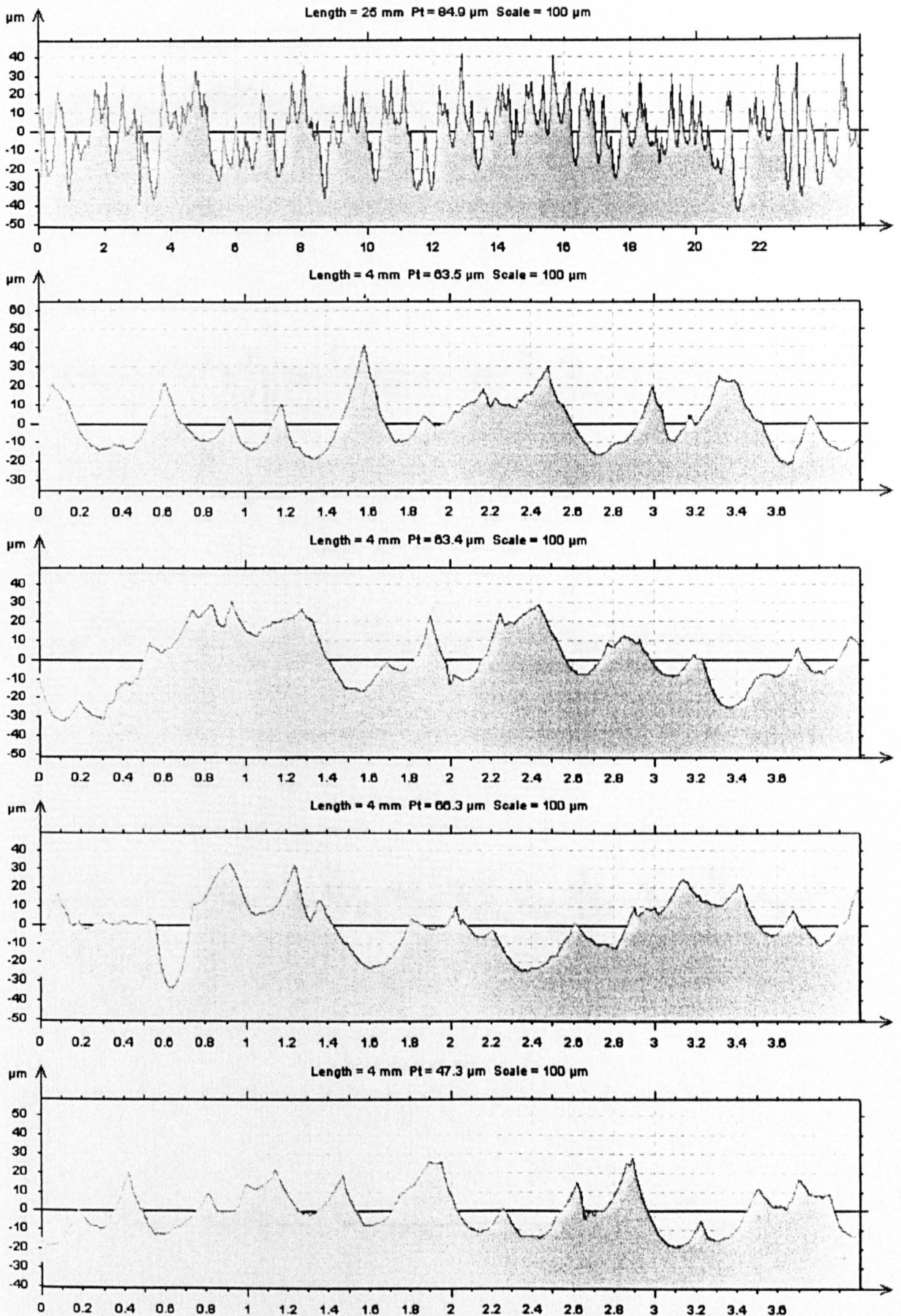


Figure 5.1.2 Roughness profile graphs of an AA-2024-T351 coupon with peening conditions: S330 (coarse shot), 100% coverage and 90° incidence angle.

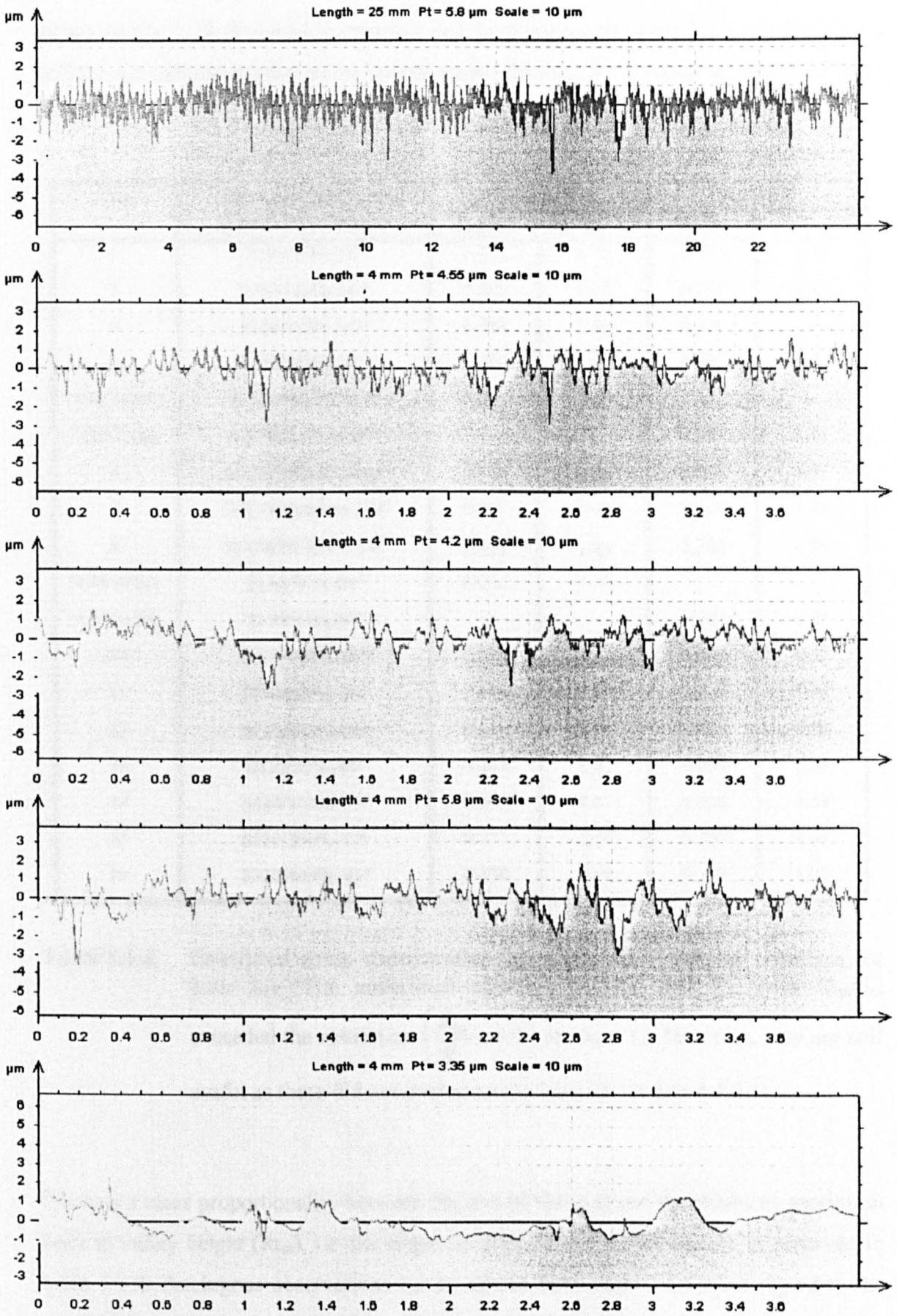


Figure 5.1.3 Roughness profile graphs of an AA-2024-T351 coupon unpeened. This roughness is basically due to machining.

Based on Eq. 3.12, the mean values R_{tm} and S_m compiled in tables 5.1.2 and 5.1.3 were utilised for calculating the stress concentration factors, K_t 's, which are listed in table 5.1.4.

Run	Peening Condition (Shot/Cover/Angle)	Al 2024		Al 7150	
		R_{tm}/S_m	K_t	R_{tm}/S_m	K_t
1.	S230/50%/30°	0.172	1.36	0.184	1.39
2.	S230/100%/89°	0.263	1.55	0.215	1.45
3.	S230/200%/45°	0.314	1.66	0.236	-
4.	S230/400%/89°	0.293	1.62	0.262	1.55
5(Al 2024).	SCCW20/75%/45°	0.265	1.56	-	-
5(Al 7150).	SCCW20/71%/45°	-	-	0.208	1.44
6.	SCCW20/100%/89°	<u>0.345</u>	<u>1.72</u>	0.272	1.57
7.	SCCW20/200%/30°	0.301	1.63	0.286	1.60
8.	SCCW20/400%/89°	<u>0.400</u>	<u>1.84</u>	<u>0.354</u>	<u>1.74</u>
9(Al 2024).	S110/96%/89°	0.262	1.55	-	-
9(Al 7150).	S110/93%/89°	-	-	0.213	1.45
10	S110/100%/45°	0.275	1.58	0.209	1.44
11	S110/200%/89°	0.271	1.57	0.234	1.49
12	S110/400%/30°	0.254	1.53	0.266	1.56
13	S330/50%/89°	0.216	1.45	0.203	1.43
14	S330/100%/30°	0.205	1.43	0.228	1.48
15	S330/200%/89°	0.271	1.57	0.225	1.47
16	S330/400%/45°	0.258	1.54	0.310	1.65

Table 5.1.4 Calculated stress concentration factors for each peening condition for both AA. The underlined numbers indicate that the ratio R_{tm}/S_m exceeded the restriction $\left(\frac{R_{tm}}{S_m} \leq 0.3\right)$ in Eq. 3.12. However, they are still useful as these did not overcome the limit of 0.4 (see § 3.2.3).

There is a clear proportionality between the size of the shot and the exhibited maximum peak to valley height (R_{tm}), i.e. the larger the shot the deeper the impact, as observed in table 5.1.2. Analogous observations can be drawn from table 5.1.3, with regard to the exhibited peak-to-peak mean values (S_m) for both AA. However, there is no discernible correlation on the calculated stress concentrations. This latter observation leads to the assertion that stress concentration is shape and not size dependent, although notch

sensitivity may be size dependent. Higher roughness aspect ratios (Rt_m / S_m) would result in higher stress concentrations.

In light of the above observations, the highest stress concentration values were found on the peened coupons with the shot type SCCW20, as can be seen in table 5.1.4. To this end, the shot geometric features previously determined in § 4.1.3.1 revealed that, the highest scatter in roundness and aspect ratio distributions were exhibited by this type of shot (see Table I-2, included in appendix I). Furthermore, the surface that was peened with this kind of shot was found to consist largely of sharp peening indentations, namely, deep penetration with narrow dents, as shown in tables 5.1.2 and 5.1.3. These findings support the observation made earlier concerning the dependence of indentation shape on the stress concentration factor.

Other features observed were: (i) surfaces peened with an impingement angle of 45° , have in general higher stress concentration than with 89° , (ii) a marginal increasing of K_t was found to be associated with an increase of the percentage of coverage. A higher coverage would significantly result in a greater dent depth, whereas a moderate incidence angle of 45° may cause the dent width to be narrower than that of a dent caused by a normal (89°) incidence angle, as graphically illustrated in Fig. 5.1.4. These conditions may still increase the stress concentrations due to higher aspect ratio values.

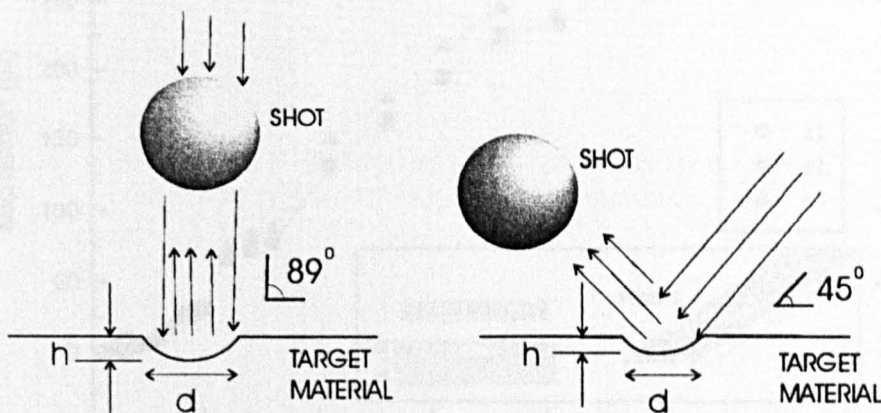


Figure 5.1.4 Schematic representation of variation of the incidence angle on the stress concentration factor (K_t). Because K_t is a function of the ratio h/d , an incidence angle of 45° may result in higher stress concentration than that for 89° .

Therefore, the geometric features of the shot, coverage and incidence angle were seen to play a major role in the stress concentration factor, K_t , which is believed to depend on the shape of the dimple left on the peened surface.

5.1.2 Residual stresses

Residual stress was measured utilising the Incremental Hole Drilling Technique (IHD), previously described in § 4.4.2.3. The experimental procedure was carried out as indicated in § 4.4.2.4. In order to determine the residual stresses for each run (or applied peening condition to a coupon) of the designed experiment matrix shown in table 5.1.1, the strain values measured directly from the strain indicator were computed in accordance with the ASTM E837 Incremental Strain Method (ISM).

An example of the typical strain relaxation curves as a function of the drilling depth is depicted in Fig. 5.1.5.

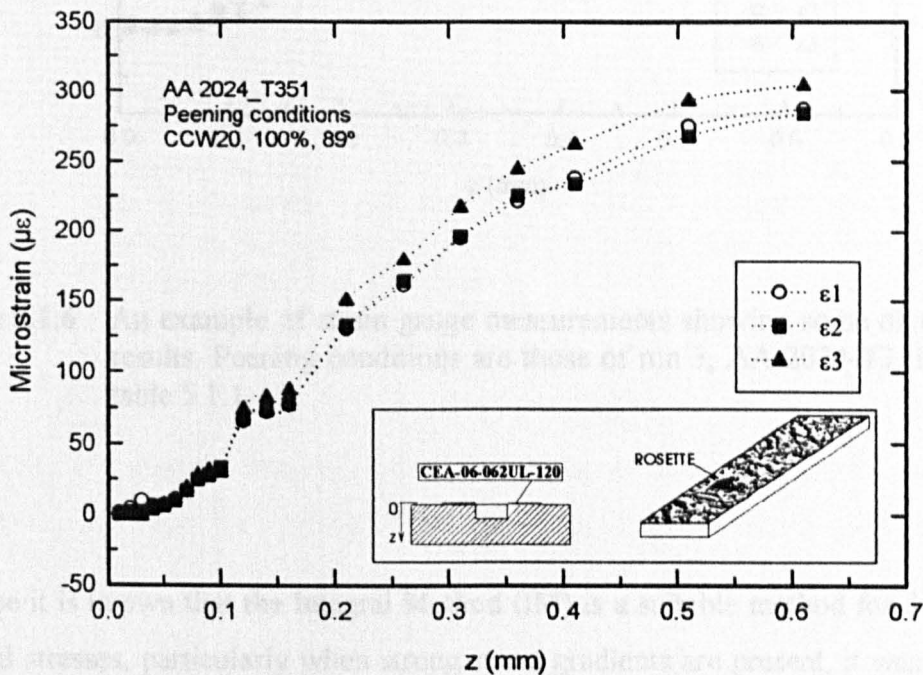


Figure 5.1.5 Measured relieved microstrains ($\mu\epsilon$) in AA 2024-T351 peened coupon. Three gauges are assembled in this specially designed rosette, from which three microstrains (ϵ_1 , ϵ_2 and ϵ_3) are recorded.

The relieved strains are believed to be independent of the measurement direction, indicating an equibiaxial stress state as discussed in §2.2.4.1, which is a characteristic of shot peening residual stresses. Although some differences in the relieved microstrains were observed, the majority of the results obtained confirmed the above. Hence, in calculating the residual stresses, a single stress component was used, corresponding to the maximum principal stress value. This latter allows for a more conservative residual stresses level, as the maximum principal stresses are less compressive. In those cases where a considerable discrepancy existed (see Fig. 5.1.6), a mean value between the minimum and maximum stress component was used.

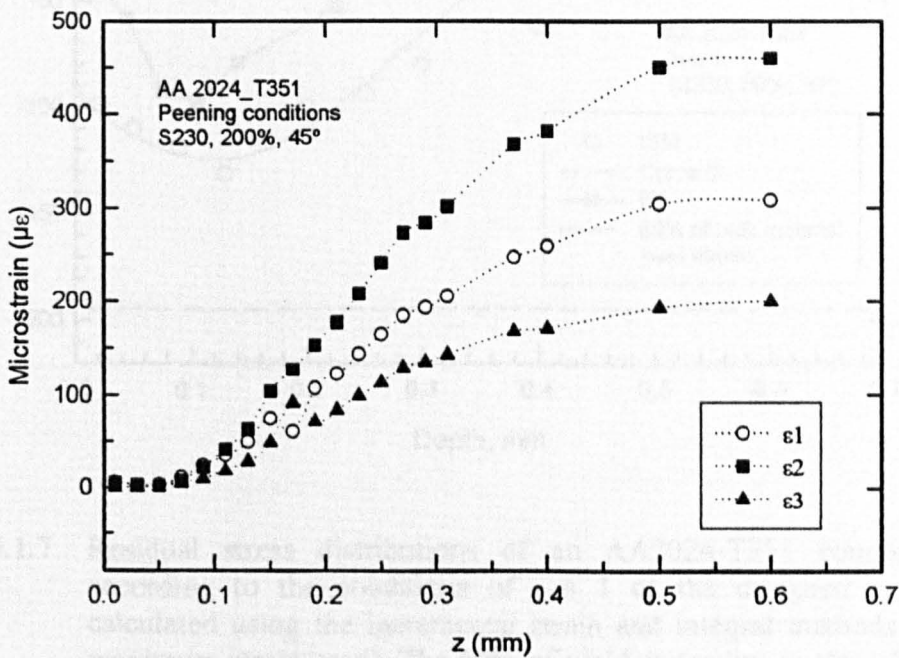


Figure 5.1.6 An example of strain gauge measurements showing some divergence of results. Peening conditions are those of run 3, AA 2024-T351 shown in table 5.1.1.

Because it is known that the Integral Method (IM) is a suitable method for determining residual stresses, particularly when strong stress gradients are present, it was employed as a means of comparing its results with those obtained with the ISM.

A few typical residual stress distributions are presented in Figs. 5.1.7 to 5.1.9. Curve fits using Eq. 3.7 or 3.8 were carried out to generate the functions that describe the residual stresses to be incorporated as the closure stresses, σ_1^i , into the CTOD estimations.

Included in the graphs, as horizontal lines (Figs. 5.1.8 and 5.1.9) are the bulk material's yield strength and the 60% of this value. These lines are used as indicators of the influence of the drilling plasticity effect¹ when the residual stresses exceed 60% of the yield strength, as reported elsewhere [225].

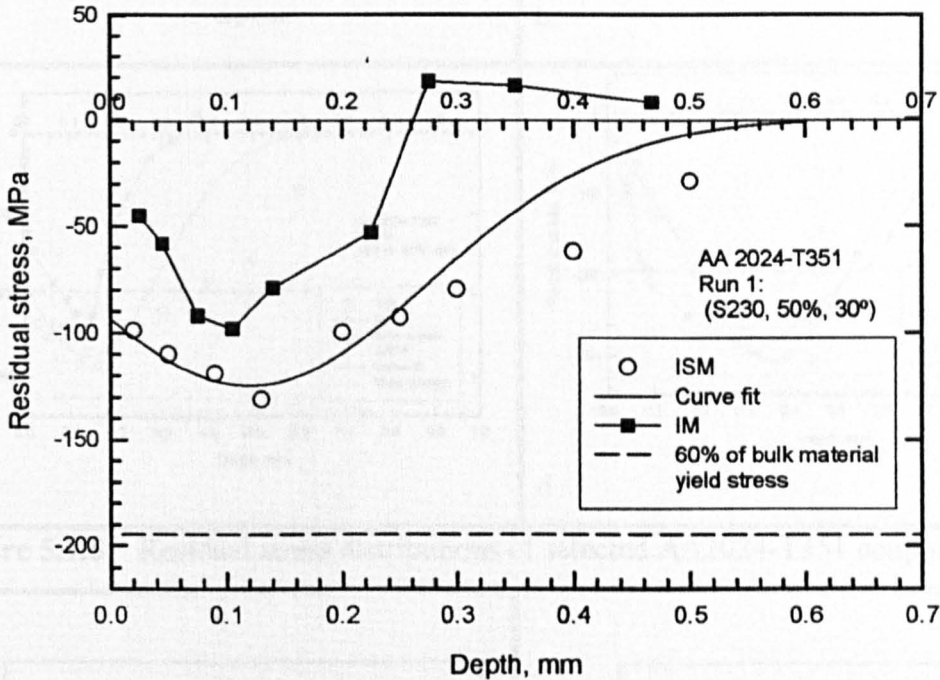


Figure 5.1.7 Residual stress distributions of an AA2024-T351 coupon, peened according to the conditions of run 1 of the designed experiments, calculated using the incremental strain and integral methods (principal maximum stress used). The 60% of yield stress line is also plotted. The bulk material's yield stress was that indicated in § 4.2.1. The curve fit was generated from ISM data.

Plots using the remainder data and corresponding curve fits can be found in appendix VI-B. Tables 5.1.5 and 5.1.6 provide a summary of the curve fit coefficients for Eq. 3.7 or 3.8.

¹ The stress concentration caused by the drilled hole itself gives rise to local plastic yielding (drilling-induced plastic deformations), which can strongly affect the residual stress determination, as the analytical procedures for computing the stresses assume linear-elastic materials behaviour.

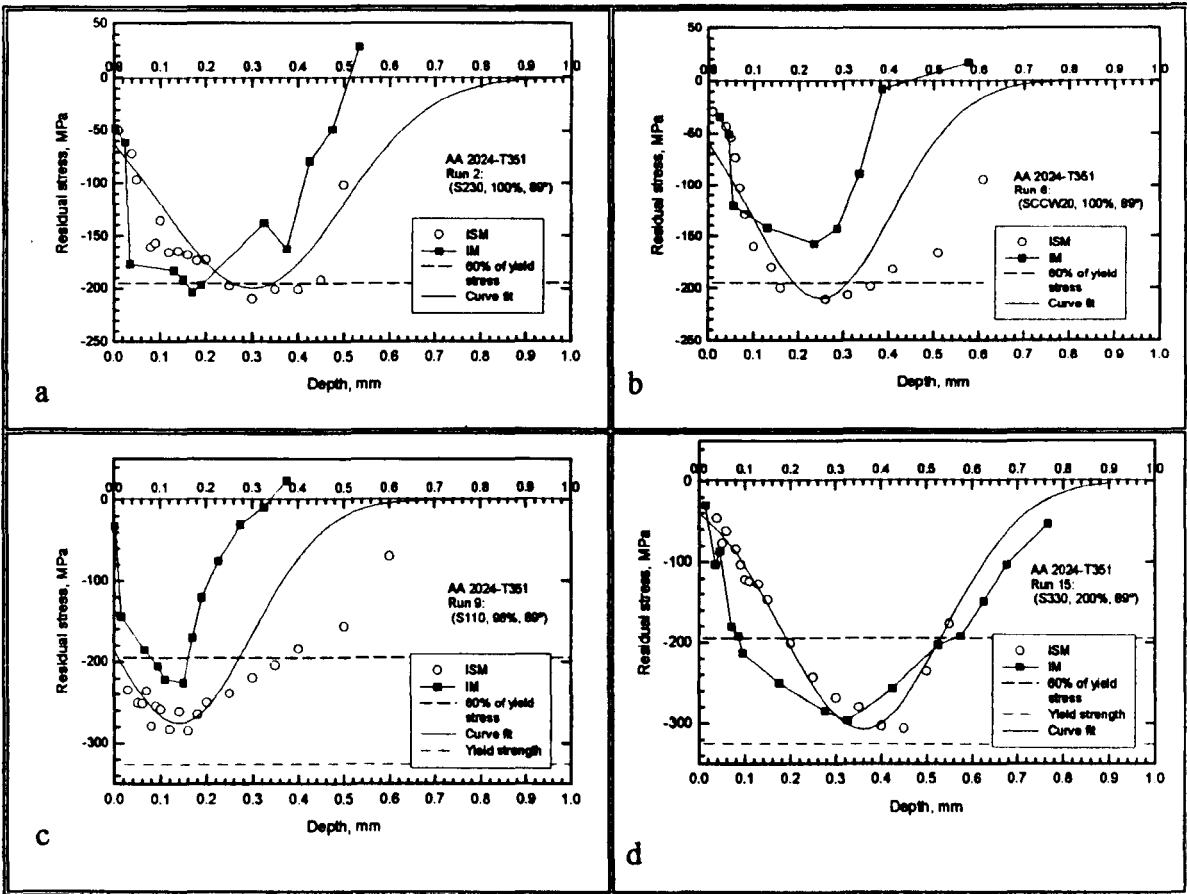


Figure 5.1.8 Residual stress distributions of selected AA2024-T351 coupons.

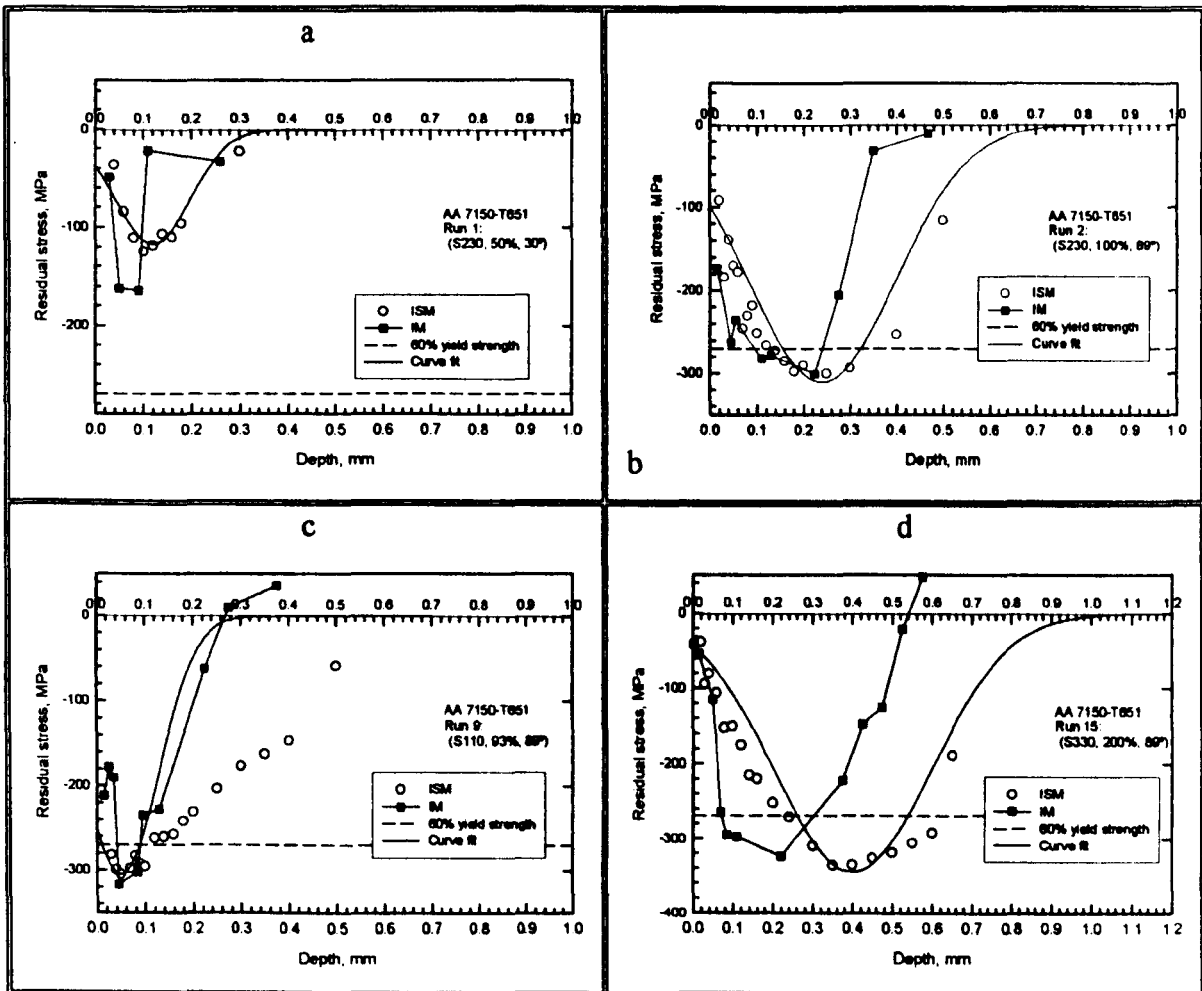


Figure 5.1.9 Residual stress distributions of selected AA7150-T651 coupons.

Run	Shot (mm)	Intensity (mm)	Coverage (%)	Angle (°)	Curve fit coefficients (2024-T351)				
					A (MPa)	B	W (mm)	Xd (mm)	n
1	S230 (0.584)	0.12A	50	30	-130.0000	0.000	0.4000	0.1300	10.0000
2		0.37A	100	89	-200.0000	0.000	0.5000	0.3000	5.0184
3		0.21A	200	45	-195.0000	0.000	0.3800	0.2801	5.0046
4		0.44A	400	89	-245.0000	0.000	0.5500	0.3000	5.0000
5	CCW20 (0.5)	0.14A	75	45	-173.1000	0.000	0.3000	0.1600	5.0000
6		0.21A	100	89	-210.0000	0.000	0.5996	0.2602	5.0114
7		0.12A	200	30	-164.8000	0.000	0.4000	0.2100	5.0000
8		0.25A	400	89	-249.9900	0.000	0.5000	0.2800	5.0040
9	S110 (0.279)	0.14A	96	89	-275.0000	0.000	0.4004	0.1401	4.9846
10		0.11A	100	45	-130.0312	0.000	0.1501	0.0901	4.9859
11		0.17A	200	89	-379.9780	0.000	0.2000	0.0700	4.9715
12		0.07A	400	30	-155.0000	0.000	0.2000	0.1200	4.9834
13	S330 (0.838)	0.57A	50	89	-255.0592	0.000	0.5002	0.2501	4.9923
14		0.27A	100	30	-170.0000	0.000	0.5700	0.2800	5.0070
15		0.72A	200	89	-307.5000	0.000	0.4000	0.3999	4.9901
16		0.4A	400	45	-292.9764	0.000	0.5000	0.3501	5.0066

Table 5.1.5 Residual stress coefficients for Eq. (3.8). Material AA 2024-T351.

Run	Shot (mm)	Intensity (mm)	Coverage (%)	Angle (°)	Curve fit coefficients (7150-T651)				
					A (MPa)	B	W (mm)	Xd (mm)	n
1	S230 (0.584)	0.12A	50	30	-117.0020	0	0.2000	0.1200	5.0030
2		0.37A	100	89	-311.0000	0	0.4002	0.2400	4.9927
3		0.21A	200	45	-235.0000	0	0.4500	0.2000	5.0210
4		0.44A	400	89	-270.0060	0	0.5000	0.3000	5.0002
5	CCW20 (0.5)	0.14A	71	45	-287.1980	0	0.1500	0.0600	4.9664
6		0.21A	100	89	-258.0000	0	0.3500	0.1600	4.9982
7		0.12A	200	30	-146.0000	0	0.2500	0.0801	4.9815
8		0.25A	400	89	-364.0720	0	0.4000	0.1200	4.9859
9	S110 (0.279)	0.14A	93	89	-306.1650	0	0.2000	0.0500	5.0000
10		0.11A	100	45	-119.9540	0	0.2000	0.1002	4.9984
11		0.17A	200	89	-132.5000	0	0.3000	0.2200	4.9871
12		0.07A	400	30	-205.0000	0	0.2000	0.0800	4.9729
13	S330 (0.838)	0.57A	50	89	-293.0000	0	0.6500	0.2200	4.9857
14		0.27A	100	30	-190.0000	0	0.4005	0.1500	4.9783
15		0.72A	200	89	-345.0000	0	0.5000	0.4000	5.0000
16		0.4A	400	45	-247.0000	0	0.4002	0.3000	4.9935

Table 5.1.6 Residual stress coefficients for Eq. (3.8). Material AA 7150-T651.

The influence of calculation procedures on the residual stress results is apparent in Figs. 5.1.7 to 5.1.9. A discernible variation between the Integral and Incremental strain methods was observed, particularly at greater distances from the surface. The observed discrepancies can be related to the theoretical shortcomings of each calculation procedure.

In the ISM method, an equivalent uniform stress takes into account the influence of the residual stresses in previous increments. This concept is based on the average stress within the total hole depth, which produces the same total strain as the actual nonuniform stress field. This latter implies that stresses at all given depth increments contribute equally to the strain relief measured at the surface. However, Flaman [243] previously showed that the residual stresses present in the increments close to the surface contribute much more to the strain relaxation than those in deeper increments. The integral method in turn, was specially proposed for correctly considering the strain contribution, when strong stress gradients are present, as pointed out by Schajer [239]. However, this method involves very accurate measurements of the relieved strains and depths for each incremental step, i.e. higher error sensitivity is prone to occur. Because the error is carried forward, the error sensitivity is proportional to the number of depth increments.

Clearly, overestimated IHD residual stress distributions under the ISM compared to the Integral procedure are present in Figs. 5.1.7 to 5.1.9. However, there is no an appreciable smooth compressive stress distribution for the IM plots. This is evidence of the carrying forward of the error due to the large number of incremental steps, specifically near to the surface. In view of the fact that all methods are limited by the decreasing sensitivity to stress relief at deeper increments, the results from the ISM were used in the subsequent stages of this study as indicated in § 4.4.2.5.

Regarding errors attributed to maximum residual stresses greater than 60% of the material's yield strength; several authors have reported estimates of the corresponding errors but without considering the local yield strength after surface treatments. It has been reported [244] than errors when residual stresses are less than 60% of the material's yield stress are approximately +10%. An overestimation of 15% can be expected for residual stress magnitudes of 70% yield stress, +20% for residual stress

magnitudes of 90% yield stress and up to +35% for stresses reaching 95% of the material's yield stress.

It has been proved that the work hardening in the surface can largely prevent plastic yielding [244]. Moreover, it was found that the plasticity effect becomes significant when the existing compressive residual stresses overcome 80% of the corresponding local yield strength of the peened material. Based on the proportionality between hardness and yield strength, the local yield strength σ_{ly} has been successfully determined using the yield strength of the bulk material σ_y and the relative variation of the microhardness according to the following relationship [244]:

$$\sigma_{ly} = \sigma_y \left(1 + \frac{\Delta H_v}{H_{v_{bulk}}} \right) \quad (5.1)$$

where σ_y is the material's yield stress (325 and 450MPa for 2024 and 7150 AA respectively). ΔH_v is the in-depth variation of the Vickers microhardness (see § 5.1.3 for hardness distributions), and $H_{v_{bulk}}$ is the Vickers microhardness of the bulk material, which was found to range between 120-130 $H_{v0.1}$ for the AA 2024-T351 and 140-145 $H_{v0.1}$ for the AA 7150-T651.

Close examination of the residual stress distributions for both peened AAs revealed that only run 11 of the AA 2024-T351 exceeded 116% of the material's yield stress. However, a high work hardening was also observed in the near surface layer, as graphically shown in Fig. 5.1.10.

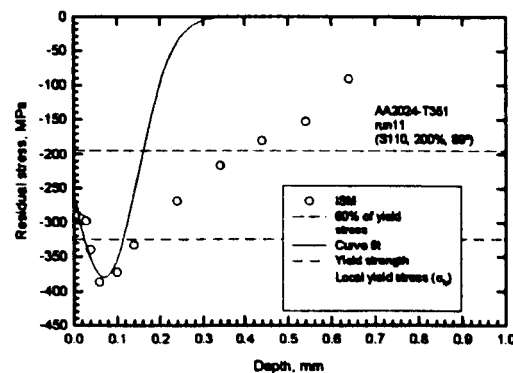


Figure 5.1.10 Residual stress distribution of the AA 2024-T351 peened coupon exceeding the material's yield stress (run 11 of the designed experiment). The local yield stress evolution shown as the dotted curve was determined by using Eq. 5.1 together with the microhardness distribution (§ 5.1.3).

It is worth commenting that in the evaluation of IHD data, the determination of the first increment size is less accurate due to e.g. the surface roughness, strain gauge thickness, etc. Thus, the uncertainty in the residual stress determination on the surface is increased. However, the majority of residual stresses results were compressive just below the surface (between 0.030 and 0.040 mm).

Observation of the compressive residual stress evolutions for each of the runs revealed the typical strong influence of the shot type (size) on the depth of the maximum residual stresses. The overall distribution of the residual stresses was found to be very similar between both AA. However, the depth to peak residual stress was marginally higher in the AA 2024-T351 than the AA 7150-T651. This understandably is a manifestation of the material's properties, e.g. hardness and yield strength. The comparatively higher number of times that the 60% of the yield stress in AA2024 is reached by the compressive residual stresses is another indication of a softer material. In table 5.1.7 are listed the maximum residual stresses and their corresponding depth below the surface according to the peening conditions of the designed experiment.

Run	Peening Condition (Shot/Coverage/Angle)	AA 2024-T351		AA 7150-T651	
		Max. RS (MPa)	Depth (mm)	Max. RS (MPa)	Depth (mm)
1.	S230/50%/30°	-124.7	0.13	-117.6	0.12
2.	S230/100%/89°	-233.7	0.3	-321.79	0.25
3.	S230/200%/45°	-197.2	0.3	-233.8	0.15
4.	S230/400%/89°	-246.7	0.3	-284.6	0.3
5(AI 2024).	SCCW20/75%/45°	-173.1	0.19		
5(AI 7150).	SCCW20/71%/45°			-287.2	0.06
6.	SCCW20/100%/89°	-243.1	0.31	-260.2	0.16
7.	SCCW20/200%/30°	-164.8	0.19	-153.9	0.08
8.	SCCW20/400%/89°	-245.6	0.28	-363.84	0.1
9(AI 2024).	S110/96%/89°	-278.0	0.14		
9(AI 7150).	S110/93%/89°			-306.7	0.03
10	S110/100%/45°	-131.5	0.09	-115.5	0.1
11	S110/200%/89°	-378.6	0.04	-135.4	0.25
12	S110/400%/30°	-149.1	0.12	-205	0.1
13	S330/50%/89°	-254.5	0.25	-290.5	0.22
14	S330/100%/30°	-170.0	0.3	-180.2	0.14
15	S330/200%/89°	-308.0	0.4	-347.9	0.4
16	S330/400%/45°	-292.4	0.35	-247.4	0.3

Table 5.1.7 Maximum compressive residual stresses and their corresponding depths.

No discernible difference of the residual stresses for unpeened material was observed for both AA. Compressive residual stresses were commonly found in the near surface (from 20 μ m depth) tending progressively to zero. The appearance of these stresses can be attributable among others to the machining process (particularly milling) during the manufacturing of the specimens. Trends of the residual stresses for the unpeened specimens are plotted in Fig. 5.1.11. Because the as received 7150-T651 AA was heat-treated (artificial ageing, according to the procedure described in appendix IV), distribution of the residual stresses for both heat-treated and non-heat treated are shown in the same Fig. 5.1.11. A complete opposite behaviour was exhibited by the AA7150 in the as received condition (W51), where a dominant tensile residual stress field was observed at the near material surface. This may be due to the 3% stretch given to the as received material (temper W51).

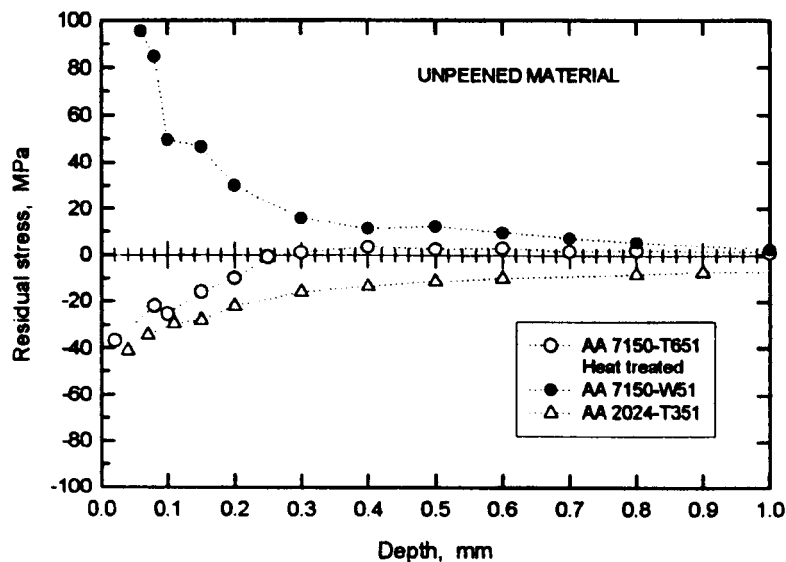


Figure 5.1.11 Comparison of the residual stress distribution for the as received and heat treated AAs. Determination of the stresses was carried out by using the ISM.

5.1.3 Work hardening

Because of the peening intensive impact, the grain and sub-grain structure of the surface layer are refined, and the dislocation density increased. This is manifested as a work hardening effect. Viewed optically, the grain structure of AA 7150-T651 is shown in micrograph, Fig. 5.1.12.

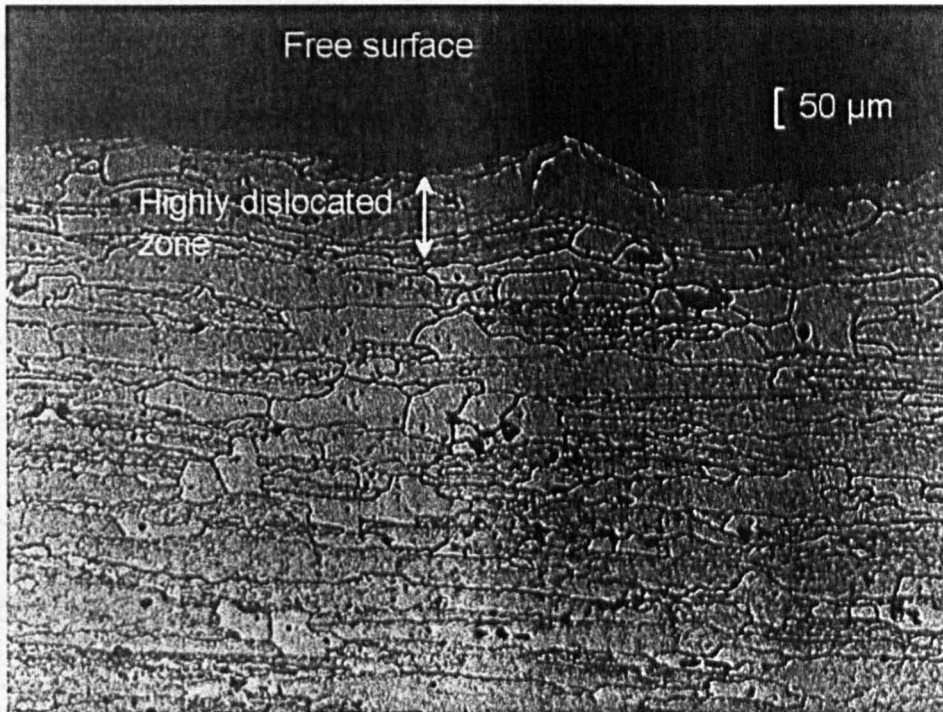


Figure 5.1.12 Microstructure of a peened AA 7150-T651 specimen. The highly distorted zone indicated by the arrowed line starts from the indented surface to approximately 100μm in-depth.

The strain hardening or the distortion in the shot peened layer was quantified according to the procedure described in § 4.4.3. Some representative microhardness variations are presented in Figs. 5.1.13 and 5.1.14.

To generate the respective function that describes the evolution of the flow stress σ_2 (detailed in §3.2.2), curve fits of the microhardness results were therefore determined by using the same Gaussian function as Eq. 3.7, with the following nomenclature:

$$f(x) = H_v = A e^{\left[\frac{-2(x-X_d)^2}{W^2} \right]} + B \quad (5.2)$$

- H_v = microhardness
- $A+B$ = maximum microhardness value
- x = depth below the surface
- X_d = depth to maximum microhardness
- W = a measure of the width of the hardness curve
- B = bulk material microhardness.

Plots of the remainder data and corresponding curve fits can be found in appendix VII. A summary of the curve fit coefficients for Eq. 5.2 is given in table 5.1.8 and 5.1.9 for each AA.

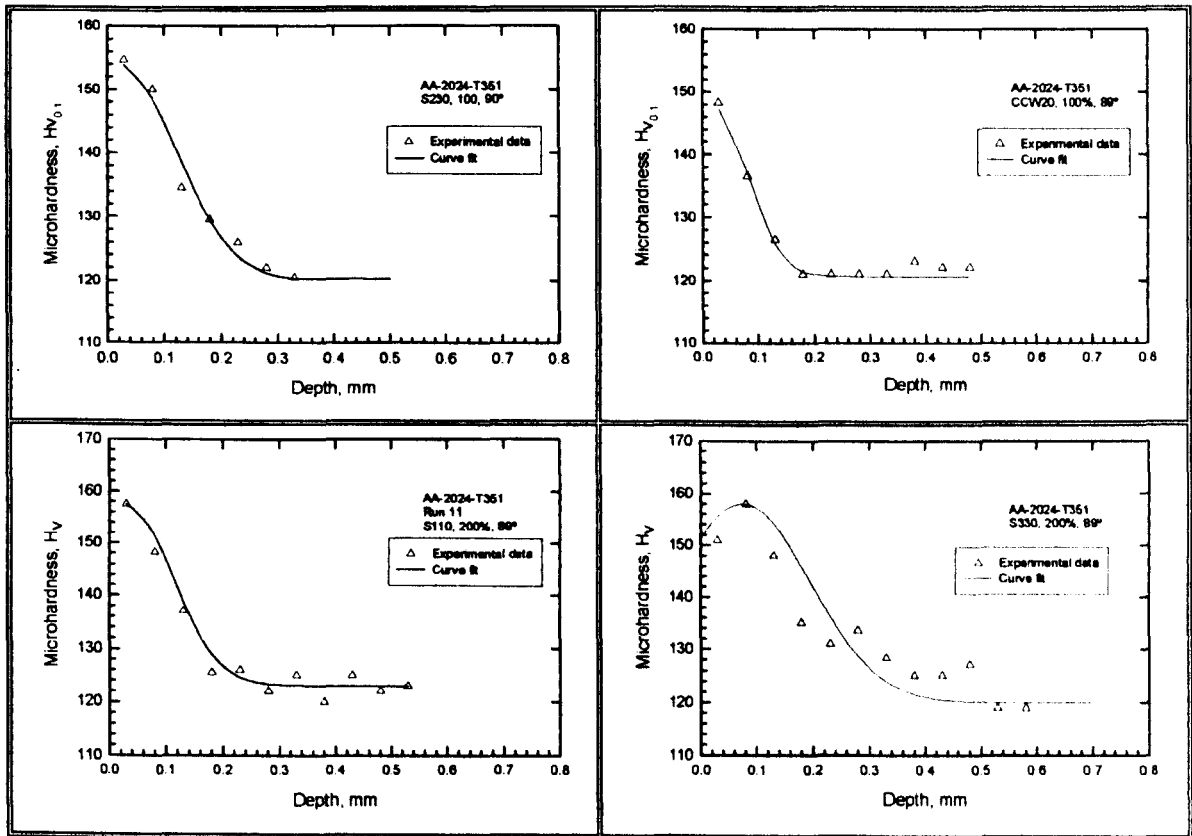


Figure 5.1.13 Representative microhardness distributions for AA 2024-T351 peened coupons.

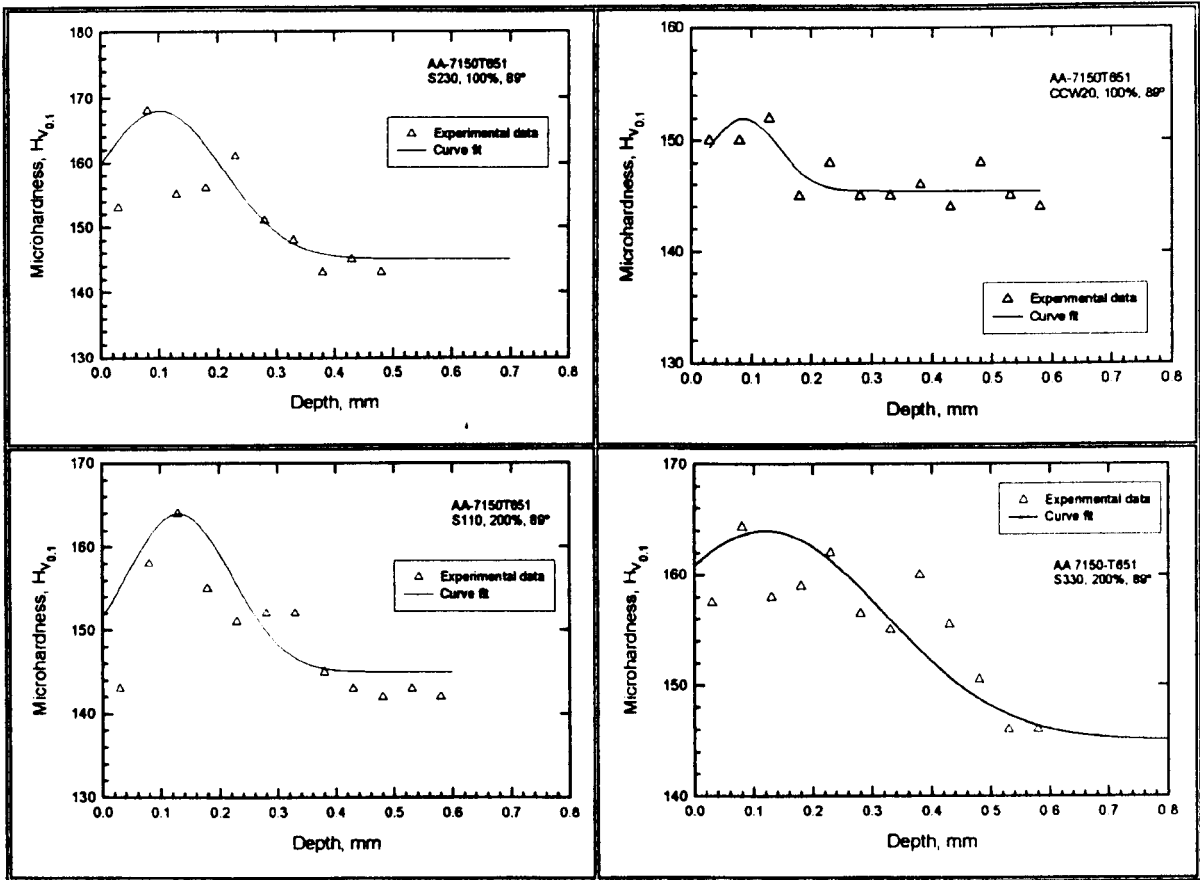


Figure 5.1.14 Representative microhardness distributions for AA 7150-T651 peened coupons.

Run	Shot (mm)	Intensity (mm)	Coverage (%)	Angle (°)	Curve fit coefficients (2024-T351)			
					A $H_{v0.1}$	B $H_{v0.1}$	W (mm)	Xd (mm)
1	S230 (0.584)	0.12A	50	30	24.0000	121.0000	0.1100	0.0200
2		0.37A	100	89	26.0000	120.0000	0.3064	-0.0004
3		0.21A	200	45	34.0000	120.0000	0.2000	0.0200
4		0.44A	400	89	43.0000	124.0000	0.3000	0.0200
5	CCW20 (0.5)	0.14A	75	45	17.0000	120.0000	0.3000	0.0800
6		0.21A	100	89	27.4040	120.6000	0.1239	0.0175
7		0.12A	200	30	29.7370	120.7600	0.1387	0.0183
8		0.25A	400	89	37.0000	120.7600	0.2200	0.0183
9	S110 (0.279)	0.14A	96	89	26.5000	120.0000	0.0800	0.0300
10		0.11A	100	45	30.5000	123.0000	0.2000	0.0300
11		0.17A	200	89	34.5000	123.0000	0.1600	0.0300
12		0.07A	400	30	30.2000	121.8000	0.0415	0.0273
13	S330 (0.838)	0.57A	50	89	12.5000	122.0000	0.0770	0.0800
14		0.27A	100	30	36.0000	123.0000	0.2100	0.0300
15		0.72A	200	89	38.0000	120.0000	0.2200	0.0739
16		0.4A	400	45	30.4999	123.7001	0.2238	0.0073

Table 5.1.8 Microhardness coefficients for Eq. 5.2 of the AA 2024-T351.

Run	Shot (mm)	Intensity (mm)	Coverage (%)	Angle (°)	Curve fit coefficients (7150-T651)			
					A Hv _{0.1}	B Hv _{0.1}	W (mm)	X _d (mm)
1	S230 (0.584)	0.12A	50	30	6.3000	145.7600	0.1270	0.0690
2		0.37A	100	89	23.0000	145.0000	0.2159	0.1015
3		0.21A	200	45	13.0000	145.0000	0.3000	0.1500
4		0.44A	400	89	18.5000	146.0000	0.1500	0.1200
5	CCW20 (0.5)	0.14A	75	45	22.0000	146.0000	0.3000	0.0300
6		0.21A	100	89	7.0000	145.0000	0.1200	0.0900
7		0.12A	200	30	10.1940	144.8100	0.1428	0.1791
8		0.25A	400	89	10.0000	145.0000	0.2500	0.1858
9	S110 (0.279)	0.14A	96	89	5.8912	145.1100	0.1414	0.1049
10		0.11A	100	45	13.0000	145.0000	0.2200	0.0300
11		0.17A	200	89	19.0000	145.0000	0.1800	0.1314
12		0.07A	400	30	17.0000	145.0000	0.2500	0.0300
13	S330 (0.838)	0.57A	50	89	18.2230	143.7800	0.2190	0.1855
14		0.27A	100	30	15.0000	145.0000	0.3000	0.1400
15		0.72A	200	89	19.0000	145.0000	0.3000	0.1855
16		0.4A	400	45	11.5000	145.0000	0.1500	0.0900

Table 5.1.9 Microhardness coefficients for Eq. 5.2 of the AA 7150-T651.

Microhardness was typically found to be higher than the bulk material near the surface (15-20 μ m) and achieve a maximum at deeper distances (20-180 μ m). Once the peak value is achieved, microhardness decreases with increasing distance from surface and, at an overall depth of approximately 500 μ m, reaches the plateau value corresponding to the hardness of the bulk material. This hardness variation exhibited by the two materials, indicates microstructural work hardening effects due to the peening induced multiplication of dislocations. In the case of the softer alloy (AA 2024), higher variations in hardness were observed than in the harder alloy (AA 7150). However, AA 2024 showed a faster drop in hardness (work softening) than in AA 7150, i.e. there exists a larger plasticised zone¹ in AA 7150 compared to AA 2024. The maximum hardness, relative microhardness variation and the plasticised zone depth are shown in Fig. 5.1.15. The corresponding magnitudes are listed in table 5.1.10.

¹ The plasticised depth is defined as the depth where micro-hardness variation returned to the corresponding values of the bulk material.

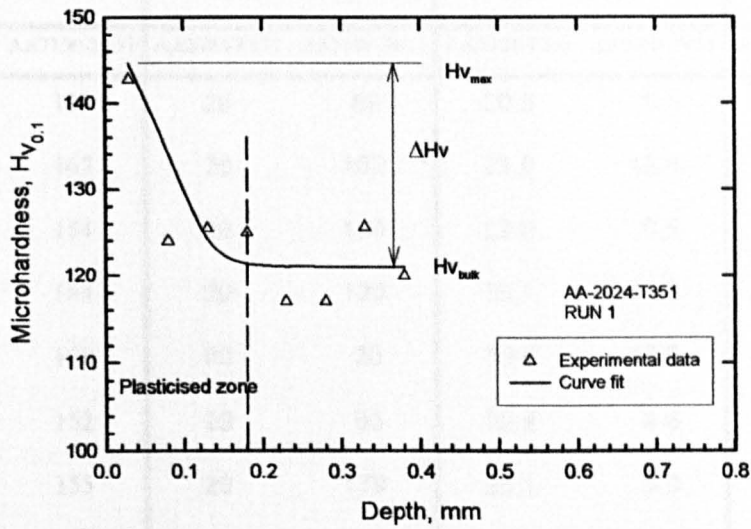
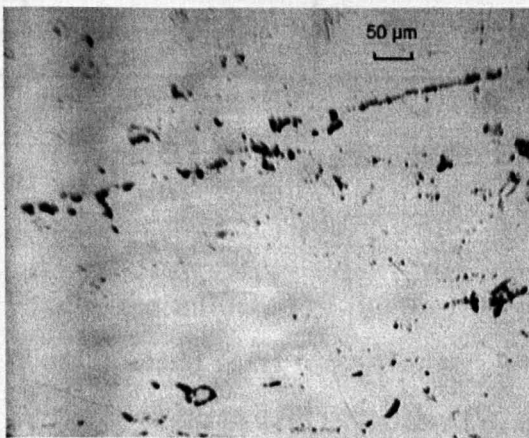
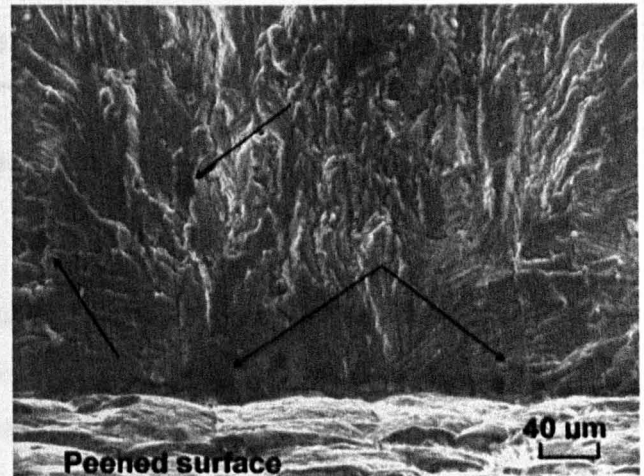


Figure 5.1.15 Microhardness distribution of a peened coupon illustrating the plasticised zone, maximum hardness, hardness bulk material and microhardness variation.

Another observation of interest is that of the scatter of data found in AA 7150 compared to the AA2024. Higher scatter of the hardness values in AA7150 can mainly be attributed to porosity, clusters and inclusions largely exhibited by this material as shown in Fig. 5.1.16.



a



b

Figure 5.1.16 Porosity, clusters and inclusions produced during the casting process were observed in AA 7150-T651 both on a polished surface (a) and below the surface as indicated for the arrows in the SEM fractograph (b).

run	Hv _{0.1 max}		Hv _{max} depth (μm)		ΔHv/Hv _{bulk} (%)		Plasticised zone depth (μm)	
	AA2024-T351	AA7150-T651	AA2024-T351	AA7150-T651	AA2024-T351	AA7150-T651	AA2024-T351	AA7150-T651
1	145	153	20	69	20.5	5.5	180	180
2	145	167	20	102	21.0	15.4	300	320
3	155	154	20	150	29.0	6.5	280	425
4	167	164	20	120	39.1	13.0	400	320
5	136	168	80	30	13.0	15.9	400	300
6	147	152	20	90	22.9	4.8	140	160
7	150	155	20	179	25.1	6.9	160	300
8	158	155	20	186	31.3	6.9	220	420
9	145	151	30	105	21.1	3.9	100	225
10	154	155	30	30	27.9	6.6	210	280
11	158	163	30	131	31.3	12.4	180	300
12	152	160	27	30	26.5	10.3	100	300
13	135	162	80	186	12.1	11.7	150	420
14	159	158	30	140	32.5	9.0	220	440
15	158	163	74	186	31.6	12.4	280	480
16	154	157	20	90	28.0	8.1	250	220

Table 5.1.10 Summary of the measured work hardening parameters.

Finally, the influence of the peening factors on the hardness distribution is not very clear. It would seem to be that shot type and coverage play the primary role and the incidence angle to a lesser extent. The design of experiments approach can also be used to determine which are the significant factors for each peening effect, as will be discussed in the following section.

5.2 THE DESIGN OF EXPERIMENT ANALYSIS

The evaluated effects were: the calculated stress concentration factor (table 5.1.4), the measured-calculated maximum compressive residual stresses (table 5.1.7) and the direct measurement of the maximum microhardness (table 5.1.10). The performance statistics utilised, i.e. the parameter MSD (§ 4.3.1.2), were selected according to two modalities: (i) Larger-the-better statistic both for the maximum compressive residual stress and for the work hardening effects, and (b) smaller-the-better statistic for the stress concentration.

5.2.1 Significant factors for each peening effect in AA-2024-T351

Results of the analysis for the compressive residual stress (RS) in AA 2024-T351 are shown in table 5.2.1.

Run	A	B	C	D	E	A shot	B cover.	C empty	D angle	E empty	MaxStress MPa	MinStress MPa	Y(mean) MPa	S/N
1	1	1	1	1	1	S230	50	1	30	1	-110.40	-139.20	-124.80	41.75
2	1	2	2	2	2	S230	100	2	89	2	-199.00	-268.40	-233.70	47.08
3	1	3	3	3	3	S230	200	3	45	3	-86.60	-307.80	-197.20	41.43
4	1	4	4	4	4	S230	400	4	89	4	-164.00	-329.30	-246.65	46.34
5	2	1	2	3	4	CCW20	75	2	45	4	-140.80	-205.50	-173.15	44.31
6	2	2	1	4	3	CCW20	100	1	89	3	-235.50	-250.50	-243.00	47.70
7	2	3	4	1	2	CCW20	200	4	30	2	-149.90	-180.00	-164.95	44.24
8	2	4	3	2	1	CCW20	400	3	89	1	-222.20	-268.90	-245.55	47.68
9	3	1	3	4	2	S110	96	3	89	2	-210.00	-350.00	-280.00	48.12
10	3	2	4	3	1	S110	100	4	45	1	-105.00	-158.00	-131.50	41.85
11	3	3	1	2	4	S110	200	1	89	4	-328.70	-429.70	-379.20	51.35
12	3	4	2	1	3	S110	400	2	30	3	-128.20	-170.54	-149.37	43.22
13	4	1	4	2	3	S330	50	4	89	3	-215.90	-299.90	-257.90	47.88
14	4	2	3	1	4	S330	100	3	30	4	-160.00	-180.00	-170.00	44.56
15	4	3	2	4	1	S330	200	2	89	1	-235.00	-382.00	-308.50	49.04
16	4	4	1	3	2	S330	400	1	45	2	-211.70	-372.90	-292.30	48.31
Average													-224.86	45.93

Table 5.2.1 Results of the design of experiments analysis for the compressive residual stresses using the larger the better statistic as the mean square deviation which measures the dispersion of the data.

Columns labelled “A”, through “E” are a repeat of the array shown in §4.3.2 (tables 4.3.7 and 4.3.8). They show the combinations of factor levels used for each run. Column “Y” shows an average of the results for each of the determined principal stresses. This column is a repeat of maximum residual stresses shown in table 5.1.7. The S/N or signal to noise ratio previously discussed in §4.3.1.2, was calculated using Eq.4.8. The best signal-to-noise ratio is that shown by the highest value, which in this case is run 11.

It may be noted from the Y and S/N columns of table 5.2.1 that, although there is an overall agreement between Y and S/N, this agreement is not always held. This is because S/N includes dispersion, while Y does not. For this reason, the principal stresses (maximum and minimum) were used rather than solely Y.

In order to find the best combination, it was necessary to construct a response table, shown in table 5.2.2. This table includes Y and S/N from which are calculated Y' and S/N', required to determine the effect of the signal-to-noise (significant variation) of each factor for the whole experiment. Here, Y' and S/N' are the average of Ys and S/Ns for each factor level. For instance, the factor Y' for A1 (factor A, level 1) is computed as follows:

$Y'_{A1} = (-124.8 - 233.7 - 197.2 - 246.65) / 4 = -200.6$, i.e. the average of all Ys for factor A at level 1 as illustrated by the shadowed values on the top left corner of table 5.2.2. SN' for factor A and level 1 is calculated in the same form.

The effect S/N for each level in the whole experiment is obtained from the difference between the averaged S/N (table 5.2.1) of the whole experiment and S/N' (table 5.2.2) for each factor and its corresponding level. Differently expressed, effect S/N' = S/N' - S/N. Thus, the effect of S/N' for the A1 = 44.15 - 45.93 = -1.8. The method of computing the effect of Y' for each factor at each level is analogous to that as for the effect S/N'.

The resulting incidence effect of S/N ratio for each factor regarding the compressive residual stresses is illustrated in Fig. 5.2.1. The control factor plot shows, in the first instance, the significant factors as those that present the highest variability of the

calculated S/N' ratio. It is, therefore observed that factor D (incidence angle) has the highest S/N' variation followed by factor A (shot). This means that incidence angle and shot type were the dominant factors for achieving the maximum compressive residual stresses. In order to evaluate the trustworthiness of this result, an analysis of variance approach was applied. The percentage contribution of the source to total variation determined for each of the factors was, for factor A (17%), B (3.5%), C (8.5%), D (62%) and E (9%) (see appendix VIII, table VIII-1 for details). These results show the same trend as the previous ones.

Run	ABCDE	Y MPa	S/N	Factor	level	Y' MPa	S/N'	Effects(S/N')	Effects (Y') MPa
1	1 1 1 1 1	-124.80	41.75	A-shot	A1	-200.6	44.15	-1.8	24.3
2	1 2 2 2 2	-233.70	47.08		A2	-206.7	45.98	0.1	18.2
3	1 3 3 3 3	-197.20	41.43		A3	-235.0	46.13	0.2	-10.2
4	1 4 4 4 4	-246.65	46.34		A4	-257.2	47.45	1.5	-32.3
5	2 1 2 3 4	-173.15	44.31		average		45.93		
6	2 2 1 4 3	-243.00	47.70	B-coverage	B1	-209.0	45.52	-0.4	15.9
7	2 3 4 1 2	-164.95	44.24		B2	-194.6	45.30	-0.6	30.3
8	2 4 3 2 1	-245.55	47.68		B3	-262.5	46.51	0.6	-37.6
9	3 1 3 4 2	-280.00	48.12		B4	-233.5	46.39	0.5	-8.6
10	3 2 4 3 1	-131.50	41.85				45.93		
11	3 3 1 2 4	-379.20	51.35	C-empty	C1	-259.8	47.28	1.3	-35.0
12	3 4 2 1 3	-149.37	43.22		C2	-216.2	45.91	0.0	8.7
13	4 1 4 2 3	-257.90	47.88		C3	-223.2	45.45	-0.5	1.7
14	4 2 3 1 4	-170.00	44.56		C4	-200.3	45.08	-0.9	24.6
15	4 3 2 4 1	-308.50	49.04				45.93		
16	4 4 1 3 2	-292.30	48.31	D-angle	D1	-152.3	43.44	-2.5	72.6
Grand average		-224.86	45.93		D2	-279.1	48.50	2.6	-54.2
					D3	-198.5	43.97	-2.0	26.3
					D4	-269.5	47.80	1.9	-44.7
							45.93		
				E-empty	E1	-202.6	45.08	-0.8	22.3
					E2	-242.7	46.94	1.0	-17.9
					E3	-211.9	45.06	-0.9	13.0
					E4	-242.3	46.64	0.7	-17.4
							45.93		

Table 5.2.2 Response table for residual stresses.

FACTOR EFFECTS FOR S/N ratio Residual Stress Al-2024-T351

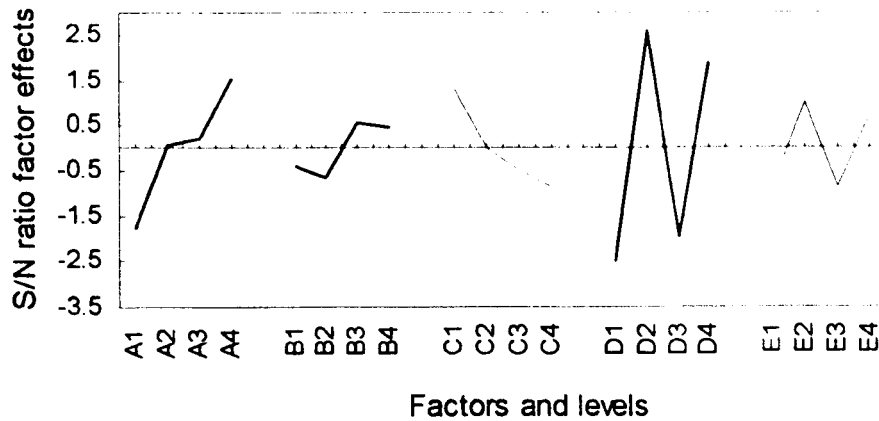


Figure 5.2.1 S/N ratio for each effect and level of the compressive residual stresses for the AA 2024-T351. A (1 through 4 level) factor stands for shot type, B for percentage of coverage, C is an empty factor, D is for incidence angle and E is another empty factor. Incidence angle (D) and shot type (A) are the significant peening factors due to the highest S/N' variation.

The plots in Fig. 5.2.1 can also be used to estimate the optimum combination of factors and their corresponding levels to attain the predicted maximum residual stress; this is achieved by selecting the set points with the highest S/N' value. In particular, the combination A4, B3, C1, D2 and E2 (S330, 200% coverage and 89° incidence angle, according to table 4.3.7), would yield the maximum theoretical residual stress. This maximum residual stress is calculated by utilising the predictive model (Eq. 4.10) and the response table 5.2.2, as follows:

$$S/N'_{\text{optimum}} = S/N \text{ average} + \text{Effects } (SN')_A \text{ maximum} + \text{Effects } (SN')_B \text{ maximum} + \text{Effects } (SN')_C \text{ maximum} + \text{Effects } (SN')_D \text{ maximum} + \text{Effects } (SN')_E \text{ maximum}$$

N.B. All these values are shadowed in the response table 5.2.2.

Substitution of the numerical values into the predictive model, gives:

$$S/N'_{\text{optimum}} = 45.93 + 1.5 + 0.6 + 1.3 + 2.6 + 1.0 = 52.93$$

Similarly, Y'_{optimum} is calculated utilising the maximum compressive Effects Y' for each factor and the general average of Y, i.e.

$$Y'_{\text{optimum}} = -224.86 - 32.3 - 37.6 - 35.0 - 54.2 - 17.9 = -401.86 \text{ MPa}$$

Evidently, the above results are higher than the maximum experimental compressive residual stress found to be $S/N = 51.35$ and $Y = -379.20$ MPa (in run 11). The worst combination of peening conditions are obtained by considering the Effect S/N' or Effects Y' with the lowest values.

Following the same argument, shot size (factor A) is a significant factor when considering the depth to the maximum compressive residual stresses as depicted in Fig. 5.2.2. These results are comparable to those observations discussed in § 5.1.2.

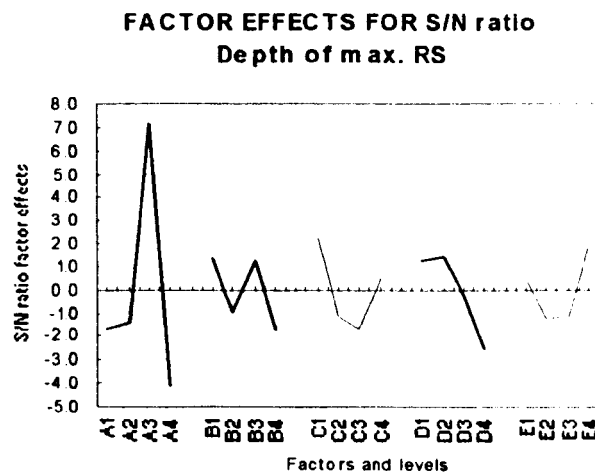


Figure 5.2.2 S/N ratio for each effect and its level on depth of the maximum compressive residual stresses for the AA 2024-T351.

The significant factors for stress concentration were shot type (A), coverage (B) and incidence angle (D). Specifically, shot type and coverage seem to affect strongly, as shown in Fig. 5.2.3.

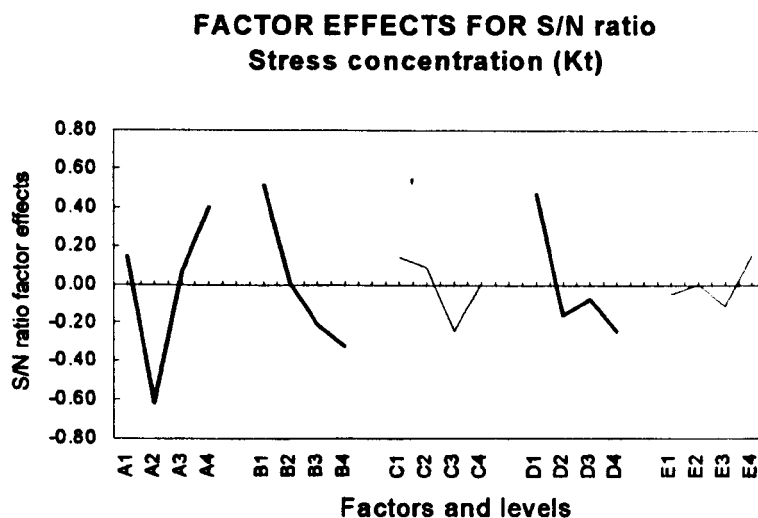


Figure 5.2.3 S/N ratio for the stress concentration peening effect.

These results support the discussion conducted in §5.1.1, where it was indicated that the geometric features of the shot, the percentage of coverage and incidence angle were seen to play a major role in the stress concentration factor, K_t , which is believed to be dependent on the shape of the dimples on the peened surface.

Regarding work hardening, coverage was found to be the significant factor for achieving maximum hardness, as can be seen in Fig. 5.2.4. This result expresses a clear indication that the shot type and incidence angle may induce a much localised distorted surface and subsurface layer. Accordingly, the degree of saturation may depend on the peening conditions and coverage.

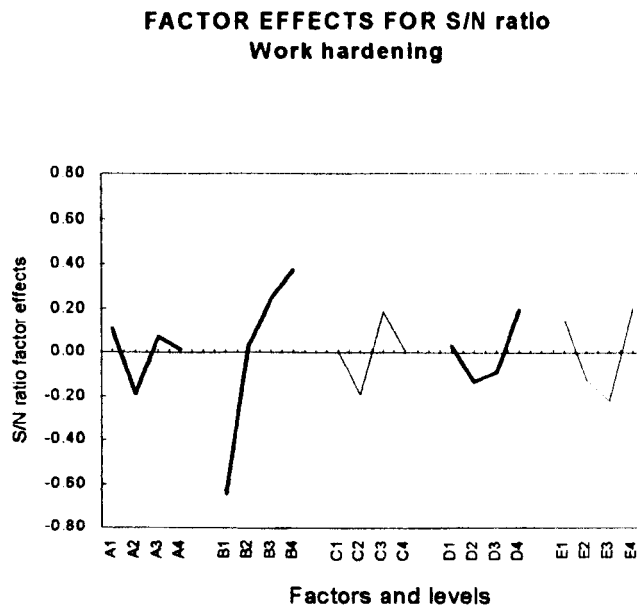


Figure 5.2.4 S/N ratio for the work hardening peening effect.

5.2.2 Optimum and worst peening conditions for AA-2024-T351

Once the calculated optimum peening conditions are known for a particular peening effect, all the remainder peening effects either optimum or worst cases can be estimated by making use of the predictive model (Eq. 4.10) and the respective response tables for each of the remainder peening effects (see appendix VIII for the response tables of

hardness and stress concentration). For example, using the conditions A4, B3, C1, D2 and E2 (as determined above), the estimated values are: optimum residual stress = -402 MPa (as determined above); depth of the optimum RS = 0.31 mm; hardness = 150.5 Hv_{0.1} and stress concentration = 1.54. A summary of the estimated optimum and worst cases is given in table 5.2.3. In this table, the estimated peening conditions are categorised by the optimum and worst residual stress (RS), hardness and stress concentration respectively. In cases where two levels of a particular factor resulted to be very close to each other, as is the case for the factor B, levels 3 and 4 from the residual stress S/N ratio shown in Fig. 5.2.1; two peening conditions were determined to avoid underestimation of possibilities.

Optimum						Worst					
Peening conditions	RS MPa	Hv	Kt	Depth mm		Peening conditions	RS MPa	Hv	Kt	Depth mm	
Residual stress (RS)						Residual stress (RS)					
A4,B3,C1,D2,E2	S330,200%,89°	-402	150	1.5	0.31	A1,B3,C4,D1,E1	S230,45%,30°	-119	160	1.5	0.19
A4,B4,C1,D2,E2	S330,400%,89°	-373	153	1.6	0.34						
Hardness (Hv _{0.1})						Hardness (Hv _{0.1})					
A1,B4,C3,D4,E4	S230,400%,89°	-270	170	1.7	0.35	A2,B1,C2,D2,E3	CCW20,75%,89°	-223	127	1.6	0.20
						A4,B1,C4,D2,E3	S330,50%,89°	-258	135	1.5	0.25
Stress concentration (Kt)						Stress concentration (Kt)					
A3,B1,C1,D1,E4	S110,96%,30°	-199	145	1.3	0.01	A2,B4,C3,D4,E1	CCW20,400%,89°	-236	163	1.8	0.35
A1,B1,C1,D1,E1	S230,50%,30°	-125	145	1.4	0.13						

Table 5.2.3 Estimated optimum and worst cases by using the DoE concepts.

It has been discussed previously that SP produces some changes that may be beneficial but others may be detrimental in terms of fatigue resistance. Thus, the balancing of beneficial and detrimental effects makes it difficult to be certain of peening behaviour and its impact on fatigue performance. Consequently, it would seem that peening conditions for optimum fatigue strength should result from a surface hardening as high as possible, peak compressive residual stresses as high as possible, a depth of this peak as short as possible and with a surface roughness as low as possible.

In this respect, to select the optimum and worst conditions to be implemented in the fatigue testing, equal weight was given to the RS, Hv and Kt, i.e. a balancing exercise of the surface changes was undertaken. The selected peening conditions and the expected values are listed in table 5.2.4.

Effects	Selected optimum conditions	Range of expected values	Selected worst conditions	Range of expected values
RS (MPa)	A3, B3, D3 (S110,200%,45°)	-200 to -299	A2, B2, D3 (CCW20,100%,45°)	-103 to -203
Hv		147 to 161		139 to 153
Kt		1.5 to 1.7		1.6 to 1.8
Depth (mm)		0.06 to 0.14		0.22 to 0.30

Table 5.2.4 Estimated optimum and worst peening conditions to be used in the fatigue testing together with their expected values.

Results of the experimental validation of the estimated optimum and worst peening conditions, as shown in table 5.2.5, were found to be slightly different to those of table 5.2.4. Such discrepancies can be attributed to several process factors such as: (i) variation in the pressure, (ii) wear (media, nozzle, and hose), (iii) highly scattered shot size, (iv) variation in the flow rate due to interferences caused by dust, debris or other objects, etc. See appendices VI-B and VII for the corresponding RS and Hv plots.

Optimum					Worst				
Peening condition	RS	Hv	Kt	Depth	Peening condition	RS	Hv	Kt	Depth
S110, 200%, 45°	-350	147	1.3	0.03	CW20,100%,45°	-247	143	1.3	0.1

Table 5.2.5 Experimental peened effects determined from the estimated peening conditions of table 5.2.4.

5.2.3 Significant factors for each peened effect in AA 7150-T651

Because the computing practice followed for the determination of the significant factors and the selection of the optimum and worst conditions is similar to that of AA 2024, the

most representative plots and results for the AA 7150-T651 will be presented in this section. Response tables are shown in appendix VIII.

Values of S/N ratio factor effect for each peening effect are shown in the control factor plots illustrated in Fig. 5.2.5.

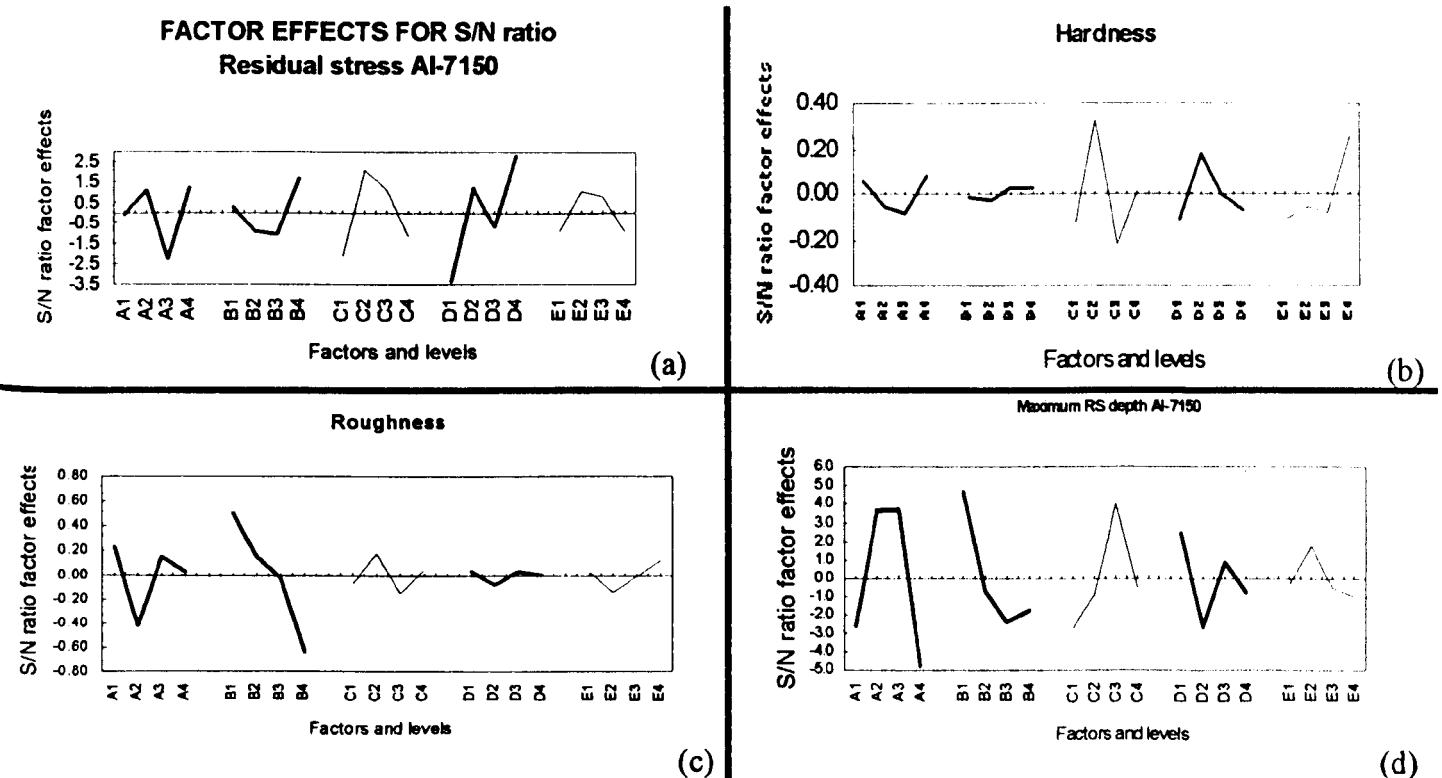


Figure 5.2.5 Summary of the S/N ratio factor effects on each of the peening outputs of the AA 7150-T651.

The S/N ratios for AA 7150 are markedly different to those of AA 2024. Whilst S/N ratios are clearly defined for the factors of interest (A, B and D) in AA 2024, the empty factor C incorporates some noise in the significance of the factors of interest, particularly concerning the Hv peening effect as evidenced in Fig. 5.2.5-b. This situation corroborates the low variability of the data, which was observed previously in table 5.1.10. This result makes it more difficult to ascertain any significant factor for hardness effect of AA-7150. Incidence angle (D) factor was highly significant for the peak RS. However, shot type and coverage exhibited higher significance for the depth to peak RS factor (Fig. 5.2.5-a, d). Coverage is a significant factor when considering

values of stress concentrations on the peened surface (Fig. 5.2.5-c), which becomes apparent when considering a surface peened to 50% coverage.

5.2.4 Optimum and worst peening conditions for the AA 7150-T651

Results of the estimated optimum and worst peening conditions determined as described in the preceded section are shown in table 5.2.6.

Optimum						Worst					
Peening conditions	RS MPa	Hv	Kt	Depth mm		Peening conditions	RS MPa	Hv	Kt	Depth mm	
Residual stress (RS)						Residual stress (RS)					
A4,B4,C2,D4,E2	CW20,400%,89°	-433	161	1.7	0.20	A3,B3,C1,D1,E1	S110, 200%,30°	-47	151	1.5	0.15
A4,B4,C2,D4,E2	S330,400%,89°	-425	164	1.6	0.37						
Hardness (Hv _{0.1})						Hardness (Hv _{0.1})					
A4,B3,C2,D2,E4	S330,200%,89°	-310	174	1.5	0.39	A3,B2,C3,D1,E1	S110,100%,30°	-122	148	1.5	0.01
A1,B4,C2,D2,E4	S230,400%,89°	-332	174	1.5	0.31	A3,B1,C3,D4,E2	S110,93%,89°	-307	151	1.4	0.03
A2,B1,C2,D3,E4	CW20,71%,45°	-287	168	1.4	0.06						
Stress concentration (Kt)						Stress concentration (Kt)					
A1,B1,C2,D1,E4	S230,50%,30°	-206	168	1.3	0.12	A2,B4,C3,D2,E2	CCW20,400%,89°	-392	156	1.8	0.08
A1,B1,C2,D3,E4	S230,50%,45°	-252	170	1.3	0.17						

Table 5.2.6 Estimated optimum and worst cases by using the DoE concepts.

Again, a balancing exercise of the values of RS, Hv and Kt was carried out. Thus, the selected optimum and worst peening conditions are listed in table 5.2.7.

Effects	Selected optimum conditions	Range of expected values	Selected worst conditions	Range of expected values
RS (MPa)		-233 to -375		-33 to 174
Hv	A1,B1,D4	152 to 169	A3, B3, D1	149 to 166
Kt	(S230,50%,89°)	1.32 to 1.143	(S110,200%,30°)	1.42 to 1.53
Depth (mm)		0.11 to 0.24		0.03 to 0.16

Table 5.2.7 Estimated optimum and worst peening conditions to be used in the fatigue testing together with their expected values.

Given the probability of premature failure of an irregular peened surface, coverage of 50% was not considered suitable. Therefore, coverages of 100% or higher were only

taken into account for fatigue testing. Consequently, the peening conditions selected for fatigue testing are shown in table 5.2.8, together with their experimental measurements.

Optimum					Worst				
Peening condition	RS	Hv	Kt	Depth	Peening condition	RS	Hv	Kt	Depth
S230,100%,89°	-288	170	1.32	0.25	S110,200%,30°	-193	157	1.23	0.05

Table 5.2.8 Experimental values of RS, Hv, Kt and depth to peak residual stress corresponding to the selected optimum and worst peening conditions for the AA 7150-T651.

5.3 FATIGUE TESTING

5.3.1 Fatigue results

5.3.1.1 AA 2024-T351

Conventional uniaxial tension-tension fatigue tests were carried out using hourglass specimens as described in §4.5. Shot peening of the specimens was undertaken according to the conditions determined in the previous section. The results of fatigue tests conducted for each AA are listed in tables 5.3.1 and 5.3.2, and graphically presented in the form of Wöhler stress versus cycles to failure (S-N) curves over a wide range of applied stress in Figs. 5.3.1 and 5.3.2. The fatigue endurance is defined as the endurance stress at or below which a specimen can sustain cycling for up to 7×10^6 cycles without failing.

Optimum peening		Worst peening		Unpeened	
σ_{max}	N_f	σ_{max}	N_f	σ_{max}	N_f
400	22952	400	25833	400	20227
360	55470	360	53676	350	66760
320	397038	320	208610	300	140990
300	865106	300	167920	270	254920
300	615200	280	334177	264	266900
280	726352	260	1043103	250	721645
270	844000	240	3490174	200	4640000
260	1350810	220	5231882	190	7000000
240	2240000	200	7000000		
240	2270642				
225	7000000				

Table 5.3.1 Experimental results of fatigue tests for peened and unpeened AA 2024-T351.

Trends observed in the fatigue life curves for AA12024 revealed that shot peened specimens have a marginally superior life compared to those unpeened, specifically at

an intermediate zone of the low¹ and high² cycle fatigue regions. It was evident, however, that peening did not impair the fatigue performance of the material. Optimum peening conditions results, on the whole, were found to be better than those given by the worst conditions, as expected from the DoE estimations. Furthermore, there was a discernable improvement in endurance by peened specimens when testing at stresses around the 300 MPa. The fatigue endurance for the unpeened material was approximately 190 MPa, whilst for the peened at worst and optimum condition was 190 and 225 MPa respectively. No discernable difference in fatigue life was observed in the low-cyclic fatigue region.

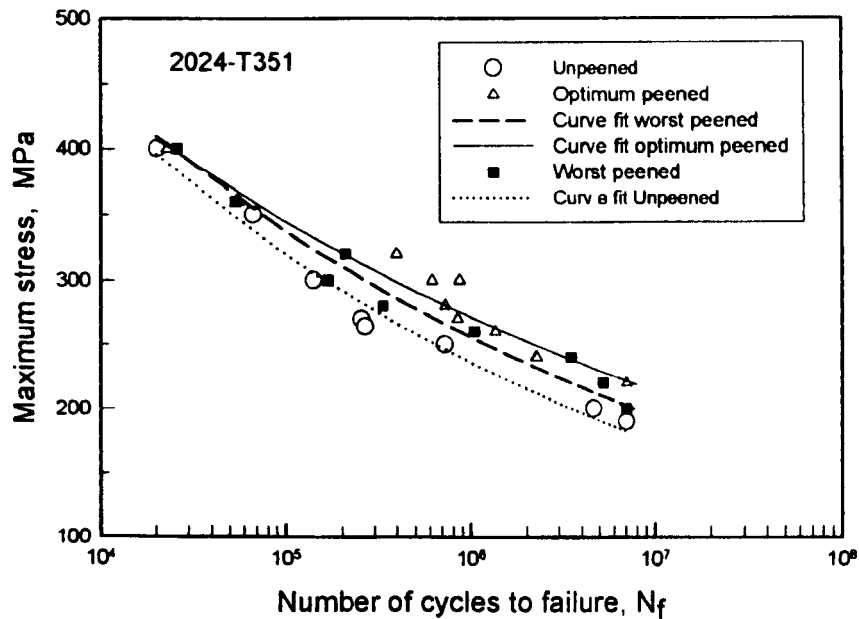


Figure 5.3.1 Axial loading, constant amplitude S-N curves for peened and unpeened specimens of AA 2024-T351.

¹ Low cyclic fatigue region is usually understood to be in the region $10^2 < N_f < 10^5$ (N_f = cycles to failure)
² $N_f > 10^5$

5.3.1.2 AA 7150-T651

Optimum peening		Worst peening		Unpeened	
σ_{max}	N_f	σ_{max}	N_f	σ_{max}	N_f
500	5647	500	7568	500	11656
460	10751	460	17211	460	24465
420	25554	420	42658	420	21642
380	47711	380	62609	400	30423
340	72057	340	84186	380	47641
300	109040	340	118000	340	85149
260	181360	300	993000	320	87318
260	142200	300	794614	280	243597
240	498000	260	1610000	260	215955
240	293871	255	3332000	250	440516
		240	8000000	240	900000

Table 5.3.2 Experimental results of fatigue tests for peened and unpeened AA 7150-T651.

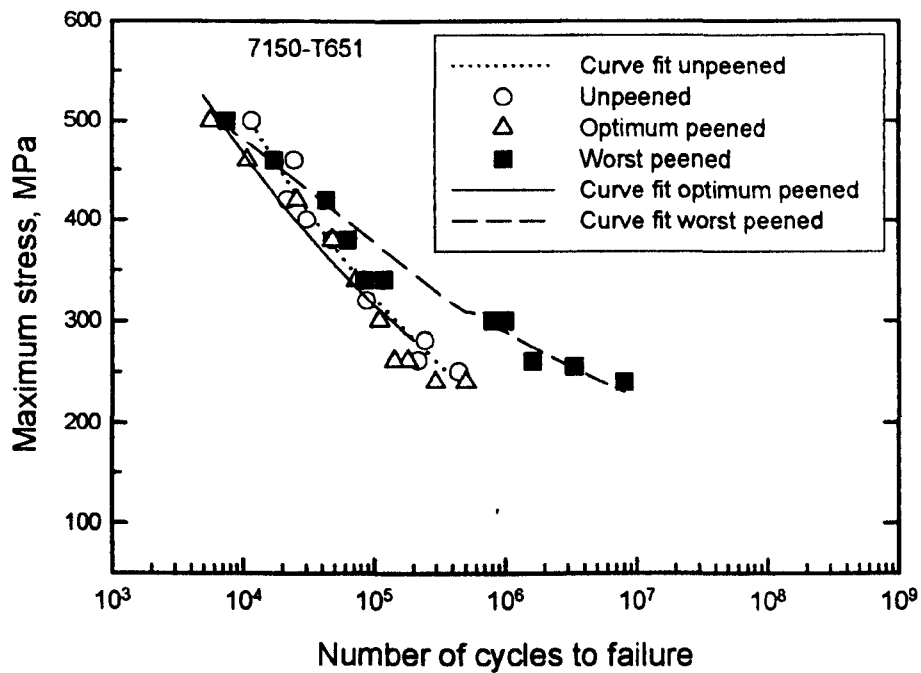


Figure 5.3.2 Axial loading, constant amplitude S-N curves for peened and unpeened specimens of AA 7150-T651.

Different behaviour was exhibited by the AA 7150 as shown by Fig. 5.3.2. Optimum peening conditions were found to give poorer results even than the unpeened material. Better fatigue results were obtained by specimens peened to the worst peening conditions particularly at stresses below the yield stress level. The fatigue limit of the peened specimens under worst conditions was 240 MPa, whereas at this stress level, those peened to optimum condition and unpeened failed at 500000 and 900000 cycles respectively. In the low-cyclic fatigue region, both peening conditions were found to be detrimental as the specimens failed slightly earlier than the unpeened.

5.3.2 Crack growth

Crack propagation measurements were carried out by taking plastic replicas of specimens tested under conditions described in table 5.3.3. This choice was based on the S-N data so that an appreciable change in crack propagation rates would be expected.

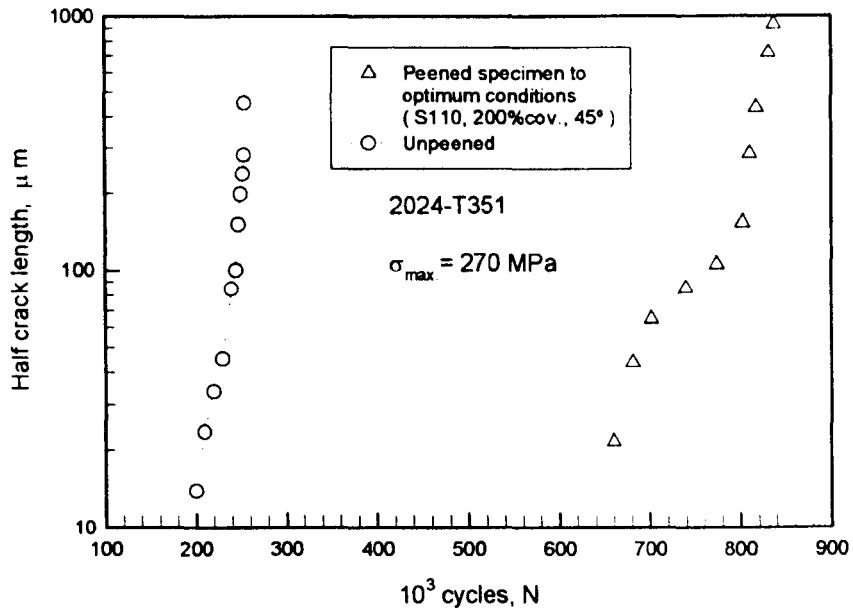
Surface condition	σ_{\max}			
	AA 2024-T351		AA 7150-T651	
Optimum	270	240	260	240
Worst			255	300
Unpeened	270		260	

Table 5.3.3 Specimen testing conditions for crack propagation measurements.

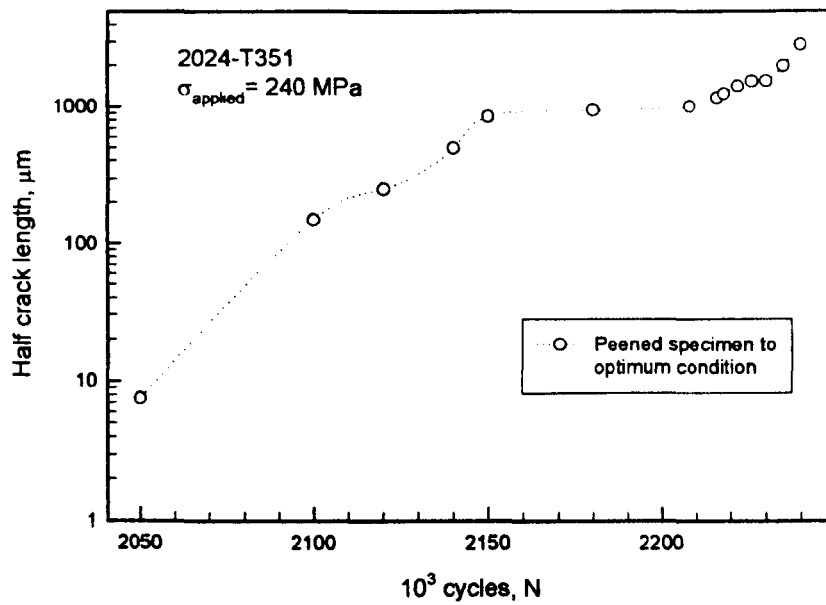
5.3.2.1 AA 2024-T351

Detection of very small cracks on the peened surfaces was increasingly difficult due to the masking effect of the rough surface and other small features. Therefore, the peened specimens were slightly polished with a 1200 grade grit paper, to surmount this limitation. Care was taken at this stage to ensure that a minimal quantity of material was removed. The growth behaviour of cracks from detection to failure was recorded for each of the replicated tests in terms of the number of cycles to initiation (N_i) and the number of cycles to failure (N_f). Crack length visible on replica is plotted as half crack

length. Crack propagation results of the AA 2024 from the observations in replicas are listed in table IX-1 of appendix IX. Fig. 5.3.3 shows two plots of the kind, half crack length versus number of cycles, for each of the replicated tests.



(a)



(b)

Figure 5.3.3 Crack propagation behaviour for peened and unpeened AA 2024-T351 specimens at different stress levels.

When comparing crack growth data of unpeened and peened specimens, Fig. 5.3.3 shows that the number of cycles needed to form a crack, of a size detectable in the replicas was increased from 200 to 660 thousand cycles after shot peening. However,

the improvement seems to be poor compared to that of AA 7150-T651, as discussed in the next section.

Surface replicas revealed that dominant cracks usually initiated at a corner edge and grew along both sides (width and thickness). Fatal cracks formed within the gauge area for both AA's in all cases. Very few isolated initiation sites at each of the applied stress levels were observed in peened specimens, whilst an increased number of such sites were observed in unpeened specimens. However, it was observed that only one crack dominated fatigue life. Furthermore, as the test progressed, coalescence was often observed both in unpeened and peened specimens as shown in Fig. 5.3.4.

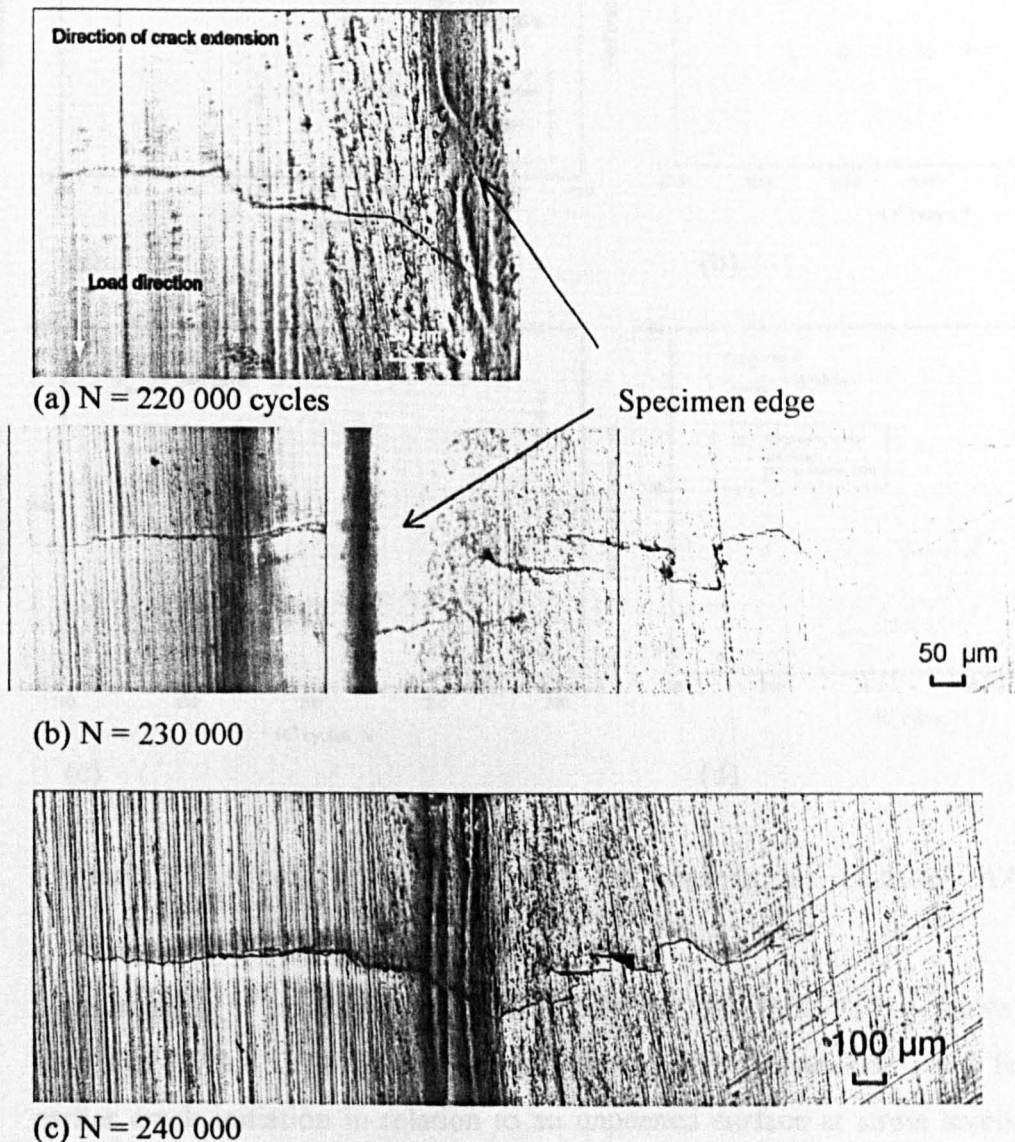


Figure 5.3.4 Crack coalescence between cracks from each side of the specimen in a AA 2024-T351 unpeened specimen ($\sigma_{\max.} = 270$ MPa): (a) a crack formed on the left side of the specimen edge, (b) Two cracks formed on the right side of the specimen edge and (c) fatal crack propagating after coalescence of the neighbouring cracks.

5.3.2.2 AA 7150-T651

Crack propagation results for the AA 7150 from replica observations are listed in table IX-2 of appendix IX, and graphically illustrated in Fig. 5.3.5.

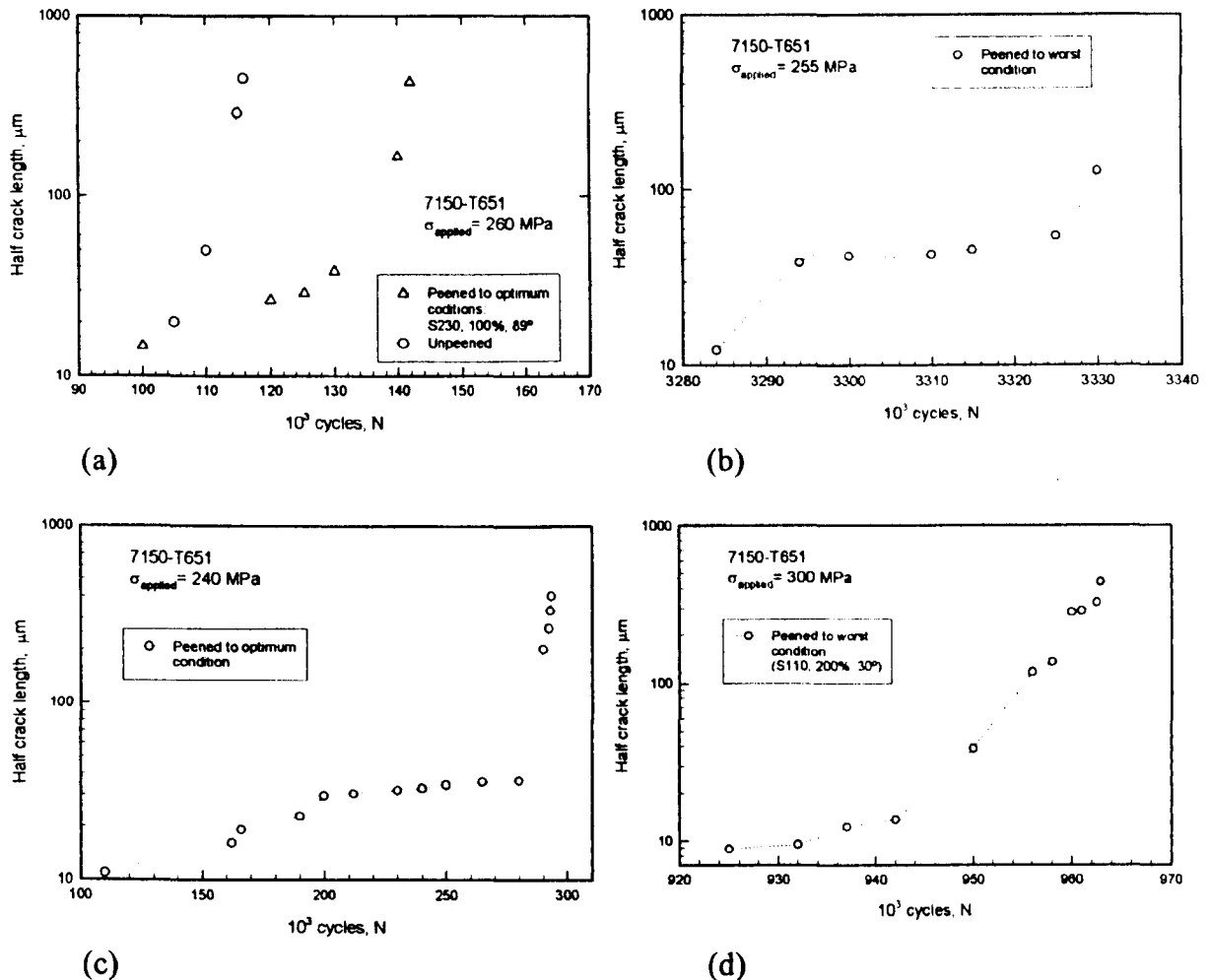


Figure 5.3.5 Crack growth behaviour for peened and unpeened AA 7150-T651 specimens at different stress levels.

Consideration of crack growth behaviour for the AA 7150-T651 is more conventional than that of AA 2024-T351. The optimum peening conditions were found to have earlier crack initiation in relation to an unpeened surface at stress levels in the high-cyclic fatigue region, as clearly shown in Fig. 5.3.5 (a). In contrast, the worst peening conditions exhibited in general a remarkably low short crack propagation rate as illustrated in Fig. 5.3.5 (b) and (d). Once this stage of crack growth is passed, the crack

grows rapidly until failure, as shown by all plots of Fig. 5.3.5. Crack coalescence was also observed in AA 7150-T651 as shown in Fig. 5.3.6.

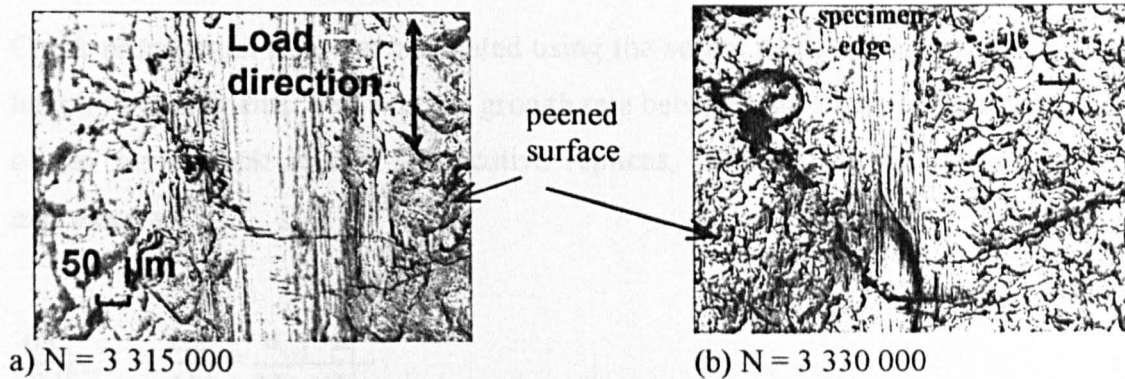


Figure 5.3.6 Crack coalescence between cracks from each side of a corner edge in an AA 7150-T651 specimen peened to worst conditions ($\sigma_{\max} = 255$ MPa).

Observations of replicas revealed that cracks propagated in a meandering fashion, which characterises the torturous path that cracks follow on overcoming the microstructural barriers presented by severely distorted grains. Also observed was some bifurcation or branching off as the crack grew. However, one branch usually dominated the crack propagation and the others arrested or coalesced as depicted in Fig. 5.3.7 (a). Overall, cracks initiate and propagate in a transverse direction almost perpendicular to the direction of axial loading. Typically of commercial materials, cracks initiated from inhomogeneous constituents such as pores or inclusions, as shown in 5.3.7 (b).

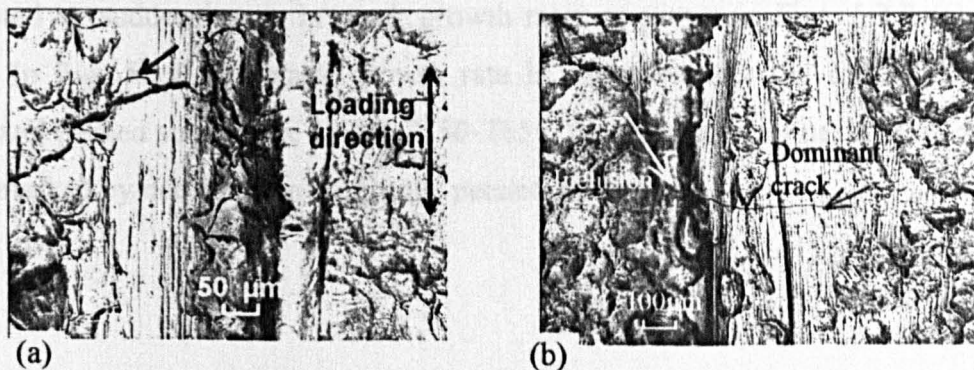


Figure 5.3.7 Crack growth features observed at the specimen edges: (a) bifurcation of a crack, indicated by the arrow and (b) initiation from an inclusion, commonly observed in AA 7150-T651.

5.3.3 Crack growth rate

Crack propagation rate was calculated using the secant method from half surface crack length measurements. The average growth rate between two crack length measurements of the same crack in two consecutive replicas, taken at known cycle lifetimes, is expressed as:

$$\left. \frac{da}{dN} \right|_{a=a_m} = \frac{\Delta a}{\Delta N} = \frac{a_{i+1} - a_i}{N_{i+1} - N_i} \quad (5.3)$$

where a_i , a_{i+1} are crack lengths at two successive stages, and N_i , N_{i+1} are the number of cycles corresponding to crack lengths a_i , a_{i+1} , respectively.

The mean growth rate $\frac{\Delta a}{\Delta N}$, during the interval is used to represent the growth rate corresponding to the mean crack length, a_m , where $a_m = \frac{a_i + a_{i+1}}{2}$.

Plots of crack propagation rates against the mean crack length are given in Figs. 5.3.8 and 5.3.9 for AA 2024-T351 and AA 7150-T651 respectively. Accelerations and decelerations were evident until steady fatigue crack growth was reached. Coalescence is manifested by sudden jumps in crack growth rates as shown in Figs. 5.3.8 (a) and 5.3.9 (b). In Fig. 5.3.8 (b) crack growth rate is approximately the same for both unpeened and peened specimens. In AA 7150-T651, the effect of shot peening on crack growth is marked by deceleration within the peened layer.

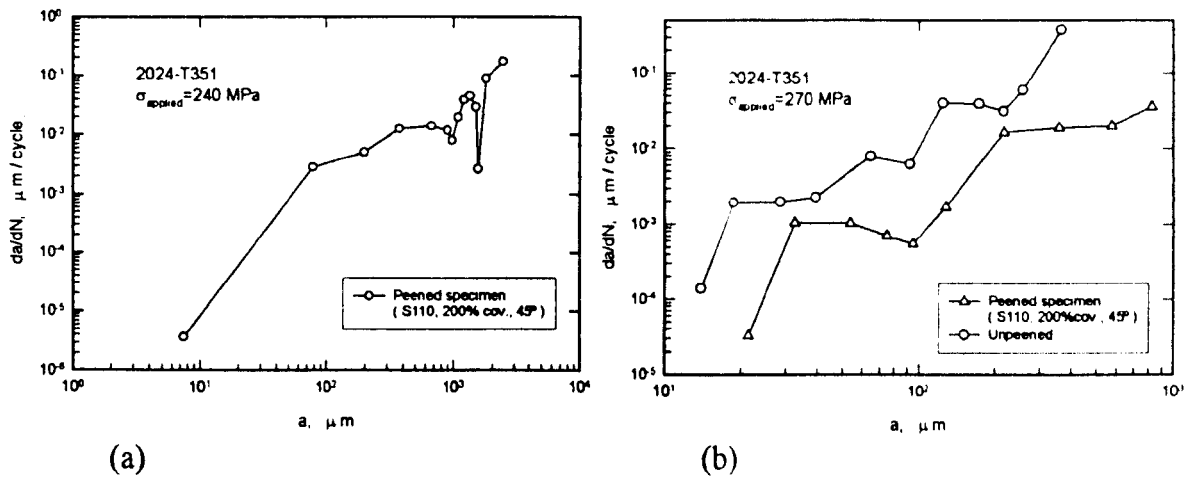


Figure 5.3.8 Crack growth rate vs. half surface crack length in AA 2024-T351.

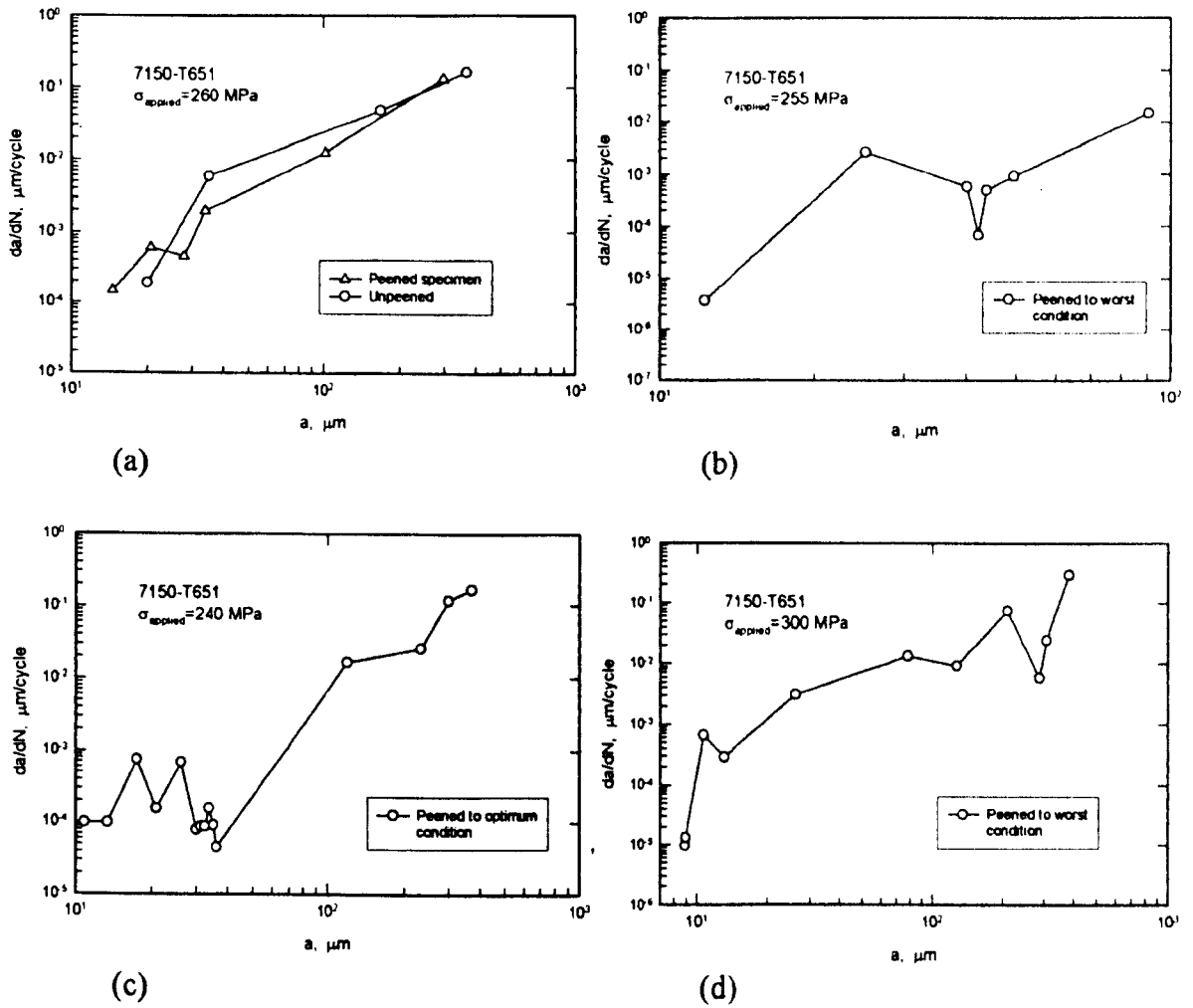


Figure 5.3.9 Crack growth rate vs. half surface crack length in AA 7150-T651.

5.3.4 Fracture surface observations

Whilst optical micrographs from replicas are useful to reveal some features of surface crack propagation such as crack initiation, crack growth and path morphology, crack bifurcation and coalescence, and even some slip patterns in relation to the growth of the crack; these are only surface observations. Generally, the location of crack initiation, local crack front geometry and microstructural interactions can be observed in a greater detail by means of scanning electron microscopy (SEM). These observations have been carried out extensively in fractured surfaces with the advantage of having a higher resolution than with the light microscope. In the present investigation, a Philips 500 scanning electron microscope was used for fractographic observations. Particular attention was paid to observe the initiation sites, and the type of fracture in the various regions (initiation, crystallographic growth, non crystallographic growth and final fracture).

5.3.4.1 AA 2024-T351

Figure 5.3.10 illustrates the initiation zone of an AA 2024-T351 unpeened specimen.

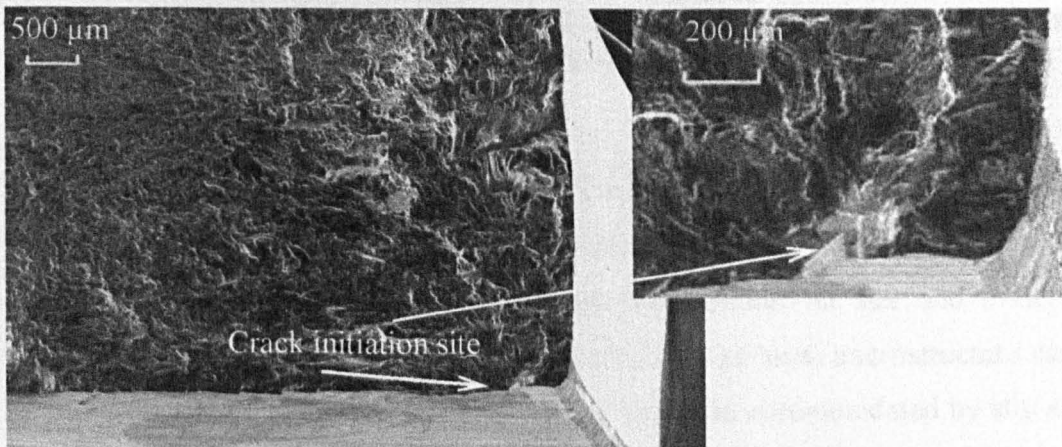


Figure 5.3.10 SEM fractograph for the AA 2024-T351 unpeened specimen at $\sigma_{\max.} = 240$ MPa. Surface initiation is clearly observed close to the corner of the specimen. The right picture is an magnified image of the initiation site indicated by the arrows.

Propagation from the initiation site was found to be transgranular in all cases. The crystallographic region at early stages of growth showing typical faceted growth is shown in Fig. 5.3.11. These differently oriented facets are mainly the result of crack propagation along primary slip planes within a grain, and then change of the growth direction to follow another slip system with different orientation in an adjacent grain as the crack front progresses. The differences exhibited with regard to the smoothness of the facets, suggest the influence of some secondary slip systems.

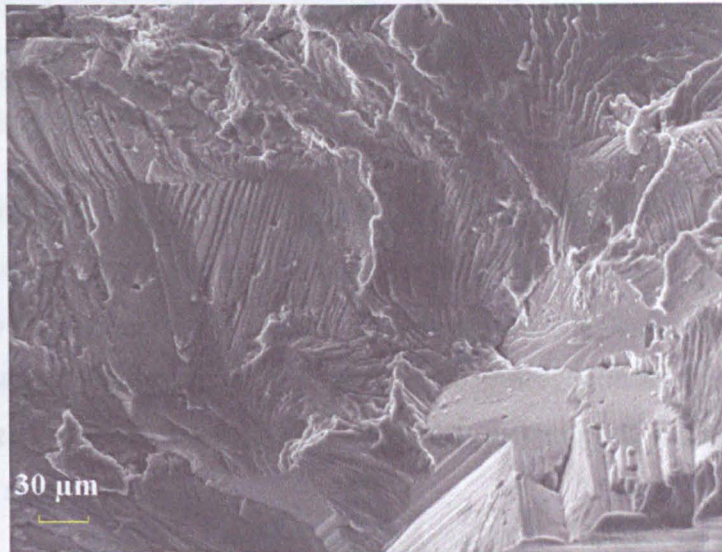


Figure 5.3.11 Transgranular Stage I crack propagation from initiation site. The appearance of the fracture surface resembles transcrystalline pseudo cleavage fracture. This initiation site corresponds to that shown in Fig. 5.3.10.

The other region of interest is that of Stage II crack propagation. The micrographs in Fig. 5.3.12 show typical striation fracture of stage II growth. Theory establishes that as the crack grows the plastic zone at the crack tip increases in size and eventually encompasses several grains to the extent that the effect of local microstructure can be neglected. This larger crack tip plasticity can no longer be accommodated by slip along a single slip system but requires multiple slip systems in two main shear directions. Precisely, this shear deformation mechanism results in a non-crystallographic crack path normal to the load direction, giving place to the characteristic fatigue striations. These marks provide a record of the passage of the crack front in each load cycle. Forsyth [245] suggested that the spacing between adjacent striations correlates with the average of crack growth rate per cycle.

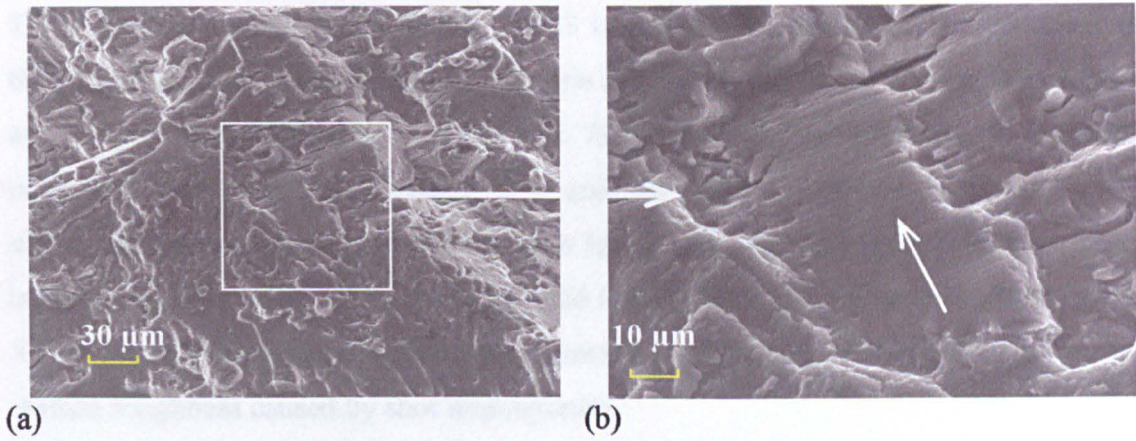


Figure 5.3.12 SEM fractograph showing the Stage II region in (a), and in (b) an amplified view from the central square of (a) with the aim of depicting the characteristic striation marks. The overall direction of the crack front is indicated by the arrow in picture (b).

In contrast, the fracture surface for the peened AA 2024-T351 to optimum conditions at the same maximum applied stress ($\sigma_{max.} = 240$ MPa) exhibited subsurface crack initiation as shown in Fig. 5.3.13. Facets can be seen which are the result of crack propagation along crystallographic planes and the grain boundaries are apparent by virtue of changes in the crack propagation direction as the crack front progresses from one grain to the next.

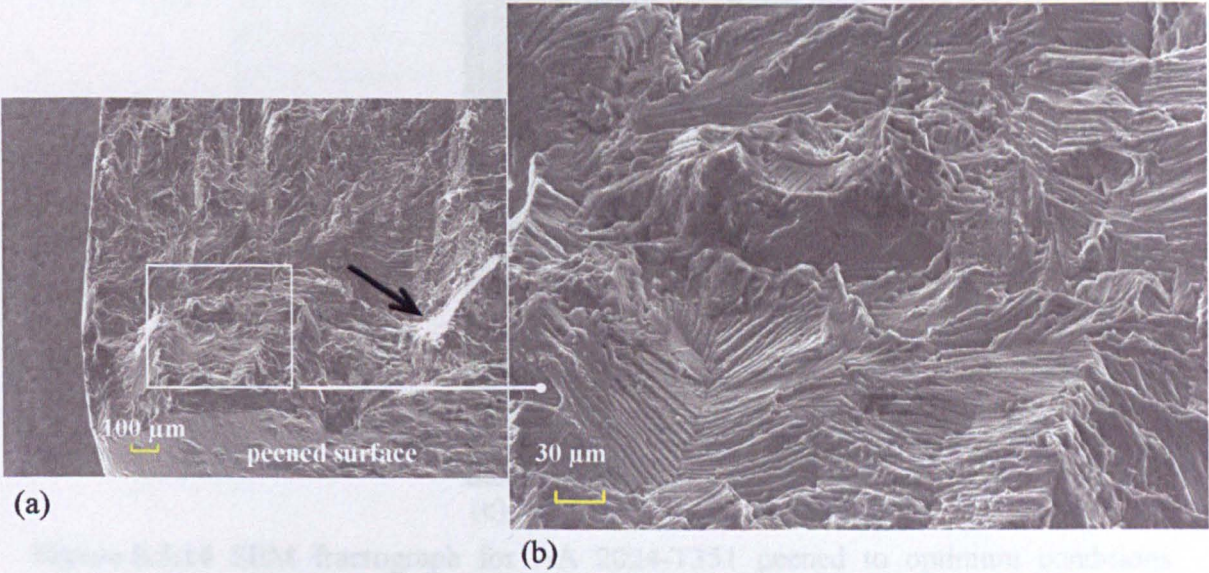


Figure 5.3.13 SEM fractograph illustrating a subsurface crack initiation indicated by the arrow in (a), which is located at 150-200μm from the surface. Facets and crystallographic planes formed are shown in the magnified picture (b) taken from the area within the square in (a).

The position of initiation site in Fig. 5.3.13 is intrinsically related to the occurrence of the transition from the compressive to tensile RS, which was found to be approximately at 180 μm from the surface for an AA 2024-T351 peened specimen to optimum conditions. Initiation sites at $\sigma_{\text{max.}} = 270$ and 300 MPa, are shown in Fig. 5.3.14. It shows subsurface initiation for both stress levels. For the 300MPa stress level, crack initiation occurred away from the corner and right below a peen dent as depicted in Fig. 5.3.14 (c). This suggests the possible influence of the stress concentration due to the surface roughness caused by shot impingement.

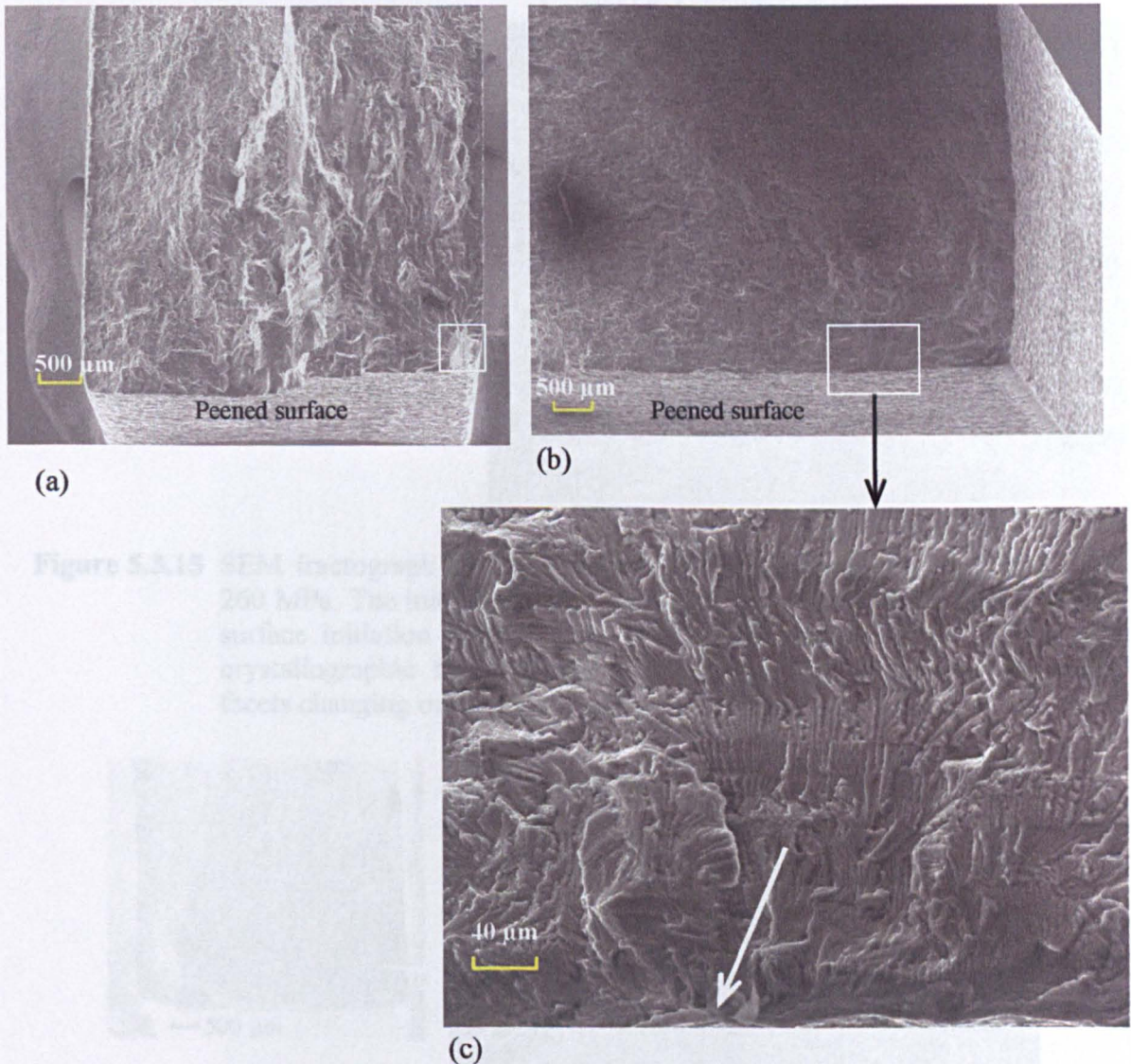


Figure 5.3.14 SEM fractograph for AA 2024-T351 peened to optimum conditions showing initiation sites (indicated by the square frames) at stress levels: (a) $\sigma_{\text{max.}} = 270$ MPa, and (b) $\sigma_{\text{max.}} = 300$ MPa respectively. The magnified picture (c) for the $\sigma_{\text{max.}} = 300$ MPa shows the initiation site right below a peening indentation as indicated by the white arrow.

Figure 5.3.16 Subsurface crack initiation site for an AA 7150-T651 peened in worst condition. The applied stress was 255 MPa.

5.3.4.2 AA 7150-T651

Similarly to results as for AA 2024-T351, surface initiation sites were exhibited by the AA 7150-T651 unpeened specimens as shown by the specimen tested at $\sigma_{\max.} = 260$ MPa. Figure 5.3.15 shows the location of the initiation site on the fractured sample. As for AA 2024, subsurface initiation was also observed in the AA 7150-T651 peened specimens, as shown in Figs. 5.3.16 and 5.3.17.

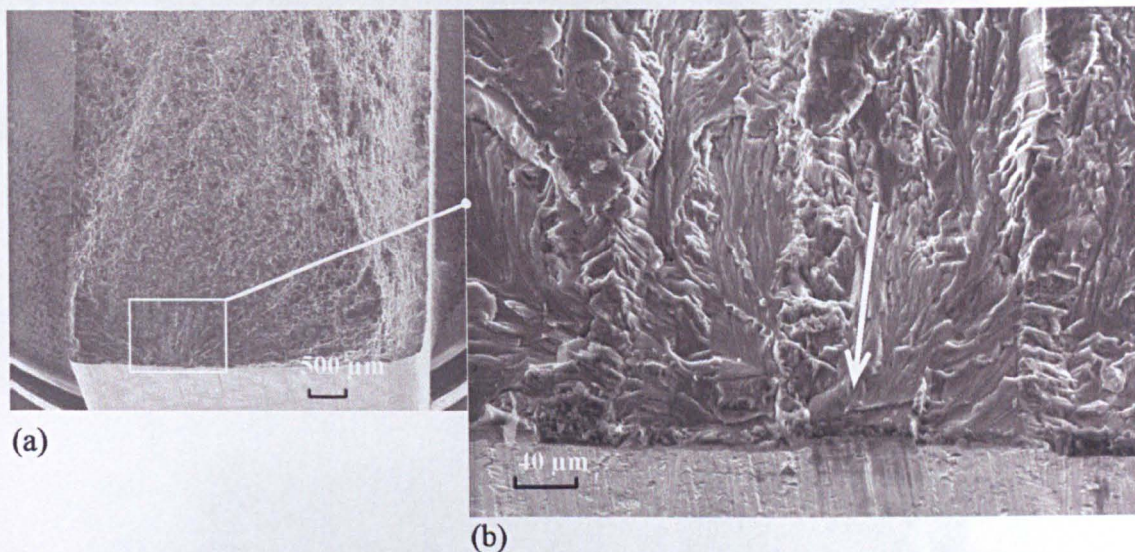


Figure 5.3.15 SEM fractograph of the AA 7150-T651 unpeened specimen at $\sigma_{\max.} = 260$ MPa. The initiation site is framed in (a). A magnified picture of the surface initiation is shown in (b). This fractograph shows the typical crystallographic facet growth of the Stage I crack propagation with facets changing orientation from grain to grain.

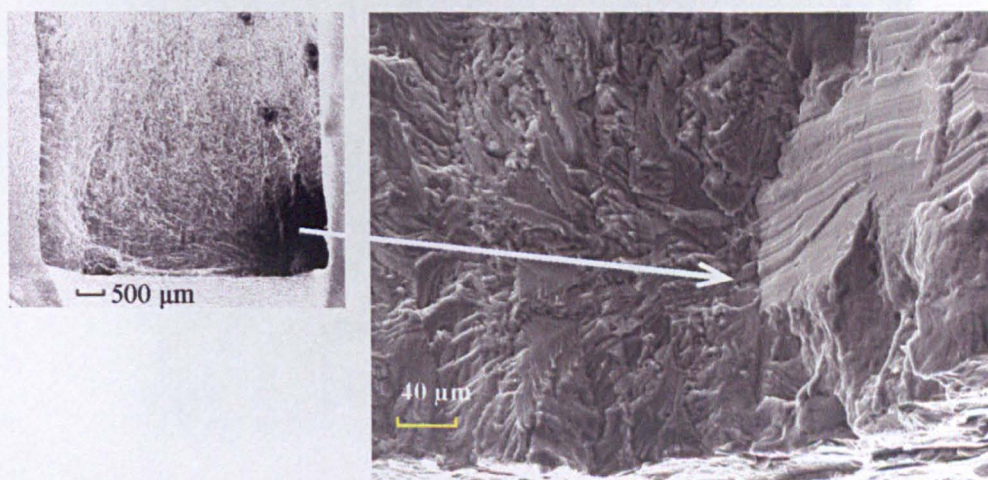


Figure 5.3.16 Subsurface crack initiation site for an AA 7150-T651 peened to worst condition. The applied stress was 255 MPa.

Fig. 5.3.18 shows clearly the influence of the peening effects (RS, hr) on the crack

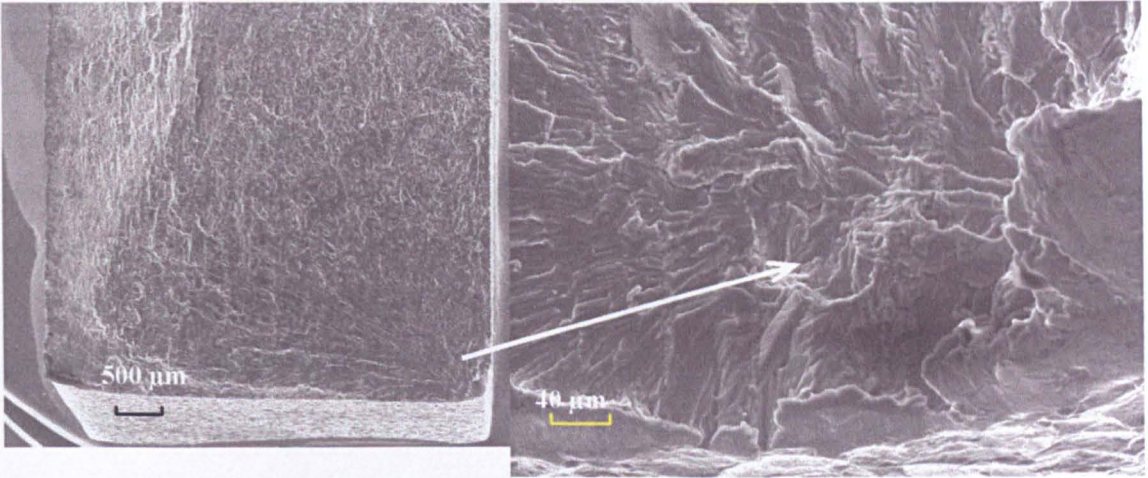


Figure 5.3.17 Subsurface crack initiation site for an AA 7150-T651 peened to worst condition. The applied stress was 300 MPa.

Subsurface initiation was also seen to take place in AA 7150-T651 peened to optimum condition tested at $\sigma_{\max} = 240$ MPa as shown in Fig. 5.3.18.

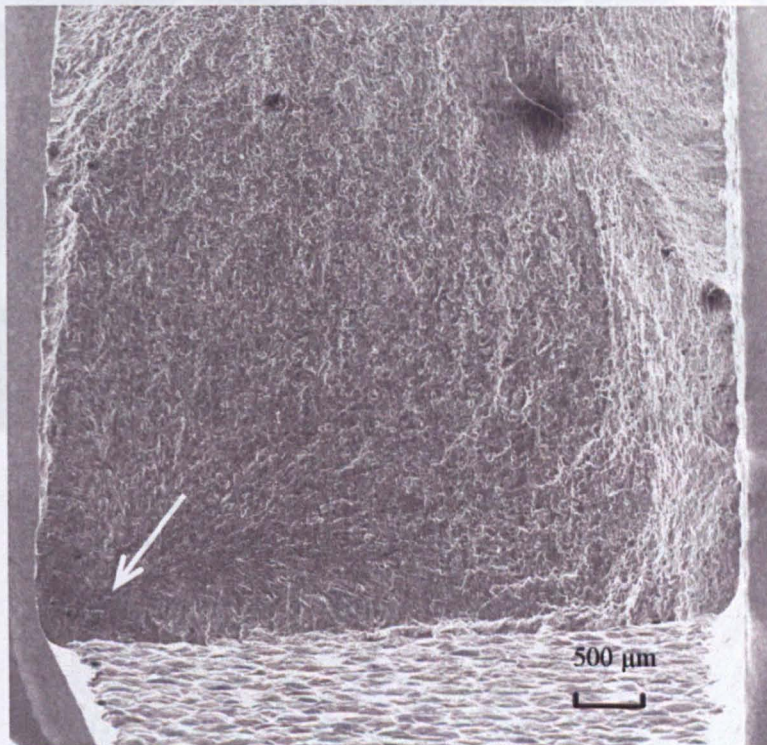


Figure 5.3.18 Subsurface crack initiation site indicated by the white arrow for an AA 7150-T651 peened to optimum condition tested at $\sigma_{\max} = 240$ MPa.

Fig. 5.3.18 shows clearly the influence of the peening effects (RS, Hv) on the location of the initiation site. The distance from the peened surface to the position of the initiation site agrees with the transition between the compressive and tensile RS and the end of the work hardened layer. Although suppression of surface initiation by peening delays crack initiation and early growth, the crack propagates later at a rate equal to the unpeened condition as shown in plots 5.3.5 (c), 5.3.9 (c) and by measurements of striation spacing. Striations are shown in Fig. 5.3.19. Crack coalescence from secondary cracks may be another characteristic associated with the rapid growth of the crack once it nucleated.

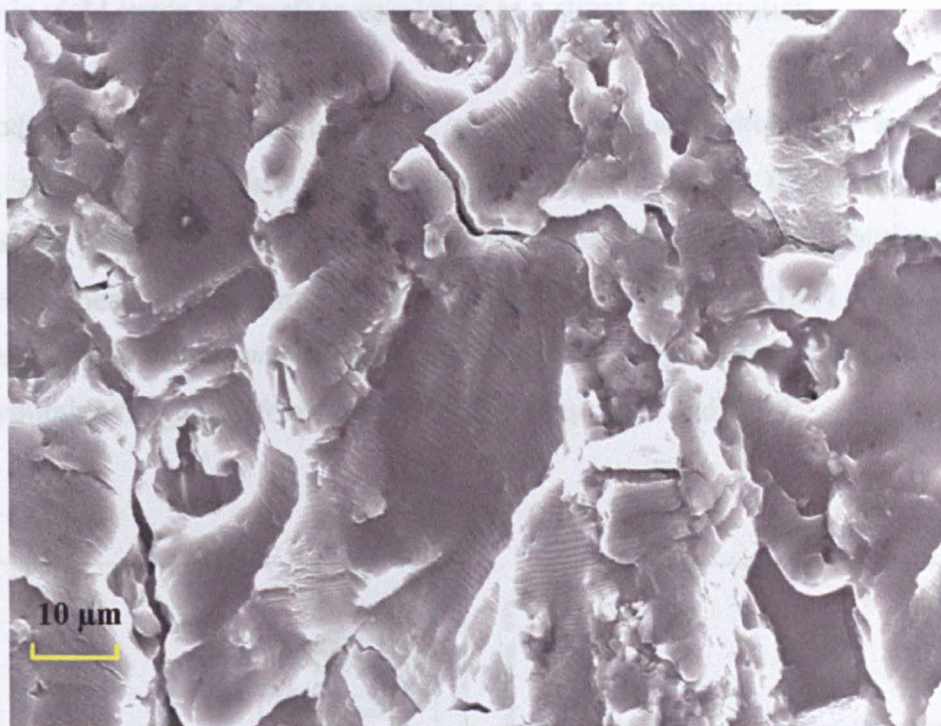


Figure 5.3.19 Stage II region with characteristic formation of striations in an AA 7150-T651 peened to optimum condition and tested at $\sigma_{\max.} = 240$ MPa.

5.3.5 Application of the Navarro-de los Rios Model to fatigue results

Experimental evidence already presented showed that the fatigue cracks propagated in the earlier stages in a crystallographic fashion. It was also shown that the changes to the material within the peened depth are comprised primarily of the development of a compressive residual stress, surface roughening and a distortion of the grain structure in the near-surface region. All these factors suggest that a suitable adaptation of the fatigue crack growth Navarro-de los Rios model would be applicable for the present case. The compressive residual stress is incorporated as a closure stress, the distortion as a local increase in yield stress and surface roughness as a stress concentration.

This model incorporates variables such as microstructure, initial flaw size, residual stresses, surface topography, work hardened layer, etc. within the system equations described in §3.2. Thus, the calculated closure and flow stress distributions for the peened specimens to optimum and worst conditions of the 2024-T351 and 7150-T351 AA's respectively are shown in Fig. 5.3.20 and 5.3.21. These conditions exhibited the most favourable fatigue performance as seen in Figs. 5.3.1 and 5.3.2.

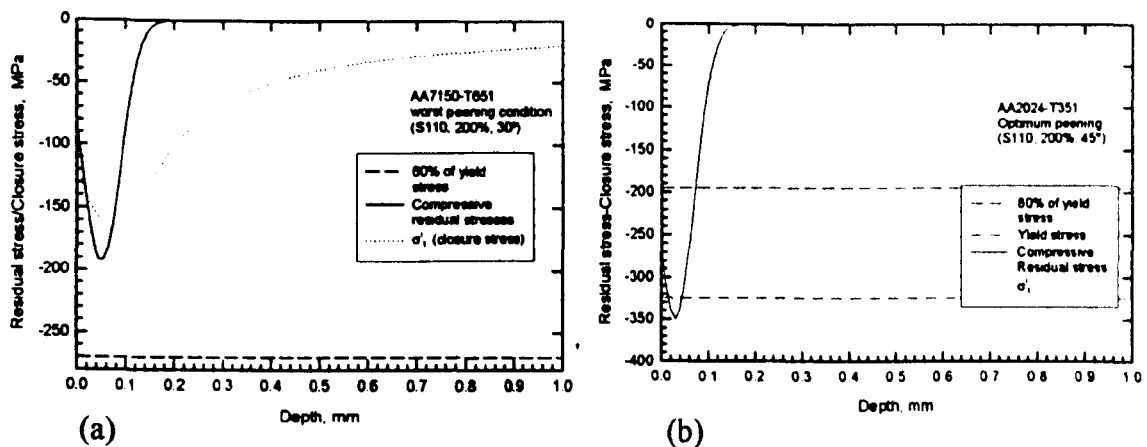
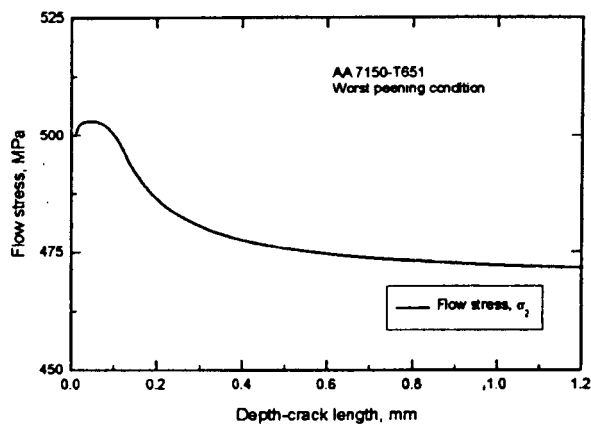
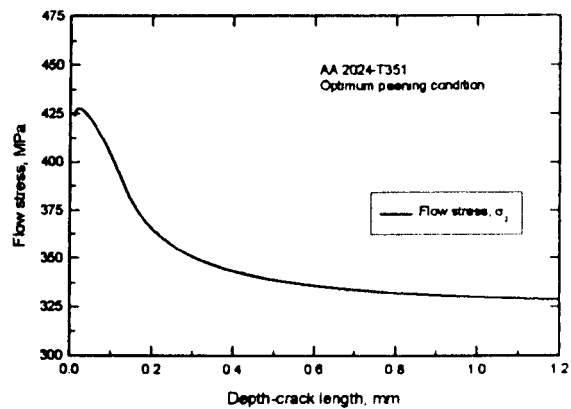


Figure 5.3.20 Closure stress distributions for the peened AA's determined by using the equations described in §3.2.1. The grain sizes utilised for calculations were those of 52.9 and 58 μm for the AA 2024-T351 and AA 7150-T651 respectively. RS data are listed in appendix VI-B.



(c)



(d)

Figure 5.3.21 Evolution of the flow stress for the peened AA's determined by using the equations described in §3.2.2. The grain sizes utilised for calculations were those of 52.9 and 58 μm for the AA 2024-T351 and AA 7150-T651 respectively. Hv data are listed in appendix VII for the validation results.

Variation in elastic stress concentration caused by the dimples on a peened surface is incorporated into the model as a function of the average width and depth of an impacted dent (aspect ratio). The equations and procedures for determining the surface Kt gradient were previously expressed in §3.2.3. In Figure 5.3.22 is depicted the decay in stress concentration as a function of the in-depth distance.

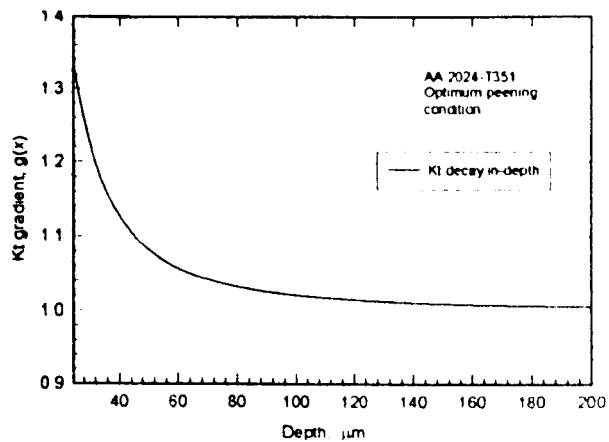
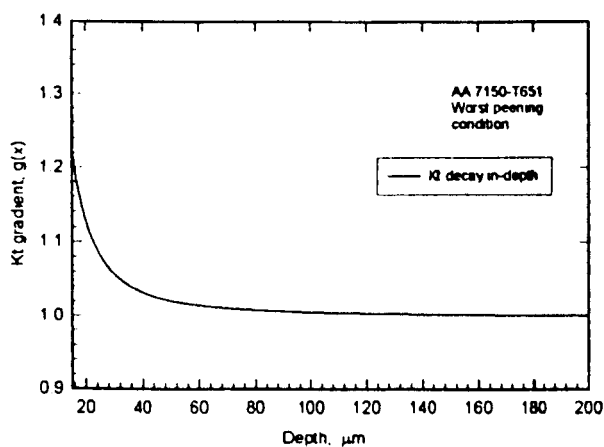


Figure 5.3.22 Elastic stress concentration gradient $g(x)$ for the peened 7150-T651 and 2024-T351 AA's to worst and optimum conditions respectively $R_{tm7150} = 14.94\mu\text{m}$ and $R_{tm2024} = 24.48\mu\text{m}$ from experimental measurements. $K_{t7150} = 1.228$ and $K_{t2024} = 1.34$ were calculated by using the equations described in §3.1.3.

Application of the equations and coefficients described in chapter 3, allows the calculation of the number of cycles to failure. The calculating procedure requires, however, a numerical solution in order to incorporate the closure, flow stresses and the stress concentration gradient to the equilibrium equation 2.13. Thus, a computer code¹, which incorporates the adapted micromechanical model, was employed for life determinations. Fig. 5.3.23 shows the estimates of cycles to failure together with experimental data. See appendix IX for input data and the computer code.

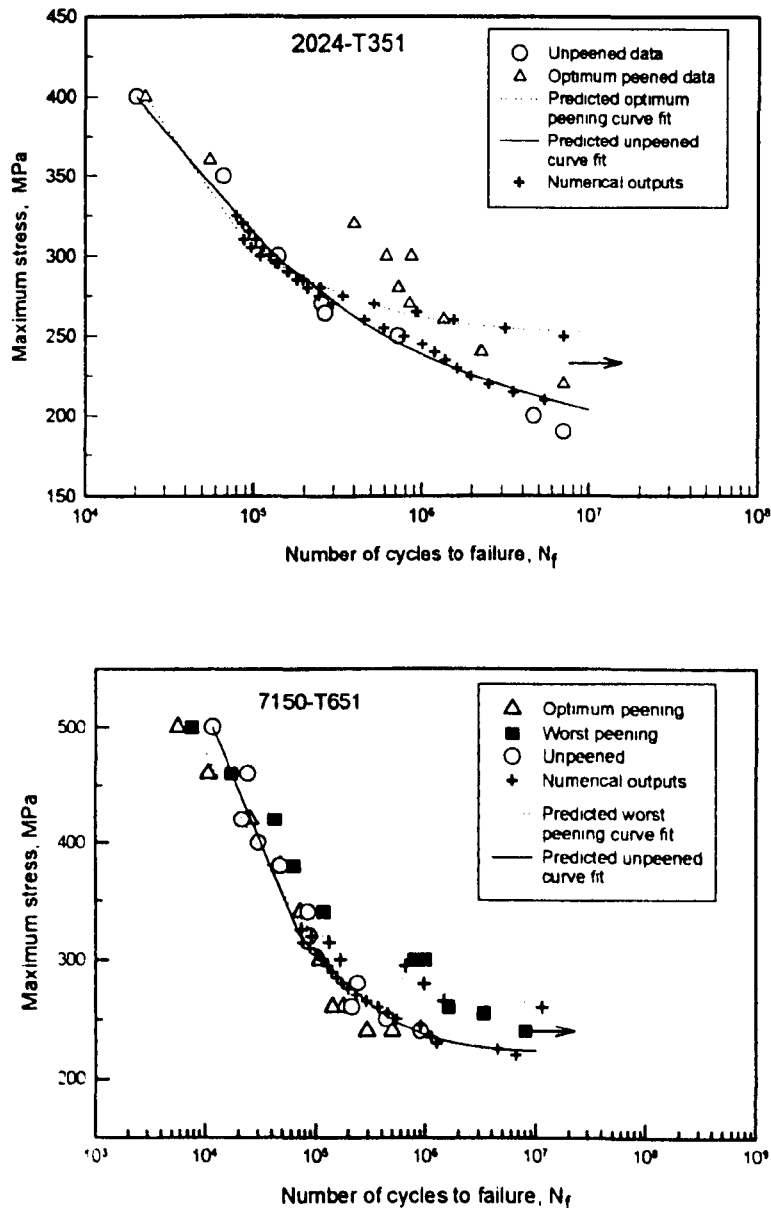


Figure 5.3.23 Fatigue life estimates by using the adapted Navarro-de los Rios model for the unpeened and peened specimens. Life predictions of peened specimens were undertaken exclusively for those exhibiting favourable results in terms of fatigue resistance.

¹ Code developed by M. Aramonov (a research visitor at the University of Sheffield)

Fig. 5.3.23 shows that the predicted values are consistent with the unpeened experimental data. There is some discrepancy though with the peened data of the AA 2024-T351. However, the predictions for the AA 7150-T651 were much better. This discrepancy between theoretical and experimental results for the AA 2024-T351 peened to optimum condition, seems to indicate that in practice the predicted benefits are not realised. The results shown in Fig. 5.3.23 for this AA, do not indicate, however, a detrimental peening effect on the fatigue performance. This latter observation will be further discussed in the next chapter.

Finally, predicted peened and unpeened lives in the range 325-500 MPa were found to be considerably low; below this stress level (high-cycle fatigue), reasonable trends were obtained compared to those of the experimental data. Therefore, stress levels above 325 MPa were not used in the calculations.

5.3.6 Summary

Based on a design of experiment method, the optimisation of the shot peening process in terms of the best combinations of surface roughness, compressive residual stresses and work hardening for fatigue resistance were quantitatively determined. Surface roughness considered as an elastic stress concentration (K_t), exhibited a dependency on the peen indent shape. Accordingly, the geometric characteristics of the shot, coverage and incidence angle were significant parameters for K_t . Compressive residual stresses (CRS) were measured by using the incremental hole drilling method and analytically determined using the incremental strain method. Comparisons with the integral method were given and discussed. CRS distributions revealed the expected strong influence of the shot size/type on the compressive residual stresses profile. Although, CRS distributions were found to be similar between both AA's, the depth to peak residual stresses was marginally higher in the AA 2024-T351 than AA 7150-T651. Higher microhardness (H_v) variations in the softer material were observed. Interestingly, faster decrease of hardening (softening) was observed in AA 2024-T351 compared to AA 7150-T651, i.e. larger plastified zones were found in the harder material. Larger hardness data scatter in AA 7150-T651 compared to the AA 2024-T351 was also

observed. This scatter was attributed to the large amount of microstructural defects observed under optical and scanning electron microscope observations.

Application of the design of experiments concepts established the major peening factors influencing each of the peening effects (RS, Hv, Kt) and allowed the estimation of the optimum combinations of such factors with their corresponding levels in order to attain the maximum CRS, Hv and minimum Kt. A balancing exercise of each of the peening effects lead to the optimum and worst conditions for fatigue resistance. These were, optimum: shot S110, 200% coverage and 45° incidence angle; worst: CCW20, 100% and 45° for AA 2024-T351. Optimum: S230, 100%, 89° and worst: S110, 200%, 30° for AA 7150-T651.

The fatigue testing results for the optimum and worst peening condition predicted for the AA 2024-T351 were found to give only marginal improvement in fatigue resistance. Although, however, the optimum condition was seen, overall, to give slightly better fatigue results, whilst the worst condition, although it did not improve life neither did it decrease. In contrast, the optimum condition in AA 7150-T651 was shown to give lower fatigue results even than the unpeened condition, whilst the worst peening condition gave the most favourable fatigue results.

Fatigue crack growth measurements were undertaken to examine further crack behaviour. Crack propagation rate was also determined, which clearly showed the influence of the peening effect in the early stages of crack growth. The study of the fracture surfaces indicated that early crack growth for all surface conditions occurred by stage I crystallographic, faceted growth. It proved difficult to ascertain the intrinsic nature of the initiation sites from fracture surface observations made in the SEM. Peened specimens exhibited subsurface initiation, whilst typical surface initiation was observed on the unpeened material, which relates to the influence of the peening in fatigue behaviour.

Peening effects were incorporated into the Navarro-de los Rios model. Fatigue life predictions showed relatively good agreement with the experimental results for peened specimens and better agreement for unpeened results.

CHAPTER 6

DISCUSSION

Controlled shot peening is a cold working treatment in which small balls (usually of cast steel but sometimes of ceramic glass, casting or cut steel wire) collide with the material surface to be treated at high speed. The particles plastically deform and indent the surface. Such inhomogeneous plastic deformation gave rise to: (i) roughening of the surface, (ii) an increase in the near surface of dislocation density (work hardening), and (iii) the development of compressive residual stresses (CRS) below the surface. The latter is beneficial to fatigue as it hinders the initiation of fatigue cracks and can slow down the propagation of small cracks because the CRS act as a crack closure stress on the crack flanks. However, propagation of cracks may be accelerated by virtue of the stress concentration effect (roughened surface). Strain hardening, in turn, will retard the propagation of cracks by increasing the resistance to crack tip plastic deformation.

It is clear that the performance of the peening process in terms of fatigue resistance depends on the competition between its beneficial and detrimental effects. Hence, the role of the effects of peening in conjunction with the interaction material-loading conditions has to be analysed and understood in order to achieve a favourable fatigue performance.

Based on the experimental results presented in chapter 5, a thorough interpretation of the effect of shot peening in the context of fatigue resistance, will be examined here. The discussion focuses on the beneficial and detrimental peening effects in connection

with fatigue damage. Particular attention is paid to the role of the peening modifications on the propagation and non-propagation of fatigue cracks.

6.1 BENEFICIAL EFFECTS

Overall, the compressive residual stress and microhardness distributions were influenced by shot intensity, shot type/size and the workpiece hardness, similarly to the observations made by Vöhringer [131], which were summarised in a rather simplified way in Fig. 6.1.3.

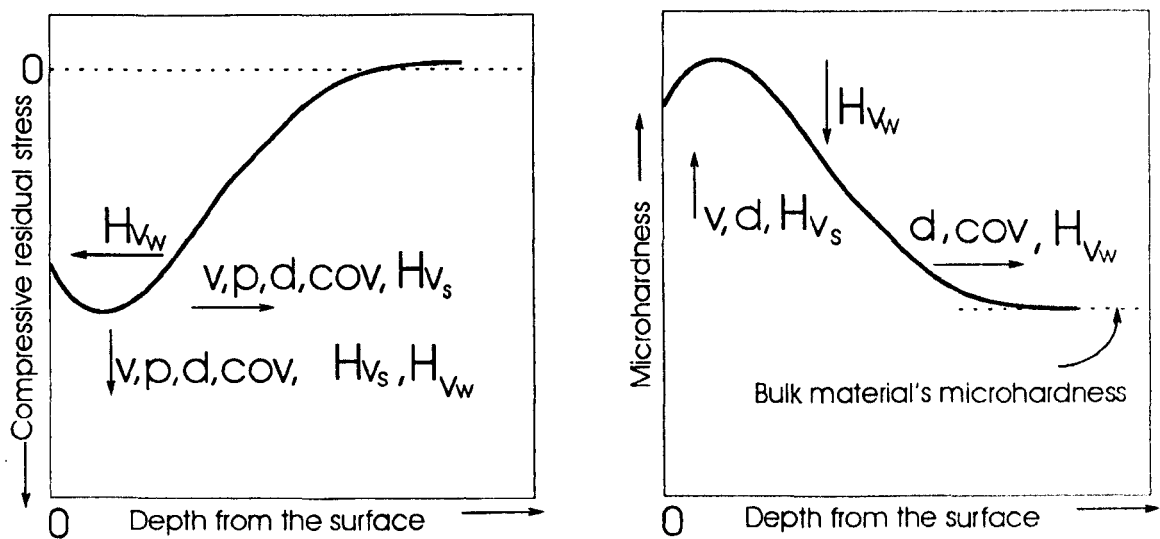


Figure 6.1.3 Peening parameters influencing the shape of the distribution in depth of the beneficial effects (compressive residual stress and microhardness), where v is the velocity of the shot, p is the applied pressure, d is the diameter of the peen, cov refers to percentage of coverage, Hv_s is the hardness of the shot and Hv_w relates to the workpiece hardness.

The curves in Fig. 6.1.3 are altered in the direction of the arrows with increasing magnitude of the peening parameters, i.e. when all the parameters increase, the maximum values of the residual stresses and the corresponding depth rise. However, increasing the workpiece hardness, the depth of the maximum residual stresses tends towards the surface.

In the following sections, a more thorough interpretation of the experimental results will be outlined by using theoretical concepts and comparison with those reported in the literature.

6.1.1 Residual stresses

The typical distribution of CRS was found to attain a maximum approximately between 30-100 μm near the surface and to extend to 100-400 μm below the surface, converging gradually towards zero stress at that depth. The variation in residual stress distribution observed can be explained considering that its development depends upon the plastic deformation of the surface during shot peening. Since the plastically deformed surface layer tends to expand, but is restrained by the adjacent undeformed substrate, it is stressed by compression. In this respect, Wohlfahrt [246] suggested a double mechanism for the formation of residual stresses because of shot peening. The first consists of plastic elongation of the upper surface layers of the material; such elongation would be caused by the tangential forces generated by multiple shot indentations as shown in Fig. 6.1.1 (b). This mechanism produces maximum plastic strain at the surface, which in turn results in a distribution of the CRS with the peak stress also remaining at the surface. The extent to which these stresses remain at the surface depends on the intensity of the plastic deformation.

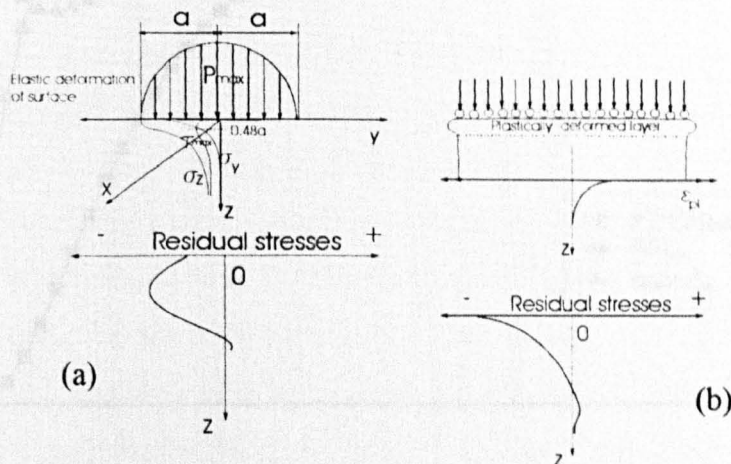


Figure 6.1.1 Schematic illustration of the formation mechanism of the residual stresses: Hertzian pressure (left) and stretching of the surface layer (right). After [246].

The second mechanism is related to the Hertz pressure (quasistatic penetration) exerted by the shot at the moment of the impact under the effect of forces normal to the surface of the material as indicated in Fig. 6.1.1 (a). If the Hertzian pressure reaches a

magnitude such that the maximum shear stress can exceed the flow stress below the surface at a depth of approximately $0.48a$, the resulting plastic deformation will generate compressive residual stress at this depth. Expressed differently, the elastic limit is first reached, at the above depth into the material, when the shear stress is maximum and $\approx 0.31p_0$, where $p_0 = \left(\frac{3P}{2\pi a^2}\right)$ P being the pressure exerted by the shot at the moment of collision. Again, the degree of plastic deformation at the depth where the shear stress is maximum, determines the maximum residual stress (see appendix X for further details).

The second mechanism for the generation of the residual stresses is graphically illustrated by plotting Equations <A.21> to <A.23> (included in appendix X) shown in Fig. 6.1.2. As stated above, the onset of plastic yielding for a normal indentation by a shot occurs at a depth of approximately $0.5a$ beneath the indented surface.

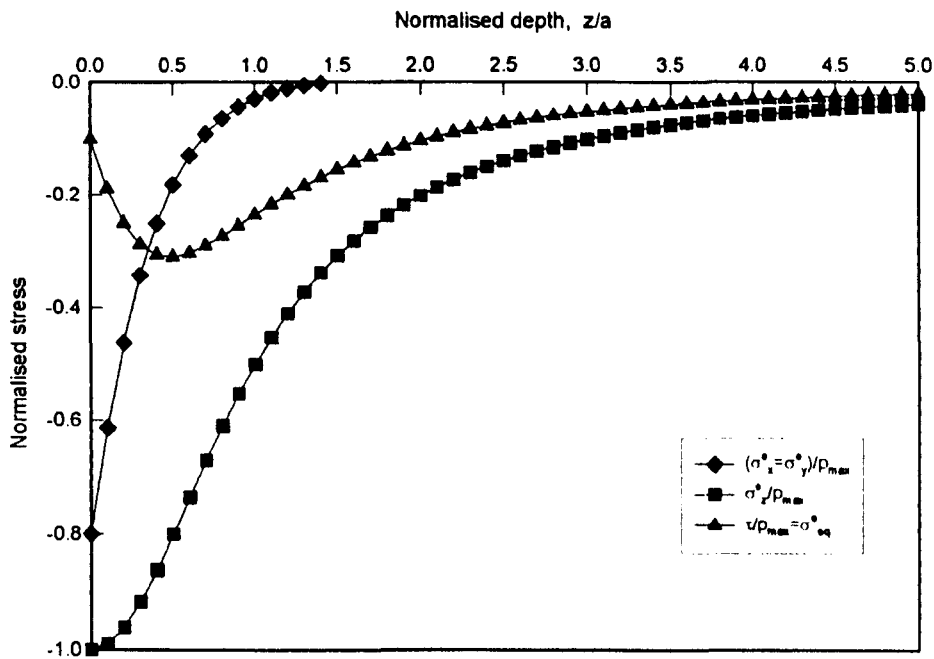


Figure 6.1.2 Static stresses occurring an elastic-perfect plastic material due to a spherical elastic indenter and with $\nu=0.3$.

Consideration of the observed CRS distributions presented in the previous chapter for the peened AAs, shows an overall Hertzian behaviour since locus of the maximum residual stress depths were found to be below the surface. In this sense, the marginal discrepancy exhibited by the two materials is due to the state of the equi-biaxial

compressive residual stress introduced, which will change according to the yield strength in compression of each material. Another possible contribution to the variation of the maximum CRS magnitudes is that found by some researchers [96, 131] in all materials, namely, a peening-induced adiabatic heat production, which is deemed to take place together with a rise in temperature. This effect is originated by the extremely short impact durations of the shot along with plastic deformation of various degrees, according to the hardness of the material. In soft materials, sufficient rise in temperature may produce plastic compression of the surface accompanied by a reduction of the CRS. Closer examination of estimated strain rates (see table 4.1.4) indicates that the shot S110 deforms plastically the surface at strain rates ranging from 6 to $9 \times 10^5 \text{ s}^{-1}$, i.e. higher strain rates, compared to the other shot. As pointed out in §2.2.2, the generated heat cannot diffuse and thus slip localization known as adiabatic shear bands may take place but simultaneously, this generated heat activates very fast moving dislocations, consistent with the fundamental equation of dislocation dynamics, expressed as [247]:

$$\dot{\epsilon} = \rho_D b \bar{v} \quad (6.1)$$

where $\dot{\epsilon}$ represents the strain rate, ρ_D is the dislocation density, b is the Burgers vector and \bar{v} the average dislocation velocity.

According to the observations made by Frost and Ashby [98], the fast moving of dislocations leads to high impact stresses; however, as the peening continues the workpiece becomes saturated due to a significantly high dislocation density, which leads to lower mean dislocation velocities and correspondingly lower impact stresses. However, relativistic effects limit the dislocation velocities at these strain rates. As the peening progresses, the material work hardens and subsequent impacts become more elastic in nature. These fundamentals may be the reason for the observed CRS distributions, particularly for the S110, which introduces high CRS very close to the surface, as shown in table 5.1.7.

Additionally, the difference in workpiece states before peening, specifically workpiece hardness is considered as one of the most important factors [246]. The magnitude of the maximum compressive residual stresses $\sigma_{\max}^{\text{rs}}$, increases with increasing hardness. The discernable difference is, however, marginal because of the stretching effects occurring during shot peening. In this case, the peening work hardening of the AA 2024-T351

leads to an increase in the residual stresses, which even exceeds the yield strength of the unpeened condition. In contrast, the higher hardness of the AA 7150-T351, means that the σ_{max}^{rs} also increases as the peening work hardening does, but the Hertzian pressure dominates by virtue of the observed deepest microhardness variations. Strictly speaking, with increasing workpiece hardness, depth and diameter of shot indentations become smaller as shown in table 6.1.1. The pressure due to the impact of the shot in conjunction with the maximum shear stress becomes higher. That is, with increasing hardness, less energy is consumed for plastic deformation of the surface peened layers, and more energy is available for plastic deformation in deeper layers [246]. Therefore, deeper deformation may occur in further layers and a higher maximum magnitude of CRS may be produced, as observed in most of the residual stress distributions for the AA 7150-T351 compared with those of the AA 2024-T351 (see appendix VI-B).

Shot type (D)	Angle	2024-T351			7150-T651		
		a, mm	2a/D	h, mm	a, mm	2a/D	h, mm
S110 (0.34 mm)	30°	0.126	0.74	0.056	0.122	0.72	0.052
	45	0.143	0.84	0.078	0.132	0.78	0.063
	90	0.151	0.89	0.092	0.149	0.88	0.088
SCCW20 (0.55)	30	0.190	0.69	0.076	0.186	0.68	0.072
	45	0.206	0.75	0.093	0.207	0.75	0.094
	90	0.213	0.77	0.101	0.208	0.76	0.095
S230 (0.72)	30	0.237	0.66	0.089	0.227	0.63	0.081
	45	0.248	0.69	0.099	0.233	0.65	0.086
	90	0.299	0.83	0.160	0.283	0.79	0.137
S330 (0.84)	30	0.344	0.82	0.179	0.316	0.75	0.143
	45	0.352	0.84	0.191	0.327	0.78	0.156
	90	0.37	0.88	0.221	0.36	0.86	0.204

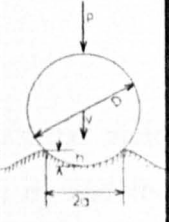


Table 6.1.1 Influence of the hardness of each alloy on the plastic deformation, defined in terms of the indentation radius (*a*) to the shot size (*D*) and its corresponding depth (*h*). This latter was calculated using Eq. <A.5> derived in appendix V. Peening conditions are listed in table 4.1.3. It should be noted that the indentation radius was measured after only one pass of the peening stream on particular coupons (designed exclusively for this purpose). The coverage in this case is less than 100% coverage.

6.1.2 Strain hardening

Shot peening introduces microstructural modifications [149], as seen in Fig. 5.1.12. A grain refinement or reduction of the grain size accompanied by multiple slip and pile-ups of dislocations is generally introduced by the intermittent shot impacts. Consequently, strain hardening either parabolic or linear [248] takes place modifying the material yield strength. This can be explained from the classical Hall-Petch assertion [249], which states that refining the grain size, d , of a polycrystalline metal, the yield strength will increase in a proportion such that:

$$\sigma_y = \sigma_0 + k_y d^{\frac{1}{2}} \quad (6.2)$$

where σ_y is the local yield stress after peening; σ_0 is the friction stress opposing the dislocation movement across the grains and includes the dislocation hardening component, and k_y is the slip band stress intensity necessary to transfer slip into and adjacent grain, accomplished by the activation of a dislocation source or by forcing a dislocation out from the grain boundary.

Based on the proportionality between hardness and yield strength, the local yield strength σ_{ly} is determined using the yield strength of the bulk material σ_y and the relative variation of the microhardness according to the following relationship [244].

$$\sigma_{ly} = \sigma_y \left(1 + \frac{\Delta H_v}{H_{v_{bulk}}} \right) \quad (6.3)$$

Hardness variations exhibited by the two AA's (listed in table 5.1.10), indicate the presence of a microstructural strain hardening effect due to an induced multiplication of dislocations caused by the inhomogeneous plastic deformation on the surface material, during shot peening. As anticipated, higher microhardness variations were found in the softer workpiece in relation to the harder workpiece. As mentioned previously for AA 7150-T351, in the shot peening of AA 2024-T351, the mechanism of plastic deformation seems to be analogous to that of stretching the surface layers. The fast moving of dislocations is related to the plastic deformations caused by collision of the

peens on the target surface, at strain rates sufficiently high. In this case, the majority of energy is consumed in the plastic deformation of the surface peened layers with less energy available for the movement of slip dislocations in deeper layers. Therefore, a more pronounced strain hardening near the surface exists, in accordance with the strain hardening behaviour of this AA. Stress concentration, rather arbitrarily used as an indicator of the plastic deformation occurring at the peened surface, shows that on average, slightly higher values of K_t are obtained for the AA 2024-T351 (see table 5.1.4).

6.2 DETRIMENTAL EFFECTS

SEM fractographs shown in Figs. 5.3.10 to 5.3.18 compare the sites of crack initiation. The induced CRS and work hardening by specific peening conditions (shot S110, 200% coverage, 45° incidence angle for AA 2024-T351, and S110, 200%, 30° for AA 7150-T351) certainly improved the fatigue limit of such AA's (see S-N curves in Figs. 5.3.1 and 5.3.2), but the effects of increasing the applied stresses above the fatigue limit are different. However, several similarities were observed:

1. The fatigue crack initiation sites of unpeened specimens are always located at the surface, whilst for different shot peened specimens, the sites of crack initiation are both, surface and subsurface, depending on the applied stress level.
2. Fatigue cracks initiated at the surface (Z_s) for peened specimens:
 - i) AA 2024-T351 = 300MPa
 - ii) AA 7150-T351 = 340MPa.
3. Fatigue cracks initiated at subsurface (Z_0)* for peened specimens:
 - i) AA 2024-T351 = 270 MPa ($Z_0 \approx 80\mu\text{m}$); 240MPa ($Z_0 \approx 180\mu\text{m}$)
 - ii) AA 7150-T351 = 300 MPa ($Z_0 \approx 130\mu\text{m}$); 255MPa ($Z_0 \approx 120\mu\text{m}$)

There is an apparent influence of the level of applied stress on the site of crack initiation for peened specimens, in short, the higher the applied stress the closer the crack

* Z_0 was measured from the closest surface edge.

initiation is to the surface. This behaviour has been largely reported both for ferrous and non-ferrous peened metals [136, 250-252]. The accepted explanation of surface crack initiation for shot peening treated materials is that cyclic deformation relaxes the surface residual stresses [253]. This adverse effect is known to readily take place in the low cyclic fatigue regime, where the magnitude of the applied stresses lies closely to or even above the yield strength of the cyclically loaded material. The magnitude of the plastic strain amplitude governs the extent of macro residual stress relaxation in fatigue-loaded materials, as concluded by Schulze, *et al.* [254]. Furthermore, concerning the evolution of CRS during fatigue, Schütz [4] observed that steel was much more stable than aluminium, which is consistent with the general assertion that the stability of CRS depends on the hardness of the material.

As a result, the magnitude of residual stress decreases when the applied fatigue stress increases. High tensile stresses are set up at stress concentration points, such as at the root of the indentations resulting from the peening treatment, or at any other irregularity existing immediately below the surface as illustrated in Fig. 5.3.14. Consequently, fatigue cracks are initiated and propagated as in surfaces without the beneficial effect of CRS. It is clear that the fatigue limit for surface initiation should be determined by the magnitudes of the surface residual stress and that of the stress concentration of the applied stress.

In subsurface initiation, the fatigue crack forms where the outer compressive stress field is balanced by the residual tensile stress field. The transition between the compressive and tensile residual stress fields and the depth of the plastically deformed layer roughly corresponds to the crack initiation sites. Cracks, however, may have also occurred due to inner defects (inclusions, pores, etc.), particularly in the AA 7150-T351, which showed a high level of microstructural defects as shown in Fig. 5.1.16 and 5.3.19.

Although crack origin is located below the surface, they soon break through the surface and become relatively larger cracks. Accordingly, the fatigue life of the subsurface crack becomes equal to that of a surface crack.

Some researchers like Wohlfahrt [155] have recognised that peening conditions for optimum fatigue strength should result from achieving a surface hardening as high as

possible, compressive residual stresses as large as possible and with a surface roughness as low as possible. Hence, selection of the optimum and worst conditions implemented in the fatigue stage were given in line with the above. From the overall fatigue results, the use of the finest shot did provide the best fatigue performance in both AA's. This suggests that both AA's are likely to be roughness-sensitive or surface damage-sensitive. The consistent degradation of fatigue life as peening media size increases may be due to one or more of these factors:

1. Broken or highly deformed media and embedded particles, which give rise to deeper surface penetration (table 6.1.1) and hence, more likely to cause crack nucleation by stress concentration.
2. Unevenness in the plastic deformation layer, 100% coverage with the finest shot is entirely impinged with some overlapping. Variations of the plastically deformed layer when peening with larger media size may be quantitatively greater than with smaller media (see Figs. 5.1.1 and 5.1.2).
3. The tendency of a larger media is to leave larger indentations and, thus, material around the indentation displaced a greater distance would indent to a greater depth and or induce impact extrusion of material parallel to the surface. It has been reported by many researchers [134, 138] that such surface damage known as peened surface extrusion folds (PSEF) or simply folds are responsible for acceleration of the crack nucleation by the stress concentration.

With the aim of further support for these theories, a sensitivity analysis was undertaken to assess the effect of surface degradation (in terms of the surface penetration, termed h in table 6.1.1) on the fatigue resistance by using the following peening conditions: (a) S110, 200%, 90°; (b) S330, 200%, 30°; (c) S330, 200%, 90°. Fatigue testing was done using a maximum stress of 300MPa under similar experimental conditions as in previous tests. The effect of increasing the penetration depth was found to be more detrimental on the fatigue resistance as seen in Figs. 6.1.3 (a) and (b). Similar findings were reported recently by Dörr *et al.* on peened aluminium and magnesium alloys [255]

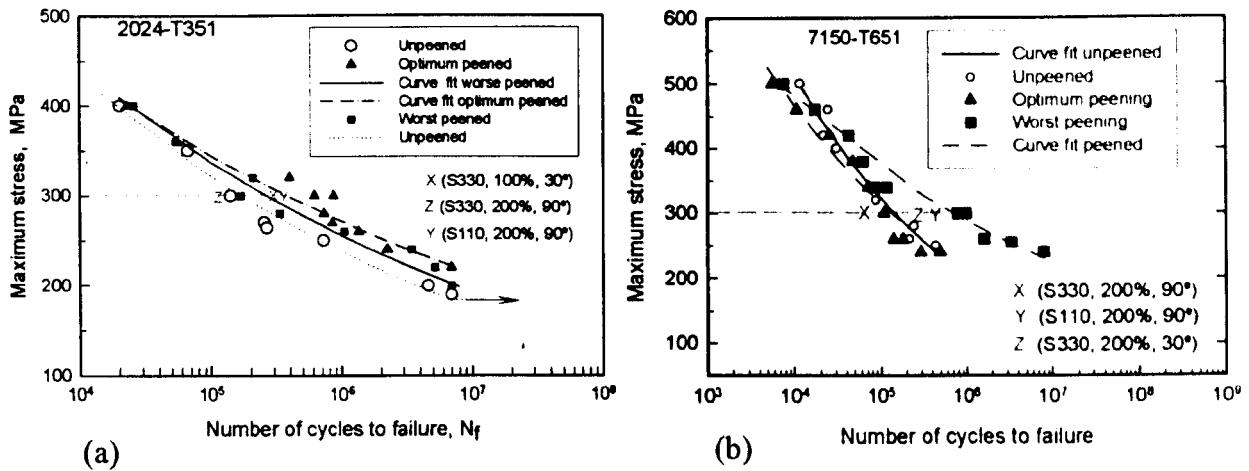


Figure 6.1.3 Effect of increasing the penetration depth on fatigue resistance.

6.2.1 Stress concentration analysis

It has been shown that the fatigue performance of peened AAs depends on the balance between its beneficial (compressive residual stress and work hardening) and detrimental effects (residual stress stability and surface degradation). For this reason, the interaction of the above effects with the microstructure has to be analysed in order to meet specific enhancements in the fatigue resistance.

6.2.1.1 Surface roughness effects under crack arrest conditions

It is well documented that the fatigue damage stages of initiation and propagation of short cracks are responsible for more than 70% of the fatigue life of a component [8]. As residual stresses, strain hardening and surface roughening will intrinsically affect the above stages, it is necessary to separate their role into propagation and non-propagation of a crack.

The micromechanical model described in §2.1.6.1, will be used in an attempt to clarify the effect of the surface stress concentration produced by the surface roughening.

In terms of the model, fatigue limit is defined as the maximum stress level below which a crack that spans over a distance between two successive microstructural barriers (inter-barrier spacing), such as grain boundaries, will not propagate (crack arrest) [69]. Specifically, crack arrest is attained when the following two boundary conditions are present: (1) the crack tip plastic zone is completely blocked by the barrier and (2) the crack driving force is unable to initiate slip beyond that barrier [69]. Cracks can be arrested even if they are longer than one inter-barrier distance, provided the above conditions are fulfilled.

Recalling the mathematical expression for crack arrest, previously given in §2.1.6.2:

$$\frac{m_i \sigma_{FL} - \sigma_1^i}{m_i \sqrt{a}} + \sigma_1^i = \sigma_{i \text{ arrest}} \quad (6.4)$$

where σ_1^i is the closure stress of a crack spanning over the i -th barrier, which is calculated by using Eq. (3.9). The grain orientation factor, $\frac{m_i}{m_1}$ as in Eq. (2.16). The fatigue damage map represented by the propagating and non-propagating regions for the peened AA 2024-T351 is illustrated in Fig.6.1.4.

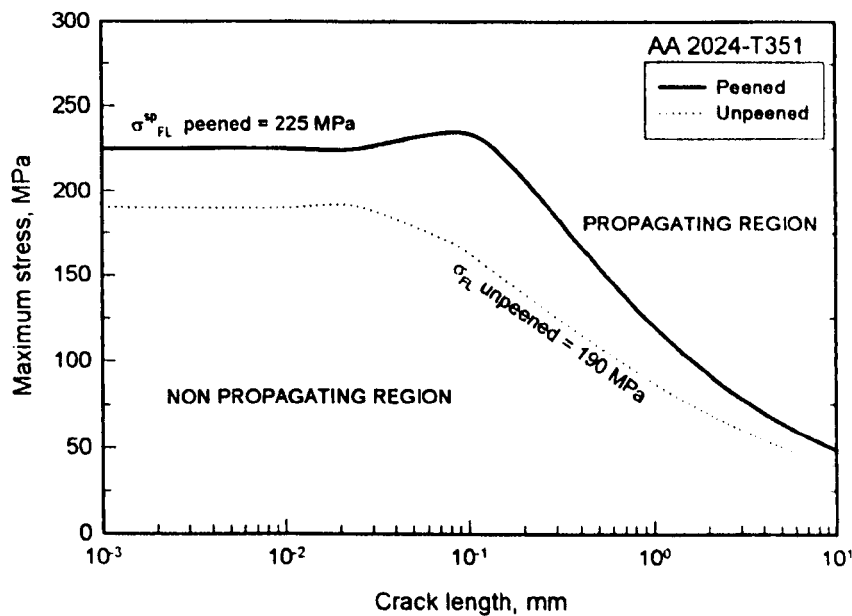


Figure 6.1.4 Comparison of the fatigue damage regions for the peened AA 2024-T351 to optimum conditions and the unpeened material. Plots were determined by using Eq. (6.4).

For $i=1$ and negligible crack closure, $\sigma_1^i=0$, Eq. (6.4) simplifies to the plain (unnotched) crack arrest as follows:

$$\sigma_{i \text{ arrest}}^P = \frac{m_1 \sigma_{FL}}{m_1 \sqrt{i}} \quad (6.5)$$

Considering the effect of the closure stress introduced by shot peening (SP), Eq. (6.4) should now read,

$$\sigma_{i \text{ arrest}}^{\text{Closure}} = \frac{m_1 \sigma_{FL}^{\text{SP}} - \sigma_1^i}{m_1 \sqrt{i}} + \sigma_1^i \quad (6.6)$$

where $\sigma_{FL}^{\text{SP}} = \sigma_{FL} + \sigma_1^i$. The parameter σ_{FL}^{SP} indicates that the fatigue limit will increase due to the closure stress. Thus, Eq. (6.6) gives,

$$\sigma_{i \text{ arrest}}^{\text{Closure}} = \frac{m_1 \sigma_{FL}}{m_1 \sqrt{i}} + \sigma_1^i \quad (6.7)$$

The effect of surface roughness considered as micro-notches (dents) is introduced utilising the Navarro & Vallellano's formulation [256], which provide a solution to a notch fatigue crack growing through the microstructure of the material. According to their work, the nominal stress in a notched member is given by,

$$\sigma_i^{\text{nom}} = \frac{\sigma^{\text{applied}}}{Z_i} \quad (6.8)$$

where σ^{applied} is the applied stress, σ_i^{nom} is the distribution of the nominal stress ahead of the notch root as a function of the distance from the notch i , mapped as $i=2a/D$, and Z_i is the fatigue notch factor given by,

$$Z_i = \frac{\sqrt{i}}{\bar{\alpha} + \beta} \left[\frac{\bar{\beta}}{\lambda_i} + \frac{\bar{\alpha}}{\sqrt{1 + \lambda_i^2}} \right]^2 \quad (6.9)$$

where $\lambda_i = \frac{1}{\alpha^2 - \beta^2} \left[\alpha \sqrt{(\alpha + iD/2)^2 - \alpha^2 + \beta^2} - \beta(\alpha + iD/2) \right]$ and $i=1,3,5,\dots$

The parameters $\bar{\alpha} = \frac{2\alpha}{D}$ and $\bar{\beta} = \frac{2\beta}{D}$ represent in a dimensionless form the notch depth α and the notch half width β . The parameter D represents the distance between two successive barriers. In the case where grain boundaries are considered as being the dominant barrier, D is regarded as the grain diameter.

The elastic stress concentration K_t introduced by multiple dents on a peened surface proposed by Li *et al.* [156], which being lower than that determined for a single notch of similar depth and width, reflects the uniformity of the micro-notches on the surface. Recalling from Eq. (3.12),

$$K_t = 1 + 2.1 \left(\frac{R_{tm}}{S_m} \right) \quad \left(\text{for } \frac{R_{tm}}{S} \leq 0.30 \right) \quad (6.10)$$

$$K_t = 1 + 4.0 \left(\frac{R_{tm}}{S_m} \right)^{1.3} \quad \left(\text{for } \frac{R_{tm}}{S} < 0.15 \right)$$

From the experimental results shown in table 5.1.4, all observed ratios R_{tm}/S were found to be higher than 0.15, therefore the resulting K_t is given by,

$$K_t = 1 + 2.1 \left(\frac{R_{tm}}{S_m} \right) \quad (6.11)$$

In the case of a semi-elliptical notch and a high degree of uniformity (>100% coverage), Eq. (6.11) can be written as,

$$K_t = 1 + 2.1 \left(\frac{\alpha}{2\beta} \right) \quad (6.12)$$

The bluntness of the notch can significantly affect the strain generated at the root of the notch and consequently the propagation rate of the crack. In the light of this, Smith and

Miller [257] proposed that $K_t = 1 + 2 \sqrt{\frac{\alpha}{\rho}}$, where ρ is the notch root radius. A semi-

elliptical notch radius can be approximated by $\rho = \frac{\gamma^2}{\alpha}$ and thus Eq. (6.12) can be

rewritten as,

$$K_t = 1 + 2 \left(\frac{\alpha}{\gamma} \right) \quad (6.13)$$

where γ is the notch half width that considers the bluntness of the notch. By equating Eq. (6.12) with Eq. (6.13), the effect of multiple micro-notches can be expressed in terms of a single notch by,

$$K_t = 1 + \left(\frac{\alpha}{\beta} \right) \quad (6.14)$$

According to Eq. (6.8), the effect of both the crack closure stress and surface roughness on the ability for a peened component to arrest cracks is given by,

$$\sigma_{i \text{ arrest}}^{\text{notch+closure}} = Z_i \sigma_{i \text{ arrest}}^{\text{closure}} \quad (6.15)$$

From Eq. (6.15), the boundary conditions that would enable the residual stress to compensate totally for the notch effect on the crack arrest capacity of the peened material is given by,

$$\sigma_{i \text{ arrest}}^{\text{Notched-SP}} = \left(\frac{m_i \sigma_{\text{Fl.}}^{\text{SP}} - \sigma_i^i}{m_i \sqrt{i}} + \sigma_i^i \right) Z_i \quad (6.16)$$

Application of Eq. (6.16) depicts the effect of roughness (notch) on the crack arrest capacity for a peened AA 2024-T351 under optimum conditions and AA 7150-T351 under worst conditions, as shown in Fig. 6.1.5 and 6.1.6 respectively.

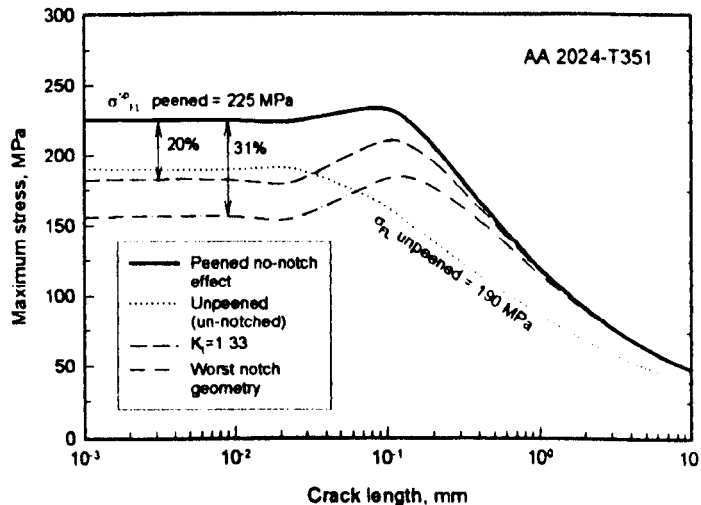


Figure 6.1.5 Effect of surface roughness on the crack arrest conditions for an AA 2024-T351 peened at predicted optimum conditions (S110, 200%, 45°). A value of $\alpha=25 \mu\text{m}$ was selected from the measured R_{tm} experimental validation data ($K_t=1.33$). The parameters for determining σ_i^i , are given in appendix VI-B. The fatigue limits for peened and unpeened material were determined experimentally (see Fig. 5.3.1). Also illustrated for comparisons the result of having the worst notch geometry, which is obtained when using values of $\alpha=78 \mu\text{m}$, $\beta=143 \mu\text{m}$ (corresponding to a 45° incidence angle according to predicted optimum peening conditions). The 20% and 31% are reductions on fatigue limit when compared to the predicted optimum conditions.

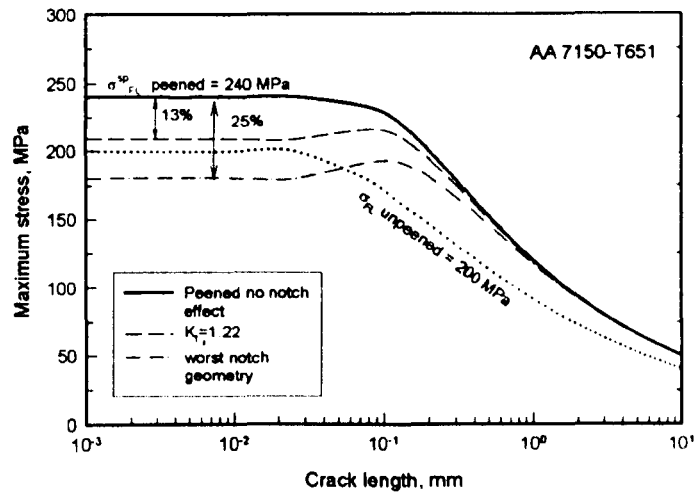


Figure 6.1.6 Effect of the surface roughness under crack arrest conditions at different K_t values for an AA 7150-T351 peened to S110, 200% cov., 30° angle. A value of $\alpha=15 \mu\text{m}$ was selected from the measured R_{tm} experimental validation data ($K_t=1.22$). The fatigue limits for peened and unpeened material were determined experimentally (see Fig. 5.3.2). Also illustrated for comparisons the result of having the worst notch geometry, which is obtained when using values of $\alpha=52 \mu\text{m}$, $\beta=122 \mu\text{m}$ (corresponding to a 30° incidence angle according to predicted optimum peening conditions). The 13% and 25% are reductions on fatigue limit when compared to the predicted worst conditions.

Examination under arrest conditions of the peened materials depicted in Figs. 6.1.5 and 6.1.6 revealed a discernable influence of the stress concentration on each peened material in relation to the stress required by a crack to overcome the i -th barrier in the notch zone. A more pronounced effect of K_t in the AA 2024-T351 compared with the AA 7150-T651 is predicted, as shown by the lower decrease in percentage terms of the peening arrest capacity when incorporating a notch effect. The crack arrest capacity for the peened AA 2024-T351 to optimum conditions decreases rapidly as K_t increases. Strictly speaking, for $\alpha=25\mu\text{m}$ and $\beta=75\mu\text{m}$, i.e. $K_t= 1.33$ (experimentally determined for AA 2024-T351, S110, 200%, 45°) no appreciable peening improvement is predicted, as the calculated inherent arrest capacity of the unpeened material is higher. Thus, the stress gradient associated with the dents at the first barrier (grain size) dominates over the closure stress effect. However, the stress gradient due to the notch will decrease with distance from the notch tip, and therefore, there will be a barrier further away which would either delay the growth of a crack or arrest it. This may be the reason for achieving a marginal fatigue improvement in the peened AA 2024-T351 when compared to the unpeened material, particularly at low fatigue applied stresses

With regard to the peened AA 7150-T351, the roughness effect on the arrest capacity is less prominent. The dent geometry of $\alpha=15\mu\text{m}$ and $\beta=68\mu\text{m}$, i.e. $K_t=1.22$ (experimentally determined for AA 2024-T351, S110, 200%, 30°) is more than compensated by the effect of the induced closure stress. This suggests the possibility of achieving an improvement in the fatigue performance of the peened material by virtue of the superior capacity for halting or delaying the propagation of cracks, including the severity of stress gradient induced by the surface roughness (notch-like effect). The size of a non-propagating crack will depend on the applied stress and the geometry of the dent [258].

These results support the previously reported experimental observations regarding the sensitivity analysis, namely, that the effect of increasing the penetration depth or varying the notch geometry was found to be detrimental to the fatigue resistance, as seen in Figs. 6.1.3 (a) and (b).

The strain hardening effect has been intentionally neglected because: a) the induced strain hardening developed by shot peening is usually overcome by the intrinsic hardening of cyclic harden materials, b) strain hardening is commonly limited to a depth close to the free surface and c) the above results are provided as a conservative analysis

6.3 ASSUMPTIONS AND LIMITATIONS

Although effort was made to undertake this research work with only few assumptions and simplifications, there were however some limitations, which need to be addressed.

- 1) Peening conditions used for the peened coupons and hourglass specimens of this investigation were determined by using design of experiments (DoE) concepts under two modalities: (i) Larger-the-better statistic both for the maximum compressive residual stress and for the work hardening effects, and (b) smaller-the-better statistic for the surface stress concentration. This selection was made in line with the general assumption that peening conditions for optimum fatigue strength should result from having a surface hardening as high as possible, a compressive residual stress as large as possible and with a surface roughness as low as possible. However, the significant influence that the geometry of the dents exert on the

fatigue resistance of the AAs was shown. In this respect, a more specific statistical method should be undertaken, which should consider among others, a shortest depth to the maximum compressive residual stress, highest local yield strength and depth of the plastified zone, and lowest surface penetration. To meet these requirements, at least 100% coverage needs to be achieved. In the present work, 50% coverage was used as one of the coverage levels within the designed experiment, which was believed to be the major contribution to the noise introduced when determined the peening effects, i.e. some anticipated tendencies were affected by the statistical variations induced by coverage less than 100%.

- 2) The designed experiment was accomplished using a fractional factorial approach, which accounts for merely 16 runs. Although the array is fully balanced, it proved difficult to correlate the peening factors and levels with the experimental results. For example, the correlation of the effect of stress concentration at 100% coverage and 30° incidence angle for all the shot types used simply could not be achieved because of lack of data, i.e. only one run provide this information. This obstacle can be surmounted by utilising the predictive model to estimate the missing data without loss of quality of the achieved results since the information used corresponds to a balanced design.
- 3) Four different type/sizes of shot media were used: cast steel (S110, S230 and S330) and conditioned cut wire steel (SCCW20). Owing to the discernable differences in the performance of each type of shot, e.g. shot velocity and the indentation shape, a separate study of each type of shot at different sizes would have been more appropriate. Due to budgetary constraints, it was not possible to consider assessing the peening effects of glass beads media.
- 4) Considerable variations were found in the size of the commercial cast steel shot media; whilst the nominal diameters for S110, S230 and S330 are respectively, 0.279, 0.584, 0.838 mm, the measured and averaged samples exhibited magnitudes of the order of 0.34, 0.72 and 0.84 mm. These were later used for calculations. In this respect, it was found that there is not a clear definition of the tolerances. Significant differences between specifications are reported. For example, whilst the dimensions of the S110 and S230 shots are consistent to MIL-S-13165C [82]

specification, these same magnitudes exceed the tolerances recommended by SAE-HS84 [87].

- 5) Because of the number of shot media tested and the levels used, only one intensity level was introduced for each of the shot media. Incorporation of two or three different intensities would have allowed comparisons to be made with regard to the penetration depth, since the pressure and flow rate would have varied. This is of great interest but also requires a considerably larger number of materials and more time.
- 6) It was assumed that surface cracks initiate at the highest local stress concentration. It is also known that failures very often originate at the most highly locally stressed tensile regions. Therefore, it was assumed that fatigue crack in peened samples initiate at the transition between the compressive and the balancing tensile stress field.
- 7) Residual strains were measured by using the incremental hole drilling method and the residual stresses were determined by using the incremental strain method. However, it is recognised that X-rays diffraction provides information that is more accurate not only for obtaining residual stresses at the surface and in-depth but also for determining the microstructural work hardening. Nevertheless, the former was used in view of its simplicity and the availability of equipment.
- 8) Simple specimen geometries were used: flat coupons and flat hourglass specimens. No cylindrical specimens, corners or bolt holes, were used since the sharpness of the edge may have a significant interaction with the shot peening conditions and would significantly affect fatigue life behaviour. This could be a task for future research.
- 9) Test conducted at 10-15 °C.
- 10) Some of the load-controlled fatigue tests were conducted at stress levels exceeding the yield stress of the material under uniaxial loading. Thus, those specimens yielded in tension.

- 11) Shot velocity data was estimated theoretically. Restrictions in availability of equipment impeded their experimental determination.
- 12) Grain size is an important microstructural factor for describing the effects of the peening process and its impact in the fatigue performance. Realistic estimations depend on the true grain size value. In the present investigation, an estimated average of grain size from limited observations was used. However, a vast number of observations involving statistic analysis are necessary for an accurate determination.
- 13) The fatigue limit of both unpeened and peened AAs, was determined from a limited number of specimens due to restrictions in the fatigue machine availability. This parameter plays an extremely important role in peened materials as it is related to the stress required to overcome the first significant microstructural barrier. A greater number of tests would be needed to accurately determine its true value

6.4 SUMMARY

As the quality of the peening process in terms of fatigue resistance depends on the competition between its beneficial and detrimental effects, the achievement of an optimum fatigue performance requires a comprehensive analysis of the factors controlling fatigue behaviour. The variation in the residual stress profiles observed was explained considering that its development on shot peened surfaces depends upon the plastic deformation of the surface during the shot peening. Two mechanisms were used to accomplish this task: 1) stretching of the surface layers and 2) the Hertzian pressure. Strain hardening or work hardening contribution was discussed in terms of the increased local yield strength undergone by the peened layers because of the changes in grain size, as described by the Hall-Petch relationship and of dislocation hardening. Surface roughness, deemed to be the detrimental effect, was discussed under crack arrest conditions derived from the N-R micromechanical model. It was clearly shown that the effect of the stress concentration induced by shot peening is considerably detrimental for AAs.

CHAPTER 7

CONCLUSIONS

The object of this study was to obtain the best fatigue performance of the shot peened 2024-T351 and 7150-T351 aluminium alloys from the application of optimised peening conditions, obtained through a systematic study using a designed experiment. The peening material modifications studied the work hardening, surface stress concentration (roughness) and compressive residual stresses. These represent the prime effects for fatigue resistance due to the shot peening process. Their interrelation is considered by means of a micromechanical fracture mechanics fatigue model. This model incorporates implicitly the peening material changes into the system equations. The residual stress is introduced as a crack closure stress (σ_1) increasing the resistance to crack opening, the work hardening as a resistance to the generation of crack tip plasticity (σ_2) and surface roughness as stress concentration factor. Fatigue life is calculated by integrating the crack propagation law from crack initiation to failure. Fatigue damage maps in the form of Kitagawa-Takahashi diagrams are drawn to establish the condition for crack arrest. In this respect, the degree of plastic deformation caused by shot impacts plays a crucial role in the fatigue life of a metallic component as it determines beneficial or detrimental effects. It is clear, that a balanced contribution between these competing mechanisms, together with the nature of the target material and the loading conditions, leads to enhanced fatigue performance.

Based upon the experimental and numerical results, the following conclusions can be drawn:

7.1 CONTROL PROCESS PARAMETERS

- Commercial cast steel shot was found to be fairly spherical with a significantly wide size distribution, whereas, conditioned cut wire has a closer size distribution but it is less spherical. Such shot variations affect considerably the stress concentration factor and coverage due to the geometry of the indentations.
- An equation of the form $H = \frac{A}{(t+b)^P} - \frac{A}{b^P}$ can satisfactorily be used to fit a curve for determining the saturation point and the Almen intensity curve.
- The Holdgate's theoretical model $C(t+\delta t) = 1 - [1 - C(t)] \left[1 - \frac{a}{S} \right]$ enables the prediction of the development of coverage with reasonable accuracy when compared to experimental measurements.
- The peening literature tends to lack rigor in reporting: i) clear definitions of the tolerances for shot sizes and type to be used, ii) intensity measurements.
- Since varied peening effects and fatigue responses can be obtained for the same intensity, it is not sufficient to characterise a peening condition indicating exclusively the value of intensity. A peening condition is completely defined by the shot (type/size), intensity, incidence angle, saturation, coverage and velocity. However, a satisfactory definition may only include shot, intensity, incidence angle and coverage, for peening to be consistently effective and reproducible
- Shot, intensity, incidence angle and coverage are independent of the peening machine used. From these, only shot type and incidence angle are controlled directly, the others are measured.
- The plethora of variables capable of altering the peening process, and hence fatigue life, is the reason that strict process control of all variables is necessary.

7.2 PEENING EFFECTS

- The shot peening process provokes plastic deformation of the surface layer. Consequently, the microstructure of deeper layers is modified by decreasing the grain size in the through thickness direction, promoting work hardening establishing a compressive residual stress and roughening the surface layer.
- The geometric features of the shot, percentage of coverage and incidence angle variations play a major role in the level of surface roughness in both aluminium alloys. Elastic stress concentration factor (K_t) was found to be largely influenced by the indentation shape and, to a lesser extent on shot size. Hence, conditioned cut wire produced the highest K_t in the cases investigated.
- Shot and incidence angle factors strongly influence the distribution of the compressive residual stress distributions (CRS). No appreciable difference in the magnitude of the maximum CRS values for both peened alloys was observed. However, the depth where the maximum CRS occurs was shorter for the AA 7150-T651 than that of AA 2024-T351.
- The mechanism for the generation of the residual stresses in the peened AA 2024-T351 resembles a stretching of surface layers type, with peak compressive stresses that even exceed the yield strength, whilst a Hertzian type mechanism accounts for AA 7150-T651.
- Coverage and shot type were identified as largely influencing the profile of the microhardness exhibited by the two AA's, which was taken to indicate a microstructural strain hardening effect due to multiplication of dislocations caused by inhomogeneous plastic deformation on the surface material, during shot peening.
- A larger plastified zone is exhibited by the harder material, which agrees with the Hertzian mechanism of plastic deformation.

7.3 FATIGUE PERFORMANCE

- The AA 2024-T351 peened to predicted optimum conditions (S110, 200%, 45°) exhibited superior fatigue performance than that peened to predicted worst or unpeened conditions. In contrast, the AA 7150-T651 peened to predicted worst conditions (S110, 200%, 30°) achieved the best fatigue performance.
- The AA 2024-T351 peened to predicted optimum conditions exhibited a marginally longer fatigue life compared to the unpeened and peened to predicted worst conditions, particularly in the high cycle fatigue region. It was evident however, that peening did not deteriorate the fatigue performance of this alloy.
- The fatigue limit of the unpeened material is approximately 190 MPa, whilst those of peened to predicted worst and optimum conditions were 190 and 225 MPa respectively.
- Material hardness has a dramatic effect on the improvement of fatigue life generated by peening. The AA 7150-T651 peened to predicted worst conditions exhibited the best fatigue performance in the high cycle fatigue region. In contrast, predicted best peening conditions were detrimental to the fatigue performance of this material.
- The fatigue limit of the unpeened AA 7150-T651 material is approximately 200 MPa, whilst that of material peened to predicted worst condition is approximately 240 MPa.
- The fatigue crack initiation sites in unpeened specimens were always located at the surface, whilst for the peened specimens, the location of crack initiation sites are either, surface or subsurface, depending on the applied stress level. Residual stress relaxation would seem to be the main cause of surface crack initiation in the low cyclic fatigue region, where the stresses are equal or even above the yield strength of the cyclically loaded material. In the high cyclic fatigue region, the fatigue crack seems to initiate where the residual stresses change from compressive to tensile.
- The best fatigue performance in both AA's was achieved using the finest shot (S110). Surface integrity degradation precedes fatigue damage. The geometry of the indentation is a prime damage feature.

- It is feasible to assess fatigue damage of peened components in terms of microstructural fracture mechanics concepts, provided the elements which characterise the material state due to peening are taken into account. The above implies the inclusion of the compressive residual stresses, the work hardening and the stress concentration factor into the appropriate model, e.g., the N-R micromechanical model, to carry out damage and lifetime calculations.

CHAPTER 8

SUGGESTIONS FOR FUTURE WORK

Although the research presented here has improved the current understanding of the shot peening control parameters and their effects on the fatigue performance of aluminium alloys, additional work is needed in order to complete the investigations of the optimisation of the shot peening in terms of fatigue resistance. Further research topics to carry out are:

- i. Examination of the current military (MIL-S-13165C) and industry (SAE-HS84 and British Airbus, process specifications) shot peening specifications for the drafting of the adequate directives for the peening process and adequate control of the process variables.
- ii. Incorporation of two or three of the following factor levels: intensity, incidence angle and coverage (>100%) to assess the surface material changes and thus, to obtain optimum peening conditions in terms of the minimum depth to peak compressive residual stress and minimum surface penetration.
- iii. Further studies on the effect of peen velocity on the size of resultant individual indentations at different incidence angles. This would give further insight into the sensitivity of the surface penetration to variation of material properties.
- iv. Investigate the fatigue resistance that can be obtained using a duplex technique by comparing specimens that have been shot peened using the sequence of coarse plus fine shot and vice versa.

- v. It has been shown that the distribution of the residual stresses plays a crucial role into the beneficial effects of peening. For this reason, further determinations of the macro and micro residual stresses will provide a better understanding of the type of changes in the material state caused by the shot peening. The use of X-ray diffraction allows the determination of the macro residual stresses and half-width values of the X-ray interference lines, which enables the estimation of dislocation densities.
- vi. The overall efficiency of the peening process as a mean of increasing fatigue life has been shown to be highly dependent on the geometry of the peen indents. Eliminating the surface roughness to a certain extent would be of particular interest.
- vii. Investigation of the adverse effect of residual stress relaxation would provide desirable information to judge the effectiveness of the peening treatment.
- viii. More extensive investigation into the determination of fatigue limits both for the unpeened and peened materials should be undertaken.
- ix. SEM, TEM and X-ray profile analysis methods are essential to understand the nature of the microstructural mechanisms of hardening and softening.
- x. Shot peening seems to be more effective in materials subjected to bending and torsional loads, where stress gradients are involved and less favourable where the applied load is uniform through the section. An extensive investigation of the optimisation of the peening treatment under different load conditions in aluminium alloys would enable interesting comparisons to be made.

CHAPTER 9

RECOMMENDATIONS

Based on the information obtained throughout this study, the following recommendations are made for future shot peening-related studies on aluminium alloys:

9.1 GENERAL RECOMMENDATIONS

- The use of the smallest and more round shot provides the best fatigue performance in AA 2024-T351 and AA 7150-T651. Geometry of the indentation is related to a primary damage feature. Hence, peening media should be geometrically characterised for: size (diameter), shape (roundness), aspect ratio (major and minor lengths). Image analysis is recommended as it provides more accurate information to that obtained from sieving. Samples of as received shots should be randomly selected by repeat sub-division of a tray of shots until approximately 100 remain as a non-biased sample, in accordance with Airbus, U.K. specifications. A PC-based image analyser, software and an optical microscope are recommended for taking such measurements. Commercial cast steel shot have fairly spherical surfaces but also possess a significantly wide size distribution, whereas, conditioned cut wire was a narrower size distribution about its nominal value, however, its roundness values are worse than those of cast steel shot. Sieves are used for the separation of fractured or contaminated shot.

- Peening specifications to be consistently effective and reproducible should include: the shot (type/size), intensity, incidence angle, coverage.
- At the beginning of a peening test program, it is recommended that a new venturi nozzle of $\frac{1}{4}$ in. (6.35 mm) or $\frac{5}{16}$ in. (7.93 mm) diameter be used. Approximate intensities provided by the manufacturer of the peening machine commissioned to the University of Sheffield are given in appendix I, Fig. II-1.
- To provide a reasonable description of shot peening intensity, a minimum of a four point saturation curve should be used. A curve fit technique is proposed in appendix-I.
- Intensities should be between 3A (0.076mmA) and 12A (0.3048mmA), which are expected not to impose the fatigue resistance when using a S110 shot.
- Incidence angles between 45° and 30° do not deform excessively the material layers and do not produce sharp indentations. Peening at these angles produce also peaks of the compressive residual stress nearer to the surface.
- Measure of the indentation size of each peening condition used in the test program. This can be done using image analysis technique for measuring the major and minor lengths of the dimple and complemented with a profilometer for measuring the corresponding dimple's height. Indentation size is useful for determining theoretical velocity and coverage, and the plastic deformation; defined in terms of the indentation radius (a) the shot size (D) and its corresponding depth (h).
- Coverage should be at least 100% and up to 400% for avoiding detrimental effects in the fatigue resistance of the material caused by surface roughness or excessive plastic deformation. Coverage can be determined by using the method proposed in appendix-III.
- Microstructures, residual stress and hardness profiles, and surface roughness measurements for all peening conditions used in a test program should be obtained. This should be done on special coupons and the information saved for future reference.
- Residual stress profiles can be determined using the hole drill method. The integral method is proposed for calculating the residual stresses, particularly when strong stress gradients are present. Care must be paid as this method involves very accurate measurements of the relieved strains and depths for each incremental step, i.e. higher error sensitivity is prone to occur.

- It is recommended to also perform some X-ray diffraction residual stress measurements for comparison purposes.
- It is proposed that surface roughness measurements follow the practice of taking at least ten measurements made at any point and in any direction that is desired, so that the average value can be used to represent the roughness of the surface. The surface roughness can then be expected to have a standard deviation of about 10%.
- Microhardness Vickers with a 50 grams force and a hold-down time of 10 seconds is recommended. It is suggested that indents should be made at depths of 30, 60, 90, 120, 150, 180 and 250 μm from the peened surface, with three indentations at each depth.
- Equation (6.15) offers quantitative capability for determining the effect of the surface roughness on the crack arrest capacity of the peened material.

9.2 PRACTICAL SHOT PEENING GUIDELINES FOR AA 2024-T351 AND AA 7150-T651.

- Shot type S110 stands for the best fatigue performance in both AAs by virtue of high peaks of residual stress and microhardness values at the near surface as long as coverage is greater than 100%. It also renders the lowest surface roughness with a shallow indentation depth, which is a crucial factor for fatigue improvements.
- The percentage of coverage for the AAs at saturation condition (Almen strip A) is as follows:

SHOT	Incidence angle	% COVERAGE AT SATURATION (ALMEN STRIP A)		Intensity at saturation (0.001" A)
		AA 2024-T351	AA 7150-T651	
S110 (recommended)	90	280	230	6
	45	250	230	4
	30	320	150	3
S230	90	280	250	15
	45	630	600	8
	30	500	420	6
S330	90	400	280	25
	45	170	150	14
	30	230	180	11
SCCW20	90	550	520	8
	45	600	490	6
	30	590	390	4

Pressure = 345 KPa (50 psi); standoff distance = 152.4mm (6 in.);
flow rate = 4.54 kg/min (10 pound/min).

- (iii) Incidence angles of less than 90° are more beneficial for achieving an improvement in fatigue resistance. It is recommended that an angle of less than 45° is used.
- (iv) The optimum and worst peening conditions predicted by design of experiments approach are as follows:

AA 7150-T651		AA 2024-T351	
Optimum	Worst	Optimum	Worst
S230,100%,89°	S110,200%,30°	S110, 200%, 45°	CW20,100%,45°

- (v) The optimum and worst peening conditions from fatigue experiments were as follows:

AA 7150-T651		AA 2024-T351	
Optimum	Worst	Optimum	Worst
S110,200%,30°	S230,100%,89°	S110, 200%, 45°	CW20,100%,45°

- (vi) The order of importance of the peening effects that largely contribute to the fatigue resistance of AAs is given as: (1) surface roughness (geometry of the indentation), (2) compressive residual stress field and (3) strain hardening.

- (vii) Overall benefits achieved in fatigue strength were as follows:

AA 2024-T351 = 18 %

AA 7150-T651 = 20 %

APPENDIX-I

GEOMETRIC FEATURES OF THE PEEN MEDIA

General guidelines for selection of the peen media (Military specification MIL-S-13165C)		
Material	Intensity ranges*	Peen media
Steels	12-25 A (0.31-0.64 mmA)	Steel cast and conditioned cut wire.
Aluminium alloys	4-14 A (0.10-0.36 mmA)	Steel cast , conditioned cut wire, ceramic and glass beads
Titanium alloys	6-12 A (0.15-0.31 mmA)	Steel cast , conditioned cut wire, ceramic and glass beads

*The exact magnitude of the intensity will depend on the component's thickness.

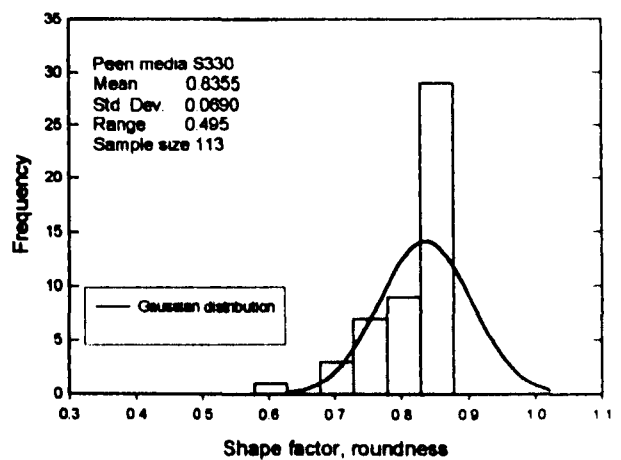
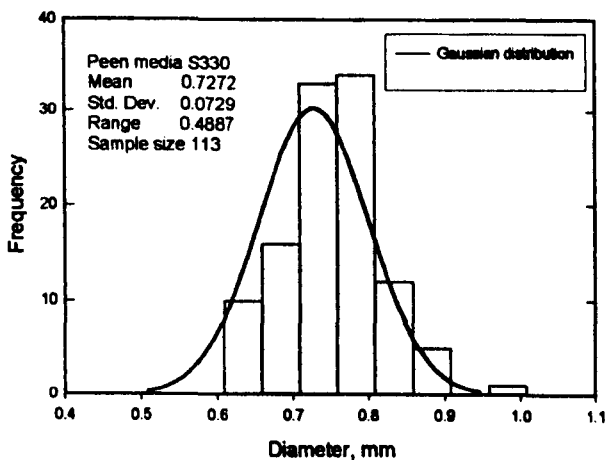


Table I-1 Distribution of the size and shape factor of the S330 shot type.

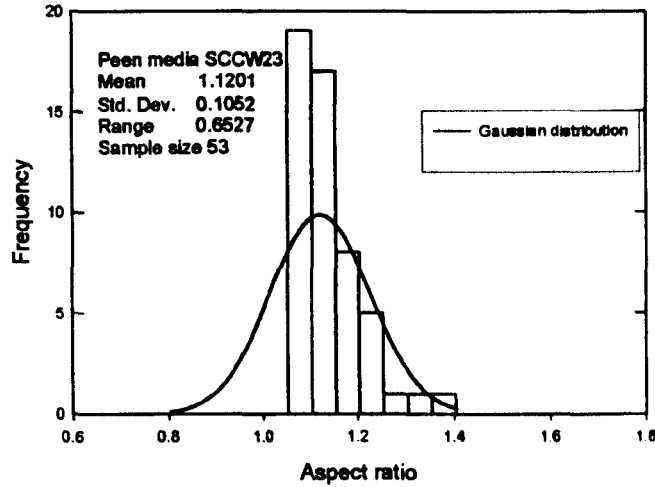
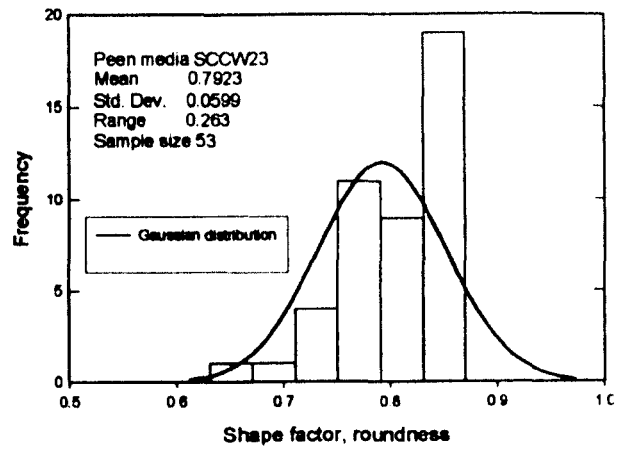
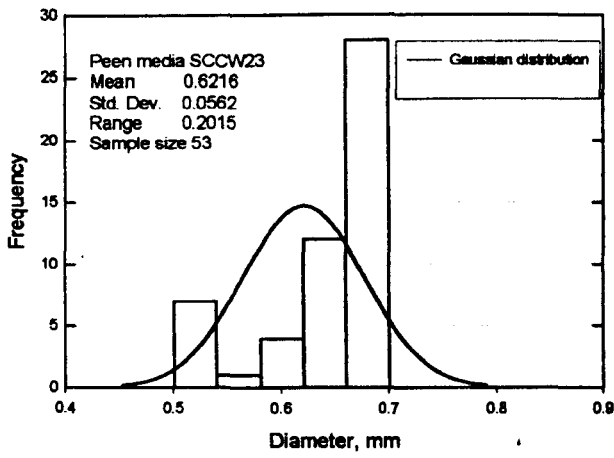


Table I-3 Distribution of the size, shape factor and aspect ratio of the SCCW 23 shot type.

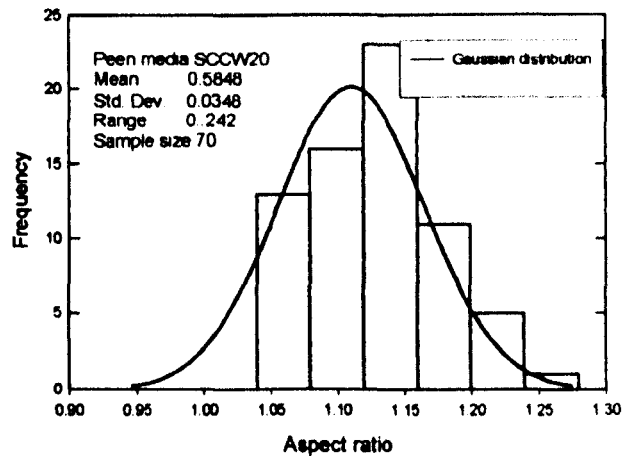
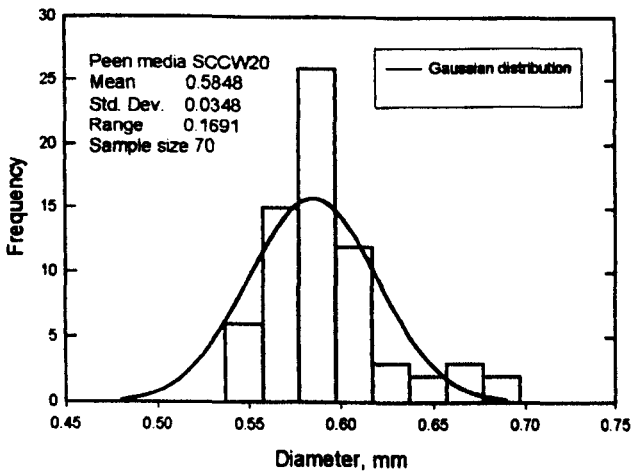


Table I-2 Distribution of the size and aspect ratio of the SCCW 20 shot type.

Distributions of the geometric features of the conditioned cut wire were found to differ from the expected circular shape (discussed in chapter 2, §2.2.3.1), whilst the statistical distribution of the size was acceptable.

APPENDIX-I

PEENING MACHINE PERFORMANCE

General Method for determining the intensity curve and saturation points (the curve fit & solution):

Note: MathCad ver. 7 (Copyright © 1986-2001 MathSoft Inc.) was used for the following numerical determinations

Sum the square of the differences i.e.

$$S := \sum_{i=1}^n \left[H_i - \left[\frac{A}{(\text{Time}_i + b)^P} - \frac{A}{b^P} \right] \right]^2$$

$$f(H, T) := H_i - \left[\frac{A}{(\text{Time}_i + b)^P} - \frac{A}{b^P} \right]$$

Partially differentiate with respect to each constant and equate to zero to achieve a minimum sum of differences.

$$\frac{\delta S}{\delta A} = -2 \cdot \sum_{i=1}^n \left[\frac{1}{(\text{T}_i + b)^P} - \frac{1}{b^P} \right] \cdot f(H, T) \quad (1)$$

$$\frac{\delta S}{\delta b} = -2 \cdot \sum_{i=1}^n \left[\frac{-A \cdot P}{(\text{T}_i + b)^{P+1}} + \frac{A \cdot P}{b^{P+1}} \right] \cdot f(H, T) \quad (2)$$

$$\frac{\delta S}{\delta P} = -2 \cdot \sum_{i=1}^n \left[\frac{-A \cdot \ln(\text{T}_i + b)}{(\text{T}_i + b)^P} + \frac{A \cdot \ln b}{b^P} \right] \cdot f(H, T) \quad (3)$$

This results in the following three equations;

$$A = \frac{\frac{1}{b^P} \cdot \sum_i H_i - \sum_i \left[\frac{H_i}{(\text{T}_i + b)^P} \right]}{\frac{2}{b^P} \sum_i \left[\frac{1}{(\text{T}_i + b)^P} \right] - \sum_i \left[\frac{1}{(\text{T}_i + b)^{2P}} \right] - \frac{n}{b^{2P}}} \quad (1)$$

$$-\sum_i \left[\frac{H_i}{(T_i+b)^{P+1}} \right] + A \cdot \sum_i \left[\frac{1}{(T_i+b)^{2P+1}} \right] - \frac{A}{b^P} \cdot \sum_i \left[\frac{1}{(T_i+b)^{P+1}} \right] + \frac{\sum_i H_i}{b^{P+1}} - \frac{A}{b^{P+1}} \cdot \sum_i \left[\frac{1}{(T_i+b)^P} \right] + \frac{A \cdot n}{b^{2P+1}} = 0 \quad (2)$$

$$-\sum_i \left[\frac{(H_i \cdot \ln(T_i+b))}{(T_i+b)^P} \right] + \sum_i \left[\frac{(\ln(T_i+b))}{(T_i+b)^{2P}} \right] - \frac{A}{b^P} \cdot \sum_i \left[\frac{(\ln(T_i+b))}{(T_i+b)} \right] + \left[\frac{\ln b \cdot \sum_i (H_i)}{b^P} \right] - \frac{A \cdot \ln b}{b^P} \cdot \sum_i \left[\frac{1}{(T_i+b)^P} \right] + \left(\frac{A \cdot \ln b \cdot n}{b^{2P}} \right) = 0 \quad (3)$$

Solution

The desired criteria considers that by doubling the exposure time ($Time_{sat}$) the measured arc height will increase by 10%, and is found as follows;

$$H_{sat} = \frac{A}{(T_{sat}+b)^P} - \frac{A}{b^P} \quad (4)$$

$$1.1 \cdot H_{sat} = \frac{A}{(2 \cdot T_{sat}+b)^P} - \frac{A}{b^P} \quad (5)$$

Therefore $1.1 \cdot A \cdot \left[\frac{1}{(T_{sat}+b)^P} - \frac{1}{b^P} \right] = A \cdot \left[\frac{1}{(2 \cdot T_{sat}+b)^P} - \frac{1}{b^P} \right]$

Therefore $\frac{1.1}{(T_{sat}+b)^P} - \frac{1}{(2 \cdot T_{sat}+b)^P} = \frac{1.1}{b^P} - \frac{1}{b^P}$

Therefore $\frac{1.1}{(T_{sat}+b)^P} - \frac{1}{(2 \cdot T_{sat}+b)^P} - \frac{1}{10 \cdot b^P} = 0 \quad (6)$

knowing b & P iterate to find $Time_{sat}$ and back substitute into 4 to find arc height.

NOZZLE PERFORMANCE - APPROXIMATE ONLY.							
PSIG at Nozzle	20	30	40	50	60	70	80
1/4" Nozzle.							
CFM with Shot.	29.1	37.6	45.8	54.2	62.2	70.7	78.8
"A" Strip S-070	0.006	0.009	0.011	0.012	0.014	0.014	0.015
"A" Strip S-110	0.006	0.009	0.011	0.013	0.014	0.015	0.016
"A" Strip S-170	0.010	0.014	0.016	0.018	0.020	0.021	0.021
"A" Strip S-230	0.012	0.016	0.019	0.021	0.023	0.024	0.025
"A" Strip S-330	0.014	0.018	0.022	0.024	0.026	0.026	0.027
"A" Strip S-390	0.014	0.019	0.023	0.025	0.027	0.028	0.029
Shot flow rate lb/min.	4.2	5.2	6.4	7.3	8.3	9.3	10.4
5/16" Nozzle.							
CFM with Shot.	43.9	56.5	69.4	81.7	95.0	106.9	119.5
"A" Strip S-070	0.007	0.010	0.012	0.014	0.015	0.016	0.017
"A" Strip S-110	0.007	0.010	0.013	0.015	0.017	0.018	0.018
"A" Strip S-170	0.011	0.018	0.021	0.022	0.024	0.024	0.025
"A" Strip S-230	0.016	0.020	0.023	0.026	0.027	0.028	0.028
"A" Strip S-330	0.017	0.022	0.026	0.028	0.030	0.031	0.032
"A" Strip S-390	0.018	0.024	0.027	0.030	0.032	0.033	0.034
Shot flow rate lb/min.	7.6	8.8	9.9	11.1	11.9	13.4	14.4
3/8" Nozzle.							
CFM with Shot.	58.0	70.0	82.0	109.0	127.0	142.0	158.5
"A" Strip S-070	0.006	0.009	0.011	0.012	0.011	0.014	0.015
"A" Strip S-110	0.006	0.009	0.011	0.013	0.014	0.015	0.016
"A" Strip S-170	0.010	0.014	0.016	0.018	0.020	0.021	0.021
"A" Strip S-230	0.012	0.016	0.019	0.021	0.023	0.024	0.025
"A" Strip S-330	0.014	0.018	0.022	0.024	0.026	0.026	0.027
"A" Strip S-390	0.014	0.019	0.023	0.025	0.027	0.028	0.029
Shot flow rate lb/min.	10.0	11.5	13.1	14.3	15.3	17.0	18.2
1/2" Nozzle.							
CFM with Shot.	87.0	111.0	138.5	165.0	192.0	212.5	238.0
"A" Strip S-070	0.006	0.009	0.011	0.012	0.014	0.014	0.015
"A" Strip S-110	0.006	0.009	0.011	0.013	0.014	0.015	0.016
"A" Strip S-170	0.010	0.011	0.016	0.018	0.020	0.021	0.021
"A" Strip S-230	0.012	0.016	0.019	0.021	0.023	0.024	0.025
"A" Strip S-330	0.011	0.018	0.022	0.024	0.026	0.026	0.027
"A" Strip S-390	0.014	0.019	0.023	0.025	0.027	0.028	0.029
Shot flow rate lb/min.	15.8	17.8	19.8	21.0	22.4	24.4	25.6

British Aerospace - CHESTER

figure 7

Figure II-1 Approximate figures provided by the manufacturer of the peening facility, in terms of the Almen intensities "A" that may be achieved when a venturi nozzle is used, for given pressure (psi), flow rate (lb/min) and shot size/type.

"A" ALMEN STRIP CHARACTERISTICS (ELECTRONICS INCORPORATED, USA)				
CHEMICAL ANALYSIS				
Carbon 0.71	Manganese 0.63	Phosphorus 0.007	Sulphur 0.004	Silicon 0.17
Chromium 0.16	Vanadium 0.01	Nickel 0.01	Aluminium 0.037	Molybdenum 0.01
MEETS THE REQUIREMENTS OF:				
MIL-S 13165C	SAE J442		SAE AMS2430L	
ELECTRONICS INCORPORATED GRADE : GRADE I Premium (9700451)				

Table II-1 Report of materials analysis/certification of compliance (April 27, 1998) of the "A" Almen strips used for measuring the intensity and saturation points.

% Vernier on the peening machine	Real time ¹ (sec)	Nozzle speed ²	Nozzle speed.	Time the nozzle spend to go over an Almen Strip (sec)	
		(mm/sec)	Tealgate ³	(76.2 mm long)	Tealgate
100	4	125	120	0.610	0.635
80	5	100	96	0.762	0.794
60	7	71	72	1.073	1.058
40	11	45	48	1.693	1.588
30	16	31	36	2.458	2.117
20	26	19	24	4.011	3.175
15	40	13	18	5.862	4.233
10	90	6	12	12.700	6.350

¹ Time the nozzle spend to complete a distance of 500 mm. This distance represents a complete run of the nozzle without stopping.
² Measured nozzle speed
³ Peening facility manufacturer

Table II-2 Velocity of the nozzle measured directly in the peening cabinet. The nozzle speeds provided by the manufacturer are also shown for comparison purposes.

When the nozzle speed is set at 71 mm/sec, it takes 1.073 seconds to go over an Almen strip of 76.2 mm long. This time was, therefore, adopted for a single pass. The latter implies that the peening time recorded in seconds is equivalent to the number of passes of the nozzle over the length of an Almen strip.

% Vernier	S330	S110	S230	S170	SCCW-20	SCCW-23
	lb/min					
100	-	-	39.25	-	-	-
90	19.5	26.5	-	17.2	-	16.8
80	17.25	20.5	-	15.4	15.3	13.4
75	-	-	-	-	-	10.0
70	14.5	14.0	-	10.0	10.0	8.8
60	11.0	10.0	11.5	7.6	7.8	5.7
55	*	-	10.0	-	5.3	-
50	5	8	5.6	5.5	-	-
45		5	3.7	-	-	-
40	-	6	-	-	-	-

* It was not possible to attain 10 lb/min flow rate. A flow rate of 11 lb/min was used instead.

Table II-3 Calibrated flow rates with different types of shot.

Calibration of the flow rate was done following the manufacturer's recommendations.

APPENDIX-III

COVERAGE DETERMINATIONS

1 AREA OF THE SHOT SPREAD

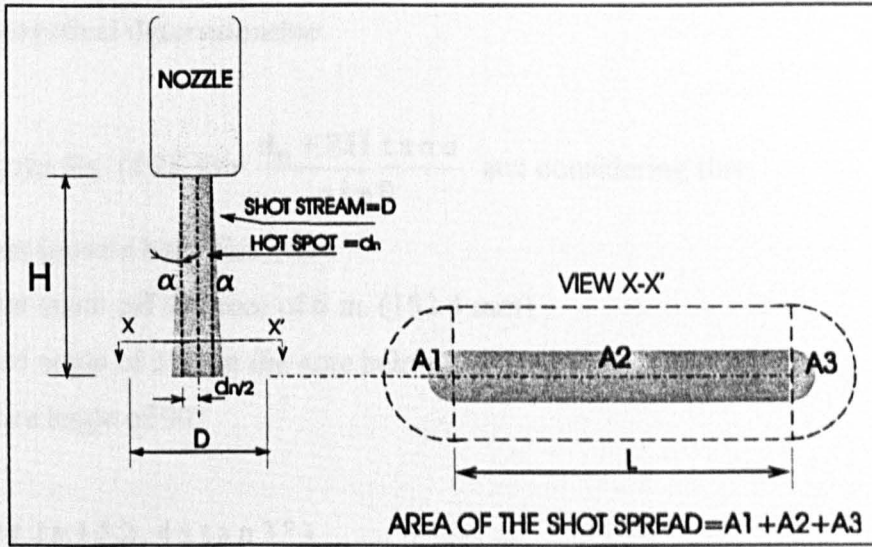


Figure III-1 Schematic of the shot stream's basic geometry.

The shot spread area common to any peening condition is calculated as follows:

$$A = (A_1 + A_3) + A_2$$

D = width of the shot spread.

L = length of the shot spread after 1 second.

$$= 2 \left(\frac{1}{2} \frac{\pi D^2}{4} \right) + (DL) = \frac{\pi D^2}{4} + DL$$

<A.1>

(a) Experimental determination

For this particular case, coverage development is determined by using the following data:

Material: 2024-T351 AA

Shot type: S230

Incidence angle: 90°

The peening process parameters were as the selected in table 4.1.3.

A shot spread of $D=21$ mm was measured when using a nozzle velocity of 125 mm/s.

The total shot spread area is given as:

$$L = (125 \text{ mm/s})(1 \text{ sec}) = 125 \text{ mm}$$

$$\therefore A = 2.971 \times 10^{-3} \text{ m}^2, \text{ by using Eq. <A.1>}$$

(b) Theoretical determination

Employing the Eq. (4.2) $D = \frac{d_n + 2H \tan \alpha}{\sin \theta}$ and considering that:

$d_n = 6.4$ mm (nozzle bore diameter)

$H =$ constant stand-off distance of 6 in. (152.4 mm)

$\alpha =$ diverged angle of 3° (see the note below)

$\theta =$ incidence angle of 90°

$$D = \frac{6.4 + (2 \times 152.4 \times \tan 3^\circ)}{\sin 90^\circ} = 22.37 \text{ mm}$$

$$A = \frac{\pi}{4} \times 22.37^2 + (22.37 \times 125) = 3.190 \times 10^{-3} \text{ m}^2$$

A comparison between the experimental and theoretical shot spread is given in table III-1.

Note:

It is well known that peening intensity varies as the reciprocal of the peened area, expressed differently,

intensity = $\frac{1}{A}$, where $A = \pi \left(\frac{d_n}{2} + H \cdot \tan \alpha \right)^2$, i.e. the larger the area, the lower the intensity. It is also

clear that for optimisation of the peening process an even intensity on the material's surface is fundamental in terms of the fatigue resistance. Bearing in mind the above and aiming to having a complete impinged surface for even intensity, the shot spread was adjusted to approximately the width of an Almen strip (19-20 mm) by varying H . The incidence angle was kept constant in $\theta = 90^\circ$. Experimental results in § 4.1.4.2 provided evidence that a standoff distance of 6 inches (152.4 mm) satisfied the recommended intensity for AA (6-16 A). Considering all these elements a value of $\alpha \approx 3^\circ$ (diverged angle) was found from Eq. 4.2. This shot spread allows for an effective intensity of about 40% (hot spot) and the rest of the shot stream will strike the surface less effectively.

Shot	Incidence Angle	Experimental D (mm)	Theoretical D(mm)	Experimental A (mm ²)	Theoretical A(mm ²)
S110	30°	28	44.8	4116	7176
	45°	24	31.6	3452	4734
	90°	20	22.4	2814	3194
SCCW20	30	40	44.8	6257	7176
	45	25	31.6	3616	4734
	90	20	22.4	2814	3194
S230	30	40	44.8	6257	7176
	45	28	31.6	4116	4734
	90	21	22.4	297	3194
S330	30	45	44.8	7215	7176
	45	32	31.6	4804	4734
	90	25	22.4	3616	3194

Table III-1 Shot spread area comparison between measured and calculated by using Eq. 4.2. It should be noted that theoretical values are shown exclusively as a reference magnitude since the target material, shot media and process variables are not embedded in Eq. 4.2.

2 COVERAGE PREDICTIONS

(a) The Avrami model

In § 2.2.3.5, the coverage concepts and models that characterise the development of coverage were discussed. Eq. (2.24) represents the well known Avrami model which can be expressed as:

$$C(t) = 100 \left\{ 1 - \exp \left(- \frac{3r^2 \dot{m} t}{4A \bar{r}^3 \rho} \right) \right\} \quad \langle A.1 \rangle$$

with the following known parameters (shot S230): The mass flow rate,

$$\dot{m} = 10 \frac{\text{lb}}{\text{min}} = 0.07576 \frac{\text{Kg}}{\text{s}}$$

The average shot radius, $\bar{r} = 0.3715 \times 10^{-3}$ m

The experimental indentation radius was: $r = 0.299 \times 10^{-3}$ m (see table III-2, below).

The shot density was taken as $\rho = 7860 \frac{\text{Kg}}{\text{m}^3}$, even though an experimental density of 7630 Kg/m^3 was found. There was not a significant difference in the results as will be seen below.

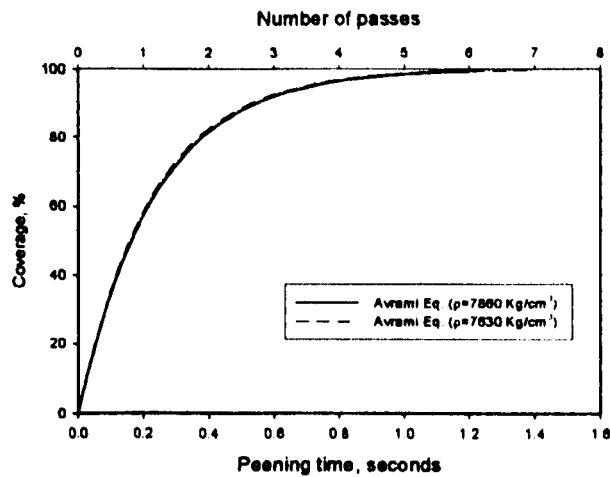
The experimentally measured shot spread area A , was used for calculations. This corresponded to a value of 2.971×10^{-3} , as determined previously.

Thus, substituting the above values into the Eq. <A.2>, it gives:

$$C(t) = 100 \left\{ 1 - \exp \left(- \frac{3 \left(0.299 \times 10^{-3} \right)^2 \times 0.07576 t}{4 \times 2.971 \times 10^{-3} \left(0.375 \times 10^{-3} \right)^3 7860} \right) \right\}$$

It reduces to $C(t) = 100 \{ 1 - \exp(-4.2427 t) \}$, which renders:

- 1st pass= $C(0.2s) = 57.2\%$
- 2nd pass= $C(0.4) = 81.7$
- 3rd pass= $C(0.6) = 92.2$
- 4th pass= $C(0.8) = 96.6$
- 5th pass= $C(1.0) = 98.6$



Figure

III-2 Coverage evolution by using the Avrami model and the experimentally determined parameters.

(b) The Holdgate model

Eq. (2.25) previously discussed in § 2.2.3.5, refers to the Holdgate's general model, in which a j^{th} number of peen sources are considered. However, our particular case is for a single peen source only. Thus, the Holdgate's model is given by:

$$C(t + \delta t) = 1 - [1 - C(t)] \left[1 - \frac{a}{S} \right] \quad \text{<A.2>}$$

under the assumptions: a) time taken for 1 pass = δt and b) at $t=0$, $C(t)=C(0)=0$

The ratio $\left(\frac{a}{S} \right)_{1 \text{ pass}} = \text{coverage ratio after 1}^{\text{st}} \text{ pass} = 0.543$ (experimentally determined)

The theoretical coverage assuming no peen overlapping was calculated as:

$$\begin{aligned} \text{Time taken to peening the sample} &= \frac{\text{Specimen length (mm)}}{\text{Nozzle speed (mm/sec)}} \\ &= 25/125 = 0.2 \text{ s} \end{aligned}$$

$$\begin{aligned} \text{Peen flow rate, } N_p &\approx \frac{3\dot{m}}{4\pi\rho\bar{r}^3} = \frac{3 \times 0.07576}{4 \times \pi \times 7860 \times (0.3715 \times 10^{-3})^3} \\ &= 44880 \text{ peens/sec} \end{aligned}$$

$$\text{Peen flow rate at } 0.2 \text{ s, } (N_p)_{0.2} = 44880 \times 0.2 = 8976 \text{ peens/0.2 s}$$

$$\begin{aligned} \text{Peens impacting the specimen} &\approx (N_p)_{0.2} \times \frac{\text{Specimen width}}{\text{Width of shot spread}} \\ &= 8976 (19/21) = 8121 \text{ peens} \end{aligned}$$

$$\text{The indentation created by single peen} = \pi r^2 = \pi (0.299)^2 = 0.28086 \text{ mm}^2$$

The total area of indentation created by the peens impacting the specimen is given by:

$$a = 8125 \times 0.28086 = 2280 \text{ mm}^2 \text{ and the total area to be peened, } S = 25 \times 19 \text{ mm} = 475 \text{ mm}^2.$$

$$\text{Hence, } \left(\frac{a}{S} \right)_{1 \text{ pass}} = \frac{2280}{475} = 4.8$$

The possible reasons why the experimental and theoretical a/S ratio differ, may be due to overlapping, irregularities in the shot size and variations of the peening process itself like pressure, flow rate and fluctuations in the oscillating movement of the nozzle. The

experimental ratio of $\left(\frac{a}{S}\right)_{1pass}$ was used for the calculation of subsequent coverage percentages, as follows:

$$C(t + \delta t) = 1 - [1 - C(t)] \left[1 - \frac{a}{S} \right] \text{ for } \delta t = 0.2 \text{ s, } C(t) = 0, \text{ and } \left(\frac{a}{S}\right)_{1pass} = 0.543$$

$$1^{st} \text{ pass} = C(0.2) = 1 - (1 - 0)(1 - 0.543) = 0.543$$

$$2^{nd} \text{ pass} = C(0.4) = 1 - (1 - 0.543)(1 - 0.543) = 0.791$$

$$3^{rd} \text{ pass} = C(0.6) = 1 - (1 - 0.791)(1 - 0.543) = 0.905$$

$$4^{th} \text{ pass} = C(0.8) = 1 - (1 - 0.905)(1 - 0.543) = 0.956$$

$$5^{th} \text{ pass} = C(1.0) = 1 - (1 - 0.956)(1 - 0.543) = 0.98$$

An output of the Holdgate's model is depicted in Fig. III-3.

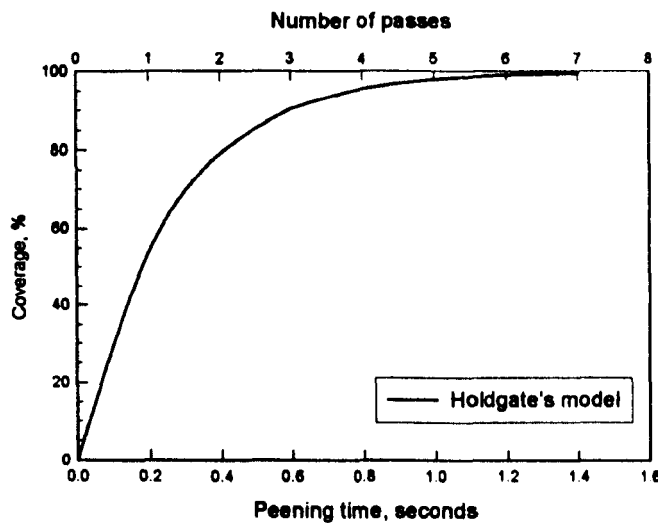


Figure III-3 Development of coverage by using the Holdgate's model.

A comparison among the experimental, Avrami and Holdgate percentage of coverage is shown in Fig. III-4.

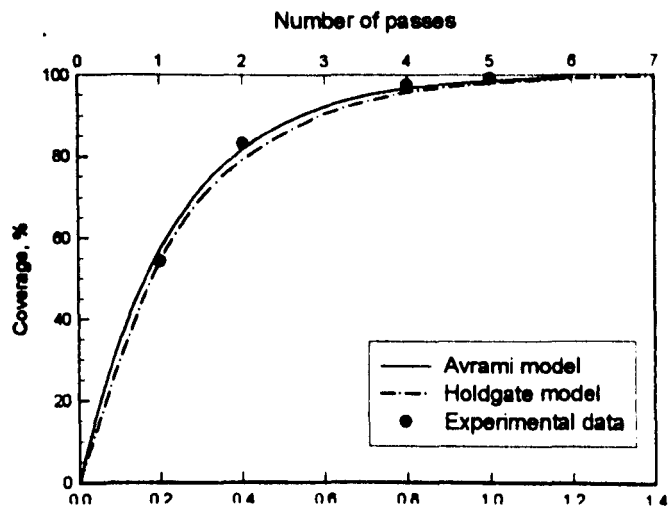
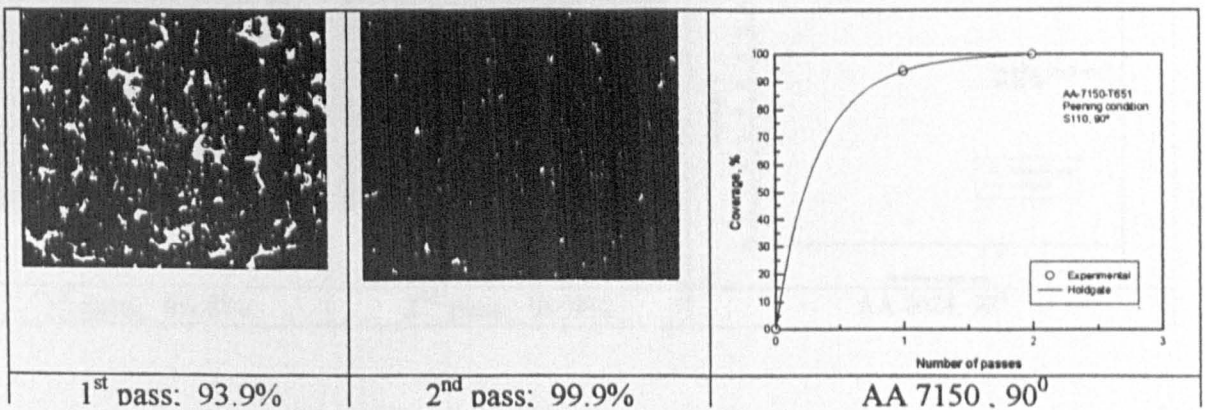
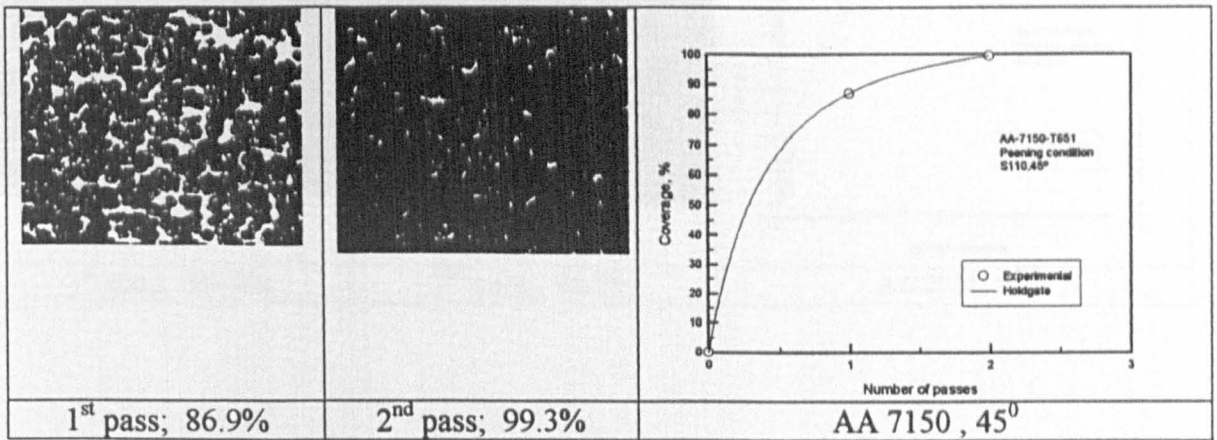
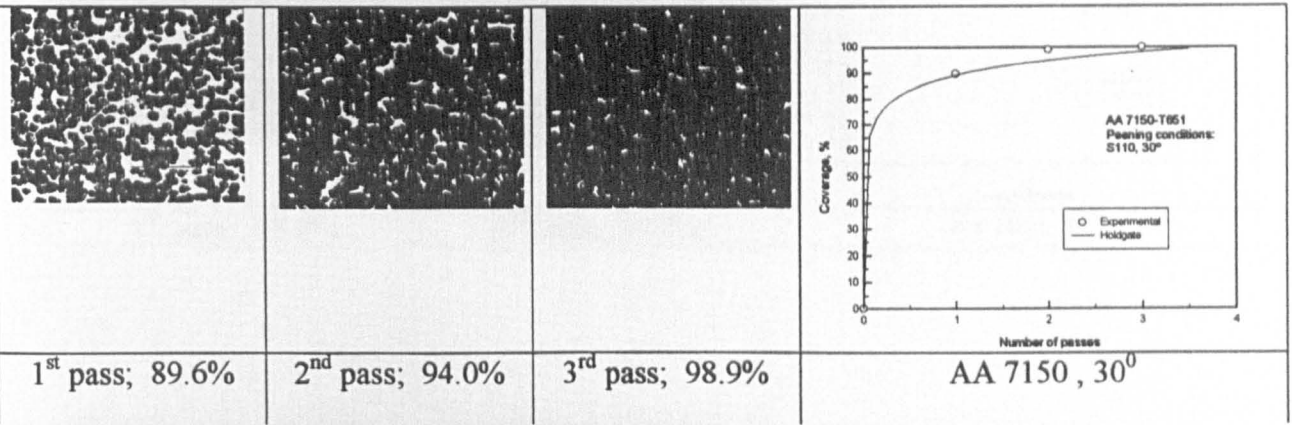
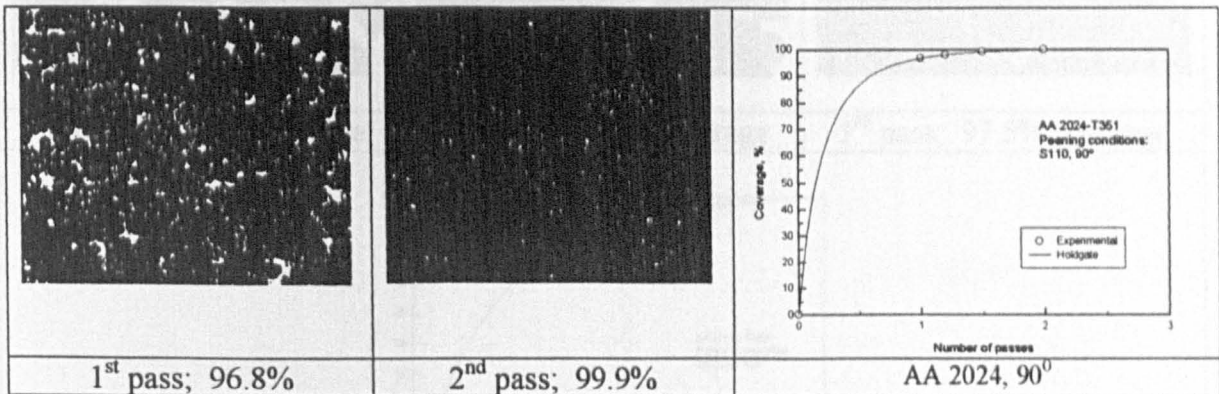
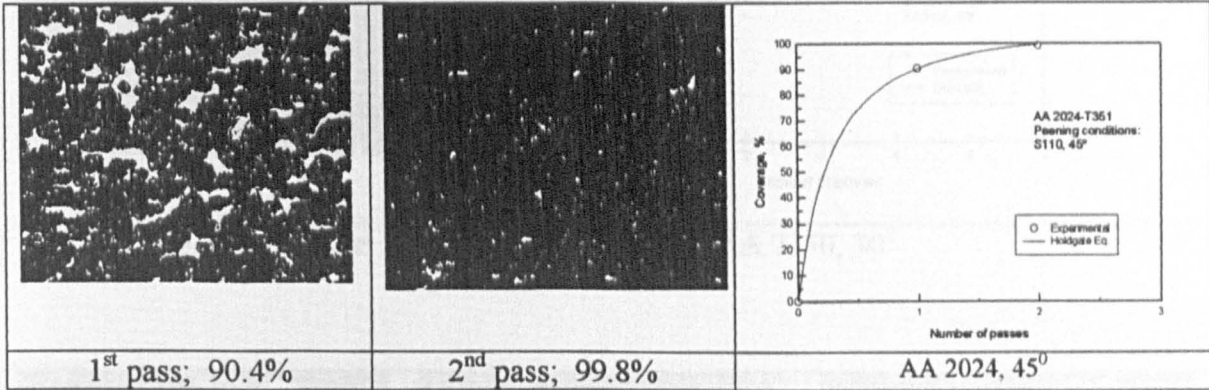
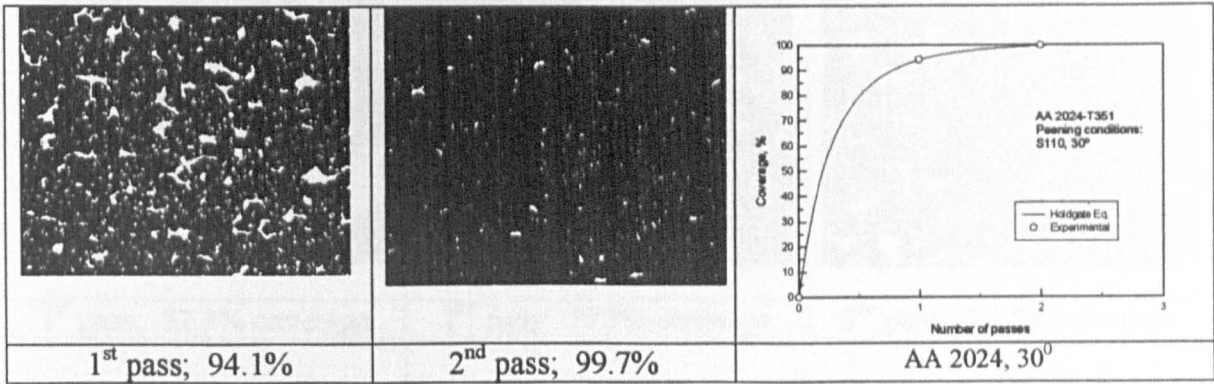


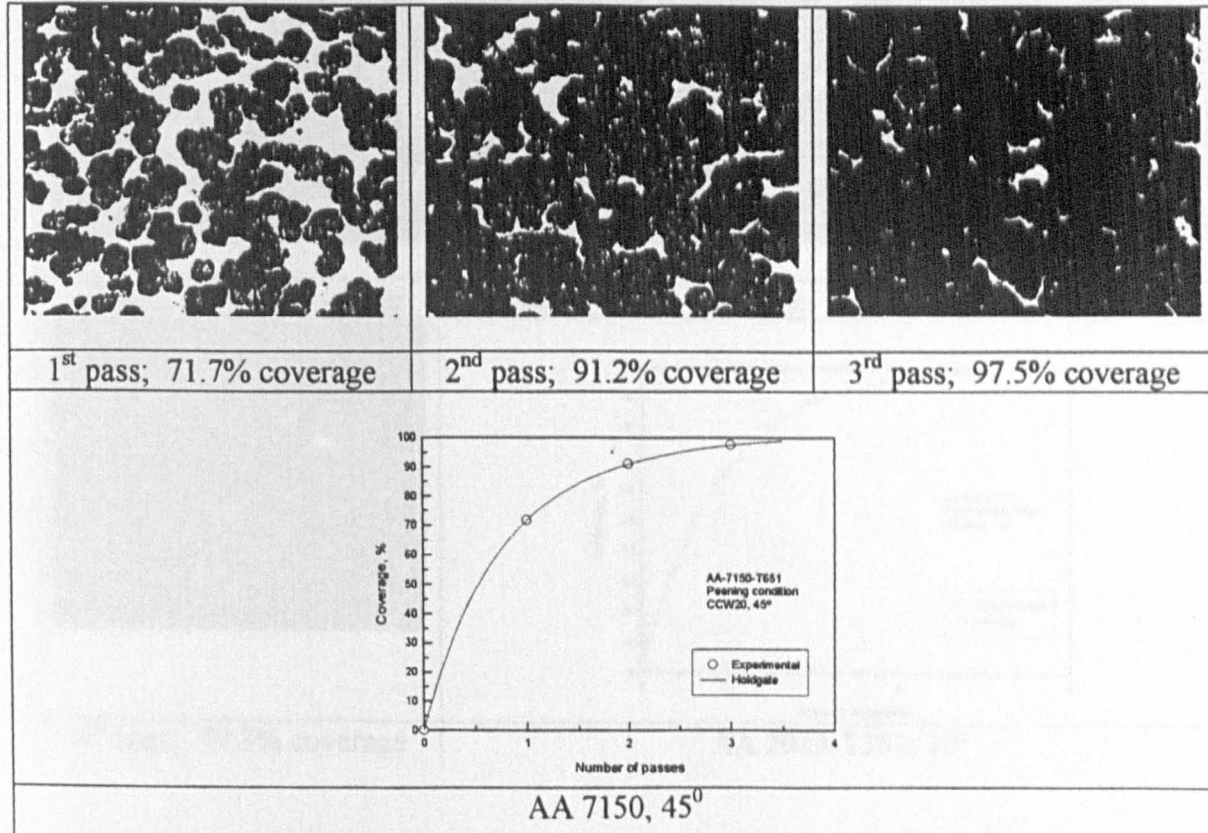
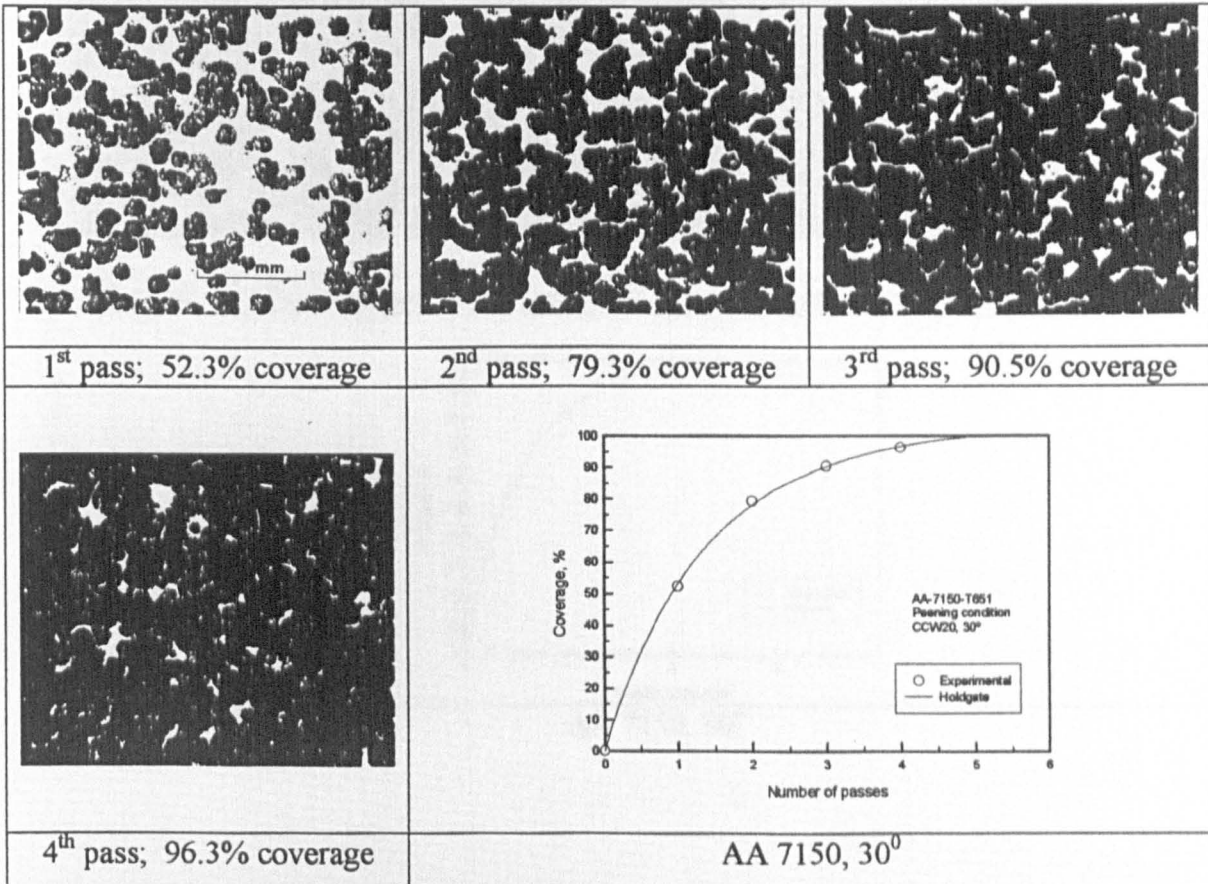
Figure III-4 Coverage comparison between theoretical models and experimental data.

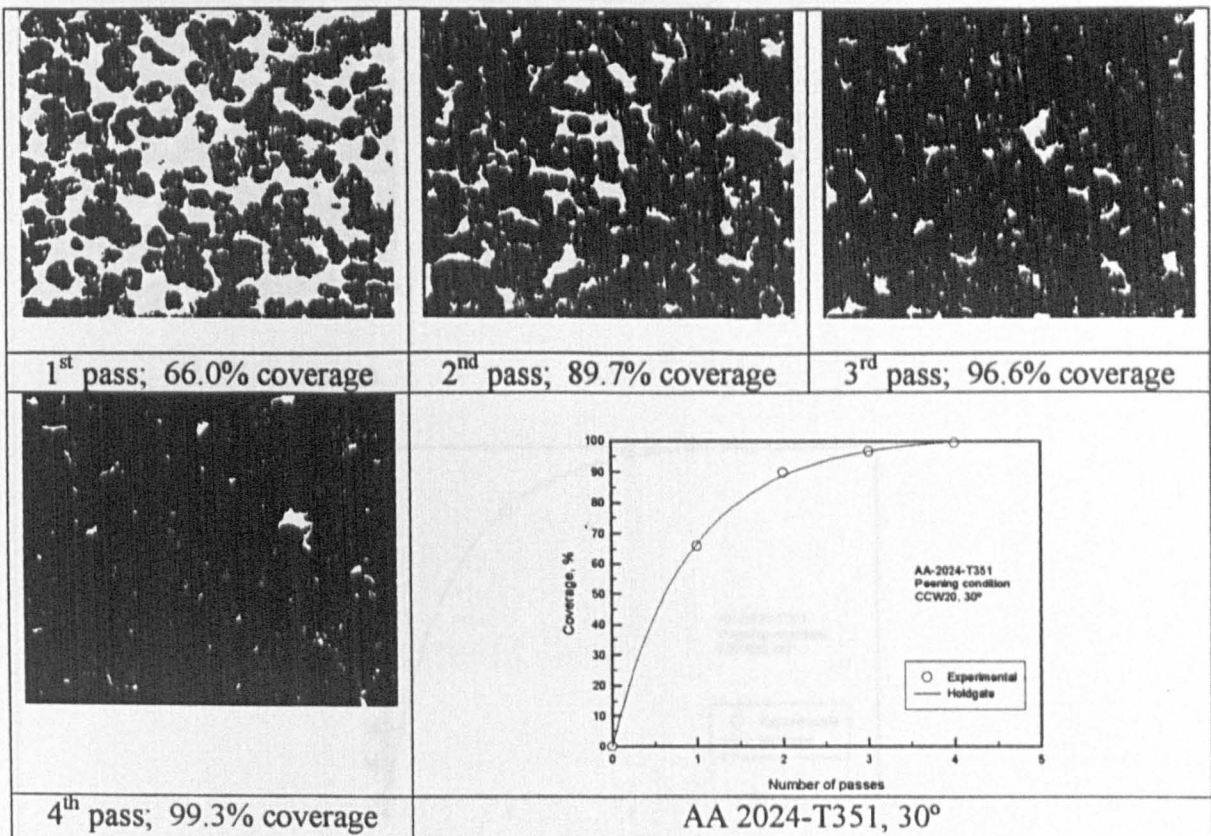
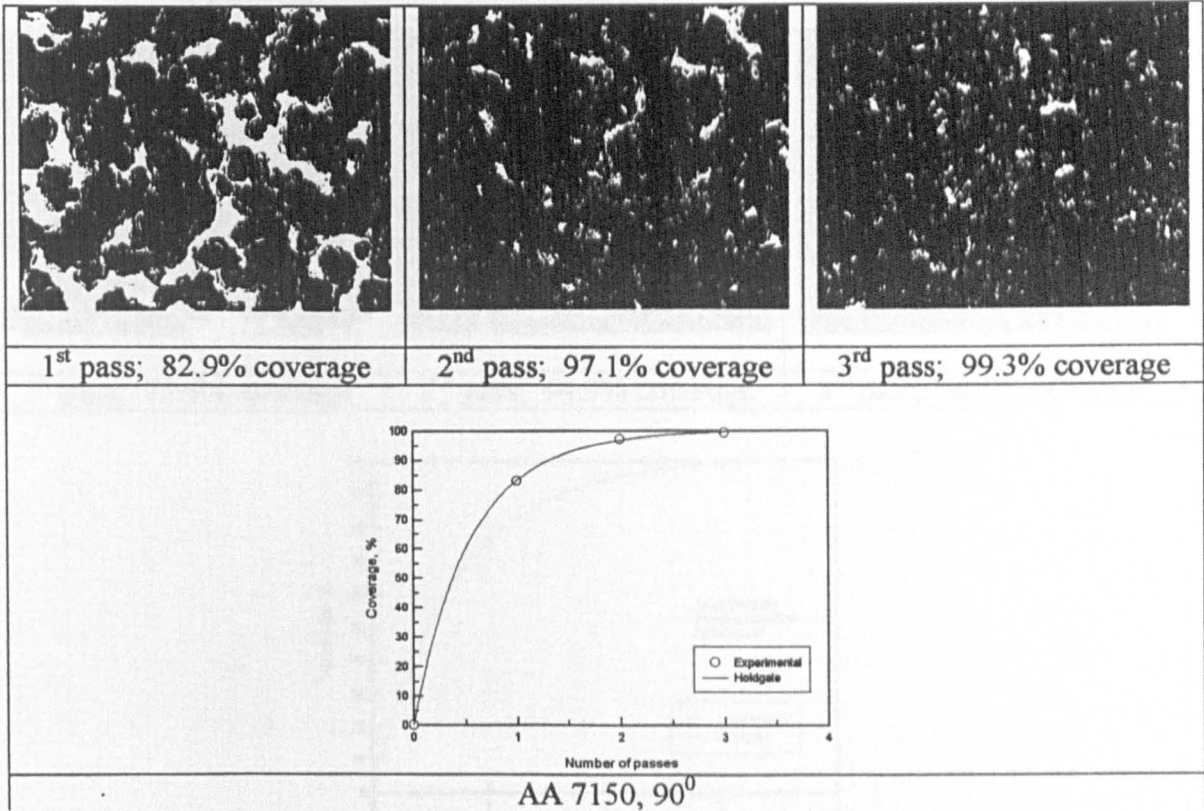
COVERAGE DEVELOPMENT BY USING SHOT TYPE S110

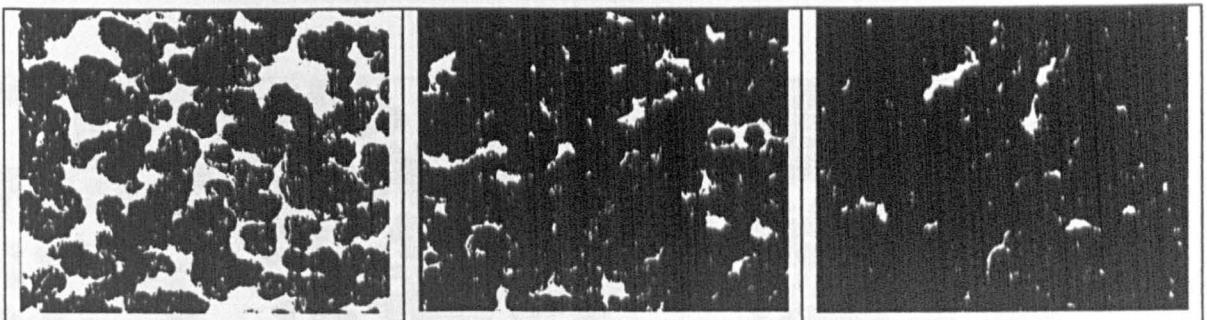




COVERAGE DEVELOPMENT FOR THE SHOT CCW20



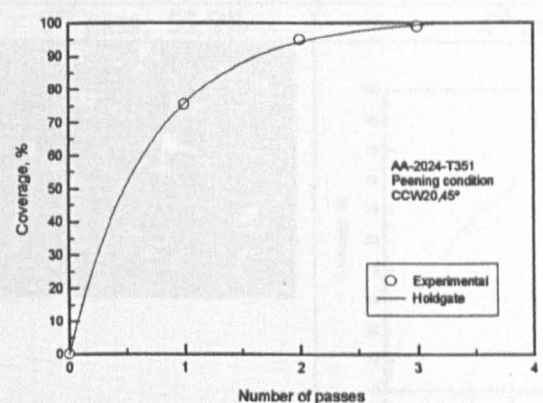




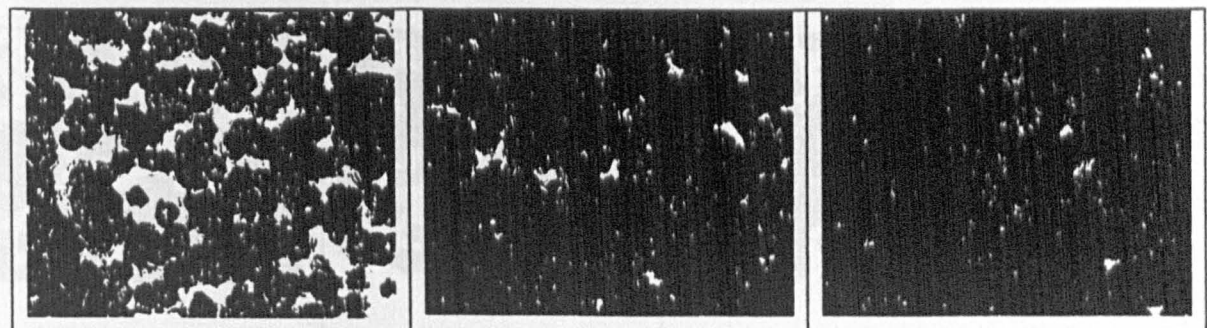
1st pass; 75.4% coverage

2nd pass; 94.9% coverage

3rd pass; 98.9% coverage



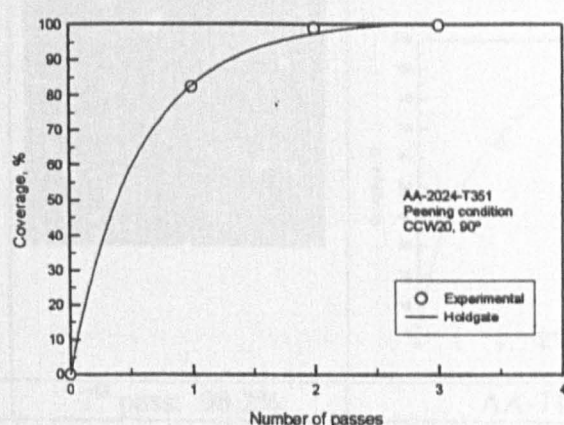
AA 2024-T351, 45°



1st pass; 82.3% coverage

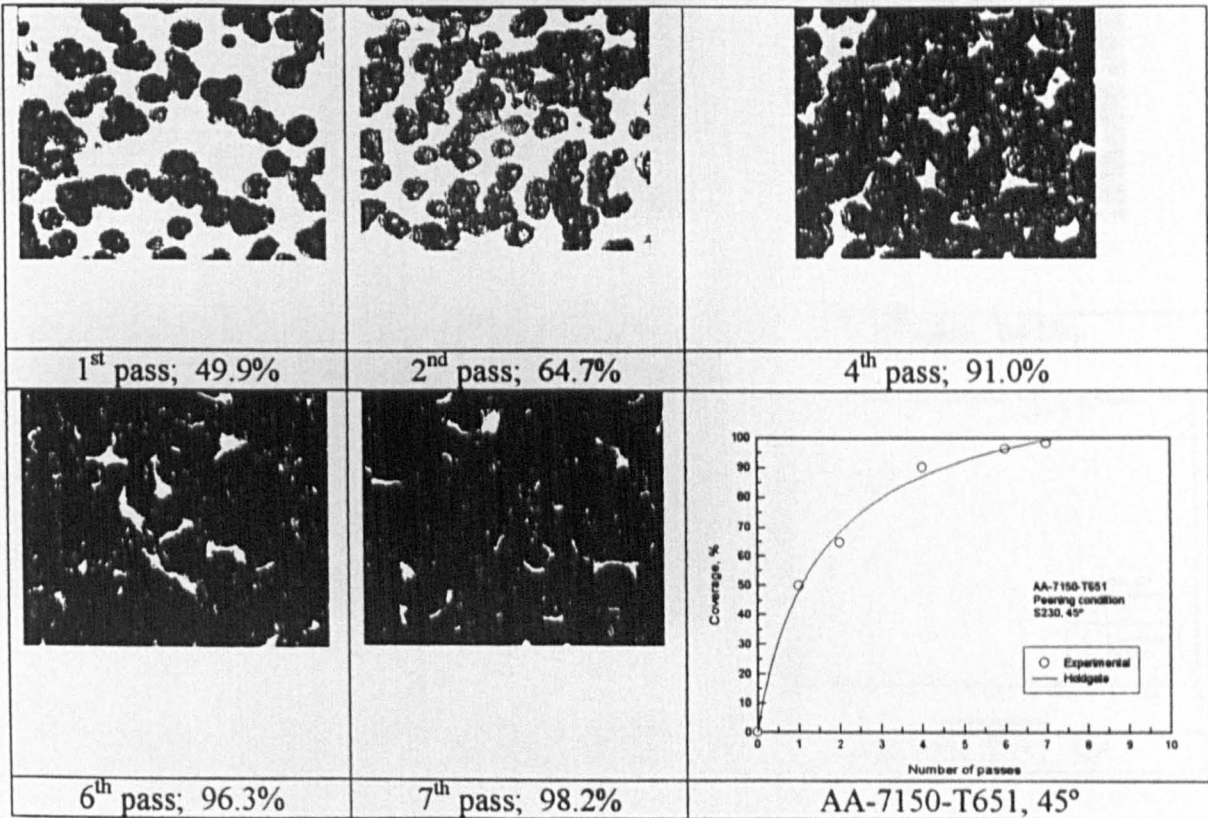
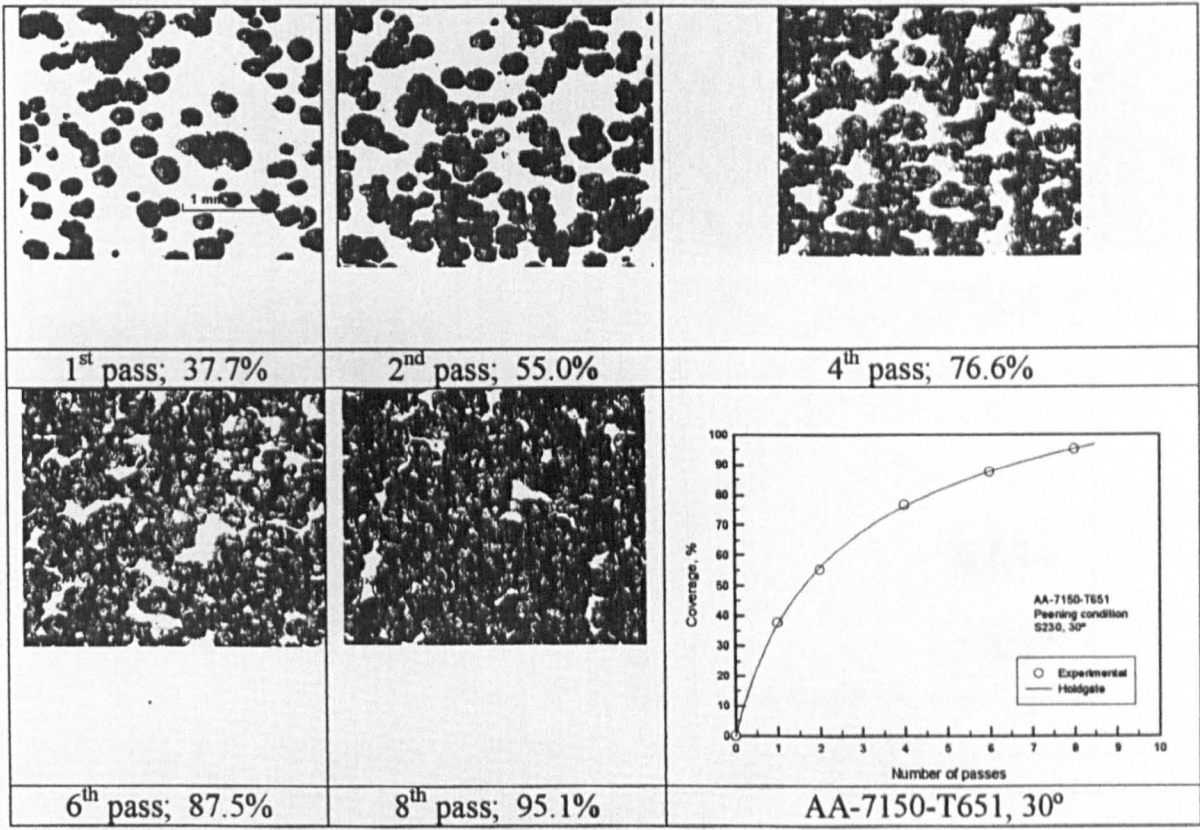
2nd pass; 98.9% coverage

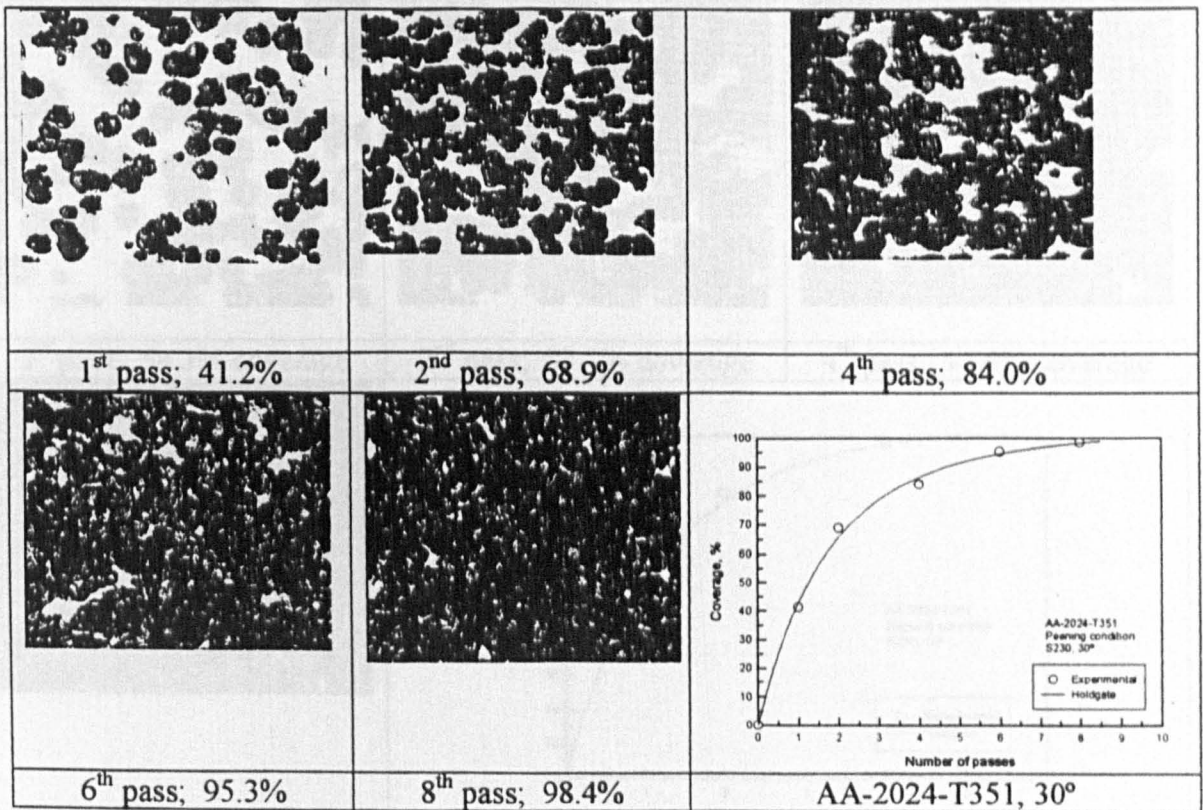
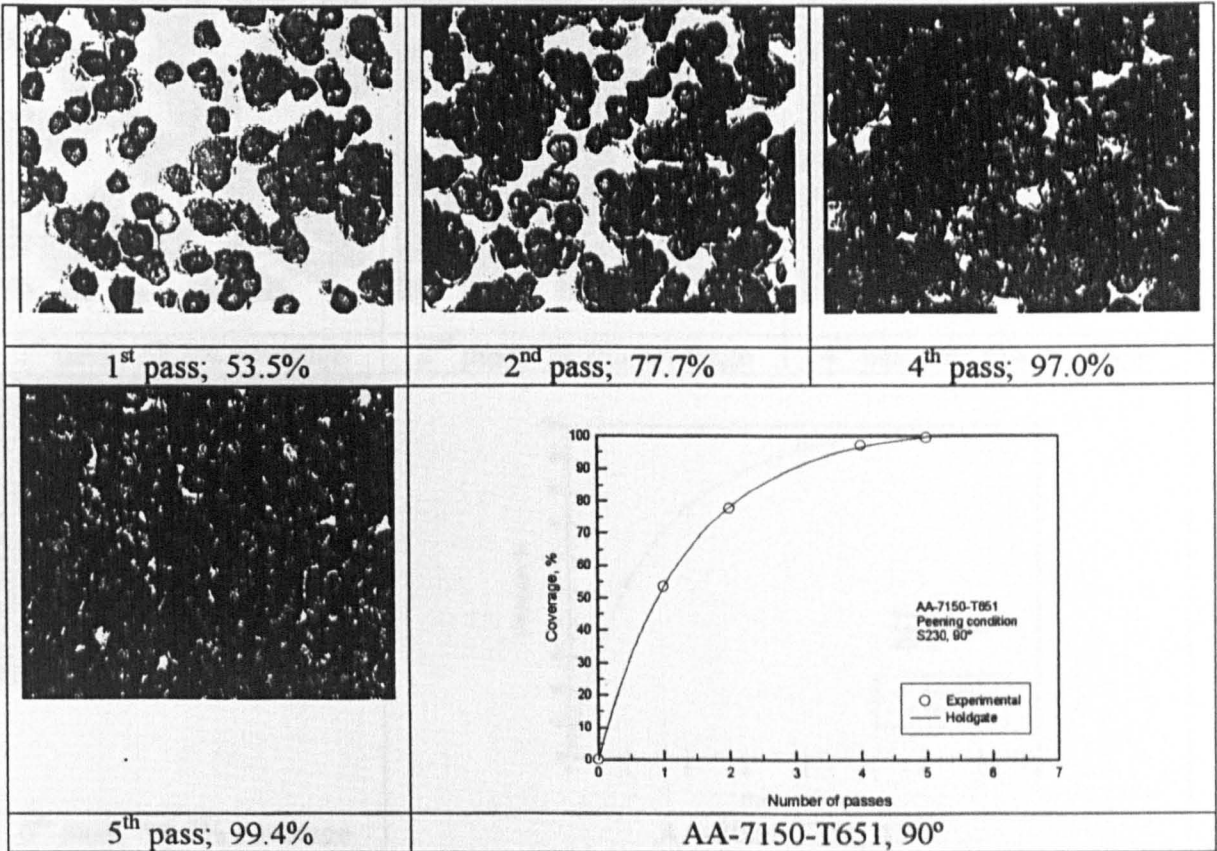
3rd pass; 99.7% coverage

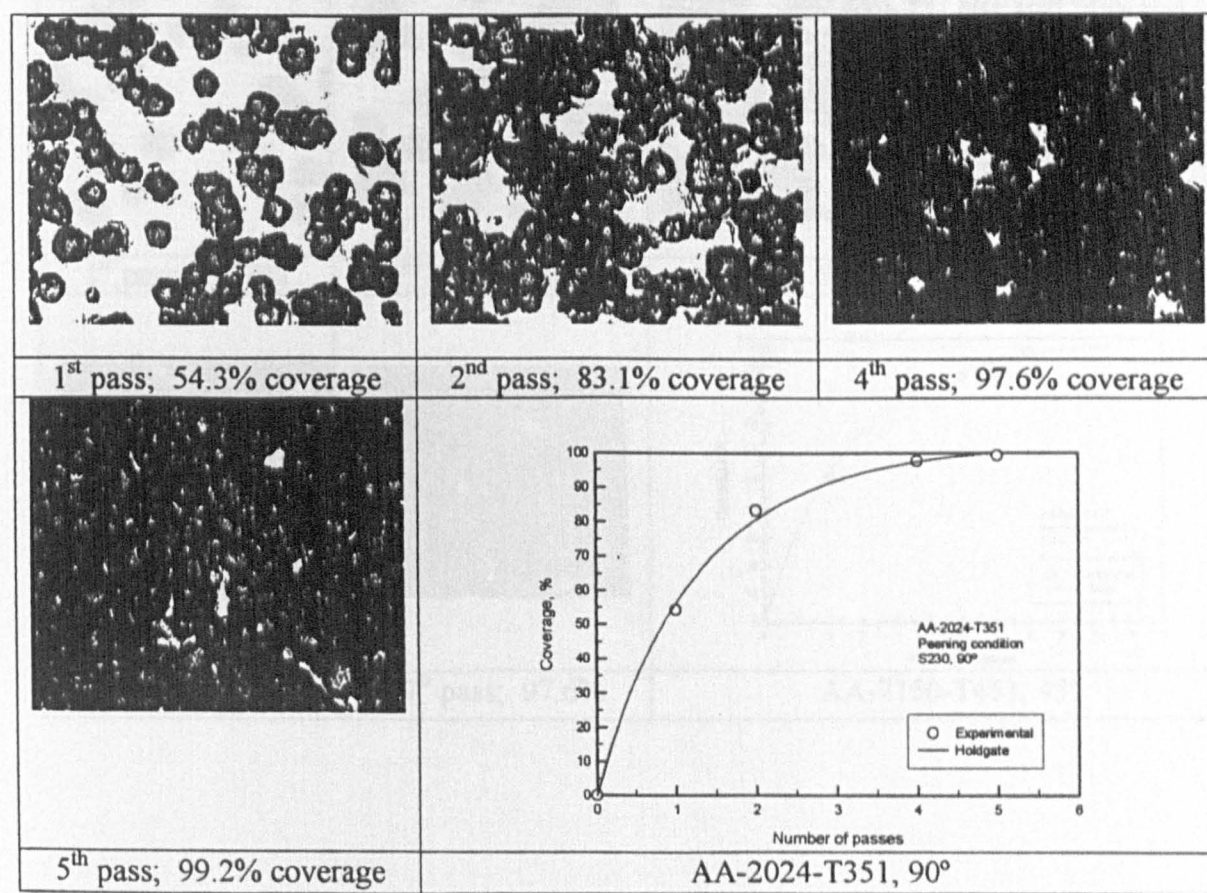
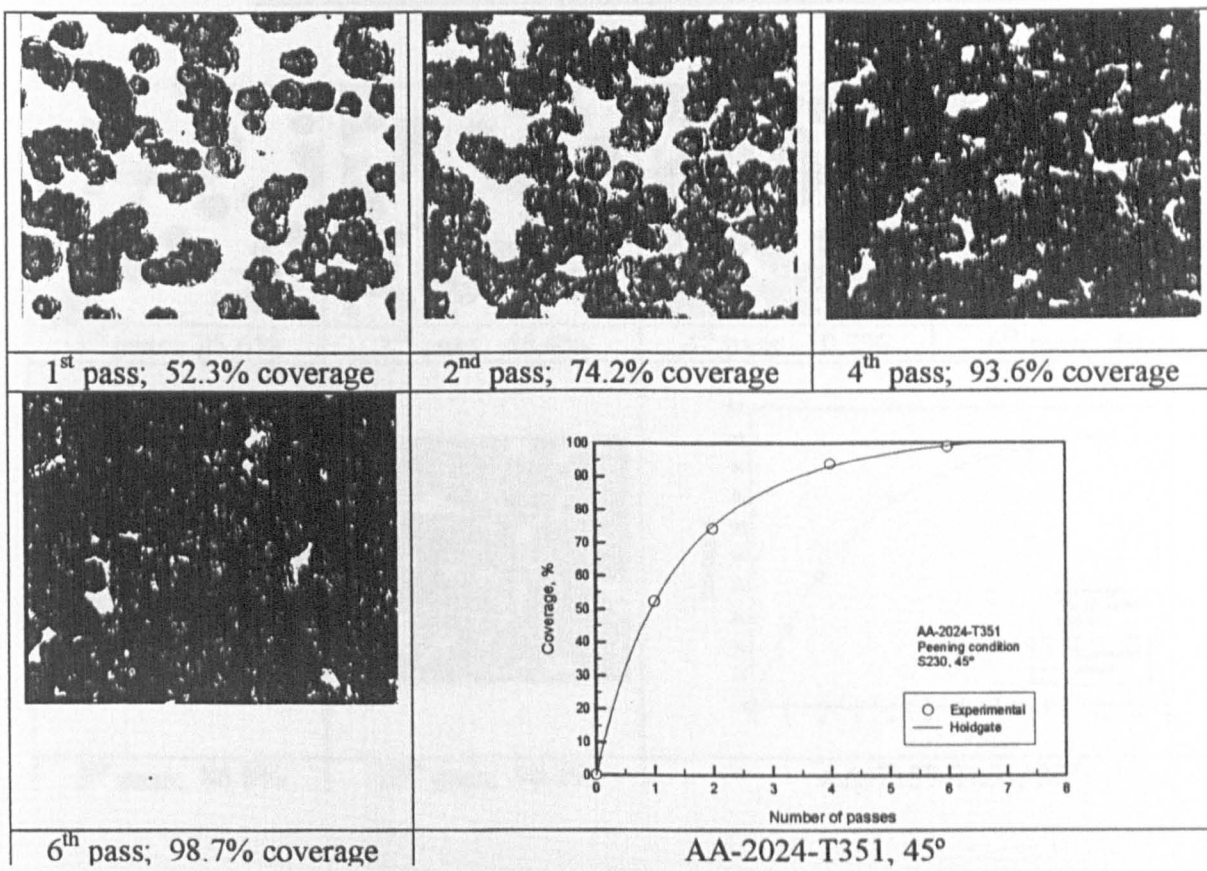


AA 2024-T351, 90°

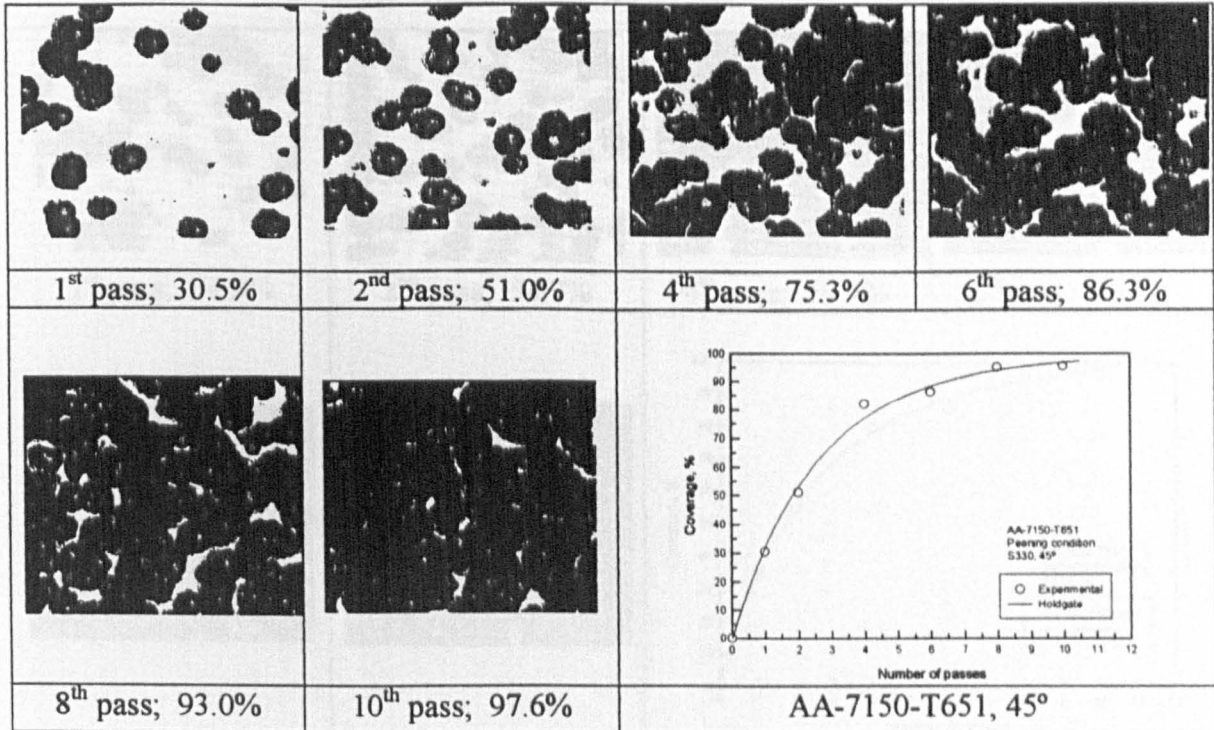
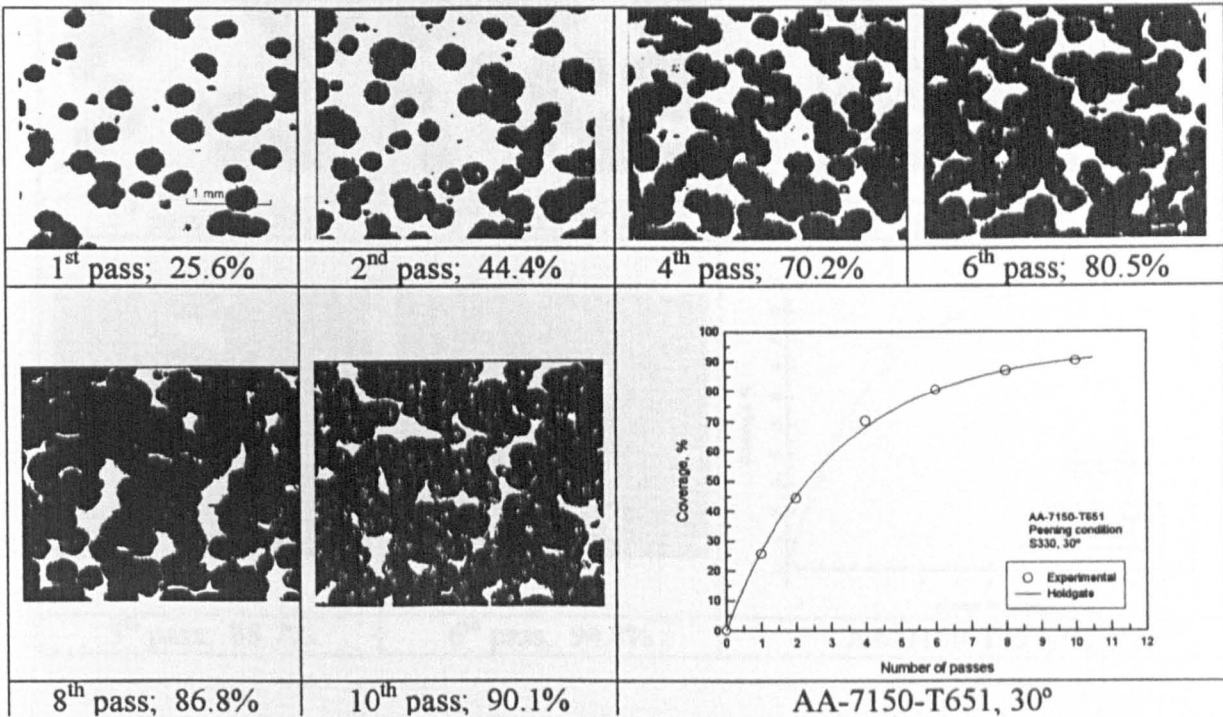
COVERAGE DEVELOPMENT FOR THE SHOT S230

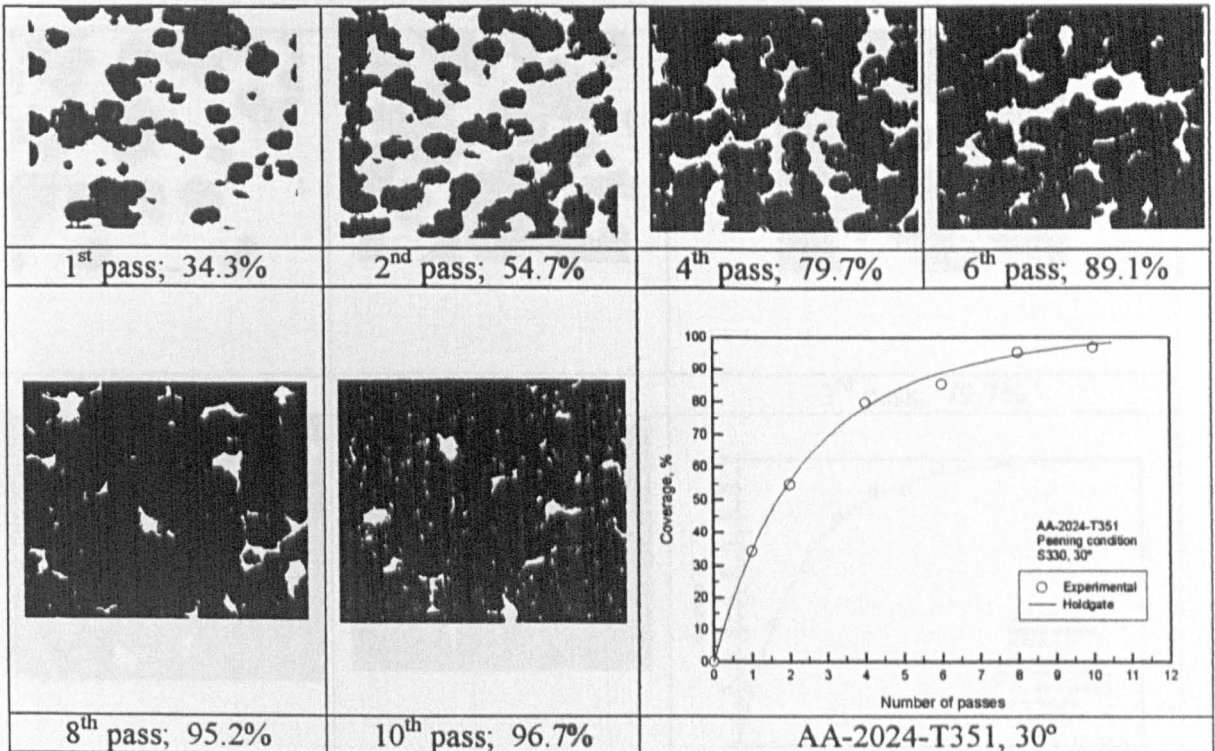
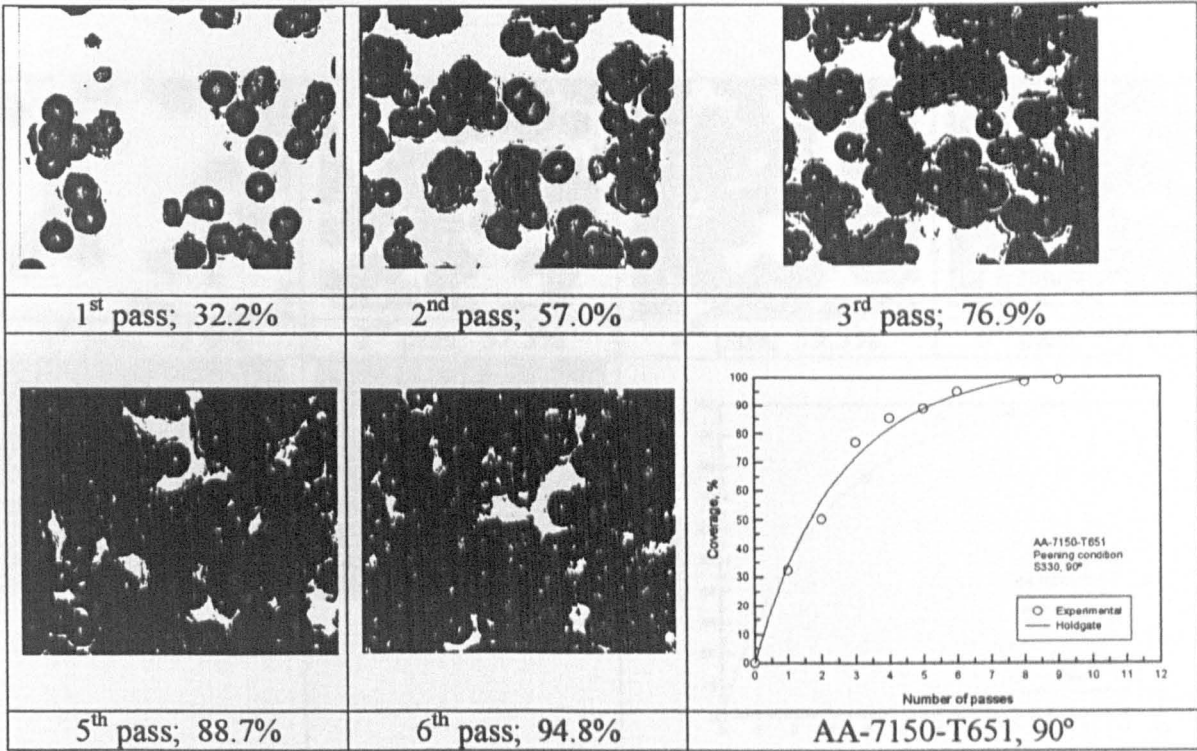


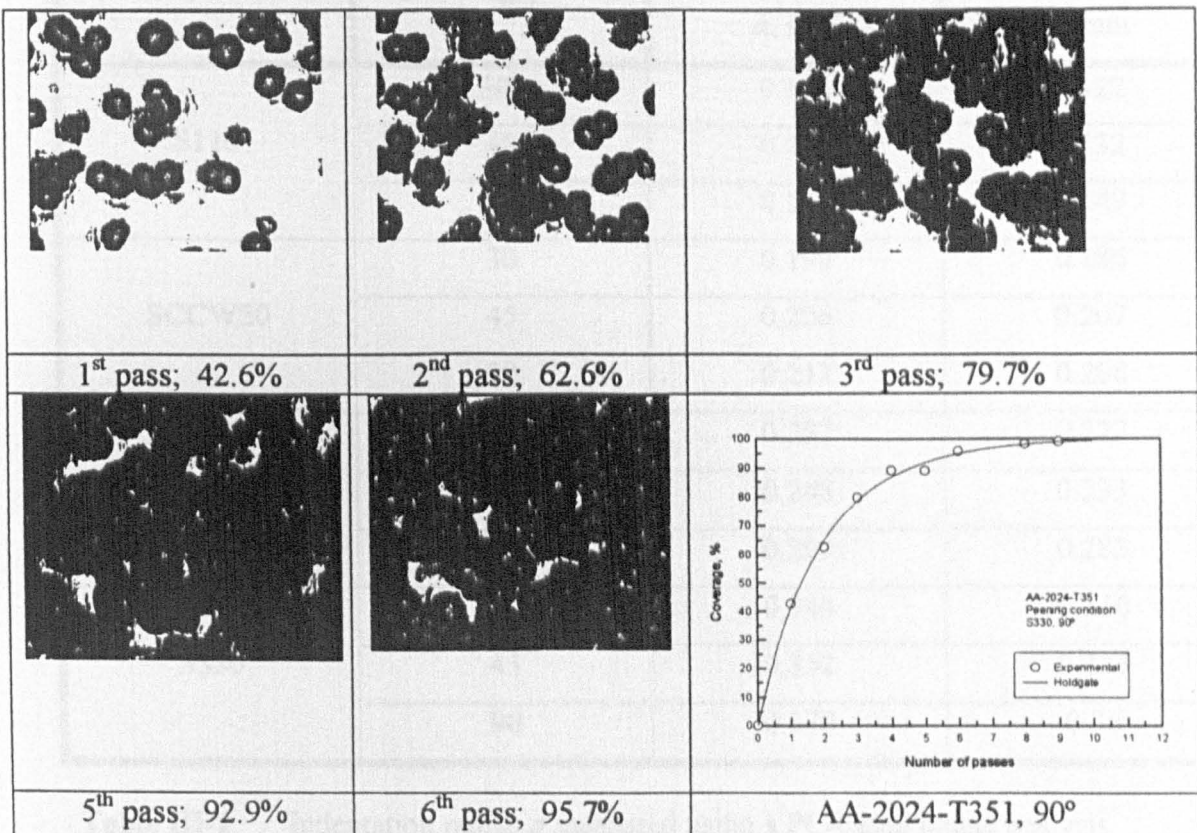
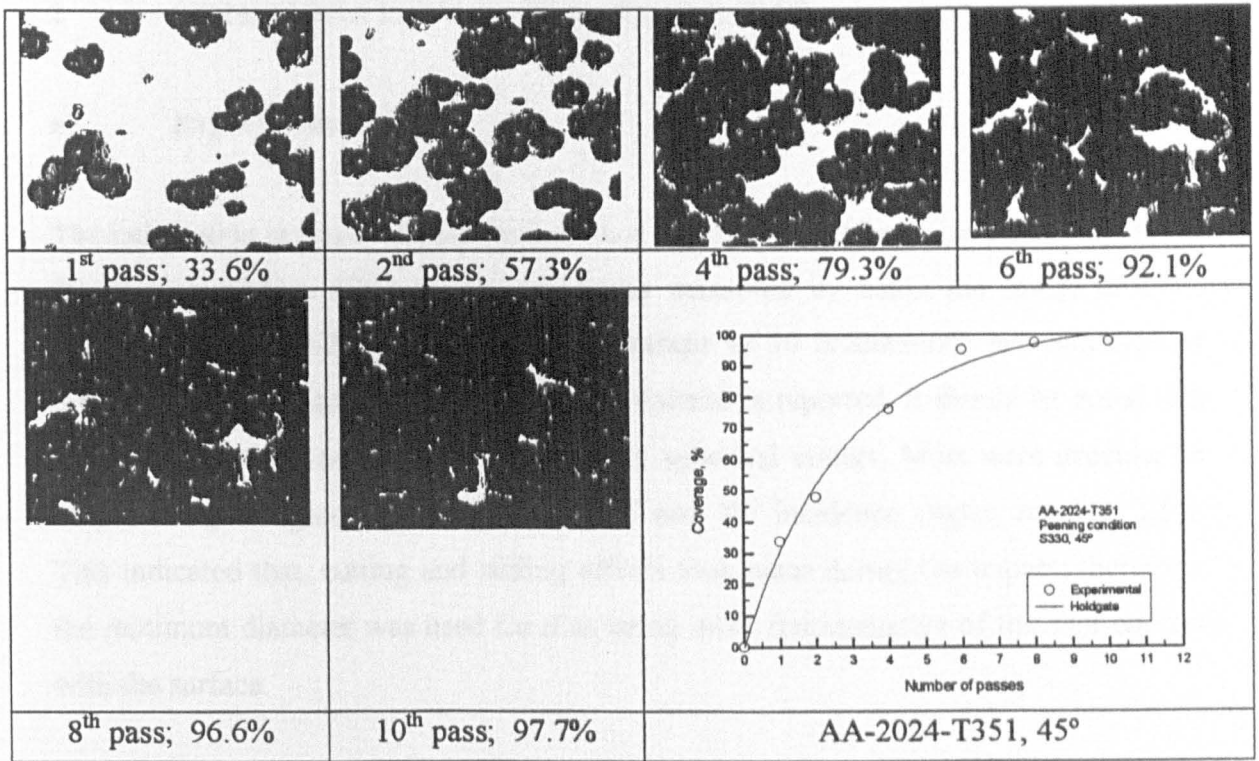




COVERAGE DEVELOPMENT FOR THE SHOT S330







3 DETERMINATION OF THE DIMPLE SIZE

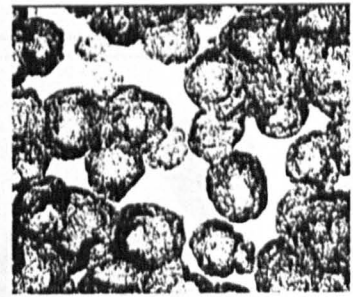
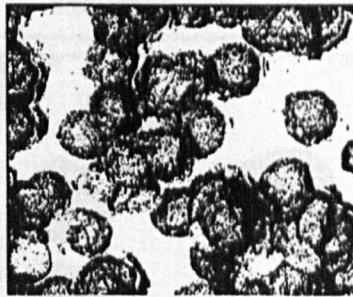
a) Experimentally

The indentation radius a of each type of shot and at three different incidence angles for the two aluminium alloys under study was measured by using the image analysis system. In table III-2 a summary of the average of 10 indentations per shot type at different incidence angles for each type of material is reported. It should be noted that the observed indentations were not perfectly spherical craters. Most were irregular in shape, being elongated, particularly for 45° and 30° incidence angles, see Fig. III-5. This indicated that, cutting and sliding effects took place during the impact; therefore, the minimum diameter was used for d as being more representative of the shot contact with the surface.

Shot	Incidence Angle	Aluminium alloy	
		2024-T351 a , mm	7150-T651 a , mm
S110	30°	0.126	0.122
	45	0.143	0.132
	90	0.151	0.149
SCCW20	30	0.190	0.186
	45	0.206	0.207
	90	0.213	0.208
S230	30	0.237	0.227
	45	0.248	0.233
	90	0.299	0.283
S330	30	0.344	0.316
	45	0.352	0.327
	90	0.370	0.36

Table III-2 Indentation radius a measured using a PC-based image analysis.

Shot type: S110
Material: AA 7150-T651

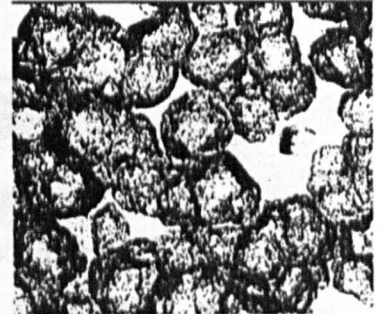
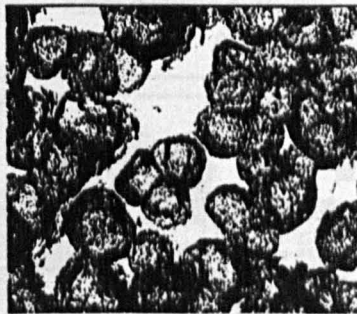
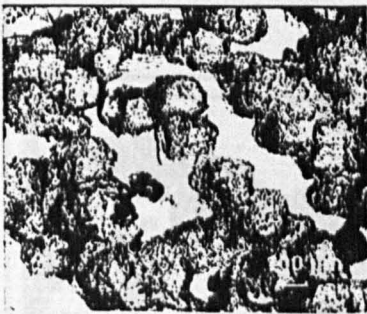


30° incidence angle

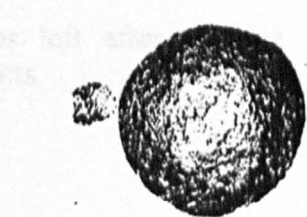
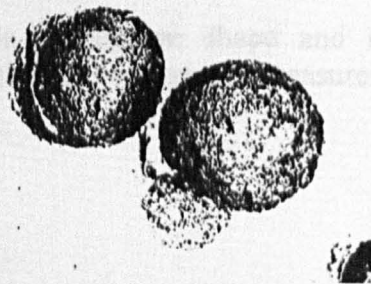
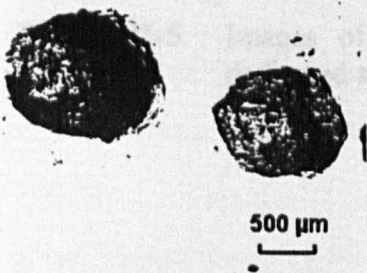
45°

90°

Shot type: S110
Material: AA 2024-T351



Shot type: S330
Material: AA 7150-T651

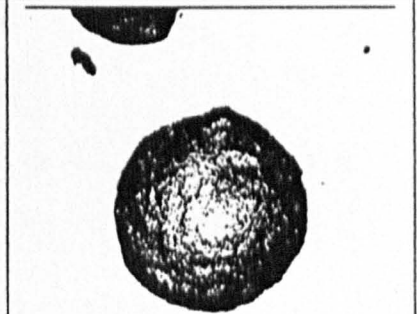
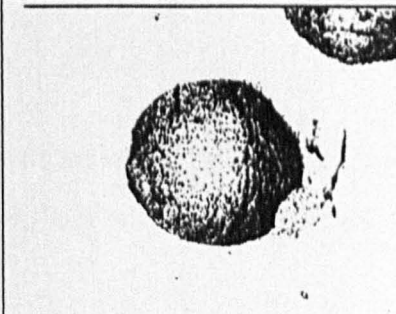
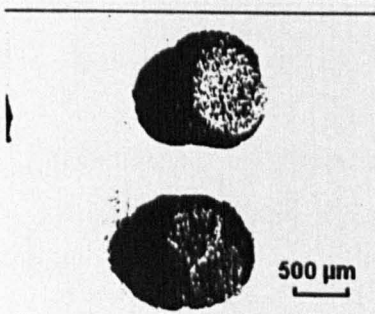


30° incidence angle

45°

90°

Shot type: S330
Material: AA 2024-T351



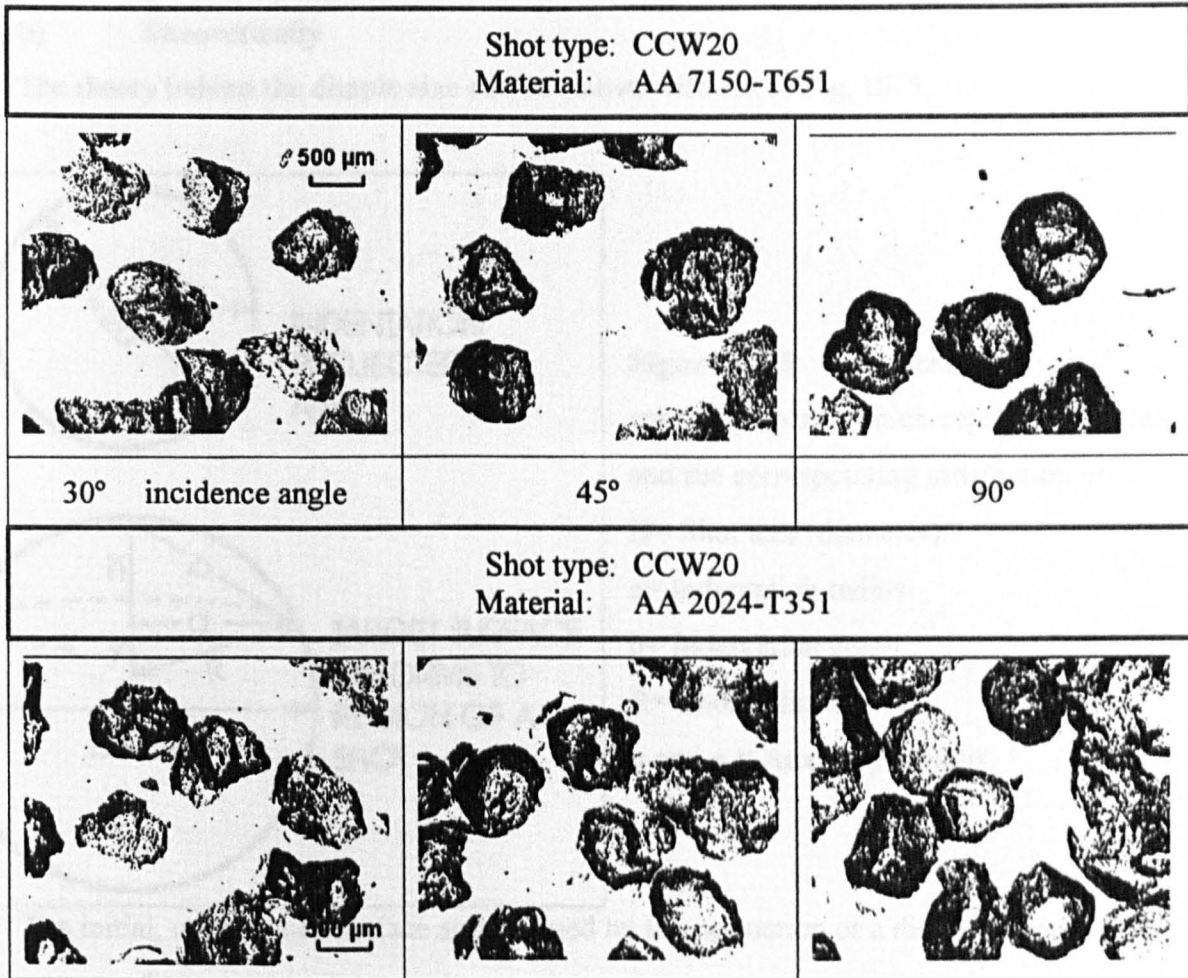


Figure III-5 Images of the indentation shape and sizes left after peening the dedicated specimens for coverage measurements.

b) Theoretically

The theory behind the dimple size can be shown with aid of Fig. III-5.

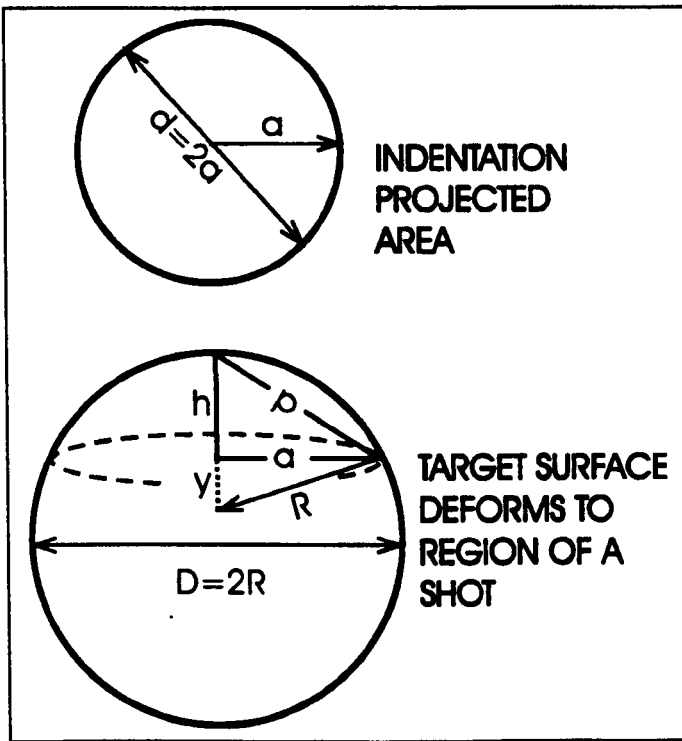


Figure III-5 Schematic of a spherical sector which represents a shot and the corresponding indentation area.

D= Shot size (diameter).

a= Indentation radius.

h= Indentation depth.

R= Shot radius.

y and p = Auxiliary lengths.

The initial, undeformed surface area defined by the projection of a dimple of radius a is:

$$A_0 = \frac{\pi d^2}{4} = \pi a^2 \tag{A.3}$$

This area will deform to approximate the surface of a sector of a sphere. The surface of such a sector of a sphere is given by:

$$S = 2\pi R h = \pi D h = \pi p^2 \tag{A.4}$$

It can be seen from Fig. III-5 that,

$$R = h + y$$

$$y = \sqrt{R^2 - a^2}$$

$$\therefore h = R - \sqrt{R^2 - a^2} = \frac{1}{2} \left(D - \sqrt{D^2 - d^2} \right) \tag{A.5}$$

The parameter h represents the theoretical indentation depth, given in terms of the shot and indentation size. This depth is specifically referred for an impingement angle of 90° .

Although still useful, the above relationships are derived merely from geometric considerations and the properties of shot and target material are taken partially into account (indentation radius). A comprehensive analysis to determine not only the indentation depth but the theoretical dimple size and its volume was developed by Iida [1]. He deemed that impact may be divided mathematically into two categories, namely, entirely elastic and ideally plastic. Assuming several factors as elastic deformation, i.e. the mechanics involved in the dynamic dent is practically the same as that occurring under static conditions, and Young's moduli for spheres and elastic body are essentially similar to static conditions. Following the Hertz's model [2]:

$$\lambda = \left\{ \frac{9 P^2}{8 D} \left(\frac{1-\nu_1^2}{E_1} + \frac{1-\nu_2^2}{E_2} \right)^2 \right\}^{\frac{1}{3}} \quad \text{<A.6>}$$

where λ is the depth of contact, P is the force, as shown in Fig. III-6-a, E_1, E_2 are the Young's moduli of the sphere and elastic material respectively, ν_1, ν_2 are the corresponding Poisson's ratio.

Iida [3] solved Eq. <A.6> as follows:

$$P = 0.943 \left(\frac{1-\nu_1^2}{E_1} + \frac{1-\nu_2^2}{E_2} \right)^{-1} D^{\frac{1}{2}} \lambda^{\frac{3}{2}}, \text{ the equation of motion of the sphere is}$$

$$m \frac{d^2 \lambda}{dt^2} = -P, \text{ then } \int_v^0 m v dv = - \int_0^\lambda 0.943 \left(\frac{1-\nu_1^2}{E_1} + \frac{1-\nu_2^2}{E_2} \right)^{-1} D^{\frac{1}{2}} \lambda^{\frac{3}{2}} d\lambda, \text{ therefore,}$$

$$P = 0.757 (\rho)^{\frac{3}{5}} \left(\frac{1-\nu_1^2}{E_1} + \frac{1-\nu_2^2}{E_2} \right)^{-\frac{2}{5}} D^2 v^{\frac{6}{5}} \quad \text{<A.7>}$$

and

$$\lambda = 0.864 \left\{ \rho \left(\frac{1-\nu_1^2}{E_1} + \frac{1-\nu_2^2}{E_2} \right) \right\}^{\frac{2}{5}} D \lambda^{\frac{4}{5}} \quad \text{<A.8>}$$

where, ρ is the density of the sphere, and from $\left(\frac{\delta}{2} \right)^2 = \lambda \cdot D$, δ is the diameter of contacted circle. Then

$$\delta = 1.728 \left\{ \rho \left(\frac{1-\nu_1^2}{E_1} + \frac{1-\nu_2^2}{E_2} \right) \right\}^{\frac{1}{5}} D v^{\frac{2}{5}} \quad \langle A.9 \rangle$$

The volume V of the dent of elastic deformation is $V = \frac{\pi}{6} \lambda \left(\frac{3}{4} \delta^2 + \lambda^2 \right) \approx \frac{\pi}{8} \delta^2 \lambda$, it gives:

$$V = 1.03 \left\{ \rho \left(\frac{1-\nu_1^2}{E_1} + \frac{1-\nu_2^2}{E_2} \right) \right\}^{\frac{4}{5}} D^3 v^{\frac{8}{5}} \quad \langle A.10 \rangle$$

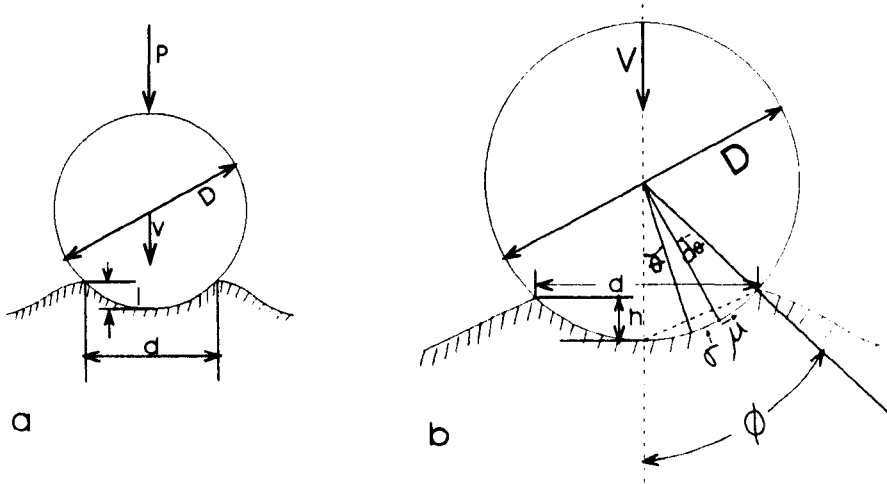


Figure III-6 Schematic illustration of: (a) elastic impact and (b) plastic impact

When a rigid sphere impinges an ideally plastic material, plastic deformation is developed as shown in Fig. III-6-b. The resistance to deformation on the area of raised lip or annulus lying on the curve of the indented surface equilibrates the impact force. Differently expressed [3]:

$$d p = \frac{\pi}{2} D \sin \theta (\cos \theta + \mu \sin \theta) d \theta \quad \langle A.11 \rangle$$

Thus,

$$\begin{aligned} P &= \int_0^\phi \frac{\pi}{2} D^2 \sigma \sin \theta (\cos \theta + \mu \sin \theta) d \theta \\ &= \frac{\pi}{2} D^2 \sigma \left\{ \frac{1}{2} \sin^2 \phi + \frac{\mu}{2} (\phi - \sin \phi \cos \phi) \right\} \\ &= \frac{\pi}{4} \sigma d \left[d + \mu \left\{ \frac{D^2 \phi}{d} - (D - h) \right\} \right] \\ &= \frac{\pi}{4} \sigma d^2 \left\{ 1 + \mu \frac{d}{4D} \right\} \end{aligned}$$

where, μ is the coefficient of friction between the sphere and plastic material, σ is the resistance to deformation per unit area and P is the impact force. The equation of motion

of the shot is $m \frac{dv}{dt} = -P$, hence,

$$\begin{aligned} m v^2 &= 2 \int_0^d \frac{\pi}{2} \sigma d^2 \left\{ 1 + \mu \frac{d}{4D} \right\} \frac{d}{2D} d d \\ &= \frac{\pi \sigma}{16D} d^4 \left(1 + \mu \frac{d}{5D} \right) \\ &= 2\sigma V \left(1 + \mu \frac{d}{5D} \right) \end{aligned}$$

Iida observed that the volume of the dent produced by steel shot on 0.2%C steel was proportional the kinetic energy of a ball. Therefore, the second term in the above formula was in practice envisaged negligible, i.e. $\mu \approx 0$. It follows that:

$$P = \pi \left(\frac{\rho \sigma}{6} \right)^{\frac{1}{2}} D^2 v \quad \text{<A.12>}$$

$$d = 2 \left(\frac{\rho}{6\sigma} \right)^{\frac{1}{4}} D v^{\frac{1}{2}} \quad \text{<A.13>}$$

$$h = \left(\frac{\rho}{6\sigma} \right)^{\frac{1}{2}} D v \quad \text{<A.14>}$$

$$\begin{aligned} V &= \frac{\pi}{8} d^2 h \\ &= \frac{\pi \rho}{12\sigma} D^3 v^2 \end{aligned} \quad \text{<A.15>}$$

The theoretical indentation depth can now be calculated from Eq. <A.14> by making use of more reliable parameters such as the force density of the shot, the yield strength of the material, the shot size and its velocity at the moment of impacting.

Thus, rearranging Eq. <A.13> for v, gives:

$$v = \left(\frac{1}{1.28} \right)^2 \left(\frac{d}{D} \right)^2 \left(\frac{\sigma}{\dot{\rho}} \right)^{\frac{1}{2}} \quad \text{<A.16>}$$

$\dot{\rho}$ is the force density, expressed in terms of $\dot{\rho} = \frac{\rho}{32.2 \times 12}$ when using $\left(\frac{\text{lb}_m}{\text{in}^3} \right)$

or $\dot{\rho} = \frac{\rho}{9.81}$ when using $\left(\frac{\text{Kg}_m}{\text{m}^3} \right)$.

The following calculating practice was adopted for estimating the velocity of a particular shot and intensity:

i. The shot is considered to have an experimental $\rho = 0.276 \text{ lb}_m/\text{in}^3$ ($7630 \text{ Kg}_m/\text{m}^3$).

Therefore, the force density gives $\dot{\rho} = \frac{0.276}{32.2 \times 12} \left(\frac{\text{lb} \cdot \text{s}^2}{\text{in}^4} \right)$ ($7630/9.81 \text{ Kg s}^2/\text{m}^4$).

ii. Considering the intensity value of the AA 2024 from Fig. 4.1.11 for a S330 shot at 90° incidence angle equal to 25.542A, hence, the indentation diameter $d = 0.029$ in (0.74 mm).

iii. The S330 shot was found to have an average diameter of $D = 0.033$ in (0.84 mm).

iv. Substituting data in Eq. <A.16>, it gives:

$$v = \left(\frac{1}{1.28} \right)^2 \left(\frac{0.029}{0.033} \right)^2 \left(\frac{47140}{7.1428} \right)^{\frac{1}{2}}$$

v. The estimated velocity is given as $v = 3850 \text{ in/s}$ (97.8 m/s). It should be noted that this estimated velocity corresponds to a normal shot velocity at the moment of impacting the workpiece surface. It is possible to estimate the particle velocity at

different incidence angles applying the following criteria: $v_\theta = \frac{V_n}{\cos \theta}$, where θ

represents the incidence angle. Hence, $v_{45^\circ} = 138.3 \text{ m/s}$ and $v_{30^\circ} = 112.93 \text{ m/s}$.

APPENDIX-IV

SPECIMENS MANUFACTURING DETAILS

The machining procedures and relevant technical data on the preparation of the coupons were as follows:

Stage of machining and brief description	Tools, and machining details
<p>1</p> <p>Saw off at 80mm long across direction of roll. Saw off at 23mm wide along direction of roll.</p>	<p>Machine: Startrite horizontal bandsaw. Cutting speed: 61m/min Feed No. 3: 51mm/min Tool M42 6/10tpi blade. Coolant: yes</p>
<p>2</p> <p>Machine sawn edges to width of 21mm, removing equal amount of material from both sides.</p>	<p>Machine: XYZ 15000 vertical milling machine. Cutting speed: 220m/min Feed No.2 45mm/min. Tool Seco R217.33 - 12 50mm dia. Tip 12 03 AZ-WM P25. Coolant: yes Depth of cut 1 @ 1.0mm each face</p>
<p>3</p> <p>Machine to 7mm thick, removing equal amount of material from both sides.</p>	<p>Machine: XYZ 15000 vertical milling machine. Cutting speed 220m/min Feed No.2 45mm/min. Tool Seco R217.33 - 12 50mm dia. Tip 12 03 AZ-WM P25. Coolant: yes Depth of cut 4 @ 2.0mm, 1 @ 1.0mm each face</p>
<p>4</p> <p>Machine to length 76mm, removing equal amount of material from both sides.</p>	<p>Machine: XYZ 15000 vertical milling machine. Cutting speed 30m/min Feed No.1 30mm/min . Tool Sandvik R390 16mm dia. Tip 11t3 P10. Coolant: yes Depth of cut 2 @ 1.0mm each face.</p>
<p>5</p> <p>Machine to finished thickness, removing equal amounts from both sides.</p>	<p>Machine: XYZ 15000 vertical milling machine. Cutting speed 300m/min Feed No.5 100mm/min Tool Seco R217.33 - 12 50mm dia. Tip 12 03 AZ-WM P25.</p>

		Coolant: yes Depth of cut 1 @ 0.5mm, 1 @ 0.25mm, 2 @ 0.125mm.
6	Set three specimens at a time in fixture, machine to width removing equal amounts from both sides Electric engrave reference number on one face, and specimen number on both ends of opposite face.	Machine: XYZ 15000 vertical milling machine. Cutting speed 300m/min Feed No. 5 100mm/m. Tool Sandvik R390 16mm dia. Tip 11t3 P10 Coolant: yes Depth of cut 1 @ 0.5, 1 @ 0.25, 2 @ 0.125 .
7	Deburr edges with fine emery cloth grade 220 longitudinally, final polishing with grade 600 wet and dry emery paper.	

Note: The as received 7150-T651 AA was not delivered with the corresponding heat treatment. Therefore, an artificial ageing treatment was conducted after the machining of the coupons, following the standard Airbus material specification, AIMS 03-02-011 [6]:

Heat treatment specifications:

Artificially aged @ $115 \leq \theta \leq 125$ °C, $1 \leq t \leq 5$ hours
+ Artificially aged @ $152 \leq \theta \leq 155$ °C, $10 \leq t \leq 12$ hours

Adopted procedure:

The oven was set to 120° C and allowed reaching the temperature. The specimens were placed into the oven and waited for oven to return to temperature. The timing to start when the oven has returned to the set temperature. The specimens were removed from the oven when completed 2 hours. Temperature was reset to 154° C and allowed reaching the set temperature. The specimens were placed into oven and waited for oven to return to the set temperature. The timing to start when the over has reached the set temperature. The specimens were removed from oven when completed 11 hours.

APPENDIX-V

ROUGHNESS PARAMETERS

a) Average roughness, R_a

The average roughness, R_a , is measured in micrometers, and is defined as the arithmetic average value of the departure of the profile from the centre line throughout the sampling length [7], i.e. the portions of the profile below the centre line within a sampling length are inverted and placed above the centre line; R_a is the mean height of the resulting profile as shown in Fig. V-1.

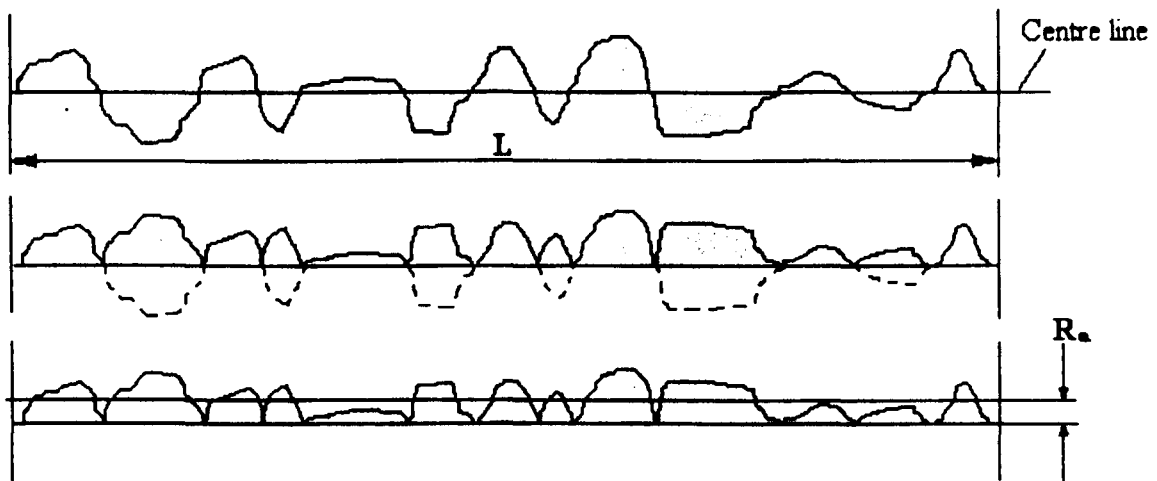


Figure V-1 Schematic representation of the surface roughness R_a

b) Roughness depth, R_t

The roughness depth, R_t , is defined as the vertical distance between the highest and lowest points within an evaluation length, so is effectively a measure of the maximum roughness, including all scratches and spurious features. It is important that this is measured from a roughness profile that has been levelled as depicted in Fig. V-2.

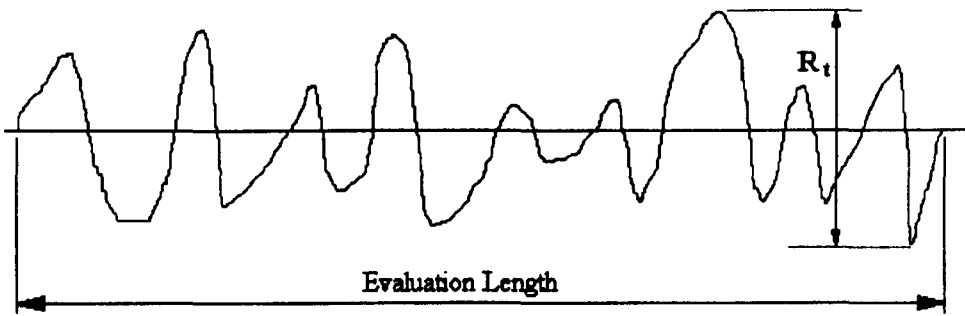


Figure V-2 Schematic representation of the surface roughness R_t .

c) Indentation peak-to-peak distance, S

S represents the peak-to-peak distance. From close analysis of the surface profile, it is possible to determine which depressions are due to a shot impact, and which are simply smaller variations in the roughness. Figure VII.3 shows an example of one such indentation, and the true distance S between the adjacent peaks. Although between the two peaks there are other smaller peaks, the easily recognisable indentation left by a piece of shot allows the true distance between peaks to be determined.



Figure V-3 Schematic representation of the peak-to-peak distance (surface irregularity caused by the impact of the shot, that resembles the size of a indentation), which is used as the parameter S .

The parameters R_t and S can be used to determine the likely stress concentration factor that will arise at the shot peening surface, K_t , which in turn, can be used in a fatigue prediction model (see *Theory*, §3.3).

APPENDIX-VI-A

RESIDUAL STRESSES THEORY

Principal advantages and disadvantages of the hole drilling technique	
Advantages	Disadvantages
– Large components	– Modest strain sensitivity
– Rapid and Inexpensive	– Limited spatial resolution
– Semi-destructive	– Interpretation of results may be a difficulty.
– Wide variety of materials: Metals, plastics, ceramics, composites, cermets, coatings, single crystals, surface treated, crystalline and amorphous, magnetic and non-magnetic.	– Limited to near surface stresses (usually between 1-30 μm).
	– Strain sensitivity varies with depth
– Portable, in situ measurements	– Induced machining stresses, although very slightly when appropriate velocity of the turbine is used, that is, the appropriate applied air pressure.
– Little specialised equipment	Surface preparation is critical and therefore demands extreme care.
– Flat and curved shapes	

a) Theoretical considerations

When residual stress distributions through the depth is measured using the incremental hole drilling technique, it usually involves taking readings from a 3-gauge rosette (Fig VI-1), through the centre of which a hole is drilled, stopping to take readings at successive depths.

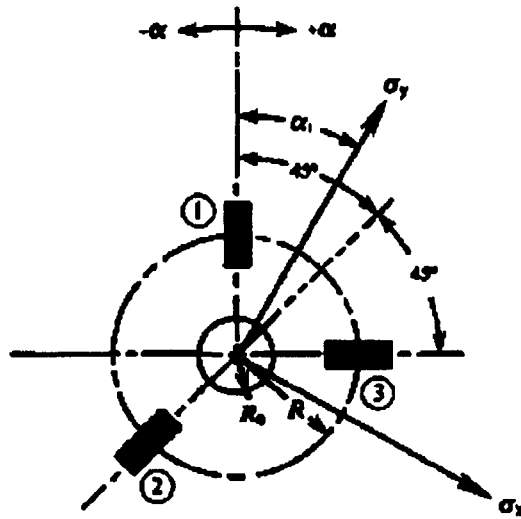


Figure VI-1 Schematic representation of the three element strain gauge rosette commonly used for measuring the released strains in the hole drilling method.

The final form for the principal stresses determined using the hole-drilling method is expressed as [8, 9]:

$$\sigma_{\max} = \frac{\varepsilon_1 + \varepsilon_3}{4\bar{A}} - \frac{1}{4\bar{B}} \sqrt{(\varepsilon_3 - \varepsilon_1)^2 + (\varepsilon_3 + \varepsilon_1 - 2\varepsilon_2)^2} \quad \langle \text{A.17} \rangle$$

$$\sigma_{\min} = \frac{\varepsilon_1 + \varepsilon_3}{4\bar{A}} + \frac{1}{4\bar{B}} \sqrt{(\varepsilon_3 - \varepsilon_1)^2 + (\varepsilon_3 + \varepsilon_1 - 2\varepsilon_2)^2} \quad \langle \text{A.18} \rangle$$

$$\tan(2\alpha) = \frac{\varepsilon_1 - 2\varepsilon_2 + \varepsilon_3}{\varepsilon_3 - \varepsilon_1} \quad \langle \text{A.19} \rangle$$

The coefficients \bar{A} and \bar{B} are the calibration coefficients which depend on the geometry of the gauge used, the elastic properties of the material and the radius and depth of the hole. Since these cannot be calculated directly from theoretical considerations they must be obtained by empirical means, i.e. experimental calibration [10] or by numerical procedures such as finite elements analysis [11].

Schajer [11] managed to incorporate intrinsically the dependence of the calibration coefficients on elastic properties by defining two dimensionless constants \bar{a} and \bar{b}

which were found to be in excellent agreement with experimental results. These new relationships are generally expressed as [8]:

$$\bar{a} = \frac{2E\bar{A}}{1+\nu} \quad \langle A.20 \rangle$$

$$\bar{b} = 2E\bar{B}$$

Note: The factors of two are included so that the constants are associated with the mean biaxial and shear stresses, $(\sigma_{\max} + \sigma_{\min})/2$ and $(\sigma_{\max} - \sigma_{\min})/2$.

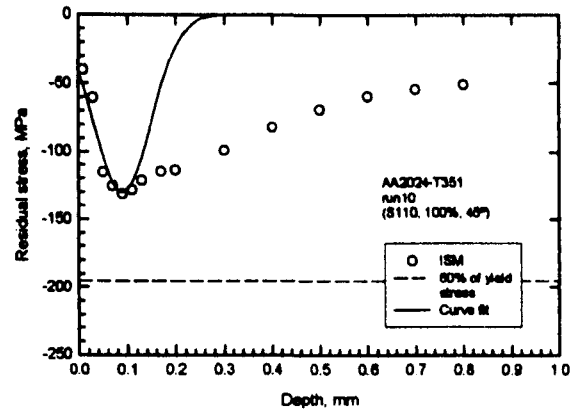
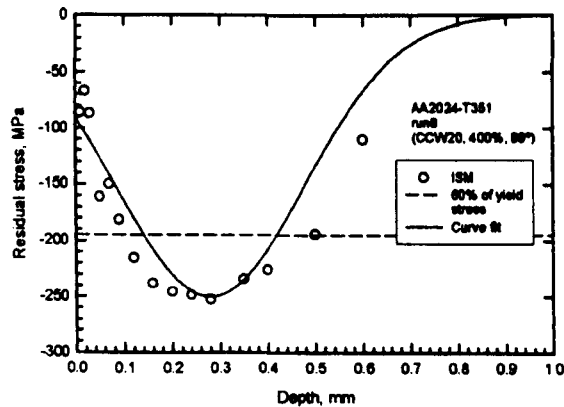
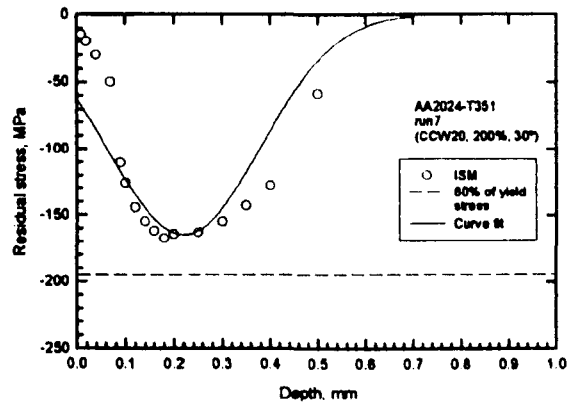
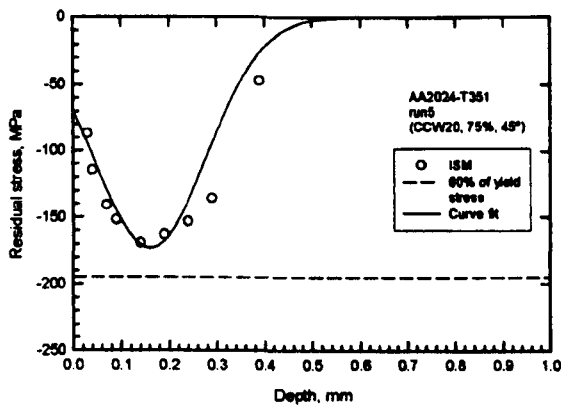
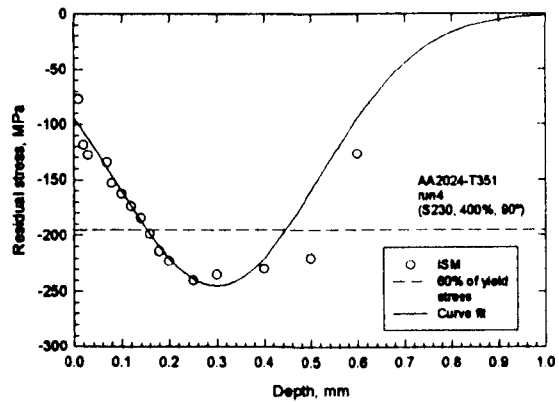
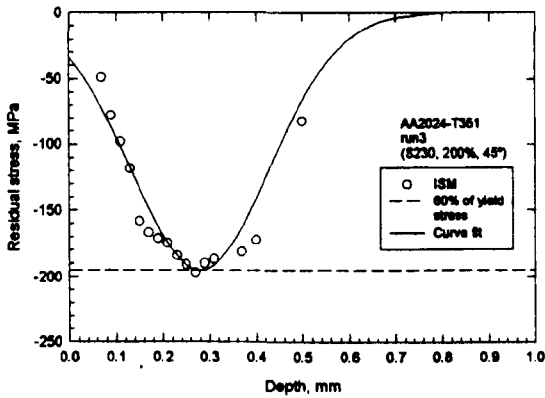
- σ_{\max} = Maximum (most tensile).
- σ_{\min} = Minimum (most compressive) principal stresses present at the hole location before drilling.
- α = Angle from the nearer principal axis to gauge number 1 (in the direction of gauge numbering, if positive; or opposite, if negative).
- $\epsilon_1, \epsilon_2, \epsilon_3$ = Strain readings at gauges 1, 2 and 3 respectively.
- E = Young's Modulus of specimen material.
- ν = Poisson's Ratio of specimen material.
- r = Ratio of gauge circle radius to hole radius.
- Z = Hole Depth.
- D = Diameter of gauge circle.

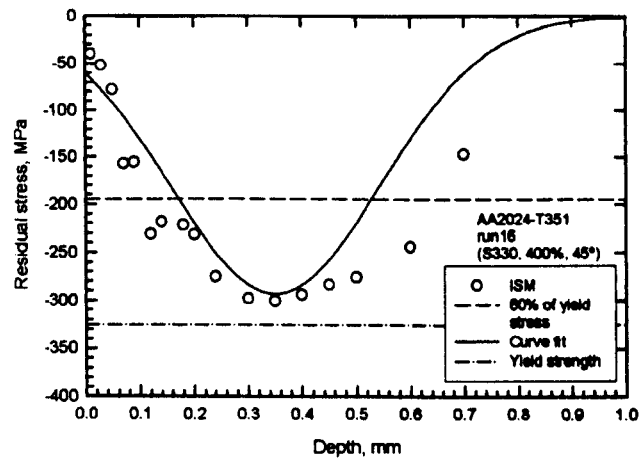
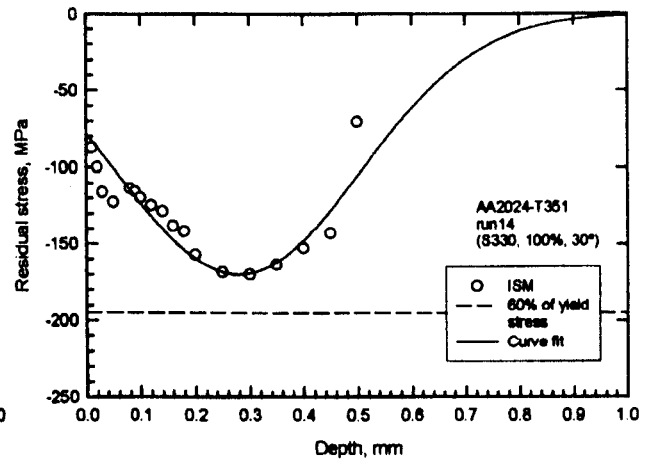
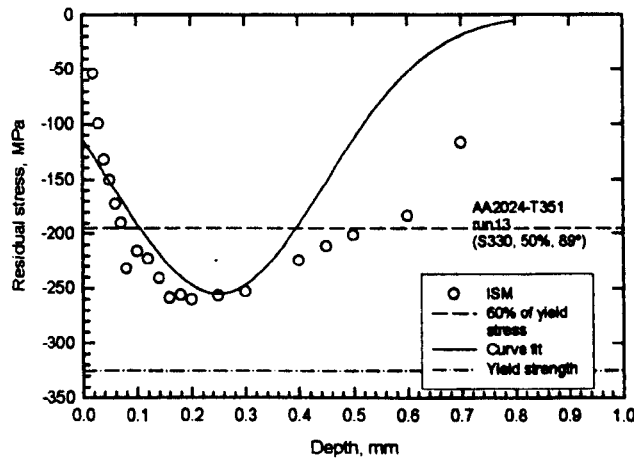
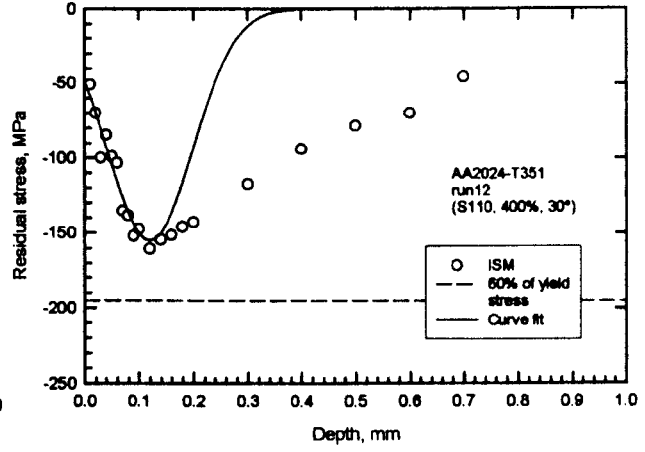
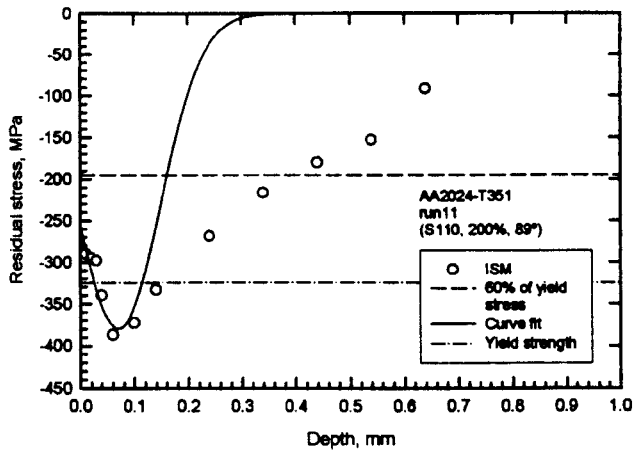
Tabulated values and graphic representations for the blind hole (as used throughout the measurements of the RS in this project) of the dimensionless constants \bar{a} and \bar{b} are found elsewhere [8, 9].

APPENDIX-VI-B

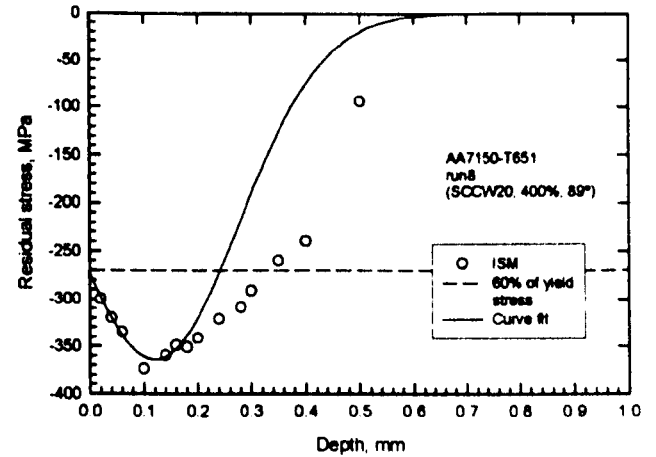
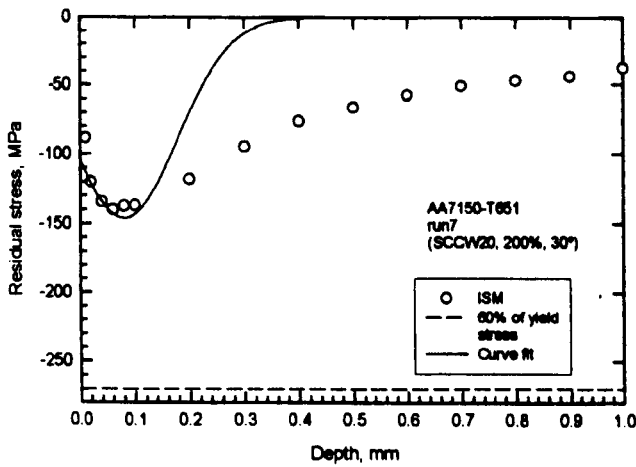
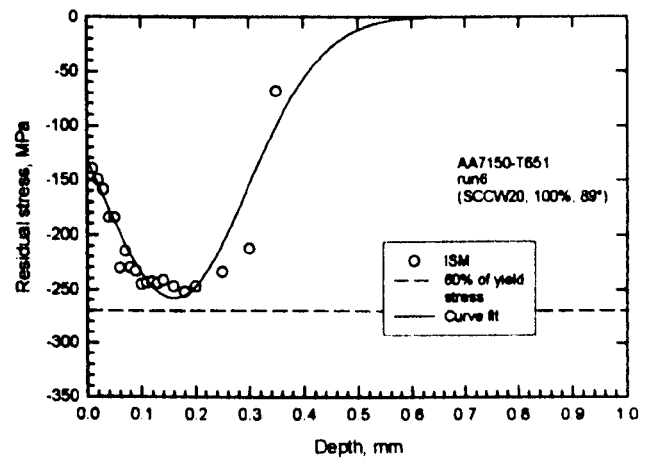
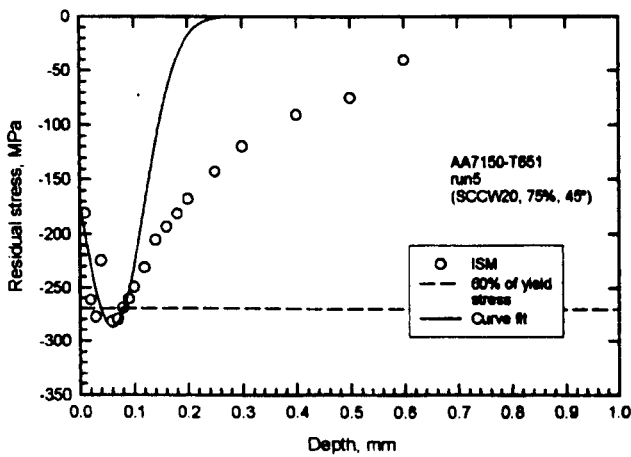
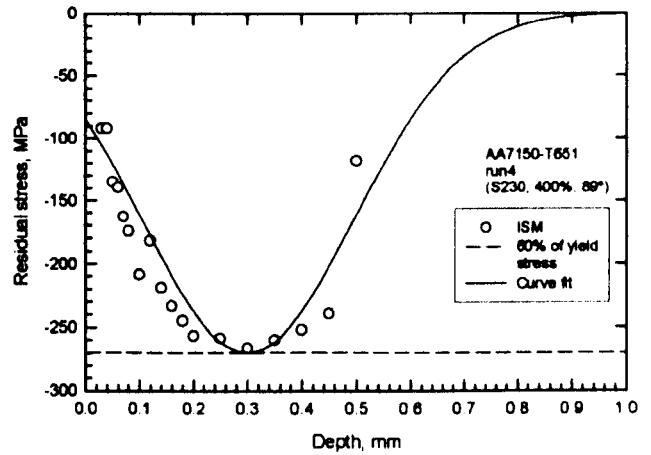
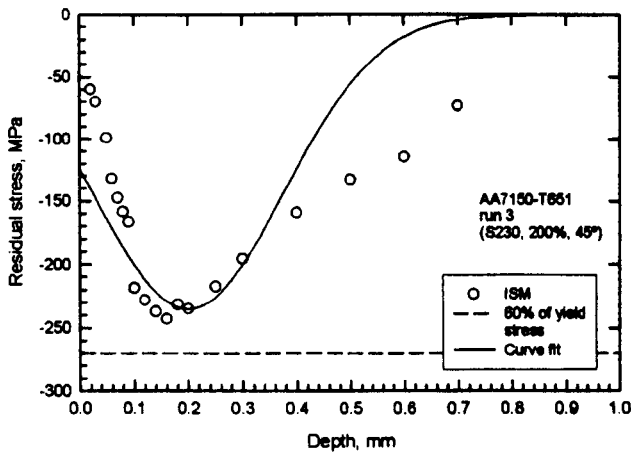
RESIDUAL STRESS RESULTS

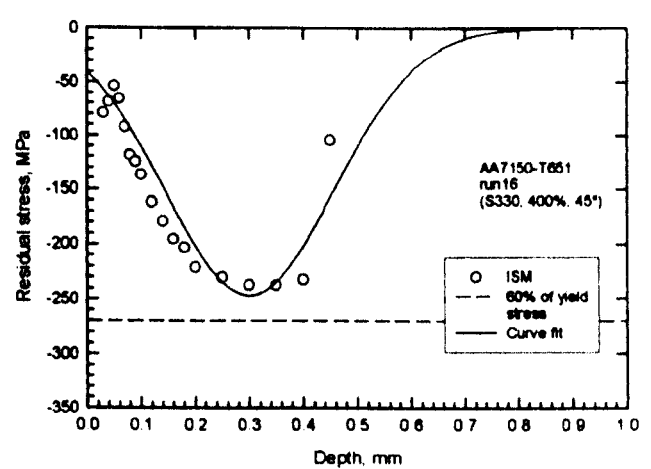
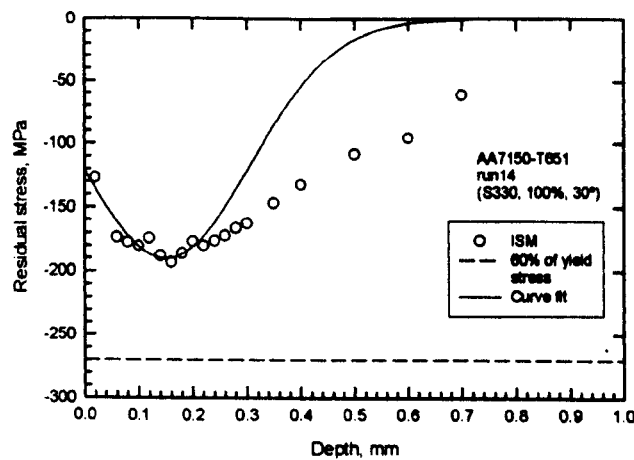
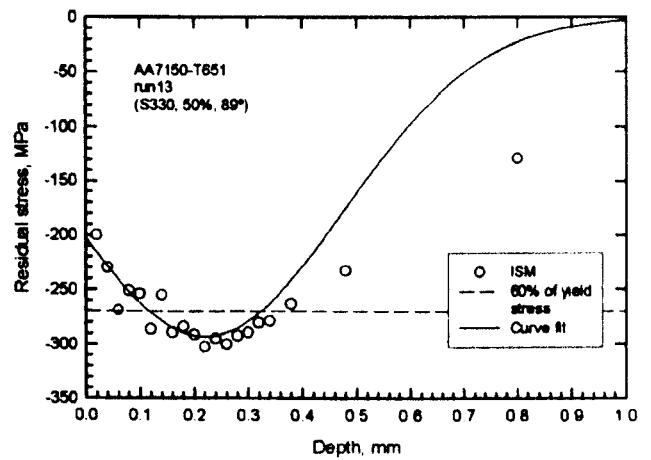
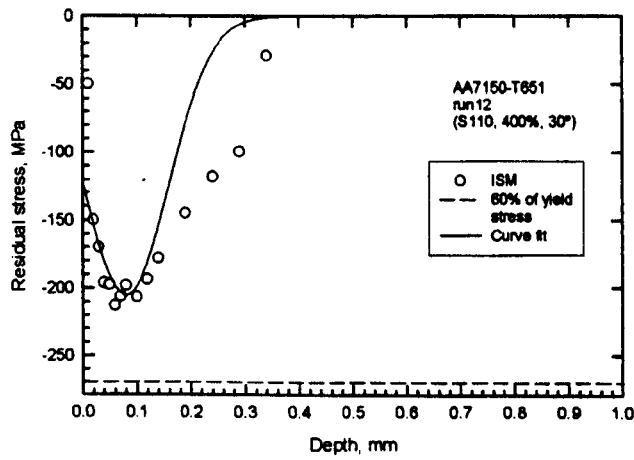
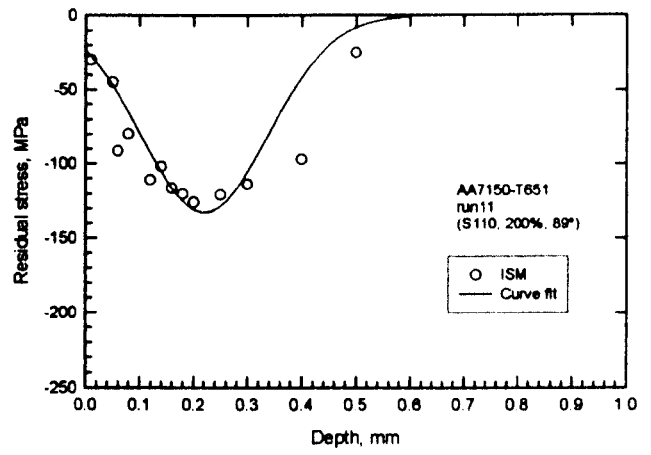
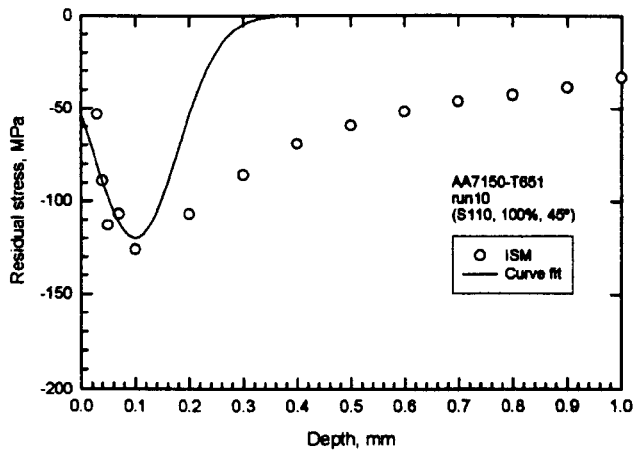
a) Residual stress distributions for AA 2024-T351 peened coupons according to the designed experiment (table 5.1.1). See § 5.1.1.2 for the rest of the plots.



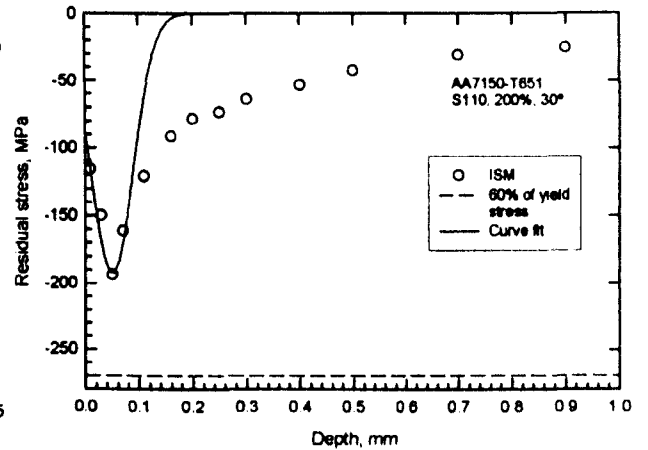
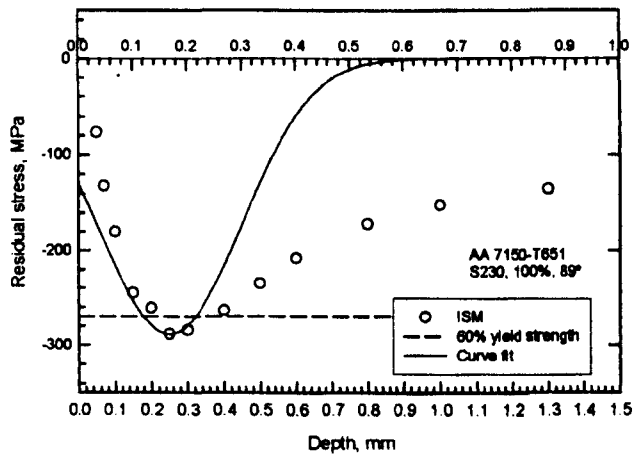
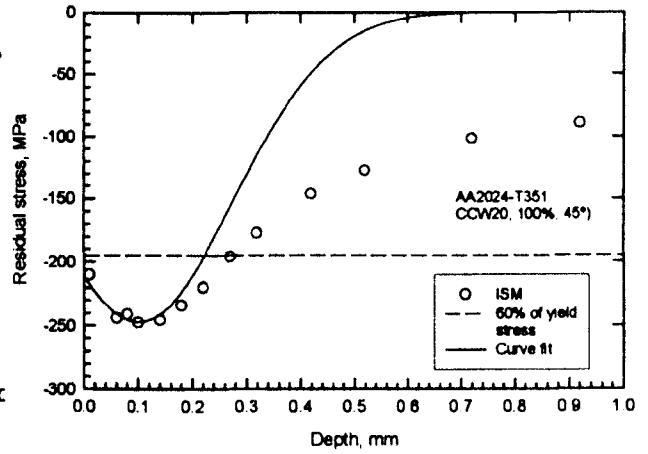
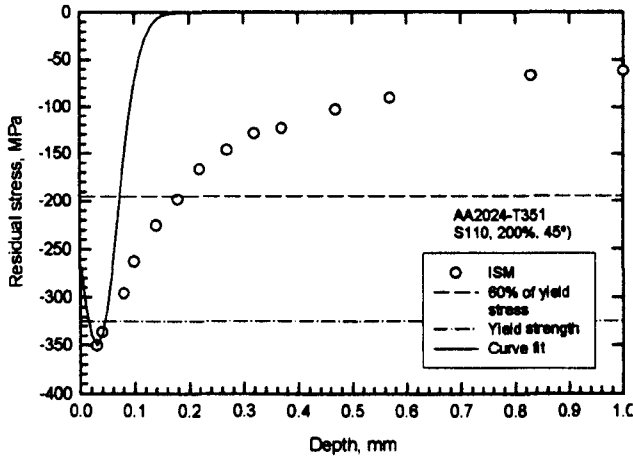


b) Residual stress distributions for AA 7150-T651 peened coupons according to the designed experiment (table 5.1.1).





c) Residual stress distributions for the AA's peened to optimum and worst conditions respectively according to table 5.2.4.



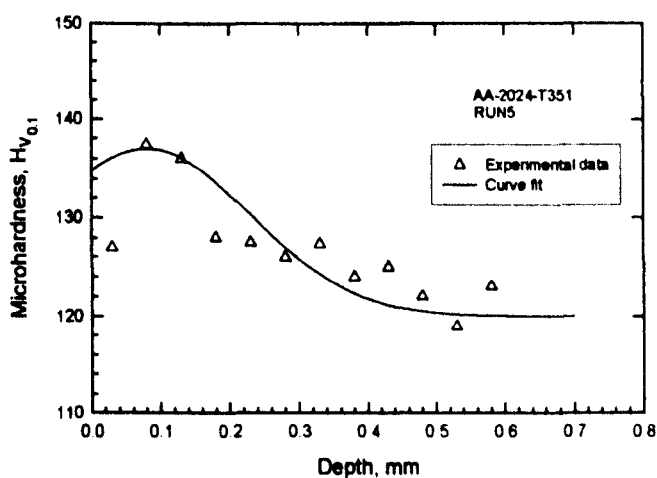
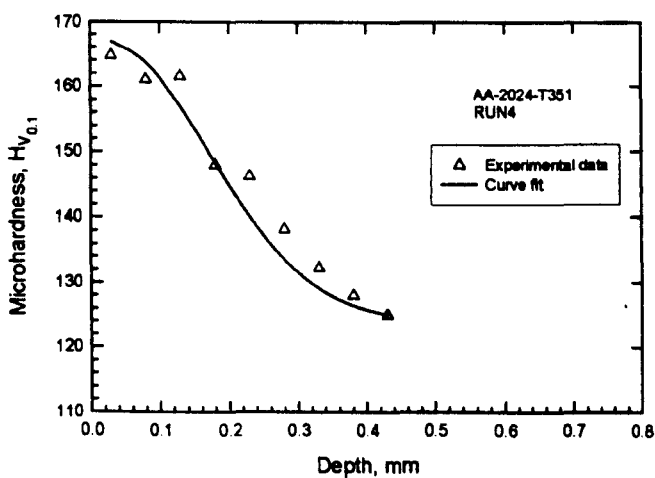
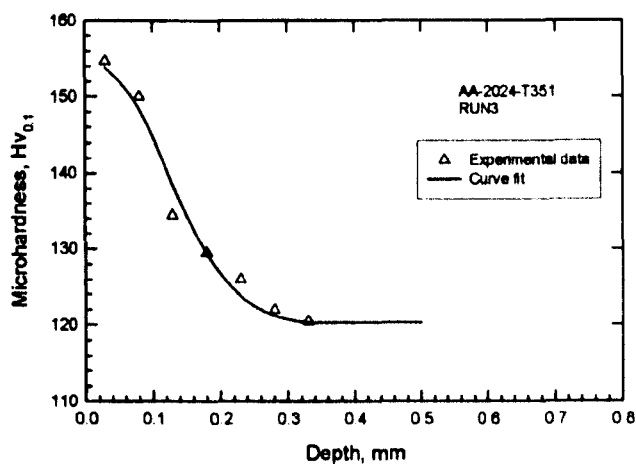
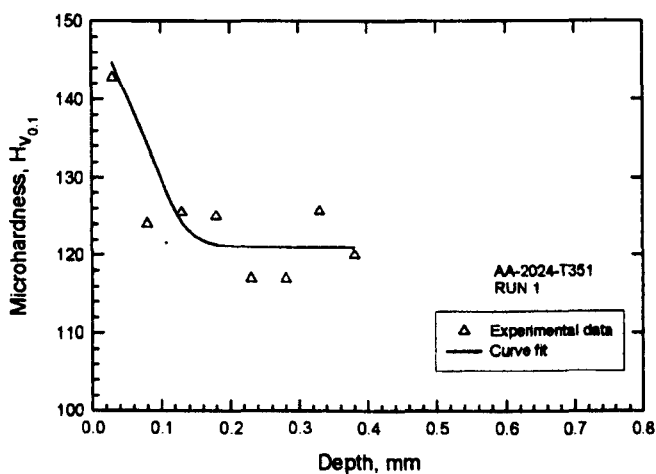
AA peened to:		A	W	Xd	B	n
AA 2024-T351	Optimum	-350	0.1	0.0300286	0	4.91758
	Worst	-247	0.45	0.10012	4.22259e-014	4.97465
AA 7150-T351	Optimum	-288.816	0.5	0.25	0	5.0142
	Worse	-192.997	0.100066	0.0500197	2.21868e-014	4.98945

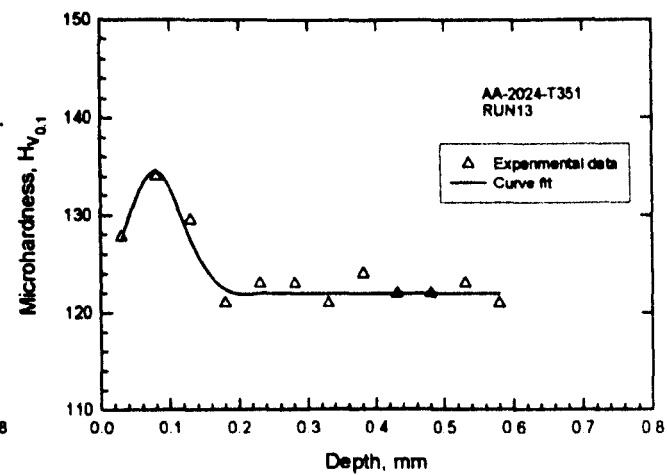
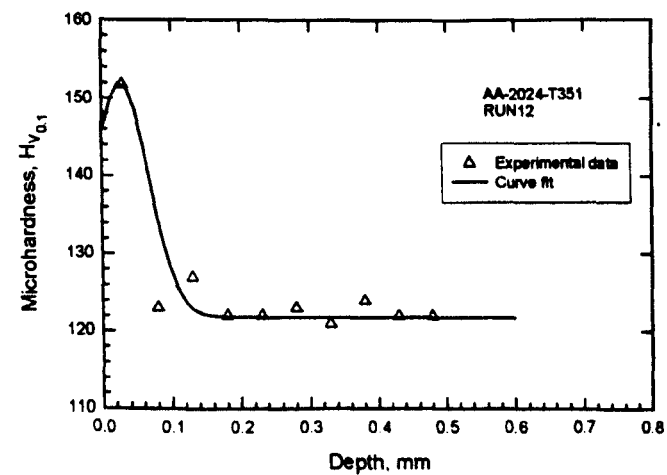
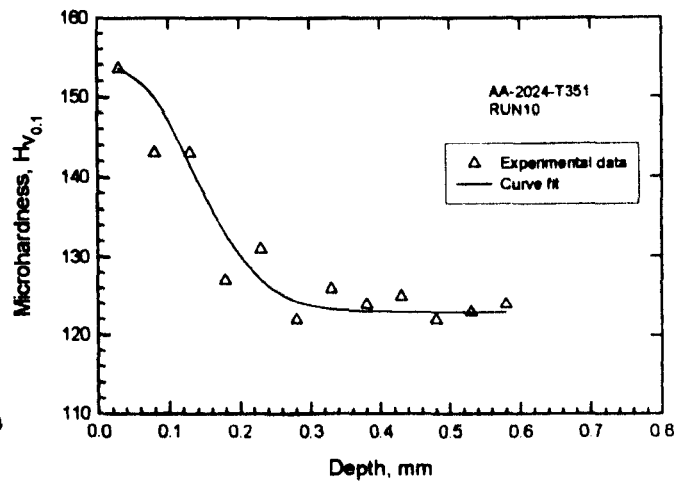
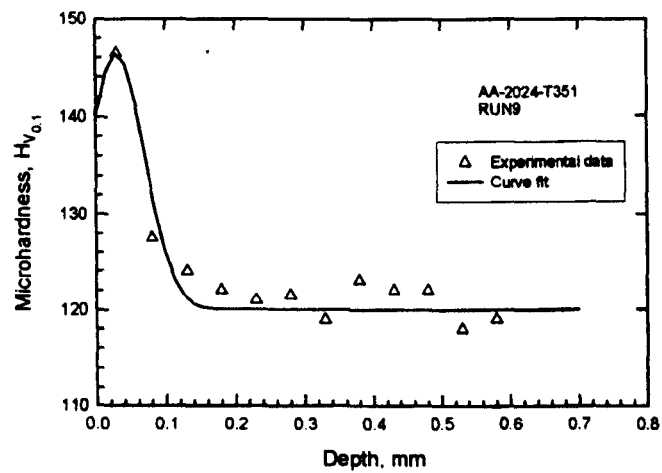
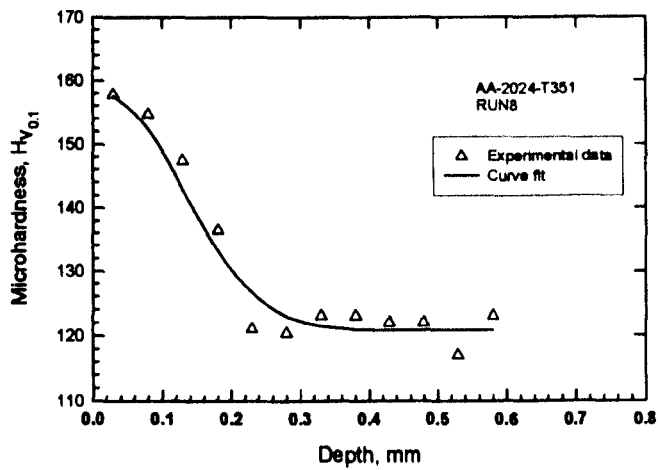
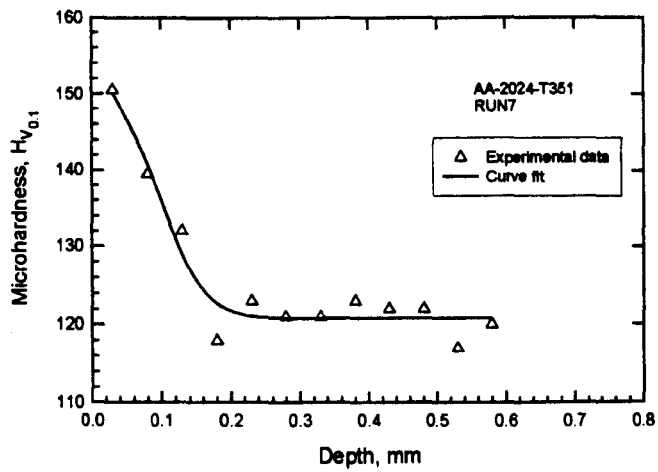
Curve fit parameters

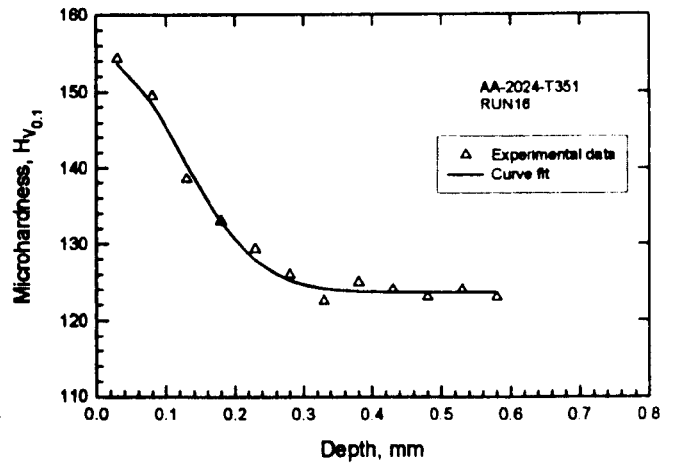
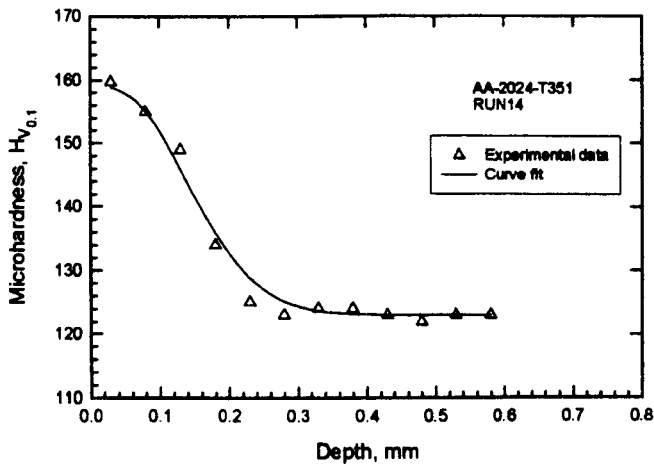
APPENDIX-VII

WORK HARDENING RESULTS

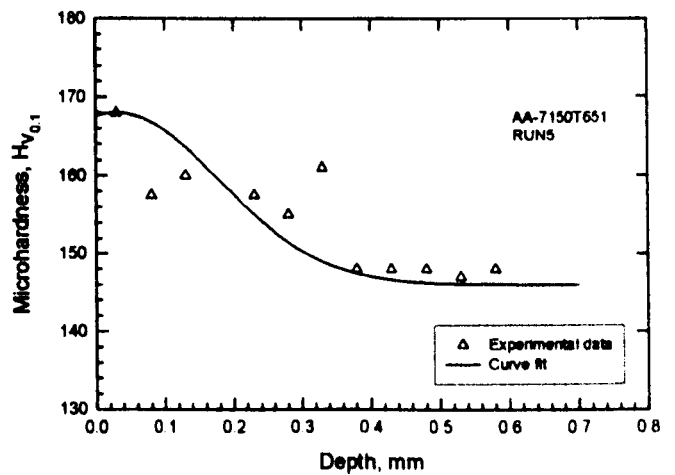
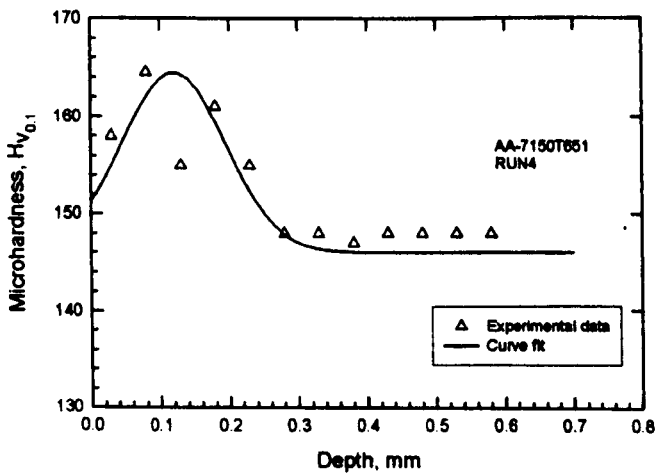
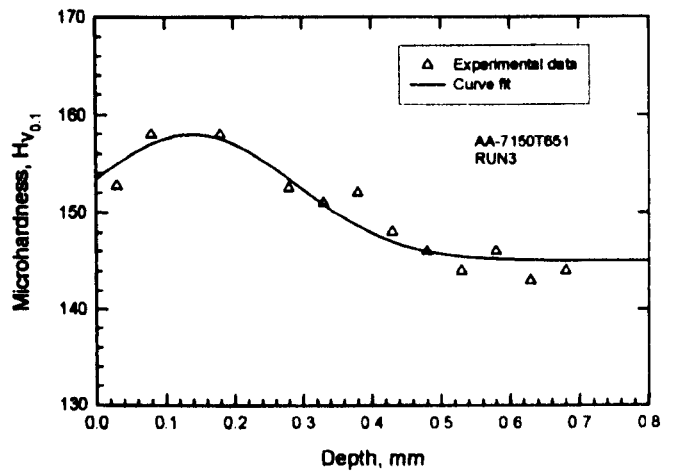
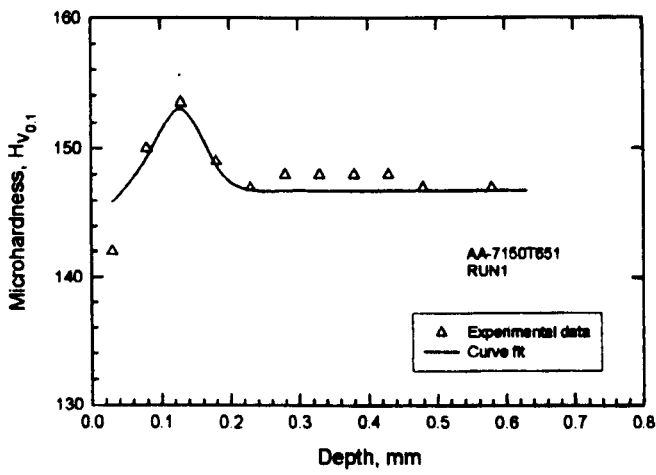
a) Microhardness distributions for AA 2024-T351 peened coupons according to the designed experiment method (table 5.1.1). N.B. Hardness distributions of runs 2,6,11 and 15 are shown in the main body of the thesis in chapter five (§ 5.1.1.3).

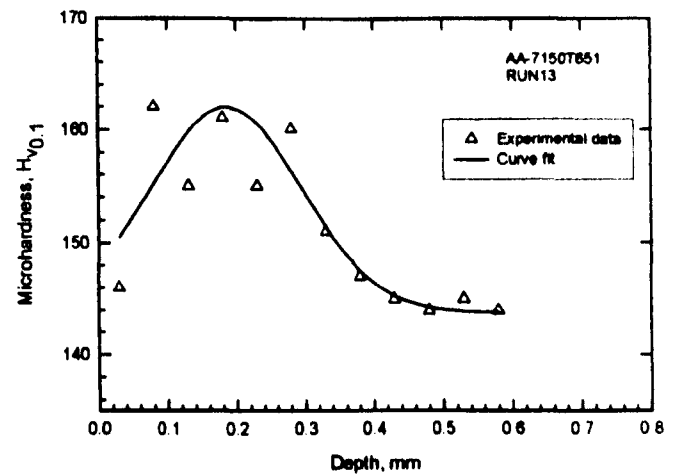
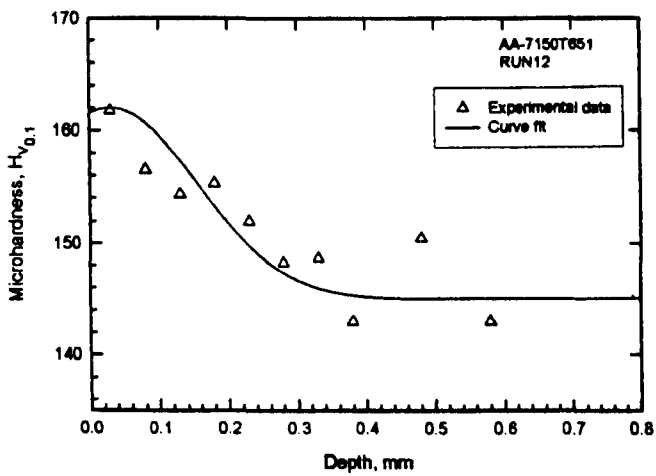
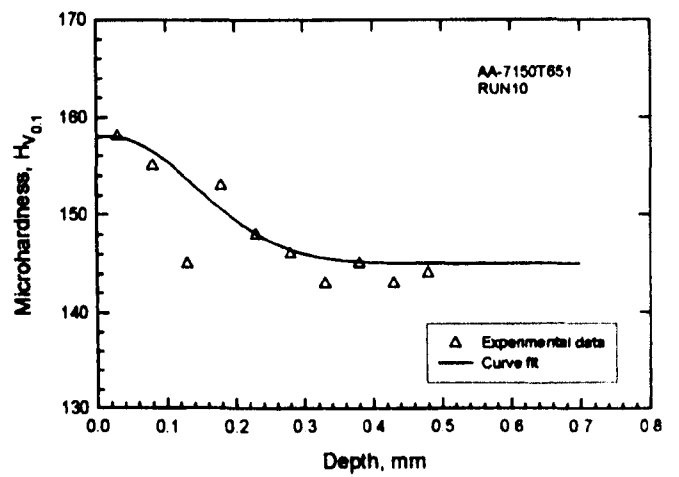
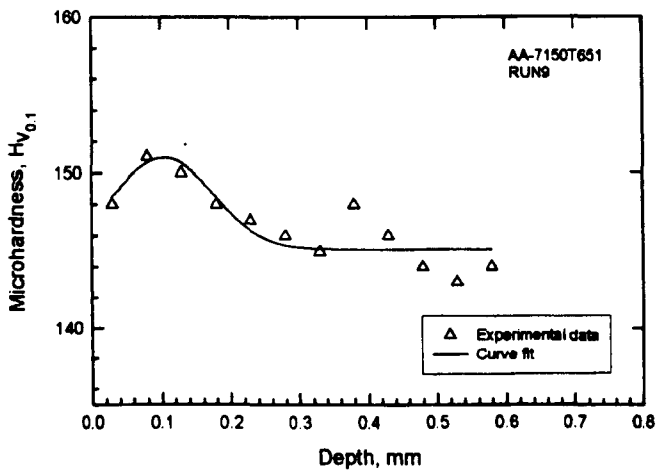
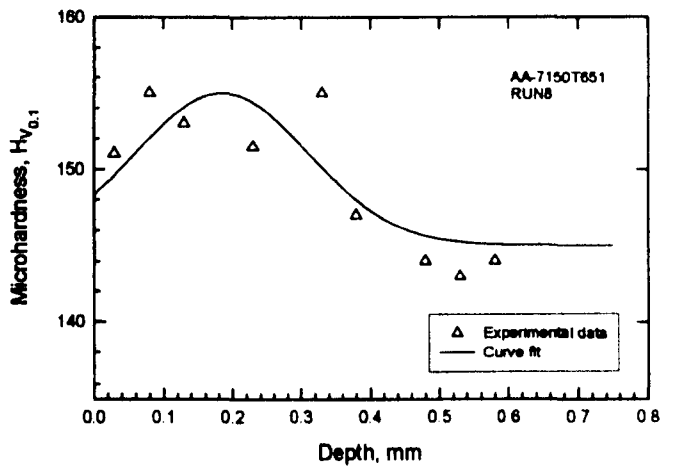
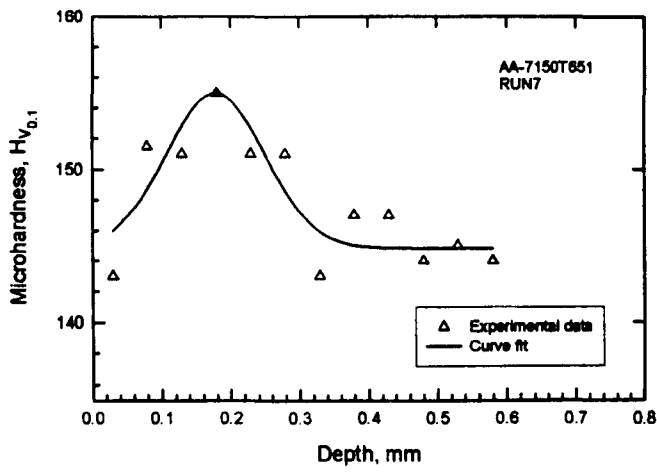


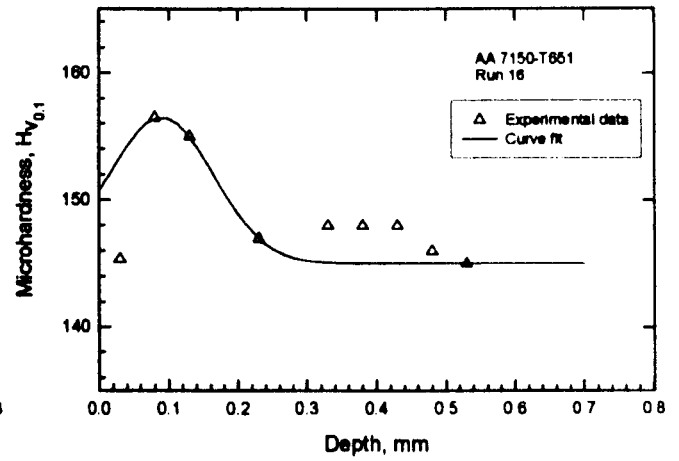
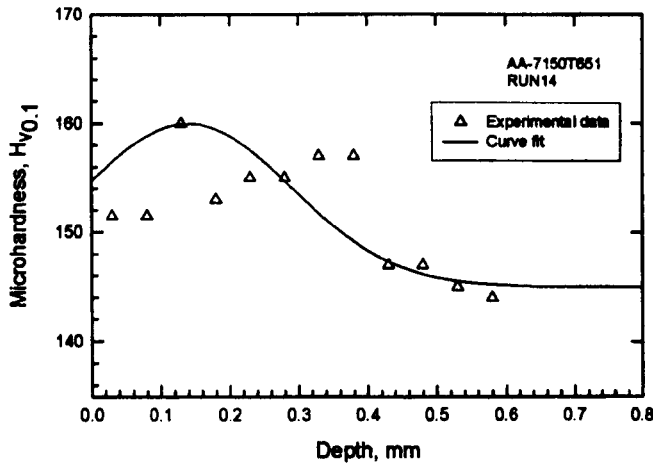




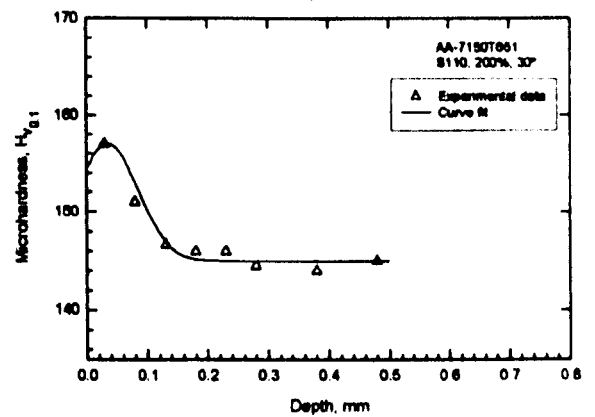
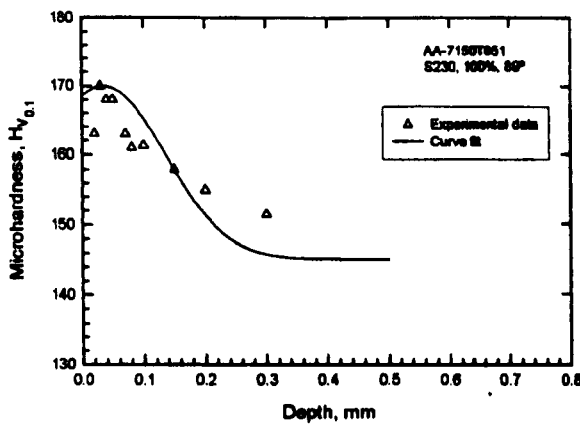
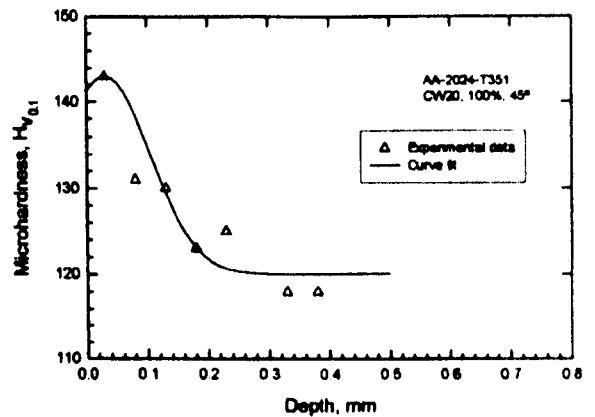
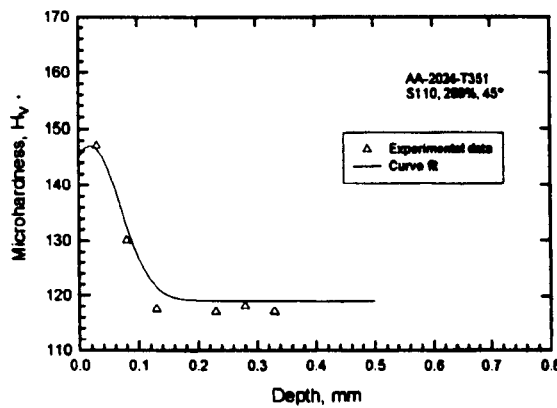
b) Microhardness distributions for AA 7150-T651 peened coupons.







c) Micro hardness distributions for the AA's peened to optimum and worst conditions respectively according to table 5.2.4.



AA peened to:		A	W	Xd	B
AA 2024-T351	Optimum	28	0.10	0.02	119
	Worst	23	0.15	0.03	120
AA 7150-T351	Optimum	25	0.2	0.035	145
	Worse	12	0.1	0.035	145

Curve fit parameters

APPENDIX-VIII

DESIGN OF EXPERIMENTS RESULTS

ANOVA table						
run	S/N	(S/N) ²	(S/N-SNtot) ²	S/N'	Source of variation factor	%Contribution
1	41.75	1743.10	17.46	44.15	12.63	
2	47.08	2216.98	1.33	45.98	0.01	
3	41.43	1716.43	20.25	46.13	0.17	
4	46.34	2147.85	0.17	47.45	9.23	
5	44.31	1963.45	2.62		Sum(22.04)	Factor A: 16.95
6	47.70	2275.26	3.13	45.52	0.69	
7	44.24	1957.04	2.86	45.30	1.59	
8	47.68	2273.84	3.08	46.51	1.36	
9	48.12	2315.47	4.80	46.39	0.85	
10	41.85	1751.05	16.68		4.49	B: 3.45
11	51.35	2636.37	29.33	47.28	7.26	
12	43.22	1868.20	7.33	45.91	0.00	
13	47.88	2292.67	3.81	45.45	0.92	
14	44.56	1985.94	1.86	45.08	2.90	
15	49.04	2404.70	9.66		11.09	C: 8.52
16	48.31	2333.99	5.67	43.44	24.71	
	45.93	33882.34		48.50	26.42	
totals	_SNtot	GTSS		43.97	15.29	
				47.80	14.00	
	33752	33882.34	130.06		80.42	D: 61.83
	S/N	S/N+TotalSS	TotalSS	45.08	2.89	
				46.94	4.07	
				45.06	3.03	
				46.64	2.03	
					12.02	E: 9.24
					Total Sums	
					130.06	100.00

Table VIII-1 Analysis of variance showing the percentage of contribution for each factor on the residual stresses of the AA-2024-T351.

where, Source of variation = $4(S/N' - S/N_{tot})^2$; %Contribution = $(\text{Sum}/\text{TotalSums})100$.

For example, the %Contribution for factor A is calculated as follows:

Source of variation = $4(44.15 - 45.93)^2 = 12.63$, $4(45.98 - 45.93)^2 = 0.01$, ... 0.17 , 9.23 .

Sum = $(12.63 + 0.01 + 0.17 + 9.23) = 22.04$, therefore,

%Contribution = $(22.04/130.06)100 = 16.95$

A	B	C	D	E	Y (Kt)	S/N	Factor	level	Y (Kt)	S/N	Effects(S/N')	Effects (Y') Kt
1	1	1	1	1	1.362	-2.684	A-shot	A1	1.547	-3.767	0.15	-0.03
2	1	2	2	2	1.553	-3.824		A2	1.689	-4.534	-0.62	0.12
3	1	3	3	3	1.659	-4.395		A3	1.558	-3.850	0.07	-0.02
4	1	4	4	4	1.616	-4.166		A4	1.499	-3.512	0.40	-0.07
5	2	1	2	3	1.556	-3.842	B-coverage	B1	1.481	-3.398	0.52	-0.09
6	2	2	1	4	1.724	-4.730		B2	1.571	-3.906	0.01	0.00
7	2	3	4	1	1.633	-4.260		B3	1.608	-4.122	-0.21	0.03
8	2	4	3	2	1.841	-5.303		B4	1.633	-4.238	-0.32	0.06
9	3	1	3	4	1.551	-3.813	C-empty	C1	1.549	-3.773	0.14	-0.02
10	3	2	4	3	1.577	-3.954		C2	1.553	-3.826	0.09	-0.02
11	3	3	1	2	1.569	-3.913		C3	1.621	-4.156	-0.24	0.05
12	3	4	2	1	1.534	-3.718		C4	1.570	-3.908	0.01	0.00
13	4	1	4	2	1.454	-3.253	D-angle	D1	1.490	-3.444	0.47	-0.08
14	4	2	3	1	1.431	-3.114		D2	1.604	-4.073	-0.16	0.03
15	4	3	2	4	1.570	-3.918		D3	1.584	-3.989	-0.07	0.01
16	4	4	1	3	1.542	-3.764		D4	1.615	-4.157	-0.24	0.04
Grand average					1.573	-3.916	E-empty	E1	1.588	-3.965	-0.05	0.01
								E2	1.570	-3.915	0.00	0.00
								E3	1.593	-4.024	-0.11	0.02
								E4	1.543	-3.759	0.16	-0.03

Table VIII-2 Response table for stress concentration of the AA 2024-T351

1	1	1	1	1	144.61	43.20	A-shot	A1	152.850	43.670	0.11	1.91
1	2	2	2	2	145.15	43.24		A2	147.683	43.374	-0.19	-3.26
1	3	3	3	3	154.74	43.79		A3	152.003	43.633	0.07	1.06
1	4	4	4	4	166.90	44.45		A4	151.243	43.574	0.01	0.30
2	1	2	3	4	135.65	42.65	B-cover	B1	140.005	42.917	-0.65	-10.94
2	2	1	4	3	147.45	43.37		B2	151.275	43.590	0.03	0.33
2	3	4	1	2	150.08	43.53		B3	155.053	43.808	0.24	4.11
2	4	3	2	1	157.55	43.95		B4	157.445	43.937	0.37	6.50
3	1	3	4	2	145.26	43.24	C-empty	C1	150.785	43.562	0.00	-0.16
3	2	4	3	1	153.50	43.72		C2	147.610	43.369	-0.19	-3.33
3	3	1	2	4	157.50	43.95		C3	154.138	43.753	0.19	3.19
3	4	2	1	3	151.75	43.62		C4	151.245	43.568	0.01	0.30
4	1	4	2	3	134.50	42.57	D-Angle	D1	151.360	43.595	0.03	0.42
4	2	3	1	4	159.00	44.03		D2	148.675	43.426	-0.14	-2.27
4	3	2	4	1	157.89	43.97		D3	149.368	43.472	-0.09	-1.58
4	4	1	3	2	153.58	43.73		D4	154.375	43.758	0.20	3.43
					150.944	43.563	E-empty	E1	153.388	43.710	0.15	2.44
								E2	148.518	43.433	-0.13	-2.43
								E3	147.110	43.340	-0.22	-3.83
								E4	154.763	43.768	0.20	3.82

Table VIII-3 Response table for work hardening of the AA 2024-T351

Run	A	B	C	D	E	Y MPa	S/N	factor	level	Y' MPa	S/N'	Effect S/N'	Effect Y'
1	1	1	1	1	1	-122.20	40.44	A-shot	A1	-240.9	46.51	-0.08	2.90
2	1	2	2	2	2	-321.78	49.98		A2	-276.0	47.71	1.12	-32.20
3	1	3	3	3	3	-235.15	46.73		A3	-190.7	44.33	-2.26	53.10
4	1	4	4	4	4	-284.55	48.90		A4	-267.6	47.81	1.22	-23.81
5	2	1	2	3	4	-287.25	48.54				46.59		
6	2	2	1	4	3	-263.95	48.29	B-cover	B1	-251.7	46.89	0.30	-7.91
7	2	3	4	1	2	-188.85	43.14		B2	-221.5	45.67	-0.92	22.32
8	2	4	3	2	1	-364.00	50.87		B3	-226.8	45.51	-1.08	16.99
9	3	1	3	4	2	-307.10	49.62		B4	-275.2	48.29	1.70	-31.41
10	3	2	4	3	1	-115.40	40.65				46.59		
11	3	3	1	2	4	-135.35	41.45	C-empty	C1	-192.2	44.50	-2.09	51.60
12	3	4	2	1	3	-205.00	45.60		C2	-290.5	48.72	2.13	-46.68
13	4	1	4	2	3	-290.35	48.95		C3	-272.8	47.74	1.15	-28.96
14	4	2	3	1	4	-184.85	43.74		C4	-219.8	45.41	-1.18	24.03
15	4	3	2	4	1	-347.95	50.74				46.59		
16	4	4	1	3	2	-247.35	47.81	D-Angle	D1	-175.2	43.23	-3.36	68.59
					Average	-243.82	46.59		D2	-277.9	47.81	1.22	-34.05
									D3	-221.3	45.93	-0.66	22.53
									D4	-300.9	49.39	2.80	-57.07
											46.59		
								E-empty	E1	-237.4	45.68	-0.91	6.43
									E2	-266.3	47.64	1.05	-22.45
									E3	-248.6	47.39	0.80	-4.80
									E4	-223.0	45.66	-0.93	20.82
											46.59		

Table VIII-4 Response table for residual stresses of AA 7150-T651

Run	A	B	C	D	E	Y Kt	S/N	factor	level	Y'	S/N'	Effect S/N'	Effect Y'
1	1	1	1	1	1	1.39	-2.839	A-shot	A1	1.471	-3.345	0.234	-0.04
2	1	2	2	2	2	1.45	-3.235		A2	1.588	-3.998	-0.419	0.08
3	1	3	3	3	3	1.50	-3.502		A3	1.484	-3.425	0.155	-0.03
4	1	4	4	4	4	1.55	-3.803		A4	1.507	-3.549	0.030	-0.01
5	2	1	2	3	4	1.44	-3.151				-14.317		
6	2	2	1	4	3	1.57	-3.926	B-cover	B1	1.424	-3.069	0.510	-0.09
7	2	3	4	1	2	1.60	-4.085		B2	1.485	-3.429	0.150	-0.03
8	2	4	3	2	1	1.74	-4.831		B3	1.516	-3.607	-0.028	0.00
9	3	1	3	4	2	1.45	-3.207		B4	1.626	-4.211	-0.632	0.11
10	3	2	4	3	1	1.44	-3.159				-14.317		
11	3	3	1	2	4	1.49	-3.476	C-empty	C1	1.525	-3.649	-0.070	0.01
12	3	4	2	1	3	1.56	-3.855		C2	1.480	-3.402	0.178	-0.03
13	4	1	4	2	3	1.43	-3.080		C3	1.541	-3.734	-0.155	0.03
14	4	2	3	1	4	1.48	-3.397		C4	1.504	-3.532	0.047	-0.01
15	4	3	2	4	1	1.47	-3.365				-14.317		
16	4	4	1	3	2	1.65	-4.355	D-Angle	D1	1.506	-3.544	0.035	-0.01
						1.51	-3.579		D2	1.528	-3.656	-0.076	0.02
									D3	1.506	-3.542	0.037	-0.01
									D4	1.510	-3.575	0.004	0.00
											-14.317		
								E-empty	E1	1.511	-3.548	0.031	0.00
									E2	1.537	-3.721	-0.141	0.02
									E3	1.513	-3.591	-0.012	0.00
									E4	1.489	-3.457	0.122	-0.02
											-14.317		

Table VIII-4 Response table for stress concentration of AA 7150-T651

Run	A	B	C	D	E	Hv	S/N	factor	level	Y' Hv	S/N'	Effect S/N'	Effect Y'
1	1	1	1	1	1	153.00	43.69	A-shot	A1	159.67	44.06	0.06	1.15
2	1	2	2	2	167.40	44.48	A2		157.50	43.94	-0.06	-1.02	
3	1	3	3	3	154.49	43.78	A3		157.00	43.91	-0.08	-1.52	
4	1	4	4	4	163.78	44.29	A4		159.90	44.08	0.08	1.38	
5	2	1	2	3	4	168.00	44.51	B-cover		175.99			
6	2	2	1	4	3	152.00	43.64		B1	158.38	43.99	-0.01	-0.14
7	2	3	4	1	2	155.00	43.81		B2	157.98	43.97	-0.03	-0.54
8	2	4	3	2	1	155.00	43.81		B3	158.87	44.02	0.02	0.36
9	3	1	3	4	2	150.60	43.56	C-empty	B4	158.85	44.02	0.02	0.33
10	3	2	4	3	1	154.50	43.78			175.99			
11	3	3	1	2	4	163.00	44.24		C1	156.18	43.87	-0.13	-2.34
12	3	4	2	1	3	159.90	44.08		C2	164.58	44.33	0.33	6.06
13	4	1	4	2	3	161.90	44.18	D-Angle	C3	154.52	43.78	-0.22	-3.99
14	4	2	3	1	4	158.00	43.97		C4	158.80	44.01	0.02	0.28
15	4	3	2	4	1	163.00	44.24			175.99			
16	4	4	1	3	2	156.70	43.90		D1	156.48	43.89	-0.11	-2.04
						158.52	44.00	D2	161.83	44.18	0.18	3.31	
								D3	158.42	43.99	-0.01	-0.09	
								D4	157.35	43.93	-0.07	-1.17	
									175.99				
								E-empty	E1	156.38	43.88	-0.12	-2.14
									E2	157.43	43.93	-0.06	-1.09
									E3	157.07	43.92	-0.08	-1.44
									E4	163.20	44.25	0.26	4.68
									175.99				

Table VIII-5 Response table for hardness of AA 7150-T651

APPENDIX-IX

FATIGUE RESULTS

Optimum peening conditions				Unpeened	
$\sigma_{\text{applied}} = 270$		$\sigma_{\text{applied}} = 240$		$\sigma_{\text{applied}} = 270$	
Half crack length μm	Cycles	Half crack length μm	Cycles	Half crack length μm	Cycles
21.46	660000 (Ni)	7.50	2050000	13.89	200000
43.50	681000	149.29	2100000	23.50	210000
64.63	702000	250.00	2120000	33.66	220000
85.00	740000	500.00	2140000	45.06	230000
104.71	775000	850.00	2150000	84.50	240000
152.08	803000	950.00	2180000	100.00	245000
284.00	811000	1012.78	2208000	150.00	247500
435.00	818000	1171.83	2216000	197.66	250000
715.93	831000	1250.00	2218000	236.79	252500
931.31	837000 (NF)	1430.68	2222000	281.07	254000
		1549.42	2226000	453.06	254920
		1560.00	2230000		
		2000.00	2235000		
		2870.43	2240000		

Table IX-1 Crack propagation results for AA 2024-T351.

Optimum peening conditions				Worst peening conditions				Unpeened	
$\sigma_{\text{applied}} = 240$		$\sigma_{\text{applied}} = 260$		$\sigma_{\text{applied}} = 255$		$\sigma_{\text{applied}} = 300$		$\sigma_{\text{applied}} = 260$	
Half crack length μm	Cycles								
10.86	110000	14.59	100000	12.21	3284000	8.91	925000	20.00	105000
16.00	162000	26.73	120000	38.34	3294000	9.00	932000	50.00	110000
19.00	166000	29.12	125280	41.82	3300000	12.28	937000	287.77	115000
22.73	190000	38.37	130000	42.50	3310000	13.72	942000	450.00	116000
29.56	200000	165.17	140000	45.00	3315000	38.48	950000		
30.50	212000	430.13	142000	54.18	3325000	118.02	956000		
32.06	230000			127.20	3330000	136.41	958000		
32.93	240000					283.61	960000		
34.47	250000					289.45	961000		
35.83	265000					326.05	962510		
36.50	280000					439.43	962900		
202.57	290000								
264.20	292400								
335.03	293000								
405.16	293424								

Table IX-2 Crack propagation results for AA 7150-T351.

PROGRAM FOR PREDICTION OF FATIGUE LIFE OF PEENED AA 2024-T351 AND AA 7150-T651 UNDER CONSTANT AMPLITUDE LOADING WRITTEN IN PASCAL CODE (by Maxim Artamonov).

```

program prog;
{ program with stress concentration and old Stresssp}
var
Ss1fl,d1:real;
angle1,angleN, stresstop,Kto,Rtm,rostart,roend,NSstart,NSstart1,dstart,dend,lchange,kstart,kend,s1le,s1ar:real;
sstart,send,dnew,dold,length1,hard1,hard2,vspeed,ff,a2,m2,s3,xb,ro,D,m,mu,sfl,sfl1,s,g,s2,s1:real;
koeff,c2a,c2xd,c2w,c2b,c2bb,c1a,c1xd,c1w,c1b,c1af,c1wf,c1bf:real; {2A,2Xd,2W,2B=koff S2 for shot peening}
f2: text;
cause,dcase,dcase1,dcase2:byte;
nameAl,namefail,note:string;
TRatio,RSequ,CorCr,Esfl,Bsfl,stop1,eqs1sp:boolean;
pn:integer;
{pns,pnc:real;}
{ff: number cycles, sfl=Sfl-fatigue limit,mu=MU-Poisson ratio,m=M,s=applied stress,g=the shear modules,
xb=x/c=1}

```

Procedure RecResStr;

```

begin
writeln(f2,'Maximum residual stess =(c1b+c1a):6:2);
writeln(f2,'Minimum residual stess =',c1b:6:2);
writeln(f2,'depth to maximum residual stess Xd=',c1xd:6:2);
writeln(f2,'W-width of the residual stess =',c1w:6:2);
writeln(f2,'use (or not) equation limit res. stress ',eqs1sp);
writeln(f2,'use (or not) equation without use integral ',RSequ);
end;

```

Procedure RecTCr;

```

begin
write(f2,' type crack= ');
if CorCr then write(f2,'corner crack')
else write(f2,'surface crack');
writeln(f2,' angle observation point =',angleL:3:0 );
end;

```

procedure RecordData;

```

begin
writeln(f2,NameAL);
writeln(f2,'Beginning length of crack=',NSstart1:1:2);
RecResStr;
writeln(f2,'Maximum S2 stess =(c2b+c2a):6:2);
writeln(f2,'Minimum S2 stess =',c2b:6:2);
writeln(f2,'depth to maximum S2 stess Xd=',c2xd:6:2);
writeln(f2,'W-width of the S2 stess =',c2w:6:2);
writeln(f2,'Koeff. of transfer Vickers to flow stress Hard1 =',hard1:6:2,' Hard2 =',hard2:6:2);
writeln(f2,'size of grain D before and behind ',lchange:3:0,' mk =',dstart:3:3,' and ',dend:3:3);
writeln(f2,'Koeff before and behind ',lchange:3:0,' mk =',kstart:3:3,' and ',kend:3:3);
if TRatio then writeln(f2,'Use linear eq. change ratio')
else writeln(f2,'Use eq. change ratio = (1-C/x)');
writeln(f2,'grain boundary width before and behind ',lchange:3:0,' mk =',rostart:1:4,' ',roend:1:4);
writeln(f2,' The angle (from side surface) line grown crack =',angleN:3:1,' and direction cal. residual
stress=',angleL:3:1);
write(f2,'The shear modules G=',g:7:1);writeln(f2,' The Poisson ratio=',mu:2:2);
writeln(f2,'A2=',a2,' m2=',m2:5:2);
writeln(f2,'Rtm=',Rtm,' Kto=',Kto:5:2);
writeln(f2,'Yield stress =',stresstop:3:0,' MPa');

```

```

RecTCr;
end;

```

procedure Al2024;

```

begin
s1le:=0;s1ar:=0;Bsfl:=true;CorCr:=true;eqs1sp:=false;Esfl:=false;
stop1:=false;RSequ:=false;TRatio:=false;
angleN:=0;

```

```

NameAl:='Allou AL 2024';

stresstop:=325;
NSstart1:=0.2;
kstart:=0.3304;
kend:=0.6;coeff:=kstart;
ro:=0.2;g:=27200;mu:=0.3;a2:=5000;m2:=1.8;

sfl1:=240;sfl:=240;
Sstart:=270;Send:=310;

dstart:=42;dend:=52.9;

lchange:=250;
rostart:=dstart/100;
roend:=dend/100;
s:=272;
hard1:=3.85;hard2:=-136.9;

Rtm:=30.1;Kto:=1.36;
c1a:=150;c1xd:=120;c1wf:=220;c1w:=560;c1bf:=0;c1b:=0;
c2a:=28;c2xd:=40;c2w:=230;c2b:=125;

angleL:=45;d:=dstart;angleN:=0;
end;

procedure Al7150;
begin
sile:=0;slar:=0;Bsfl:=true;CorCr:=true;eqslsp:=false;Esfl:=false;
stop1:=false;d:=dstart;RSequ:=false;TRatio:=FALSE;
angleN:=0;

NameAl:=' Allou AL 7150';
stresstop:=510;Sstart:=381;Send:=510;
NSstart1:=0.4;kstart:=0.3304;
kend:=0.6;coeff:=kstart;
g:=28070;mu:=0.3;a2:=300;m2:=1.5;
sfl:=380;sfl1:=350;
dstart:=7.85;dend:=9.34;
lchange:=100;
rostart:=dstart/100;
roend:=dend/100;
s:=420;
hard1:=3.215;hard2:=15.548;
c2a:=23;c2xd:=50;c2w:=280;c2b:=152;
c1a:=310;c1xd:=100;c1w:=120;c1b:=0;
c1wf:=120;c1bf:=0;
Rtm:=33.0;Kto:=1.39;
angleL:=45;d:=dstart;angleN:=0;
end;

function lengthAN(x,y,z:real):real;{length x-n1 y-i z-angle}
begin
{al:=coeff/(sqrt(1+coeff*coeff))*(x*(y*d/2+ro)-Rtm/2);}
{lengthAN:=sqrt((x*(y*d/2+ro)-Rtm/2)/(1-sqr(sin(z*Pi/180))+sqr(sin(z*Pi/180))*sqr(coeff)))};
{lengthAN:=(x*(y*d/2+ro)-Rtm/2)/sqrt(1+sqr(sin(z*Pi/180))*(sqr(coeff)-1));}
lengthAN:=(x*(y*d/2+ro)-Rtm/2)*sqrt((1+sqr(sin(angleN*Pi/180))*(sqr(coeff)-1))/(1+sqr(sin(z*Pi/180))*(sqr(coeff)-1)));
end;

function lengthCS(x:real):real;
begin
if CorCr then begin
if angleL>45 then lengthCS:=x*sqrt(1-sqr(sin(angleL*Pi/180)))
else lengthCS:=x*sin(angleL*Pi/180);
end
end;

```

```

else lengthCS:=x*sqrt(1-sqr(sin(angleL*Pi/180)));
end;

procedure NewSfl;
var a1,q1,b1:real;
begin
if Rtm = 0 then sfl:=sfl1
else begin
a1:=Rtm/Dstart*2;b1:=1/(Kto-1)*2.1*Rtm/dstart*2;
q1:=1/(a1*a1-b1*b1)*(a1*sqrt(sqr(a1+1)-(a1*a1-b1*b1))-b1*(a1+1));
sfl:=sfl1/(a1+b1)*sqrt(a1/sqrt(q1*q1+1)+b1/q1);
end;
end;

procedure NewSfl1;
var z:real;
begin
z:=sfl1+c1a*exp(-2*sqrt(c1xd)/sqrt(c1wf))+c1bf;
if z> send then send:=z+50;
sfl:=z;
end;

FUNCTION arccos(x:real):real;
begin
arccos:=arctan(x/sqrt(1-x*x))+pi/2;
end;
FUNCTION N2(x: real):real;
begin
N2:=(x*D/2)/((x*d/2)+ro); {x=i}
end;

FUNCTION Scon(x,y: real):real; {x=n,y=i}
var al,sconn,rmid:real;
begin
al:=x*(y*d/2+ro);

Sconn:=s*((Kto-1)*Rtm/2/al+1);
{Sconn:=s*((Kto-1)*Rtm/(al)+1);}
if sconn>=stresstop then begin
{scon:=stresstop+(sconn-stresstop)*(stressc-stresstop)/(ec*E+(stressc-stresstop));}
scon:=stresstop; end
else scon:=sconn;
{Sconn:=sconn;}
end;

FUNCTION mi(x: real):real; {orientation factor}
begin
{mi:=1+0.5*ln(x);}
if x=1 then mi:=1
else mi:=1+2.07*exp(1.86*ln(2/Pi*arctan(0.522*(x-1)))); {x=i}
end;

FUNCTION far(z,y:real):real; {s arrest z:=s1,y=i}
begin
if y = 1 then far:=mi(y)*(sfl-z)/sqrt(y)+z
else far:=mi(y)*(sfl-s1fl)/sqrt(y)+z;
end;

FUNCTION fs3(x,y,z,b,Scon1: real):real;
begin
fs3:=((x-y)*arctan(z/sqrt(1-z*z))-x*arctan(b/sqrt(1-b*b))+Pi/2*Scon1)/arccos(b);
{x=S2,y=S1,z=N1,b=N2 scon1 = applied stress}
end;

FUNCTION s2x(x: real):real; {after shot peening}
begin
s2x:=Hard1*(c2a*exp(-2*sqrt(x-c2xd)/sqrt(c2w))+c2b)+hard2;
end;

```

```

FUNCTION s2sp(x,y: real):real; {after shot peening}
var al:real;
begin {dimensioned!}
{x,y=A,z=Xd,b=W,dd=B}
{al:=(x*(y*d/2+ro)-Rtm);}
{ koefl/(sqrt(1+koefl*koefl))*((x*(y*d/2+ro)-Rtm/2));}

al:=lengthCS(lengthAN(x,y,angleL));
s2sp:=s2x(al);

end;

FUNCTION s1x(x: real):real; {x-length}
var S1xtm:real;
begin
if x>c1xd then s1xtm:=((c1a-c1b)*exp(-2*sqrt(x-c1xd)/sqrt(c1w))+c1b)
else s1xtm:=((c1a-c1bf)*exp(-2*sqrt(x-c1xd)/sqrt(c1wf))+c1bf);

if ((s1xtm>stresstop) and (eqs1sp)) then s1xtm:=stresstop;
s1x:=s1xtm;
end;

FUNCTION s1sp(x,y: real):real; {after shot peening x=n,y=i}
var kk,al,als,sum1,vir2,steps2:real;
nns,ns:word;
begin

if RSequ then s1sp:=s1x(lengthCS(lengthAN(x,y,angleL)))
else begin
al:=lengthAN(x,y,angleL);
sum1:=0;
nns:=40;
steps2:=al/nns;
for ns:=0 to nns do
begin
als:=ns*steps2;
vir2:=s1x(lengthCS(als));
if odd(ns) then kk:=4
else kk:=2;
if ((ns=0) or (ns=nns)) then kk:=1;
sum1:=sum1+kk*vir2;
end;
s1sp:=sum1/al*steps2/3;
end;

end;

FUNCTION ncr(y,b,z,Scon1: real):real;
{var ncr1:real;}
begin
ncr:=cos(pi/2*(Scon1-far(z,y))/(b-z));{y=i,b=s2 z=s1 Scon =s aplaind mod con}
{ if ncr1>1 then write('exit');}
ncr:=ncr1;}
end;

procedure change2(y:real);
var x:real;
begin
y:=y-Rtm/2;
If TRatio then begin
if y<lchange then koefl:=(y-Nsstart1*(dstart/2+ro))*(kend-kstart)/(lchange-Nsstart1*(dstart/2+ro))+kstart
else koefl:=kend;
end
else begin
x:=1-(1-kend)*lchange/y;
if y<lchange then begin
if x<kstart then koefl:=kstart
else koefl:=1-(1-kend)*lchange/y;

```

```

                end
            else koeff:=kend;
        end;
    end;
end;

procedure change1(x:integer;y:real); {x=i,y=ns}
var alen,kold,knew:real;
begin
    alen:=(x*d/2+ro)*y;
    dold:=d;kold:=koeff;
    if alen<(lchange+Rtm/2) then
        begin
            dnew:=dstart;
            ro:=rostart;
            {   knew:=kstart;}
            {   knew:=(alen-Nsstart*(d/2+ro))*(kend-kstart)/(lchange-Nsstart*(d/2+ro))+kstart;}
            end
        else
            begin
                dnew:=dend;
                ro:=roend;
                {   knew:=kend;}
            end;
        end;
end;

if x=1 then begin dnew:=dold;ro:=rostart;knew:=kstart; end;

d:=(2*dnew+(x-2)*dold)/x;
{koeff:=knew;}
change2(alen);
{koeff:=(2*dnew*knew+(x-2)*kold*dold)/x/dold;}
{s1ar:=area(alen);s1le:=alen;}
end;

function speen1 (c2,q2:real):real; {c2=i,q2=ns  find nc peening}
var
    m,x,y,q1:double;
    qq:integer;
begin
    m:=1E-10;
    q1:=1;
    x:=(q1-ncr(c2,s2sp(q1,c2),s1sp(q1,c2),Scon(q1,c2)));
    y:=(q2-ncr(c2,s2sp(q2,c2),s1sp(q2,c2),Scon(q2,c2)));

    if (((x>0) and (y>0)) or ((x<0) and (y<0))) then
        begin
            cause:=2;
            stop1:=true; exit;
        end;

    qq:=1;
    repeat
        x:=(q1+q2)/2;
        y:=(x-ncr(c2,s2sp(x,c2),s1sp(x,c2),Scon(x,c2)));
        {writeln(x,y);}
        qq:=qq+1;
        if y>0 then q1:=x
            else q2:=x;
        until ((abs(y)<m) or (qq=250));

    if qq=250 then
        begin
            cause:=2;
            stop1:=true; exit;
        end;

    speen1:=x;
end;

```

```

function cod(x,y,z,a,nn1,nn2:real):real;
{x=i,y=s2,z=s1,a=s3,nn1=nn1,nn2=nn2}
var
cosh22,cosh41,cosh42,codd:real;
begin
cosh22:=2*nn1*ln(abs((1+nn1*nn1)/2/nn1)+sqrt(sqrt((1+nn1*nn1)/2/nn1)-1));
cosh41:=(nn1-nn2)*ln(abs((1-nn2*nn1)/(nn2-nn1))+sqrt(sqrt((1-nn2*nn1)/(nn2-nn1))-1));
cosh42:=(nn1+nn2)*ln(abs((1+nn2*nn1)/(nn2+nn1))+sqrt(sqrt((1+nn2*nn1)/(nn2+nn1))-1));

codd:=2*(x*d*0.5+ro)*(1e-6)*(1-mu)/g/pi*((y-z)*cosh22+(a-y)*(cosh42-cosh41));
{if x=2 then begin
writeln(codd,(x*d/2+ro),y,z,a,nn1,nn2);end;}
cod:=codd;
end;

function intspar(x1,ns,nc:real;nn:integer):real;{for peening x1=i}
var n,k :integer;
st,l,n2,s1,s2,s3,c1,c2:double;
sum:double;
begin
n2:=x1*d*0.5/(x1*d*0.5+ro);
sum:=0;
st:=(nc-ns)/nn;
for n:=0 to nn do
begin
l:=ns+n*st;
s2:=s2sp(l,x1);s1:=s1sp(l,x1);s3:=fs3(s2,s1,l,n2,Scon(l,x1));c2:=cod(x1,s2,s1,s3,l,n2);
{writeln(l2,'l=',l*(x1*d*0.5+ro),' s1=',s1,' s2=',s2,' s3=',s3,' codd=',c2,' dA/dN=',exp(-m2*ln(c2)));}
{writeln(' l=',l*(x1*d*0.5+ro),' s1=',s1,' s2=',s2,' codd=',c2);}
if c2<0 then begin
{write ('stop') ;}
cause:=1;stop1:=true;exit;
end;
if odd(n) then k:=4
else k:=2;
if ((n=0) or (n=nn)) then k:=1;
sum:=sum+k*exp(-m2*ln(c2));
end;
intspar:=sum/a2/3*st*(x1*d*0.5+ro)*1E-6;
end;

function intsp(x1,ns1,nc1:real):real;{for peening x1=i}
var nn,nn1 :integer;
ns,nc:real;
sum:double;
begin
nn1:=20;nn:=20;
ns:=ns1;nc:=((nc1-ns1)/nn*(nn-1)+ns1);sum:=0;
sum:=intspar(x1,ns,nc,nn);
if stop1 then exit;
ns:=nc;nc:=nc1;
sum:=sum+intspar(x1,ns,nc,nn1);
if stop1 then exit;
intsp:=sum;
end;

procedure start1;{for peening}
var xn,pn,pn4,nn:integer;
meglen:byte;
dstart1,pns,pnc,sec,al,als,ndcycl:real;
begin
meglen:=1;dstart1:=dstart;
koef:=kstart;
ro:=rostart;
ff:=0;length1:=0;

d:=Rtm+dstart1;Nsstart:=(Rtm/2+Nsstart1*(dstart1/2+ro))/(Rtm/2+(dstart1/2+ro));

```

```

{d:=dstart;Nsstart:=Nsstart1;}

pns:=NSstart;
als:=(d/2+ro)*pns;

pnc:=speen1(1,pns);
if stop1 then exit;
Ss1fl:=sisp(pnc,1);

for pn4:=1 to 70 do
begin
pn:=pn4*2-1;

change1(pn,pns);
if pn<>1 then pns:=pnc*(pn-2)*dold/pn/d;
pnc:=speen1(pn,pns);
al:=(pn*d/2)*pnc;
als:=(pn*d/2)*pns;
if stop1 then exit;
ndcycl:=intsp(pn,pns,pnc);
ff:=ff+ndcycl;
if stop1 then exit;
{writeln(' ',pn4,' ',pnc,' ',ff);}
{writeln(' ',pn4,' len= ',al,' ',sqrt(d1/d/pn),d,d1);}
{writeln(' ',pn4,' a=',al:3:1,' ns=',pns,' nc=',pnc,' s1=',s1:3:2,' s2=',s2:3:2,' ',ff:2:4);}

if((((al-als)/ndcycl)>1) and (meglen=1)) then begin
length1:=al/koeff;meglen:=0;
{exit;}
end;

als:=(pn*d/2+ro)*pnc;
end;
end;

procedure startpeen;
var a:real;
ch:boolean;
begin

stop1:=false;cause:=0;ch:=false;
a:=send;
writeln(f2,' Stress   Cycles ');
repeat
s:=a;
start1;
if((cause=1) and ch) then cause:=4;
case cause of
4:begin end;
1:begin
writeln(f2,'s=',a:3:0,'          cycles=not          COD<0');
writeln('s=',a:3:0,' cycles=not          COD<0');
ch:=true;
end;
2:begin
writeln(f2,' ',a:3:0,' ',ff,' ',length1:4:0,' nc ');
writeln(' s=',a:3:0,' ff=',ff,' length=',length1:4:0,' nc ');
ch:=false;
end;
else
begin
writeln(f2,' ',a:3:0,' ',ff,' ',length1);
writeln(' s=',a:3:0,' ff=',ff);
ch:=false;
end;
end;
end;
end;

```

```

    stop1:=false;cause:=0;
a:=a-5;
until a<Sstart;
end;

procedure un1;
var nombe1:integer;
begin
RecordData;
writeln(f2);
for nombe1:=1 to 1 do
begin
if Esfl then NewSfl;
writeln(f2,'The fatigue limit =',sfl:7:1);
if Bsfl then sstart:=sfl;
startpeen;
{sfl:=sfl+5;}
end;
{sfl:=sfl-5*nombe1;}
end;

procedure EqArSt;
var pn,pn4:integer;
Sn:real;
begin
RecordData;d:=Rtm+dstart;
Ss1fl:=s1sp(1,1);

writeln(f2,'The fatigue limit =',sfl:7:1);
writeln(f2,'s1 Sarrest (i+1)/2 ');
writeln('s1 Sarrest (i+1)/2 ');

for pn4:=1 to 70 do
begin
pn:=pn4*2-1;
change1(pn,1);
sn:=s1sp(1,pn);
writeln(sn,' ',far(sn,pn),' ',pn4);
writeln(f2,sn,' ',far(sn,pn),' ',pn4);
end;
end;

Procedure ResStress1(mm,mm1:integer,lt,lb,amax,amin,an3:real; ch:boolean);
var x,y,x1,y1:integer;
ll,sum1,sum2,ll1:real;
begin
ro:=0;
sum1:=0;sum2:=0;Rtm:=0;
RecResStr;
RecTCr;
writeln('coeff ratio - ',coeff:2:2);
writeln(f2,'coeff ratio - ',coeff:2:2);

x1:=mm;y1:=mm1;
if lb>=lt then x1:=0;
if amin>=amax then y1:=0;
for x:=0 to x1 do begin
ll:=lt-(lt-lb)/mm*x;
for y:=0 to y1 do begin
angle1:=amax-(amax-amin)/mm1*y;
sum2:=s1sp(ll/(d/2+ro),1);
sum1:=sum1+sum2;
if ch then begin
writeln(angle1:3:0,' ',sum2:3:1);
writeln(f2,angle1:3:0,' ',sum2:3:1);
end;
end;
end;
ll1:=lengthAN(ll/(d/2+ro),l,an3);

```

```

writeln(l11:3:1,'     ',(sum1/(y1+1)):3:1);
writeln(l2,l11:3:1,'     ',(sum1/(y1+1)):3:1);
sum1:=0;
if ch then begin
writeln(' ');
writeln(l2,' ');
      end;
end;
end;

procedure Menykoef;
var dcase2:byte;
begin
repeat
  writeln(' ');
  writeln('Menu 10 ');
  writeln('0: back');
  writeln('1:k start, Current parameter=',kstart:1:3 );
  writeln('2:k finish, Current parameter=',kend:1:3);
  writeln('3:use linear eq. change ratio (TRUE) or eq. (1-C/x) (FALSE), Cur. P.=',TRatio);
  readln(dcase2);
  case dcase2 of
    1:read(kstart);
    2:read(kend);
    3:Tratio:=not(Tratio);
  end;
until dcase2=0;
end;

procedure Menyro;
var dcase2:byte;
begin
repeat
  writeln(' ');
  writeln('Menu 11 ');
  writeln('0: back');
  writeln('1:ro start, Current parameter=',rostart:1:3 );
  writeln('2:ro finish, Current parameter=',roend:1:3);

  readln(dcase2);
  case dcase2 of
    1:read(rostart);
    2:read(roend);
  end;
until dcase2=0;
end;

procedure MenRes;
var dcase2:byte;
begin
repeat
  writeln(' ');
  writeln('Menu 8 ');
  writeln(' Parameters of the curve of residual stresses');
  writeln('0: back');
  writeln('1:a Current parameter=',c1a:3:0 );
  writeln('2:xd Current parameter=',c1xd:3:0,' mkm');
  writeln('3:Wf Current parameter=',c1wf:3:0,' mkm');
  writeln('4:bf Current parameter=',c1bf:3:0);
  writeln('5:W Current parameter=',c1w:3:0,' mkm');
  writeln('6:b Current parameter=',c1b:3:0);
  writeln('7:use limit eq. CPar=',eqslsp);
  writeln('8:use eq. without use integ. CPar=',RSequ);
  readln(dcase2);
  case dcase2 of
    1:read(c1a);
    2:read(c1xd);
    3:begin read(c1wf);c1w:=c1wf;end;
  end;
end;
end;

```

```

4:begin read(c1bf);c1b:=c1bf;end;
5:read(c1w);
6:read(c1b);
7:eqs1sp:=not(eqs1sp);
8:RSequ:=not(RSequ);
end;
until dcase2=0;
end;
procedure MenHardness;
var dcase2:byte;
begin
repeat
writeln(' ');
writeln('Menu 7 ');
writeln(' Parameters of the Hardness curve');
writeln('0: back');
writeln('1:a Current parameter=',c2a:3:0 );
writeln('2:xd Current parameter=',c2xd:3:0,' mkm');
writeln('3:W Current parameter=',c2w:3:0,' mkm');
writeln('4:b Current parameter=',c2b:3:0);
writeln('5:Hard1 Current parameter=',hard1:3:3);
writeln('6:Hard2 Current parameter=',hard2:3:3);
readln(dcase2);
case dcase2 of
1:read(c2a);
2:read(c2xd);
3:read(c2w);
4:read(c2b);
5:read(hard1);
6:read(hard2);
end;
until dcase2=0;

end;
Procedure MenyMaterial;
var dcase1:byte;
Begin
repeat
writeln(' ');
writeln('Menu 3 ');
writeln('0: back');
writeln('1: material Al2024');
writeln('2: material Al7150');
writeln('3: unpeen');
writeln('4: polish');
writeln('5: angle observation point, current angle=',angleL:3:0 );
writeln('6: angle of crack grow direction, current angle=',angleN:3:0 );
write('7: changing type crack current type= ');
if CorCr then writeln('corner crack')
else writeln('surface crack');
readln(dcase1);
case dcase1 of
1:begin Al2024;{dcase1:=0;}end;
2:begin Al7150;{dcase1:=0;}end;
3:begin lchange:=0;Rtm:=0;c1a:=0;Kto:=1;c1b:=0;c1bf:=0;c2a:=0;end;
4:begin Rtm:=0;Kto:=1;end;
5:begin read (angleL); end;
6:begin read (angleN); end;
7:begin CorCr:=not(CorCr);
if CorCr then angleL:=45
else angleL:=0;
end;
end;
until dcase1=0;
end;

Procedure MenyFL;

```

```

var dcase2:byte;
Begin
  repeat
    writeln(' ');
    writeln('Menu 6 ');
    writeln(' Fatigue Limit');
    writeln('0: back');
    writeln('1:the fatigue limit, sfl=',sfl:3:0);
    writeln('2:fatigue limit without the effect of stress conc., sfl1=',sfl1:3:0);
    writeln('3:use equation ');
    writeln('4:use equation auto- curr. par. ',Esfl);
    readln(dcase2);
    case dcase2 of
      1:read(sfl);
      2:read(sfl1);
      3:NewSfl;
      4:Esfl:=not(Esfl);
    end;
  until dcase2=0;

end;

Procedure MenySCon;
var dcase2:byte;
Begin
  repeat
    writeln(' ');
    writeln('Menu 9 ');
    writeln('0: back');
    writeln('1: Rtm Current parameter= ',Rtm:3:2);
    writeln('2: Kto Current parameter= ',Kto:3:2);
    readln(dcase2);
    case dcase2 of
      1:read(Rtm);
      2:read(Kto);
    end;
  until dcase2=0;

end;

Procedure MenyParM;
var dcase2:byte;
Begin
  repeat
    writeln(' ');
    writeln('Menu 5 ');
    writeln('0: back');
    writeln('1:Indentification of the material - ',nameA1);
    writeln('2:Grain Size in the Shot-peened zone ,Current parameter =',dstart:3:1,' mkm' );
    writeln('3:Grain Size - D, Current parameter =',dend:3:1,' mkm' );
    writeln('4:CTOD Curve Parameter-A2 Current parameter =',a2);
    writeln('5:CTOD Curve Parameter-M2 Current parameter =',m2);
    writeln('6: Nsstart Current parameter= ',Nsstart:3:2);
    writeln('7: depth change the size of grain Current parameter= ',lchange:3:2,' mkm');
    writeln('8:Yield stress Current parameter =',stresstop:3:0,' MPa');
    writeln('9:crack-shape ratio curve parameter, k start=',kstart:1:3,' k finish=',kend:1:3);
    writeln('10:the ro - width of grain boudary');
    writeln('11:The shear modules G=',g:7:1);
    writeln('12:The Poisson ratio=',mu:2:2);
    readln(dcase2);
    case dcase2 of
      1:read(nameA1);
      2:begin read(dstart);rostart:=dstart/100;end;
      3:begin read(dend);roend:=dend/100;end;
      4:read(a2);
      5:read(m2);
      6:read(NSstart);
      7:read(lchange);
      8:read(stresstop);
    end;
  until dcase2=0;
end;

```

```

9:menykoeff;
10:menyro;
11:read(g);
12:read(mu);
end;
until dcase2=0;

End;

procedure EqSPAg;
var x,y,mm,mm1,x1,y1:integer;
ch:boolean;
lt,lb,amax,amin,ll,an3:real;
begin
mm:=20;mm1:=20;
lt:=100;lb:=100;amax:=45;amin:=45;koeff:=0.8;ch:=true;an3:=90;

repeat
writeln(' ');
writeln('Menu 13 ');
writeln('0: back');
writeln('1:changing top length, lt=',lt:3:0);
writeln('2:changing botton length lb=',lb:3:0);
writeln('3:changing maximum angle amax=',amax:3:0);
writeln('4:changing minimum angle amin=',amin:3:0);
writeln('5:number of steps covering crack length =',mm);
writeln('6:number of steps covering the angle of crack =',mm1);
writeln('7:crack-shape ratio=',koeff:2:3);
writeln('8: Parameters of the residual stress equation');
writeln('9:Fatigue Limit      Current parameter =',sfl:3:0,' MPa');
writeln('10: Choose of material and type of crack');
writeln('12: record of all data, current par=',ch);
writeln('13: angle from specimen side surface for crack growth direction, cur. p=',an3:3:0);
writeln(' ');
writeln('11: calculation of the res. stress distribution profile');

readln(dcase2);
case dcase2 of
  11:begin ResStress1(mm,mm1,lt,lb,amax,amin,an3,ch); end;
  1:begin read(lt);lb:=lt;end;
  2:read(lb);
  3:begin read(amax);amin:=amax;end;
  4:read(amin);
  5:read(mm);
  6:read(mm1);
  7:read(koeff);
  8:begin MenRes; end;
  9:begin MenyFL;end;
  10:begin MenyMaterial; end;
  12:begin ch:=not(ch); end;
  13:begin read(an3); end;

end;
until dcase2=0;
{A12024;}
end;

Procedure MenyArCr;
Begin
repeat
writeln(' ');
writeln('Menu 12 ');
writeln('0: back');
writeln('1:Fatigue Limit      Current parameter =',sfl:3:0,' MPa');
writeln('2: Parameters of the residual stress curve');
writeln('3: Choose of material and type of crack');
writeln('4: Calculation');
readln(dcase2);

```

```

        case dcase2 of
            1:begin MenyFL;end;
            2:begin MenRes; end;
            3:begin MenyMaterial; end;
            4:EqArSt;
            end;
        until dcase2=0;
    {Al2024;}
End;

begin
{var s0,xb,ro,i,D,m,mu,sfl,s,g,s2,s3,s1:real;}
{sfl=Sfl-fatigue limit,mu=MU-Poisson ratio,m=M,s=applied stress,g=the shear modules,xb=x/c=1}

Al2024;
writeln(' ');

{NewSfl;}

namefail:='FLdata.txt';
s1le:=0;s1ar:=0;Bsfl:=true;eqs1sp:=false;Esfl:=false;
stop1:=false;d:=dstart;coeff:=kstart;
assign(f2,namefail);  rewrite(f2);

repeat
writeln(' ');
writeln('Menu 1 ');
writeln('0: exit');
writeln('1: enter note');
writeln('2: enter data for the calculation fatigue life');
writeln('3: Choice of material and type of crack');
writeln('4: Computation of fatigue life');
writeln('5: Programs');
readln(dcase);
case dcase of
    1: begin
        readln(note);
        writeln(f2,' ');
        writeln(f2,' ');
        writeln(f2,' ',note);
        end;
    2:begin
        repeat
            writeln(' ');
            writeln('Menu 2 ');
            writeln('0: back');
            writeln('1:material parameters' );
            writeln('2:Top applied stress  Current parameter =',Send:3:0,' MPa');
            writeln('3:Bottom applied stress  Current parameter =',Sstart:3:0,' MPa');
            writeln('4:use eq. Bottom s.=sfl  Current parameter =',Bsfl);
            writeln('5:Yield stress  Current parameter =',stresstop:3:0,' MPa');
            writeln('6:Fatigue Limit  Current parameter =',sfl:3:0,' MPa');
            writeln('7: Parameters of the Hardness curve');
            writeln('8: Parameters of the residual stress curve');
            writeln('9: Stress con. factor Curr. par. Rtm= ',Rtm:3:2,' Kto=',Kto:3:2);

        readln(dcase1);
        case dcase1 of
            1:begin MenyParM;end;
            2:read(Send);
            3:read(Sstart);
            4:Bsfl:=not(Bsfl);
            5:read(stresstop);
            6:begin MenyFL;end;
            7:begin MenHardness; end;
            8:begin MenRes; end;
            9:MenySCon;
            end;
    end;
end;

```

```

until dcase1=0;
end;
3:begin MenyMaterial; end;
4:unl;
5:begin
repeat
writeln(' ');
writeln('Menu 4 ');
writeln('0: back');
writeln('1:arrest stress EqArSt ');
writeln('2:residual stress - angle EqSPAg ');
readln(dcase1);
case dcase1 of
1:MenyArCr;
2:EqSPAg;
end;
until dcase1=0;
end;
end;
until dcase=0;

```

```

{Start2;}
{startpeen;}

```

```

close(f2);
end.

```

INPUT DATA	
AA 7150-T651 PEENED TO WORST CONDITION	AA 2024-T351 PEENED TO OPTIMUM CONDITION
Allou AL 7150 Beginning length of crack=0.40 Maximum residual stress =-193.00 Minimum residual stress = 0.00 depth to maximum residual stress Xd= 50.00 W-width of the residual stress =100.00 use (or not) equation limit res. stress FALSE use (or not) equation without use integral TRUE Maximum S2 stress =157.00 Minimum S2 stress =145.00 depth to maximum S2 stress Xd= 50.00 W-width of the S2 stress =100.00 Koeff. of transfer Vickers to flow stress Hard1 = 3.22 Hard2 = 15.55 size of grain D before and behind 100 mk =35.000 and 58.000 Koeff before and behind 100 mk =0.330 and 0.600 Use eq. change ratio = (1-C/x) grain boundary width before and behind 100 mk =0.3500 0.5800 The angle (from side surface) line grown crack =0.0 and direction cal. residual stress=45.0 The shear modules G=28070.0 The Poisson ratio=0.33 A2= 3.000000000000000E+0002 m2= 1.50 Rtm= 1.450000000000000E+0001 Kto= 1.23 Yield stress =450 MPa type crack= corner crack angle observation point = 45 The fatigue limit = 240.0	Allou AL 2024 Beginning length of crack=0.20 Maximum residual stress =-260.00 Minimum residual stress = 0.00 depth to maximum residual stress Xd= 30.00 W-width of the residual stress =100.00 use (or not) equation limit res. stress FALSE use (or not) equation without use integral TRUE Maximum S2 stress =147.00 Minimum S2 stress =119.00 depth to maximum S2 stress Xd= 20.00 W-width of the S2 stress =100.00 Koeff. of transfer Vickers to flow stress Hard1 = 3.85 Hard2 =-136.90 size of grain D before and behind 150 mk =15.000 and 52.900 Koeff before and behind 150 mk =0.330 and 0.600 Use eq. change ratio = (1-C/x) grain boundary width before and behind 150 mk =0.1500 0.5290 The angle (from side surface) line grown crack =0.0 and direction cal. residual stress=45.0 The shear modules G=27200.0 The Poisson ratio=0.30 A2= 5.000000000000000E+0003 m2= 1.80 Rtm= 2.448000000000000E+0001 Kto= 1.34 Yield stress =325 MPa type crack= corner crack angle observation point = 45 The fatigue limit = 225.0

APPENDIX-X

DISCUSSION

a) Elastic and plastic stress analysis for the residual stress distribution

The principal elastic stresses in the material under an indenter are given by Equations <A.21> and <A.21>. The maximum shear stress is given as an equivalent stress defined in Eq. <A.23>.

$$\sigma_x^e = \sigma_y^e = -p_{\max} \left[(1 + \nu_1) \left(1 - \frac{z}{a} \tan^{-1} \left(\frac{a}{z} \right) - \frac{1}{2} \left(1 + \frac{z^2}{a^2} \right)^{-1} \right) \right] \quad \text{<A.21>}$$

where σ^e denotes principal stress in the elastic regime.

$$\sigma_z^e = -p_{\max} \left(1 + \frac{z^2}{a^2} \right)^{-1} \quad \text{<A.22>}$$

$$\tau_{\max} = \sigma_{\text{eq}}^e = \frac{1}{\sqrt{2}} \left[(\sigma_x^e - \sigma_y^e)^2 + (\sigma_y^e - \sigma_z^e)^2 + (\sigma_z^e - \sigma_x^e)^2 \right]^{\frac{1}{2}} \quad \text{<A.23>}$$

where σ_{eq}^e denotes principal equivalent stress in the elastic regime.

The maximum pressure and the indentation radius are given by $a = \frac{\pi p_{\max} D}{4E^*}$ where D is the diameter of the peen. E^* is the single combined value of the Young's modulus, obtained by using the equivalent Young's modulus $\frac{1}{E^*} = \frac{1 - \nu_1^2}{E_1} + \frac{1 - \nu_2^2}{E_2}$ where E_1 , ν_1 , E_2 , and ν_2 are the Young's modulus and Poisson's ratios of the shot and of the material respectively, as described in §2.2.3.2.

For the spherical indenter, the maximum Hertzian pressure at the commencement of plastic flow is given by Johnson's relationship [12]:

$$P_{\max} = \frac{3P}{2\pi a^2} \approx 1.6 \sigma_{\text{yield}} \quad \text{<A.24>}$$

where σ_{yield} represents the yield strength of the indented material in compression.

It is clear that the indented material undergoes strain hardening during the loading and unloading peening process and therefore, the above analysis has to be corrected to obtain more realistic estimations. Particularly, when σ_{yield} in compression is replaced by a representative flow stress $\bar{\sigma}_{\text{yield}}$, measured at a compressive strain of $\epsilon_R=0.2a/R$, as proposed by Tabor [13]. For an ideally plastic solid, the stress distribution directly beneath the surface the shot (along the z axis), according to the Tresca yield criterion is given by:

$$\sigma_z - \sigma_r = -\sigma_y \quad \text{<A.25>}$$

where σ_z and σ_r are the normal and the radial stresses (as these stresses are principal, the shear stresses are zero along the z axis).

The elastic unloading gives rise to an effective superposition of a uniform tension (negative pressure) $\approx 3\sigma_y$ at the contact interface. It is also well documented that upon unloading, a uniform tension of $3\sigma_y$ acting on the contact area is [14],

$$(\sigma_z - \sigma_r)_{\text{max}} = 0.66(3\sigma_y) \quad \text{at } z = 0.64a \quad \text{<A.26>}$$

where $0.64a$ is the depth at which the maximum Tresca and von Mises effective stresses take place.

Combining Eqs. <A.25> and <A.26>,

$$(\sigma_z - \sigma_r)_{\text{unloading}} = [3 \times 0.66 - 1]\sigma_y = 0.98\sigma_y \quad \text{<A.27>}$$

This result represents the residual stress developed in the material at the point of reverse plastic flow upon shot rebounding. Furthermore, at the surface outside the contact area, the stress state during elastic-plastic loading involves radial compression and a small circumferential tension. Plastic flow is thus assisted by the uniform stress during unloading. The elastic-plastic boundary can be determined by using Eq. <A.28> for a spherical indenter.

$$c = a \left(\frac{\frac{2E^*a}{D\sigma_y} + 4(1-\nu)}{6(1-\nu)} \right)^{\frac{1}{3}} \quad \text{<A.28>}$$

where c is the radius from the point of contact, D is the diameter of the shot and σ_y refers to yield strength in compression. A representation of the elastic-plastic boundary is shown in Fig. IX-1.

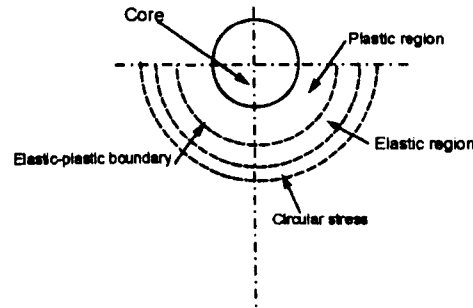


Figure IX-1 The spherical cavity model which assumes that there is no plastic deformation of the indenter such that a perfectly spherical indentation is made.

The beneficial effect of the CRSF was derived in simple terms from the equi-biaxial stresses produced ($\sigma_x|_R = \sigma_y|_R$) by a sphere pressing a flat surface [15]. Assuming a frictionless contact, an indented surface will contain $\sigma_x|_R = \sigma_y|_R \rightarrow -\sigma_y$; $\sigma_z|_R = 0$ on planes parallel to the indented surface. If the radial stress is added, it gives a net radial stress of $[\sigma_r + \sigma_x|_R]$. When the sphere is indented on to the surface with a load P , plastic yielding is undeveloped if $|\sigma_r + \sigma_x|_R - \sigma_z| \leq \sigma_y$ (according to Tresca's yield condition). Considering compressive residual stresses approaching to the yield strength, $|\sigma_x|_R = |\sigma_y|_R \rightarrow \sigma_y$. Therefore, $|\sigma_r + \sigma_y| - \sigma_z| \leq \sigma_y$ and equal to $\sigma_r - \sigma_z \leq 2\sigma_y$. This theoretical analysis shows that $(\sigma_r - \sigma_z)|_{\max} = 2\tau_{\max} = 0.62 P_{\max}$ at $z = 0.48 a$. Hence, $0.62 P_{\max} \leq 2 \sigma_y$ or $P_{\max} \leq 3.2 \sigma_y$, where, if compared to Eq. <A.24>, readily shows that the maximum Hertzian contact imposed by the shot on the surface is elevated by a factor of two when a state of equi-biaxial compressive residual stress, approaching to the yield strength in compression, is introduced.

Dynamic considerations show that impact of the shots at moderate speeds can be treated as quasi-static, if a non-dimensional velocity parameter is sufficiently low [16]. Thus, the impact of the peens is approximated to the static situation as long as some correction factors due to the peen velocity are taken into account. Commonly $\frac{\rho v^2}{\sigma_{y-\text{dynamic}}}$ represents the parameter used to determine the regime of impact, where ρ is the density of the target material, v is the velocity of the shot and $\sigma_{y-\text{dynamic}}$ is the dynamic yield strength of the material. The elastic regime is given by $\frac{\rho v^2}{\sigma_{y-\text{dynamic}}} < 10^{-6}$. In this case, if a velocity of

113 ms^{-1} (see table 4.1.4 for a S110 shot and normal impact to the surface) was taken as the upper limit of the peen velocity; the parameter would approximately be 3×10^{-2} for

the AA 2024-T351. The value shows that provided the dynamic yield strength is defined, the use of the static indentation theory for shot peening is still applicable, as previously mentioned in §2.2.2.

Appendix references

1. Fathallah, R., (1998), "Prediction of plastic deformation and residual stresses induced in metallic parts by shot peening." *Materials Science and Technology*. Vol. 14, pp. 631-639.
2. Johnson, K.L., (1985), *Contact mechanics*. Cambridge Univ. Press.
3. Iida, K., (1984), "Dent and affected layer produced by shot peening". In: *Second International Conference on Shot Peening. Proceedings of the International Conference on Shot Peening (ICSP-2)*. Chicago. Ed. H.O. Fuchs. The American Shot Peening Society: pp. 283-292
4. Tufft, Marsha Klopmeier, (1999), "Shot peening impact on life, part 2: single particle impact tests using production shot". In: *Shot Peening: Present and Future. The 7th Conference on Shot Peening (ICSP-7)*. Warsaw, Poland. Ed. Aleksander Nakonieczny. Institute of Precision Mechanics <IMP>: pp. 254-263
5. Bailey, P.G., 1994, "Letter to the Editor", in *The shot peener*, Spring 1994. p. 17.
6. Airbus Industrie Material Specification, (AIMS 03-02-011), 1996, "Aluminium Alloy (7150) Solution treated, controlled stretched and artificially aged (T651) plate." AIRBUS INDUSTRIE, Editor. Airbus industrie: Blagnac cedex, France. p. 1-6.
7. DeGarmo, Black, E.P., Kohser, J. T. and R.A., (1999), *Materials and processes in manufacturing*. John Wiley and Sons.
8. E837-95, ASTM, (1995), Standard test method for determining residual stresses by the hole-drilling strain-gage method. Annual book of ASTM standards, American Society for Testing and Materials. Vol. 03.01. Philadelphia, PA 19103.: pp. 642-648.
9. Vishay-Measurements Group, Inc., Nov. 1996, "Measurement of residual stresses by the hole-drilling strain gage method." in *Measurements Group, Tech note, TN-503-5 (Residual stress measurement)*. p. 1-19.
10. Kelsey, R.A., (1956), "Measuring non-uniform residual stresses by the hole drilling method". In: *Proc. Soc. Exp. Stress Anal.*: pp. 181-194
11. Schajer, G.S., (1981), "Application of the finite elements calculations to residual stress measurements". *Journal of engineering materials and technology (Trans. ASME)*. Vol. 103, pp. 157-163.
12. Johnson, K.L., (1983), "Inelastic contact: plastic flow and shakedown". In: *Contact mechanics and wear of rail/wheel systems*. Waterloo, Ontario, Can. University of Waterloo Press: pp. 79-101
13. Tabor, D., (1951), *Hardness of metals*. Oxford. Oxford University Press.
14. Timoshenko, S. and Goodier, J.N., (1951), *Theory of elasticity*, ed. 3rd. edition. New York. McGraw-Hill.
15. Hills, D.A. and Ashelby, D.W., (1982), "The influence of residual stresses on contact load bearing capacity". *Wear*. Vol. 75, pp. 221-240.
16. Johnson, W., (1972), *Impact strength of materials*. London. Edward Arnold.

References

1. Miller, K. J., (1993), "Materials science perspective of metals fatigue resistance". *Materials Science and Technology*. Vol. 9, pp. 453-462.
2. de los Rios, E. R., Mercier, P. and El-Sehily, B. M., (1996), "Short crack growth behaviour under variable amplitude loading of shot peened surfaces". *Fatigue and Fracture of Engineering Materials and Structures*. Vol. 19, No. 2/3: pp. 175-184.
3. de los Rios, E.R., Walley, A., Milan, M.T. and Hammersley, G., (1995), "Fatigue crack initiation and propagation on shot peened surfaces in A316 stainless steel". *International Journal of Fatigue*. Vol. 17, No. 7: pp. 493-499.
4. Schütz, W., (1981), "Fatigue life improvement of high-strength materials by shot peening". In: *First International Conference on Shot Peening. Proceedings of the International Conference on Shot Peening (ICSP-1)*. Paris. Ed. A. Niku-Lari. Pergamon press: pp. 423-433
5. Clayton, J.Q. and Clark, G., (1988), "The effect of steel shot and glass bead peening treatments on the fatigue resistance of 7050-T76351 aluminium alloy". In: *Proc. Australian fracture group, "fracture mechanics in engineering practice"*. Melbourne, Australia. pp. 44-51
6. Eckersley, John S., (1984), "Shot peening plays a vital roll in rejuvenation of aging aircraft". In: *Second International Conference on Shot Peening. Proceedings of the International Conference on Shot Peening (ICSP-2)*. Chicago. Ed. H.O. Fuchs. The American Shot Peening Society: pp. 241-255
7. Yokobori, Takeo, (1964), *The strength, fracture and fatigue of materials*. The Netherlands. P. Noordhoff/Groningen/The Netherlands: pp. 108-116.
8. Suresh, Subra, (1998), *Fatigue of Materials*. Second ed. Cambridge, University press, Cambridge.
9. Yates, John R., 1999, "Fatigue of engineering materials. MSc in Structural Integrity (MPE603), course notes". Department of Mechanical Engineering. The University of Sheffield: Sheffield, U.K.
10. Whöler, A., (1860), "Versuche über die festigkeit der eisenbahnwagenachsen; English summary (1867). *Engineering 4*", *Zeitschrift für Bauwesen*. No. 10: pp. 160-161.
11. Griffith, A.A., (1921), "The phenomenon of rupture and flow in solids". *Philosophical transactions of the Royal Society, London*. No. A221: pp. 163-197.
12. Irwin, G.R., (1957), "Analysis of stresses and strains near the end of a crack transversing a plate". *Journal of applied mechanics*. No. 24: pp. 361-364.
13. Paris, P.C. and Erdogan, F.J., (1963), "A critical analysis of crack propagation law." *Journal of basic Engineering, Trans. ASME, Series D*. Vol. 85, No. 4: pp. 528-535.
14. Paris, P.C., (1998), "Fracture mechanics and fatigue: A historical perspective". *Fatigue and Fracture of Engineering Materials and Structures*. No. 21: pp. 535-540.
15. Forsyth, P.J.E., (1962), "A two stage process of fatigue crack growth, in crack propagation". In: *Proceedings of Cranfield Symposium*. London: Her Majesty's Stationery Office. pp. 76-94
16. Kitagawa, H. and Takahashi, S., (1976), "Applicability of fracture mechanics to very small cracks or the cracks in the early stage". In: *2nd International conference on mechanical behaviour of materials (ICM2)*. Boston, USA. American Society of Metals, Metal park, Ohio.: pp. 627-631
17. Lukáš, Petr, (1996), in: *Fatigue and Fracture, Fatigue crack nucleation and microstructure*, ASM Handbook, Volume 19, Vol. 19. ASM International: Materials Park, Ohio. pp. 96-109.
18. Miller, K.J., (1985), "Fundamentals of deformation and fracture". In: *Proc. Eshelby Memorial Symposium*. Cambridge, U.K. Ed. B.A. Bilby. Cambridge University Press: pp. 477-500
19. Hoepfner, D.W., (1978), "Model for prediction of fatigue lives based upon a pitting corrosion fatigue process. *Fatigue Mechanisms*". In: *Proc. of an ASTM-NBS-NSF symposium*. Kansas, City, Mo. Ed. J.T. Fong. ASTM STP 675: pp. 841-870
20. Hertzberg, R.W., (1989), *Deformation and fracture mechanics of engineering materials*. 3rd. ed. New York, USA. John Wiley & Sons: p. 491.
21. Guin F., Dulniak R. and Edwards, B.C., (1982), "On the nucleation of fatigue cracks in pure polycrystalline α -iron". *Fatigue and Fracture of Engineering Materials and Structures*. No. 5: p. 311.
22. Radhakrishnan, V.M. and Mutoh, Y., (1986), "On fatigue crack growth in stage I". In: *The behaviour of short fatigue cracks*, EGF Pub. 1. Great Britain. Eds. K.J. Miller and E.R. de los Rios. Mechanical Engineering Publications Limited: pp. 87-99
23. Brown, M.W., (1986), "Interfaces between short, long and non-propagating cracks." In: *The behaviour of short fatigue cracks*, EGF Pub. Sheffield, U.K. Eds. K.J. Miller and E.R. de los Rios. Mechanical Engineering Publications, London: pp. 423-439
24. Mutoh, Y. and Radhakrishnan, V.M., (1986), "An analysis of grain size and yield stress effects on stress at fatigue limit and threshold stress intensity factor". *Journal of engineering materials and technology*, No. 103: pp. 229-233.
25. Hay, E. and Brown, M.W., (1986), "Initiation and early growth of fatigue cracks from a circumferential notch loaded in torsion". In: *The behaviour of short fatigue cracks*, EGF Pub.

- Sheffield, U.K. Eds. K.J. Miller and E.R. delosRios. Mechanical Engineering Publications, London: pp. 309-321
26. Ritchie, R.O., McClintock, F.A., Nayeb-hashemi, H. and Ritter, M.A., (1982), "Mode III fatigue crack propagation in low alloy steel". *Metallurgical transactions*. Vol. 13A, pp. 101-110.
 27. Knott, J.F., (1973), *Fundamentals of fracture mechanics*. London. Butterworths, London, p. 134.
 28. Smith, R.A., (1978), "An introduction to fracture mechanics for engineers part I: Stresses due to notches and cracks." *Materials in engineering applications*. Vol. 1, No. December: pp. 121-128.
 29. Rice, J.R., (1968), "A path independent integral and the approximate analysis of strain concentrations by notches and cracks". *Journal of applied mechanics*. No. 35: pp. 379-386.
 30. Walls, A.A., (1961). In: *Crack propagation symposium proceedings*. Cranfield, England. Ed. Cranfield college of aeronautics.
 31. Knott, John and Withey, Paul, (1998), *Fracture mechanics: worked examples*. London. The Institute of Materials.
 32. Hutchinson, J.W., (1968), "Singular behaviour at the end of a tensile crack in a hardening material". *Journal of the mechanics and physics of solids*. No. 16: pp. 13-31.
 33. Rice, J.R. and Rosengren, G.F., (1968), "Plain strain deformation near a crack tip in a power low hardening material". *Journal of the mechanics and physics of solids*. No. 16: pp. 1-12.
 34. Shih, C.F., (1981), "Relationships between the J- integral and the crack opening displacement for stationary and extending cracks". *Journal of the mechanics and physics of solids*. No. 29: pp. 305-326.
 35. Richards, C.E. and Lindley, T.C., (1972), "The influence of stress intensity and microstructure on fatigue crack propagation in ferritic materials". *Engineering fracture mechanics*. No. 4: pp. 951-978.
 36. Elber, W., (1970), "Fatigue crack closure under cyclic tension". *Engineering fracture mechanics*. Vol. 2, pp. 37-45.
 37. Dowling, N.E. and Begley, J.A., (1976), "Fatigue crack growth during gross plasticity and the J-integral. In *mechanics of crack growth*". STP 590. Philadelphia:ASTM. pp. 82-103.
 38. Suresh, S. and Ritchie, R.O., (1984), "The propagation of short fatigue cracks". *International metals review*. Vol. 29, No. 6: p. 445.
 39. Louat, N., Sadananda, K., Duesbery, M. and Vasudevan, A.K., (1993), "A theoretical evaluation of crack closure". *Metallurgical transactions*. Vol. 24-A, pp. 2225-2232.
 40. Ritchie, R.O., Suresh, S. and Moss, C.M., (1980), "Near threshold fatigue crack growth in 21/4 Cr 1Mo pressure vessel steel in air and hydrogen". *Journal of engineering materials and technology (Trans. ASME)*. No. 102: p. 293.
 41. Suresh, S. and Ritchie, R.O., (1982), "A geometric model for fatigue crack closure induced by fracture surface roughness". *Metallurgical transactions A*. Vol. 13A, pp. 1627-1631.
 42. Pearson, S., (1975), "Initiation of fatigue cracks in commercial aluminium alloys and the subsequent propagation of very short cracks". *Engineering fracture mechanics*. Vol. 7, pp. 235-247.
 43. Lankford, J., (1982), "The growth of small fatigue cracks in 7075-T6 aluminum". *Fatigue and Fracture of Engineering Materials and Structures*. Vol. 5, No. 3: pp. 233-248.
 44. Kujawski, D. and Ellyin, F., (1992), "A microstructurally motivated model for short crack growth rate". *Short Fatigue Cracks, ESIS 13 (Edited by K.J. Miller and E.R. de los Rios)*. Mechanical Engineering Publications, London. pp. 391-405.
 45. Taylor, D. and Knott, J. F., (1981), "Fatigue crack propagation behaviour of short cracks: The effect of microstructure". *Fatigue and Fracture of Engineering Materials and Structures*. Vol. 4, No. 2: pp. 147-155.
 46. Miller, K. J., (1987), "The Behaviour of short fatigue cracks and their initiation. Part I - A review of two recent books". *Fatigue and Fracture of Engineering Materials and Structures*. Vol. 10, No. 1: pp. 75-91.
 47. Miller, K. J., (1987), "The Behaviour of short fatigue cracks and their initiation. Part II - A general summary". *Fatigue and Fracture of Engineering Materials and Structures*. Vol. 10, No. 1: pp. 75-91.
 48. Tokaji, K. and Ogawa, T., (1992), "The growth behaviour of microstructurally small fatigue cracks in metals". *Short Fatigue Cracks, ESIS 13 (Edited by K.J. Miller and E.R. de los Rios)*. Mechanical Engineering Publications, London. pp. 85-99.
 49. Taylor, D., (1986), "Fatigue of short cracks: the limitations of fracture mechanics". In: *The behaviour of short fatigue cracks*, EGF Pub. Sheffield, U.K. Eds. K.J. Miller and E.R. delosRios. Mechanical Engineering Publications, London: pp. 479-490
 50. Kendall, J.M., James, M.N. and Knott, J. F., (1986), "The behaviour of physically short fatigue cracks in steels". In: *The behaviour of short fatigue cracks*, EGF Pub. Sheffield, U.K. Eds. K.J. Miller and E.R. delosRios. Mechanical Engineering Publications, London: pp. 241-258
 51. James, M.R. and Morris, W.L., (1983), "Effect of fracture surface roughness on growth of short fatigue cracks". *Metallurgical transactions*. No. 14A: pp. 153-155.

52. Newman, J.C., (1983), "A non linear fracture mechanics approach to the growth of small cracks". In: Behaviour of short cracks in airframe components, Proceedings 328. Advisory group for aerospace research and development. Neuilly sur Seine (France). pp. 6.1-6.20
53. Venkateswara-Rao, K.T., Yu, W. and Ritchie, R.O., (1988), "On the behaviour of small fatigue cracks in commercial Aluminium-Lithium alloys". Engineering fracture mechanics. Vol. 31, No. 4: p. 623.
54. Zaiken, E. and Ritchie, R.O., (1985), "On the development of crack closure and the threshold condition for short and long fatigue cracks in 7150 aluminum alloy". Metallurgical transactions A. Vol. 16A, pp. 1467-1477.
55. Boettner, R.C., Laird, C. and McEvily, A.J., (1965), "Crack nucleation and growth in high strain-low cycle fatigue". Transactions of Metallurgical Society, AIME. Vol. 233, pp. 379-385.
56. Chang, R., Morris, W.L. and Buck, O., (1979), "Fatigue crack nucleation at intermetallic particles in alloys-A dislocation pile-up model". Scripta Metallurgica. Vol. 13, p. 191.
57. Chan, K.S. and Lankford, J., (1983), "A crack tip model for the growth of small fatigue cracks". Scripta Metallurgica. Vol. 17, pp. 529-538.
58. Tanaka, K., (1986), "Modelling of propagation and non-propagation of small cracks". In: In Small Fatigue Cracks. Ed. Ed. Ritchie R.O. and Lankford J. Metallurgical Society Inc.: pp. 343-362
59. Hobson, P. D., (1982), "The formulation of a crack growth equation for short cracks". Fatigue and Fracture of Engineering Materials and Structures. Vol. 5, No. 4: pp. 323-327.
60. Hobson, P.D., Brown, M.W. and de los Rios, E.R., (1986), "Two phases of short crack growth in a medium carbon steel". In: The behaviour of short fatigue cracks, EGF Pub. Sheffield, U.K. Eds. K.J. Miller and E.R. de los Rios. Mechanical Engineering Publications, London: pp. 441-459
61. Angelova, D. and Akid, R., (1998), "A note on modelling short fatigue crack behaviour". Fatigue and Fracture of Engineering Materials and Structures. Vol. 21, pp. 771-779.
62. Navarro, A. and de los Rios, E.R., (1987), "A model for short fatigue crack propagation with an interpretation of the short-long crack transition". Fatigue and Fracture of Engineering Materials and Structures. Vol. 10, No. 2: pp. 169-186.
63. Xiaojiang, Xin, (1992), Experimental and theoretical aspects of microstructural sensitive crack growth in Al-Li 8090 alloy. PhD thesis, Department of Mechanical Engineering, Sheffield: The University of Sheffield.
64. Rodopoulos, C.A., (1996), Fatigue studies under constant and variable amplitude loading in MMCs. PhD thesis, Department of Mechanical Engineering, Sheffield, U.K.: The University of Sheffield.
65. Hanlon, David Neal, (1994), Fatigue fracture initiation and short crack propagation in the high strength aluminium alloy AA7150. PhD thesis, Department of Engineering Materials, Sheffield, U.K.: The University of Sheffield.
66. Bilby, B.A., Cottrell, A. H. and Swinden, K. H., (1962), "The spread of plastic yield from a notch". Proc. R. Soc. Lond. A. Vol. A-272, pp. 304-314.
67. Navarro, A. and de los Rios, E. R., (1988), "Compact solution for a multizone BCS crack model with bounded or unbounded end conditions". Philosophical Magazine A. Vol. 57, No. 1: pp. 43-50.
68. Navarro, A. and de los Rios, E.R., (1988), "An alternative model of the blocking of dislocations at grain boundaries". Philosophical Magazine A. Vol. 57, pp. 37-42.
69. Navarro, A. and de los Rios, E.R., (1992), "Fatigue crack growth modelling by successive blocking of dislocations". Proc. R. Soc. Lond. A. No. 437: pp. 375-390.
70. de los Rios, E.R., Mohamed, H.J. and Miller, K. J., (1985), "A micro-mechanics analysis for short fatigue crack growth". Fatigue and Fracture of Engineering Materials and Structures. Vol. 8, No. 1: pp. 49-63.
71. de los Rios, E.R., Navarro, A. and Hussain, K., (1992), "Microstructural variations in short fatigue crack propagation of a C-Mn steel". Short Fatigue Cracks, ESIS 13 (Edited by K.J. Miller and E.R. de los Rios). Mechanical Engineering Publications, London., pp. 115-132.
72. de los Rios, E.R., (1998), "Dislocation modelling of fatigue crack growth in polycrystals". Engineering mechanics. Vol. 5, No. 6: pp. 363-368.
73. de los Rios, E.R. and Navarro, A., (1990), "Grain orientation and work hardening considerations on short fatigue crack modelling". Philosophical Magazine A. Vol. 61(3), pp. 435-449.
74. Taylor, G.I., (1938), "Plastic strain in metals". Journal of the institute of metals. Vol. 62, pp. 307-324.
75. Navarro, A. and de los Rios, E.R., (1988), "Short and long fatigue crack growth: A unified model". Philosophical Magazine A. Vol. 57, No. 1: pp. 15-36.
76. Xin, X. J., de los Rios, E.R. and Navarro, A., (1992), "Modelling strain hardening at short fatigue cracks". In: Short fatigue cracks, ESIS 13. Eds. K. J. Miller and E. R. de los Rios. Mechanical Engineering Publications, London: pp. 369-389
77. de los Rios, E.R., Trull, M. and Levers, A., (2000), "Modelling fatigue crack growth in shot peened components of Al 2024-T351". Fatigue and Fracture of Engineering Materials and Structures. No. 23: pp. 209-216.

78. Kloos, K.H. and Macherauch, E., (1987), "Development of mechanical surface strengthening processes from the beginning until today". In: Shot Peening- Science-Technology-Application. Third International Conference on Shot Peening (ICSP-3). Germany. Eds. H. Wohlfahrt, R. Koop and O. Vohringer. Deutsche Gesellschaft für Metallkunde e.V.: pp. 3-27
79. Cary, P.E., (1981), "History of shot peening". In: First International Conference on Shot Peening. Proceedings of the International Conference on Shot Peening (ICSP-1). Paris. Ed. A. Niku-Lari. Pergamon press: pp. 23-28
80. Zimmerli, F.P., (1940), "Shot blastig and its effect on fatigue life". Machine Design. No. 12: p. 62.
81. Almen, John O. and Black, Paul H., (1963), Residual stresses and fatigue in metals. USA. McGraw Hill book company. Inc.
82. Military Specification, MIL-S-13165C, 7 June 1989, "Shot peening of metal parts". The Wheelabrator Corporation: USA.
83. Grasty, L. V. and Andrew, C., (1996), "Shot peening forming sheet metal: Finite element prediction of deformed shape". Proceedings of the Institution of the Mechanical Engineers. Vol. 210, pp. 361-366.
84. Tatton, R.J.D., (1986), "Shot peen-forming". In: Proceedings of the 2nd. International Conference on Impact Treatment Process. U.K. Ed. S.A. Meguid. Elsevier applied science: pp. 134-143
85. Corporation, American Wheelabrator & Equipment, (1947), Shot Peening. 3rd ed. USA. Mishawaka, Indiana: p. p. 82.
86. Inc., Metal Improvement Company, (1989), Shot peening applications. 7th ed. ed. USA. Paramus.
87. Committee, SAE Fatigue Design and Evaluation, (1991), SAE Manual on Shot Peening (SAE HS-84). 3rd ed. Society of Automotive Engineers, Inc.: pp. 19-20.
88. Baughman, D.L., (1981), "Evolution of centrifugal wheel shot peening in the aerospace industry and recent applications". In: First International Conference on Shot Peening. Proceedings of the International Conference on Shot Peening (ICSP-1). Paris. Ed. A. Niku-Lari. Pergamon press: pp. 101-108
89. Plaster, H.J., (1981), "Technical aspects of shot peening machinery and media". In: First International Conference on Shot Peening. Proceedings of the International Conference on Shot Peening (ICSP-1). Paris. Ed. A. Niku-Lari. Pergamon press: pp. 83-94
90. Lecoffre, Yves and Xavier, Helispire Bonazzi, (1993), "TRAVEL: A real time particle velocity measuring system for use in shot peening". In: The fifth International Conference on Shot Peening (ICSP-5). Oxford, U.K. Ed. D Kirk. Coventry University: pp. 61-68
91. Fathallah, R., (1998), "Prediction of plastic deformation and residual stresses induced in metallic parts by shot peening." Materials Science and Technology. Vol. 14, pp. 631-639.
92. Johnson, W., (1972), Impact strength of materials. London. Edward Arnold.
93. Hills, D.A., Waterhouse, R.B. and Noble, B., (1983), "An analysis of shot peening". Journal of strain analysis. Vol. 18, No. 2: pp. 95-100.
94. Al-Obaid, Y.F., (1990), "A rudimentary analysis of improving fatigue life of metals by shot peening". Journal of applied mechanics. Vol. 57, pp. 307-312.
95. Boyce, B.L., Chen, X., Hutchinson, J.W. and Ritchie, R.O., (2001), "The residual stress state due to a spherical hard-body impact". Mechanics of materials. Vol. 33, pp. 441-454.
96. Al-Hassani, S.T.P., (1982), "The shot peening of metal-mechanics and structures". Shot peening for advance aerospace design. SP-528, Society of Automotive Engineers: Warrendale, PA., p. 2.
97. Kobayashi, M., Matsui, T. and Murukami, Y., (1998), "Mechanism of creation of compressive residual stress by shot peening". International Journal of Fatigue. Vol. 20, No. 5: pp. 351-357.
98. Frost, H.J. and Ashby, M.F., (1982), Deformation-Mechanism Maps: The plasticity and creep of metals and ceramics. NY, Oxford. Pergamon Press.
99. Simpson, R.S. and Chiasson, G.L., (1986), "A new concept for defining optimum levels of a critical shot peening process variable." In: Impact surface treatment (Second International Conference on Impact Treatment Processes). Bedford, U.K. Ed. S.A. Meguid. Elsevier applied science: pp. 101-114
100. Eckersley, John S., (1984), "Shot peening process controls ensure repeatable results". In: Second International Conference on Shot Peening. Proceedings of the International Conference on Shot Peening (ICSP-2). Chicago. Ed. H.O. Fuchs. The American Shot Peening Society: pp. 133-142
101. Simpson, Roger S. and Robert, Barnesky, (1993), "A statistical analysis of the internal statistical capability of several common controlled shot peening specifications". In: The Fifth International Conference on Shot Peening (ICSP-5). Oxford, UK. Ed. David Kirk. Coventry University: pp. 69-80
102. British Aerospace (operations), limited, 1997, "Shot peening for improved fatigue and stress corrosion resistance. British Aerospace (Airbus), PROCESS SPECIFICATION (ABP 1-2031)". England. UK. pp. 1-23.

103. Natkaniek-Kocanda, D., Kocanda, S. and Miller, K.J., (1996), "Influence of shot peening on short crack behaviour in a medium carbon steel". *Fatigue & Fracture of Engineering Materials & Structures*. Vol. 19, No. 7: pp. 911-917.
104. Solis-Romero, J., de los Rios, E.R., Fam, Y.H. and Levers, A., (1999), "Optimisation of the shot peening in terms of the fatigue resistance." In: *Shot Peening: Present and Future. The 7th Conference on Shot Peening (ICSP-7)*. Warsaw, Poland. Ed. Aleksander Nakonieczny. Institute of Precision Mechanics <IMP>: pp. 117-126
105. Bailey, PG, Lombardo, DR, Popp, HG and Thompson, RA, (1996), "Full assurance shot peening of aircraft gas turbine engine components". In: *Sixth International Conference on Shot Peening. Proceedings of the International Conference on Shot Peening (ICSP-6)*. California, USA. Ed. Jack Campaigne. pp. 320-327
106. Gillespie, R.D., (1993), "Shot peening media: Its effect on process consistency and resultant improvement in fatigue characteristics." In: *The Fifth International Conference on Shot Peening (ICSP-5)*. Oxford, UK. Ed. David Kirk. Coventry University: pp. 81-90
107. Gillespie, R.D. and Gloerfeld, H., (1990), "An investigation of the durability and breakdown characteristics of shot peening media". In: *Shot peening: Proceedings of the fourth international conference on shot peening (ICSP-4)*. Tokyo, Japan. Ed. k. Iida. The Japan Society of precision engineering: pp. 27-36
108. British Aerospace PLC, 1994, 1995, "Carbon steel spherically conditioned cut wire for shot peening. British Aerospace (Airbus), PROCESS SPECIFICATION (ABM 9-9076)": England, UK. pp. 1-7.
109. Flavenot, J.F. and Lu, J., (1990), "Influence of ageing of a cut steel wire shot during shot peening". In: *Shot peening: Proceedings of the fourth international conference on shot peening (ICSP-4)*. Tokyo, Japan. Ed. k. Iida. The Japan Society of precision engineering: pp. 83-93
110. Edwards, P.E., (1993), "A comparison of the effect of peening using cut wire and cast steel shot on fatigue performance of 7010-T7651 aluminium alloy plate". In: *The fifth International Conference on Shot Peening (ICSP-5)*. Oxford, U.K. Ed. D. Kirk. Coventry University: pp. 154-165
111. Muller, P.P., Koln and Urffer, D., (1987), "Peening with fused ceramic beads". In: *Shot Peening-Science-Technology-Application. Third International Conference on Shot Peening (ICSP-3)*. Germany. Eds. H. Wohlfahrt, R. Koop and O. Vohringer. Deutsche Gesellschaft fur Metallkunde e.V.: pp. 49-54
112. Barzoukas, H. and Jauffret, J., (1990), "Peening with ceramic shot". In: *Shot peening: Proceedings of the fourth international conference on shot peening (ICSP-4)*. Tokyo, Japan. Ed. k. Iida. The Japan Society of precision engineering: pp. 47-56
113. Gillespie, Bob, (1996), "Image Analysis of shot peening media". In: *Sixth International Conference on Shot Peening. Proceedings of the International Conference on Shot Peening (ICSP-6)*. California, USA. Ed. Jack Campaigne. pp. 213-222
114. Bohn, Per, (1993), "The control of the shot peening media by sieve analysis." In: *The Fifth International Conference on Shot Peening (ICSP-5)*. Oxford, UK. Ed. David Kirk. Coventry University: pp. 91-98
115. Iida, K., (1984), "Dent and affected layer produced by shot peening". In: *Second International Conference on Shot Peening. Proceedings of the International Conference on Shot Peening (ICSP-2)*. Chicago. Ed. H.O. Fuchs. The American Shot Peening Society: pp. 283-292
116. British Aerospace, PLC, 1993, "Determination of the shot peening and blasting intensity by Almen gauge. British Aerospace (Airbus), PROCESS SPECIFICATION (ABM 1-2031)": England, UK. pp. 1-11.
117. Campaigne, Jack, (1993), "Almen gauge accuracy and repeatability". In: *The fifth International Conference on Shot Peening (ICSP-5)*. Oxford, U.K. Ed. David Kirk. Coventry University: pp. 15-26
118. Niku-Lari, A., (1981), "Méthode de la flèche, méthode de la source de contraintes résiduelles". In: *First International Conference on Shot Peening. Proceedings of the International Conference on Shot Peening (ICSP-1)*. Paris. Ed. A. Niku-Lari. Pergamon press: pp. 237-253
119. Person, Neal L., (1981), "Effect of the shot peening variables on fatigue of aluminum forgings". *Metal Progress*. No. July: pp. 33-35.
120. Wieland, Richard C., (1993), "A statistical analysis of the shot peening intensity measurement". In: *The fifth International Conference on Shot Peening (ICSP-5)*. Oxford, U.K. Ed. D. Kirk. Coventry University: pp. 27-38
121. Happ, Marvin B. and Rumpf, David L., (1993), "Almen strip variability-A statistical treatment". In: *The fifth International Conference on Shot Peening (ICSP-5)*. Oxford, U.K. Ed. D. Kirk. Coventry University: pp. 302-311
122. Kirk, D., (1996), "Developments in interactive control of shot peening intensity". In: *Sixth International Conference on Shot Peening. Proceedings of the International Conference on Shot Peening (ICSP-6)*. California, USA. Ed. Jack Campaigne. pp. 95-106

123. Fuchs, H.O., (1984), "Defects and virtues of the Almen intensity scale". In: Second International Conference on Shot Peening. *Proceedings of the International Conference on Shot Peening (ICSP-2)*. Chicago. Ed. H.O. Fuchs. The American Shot Peening Society: pp. 74-78
124. Guagliano, M., (2001), "Relating Almen intensity to residual stresses induced by shot peening: a numerical approach". *Journal of Materials Processing Technology*. No. 110: pp. 277-286.
125. Kirk, D. and MY, Abyaneh, (1993), "Theoretical basis of shot peening coverage control". In: The fifth International Conference on Shot Peening (ICSP-5). Oxford, U.K. Ed. D. Kirk. Coventry University: pp. 9-14
126. Abyaneh, M.Y., (1996), "Fundamental aspects of shot peening coverage control part one: formulation of single and multiple impacting". In: Sixth International Conference on Shot Peening. *Proceedings of the International Conference on Shot Peening (ICSP-6)*. California, USA. Ed. Jack Campaigne. pp. 438-447
127. Kirk, D., (1999), "Shot peening". *Aircraft engineering and aerospace technology: An international journal*. Vol. 71, No. 4: pp. 349-361.
128. Meguid, S.A. and Duxbury, J.K., (1981), "A practical approach to forming and strengthening of metallic components using impact treatment". In: First International Conference on Shot Peening. *Proceedings of the International Conference on Shot Peening (ICSP-1)*. Paris. Ed. A. Niku-Lari. Pergamon press: pp. 217-228
129. Mason, Charly, (1996), "The practical use of statistical process control and computer monitored equipment in the shot peening process". In: Sixth International Conference on Shot Peening. *Proceedings of the International Conference on Shot Peening (ICSP-6)*. California, USA. Ed. Jack Campaigne. pp. 328-337
130. Kittel, S., Linnemann, W., Wüstefeld, F. and Kopp, R., (1999), "Tight tolerance peen forming with on-line shape control". In: Shot Peening: Present and Future. 7th International Conference on Shot Peening (ICSP-7). Warsaw, Poland. Ed. Aleksander Nakonieczny. Institute of precision mechanics <IMP>: pp. 301-307
131. Vöhringer, O., (1987), "Changes in the state of the material by shot peening". In: Shot Peening-Science-Technology-Application. Third International Conference on Shot Peening (ICSP-3). Germany. Eds. H. Wohlfahrt, R. Koop and O. Vöhringer. Deutsche Gesellschaft für Metallkunde e.V.: pp. 185-204
132. Tosha, Katsuji, (1999), "Papers on shot peening published in the world for the last thirteen years". In: Shot Peening: Present and Future. The 7th International Conference on Shot Peening (ICSP-7). Warsaw, Poland. Ed. Aleksander Nakonieczny. Institute of Precision Mechanics <IMP>: pp. 5-10
133. Leadbeater, G., Noble, B. and Waterhouse, R.B., (1984), "The fatigue of aluminium alloy produced by fretting on a shot-peened surface". In: *Proceedings of the 6th International conference on fracture*. New Dehli. Pergamon Press, Oxford: pp. 2125-2132
134. Simpson, Roger S., 1984, "Development of a mathematical model for predicting the percentage fatigue life increase resulting from shot peened components, phase I." Airtech Precision Shot Peening, Inc. Flight dynamics laboratory. Air force wright aeronautical laboratories. air force systems command wright-patterson AFB, Ohio 45433. Final report for period September 1983- April 1984: pp. 1-37.
135. Daly, H.O Fuchs and J.J., (1987), *Mechanical production of residual stresses. Advances in surface treatments : Technology/Applications/Effects*, ed. A. Niku-Lari. Vol. 4, International guidebook on residual stresses. UK. Pergamon press: pp. 73-86.
136. Starker, P., Wohlfahrt, H. and Macherauch, E., (1979), "Subsurface crack initiation during fatigue as a result of residual stresses". *Fatigue of Engineering Materials and Structures*. Vol. 1, pp. 319-327.
137. Gurova, T., Teodosio, J. R., Rebello, J M A and Monin, A., (1998), "Model for the variation of the residual stress state during plastic deformation under uniaxial tension". *Journal of strain analysis*. Vol. 33, No. 5: pp. 367-372.
138. Mutoh, Y., Fair, G. H., Noble, B. and Waterhouse, R. B., (1987), "The effect of residual stresses induced by shot-peening on fatigue crack propagation in two high strength aluminium alloys". *Fatigue and Fracture of Engineering Materials and Structures*. Vol. 10, No. 4: pp. 261-272.
139. Song, P. S. and Wen, C. C., (1999), "Crack closure and crack growth behaviour in shot peened fatigued specimen". *Engineering fracture mechanics*. No. 63: pp. 295-304.
140. Sharp, P. K., Clayton, J. Q. and Clark, G., (1994), "The fatigue resistance of peened 7050-T7451 aluminium alloy - repair and re-treatment of a component surface". *Fatigue and Fracture of Engineering Materials and Structures*. Vol. 17, No. 3: pp. 243-252.
141. Farrahi, G.H., Lebrun, J.L. and Couratin, D., (1995), "Effect of shot peening on residual stress and fatigue life of a spring steel". *Fatigue and Fracture of Engineering Materials and Structures*. Vol. 18. No. 2: pp. 211-220.
142. Al-Hassani, S.T.S., (1981), "Mechanical aspects of residual stress development in shot peening". In: First International Conference on Shot Peening. *Proceedings of the International Conference on Shot Peening (ICSP-1)*. Paris. Ed. A. Niku-Lari. Pergamon press: pp. 583-602

143. Meguid, S.A., (1975), The mechanics of the shot peening process. PhD Thesis, Manchester, UK: Manchester Institute of Science and Technology.
144. Meguid, S.A., (1996), "Elasto-plastic finite-element study of the effect of residual stress upon double edge-cracked plate". *Engineering fracture mechanics*. Vol. 23, No. 4: pp. 735-744.
145. Cao, W., Fathallah, R. and Castex, L., (1995), "Correlation of Almen arc height with residual stresses in shot peening process". *Materials Science and Technology*. Vol. 11, No. September: pp. 967-973.
146. Ogawa, Kazuyoshi and Asano, Takashi, (2000), "Theoretical prediction of residual stress produced by shot peening and experimental verification for carburized steel". *Materials Science Research International*. Vol. 6, No. 1: pp. 55-62.
147. Guagliano, M., Vergani, L., Bandini, M and Gili, F., (1999), "An approach to relate the shot peening parameters to the induced residual stresses". In: *Shot Peening: Present and Future. The 7th Conference on Shot Peening (ICSP-7)*. Warsaw, Poland. Ed. Aleksander Nakonieczny. Institute of Precision Mechanics <IMP>: pp. 274-288
148. Lillamand, I., Barrallier, L., Lalanne, B. and Castex, L., (2001), "Cyclic modelling of the mechanical state produced by shot peening". *Fatigue and Fracture of Engineering Materials and Structures*. Vol. 24, pp. 93-104.
149. Renzhi, Wang, Xiangbin, Li, Yonggui, Tan and Minggao, Yan, (1981), "Investigation on the microstructure in shot-peening surface straining layer of materials". In: *First International Conference on Shot Peening. Proceedings of the International Conference on Shot Peening (ICSP-1)*. Paris. Ed. A. Niku-Lari. Pergamon press: pp. 185-192
150. Jilai, Ru, Renzhi, Wang and Xiangbin, Li, (1996), "Investigation on shot peening strengthening of rene'95 powder alloy". In: *Sixth International Conference on Shot Peening. Proceedings of the International Conference on Shot Peening (ICSP-6)*. California, USA. Ed. Jack Campaigne. pp. 338-347
151. Timothy, S.P. and Hutchings, I.M., (1981), "Microstructural features associated with ballistic impact in Ti6Al4V". In: *7th International conference on high energy rate fabrication*. pp. 19-28
152. Wagner, L. and Luetjering, G., (1981), "Influence of shot peening on the fatigue behaviour of titanium alloys". In: *First International Conference on Shot Peening. Proceedings of the International Conference on Shot Peening (ICSP-1)*. Paris. Ed. A. Niku-Lari. Pergamon press: pp. 453-460
153. Bonnafé, J.P. and Bathias, C., (1987), "Study of fatigue damage in shot peened aluminium alloys using acoustic emission and macro/microscopic x-ray diffraction investigations". In: *Shot Peening- Science-Technology-Application. Third International Conference on Shot Peening (ICSP-3)*. Germany. Eds. H. Wohlfahrt, R. Koop and O. Vohringer. Deutsche Gesellschaft für Metallkunde e.V.: pp. 485-497
154. Simpson, Roger S. and Probst, Robert L., (1987), "Topography and fracture studies of surfaces shot peened at different intensities". In: *Shot Peening- Science-Technology-Application. Third International Conference on Shot Peening (ICSP-3)*. Germany. Eds. H. Wohlfahrt, R. Koop and O. Vohringer. Deutsche Gesellschaft für Metallkunde e.V.: pp. 261-267
155. Wohlfahrt, H., (1987), "Practical aspects of the application of shot peening to improve the fatigue behaviour of metals and structural components". In: *Shot Peening- Science-Technology-Application. Third International Conference on Shot Peening (ICSP-3)*. Germany. Eds. H. Wohlfahrt, R. Koop and O. Vohringer. Deutsche Gesellschaft für Metallkunde e.V.: pp. 563-584
156. Li, J.K., Mei, Yao, Duo, Wang and Renzhi, Wang, (1992), "An analysis of stress concentrations caused by shot peening and its application in predicting fatigue strength." *Fatigue and Fracture of Engineering Materials and Structures*. Vol. 15, No. 12: pp. 1271-1279.
157. Neema, M.L. and Pandey, P.C., (1981), "A study of controlled peening parameters on the properties of machined surfaces". In: *Proceedings of the First International Conference on Shot Peening (ICSP-1)*. France. Ed. A. Niku-Lari. Pergamon press: pp. 201-207
158. Horwath, J.A., (1981), "Effect of shot peening variables on bending fatigue". In: *Proceedings of the First International Conference on Shot Peening (ICSP-1)*. France. Ed. A. Niku-Lari. Pergamon press:
159. Garibay, Adam J. Vahratian and Robert P., (1993), "Application of statistically capable shot peening to automotive component design". In: *The Fifth International Conference on Shot Peening (ICSP-5)*. Oxford, UK. Ed. David Kirk. Coventry University: pp. 99-110
160. Nevarez, Ivan M. and Nelson, Drew V., (1996), "Shot peening and robust design for fatigue performance". In: *Sixth International Conference on Shot Peening. Proceedings of the International Conference on Shot Peening (ICSP-6)*. California, USA. Ed. Jack Campaigne. pp. 517-529
161. Freddi, A., Veshi, D., Bandini, M. and Giovani, G., (1997), "Design of experiments to investigate residual stresses and fatigue life improvement by surface treatment." *Fatigue Fract. Engng Mater. Struct.* Vol. 20, No. 8: pp. 1147-1157.

162. Baragetti, S., (1997), "Shot peening optimisation by means of "DoE": Numerical simulation and choice of treatments parameters". *Int. J. of Materials and Product Technology*. Vol. 12, No. 2/3: pp. 83-109.
163. Condra, Lloyd W., (1993), *Reliability Improvement with Design of experiments*. 1 ed. Quality and Reliability, ed. Edward G. Shilling. New York, USA. Marcel Dekker.
164. Nachman, Gerald, (1987), "Modern shot peening technology". In: *Shot Peening- Science-Technology-Application*. Third International Conference on Shot Peening (ICSP-3). Germany. Eds. H. Wohlfahrt, R. Koop and O. Vohringer. Deutsche Gesellschaft fur Metallkunde e.V.: pp. 37-47
165. Fuchs, H.O., (1987), "Optimum peening intensities". In: *Shot Peening- Science-Technology-Application*. Third International Conference on Shot Peening (ICSP-3). Germany. Eds. H. Wohlfahrt, R. Koop and O. Vohringer. Deutsche Gesellschaft fur Metallkunde e.V.: pp. 639-646
166. Bucci, R.J., (1996), in: *ASM Handbook: Fatigue and fracture, Selecting Aluminum alloys to resist failure by fracture mechanics*, Vol. 19, Ed. ASM International committee. pp. 771-773.
167. Quist, W.E., Wingert, A.L. and Narayanan, G.H., (1986), in: *Aluminum-Lithium, Development, application, and super-plastic forming.*, Editors S.P. Agrawal and R.J. Kar. ASM International: Metals Park, OH. pp. 227-279.
168. *ASM-handbook*, (1994), in: *Aluminum and aluminum alloys, Physical metallurgy*, Ed. J.R. Davis. p. 31.
169. *METALS-HANDBOOK*, (1989), in: *METALS-HANDBOOK*, Desk edition, Alloy and temper designation systems for aluminum, Ed. ASM International committee. pp. 6.8-6.11.
170. Hatch, J.E., (1984), in, *Constitutions of alloys, Aluminum: Properties and physical metallurgy*, Ed. American Society for Metals. pp. 25-57.
171. Martin, J.W., (1986), in, *Precipitation hardening*. Pergamon press, Oxford. p. 129.
172. Gao, Ming, Feng, C.R. and Wei, Robert P., (1998), "An analytical electron microscopy study of constituent particles in commercial 7075-T6 and 2024-T3 alloys". *Metallurgical and materials transactions A*. Vol. 29A, pp. 1145-1151.
173. Mandolfo, L.F., (1971). *Int. met. rev.* Vol. 16, p. 95.
174. Raghaven, m., (1980). *Metalurgical transactions A*. Vol. 12A, p. 1356.
175. Thompson, David S., (1975), "Metallurgical factors affecting high strength aluminum alloy production". *Metallurgical transactions A*. Vol. 6A, pp. 671-682.
176. Hahn, G. T. and Rosenfield, A. R., (1975), "Metallurgical factors affecting structure toughness of aluminum alloys". *Metalurgical transactions A*. Vol. 6A, pp. 653-670.
177. Santner, J.S. and Eylon, D., (1979), "Fatigue behaviour and failure mechanisms of modified 7075 aluminium alloys". *Metallurgical and material transactions A*. Vol. 10A, pp. 841-848.
178. Hempel, M.R., (1959), *Fracture*. Technology press, MIT: p. 376.
179. GrossKreutz, J.C. and Shaw, G.C., (1969), *Fracture*, ed. P.L. Pratt. Chapman and Hall, London: p. 620.
180. James, M.R. and Morris, W.L., (1983), in: *ASTM STP 811*.
181. VanOrden, J.M., Krupp, W.E., Walden, E. and Ryder, J.T., (1979), "Effects of purity of fatigue and fracture of 7xxx-T76511 aluminum extrusion". *Journal of Aircraft*. Vol. 16, pp. 327-335.
182. de.los.Rios, E.R., (1999), "Improving the fatigue crack resistance of 2024-T351 aluminium alloy by shot peening." In: *Proceedings Ceas Forum: Life Extension-Aerospace Technology Opportunities*. Cambridge, U.K. Ed. Cambridge. Churchill College. pp. 26.1-26.8
183. de.los.Rios, E.R., "Extending the fatigue life of aerospace materials by surface engineering."
184. Newman, J.C. and I.S.Raju, (1983), "Stress intensity factor equations for cracks in three dimensional finite bodies". In: *Fracture mechanics: Fourteenth Symposium-Vol.1. Theory and analysis*, ASTM STP 791. Eds. J.C. Lewis and G. Sines. pp. 1-238-1-265
185. Sharp, R.P., (1995), "Representacion of crack growth data for design". In: *Estimation, Enhancement and Control of Aircraft Fatigue Performance*. Birmingham, U.K. Eds. J.M. Grandage and G.S. Jost. EMAS: pp. 1095-1106
186. *Airbus Industrie Material Specification*, (AIMS 03-02-011), 1996, "Aluminium Alloy (7150) Solution treated, controlled stretched and artificially aged (T651) plate." AIRBUS INDUSTRIE. Editor. Airbus industrie: Blagnac cedex, France. p. 1-6.
187. de.los.Rios, E.R., Xin, X. J. and Navarro, A., (1994), "Modelling microstructurally sensitive fatigue short crack growth". *Proc. R. Soc. London A.*, No. 447: pp. 111-134.
188. de.los.Rios, E.R., Artamonov, M., Rodopoulos, C.A., Peyre, P. and Levers, A., (2001), "How to extend fatigue life by understanding and applying surface-engineering principles". In: *ICAF 2001*. Toulouse, France.
189. Robertson, G.T., (1997), "The effects of shot size on the residual stresses resulting from shot peening". *The shot peener*. Vol. 11, No. 3: pp. 46-48.
190. de.los.Rios, E.R., X.D. Wu and Miller, K.J., (1996), "A micro-mechanics model of corrosion-fatigue crack growth in steels". *Fatigue and Fracture of Engineering Materials and Structures*. Vol. 19, No. 11: pp. 1383-1400.

191. Tealgate, 1998, "The precifeed system by tealgate. Operator handbook for", in British Aerospace Airbus Division, special peening facility installed at the University of Sheffield.: Chalgrove, Oxfordshire, U.K. p. 1-13.
192. (EI), Electronics Incorporated, 1997, "#2 Almen Gage. Owner's instruction manual, vol.1". p. 1-16.
193. Solis-Romero, J., de los Rios, E.R., Levers, A. and Karuppanan, S., (2001), "Toward the optimisation of the shot peening process in terms of fatigue resistance of the 2024-T351 and 7150-T651 aluminium alloys". In: Surface treatment V: Computer methods and experimental measurements for surface treatment effects. Spain. Ed. C.A. Brebbia. WIT press, Southampton, U.K.: pp. 343-355
194. Hammond, D. W., (1990), "Crack propagation in the presence of shot-peening residual stresses". Engineering fracture mechanics. Vol. 37, No. 2: pp. 373-387.
195. Holdgate, N.M.D., (1993), Peen mechanics in the shot peening process. PhD thesis, Mechanical Engineering., Cambridge, U.K.: Cambridge.
196. Tufft, Marsha Klopmeier, (1999), "Shot peening impact on life, part 2: single particle impact tests using production shot". In: Shot Peening: Present and Future. The 7th Conference on Shot Peening (ICSP-7). Warsaw, Poland. Ed. Aleksander Nakonieczny. Institute of Precision Mechanics <IMP>: pp. 254-263
197. Bailey, P.G., 1994, "Letter to the Editor", in The shot peener, Spring 1994. p. 17.
198. Meyers, Marc, (1994), Dynamic behavior of materials. New York. John Wiley and Sons.
199. Handbook, ASM, 1996, "Fatigue and Fracture". p. 231.
200. Airbus Industrie Test Method, (AITM 1-0011), 1996, "Constant amplitude fatigue testing of metallic materials", AIRBUS INDUSTRIE, Editor. Airbus industrie, Engineering Directorate: Blagnac cedex, France. p. 1-24.
201. ASTM, E466-82, 1982, "Standard practice for conducting constant amplitude axial fatigue tests of metallic materials", American Society of Testing and Materials, Editor.
202. BS, 7270, 1990, "Standard practice for conducting constant amplitude axial fatigue tests of metallic materials", British Standards, Editor.
203. Kacker, R.N., (1985), "Off-line quality control, parameter design and the taguchi method". Journal of Quality technology. Vol. 17, No. 4: pp. 176-188.
204. Box, G.E.P., Hunter, W.G. and Hunter, J.S., (1978), Statistics for experimenters: An introduction to design, data analysis and model building. John Wiley & Sons, New York.
205. Fisher, R.A., (1974), The design of experiments. 9th edn ed. New York, Hafner.
206. Taguchi, G., (1986), "Introduction to quality engineering". American Supplier Institute, Dearborn, MI.
207. Wagner, L., Müller, C. and Gregory, J.K., (1993), "The effect of surface rolling and shot peening on notched fatigue strength in Al 2024". Surface engineering. pp. 181-186.
208. Lumsdaine, Edward and Cherng, John, (1987), "Parameter design for a disk break system". In: Fifth symposium on Taguchi methods. Dearborn, Michigan. American Supplier Institute, Inc.: pp. 803-819
209. Shoemaker, Anne C. and Kacker, Raghu N., (1988), "A methodology for planning experiments in robust product and process design". Quality and reliability engineering international. Vol. 4, pp. 95-103.
210. Fowlkes, William, (1995), Engineering methods for robust product design using Taguchi methods in technology and product development. 1 ed. Addison-Wesley Co.
211. Tsui, Kwor-Leung, (1988), "Strategies for planning experiments using orthogonal arrays and confounding tables". Quality and reliability engineering international. Vol. 4, pp. 113-122.
212. Rao, C.R., (1947), "Factorial experiments derivable from combinatorial arrangements of arrays". Journal of the Royal statistical society. Vol. Supplement, No. 9: pp. 128-139.
213. Kapur, Kailash C. and Chen, Guangming, (1988), "Signal-to-noise ratio development for quality engineering". Quality and reliability engineering international. Vol. 4, pp. 133-141.
214. Box, George, Bisgaard, Soren and Fung, Conrad, (1988), "An explanation and critique of Taguchi's contributions to quality engineering". Quality and reliability engineering international. Vol. 4, pp. 123-131.
215. Shainin, Dorian and Shainin, Peter, (1988), "Better than Taguchi orthogonal tables". Quality and reliability engineering international. Vol. 4, pp. 143-149.
216. Bandurek, G.R., Disney, J. and Bendell, A., (1988), "Application of Taguchi methods to surface mount processes". Quality and reliability engineering international. Vol. 4, pp. 171-181.
217. ISO, 4288, 1996, "Geometrical product specifications-Surface texture: profile method-rules and procedures for the assessment".
218. Clausen, R., (1999), "Roughness of shot-peened surfaces-Definition and measurement." In: Shot Peening: Present and Future. 7th International Conference on Shot Peening (ICSP-7). Warsaw. Poland. Ed. Aleksander Nakonieczny. Institute of precision mechanics <IMP>: pp. 69-77
219. Noyan, I.C. and Cohen, J.B., (1985), Residual stresses. Elsevier, New York.

220. Lu, J. and (ed.), M.R. James, (1996), Handbook of measurement of residual stresses. Lilburn, GA. Fairmount press.
221. Ma., Q. and Clarke, D.R., (1993). *Acta metallurgical mater.*, No. 41: p. 1811.
222. Chang, Hong, Fred C. Schoenig, Jr. and Soules, Jack A., (1996), "Non destructive residual stresses measurement using Eddy current". In: Sixth International Conference on Shot Peening. Proceedings of the International Conference on Shot Peening (ICSP-6). California, USA. Ed. Jack Campaigne. pp. 356-384
223. Suresh, S. and Giannakopoulos, E., (1998), "A new method for estimating residual stresses by instrumented sharp indentation". *Acta metallurgical*. Vol. 46, No. 16: pp. 5755-5767.
224. Prime, Michael B., (1999), "Residual stress measurement by successive extension of a slot: the crack compliance method". *Applied mechanics reviews*. Vol. 52, No. 2: pp. 75-96.
225. Vishay-Measurements Group, Inc., Nov. 1996, "Measurement of residual stresses by the hole-drilling strain gage method." in Measurements Group, Tech note, TN-503-5 (Residual stress measurement). p. 1-19.
226. Prevéy, Paul S., (1986), "Residual stress distributions produced by strain gage surface preparation". In: Proceedings of the 1986 SEM spring conference on experimental mechanics, Society for experimental mechanics. Inc., Bethel, CT.: pp. 216-223
227. Prevéy, Paul S., (1996), Developments in materials characterisation technologies, eds. G.Vander Voort and J. Friel. ASM International, Materials Park, OH: pp. 103-110.
228. National Physics Laboratories (NPL), United Kingdom.,2001,Survey (residual stresses methods).<http://www.npl.co.uk>.
229. Niku-Lari, A., Lu, J. and Flavenot, J.F., (1985), "Measurement of residual stress distribution by the incremental hole-drilling method". *Journal of mechanical working technology*. Vol. 11, pp. 165-188.
230. Nobre, J.P., Kornmeier, M., Dias, A.M. and Scholtes., B., (2000), "Use of the hole-drilling method for measuring residual stresses in highly stressed shot-peened surfaces". *Experimental Mechanics*. Vol. 40, No. 3: pp. 289-297.
231. Mathar, J., (1934), "Determination of the initial stresses by measuring the deformation around drilled holes". *Trans., ASME*. Vol. 56, No. 4: pp. 249-254.
232. Kelsey, R.A., (1956), "Measuring non-uniform residual stresses by the hole drilling method". In: *Proc. Soc. Exp. Stress Anal.*: pp. 181-194
233. Flaman, Michael T., (1982), "Brief investigation of induced drilling stresses in the center-hole method of residual-stress measurement." *Experimental Mechanics*. Vol. 22, pp. 26-30.
234. Measurements Group, Inc.,2001,RS-200 Milling guide for measuring residual stresses. <http://www.Measurementsgroup.co.uk>.
235. E837-95, ASTM, (1995), Standard test method for determining residual stresses by the hole-drilling strain-gage method. Annual book of ASTM standards, American Society for Testing and Materials. Vol. 03.01. Philadelphia, PA 19103.: pp. 642-648.
236. Nickola, W.E., (1986), "Practical subsurface residual stress evaluation by the hole drilling method". In: Proceedings of the spring conference on experimental mechanics. New Orleans. Ed. Society for Experimental Mechanics. Society for Experimental Mechanics: pp. 47-58
237. Schajer, G.S., (1981), "Application of the finite elements calculations to residual stress measurements". *Journal of engineering materials and technology (Trans. ASME)*. Vol. 103, pp. 157-163.
238. Flaman, M.T. and Manning, B.H., (1985), "Determination of residual stress variation with depth by the hole-drilling method". *Experimental Mechanics*. Vol. 25, No. 9: pp. 205-207.
239. Schajer, G.S., (1988), "Measurement of non-uniform residual stresses using the hole drilling method. Part1-stress calculation procedures." *Journal of engineering materials and technology*. Vol. 110, No. October: pp. 338-343.
240. E739-91., ASTM and 1998), (Reapproved, (1991), Standard practice for statistical analysis of linear or linearized stress-life (S-N) and strain-life (ϵ -N) fatigue data. Annual book of ASTM standards. American Society for Testing and Materials. Vol. 03.01. Philadelphia, PA 19429-2959.: pp. 631-6637.
241. de los Rios., E.R. and Brown, M.W., (1991), in: Fatigue crack measurements: Techniques and applications, Chapter 9: Microscope techniques, Editors K.J. Marsh, R.A. Smith and R.O. Ritchie. Warley: Engineering Materials Advisory Services. pp. 289-313.
242. de los Rios, E.R., (1988), "Experimental techniques to observe and monitor short fatigue cracks". In: 1989 Advances in fatigue science and technology. Alvor, Portugal. Eds. C. Moura Branco and L. Guerra Rosa. Kluwer Academic Publishers: pp. 265-280
243. Flaman, M.T., Mills, B.E. and Boag, J.M., (1987), "Analysis of the stress variation-with-depth measurement procedures for the center-hole-method of residual stress measurement". *Experimental Techniques*. Vol. 11, pp. 35-37.

244. Nobre, J. P., Kornmeier, M., Dias, A.M. and Scholtes., B., (2000), "Comparative analysis of shot-peening residual stresses using hole-drilling and X-ray diffraction methods". *Materials Science forum*. Vol. 347-349, pp. 138-143.
245. Forsyth, P.J.E. and Ryder, D.A., (1960). *Fatigue fracture, Aircraft. Engng*. Vol. 32, pp. 96-99.
246. Wohlfahrt, H., (1984), "The influence of peening conditions on the resulting distribution of residual stress". In: *Second International Conference on Shot Peening. Proceedings of the International Conference on Shot Peening (ICSP-2)*. Chicago. Ed. H.O. Fuchs. The American Shot Peening Society: pp. 316-331
247. de.Rosset, W. and Granato, A.V., (1970), in: *Fundamental aspects of dislocation theory, Strain rates in dislocation dynamics*, Vol. II. National Bureau of standards special publication 317: Washington, D.C. pp. 1099-1113.
248. Turnbull, A. and Rios, E.R. de los, (1995), "The effect of grain size, strain and temperature on the monotonic stress-strain behaviour of polycrystalline aluminium and Al alloys". *Fatigue and Fracture of Engineering Materials and Structures*. Vol. 18, pp. 1343-1354.
249. Petch, N.J., (1953), "The cleavage strength of polycrystals". *Journal of the Iron Steel Institution*. No. 174: pp. 25-28.
250. Ochi, Yasuo, Masaki, Kiyotaka, Matsumura, Takashi and Sekino, Takeshi, (2001), "Effect of shot-peening treatment on high cycle fatigue property of ductile cast iron". *Int J Fatigue*. Vol. 23, pp. 441-448.
251. Shengping, Wang, Yongjun, Li, Mei, Yao and Renzhi, Wang, (1998), "Fatigue limits of shot peened metals". *Materials processing technology*. No. 73: pp. 57-63.
252. Jaensson, Bernt and Magnusson, Lennart, (1987), "An investigation into the influence on the fatigue strength of aluminium alloy parts of load spectrum base level and residual stresses induced by shot peening or strengthening". In: *Shot Peening- Science-Technology-Application. Third International Conference on Shot Peening (ICSP-3)*. Germany. Eds. H. Wohlfahrt, R. Koop and O. Vohringer. Deutsche Gesellschaft fur Metallkunde e.V.: pp. 423-430
253. Landgraf, Ronald W and Chernenkoff, Russell A., (1988), in: *Analytical and experimental methods for residual stress effects in fatigue, ASTM STP 1004, Residual stress effects on fatigue of surface processed steels*, Editors R.L. Champoux, J.H. Underwood and J.A. Kapp. American Society for Testing and Materials: Philadelphia. pp. 1-12.
254. Schulze, V., Lang, K.H., Vohringer, O. and Macherauch, E., (1996), "Relaxation of shot peening induced residual stresses in quenched and tempered steel AISI 4140 due to uniaxial cyclic deformation". In: *Sixth International Conference on Shot Peening. Proceedings of the International Conference on Shot Peening (ICSP-6)*. California, USA. Ed. Jack Campaigne. pp. 403-415
255. Dörr, T., Hilpert, M., Beckmerhagen, P., Kiefer, A. and Wagner, L., (1999), "Influence of shot peening on fatigue performance of high-strength aluminum-and magnesium alloys". In: *Shot Peening: Present and Future. The 7th Conference on Shot Peening (ICSP-7)*. Warsaw, Poland. Ed. Aleksander Nakoneczny. Institute of Precision Mechanics <IMP>: pp. 153-160
256. Navarro, A., Vallengano, C., Rios, E.R. de los and Xin, X. J., (1999), in: *Engineering against fatigue, Notch sensitivity and size effects described by a short crack propagation model*, Editors J.H. Beynon, M.W. Brown, R.A. Smith, T.C. Lindley, and B. Tomkins. A.A. Balkema: Sheffield, UK. pp. 63-72.
257. Smith, R.A. and Miller, K.J., (1978), "Prediction of fatigue regimes in notched components". *Inter. J. Mech. Sci.*, No. 20: pp. 201-206.
258. El-Haddad, M.H., Topper, T.H. and Smith, K.N., (1979), "Prediction of non propagating cracks". *Engineering fracture mechanics*. No. 11: pp. 573-584.